Gitelman & Gordon: Mirror image syndromes reveal the roles of WNKs in blood pressure homeostasis and novel anti-hypertensive targets

A dissertation by

Keith Siew

This dissertation is submitted for the degree of Doctor of Philosophy

February 2018

Supervisor: Dr. Kevin O'Shaughnessy

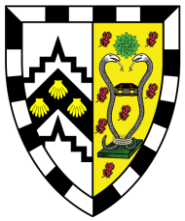

Gonville & Caius College,
University of Cambridge

Experimental Medicine & Immunotherapeutics,
Department of Medicine,
University of Cambridge

"It seems to me that the natural world is the greatest source of excitement; the greatest source of visual beauty; the greatest source of intellectual interest. It is the greatest source of so much in life that makes life worth living."

– Sir David Attenborough

Gitelman & Gordon: Mirror image syndromes reveal the roles of WNKs in blood pressure homeostasis and novel anti-hypertensive targets

Abstract for a dissertation submitted for the degree of Doctor of Philosophy by

Keith Siew

Study of Gordon (PHAII) and Gitelman (GS) syndromes revealed the importance of the WNK pathway and thiazide-sensitive Na-Cl Cotransporter (NCC) in the renal control of blood pressure. PHAII mutations lead to WNK accumulation resulting in the hyperphosphorylation of the downstream effector, SPAK, which overactivates NCC causing salt retention and hypertension. Mutations causing deletion of exon-9 in Cullin-3, which normally ubiquitylates WNKs for degradation, were recently discovered to cause the severest subtype of PHAII (PHA2E) with early onset salt-sensitive hypertension and hyperkalaemia. The reasons for this severity have remained elusive, however clues came from SPAK knock-out mice which recapitulate GS, the phenotypic mirror image of PHAII, typically caused by activation-inhibiting NCC phosphorylation site mutations resulting in salt-wasting and hypotension. As these mice were also discovered to have reduced vascular tone, it suggests the WNK pathway may have extra-renal roles in vascular smooth muscle function and highlights inhibition of SPAK function as a promising anti-hypertensive strategy with multiple sites of action. To address these possibilities the work aimed to phenotype: (1) heterozygous $CUL3^{WT/\Delta 403-459}$ mice to investigate a possible vascular contribution to PHAII pathophysiology, (2) homozygous knock-out mice of MO25, a master regulator known to increase SPAK activity up to 100-fold independent of WNKs, and (3) homozygous $SPAK^{L502A/L502A}$ knock-ins, predicted to have disrupted SPAK binding to WNK/NCC, in order to validate SPAK signalling inhibition as a viable anti-hypertensive strategy. In mice, the $CUL3^{\Delta 403-459}$ proteins are hyperflexible, hypermodified and ultimately have reduced WNK ubiquitylation. This lead to hypertension, hyperkalaemia, hyperchloraemia with compensated metabolic acidosis and growth retardation, which closely recapitulates human PHA2E. The discovery of increased vascular tone suggests an explanation for the severity of $CUL3^{\Delta ex9}$ PHAII. In mice, homozygous MO25α knock-out proved embryonically lethal, while homozygous MO25β knock-out did not meaningfully alter blood pressure or electrolyte homeostasis. However, the $SPAK^{L502A}$ protein had a decreased ability to bind WNKs and cation-chloride cotransporters NCC and NKCC1/2, serving to reduce their activation. $SPAK^{L502A/L502A}$ mice showed typical features of GS with mild hypokalaemia, hypomagnesaemia, hypocalciuria and salt-wasting hypotension. The mice also presented with decreased markers of vascular tone potentially due to effects on cardiovascular and neuronal NKCC1. These results show that SPAK binding is crucial for blood pressure control and pharmacological inhibition of this binding is an attractive anti-hypertensive strategy.

Thesis at a Glance

Study I — Constitutive CUL3$^{WT/\Delta 403-459}$ Knock-in Mouse Model

Aim: Determine how *CUL3* mutations causes PHA2E, a severe form of Gordon syndrome.

Methods: Structural modelling, mass spectrometry and biochemical analysis of CUL3$^{\Delta 403-459}$. *In vivo* pulse wave analysis, vasopressor responses and electrolytes. Fluorescent and electron microscopy.

Results: CUL3$^{\Delta 403-459}$ enhances structural flexibility, promoting auto-ubiquitylation and its own degradation. CUL3$^{WT/\Delta 403-459}$ mice are hyperkalaemic, hypertensive with enhanced vascular contractility. Renal WNK accumulation and pathway overactivation leads to puncta formation.

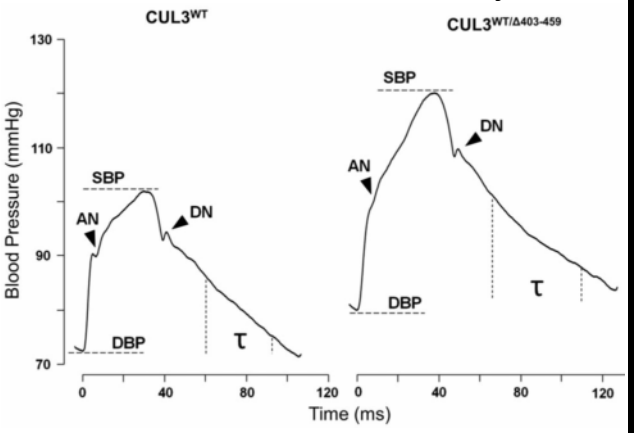

CUL3$^{WT/\Delta 403-459}$ mice have elevated markers of artery stiffening and increased peripheral vascular resistance.

Conclusion: The previously unreported vascular contribution to hypertension explains PHA2E severity, suggesting concomitant thiazide/vasodilator treatment for PHA2E.

Study II — Constitutive MO25β$^{-/-}$ Knock-out Mouse Model

Aim: Explore role of MO25β in blood pressure control.

Methods: *In vivo* blood pressure, dietary manipulations and electrolytes. Microscopy and immunoblotting.

Results: No differences in blood pressure or electrolyte homeostasis were observed between MO25β$^{-/-}$ and WT mice, with the exception of $[Mg^{2+}]_U$ on a NNa diet.

Conclusion: MO25β has a no significant role in blood pressure control, or its loss is compensated by MO25α, the physiologically dominant isoform.

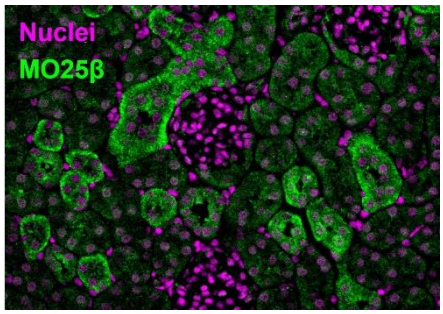

MO25β is most abundant in the distal nephron segments of the renal cortex.

Study III — Constitutive SPAK$^{L502A/L502A}$ Knock-in Mouse Model

Aim: Investigate if *in vivo* SPAK binding inhibition produces a Gitelman syndrome-like phenotype.

Methods: *In vivo* pulse wave analysis, vasopressor responses, diet manipulations and electrolytes. Microscopy, immunoblotting and *in vitro* SPAK-WNK binding assays and biochemical analyses.

Results: Gitelman syndrome is recapitulated by SPAK$^{L502A/L502A}$ mice, with lower vascular tone, hypotension and decreased phosphorylation of SPAK, NCC and NKCC1/2 in multiple tissues.

Conclusion: SPAK binding is an attractive druggable target for a new class of thiazide-like anti-hypertensives without unwanted off-target effects.

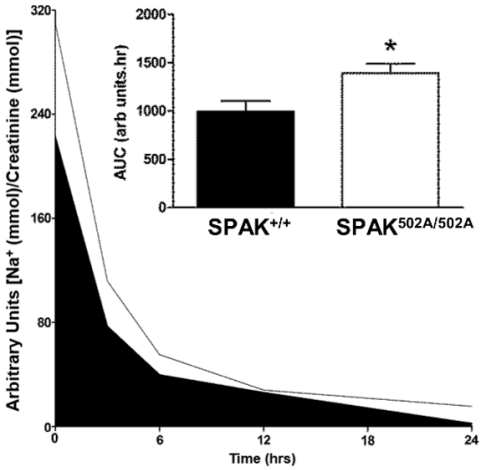

SPAK$^{L502A/L502A}$ urinary Na^+ wasting during acute HNa to LNa diet-switch

WT = wild-type; SBP = systolic blood pressure; DBP = diastolic blood pressure; τ = DBP decay time constant; AN = anacrotic notch; DN = dicrotic notch; NNa = Normal Na^+ diet; HNa = High Na^+ diet; LNa = Low Na^+ diet

Contents

List of Figures

List of Tables

Appendices

Declaration

This dissertation is the result of my own work and includes nothing which is the outcome of work done in collaboration except as declared in the Preface and specified in the text.

It is not substantially the same as any that I have submitted, or, is being concurrently submitted for a degree or diploma or other qualification at the University of Cambridge or any other University or similar institution except as declared in the Preface and specified in the text. I further state that no substantial part of my dissertation has already been submitted, or, is being concurrently submitted for any such degree, diploma or other qualification at the University of Cambridge or any other University or similar institution except as declared in the Preface and specified in the text

This thesis does not exceed 60,000 words.

Collaborations

The animal models in this work were generated and phenotyped in collaboration with the Alessi and Kurz groups at the MRC Phosphorylation and Ubiquitylation Unit (MRC-PPU), University of Dundee.

Guidance and advice on technical and experimental matters and materials are gratefully acknowledged.

Further information on collaborative efforts are detailed in Chapter 2: Materials & Methods.

Keith Siew, BSc(Hons) MSc NQEMT FRMS

February 2018

Acknowledgements

My sincerest thanks to my supervisor, Dr. Kevin O'Shaughnessy for taking a chance on me back when I was just an overenthusiastic undergraduate attending his first scientific meeting. As the first in my family to attend university and gone this far, I am eternally grateful for the opportunity of a lifetime, your mentorship and unwavering support.

I wish to thank my colleagues both past and present at the EMIT division for their friendship, guidance and lively debate. In particular, to Dr. Yasmin and Sarah Cleary for opening up their hearts and homes to me. I felt very much part of the family, and I can never thank you enough. To Nikki Figg, Janet Maguire, Meena Murthy and Carmen Methner, I thank you for imparting your knowledge and techniques with near saintly patience during my training.

I am very grateful to Prof. Dario Alessi, Dr. Thimo Kurz, Dr. Jinwei Zhang, Dr. Frances-Rose Schumacher, Elaine Forsyth and Gail Gilmour at the MRC-PPU, University of Dundee for the opportunity to learn from you, collaborate on exciting projects, and making me feel welcome on my many sojourns past Hadrian's wall.

To the staffs of the core biochemical assay laboratory, central biomedical services, joint animal facility, geography science laboratories, Cambridge advanced imaging centre and CRUK light microscopy facility at Cambridge University, thank you for supporting my work and sharing in my eagerness to develop new approaches to address research questions.

I also want to thank my friends for providing moral support and comedic relief on this journey. Especially to Lalarukh Haris Shaikh and Paul Gallagher, you picked me up when things were looking down and pushed me to do more and be better.

I dedicate this to my family; Monica Collins, Khay Hean Siew, Steven Siew, Catherine Collins, and Rose Collins, who believed in me every step of the way and came to call Cambridge a home away from home. The road was long and not without its fair share of bumps, and I could not have done it without your love, support and belief.

And finally, my most heartfelt of thanks must go to my late Nana, Kitty Trunk, for kindling my love of nature and indulging the curiosities of a young boy who dreamed of being a scientist since the age of 5. While you did not get to see it, you always knew I'd get here eventually.

Le grá gan deireadh

Publications and Abstracts

** Joint First Author*

Original Articles

Ware JS, Wain LV, Channavajjhala SK, Jackson VE, Edwards E, Lu R, **Siew K**, Jia W, Shrine N, Kinnear S, Jalland M, Henry AP, Clayton J, O'Shaughnessy KM, Tobin MD, Schuster VL, Cook S, Hall IP, Glover M (2017). Phenotypic and pharmacogenetic evaluation of patients with thiazide-induced hyponatremia. *The Journal of Clinical Investigations* 127:3367-3374

Schumacher FR, **Siew K***, Zhang J, Johnson C, Wood N, Cleary SE, Al Maskari RS, Ferryman JT, Hardege I, Yasmin, Figg NL, Enchev R, Knebel A, O'Shaughnessy KM, Kurtz T (2015). Characterisation of the Cullin-3 mutation that causes a severe form of familial hypertension and hyperkalaemia. *EMBO Molecular Medicine* 7:1285-1306

Zhang J, **Siew K***, Macartney T, O'Shaughnessy KM, Alessi DR (2015). Critical role of the SPAK protein kinase CCT domain in controlling blood pressure. *Human Molecular Genetics* 24:4545-4558

Kuc RE, Maguire JJ, **Siew K**, Patel S, Derksen DR, Margaret Jackson V, O'Shaughnessy KM, Davenport AP (2014). Characterization of [^{125}I]GLP-1(9-36), a novel radiolabeled analog of the major metabolite of glucagon-like peptide 1 to a receptor distinct from GLP1-R and function of the peptide in murine aorta. *Life Sciences* 102:134-138

Review Articles

† Invited

Siew K† and O'Shaughnessy KM (2013). 'Extra-renal Roles of WNKs'. *Clinical and Experimental Pharmacology and Physiology* 40:885-894

Oral Communications

[#] Award/Shortlist | [†] Invited Speaker

Siew K# (2018). Gitelman & Gordon – Mirror image syndromes reveal the roles of WNKs in blood pressure homeostasis and novel anti-hypertensive targets. *London Cardiovascular Society Meeting*, January 2018, London, UK.

Siew K† (2015). Gitelman & Gordon – Mirror image syndromes reveal the roles of WNKs in blood pressure homeostasis and novel anti-hypertensive targets. *American Heart Association – Council on Hypertension 2015 Scientific Sessions*, September 2015, Washington, D.C., USA.

Siew K#, Zhang J, Alessi DR, O'Shaughnessy KM (2014). Disruption of STE20/SPS1-related proline/alanine-rich kinase (SPAK) targeted mouse model of Gitelman Syndrome. *Journal of Human Hypertension* 28:617-48, OA1. *British Hypertension Society Annual Scientific Meeting,* September 2014, Edinburgh, UK.

Poster Communications

 # Award/Shortlist

Siew K, Schumacher FR, Kurtz T, O'Shaughnessy KM (2015). Characterisation of the Cullin-3 Mutation That Causes a Severe Form of Familial Hypertension and Hyperkalaemia. *Journal of the American Society of Nephrology* 26 (Abstract Edition): 2015:188A, TH-PO948. *American Society of Nephrology Kidney Week 2015 Annual Meeting*, November 2015, San Diego, USA.

Siew K, Zhang J, Schumacher FR, Alessi DR, Kurtz T, O'Shaughnessy KM (2015). Pulse waveform analysis reveals vascular contributions to Gordon Syndrome and Gitelman Syndrome blood pressure homeostasis. *Proceedings of The Physiological Society* 34, PC267. *Physiology 2015*, July 2015, Cardiff, UK.

Siew K, Zhang J, Alessi DR, O'Shaughnessy KM (2014). Disruption of STE20/SPS1-related proline/alanine-rich kinase (SPAK) targeted mouse model of Gitelman Syndrome. *Journal of the American Society of Nephrology* 25 (Abstract Edition): 2014:375A, FR-P0012. *American Society of Nephrology Kidney Week 2014 Annual Meeting*, November 2014, Philadelphia, USA.

Siew K, Glover M, O'Shaughnessy KM (2014). Sex differences in bone mineral density of the STE20/SPS1-related proline/alanine-rich kinase (SPAK) targeted mouse model of Gitelman Syndrome. *Proceedings of The Physiological Society* 31, PCB109. *Physiology 2014*, July 2014, London, UK.

Siew K, Glover M, O'Shaughnessy KM (2014). Sex differences in bone mineral density of the STE20/SPS1-related proline/alanine-rich kinase (SPAK) binding lowers blood pressure and recapitulates Gitelman Syndrome in Mice. *The FASEB Journal* 28 (1 Suppl), 1083.4. *Experimental Biology 2014*, April 2014, San Diego, USA.

Siew K, Maguire JJ, Davenport AP, O'Shaughnessy KM (2014). Vascular phenotype of STE20/SPS1-related proline/alanine-rich kinase targeted hypotensive mouse model of Gitelman Syndrome. *The FASEB Journal* 28 (1 Suppl), 697.6. *Experimental Biology 2014*, April 2014, San Diego, USA.

Siew K, Maguire JJ, Davenport AP, O'Shaughnessy KM (2013). Vascular Phenotype of STE20/SPS1-related Proline/Alanine-rich Kinase (SPAK) Targeted Mouse Model of Gitelman Syndrome. *pA2 Online* 11 (3), 136P. *Pharmacology 2013*, December 2013, London, UK.

Siew K#, de los Heros P, Alessi DR and O'Shaughnessy KM (2013). MO25β has no physiological role in electrolyte homeostasis or systemic blood pressure maintenance in the mouse. *Journal of Human Hypertension* 27:635-55, PD1. *British Hypertension Society Annual Scientific Meeting*, September 2013, London, UK.

Siew K, de los Heros P, Alessi DR and O'Shaughnessy KM (2013). MO25β has no physiological role in electrolyte homeostasis or systemic blood pressure maintenance. *Proceedings of the 37th IUPS*, PCD227. *XXXVII International Congress of Physiological Sciences*, July 2013, Birmingham, UK.

Prizes and Awards

Runner-up for the JRSM Cardiovascular Disease – Young Investigator Award at the London Cardiovascular Society Meeting – London, UK 2018.

Winner of BHS Young Investigator's Oral Prize at the British Hypertension Society Annual Scientific Meeting – Edinburgh, UK 2014. Invited Young Investigator Speaker at AHA Council on Hypertension 2015, USA.

ASN Kidney STARS Program Participant – Competitive American Society of Nephrology program for networking with training program directors and key faculty members from special renal interest groups.

Irish delegate to the European Society of Hypertension Summer School - Porto, Portugal 2013; once-in-a-lifetime event with two persons selected per country per year for training and networking.

Runner-up BHS Jack Ledingham Young Investigator's Poster Prize at the British Hypertension Society Annual Scientific Meeting – London, UK 2013.

Winner of the Hormone Zone - I'm a Scientist Get Me Out of Here – UK, June 2013; 3 week eviction style competition of live web chats with children about science. £500 prize was awarded for public engagement activities.

List of Abbreviations

%	Percent
°C	Degree Centigrade
AFU	Arbitrary Fluorescent Units
AIx	Augmentation Index
Ala or A	Alanine
AMPK	Adenosine Monophosphate-Activated Protein Kinase
AN	Anacrotic Notch
AP	Augmentation Pressure
Arg or R	Arginine
ATP	Adenosine Tri Phosphate
AU	Arbitrary Units
BE	Base Excess
BMD	Bone Mineral Density
BP	Blood Pressure
BW	Body Weight
Ca^{2+}	Calcium ion
CAB39	Calcium-Binding Protein 39
CAB39L	Calcium-Binding Protein 39-Like
CACO-2	Human Colon Adenocarcinoma
CAND1	Cullin-associated Nedd8-dissociated protein 1
CCC	Cation-coupled Chloride Cotransporters
CCD	Cortical Collecting Duct
CCT	Conserved C-Terminal
CD	Collecting Duct
Cl^-	Chloride ion
cm	Centimetre
CNT	Connecting Tubule
CO_2	Carbon dioxide
COP9	Constitutive photomorphogenesis 9
Creat	Creatinine
CRL	Cullin-RING ligase
cRNA	complementary RiboNucleic Acid
CSN	COP9-Signalosome
CTD	C-Terminal Domain
CUL3	Cullin-3

DBP	Diastolic Blood Pressure
DCT	Distal Convoluted Tubule
DCT1	Early Segment of DCT
DCT2	Late Segment of DCT
DMEM	Dulbecco's Modified Eagle's Medium
ED_{50}	Half Maximal Response
EEA1	Early Endosome Antigen 1
E_{max}	Maximal Response
ENaC	(Amiloride-sensitive) Epithelial Sodium Channel
eNOS	Endothelial nitric oxide synthase
ERK1/2	Extracellular Signal-Regulated Kinase 1/2
EUCOMM	European Conditional Mouse Mutagenesis Program
FGF23	Fibroblast Growth Factor 23
FHHt	Familial Hyperkalaemia Hypertension
FRT	Flippase-Recognition Target
GCK	Germinal Centre Kinase
gDNA	Genomic DNA
Gln or Q	Glutamine
Glu or E	Glutamic Acid
h	Hour
H_2O	Water
HCO_3^-	Bicarbonate
HEK293	Human Embryonic Kidney-293
HNa	High sodium diet
HSAN2	Hereditary sensory and autonomic neuropathy type 2
HTRF	Homogeneous Time-Resolved Fluorescence
IB	Immunoblot
ICP-OES	Inductively coupled plasma – optical emission spectrometer
IKMC	International Knockout Mouse Consortium
Ile or I	Isoleucine
IMPC	International Mouse Phenotyping Consortium
IMPReSS	International Mouse Phenotyping Resource of Standardised Screens
IMSR	International Mouse Strain Resource
IP	Immunoprecipitation
K^+	Potassium ion
KCC	K+-Cl- Cotransporter
KI	Knock-In

KLHL3	Kelch-like protein 3
KO	Knock-Out
KS-SPAK	Kidney Specific Kinase Inactive SPAK isoform (~34kDa)
KS-WNK1	Kidney Specific WNK1 Isoform
L-WNK1	Full Long Sequence WNK1
LAMP1	Lysosomal-associated membrane protein 1
Leu or L	Leucine
LKB1	Liver Kinase B1
LNa	Low sodium diet
M	Molar
MAP	Mean Arterial Pressure
MAPK	Mitogen-Activated Protein Kinase
mg/L	Milligram per Litre
Mg^{2+}	Magnesium ion
MGI	Mouse Genome Informatics
min	Minute
mM	Millimolar
mm	Millimetre
mmHg	Millimetres of Mercury
MO25	Mouse Protein-25
mRNA	messenger RiboNucleic Acid
mTOR	Mammalian Target of Rapamycin
MYPT1	Myosin phosphatase target subunit 1
Na^+	Sodium ion
NAE	Nedd8 Activating Enzyme
NCC	(Thiazide-sensitive) Na^+-Cl^- Cotransporter
Nedd4-2	Neural precursor cell expressed developmentally down-regulated protein 4-2
Nedd8	Neural precursor cell expressed developmentally down-regulated protein 8
NKCC	(Bumetanide-sensitive) Na^+-K^+-$2Cl^-$ Cotransporter
nM	Nanomolar
nm	Nanometre
NNa	Normal sodium diet
NTD	N-Terminal Domain
OMIM	On Mendelian Inheritance In Man
OSR1	Oxidative Stress-Response Kinase-1
P	Plasma
pCO_2	Partial Pressure of Carbon dioxide

PCR	Polymerase Chain Reaction
PCT	Proximal Convoluted Tubule
PHAII	Pseudohypoaldosteronism Type II
PHA2	Pseudohypoaldosteronism Type II
Phe or F	Phenylalanine
pMYPT1	Phospho-myosin phosphatase target subunit 1
pNCC	Phospho-NCC
pNKCC	Phospho-NKCC
PO_4^{3-}	Phosphate
pOSR1	Phospho-OSR1
PP	Pulse Pressure
PP1	Protein Phosphatase 1
PP2A	Protein Phosphatase 2A
PP3	Protein Phosphatase 3
PP4	Protein Phosphatase 4
PPP4C	Protein Phosphatase 4 Gene
pSPAK	Phospho-SPAK
PuroR	Puromycin Resistance
PVALB	Parvalbumin
RasGRP1	Ras Guanyl-Releasing Protein 1
RBC	Red Blood Cell
RBX1	RING-box protein 1
RFxV	[S/V/G]RFx[V/I]xx[T/I/S/V]xx docking site motif
RING	Really interesting new gene finger domain
RNA	RiboNuleic Acid
ROCK	RhoA/RhoA Kinase
ROMK	Renal Outer Medullary Potassium Channel
RPL22	60s Ribosomal Subunit L22
rpm	Rotations per minute
RT	Room Temperature
RT-PCR	Real Time-PCR
s	Seconds
SBP	Systolic Blood Pressure
SCL12	Solute Carrier Family 12
SEM	Standard Error of the Mean
Ser or S	Serine
SGK1	Serum/Glucocorticoid-induced Kinase 1

siRNA	small interfering RiboNucleic Acid
SPAK	STE20(sterile-20)/SPS1-related Proline/Alanine-rich Kinase
SPAK2	Short Sequence Kinase Impaired SPAK isoform (~49kDa)
STE20	Sterile-20
STK	Serine-Threonine Kinase
STK39	Serine/Threonine Kinase 39 gene encoding SPAK
STRAD	STE20-related Adaptor Pseudo-kinase
TAL	Thick Ascending Limb of Loop of Henle
Thr or T	Threonine
tNCC	Total NCC
tNKCC2	Total NKCC2
Trp or W	Tryptophan
TRPC	Transient Receptor Potential Canonical
TRPV	Transient Receptor Potential Vanilloid
TTBS	TBS-Tween Buffer
U	Urinary
UPS	Ubiquitin Proteasome System
v/v	Volume/Volume
Val or V	Valine
VSMC	Vascular Smooth Muscle Cell
w/v	Weight/Volume
WBC	White Blood Cell
WNK	With-No-Lysine Kinase
WT	wildtype
WTSI	Wellcome Trust Sanger Institute
µg/kg.bw	Micrograms per kilogram of bodyweight
µg/mL	Microgram per Millilitre
µm	Micrometre
µM	Micromolar
$\tau_{bourgeois}$	Diastolic Pressure Time Decay Constant

Chapter 1 : Introduction

[*This chapter is written principally as a contemporaneous overview of the state of knowledge prior to these studies. In-depth reviews of the recent literature appears in subsequent chapters*]

1.1 Hypertension

1.1.1 The problem and therapies

According to the World Health Organisation, systemic high blood pressure, or hypertension remains one of the largest risk factors to health globally, affecting approximately 1 in 4 over the age of 25 years. It is estimated that an astonishing 12.8% of global death can be attributed to hypertension; causing 51% of deaths from stroke and 45% from coronary heart disease (World Health Organisation, 2012).

Although the strict definition of what constitutes hypertension can vary, given the normal Gaussian distribution amongst the normal population, it is most commonly defined by learned bodies as a blood pressure of ≥140/90 mmHg (but has recently been redefined in the USA as ≥130/80mmHg). Broadly speaking hypertension can be classified into two categories: Secondary hypertension which accounts for the minority of cases, in which there is a known cause of hypertension that results secondary to disease of other organs or systems, drugs or genetic syndromes; or essential hypertension which is estimated to account for as many as ~90% of cases, in which the exact cause of hypertension is unknown (Carretero & Oparil, 2000; Messerli *et al.*, 2007; Bolívar, 2013). In the latter, genetic influence is reported to account for anywhere between 34-67% of blood pressure variation between persons in the population (Vinck WJ Loos R, Vlietinck R., 2001; Hottenga *et al.*, 2005); additionally numerous environmental risk factors such as poor diet, lack of exercise, obesity, sodium intake, smoking and excess alcohol consumption are documented to contribute significantly to onset of the condition (World Health Organisation, 2007). Due to this immense complexity progress has been quite slow in the identification of gene candidates that may be causative or contribute to hypertension onset. Thus, although rare, monogenetic diseases have been a great resource in the discovery of hypertension aetiology.

Blood pressure is primarily controlled by the cardiovascular and renal systems working in concert with one another; the heart capable of modulating heartbeat rate and stroke volume to alter cardiac output, while blood vessels dilate or constrict to provide vascular resistance and alter the circulatory volume capacity, and finally the renal system can regulate the volume of plasma in the cardiovascular system. It is at the level of the kidney that numerous pharmacological therapies have emerged to treat and ameliorate the cardiovascular impact of hypertension. Diuretics are a key part of these therapies with thiazide drugs still considered to be first-line agents in many hypertension guidelines. They act to reduce blood pressure, in part, by inhibition of thiazide-sensitive Na^+-Cl^- cotransporter (NCC) activity in the distal convoluted tubule of the kidney. Subsequently resulting in a reduction of circulating plasma volume and extracellular fluid via salt and water loss. However, reductions in circulating volume only last up to 4 – 6 weeks of chronic treatment, and the long-term maintenance of reduced blood pressure is purported to involve a concomitant decrease in total peripheral vascular resistance via thiazide action on the vascular smooth muscle cell (VSMC) or endothelial cell function (Duarte & Cooper-DeHoff, 2010).

The physiological processes that regulate NCC activity *in vivo* have only been recently under investigation for the past decade or so, and the elucidation of such could perhaps lead to better understanding of thiazides' mechanisms of action and discovery of novel therapeutic targets.

1.1.2 Genetic disorders

Until recently, understanding of the mechanisms that regulate renal sodium reabsorption on a molecular physiology level have been extremely limited. However breakthroughs in the profiling of rare genetic diseases such as Bartter syndrome, Gitelman syndrome and Gordon syndrome have permitted dissection of the signalling pathways involved in the pathophysiology of these conditions. This has not only improved treatment of these conditions but allowed exploration of new therapeutic targets for treating hypertension generally (Figure 1.1).

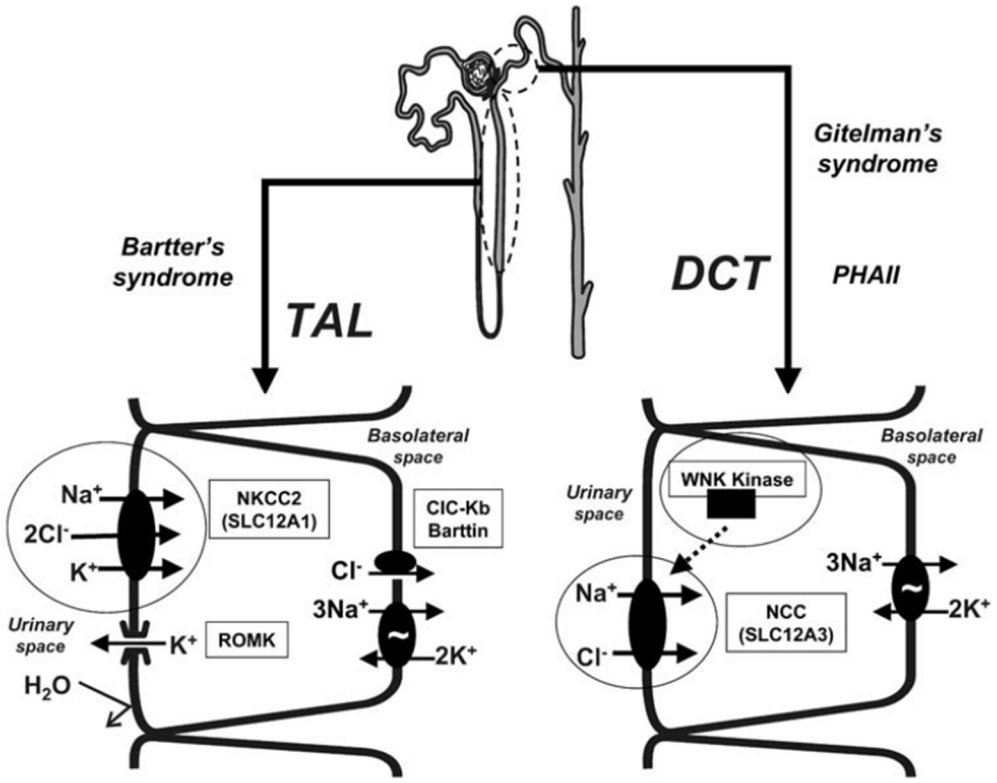

Figure 1.1: Diagram illustrating the sites at which Bartter, Gitelman and Gordon syndrome exert their effects in the nephron.

Bartter syndrome results from impaired electroneutral influx of a Na^+, K^+, and two Cl^- ions from thick ascending limb (TAL) tubule fluid. This can occur via loss-of-function mutations in the NKCC2 cotransporter which directly impairs this influx, or indirectly via mutations in proteins like ROMK, Barttin or CLC-Kb which impair the efflux of K^+ or Cl^- from the cell that NKCC2 activity is dependent on. Gitelman syndrome and Gordon syndrome (PHAII) result from the impaired or enhanced electroneutral influx of Na^+ and Cl^- form distal convoluted tubule (DCT) fluid, respectively. For Gitelman syndrome this is due to loss-of-function mutations to NCC, while Gordon syndrome mutations lead to increased WNK activity which stimulates Na^+-Cl^- influx via NCC. With all of these activities ultimately dependent on the basolateral sodium-potassium pump ($3Na^+/2K^+$-ATPase). [Taken from (Hebert *et al.*, 2004) with a typo in "SLC12A1" corrected].

1.1.2.1 Bartter Syndrome

Patients often present early in childhood and the syndrome manifests with hypotension, renal salt wasting, hypokalaemia, hypercalciuria with normal serum magnesium and calcium levels, and an activated renin-angiotensin system. The phenotype of these patient mimics that of someone on long-term chronic administration of loop diuretics (Amirlak & Dawson, 2000; Unwin & Capasso, 2006; Seyberth & Schlingmann, 2011). The genetic mutations that present in Bartter's syndrome are heterogeneous with at least five known genes: *SLC12A1* (encodes NKCC2)*; KCNJ1* (encodes ROMK1); *BSND* (encodes Barttin)*; CLCNKA (*encodes CLC-K1

or CLC-Ka)*; CLCNKB* (encodes CLC-K2 or CLC-Kb) (Figure 1.1) (Seyberth & Schlingmann, 2011). Nonetheless they all relate to either a direct loss of bumetanide-sensitive Na^+-K^+-$2Cl^-$ cotransporter (NKCC) activity, specifically NKCC2 function (Bartter syndrome type 1), and/or mutations that effect the channel indirectly, for example, loss of inward-rectifier renal outer medullar potassium channel (ROMK) activity (Bartter syndrome type 2) on which NKCC2 activity is dependent (Figure 1.1) (O'Shaughnessy & Karet, 2004). This is supported not only by the mimicry of chronic loop diuretic administration which inhibits NKCC2 (Amirlak & Dawson, 2000; Unwin & Capasso, 2006; Seyberth & Schlingmann, 2011), but also by animal models in which NKCC2 has been mutated (Kemter *et al.*, 2010), NKCC2 activity suppressed indirectly by loss of ROMK activity (Cantone *et al.*, 2008; Wagner *et al.*, 2008) or the absence of a positive regulator such as oxidative stress-response kinase 1 (OSR1) (Lin *et al.*, 2011). For more details on the gene-phenotype relationship and clinical features see OMIM: #241200, #300971, #601678, #602522, #607364, #613090.

1.1.2.2 Gitelman Syndrome

At one point Bartter and Gitelman syndromes were thought to be variations of the same disease (Simon *et al.*, 1996); although recent advances have distinguished Gitelman as separate from Bartter syndrome (Unwin & Capasso, 2006; Seyberth & Schlingmann, 2011). Gitelman patients can often be asymptomatic with evidence of the syndrome not present until late childhood or in some cases adulthood; reporting joint problems, lethargy, growth retardation and usually a preference for salty foods. The phenotype of Gitelman syndrome mimics Bartter syndrome in many respects, with hypotension, salt wasting, hypokalaemia and an activated renin-angiotensin system. Although the other biochemical characteristics of the syndrome better emulate chronic thiazide administration, as patients also have hypocalciuria, hypomagnaesemia and renal magnesium wasting (Unwin & Capasso, 2006; Seyberth & Schlingmann, 2011). All reported cases of Gitelman syndrome with a genetic diagnosis have resulted from mutations in NCC which either reduce or abolish activity (O'Shaughnessy & Karet, 2004). Unsurprisingly, knock-out (KO) and knock-in (KI) animal models which exhibit a Gitelman syndrome phenotype include NCC-KO and loss-of-function NCC-KI mice (Loffing *et al.*, 2004; Yang *et al.*, 2010*b*) and those deficient in positive upstream regulators such as STE20/SPS1-related proline-alanine-rich protein kinase (SPAK) activity (see section 1.3.2)

(Rafiqi *et al.*, 2010; Yang *et al.*, 2010*c*). For more details on the gene-phenotype relationship and clinical features see OMIM: #263800.

1.1.2.3 Gordon Syndrome

Gordon syndrome, also known as pseudohypoaldosteronism type II (PHAII) or familial hyperkalaemia and hypertension (FHHt), is the mirror image of Gitelman syndrome in terms of clinical presentation. Patients present with hypertension, salt retention and elevated serum potassium with a metabolic acidosis. Despite the genetic heterogeneity of the syndrome, the pathophysiological endpoint remains the same, resulting in elevated NCC activity via either increased apical membrane expression and/or increased intrinsic cotransporter activity (Cope *et al.*, 2005; Boyden *et al.*, 2012; Louis-Dit-Picard *et al.*, 2012; Osawa *et al.*, 2013). Mutations in the With-No-Lysine kinases (WNK) have traditionally been associated with the syndrome, namely exonic mutations in WNK4 and or intronic mutations in WNK1 which result in the overexpression of WNK1 that inhibits WNK4 activity, thus indirectly increasing apical membrane expression (Cope *et al.*, 2005). The most recently reported kelch-like 3 (KLHL3) and cullin-3 (CUL3) proteins, which are known to negatively regulate NCC membrane abundance, have also been identified as causative sites of genetic mutation (Boyden *et al.*, 2012; Louis-Dit-Picard *et al.*, 2012). Additionally it was found that transplant patients on long-term chronic administration of protein phosphatase 3 inhibitors, Tacrolimus and Cyclosporine exhibited many of the hallmarks of Gordon syndrome. These drugs act to remove a negative regulator of NCC activity (see section 1.3.5), and it was found that the clinical features resulting from this increase in NCC activity were reversible with thiazide administration (Hoorn *et al.*, 2011; Melnikov *et al.*, 2011). Furthermore, animal models mimicking these mutations have allowed exploration of the regulation of NCC *in vivo* and given insight into new potential therapeutic strategies (Yang *et al.*, 2007*b*; Chowdhury *et al.*, 2013; Vidal-petiot *et al.*, 2013). For more details on the gene-phenotype relationship and clinical features see OMIM: #145260, #614491, #614492, #614495, #614496.

1.2 Renal Salt Handling

1.2.1 Nephron segments

The average daily intake of sodium is approximately 9-12g (World Health Organisation, 2016), the vast majority of which is subsequently lost in the urine, with some minor loss also via the faeces and sweat. Within a day an average human will filter 170-180L of plasma, which equates to approximately 25 moles of sodium. Thus to maintain salt homeostasis the kidneys must reabsorb sodium; which is done at all segments of the nephron except the descending thin limb of the loop of Henle (Figure 1.2) (O'Shaughnessy & Karet, 2006).

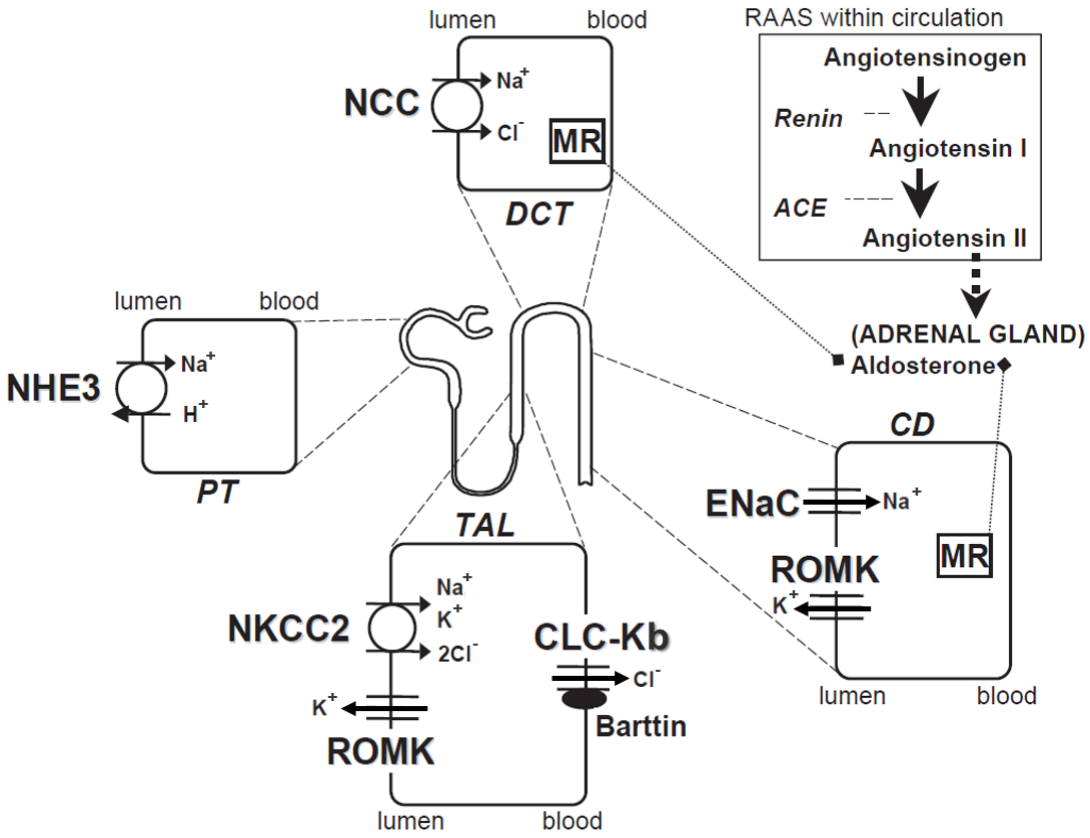

Figure 1.2: Schematic of the major sites of Na^+ reabsorption along the mammalian nephron.

The kidneys are capable of reabsorbing ~99% of filtered sodium in the nephron. The vast majority of sodium reabsorption occurs in the proximal tubule (PT) through the Na^+/H^+ exchanger (NHE3), with the second largest bulk of sodium uptake in the thick ascending limb (TAL) of the loop of Henle by the electroneutral NKCC2 cotransporter; a process dependent on TAL K^+ and Cl^- efflux by ROMK, CLC-Kb and Barttin. Fine tuning of the final sodium excretion is determined by the distal convoluted tubule

(DCT) via electroneutral NCC cotransporter activity and in the collecting duct (CD) through electrogenic reabsorption mediated by epithelial sodium channel (ENaC). Additionally sodium reabsorption can be modulated by the renin-angiotensin-aldosterone system (RAAS) in the aldosterone-sensitive segments of the distal tubule expressing the mineralocorticoid receptor (MR). [Adapted from (Cope *et al.*, 2005) with changes to labels].

The majority of sodium is reabsorbed in the proximal convoluted tubule (PCT) with approximately 60% via primary active transport of the Na^+/H^+ exchanger (NHE3). A further 25% is then reabsorbed by the thick ascending limb of the loop of Henle (TAL) via the electroneutral NKCC2; the function of which is dependent on recycling of potassium into the tubular fluid via ROMK. In the distal convoluted tubule (DCT), up to 10% of total sodium reabsorption is regulated by the electroneutral NCC. Finally amiloride-sensitive epithelial sodium channels (ENaC) reabsorb the remaining 2-3% of sodium in the collecting ducts (CD) (Figure 1.2) (O'Shaughnessy & Karet, 2006).

1.2.2 NCC and the *SLC12* gene family

The solute carrier family 12 (*SLC12*) genes which encode for electroneutral cation-coupled chloride cotransporters (CCC) and can be divided into two divergent groups: a K^+-Cl^- cotransporter (KCC) group which has four members, KCC1 – 4 encoded by *SLC12A4 – 7* respectively, and the other group containing a thiazide-sensitive Na^+-Cl^- cotransporter (NCC) encoded by the *SLC12A3* gene and two bumetanide-sensitive Na^+-K^+-$2Cl^-$ cotransporters (NKCC) encoded by *SLC12A2* (NKCC1) and *SLC12A1* (NKCC2) (Figure 1.3). Two more orphan members of the *SLC12* family exist, namely *SLC12A8* (CCC8) which has been linked with psoriasis and *SCL12A9* (CCC9; also known as CCC interacting protein, CIP) which has been shown to inhibit the functional expression of NKCC1, however both of these await further characterisation (Hebert *et al.*, 2004; Gagnon & Delpire, 2013).

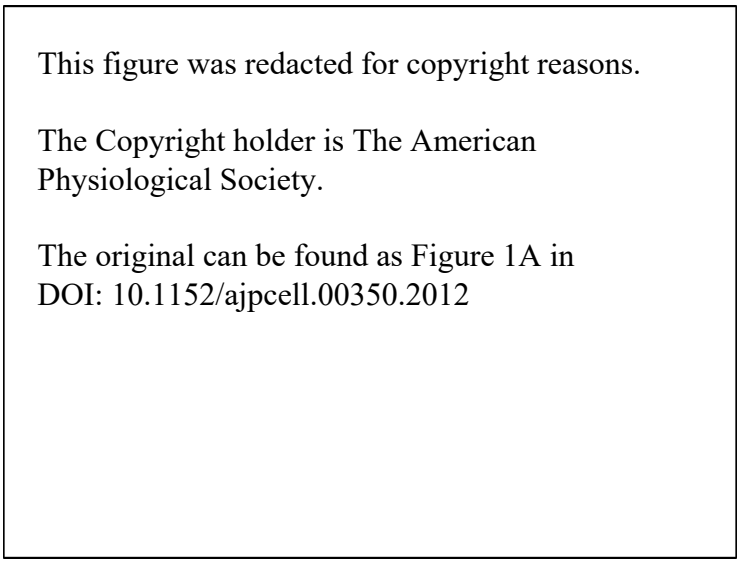

Figure 1.3: Cluster dendrogram of the SLC12 family members.

The cluster dendrogram shows a visual representation of the evolutionary relationships of the human SLC12 gene family. Length of tree branches can be compared with the reference bar, which represents 0.1 amino acid substitutions per site. The closely related K^+-Cl^- cotransporters (KCC) 1 – 4 are responsible for cellular efflux of these ions, while Na^+-K^+-$2Cl^-$ (NKCC) 1 – 2 and Na^+-Cl^- (NCC) cotransporters control cellular influx of these ions. The exact transporter substrates of cation-coupled cotransporter (CCC) 8 – 9 are not known, although the evolutionary older CCC8 is more closely related to the Na^+-independent branch of the family while CC9 branched off early from Na^+-dependent cotransporters. [Taken from (Gagnon & Delpire, 2013)].

The *SLC12A3* gene located on chromosome 16q13, was originally characterised in the urinary bladder of the winter flounder, *Pseudopleuronectes americanus* (Gamba *et al.*, 1993). The expression of its product, NCC, is restricted to the DCT of the kidney where it plays an important role in water and salt homeostasis. Regulation of NCC activity is controlled by two mechanisms: membrane trafficking of the protein to govern levels of apical membrane expression, and the phosphorylation status of highly conserved serine (S)/threonine (T) residues (Hebert *et al.*, 2004) that control the level of intrinsic channel activity . It was once thought that NCC expression was relatively static in the apical membrane of the DCT, but in the last decade or so it has become apparent that a highly complex, multi-level system of upstream regulators exists (Dimke, 2011). In particular these upstream regulators phosphorylate or dephosphorylate at key residues T46, T55 and T60 in humans (T53, T58 and S71 in mice) to increase or decrease activity (Figure 1.4), respectively (Rafiqi *et al.*, 2010); the most functionally important of which has been shown to be T60 (equivalent to T58 in mice) which likely induces conformational change (Richardson *et al.*, 2008).

Figure 1.4: NCC and NKCC1 conserved phosphorylation sites

N-terminal sequence alignment of human and mouse NCC, NKCC1 and NKCC2 residues showing the highly conserved nature of a region known to increase cotransporter activity when phosphorylated. Characterised phosphorylation sites are shown in red boxes, identical residues are shown in black and similar residues are in grey. [Adapted from (Richardson *et al.*, 2008) with changes to sequence order and labelling].

Due to the high degree of homology between the *SLC12* family members the S/T residues are conserved in the NKCCs, and the upstream regulators which act on these residues often solicit responses similar to those seen in NCC. Hence in NKCC1, the more ubiquitously expressed of the two, expression tends to be localised to the basolateral membrane in epithelia and it is activated by phosphorylation of T203, T212 and T217 (Figure 1.4) (Richardson *et al.*, 2008; Thastrup *et al.*, 2012). While NKCC2, whose expression is confined to apical membrane expression in the TAL of the kidney, has phosphorylation sites at T91, T100 and T105 (Figure 1.4) (Hebert *et al.*, 2004). Also of note is that NCC and the NKCCs share a conserved docking site, the [S/V/G]RFx[V/I]xx[T/I/S/V]xx motif (abbreviated to RFxV), that is integral for binding to the conserved C-Terminal (CCT) of their upstream regulators, SPAK and OSR1 to enable phosphorylation (Figure 1.5) (Richardson *et al.*, 2008).

1.3 The Role and Regulation of the WNK Pathway in the kidney

1.3.1 WNK: The original regulators of NCC

Four novel members of the MEK kinase family, the so called With-No-Lysine kinases (WNK) were the first proteins to be investigated for a role in the regulation of CCC activity. The members of the WNK family also share a conserved RFxV binding motif, present in the CCC substrates. This facilitates binding to and phosphorylation of SPAK/OSR1 which are the downstream effectors of the WNKs (Figure 1.5).

The best profiled of these to date is WNK4. Tissue expression of WNK4 in humans and mice is localised to many polarised epithelial cell types such as the pancreas, liver, epididymis, colon, kidney, in addition to blood-brain barrier endothelia (Kahle *et al.*, 2004). In renal tissue, WNK4 expression is highest in the DCT, predominantly associated with tight junctions (evidenced by colocalisation with zona-occludens-1 tight junction protein), and the cortical CD (CCD), in which expression is cytosolic with some intercellular junction localisation (Wilson *et al.*, 2001). Amphibian oocyte and mammalian cell line experiments have demonstrated that WNK4 can act indirectly to positively regulate CCCs; WNK4 phosphorylates its downstream effectors SPAK/OSR1, which in turn mediate its action by phosphorylating CCCs at key residues to stimulate transporter activity (Figure 1.5) (see section 1.3.2) (Vitari *et al.*, 2005; Ahlstrom & Yu, 2009). Mutation of the WNK4 kinase domain in most cases was capable of abolishing this effect, as were experiments utilising kinase-dead forms of SPAK/OSR1, thus demonstrating the necessity for these downstream effectors to mediate WNK4 positive regulation of CCCs (Vitari *et al.*, 2005; Ahlstrom & Yu, 2009). However in contrast to this, native/wildtype WNK4 acting in isolation is known to have a direct negative regulatory effect on CCCs, via inhibition of anterograde trafficking of proteins resulting in a reduction of membrane expression (Yang *et al.*, 2003). *In vitro* experiments demonstrate that co-expression of WNK4 with NCC or NKCC1 will inhibit the transporter activity by dramatically reducing surface membrane levels of CCCs which can be reversed by introduction of Gordon syndrome-causing mutations into WNK4. This mechanism acts independent of dynamin-dependent endocytosis to inhibit anterograde trafficking of NCC from the trans-Golgi network (Yang *et al.*, 2003; Golbang *et al.*, 2006); instead channels are diverted to lysosomes for degradation via a mechanism reliant on the MAPK ERK1/2 signalling pathway (Zhou *et al.*, 2012) and stimulation of AP-3 interaction with NCC (Subramanya *et al.*, 2009). WNK4 reduction of surface membrane NCC can be inhibited through serum/glucocorticoid-induced kinase 1 (SGK1), an aldosterone effector, directly phosphorylating human WNK4 at S1190, the same site targeted by full length WNK1 (L-WNK1) to halt the process and encourage NCC membrane anterograde trafficking (Figure 1.5) (Rozansky *et al.*, 2009).

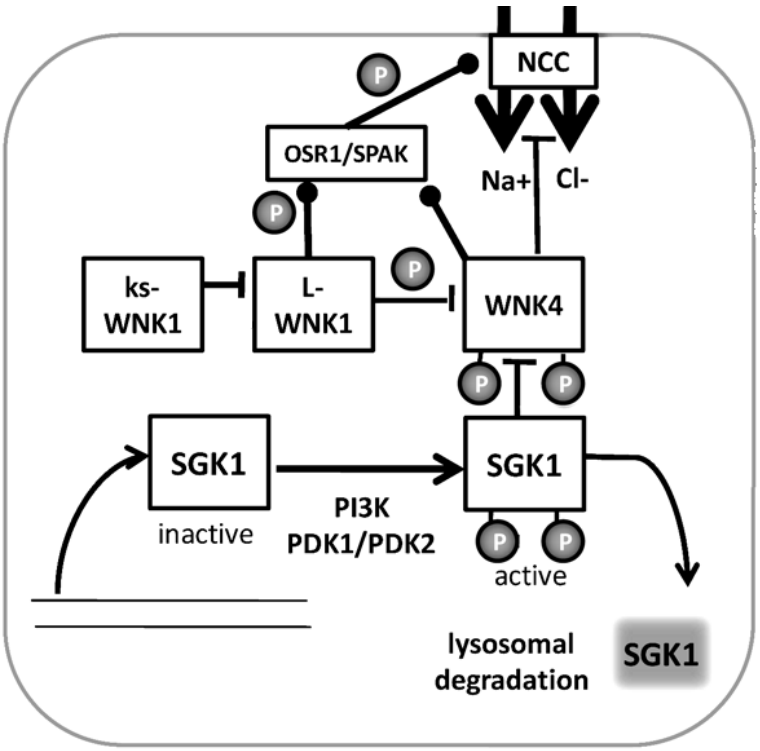

Figure 1.5: Schematic diagram of NCC regulation by WNK 1 and WNK4.

Serum/glucocorticoid-induced kinase 1 (SGK1) is transcriptionally induced by aldosterone and phosphorylated (P) by phosphoinositide 3-kinase (PI3K) and phosphoinositide-dependent kinase (PDK) 1 – 2 signalling, which activates SGK1 and incidentally promotes its degradation. Both SGK1 and full length WNK1 (L-WNK1) can phosphorylate WNK4 to inhibit its negative regulation of NCC activity, which WNK4 normally achieves through disruption of anterograde trafficking of NCC from the trans-Golgi network to the plasma membrane. WNK4 and L-WNK1 can also positively regulate NCC activity through phosphorylation of SPAK/OSR1 which in turn phosphorylate NCC to increase transporter activity. However, the actions of L-WNK1 can also be inhibited by a kidney-specific WNK1 (KS-WNK1) shorter splice variant. [Taken from (Rozansky *et al.*, 2009)].

Similar to SGK1 inhibition of WNK4, WNK1 the first of the WNKs to be discovered and the oldest phylogenetically (Xu *et al.*, 2000), is also capable of interacting with WNK4 to inhibit its negative effect on NCC anterograde trafficking (Yang *et al.*, 2003, 2005). WNK1 phosphorylates WNK4 at the same site as SGK1 to disable its inhibitory effect on NCC activity (Rozansky *et al.*, 2009), and it is also worth noting that WNK1 has been shown to interact with and activate SGK1 to regulate ENaC activity and a similar process may occur in the DCT to further suppress WNK4 (Xu *et al.*, 2005). WNK1 has a broad tissue expression profile and numerous isoforms with putatively different functional roles. In the renal tissue WNK1 colocalises with WNK4 in the DCT and CCD with a diffuse cytosolic distribution (Wilson *et al.*, 2001). In fact a kidney-specific shortened sequence of WNK1 (KS-WNK1) which is kinase inactive and confined to the distal nephron accounts for 90% of WNK1 in this area. The other

10% is made up of L-WNK1, whose tissue distribution is ubiquitous (Yu, 2006; Lee *et al.*, 2009; Rozansky *et al.*, 2009). KS-WNK1 exerts an inhibitory effect on L-WNK1by removing L-WNK1 inhibition of WNK4, which increases inhibition of NCC anterograde trafficking and thus NCC activity (Subramanya *et al.*, 2006; Rozansky *et al.*, 2009). Evidence from KS-WNK1-KO mice have demonstrated this effect *in vivo* with mice demonstrating elevated diastolic blood pressure due to increased NCC expression and phosphorylation (Hadchouel *et al.*, 2010). *In vitro* data also shows L-WNK1 is also capable of increasing NCC activity by phosphorylating SPAK/OSR1 (Moriguchi *et al.*, 2005; Vitari *et al.*, 2005), although given the high ratio of KS-WNK1 to L-WNK1 in the kidney it is likely this effect is typically suppressed *in vivo* (Figure 1.5).

A third member of the WNK family, WNK3, is known to present in at least two isoforms, renal and brain, which exhibit opposite regulatory effects on NCC (Glover *et al.*, 2009). The renal form of WNK3 is expressed along the entire length of the nephron, with the highest levels in PCT and TAL; exhibiting a subcellular localisation to intercellular junctions (zona-occludens-1, tight junction marker protein) (Rinehart *et al.*, 2005). WNK3 has been shown to promote surface membrane expression of NCC by up to 3-fold in amphibian oocyte experiments. Unexpectedly when WNK3 is mutated to remove its activity it gains WNK4-like attributes reducing NCC membrane surface expression (Rinehart *et al.*, 2005). WNK3 is also involved in a chloride sensing mechanism, and like WNK1 and WNK4, SPAK activity is essential to mediate the actions of WNK3 on the downstream substrate NKCC2 (Ponce-Coria *et al.*, 2008). It was the study of WNK3 that provided further confirmation of the two distinct methods of modulating CCC activity; first by control of surface membrane protein abundance and secondly, by altering channel phosphorylation status to increase or decrease the intrinsic activity of the individual transporters inserted into the membrane (Glover *et al.*, 2009).

1.3.2 SPAK/OSR1: The recent focus of NCC regulation

STE20/SPS1-related proline-alanine-rich protein kinase (SPAK) encoded by the *STK39* gene and oxidative stress-response kinase-1 (OSR1) encoded by the *OXSR1* gene, belong to the germinal centre kinase (GCK) subgroup of the STE kinase group (Figure 1.6) (Filippi *et al.*, 2011). Originally discovered for the their ability to stimulate NKCC1 activity, these two closely related kinases sterile-20 (STE20) kinases (Figure 1.7) share 68% sequence identity with one

another, as well as 79% conserved C-terminal (CCT) domain and 96% N-terminal catalytic domain sequence homology (Delpire & Gagnon, 2008).

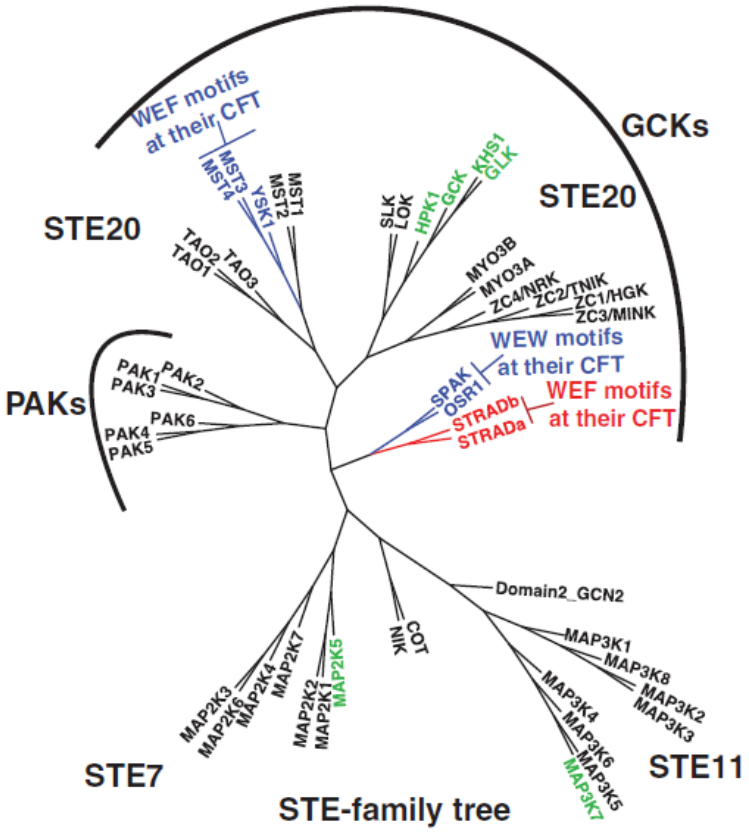

Figure 1.6: STE kinase group classification and relationships.

Neighbour-joining distance tree illustrating the evolutionary relationships of the human sterile (STE) serine/threonine kinase family members. Kinases with all four putative MO25α binding sites are in blue with either a conserved tryptophan-glutamic acid-phenylalanine/tryptophan (WEF/WEW) motifs at their C-terminal flanking tail (CFT) of the kinase domain, STRADα/β are in red and those with three of the putative sites are in green; the majority of these belong to the germinal centre kinase (GCK) subgroup. [Adapted from (Filippi *et al.*, 2011)].

Of the two, OSR1 is more ubiquitously expressed and present in the tissues of the brain, heart, kidney, lung, spleen, testis, liver and skeletal muscle; likely indicative of the more global regulatory actions of OSR1, evidenced by the embryonic lethality of constitutive OSR1-KO (Delpire & Gagnon, 2008; Rafiqi *et al.*, 2010). While SPAK, which has most likely evolved to perform more specialised function has a more restricted expression profile limited to specific areas in the brain, heart, testis, spleen, lung and kidneys, where expression is confined to the

TAL and DCT portions of the mouse nephron (Rafiqi *et al.*, 2010) and TAL, DCT and CCD of human kidneys (Wang *et al.*, 2009). This tissue specific expression correlates well with the expression patterns of the known substrates of OSR1 and SPAK, namely NCC, NKCC1 and NKCC2 which they directly phosphorylate at conserved key S/T residues to positively regulate transporter activity (Moriguchi *et al.*, 2005).

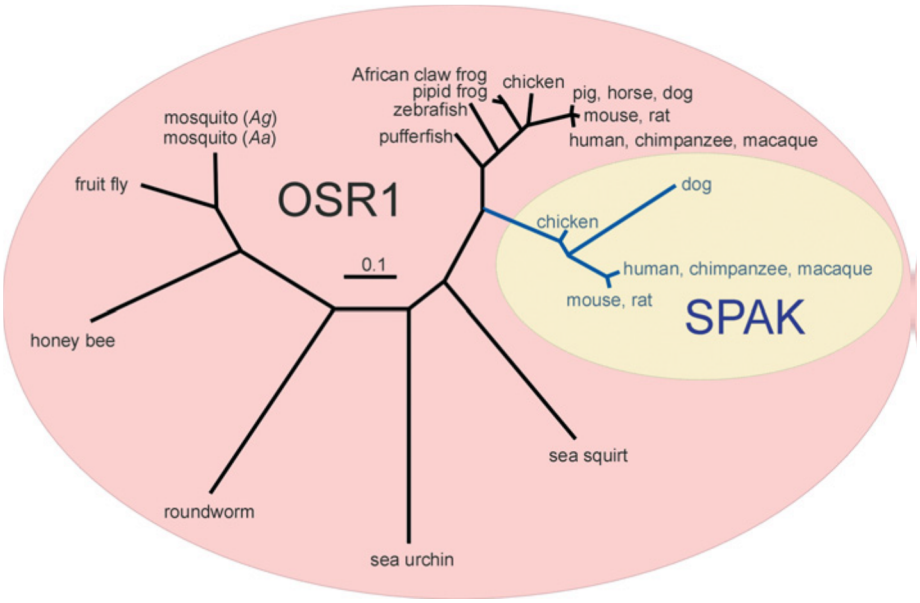

Figure 1.7: SPAK and OSR1 evolutionary relationship.

Phylogenetic cluster dendrogram of SPAK and OSR1 in the animal kingdom. Length of tree branches can be compared with the reference bar, which represents 0.1 amino acid substitutions per site. SPAK branched from OSR1 in avian and mammalian species. Notably, due to the close relationship between mouse, rat and human OSR1/SPAK these animals have proved useful models for studying OSR1/SPAK in human physiology. [Taken from (Delpire & Gagnon, 2008)].

The CCTs of both SPAK and OSR1 are capable of binding with a conserved motif of both substrates (CCCs) and upstream regulators (WNKs), [S/V/G]RFx[V/I]xx[T/I/S/V]xx, more commonly referred to as RFxV (Delpire & Gagnon, 2008), and an example of this binding complex, OSR1-WNK4 has been confirmed by x-ray crystallography (Villa *et al.*, 2007). In order to activate SPAK or OSR1, key T and/or S residues must be phosphorylated; SPAK at S373 (mouse S383) and T233 (mouse T243), and OSR1 at S325 and T185 (Rafiqi *et al.*, 2010; Gagnon *et al.*, 2011). These residues are typically phosphorylated by upstream regulators WNK1, WNK3 and WNK4. This has been verified *in vitro* with experiments employing mutated kinase-dead WNKs and SPAK/OSR1 with key S/T residues mutated such that CCCs

cannot be activated (Vitari *et al.*, 2006; Delpire & Gagnon, 2008; Ponce-Coria *et al.*, 2008). The WNK-SPAK/OSR1-NCC signalling cascade has circadian rhythm, with phosphorylated levels of NCC, SPAK and OSR1 increased at the start of the active period (night in mice/rats) and decreased at the start of the rest period (day in mice/rats) in the nocturnal mouse (Susa *et al.*, 2012). It has also been shown that OSR1 and SPAK, can form functional homodimers and heterodimers with one another that may be capable of activation by trans-autophosphorylation, bypassing normal upstream WNK activation and utilising a stabilising regulator Mouse protein-25 (MO25) (see section 1.3.3) (Lee *et al.*, 2009; Ponce-Coria *et al.*, 2012).

Independently generated SPAK-KO (Geng *et al.*, 2009; Yang *et al.*, 2010*c*) and kinase inactive SPAK-KI mouse models (Rafiqi *et al.*, 2010) have provided viable animals exhibiting sodium-wasting hypotensive phenotypes similar to Gitelman's syndrome or chronic thiazide use. These mice have significantly reduced expression of total and phospho-NCC (pNCC), thus verifying the dominant role of SPAK in DCT regulation of NCC activity *in vivo* (Geng *et al.*, 2009; Rafiqi *et al.*, 2010; Yang *et al.*, 2010*c*). Notably SPAK-KO mice also exhibit an increase in TAL phospho-NKCC2 (pNKCC2) which cannot be entirely attributed to an increase in phospho-OSR1 (pOSR1), but rather may be explained by the emergence of a novel theory supporting a role for shorter sequence SPAK isoforms that exert a negative regulatory effect on CCCs reminiscent of the KS-WNK1/L-WNK1 story (Mccormick *et al.*, 2011; Grimm *et al.*, 2012).

Two of these isoforms that have been discovered in the kidney differ from full length SPAK (~60kDa) in predicted molecular weight and kinase activity. The first isoform, SPAK2, (~49kDa) is missing part of the N-terminus of the kinase domain and presumed to be kinase impaired, while the second isoform, KS-SPAK (~34kDa), is kidney-specific and kinase inactive with loss of the entire kinase domain (Grimm *et al.*, 2012). As the CCT domain is intact in these isoforms, it is presumed that they compete with full length SPAK and OSR1 for RFxV docking sites, thus inhibiting CCC activity. Another distinguishing factor is the differential expression of these isoforms along the nephron: of particular note in the TAL where SPAK2 and KS-SPAK are significantly higher than full length SPAK, and the DCT where the converse is true (Mccormick *et al.*, 2011). It was noted in *Xenopus* oocyte and HEK-293 cell line experiments that SPAK2 significantly decreased NKCC1 activity and that KS-SPAK attenuates levels of pNCC. *In vivo*, the predominance of these truncated SPAK isoforms in the TAL would be expected to supress full-length SPAK activity and partially dampen down OSR1-dominated positive regulation of NKCC2 by competing for docking sites. However, in

the DCT full-length SPAK is the dominantly-expressed isoform allowing it to outcompete SPAK2 and KS-SPAK, overcoming their inhibitory effects. This is evidenced by *in vitro* co-expression of full length SPAK, which serves to significantly diminish the inhibitory effects of SPAK2 on NKCC1 activity (Mccormick *et al.*, 2011; Grimm *et al.*, 2012). Perhaps the most intriguing report has been the presence of an isoform ratio switch in response to extracellular fluid depletion; in which a low sodium diet decreased the abundance of KS-SPAK while simultaneously increasing levels of full length SPAK to promote sodium retention (Figure 1.8) (Grimm *et al.*, 2012). It is therefore likely that complete SPAK-KO wipes out all SPAK isoform-dependent competition, leaving OSR1 to increase NKCC2 activity uninhibited, thus accounting for increased pNKCC2 observed in these models (Geng *et al.*, 2009; Yang *et al.*, 2010*c*). Furthermore, this may explain the absence of any change in NKCC2 activity in SPAK-KI mice, as the ratios of full length SPAK (although mutated), SPAK2 and KS-SPAK are maintained with OSR1 operating in a relatively intact environment (Rafiqi *et al.*, 2010).

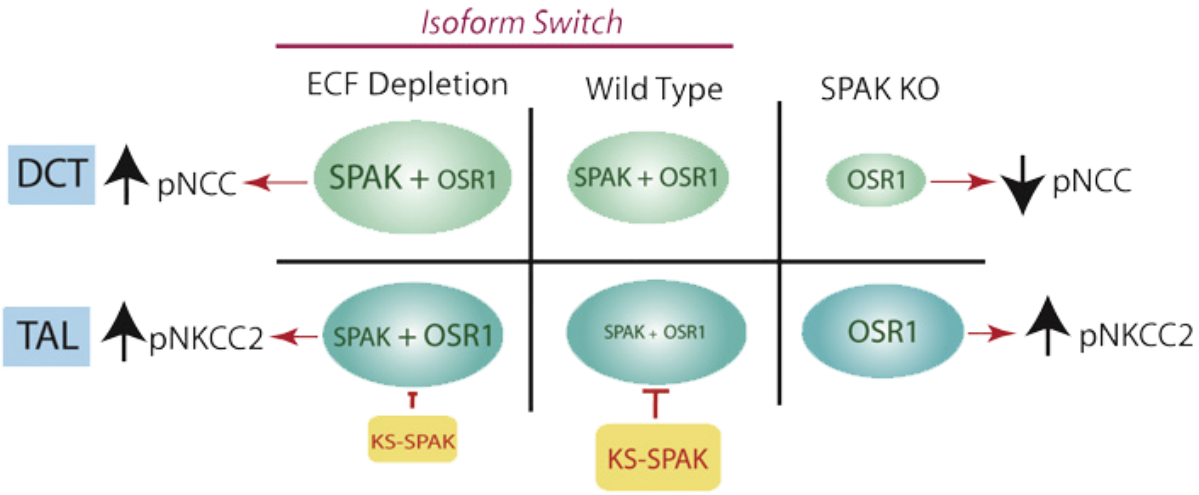

Figure 1.8: Model of SPAK isoform switch mechanism controlling NCC and NKCC2 activity.

In volume replete wildtype animals SPAK/OSR1 stimulates baseline NCC and NKCC2 activity, although full length SPAK/OSR1 activity is largely dampened by the high abundance of kinase-inactive kidney-specific SPAK (KS-SPAK) isoform in the TAL ("switched-off" = high KS-SPAK vs. low full length SPAK/OSR1 levels). During extracellular fluid (ECF) depletion the KS-SPAK is downregulated in the TAL while levels of full length SPAK and OSR1 are increased in DCT/TAL, thereby promoting phosphorylation of NCC and NKCC2 ("switched-on" = low KS-SPAK vs. high full length SPAK/OSR1 levels). Whereas in SPAK-KO animals the absence of any SPAK isoforms leads to a decrease in phospho-NCC (pNCC) as full-length SPAK is the principal kinase in DCT, and an increase in phospho-NKCC2 levels as OSR1 has no competition for binding sites in the TAL in the absence of KS-SPAK. The size of the oval and text is indicative of protein abundance. Red pointed arrows indicate a promotion

of indicated effect, while red flat-head arrows indicate inhibition of effect [Taken from McCormick *et al*, 2011 (42)].

While a homozygote constitutive OSR1-KO mouse model resulted in embryonic death (Delpire & Gagnon, 2008; Rafiqi *et al.*, 2010), heterozygote constitutive OSR1-KO and homozygote kidney tubule-specific OSR1-KO produced viable animals that could be physiologically characterised (Lin *et al.*, 2011). These mice present with a hypotensive phenotype accompanied by sodium/potassium/calcium-wasting, similar to Bartter's syndrome or chronic use of loop diuretics. TAL expression of NKCC2 in these mice was relatively unaffected but levels of phospho-NKCC2 were dramatically decreased, thus supporting the role of OSR1 as the principal regulatory force in TAL NKCC2 activity. Interestingly, levels of SPAK, phospho-SPAK, total NCC and phospho-NCC were all markedly increased in the DCT (Lin *et al.*, 2011), perhaps as a compensatory mechanism for Na^+ handling or due to a yet unexplored mechanism involving previously identified but uncharacterised OSR1 lower molecular weight isoforms present in the kidney that may be operating in a similar fashion to the SPAK isoforms described above (Piechotta *et al.*, 2003).

Additionally, it was reported that SPAK-KO mice have a reduction in aortic contractility which contributes to hypotension, purportedly due to diminished NKCC1 phosphorylation (Yang *et al.*, 2010*c*); activation of NKCC1 in VSMCs causes a rise in intracellular Cl^- which in turn stimulates the influx of Ca^{2+} via L-type calcium channels and subsequent vessel contraction (Akar *et al.*, 2001; Anfinogenova *et al.*, 2004; Orlov & Mongin, 2007). Similarly heterozygote constitutive OSR1-KO mice exhibit significant reductions in aortic levels of phospho-NKCC1 (pNKCC1), pOSR1 and phospho-SPAK (pSPAK) without changes to the total levels of NKCC1 and SPAK, and thus likely exhibit reductions in aortic contractility similar to that observed in SPAK-KO mice (Yang *et al.*, 2010*c*; Lin *et al.*, 2011). Although, to account for the lack of compensation in these KO models by the other remaining kinases that may activate NKCC1, one may argue that evidence shows SPAK and OSR1 interactions with one another stabilise the intracellular localisation of expression, which is required to facilitate their activation (Grimm *et al.*, 2012). Therefore it is conceivable that the absence of one may destabilise and impair the function of the other in the vasculature.

1.3.3 MO25: The master regulator of SPAK/OSR1

Mouse protein-25 (MO25), also known as calcium-binding protein 39 (CAB39), was first discovered to be a highly conserved protein expressed in the cleavage stage of mouse embryos (Miyamoto *et al.*, 1993). Since then much progress has been made in the elucidation of its role as a scaffold protein in the binding to and stabilisation of STE20-related adaptor (STRAD) pseudo-kinase in an active conformation (Figure 1.9), so that it may stimulate liver kinase B1 (LKB1) tumour suppressor protein kinase activity (Boudeau *et al.*, 2003; Milburn *et al.*, 2004; Zeqiraj *et al.*, 2009*b*, 2009*a*). The Alessi group were the first to establish a role for MO25 as a potential master regulator of SPAK and OSR1; both of which are closely related to STRAD and possesses the same four key sites for MO25 interaction (Figure 1.6) (Filippi *et al.*, 2011).

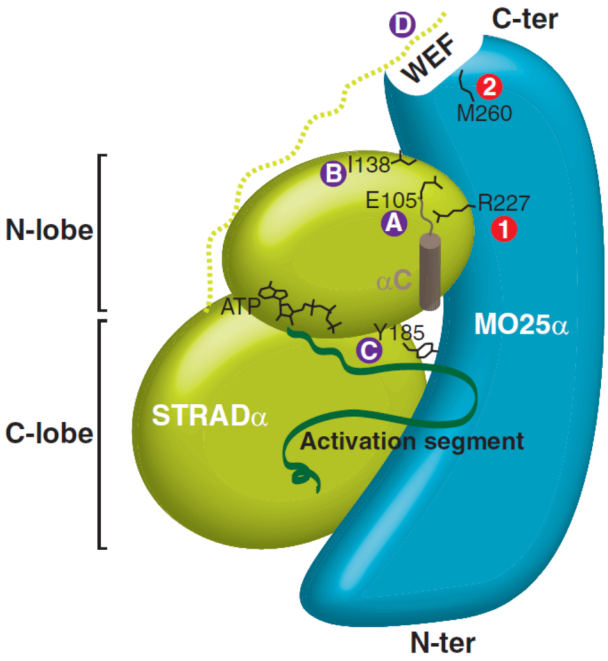

Figure 1.9: STRAD-MO25 interaction sites

Schematic representation of the STRAD–MO25 interaction based on the crystal structure (PDB: 3GNI). Highlighted are key interaction sites referred to as sites 1 and 2 (in red circles) on MO25α (shown in blue) and sites A, B, C and D (in purple circles) on STRADα (shown in green).

There exists two isoforms of MO25 within mammals, namely MO25α and MO25β (also known as CAB39L), which share approximately 73% sequence homology and have similar biological actions on LKB1 (Boudeau *et al.*, 2003). However, it was MO25α that was found *in vitro* to increase the activation of SPAK and OSR1 constitutively active mutants by up to 100-

fold. This effect was found to be dose-dependent with an activity plateau reached around a 10-fold molar excess of MO25α versus SPAK/OSR1; MO25β exhibited similar effects, although was not as potent. Additionally, siRNA-mediated ~70% knockdown of MO25α in a mammalian cell line was shown to decrease hypotonic low-chloride stimulated phosphorylation of NKCC1 by SPAK/OSR1 in a manner rescuable by re-expression of MO25α (Filippi *et al.*, 2011).

Immunofluorescent studies of mouse renal tissue have shown MO25α to specifically colocalise with SPAK and OSR1 at the apical membrane of the TAL and DCT, thus providing evidence to support a role for MO25α-SPAK/OSR1 signalling *in vivo*. Interestingly, in SPAK-KO mice MO25α expression levels and localisation appear unaltered, while OSR1 in the DCT redistributes to punctate structures containing WNK1, but does not in the TAL. This suggests SPAK stabilises OSR1 apical localisation in the DCT and perhaps explains why OSR1 is incapable of compensating for the loss of positive SPAK regulation on NCC activity, as MO25α it is no longer in proximity to promote OSR1 activation (Grimm *et al.*, 2012).

Work by Delpire *et al* in *Xenopus* oocytes, has shown that SPAK and OSR1 are capable of forming functional homo- and heterodimers with one another; and while the functional unit of SPAK is the monomeric form, dimerisation can facilitate monomer activation. Importantly, this dimer-facilitated activation of monomeric kinase activity is mediated by MO25α, in a manner that bypasses the usual upstream phosphorylation requirement of SPAK/OSR1 by WNK (Figure 1.10). Also it was shown that MO25α is incapable of increasing NKCC1 activation if SPAK is solely an unactivated monomer, although could significantly increase NKCC1 activity if the SPAK monomer was already in an active form (Ponce-Coria *et al.*, 2012). In another study MO25α was demonstrated to potentially stabilise and facilitate the active conformation of OSR1 kinase as either a monomer or dimers (Figure 1.11) (Gagnon *et al.*, 2011).

Of particular note is the ability of MO25α to facilitate the rescue of non-functional SPAK mutants by P+1 loop domain swapping with another non-functional SPAK mutant in a homodimer or wildtype (WT) OSR1 in a heterodimer. This demonstrated an exciting new MO25α facilitated interplay between and within SPAK/OSR1 co-expressed in the TAL and DCT that had not previously been studied (Ponce-Coria *et al.*, 2012). It should also be considered that due to the ability of MO25α to stimulate SPAK/OSR1 activity independent of the usual upstream WNK-mediated phosphorylation, caution should be exercised in

interpreting various phosphorylated NCC residues as an absolute indicator of channel activity/stimulation (Gagnon *et al.*, 2011).

This figure was redacted for copyright reasons.

The Copyright holder is The American Physiological Society.

The original can be found as Figure 8 in
DOI: 10.1152/ajpcell.00284.2012

Figure 1.10: Proposed mechanisms for mouse SPAK activation.

[I] A monomer of unactivated SPAK with unmodified T243 (T) and S383 (S) phosphorylation sites and P+1 loop T247 hidden between. **[II]** Inactive SPAK monomers can dimerise. **[III]** WNK4 binds to SPAK and phosphorylates T243 and S383 (shown as *). **[IV]** A conformational change unmasks the P+1 loop T247 residue permitting domain-swapping (shown as swapped coloured "T" circles); it is unclear if WNK4 remains in complex with the active SPAK (shown as faded). **[V]** MO25α (also known as CAB39, and shown as CAB in the figure) binds to SPAK and induces a conformational change unmasking the P+1 loop T247. **[VI]** Domain swapping of the P+1 loop and phosphorylation of T243 activate SPAK; it is unclear if MO25α remains in complex with active SPAK (shown as faded). [Taken from (Ponce-Coria *et al.*, 2012)]

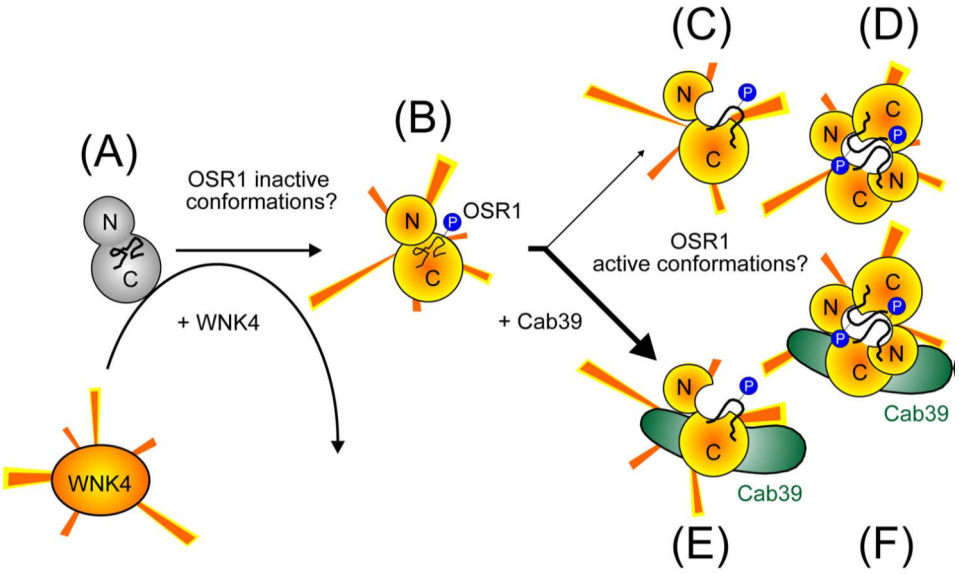

Figure 1.11: Proposed mechanisms of mouse OSR1 activation.

[A] WNK4 phosphorylates an inactive OSR1 (shown in grey), **[B]** active OSR1 (shown in yellow) is phosphorylated (P in blue circle) at S325 and T185, **[C]** active conformation phospho-OSR1 monomer or **[D]** dimer, **[E]** MO25α (CAB39) facilitates and stabilises an active conformation of phospho-OSR1 monomer or **[F]** domain-swapped dimer. [Adapted from (Gagnon *et al.*, 2011)].

1.3.4 CUL3/KLHL3: The New Players

Two new gene candidates involved in the pathophysiology of Gordon's syndrome were identified by whole-exome sequencing; namely *KLHL3* which encodes kelch-like 3 (KLHL3) and *CUL3* (CUL3) which encodes cullin-3 involved in the formation of a ubiquitin ligase complex (Boyden *et al.*, 2012; Louis-Dit-Picard *et al.*, 2012). A striking finding of this work was that mutations between these two new genes accounted for 79% of Gordon syndrome patients who did not possess traditional mutations in either WNK1 or WNK4 (WNK1/WNK4 mutations account for 13%) in the examined patient cohort (Boyden *et al.*, 2012). Characterisation of KLHL3 expression within the kidneys demonstrated a restriction of expression to DCT and CNT with apical localisation in the DCT, and thus can be assumed to colocalise with NCC. While CUL3 was found to be ubiquitously expressed in all renal tubules, but with highest expression in the PCT, DCT and CCD (Boyden *et al.*, 2012; Louis-Dit-Picard *et al.*, 2012). The ability of KLHL3 to negatively regulate NCC membrane expression is in part dependent on the ability to colocalise with NCC; they have been shown to co-immunoprecipitate and a reduction of KLHL3 at the membrane increases NCC surface localisation, presumably through a reduction in NCC ubiquitination (Louis-Dit-Picard *et al.*, 2012). It was proposed that these represent a promising third candidate for a pathway regulating NCC endocytosis/degradation, although significant investigation is warranted to establish if KLHL3 and CUL3 administer their actions solely through an endocytotic process or by ubiquitination of other NCC regulators.

1.3.5 PP4/PP3: The counter-regulatory system

As phosphorylation of NCC by SPAK/OSR1 has a positive regulatory effect on transporter activity, it is logical to assume that a counter-regulatory mechanism of dephosphorylation must exist, presumably executed by protein phosphatases (PP). For example, PP1 has already been reported to reduce NKCC1 activity, by direct dephosphorylation of the channel or indirectly by dephosphorylation of SPAK (Gagnon & Delpire, 2010). Data has also shown that PP1 is capable of recognising the RFxV motif in conjunction with its regulatory subunits and is capable of binding with WNK1 and WNK4, thus potentially negatively regulating channel activity at several levels (Villa *et al.*, 2007). PP2A has been found to inhibit NKCC1 activity by dephosphorylation, and studies have shown co-immunoprecipitation with SPAK,

suggesting perhaps indirect reduction in NKCC1 phosphorylation status by dephosphorylation of SPAK, similar to PP1 (Liedtke *et al.*, 2005).

PP4 which shares 65% of its amino acid sequence with PP2A (Hu *et al.*, 2001), is primarily found in the DCT, distal CNT and CD cells (Glover *et al.*, 2010). The human S/T protein phosphatase 4 gene (*PPP4C*) which encodes for PP4 is located on chromosome 16p11-p12 (Bastians *et al.*, 1997), and although the mouse and human genes sequences differ, the resulting amino acid sequence of the protein remains the same for both species (Hu *et al.*, 1998). PP4 is a developmentally regulated protein phosphatase playing important roles in embryonic development; in adult life the protein is abundantly expressed in numerous tissues such as the kidneys, heart and skeletal muscle (Hu *et al.*, 2001). Thus constitutive PP4-KO has proved to be embryonically lethal in mice and subsequently a conditional knock-out was later developed (Shui *et al.*, 2007). The wide and complex activities of PP4 are in part controlled by regulatory subunits, namely R1 and R2, which can form complexes and thus in turn help govern the specificity of PP4 actions (Cohen *et al.*, 2005). Data from *Xenopus* oocyte $^{22}Na^{+}$ flux experiments have illustrated that PP4 can directly reduce NCC activity by dephosphorylation of T58 residues. This regulation is dependent on the phosphatase actions of PP4, as demonstrated by phosphatase inactive mutants, and the effect is also shown to be completely independent of WNK4 regulation of NCC membrane trafficking, which is not impacted by T58 phosphorylation status (Glover *et al.*, 2010). *In vivo* evidence for a physiological role of PP4 may be found in the clinical outcomes of anti-tumour anti-biotic drugs such as fostriecin which is a potent and selective inhibitor of PP2A and PP4 (Walsh *et al.*, 1997; Hastie & Cohen, 1998) as has been observed previously for other phosphatase inhibitors (Hoorn *et al.*, 2011; Melnikov *et al.*, 2011).

Strong evidence for PP3 (also known as calcineurin) regulation of NCC activity was discovered from studying the clinical side effects of immunosuppressive drugs tacrolimus or cyclosporine (calcineurin inhibitors), often prescribed to patients who have undergone transplant surgery. Administration of either of these drugs has been known to induce hypertension, which may be ameliorated with the application of thiazides, furthermore these drugs cannot induce elevated blood pressure in NCC-KO mice, thus reinforcing the evidence that phosphatase activity is required for negative regulation of NCC activity. It should also be noted that PP3 and NCC colocalise, and PP3 inhibitors increase WNK1, WNK4, SPAK and NCC levels in addition to increasing phosphorylation of NCC and SPAK (Hoorn *et al.*, 2011; Melnikov *et al.*, 2011). Thus it is likely that PP3 is working to negatively regulate NCC activity

in vivo directly at the level of NCC and via inhibition of its upstream regulators, though the precise mechanisms of this regulation remain unknown.

1.3.6 Parvalbumin: An unexpected regulator of NCC and diuretic response

A member of the EF-hand Ca^{2+} binding proteins, parvalbumin (PVALB) is encoded by the *PVALB* gene on chromosome 22q12-q13.1. This Ca^{2+} sensing and/or buffering protein contains a pair of EF-hand motifs capable of binding two Ca^{2+} ions with high affinity leading to conformational change (Belge *et al.*, 2007). In 1986, renal DCT specific expression of PVALB was first characterised in rats (Schneeberger & Heizmann, 1986), and later in 2001, also profiled in mouse kidneys where expression was specifically confined to the early portion of the DCT (DCT1) colocalising with NCC (Loffing *et al.*, 2001), as is also the case in human kidneys (Belge *et al.*, 2007). As a result of this specificity, PVALB has been used in studies as a marker for distinguishing DCT1 (Grimm *et al.*, 2012), which specifically expresses PVALB and NCC only with weak Calbindin D_{28K}, from the late portion of the DCT (DCT2) which strongly expresses Calbindin D_{28K} but not PVALB with a progressive decline in NCC expression and rise in ENaC expression along the DCT2 as it approaches the connecting tubule (CNT) (Câmpean *et al.*, 2001; Loffing *et al.*, 2001).

The role of PVALB in the DCT has been somewhat of a mystery for a while and has been postulated to play a role in Ca^{2+} and Mg^{2+} transport activity (Câmpean *et al.*, 2001). Although it was Belge *et al* that demonstrated that PVALB in fact has an important functional role in the maintenance of NCC expression; but is not likely to have a direct role in DCT transport of Ca^{2+} or Mg^{2+} (Belge *et al.*, 2007; Belge & Devuyst, 2010). Using *PVALB*-KO mice they demonstrated decreases in NCC, WNK1 and WNK4 expression at mRNA and protein levels (Belge *et al.*, 2007; Zacchia & Capasso, 2008). Interestingly this relationship with NCC is also apparent in SPAK-KO mice where SPAK has been found to be necessary for DCT1 integrity. Mass and lengths of DCT1 are severely diminished with corresponding decreases in NCC and PVALB in SPAK-KO mice when compared with WT (Grimm *et al.*, 2012).

Using mouse DCT cell lines, the expression of NCC was found to be Ca^{2+}-dependent and can be modulated by parvalbumin levels which in turn regulate intracellular Ca^{2+} signalling. This novel finding places parvalbumin as an important player within the intricate

network of NCC regulators; although work has not been done to elucidate if the effects of its control are solely at the level of NCC membrane abundance or if phosphorylation status is affected via PVALB regulation of WNK1 or WNK4. Perhaps most strikingly was their discovery that *PVALB*-KO impairs the diuretic response to hydrochlorothiazide and induces marked hypocalciuria when compared with WT; possibly due to several tubular compensatory mechanisms (Belge *et al.*, 2007). At first the discovery of a *PVALB*-KO phenotype akin to that seen in Gitelman syndrome patients was a source of great excitement (Zacchia & Capasso, 2008), however initial evaluation of *PVALB* as a candidate gene for *SLC12A3*-negative cases of Gitelman syndrome revealed no hits within this subset of patients (Riveira-Munoz *et al.*, 2008). This does not however preclude a role for mutations of the *PVALB* gene contributing to the pathophysiology of other distal tubulopathies or indeed variations in individual patient response to thiazide diuretics (Belge & Devuyst, 2010).

1.3.7 RasGRP1/Nedd4-2: Negative regulation of NCC by endocytosis

Work published by the Hoover group in 2007 (Ko *et al.*, 2007) and 2010 (Ko *et al.*, 2010), was the first to demonstrate the role of an endocytotic process in NCC activity regulation. Through the use of phorbol ester, TPA, a functional analog of diacylglycerol (DAG) they stimulated the Ras guanyl-releasing protein 1 (RasGRP1) which triggered a cascade activating the ERK1/2 MAPK pathway resulting in a decrease of NCC activity *in vitro* (Ko *et al.*, 2010). They discovered that activation of the ERK1/2 MAPK pathway by TPA simulated RasGRP1 activity that was independent of protein kinase C (Ko *et al.*, 2007), and the decrease in NCC activity was mediated by a decrease of NCC membrane expression by an active promotion of dynamin-dependent endocytosis. This process relied on ubiquitination of NCC by ERK1/2, which could be disabled by inhibition of ubiquitin-activating enzyme E1 with UBEI-41 (Ko *et al.*, 2010). How this pathway may be activated *in vivo* still awaits further investigation.

Later in 2011, a second system of NCC endocytosis was discovered involving aldosterone, SGK1 and the ubiquitin-protein ligase neuronal precursor cell expressed developmentally down-regulated protein (Nedd4-2). This pathway had previously been characterised in the regulation of ENaC (Abriel & Staub, 2005; Rotin & Staub, 2012), but through *in vivo* site-specific conditional knock-out of Nedd4-2 in renal tubules, it was also discovered to be involved in NCC regulation (Arroyo *et al.*, 2011). *In vivo,* Nedd4-2 interacts with NCC to cause ubiquitination and endocytosis; though once Nedd4-2-KO is induced the

DCTs of these mice exhibit a huge increase in NCC expression (Arroyo *et al.*, 2011). In *Xenopus* oocyte and HEK-293 cell work they demonstrated that SGK, a mediator of aldosterone action, regulates NCC expression indirectly by inhibiting Nedd4-2 through S328 and/or S222 phosphorylation, and can interact with NCC directly to compete with and prevent Nedd4-2-mediated inhibition of NCC (Arroyo *et al.*, 2011). The importance of SGK1 in this process is emphasised with *in vivo* kidney specific knock-out of SGK1 which results in a hypotensive sodium-wasting phenotype with reduced NCC expression (Rotin & Staub, 2012).

1.4 Extrarenal roles of the WNK Pathway

[*This section is principally based on content from the paper in Appendix 2* (Siew & O'Shaughnessy, 2013)]

Although the research focus has been predominantly on the renal functions of WNKs, they are both highly conserved among various species and widely expressed in a variety of tissues, suggesting many more diverse physiological roles (Xu *et al.*, 2000; Veríssimo & Jordan, 2001; Wilson *et al.*, 2001; O'Reilly *et al.*, 2003; Vidal-Petiot *et al.*, 2012). It has been proposed that the WNK–STE20 interactions and functions are evolutionarily ancient, conserved over millions of years and having coincided with the evolution of multicellularity and polarised epithelia. This is demonstrated in *Caenorhabditis elegans*, in which interference of this system causes a complete breakdown of osmotic homeostasis and drastically reduces survivability in response to hypertonic-induced shrinkage (Choe & Strange, 2007; Lee *et al.*, 2010). In fact, the various biological roles of WNKs may be evidenced in the other features of Gordon syndrome, which include hyperchloraemic metabolic acidosis, hypercalciuria with accompanying low bone mineral density (BMD) and, in some cases, dental abnormalities, short stature, muscle weakness and intellectual impairment (Licht *et al.*, 1985; Mayan *et al.*, 2002).

1.4.1 Musculoskeletal system

Osteoporosis, marked by an abnormally low BMD, has been linked with a downregulation of WNK1 and a rare mutation in Exon 17 of WNK4 that does not cause hypertension (Xiao *et al.*,

2008; Mendes *et al.*, 2011). In addition, Gordon syndrome patients and mice with the same WNK mutations have been documented with hypercalciuria, low BMD, short stature and dental abnormalities (Licht *et al.*, 1985; Mayan *et al.*, 2002, 2004; Yang *et al.*, 2010*a*). Another monogenetic disease, namely Gitelman syndrome, which is the phenotypic mirror of Gordon syndrome, is caused by loss-of- function mutations in NCC, the downstream target of WNKs. Gitelman syndrome patients and mouse models with inactive NCC or disrupted WNK–SPAK signalling exhibit a high BMD, hypocalciuria, and in some cases hypophosphataemia and hyperphosphaturia (Nicolet-Barousse *et al.*, 2005; Akhtar & Hafeez, 2009; Rafiqi *et al.*, 2010; Yang *et al.*, 2010*c*; Viganò *et al.*, 2012; Pathare *et al.*, 2012). A report also suggests that Ca2+ increases the positive actions of WNK4 on NCC activity by enhancing OSR1 phosphorylation and that Gordon syndrome mutations disrupt the sensitivity of WNK4 activity to Ca2+, locking it chronically in a Ca^{2+}-activated type state (Na *et al.*, 2012). These data provide strong support for the hypothesis that WNKs regulate bone, PO_4^{3-} and Ca^{2+} homeostasis.

Data from as far back as the late 1960s show a link between thiazides and increased BMD, hypocalciuria and hypophosphataemia, suggesting the role of WNKs in bone homeostasis was indirect and via renal Ca^{2+} homeostasis (Condon & Nassim, 1970; Rejnmark *et al.*, 2003; Olmos *et al.*, 2010). This was further supported by research showing that the renal transient receptor potential vanilloid (TRPV) ion channels involved in Ca^{2+} transport are WNK regulated. In fact, TRPV5 expression is localised to the apical membrane of the DCT, the nephron segment involved in active Ca^{2+} reabsorption, which is positively regulated by both WNK4 and WNK3 (Jiang *et al.*, 2006, 2008; Zhang *et al.*, 2008; Jing *et al.*, 2011). Interestingly coexpression of NCC with WNK4 and TRPV5 *in vitro* blocks the positive regulatory effect of WNK4, which is consistent with the changes in NCC activity and altered Ca^{2+} homeostasis observed in Gordon or Gitelman syndromes and may also account for thiazide-induced hypocalciuria (Jiang *et al.*, 2006). In contrast, TRPV6, which is expressed along the DCT and adjacent CD, is regulated by WNK3 (but not WNK4) in a similar manner to TRPV5 (Zhang *et al.*, 2008). However, TRPV6 is considered to be a minor player in Ca^{2+} reabsorption and although upregulated in knock-in mice carrying a WNK4 mutation known to cause Gordon syndrome, this does not correct the hypercalciuria phenotype (Yang *et al.*, 2010*a*).

The NCC and TRPVs are not restricted to the kidney. Hence, NCC and TRPV6 are expressed in the small intestine and may be involved with intestinal Ca^{2+} absorption under WNK–SPAK/OSR1 regulation (Bazzini, 2005; Lieben & Carmeliet, 2012; Pasham *et al.*, 2012*a*). Thiazides also inhibit intestinal NCC, suggesting that the gut may be important for the

increased BMD seen in both Gitelman syndrome and thiazide-treated patients (Bazzini, 2005). Furthermore, NCC and TRPVs have been implicated in osteocyte, osteoblast and osteoclast function, thus representing a second avenue for WNK regulation of Ca^{2+}, PO_4^{3-} and bone homeostasis. Numerous studies have shown osteoblasts, the cells responsible for new bone formation, express NCC and can be influenced by thiazide administration *in vitro*. For example, pharmacological inhibition of NCC has been shown to induce membrane depolarisation, increase intracellular Ca^{2+}, promote osteoblast differentiation and raise alkaline phosphatase activity, which stimulates bone mineralisation (Aubin *et al.*, 1996; Barry *et al.*, 1997; Lalande *et al.*, 2001; Dvorak *et al.*, 2007). This antiresorptive effect observed during chronic thiazide treatment or Gitelman syndrome is compounded by osteoclast inhibition and hence a reduction in their usual catabolic effect on bone and release of Ca^{2+} and PO_4^{3-} stores. Osteoblasts produce macrophage colony stimulating factor (M-CSF), which promotes recruitment and differentiation of precursor osteoclast cells; thiazides have been shown to reduce levels of M-CSF (Aubin *et al.*, 1996; Lalande *et al.*, 2001). However, thiazides may have direct effects on osteoclasts, because a subpopulation express NCC (Hall & Schaueblin, 1994; Dvorak *et al.*, 2007) and NCC-null mice are reported to have a significantly reduced endosteal osteoclastic surface in long bones such as the femur (Nicolet-Barousse *et al.*, 2005). Osteoclasts also express TRPV5 on their apical membrane, which is regulated by WNK4 and NCC and provides another mechanism to explain the dichotomous BMD in Gitelman and Gordon syndrome (Lieben & Carmeliet, 2012). The close paralogue TRPV4 is expressed on the basolateral membrane of osteoclasts and is essential for regulating intracellular Ca^{2+} and differentiation but, in contrast with the other TRPVs, WNK4 and WNK1 have been shown to decrease surface expression of TRPV4 (Fu, 2006; Lieben & Carmeliet, 2012). Perhaps it is disruption of this dynamic regulation of TRPVs and NCC in osteoblasts and/or osteoclasts caused by WNK mutations that leads to a low BMD in Gordon syndrome rather than isolated alterations in renal Ca^{2+} homeostasis. A graphical representation of these mechanisms can be seen in (Figure 1.12).

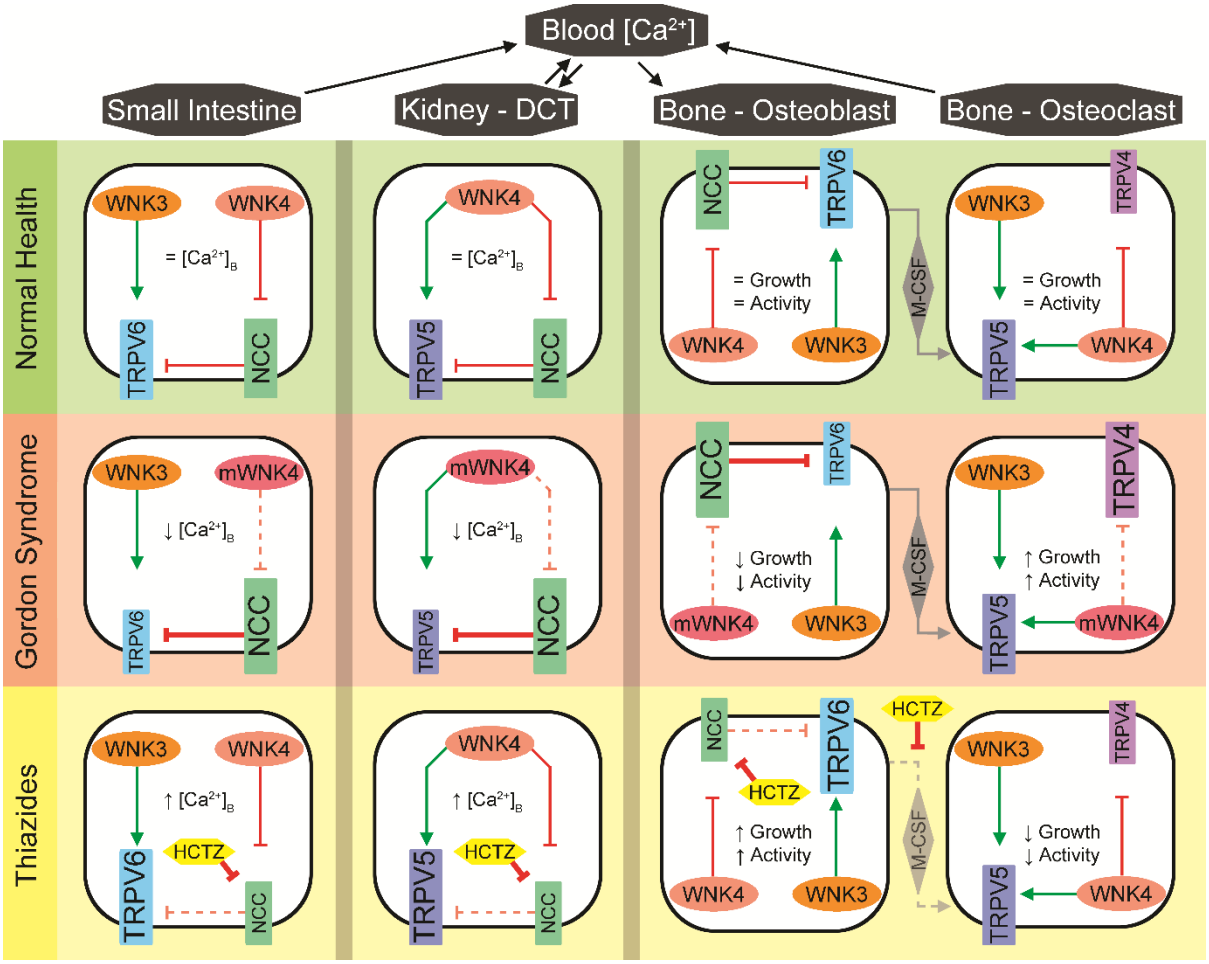

Figure 1.12: WNK kinases in Ca^{2+} homeostasis.

Transient receptor potential vanilloid (TRPV) ion channels allow the influx of Ca^{2+} into cells for the purposes of absorption, reabsorption and regulating bone homeostasis. The TRPV5/6 channels, present in the kidneys and small intestine, enable the transport of Ca^{2+} from the lumen into the blood. In addition, TRPV5 is present on the bone-facing side of osteoclasts for bone resorption. Basolateral TRPV4 activity stimulates osteoclast differentiation, as does the release of macrophage colony-stimulating factor (M-CSF) from osteoblasts, which are themselves stimulated to differentiate by TRPV6 activity. These TRPV channels are regulated directly by WNKs and indirectly by the actions of WNKs on the Na+-Cl^- cotransporter (NCC). As a result, Gordon syndrome patients present with low bone mineral density and hypercalciuria, whereas chronic thiazide (HCTZ) treatment indirectly elicits the opposite phenotype via effects on the NCC. Green-pointed arrows indicate stimulation; red flat arrows indicate inhibition; dashed lines indicate diminished effect, and the size and thickness of the NCC and TRPV symbols and arrows represent the relative strength of the activity and/or effect. Cell diagrams are orientated so that the basement membrane is uppermost and apical on the bottom. Gordon syndrome WNK4 mutations (mWNK4); Differentiation and proliferation (growth); Blood Ca^{2+} concentration ($[Ca^{2+}]_B$). [Taken from (Siew & O'Shaughnessy, 2013)].

Perhaps the least understood aspects of Gitelman syndrome and chronic thiazide administration, namely the hypophosphataemia and/or hyperphosphaturia observed in animal models and handful of patient case reports, may also be explained by integrated signalling

between kidney, osteoblasts and osteocytes governed by the WNK signalling pathway (Condon & Nassim, 1970; Katopodis *et al.*, 1996; Viganò *et al.*, 2012; Pathare *et al.*, 2012). Fibroblast growth factor (FGF) 23 is produced by osteoblasts and osteocytes and acts as a potent inhibitor of PO_4^{3-} reabsorption in the renal proximal convoluted tubules (PCT) and of calcitriol (1,25-(OH)2D), a promoter of intestinal Ca^{2+} and PO_4^{3-} absorption and renal Ca^{2+} reabsorption (Liu & Quarles, 2007). Of note, the initial FGF23-mediated signalling that takes place within the DCT occurs in tubules adjacent to PCT tubules, where PO_4^{3-} reabsorption is reduced, suggesting a paracrine action (Farrow *et al.*, 2009). This may be necessary if the fine-tuning of Ca^{2+} homeostasis is to take place in the DCT. Production of FGF23 is increased with rising plasma Ca^{2+} levels and shares a strong positive exponential correlation with the Ca^{2+} x PO_4^{3-} product (Quinn *et al.*, 2012; Rodriguez-Ortiz *et al.*, 2012; Yasin *et al.*, 2013). When the presence of NCC and TRPV6 in osteoblasts and osteocytes is taken into account (Dvorak *et al.*, 2007; Little *et al.*, 2011), it is possible to imagine that changes in phosphate excretion are elicited by osteoblasts and/or osteocytes in an attempt to correct an abnormal Ca^{2+} x PO_4^{3-} product and prevent calciphylaxis, which becomes exaggerated in Gitelman syndrome and thiazide treatment or dysfunctional when WNK–STE20 signalling is disturbed (Quinn *et al.*, 2012; Pathare *et al.*, 2012; Yasin *et al.*, 2013).

1.4.2 Cardiovascular system

Early attempts to investigate WNK function *in vivo* suffered several setbacks as the phenotype of WNK1 homozygote knock-out (KO) mice proved to be embryonically lethal. However this difficulty did at least confirm the importance of WNK1 for early cardiovascular development. Hence, WNK1 is highly expressed in the early heart, endothelium of blood vessels and in the extra-embryonic tissues, including the placenta and yolk sac (Delaloy *et al.*, 2006). It is probably no surprise that WNK1 homozygote KO embryos developed obvious cardiovascular malformations, including smaller heart chambers, reduced myocardial trabeculation and underdevelopment of yolk sac vasculature, failed angiogenesis and aberrant gene expression within vascular tissues. The changes led to death before embryonic day 13 (Gamba, 2005). The absence of WNK1 from endothelial tissues appears to be the key problem, because the phenotype of endothelial-specific KO mice closely matched that of global KO, and global KO tissues could be rescued with endothelial-specific transgenic expression of WNK1 (Xie *et al.*, 2009). The vasculopathy caused by WNK1-KO may extend to other members of the WNK

family; in a Japanese cohort, polymorphisms in WNK2 were associated with a higher incidence of intracerebral haemorrhage (Yoshida *et al.*, 2010). In fact, Richard Gordon may have been premature in assuming that four cases of heart murmur and one of pulmonary stenosis were unrelated to Gordon syndrome (Gordon, 1986).

The WNK1 heterozygote KO mice are viable, although present with a variable hypotensive phenotype. Pronounced nitric oxide independent reductions in the contractility of the thoracic aorta and mesenteric arteries, as well as a severe decrease in the myogenic response to resistance vessels, were also noted (Zambrowicz *et al.*, 2003; Bergaya *et al.*, 2011). The partial loss of WNK1 reduced the subsequent phosphorylation of SPAK by approximately 40% and, in turn, the phosphorylation of the bumetanide-sensitive Na^+-K^+-$2Cl^-$ cotransporter 1 (NKCC1) by approximately 30%; both are present in arterial vascular smooth muscle (VSM) cells (Zambrowicz *et al.*, 2003; Bergaya *et al.*, 2011). Typically NKCC1 activity will increase Cl^- influx, causing depolarisation and increased contraction of VSM cells (Orlov *et al.*, 2012); however, this effect is diminished when the WNK–SPAK/OSR1 pathway is disrupted because NKCC1 activity is phosphorylation dependent. This was demonstrated by homozygote SPAK KO mice and heterozygote OSR1 KO mice that showed marked hypotension, significant reductions in aortic contractility, decreased levels of phosphorylated (p) NKCC1 and phenotypes that closely recapitulate Gitelman and Bartter syndrome, respectively (Yang *et al.*, 2010*c*; Lin *et al.*, 2011).

In addition, WNK4 has been implicated in the modulation of vascular tone by tonic inhibition of transient receptor potential canonical (TRPC) 3, which is a major component of the Ca^{2+}-dependent vasoconstrictive mechanism. Using *ex vivo* tissues from rats, WNK4 was depleted via short interference (si) RNA silencing, which, in turn, increased apical membrane expression of TRPC3 in the VSM cells of mesenteric arteries, enhancing vasoconstriction (Park *et al.*, 2011). The TRPC3 activity was also capable of inducing hypertrophic growth of VSM cell primary cultures when WNK4 was suppressed (Park *et al.*, 2011), which, *in vivo*, would likely contribute to an increased vessel wall thickness/lumen diameter ratio, causing higher vascular resistance and lower vascular compliance. Coexpression of Gordon syndrome-causing WNK4 mutations in human cells with TRPC3 suggested that the mutations would have a reduced effect on TRPC3 inhibition in vivo (Park *et al.*, 2011). This could raise vascular resistance and compound the systemic hypertension caused by salt retention in the DCT and subsequent hypervolaemia (Park *et al.*, 2011). A graphical representation of these mechanisms can be seen in (Figure 1.13).

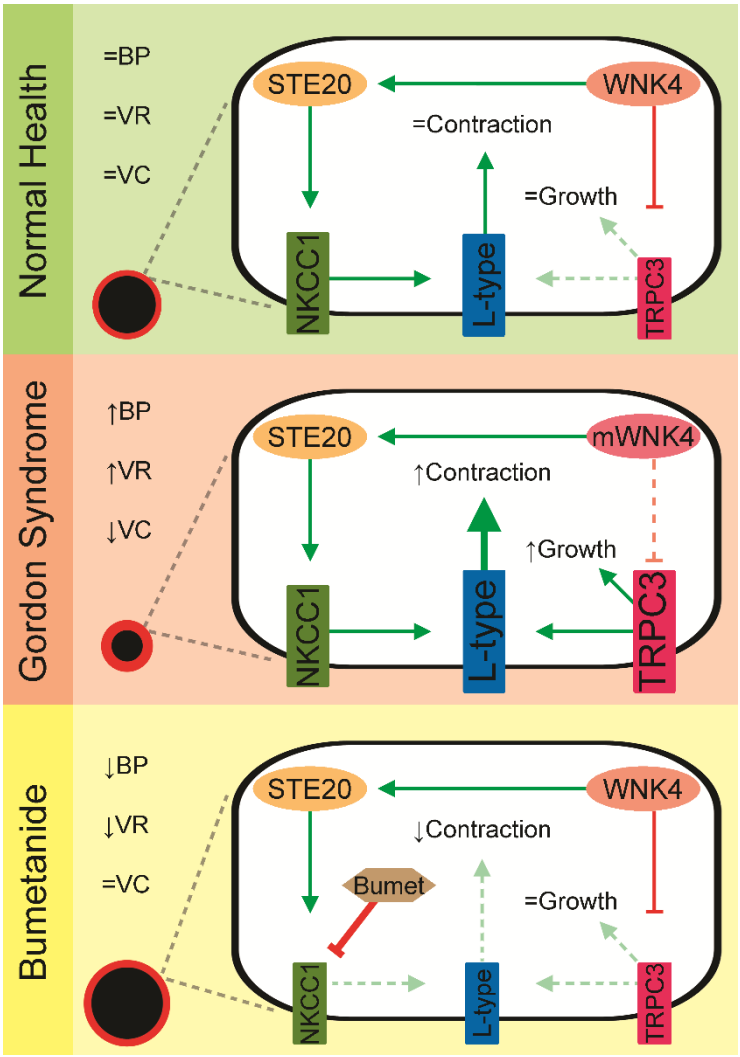

Figure 1.13: WNKs in vascular smooth muscle cells and the contribution to blood pressure control.

As indicated, WNK4-stimulated Na^+-K^+-$2Cl^-$ cotransporter 1 (NKCC1) activity raises intracellular Cl^-, depolarising the vascular smooth muscle cell (VSMC), triggering Ca^{2+} influx via L-type Ca^{2+} channels, which induces vasoconstriction; inhibition of NKCC1 results in vasodilatation. When WNK4 is mutated (mWNK4), it can no longer inhibit Ca^{2+} influx via transient receptor potential canonical (TRPC) 3 channels and so intracellular Ca^{2+} increases, triggering intense vasoconstriction and hypertrophic growth of VSMC, thus increasing vascular resistance and reducing vascular compliance. Green-pointed arrows indicate stimulation; red flat arrows indicate inhibition; dashed lines indicate diminished effect, and the size and thickness of the NKCC1, TRPC3 and L-type symbols and arrows represent the relative strength of the activity and/or effect. Vasoconstrictor status and the ratio of wall thickness to lumen diameter are represented graphically with an example VSMC shown in frame. Sterile 20 kinase (STE20); Bumetanide (Bumet); Blood pressure (BP); Vascular resistance (VR); Vascular compliance (VC). [Taken from (Siew & O'Shaughnessy, 2013)].

1.4.3 Nervous system

It has become apparent in recent years that WNKs are more dynamic and complex than was first imagined. The WNKs have many yet uncharacterised splice variants with diverse tissue specific expression and functions (O'Reilly *et al.*, 2003; Glover *et al.*, 2009; Vidal-Petiot *et al.*, 2012). The latest focus of attention has been on a previously unknown isoform of WNK1 in which a nervous system-specific exon of WNK1, named WNK1/HSN2, when mutated causes hereditary sensory and autonomic neuropathy type 2 (HSAN2). Patients with HSAN2 lose peripheral sensory nerves and have limited or no perception of touch, heat or pain (Shekarabi *et al.*, 2008; Potulska-Chromik *et al.*, 2012). Interestingly, heterozygous carriers of the recessive WNK1/HSN2 mutation paradoxically experience heightened sensitivity to thermal stimuli (Loggia *et al.*, 2009). Clues to the molecular basis of HSAN2 have come from transgenic zebrafish expressing mutant WNK1/HSN2; these fish have significantly increased K^+-Cl^- cotransporter 2 (KCC2) expression, which is known to be important in peripheral nerve development and control of intracellular Cl^- concentrations, and it is this disruption of normal KCC2 expression that may account for pathogenic peripheral sensory nerve development (Bercier *et al.*, 2013).

A WNK3 brain isoform expressed in the nervous system regulates NKCC1 and KCC2 by altering their phosphorylation state via SPAK/OSR1; pNKCC1 is activated and increases intracellular Cl^-, whereas pKCC2 is deactivated and reduces the efflux of Cl^- from the cell (Kahle *et al.*, 2005; Glover *et al.*, 2009). Therefore, WNK3 simultaneously promotes complementary actions on NKCC1 and KCC2. This regulation of intracellular Cl^- is very important for neuronal excitability and is particularly relevant to GABA signalling (Kahle *et al.*, 2005). This system may be important in the pathogenesis of autism, in which mutations in SPAK (Ramoz *et al.*, 2008) and WNK3 (Qiao *et al.*, 2008) have been identified. Further support has come from an intriguing small clinical trial involving five children with infantile autistic syndrome who were effectively treated with bumetanide, an inhibitor of NKCC1, decreasing their autistic behaviour over a 3 month period (Lemonnier & Ben-Ari, 2010). WNK3 may also be involved through its role in RNA processing by regulating the neuronal mRNA splicing factor Fox-1. Both WNK3 and Fox-1 are purported to have roles in neurodevelopment, so further research into the association of WNKs and autism is warranted (Lee *et al.*, 2012*a*).

Numerous studies have linked mutations at virtually each point in the WNK2/WNK3–SPAK/OSR1–NKCC1/KCC2 axis to the development of schizophrenia in which GABA signalling is dysfunctional (Arion & Lewis, 2011; Hyde *et al.*, 2011; Kalkman, 2011; Wang & Kriegstein, 2011). Of particular note is the position of WNK3 on the X-chromosome, mutations in which may contribute to the higher number of males with schizophrenia and autism than females (Veríssimo & Jordan, 2001; Qiao *et al.*, 2008). In normal health, developing neurons of the prefrontal cortex and hippocampus have a high NKCC1:KCC2 ratio, thus increasing intracellular Cl^- under the control of WNK2–SPAK, and the resulting reversal potential ensures that $GABA_A$ receptor activation causes depolarisation. This excitatory behaviour of GABA is required for stimulating the differentiation and proliferation of neurons, as well as the growth and formation of dendrites and synapses. As the GABA system matures, the ratio is shifted from a high to low NKCC1:KCC2 ratio and becomes increasingly regulated by WNK3–OSR1, which reduces intracellular Cl^- and shifts its reversal potential so that GABA becomes an inhibitory transmitter with $GABA_A$ receptor activation causing hyperpolarisation. However, in a large cohort of adult schizophrenic patients, the aberrant 'immature' GABA physiology remains intact with higher NKCC1:KCC2 ratios, lower KCC2 levels and a marked increase in WNK3 and OSR1 (Arion & Lewis, 2011; Hyde *et al.*, 2011; Kalkman, 2011; Rinehart *et al.*, 2011). Perturbation of the signalling axis can also predispose people to or induce schizophrenia. For example, seizures that may be made more likely due to the increased neuronal excitability promote undesirable acceleration of neuronal development through increased GABA excitatory activity (Kalkman, 2011). Strikingly, Danish cohort studies found that those with a history of juvenile febrile seizures were at a 44% higher risk of schizophrenia, whereas those who also had a history of epilepsy were at a 204% increased risk (Arion & Lewis, 2011). However, inappropriate pharmacological manipulation of GABA physiology can also be dangerous, because early administration of bumetanide to inhibit NKCC1 activity in neonatal seizures can inhibit neuronal development and lead to inhibition of anxiety-related behaviours or impairment of the prepulse inhibition of the startle reflex; both are hallmarks of schizophrenia (Wang & Kriegstein, 2011). A graphical representation of these mechanisms can be seen in (Figure 1.14).

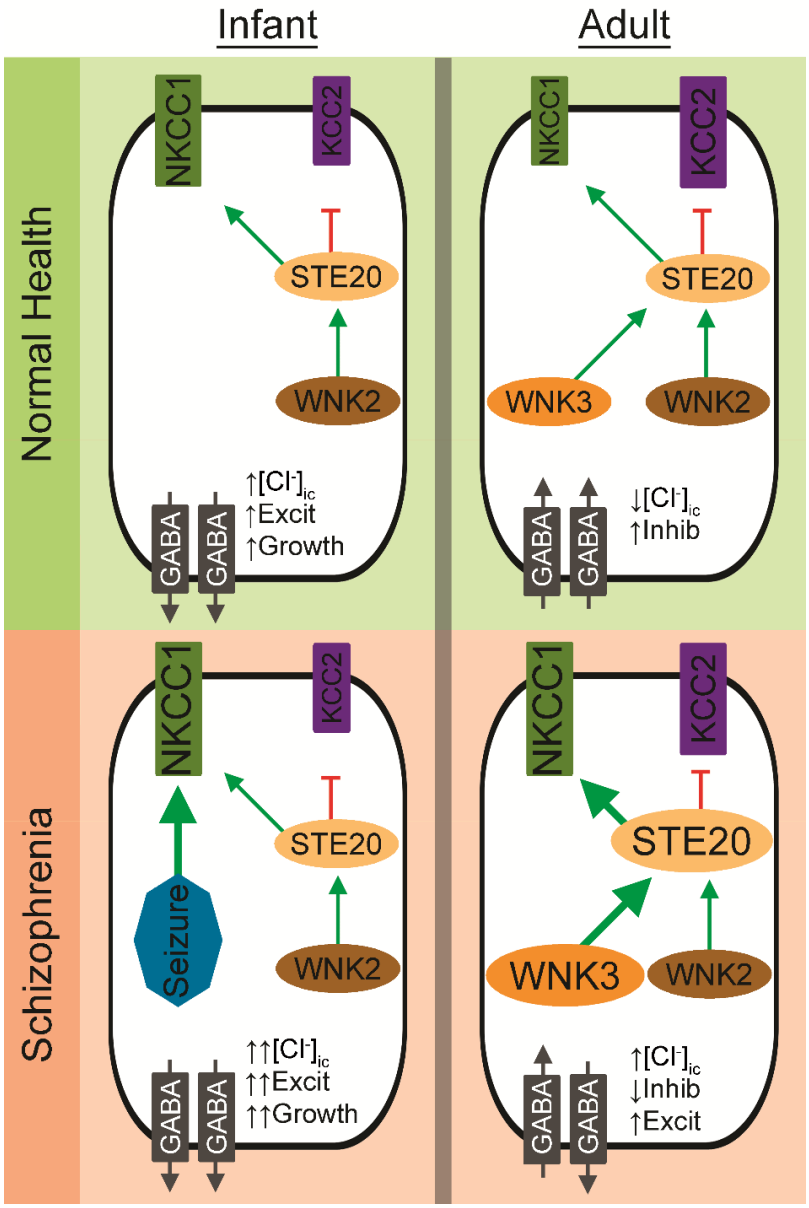

Figure 1.14: WNK, GABA and the development of schizophrenia.

In the developing brain there is a higher ratio of Na^+-K^+-$2Cl^-$ cotransporter 1 (NKCC1) to K^+-Cl^- cotransporter 2 (KCC2), with activity regulated by WNK2. This raises intracellular Cl^- due to increased influx from NKCC1 and reduced efflux from KCC2. This results in excitatory GABA signalling, which stimulates the differentiation and proliferation of neurons. Later in adulthood, WNK3 becomes the dominant regulator and the ratio of NKCC1:KCC2 is inversed, intracellular Cl^- is decreased and GABA signalling becomes inhibitory. In the young brain, schizophrenia can be induced by environmental insult, such as febrile seizure, which can exaggerate the excitatory GABA signalling, leading to undesirable premature differentiation of neurons. This increased NKCC1 can persist into adulthood, accompanied by overexpression of WNK3/sterile 20 kinase (STE20), which leaves inappropriate GABA excitatory activity intact. Green-pointed arrows indicate stimulation; red flat arrows indicate inhibition; dashed lines indicate diminished effect, and the size and thickness of the WNK, STE20, NKCC1, KCC2 symbols and arrows represent the relative strength of the activity and/or effect. Intracellular Cl^- concentration ($[Cl^-]_{ic}$); GABA excitatory activity (Excit); GABA inhibitory activity (Inhib); neuronal differentiation and proliferation (Growth). [Taken from (Siew & O'Shaughnessy, 2013)].

1.4.4 Immune system and cellular regulation

As multicellular organisms evolved, so did the requirement to regulate an internal environment, maintain a secure external barrier, recover from injury and defend against hostile organisms and environmental insult. The WNKs–STE20 represent a signalling axis that integrates these things, and an early example can be seen in *C. elegans*, in which antimicrobial peptide neuropeptide-like protein 29 (nlp-29) is released in response to infection, wounds or osmotic stress. In *C. elegans*, WNK1 is activated when osmotic stress is detected, which may often be accompanied by infection or injury, and this in turn activates germinal centre kinase (GCK)-3 (a STE20 kinase), which stimulates nlp-29 to trigger the maintenance of epidermal integrity and the innate immune system (Choe & Strange, 2007; Lee *et al.*, 2010).

In mammals, the role of WNKs in immunity and regulating cellular processes is conserved, although poorly understood. For example, WNK2 is a potent tumour suppressor, inhibiting up to 78% of glioma cell colony formation *in vitro* (Hong *et al.*, 2007). Deletions and epigenetic silencing of WNK2 strongly correlate with certain central nervous system cancers (Hong *et al.*, 2007). For more detailed reviews of WNKs and cancer than is provided here, readers are referred to (McCormick & Ellison, 2011) and (Moniz & Jordan, 2010). It has been demonstrated that WNK1 and WNK3 can independently, or in synergy with IL-1, increase nuclear factor-κB (Pichlmair *et al.*, 2012), a major component of the mammalian innate and adaptive immune response. However, WNK1 and WNK3 are also viral targets for disruption as part of a viral strategy to impair the host immune response; WNK3 and IL-1, which can stimulate IL-8, can also be potently inhibited by the K7 protein of the Vaccinia virus (Pichlmair *et al.*, 2012).

Dendritic cells, which are the antigen-presenting cells that bridge the gap between innate and adaptive immunity, express WNK1, WNK3, OSR1, NCC and NKCC1. These cells in OSR1 heterozygote KO mice have lower levels of pNKCC1, but higher baseline Na^+/H^+ exchanger activity and increased production of reactive oxygen species. One would assume this is beneficial for fighting off pathogens, although, when responding to oxidative stress or a foreign antigen, the responses of normal dendritic cells were significantly blunted, illustrating the importance of an intact WNK–OSR1–NKCC1 axis for immunity (Pasham *et al.*, 2012*b*).

1.5 Aims

Given the mounting evidence for the WNK pathway in the regulation of blood pressure and electrolyte homeostasis, it has become an intense area of focus for prospective anti-hypertensive drug targets or to further elucidate the mechanisms which underlie hypertension. With this trend in mind, the study had three objectives:

1) To investigate the aetiology of PHA2E, the most severe form of Gordon syndrome, with the goal of developing novel anti-hypertensive strategies. Recent evidence supports a role for the WNK pathway in vascular physiology, and it was hypothesised an additional vascular phenotype drove the early onset and intensity of hypertension seen in PHA2E patients.

2) Explore MO25 as an anti-hypertensive drug target. As MO25 is known to be involved in WNK-independent activation of CCCs, its ablation was hypothesised to lower blood pressure.

3) Verify SPAK binding disruption as a viable anti-hypertensive strategy for drug targeting. As loss of SPAK signal by genetic knock-out or inhibition of kinase activity produces Gitelman syndrome, it was hypothesised that genetic disruption of SPAK binding to its regulator and substrate would do the same.

Chapter 2 : Materials & Methods

[*This chapter is principally based on and expands upon the content from the abstracts in Appendix 1, and papers in Appendix 3* (Schumacher *et al.*, 2015)] *and Appendix 4* (Zhang *et al.*, 2015).

2.1 *Mus musculus* Animal Models

All animal procedures were approved by local ethical committees and performed under a UK Home Office-approved licence in accordance with the regulations set by the Universities of Cambridge and Dundee.

2.1.1 Generation

Taconic Biosciences (formerly Taconic Artemis) generated two constitutive knock-in mouse models; a deletion of CUL3 exon 9 (Δ403-459) and a leucine to alanine mutation at SPAK residue 502 (L502A). In brief, targeting vectors containing the desired mutations were constructed, cloned and sequenced before electroporation into competent germline C57BL/6NTac embryonic stem cell lines. After homologous recombination, clones with targeted alleles containing the positive selection puromycin cassette (which was later removed by Flp recombinase) were isolated, validated, injected into mouse blastocysts and transferred into pseudo-pregnant females (Figure 2.1; Figure 2.2). The resulting chimeras were bred with wild-type mice to ensure germline transmission and produce heterozygous founder males and females on a C57Bl/6N background.

The MO25β null (MO25β$^{-/-}$) mice on a C57BL/6 x CBA mixed background were sourced as frozen embryos from the CARD resource at the University of Kunamoto, Japan. To generate this model the MO25β allele was gene trapped at the first exon by using the pU-21W promotor trap vector (http://egtc.jp/action/access/vector_detail?vector=pU-21W) on the KTPU8 embryonic stem cell line (http://egtc.jp/action/access/cellline_detail?cellline=KTPU8) to produce the strain B6;CB-*Cab39l*$^{Gt(pU\text{-}21W)191Card}$ (http://cardb.cc.kumamoto-u.ac.jp/transgenic/strainsDetailAction.do?strainId=1287).

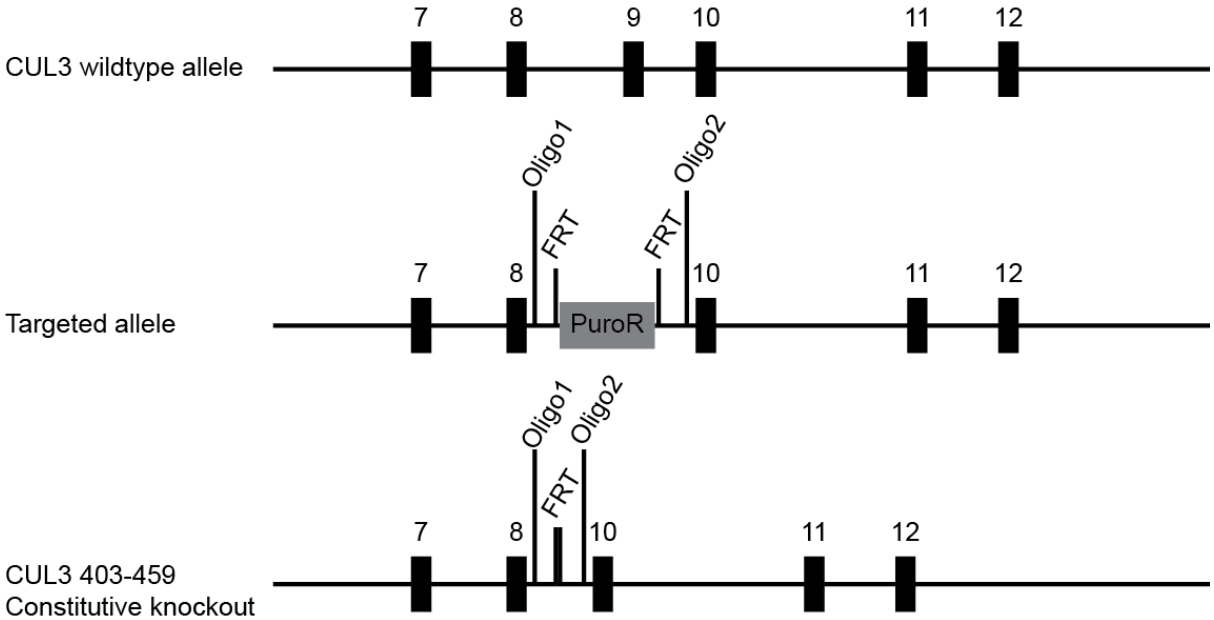

Figure 2.1: CUL3 mouse model generation.

The knock-out strategy of exon 9 of endogenous Cullin3. The endogenous allele is represented and the target allele with the puromycin cassette (PuroR) removed by Flp recombinase. The black rectangles represent exons, the flippase-recognition target (FRT) sites and primer targets (Oligo) for PCR-based genotype confirmation are indicated. [Taken from (Schumacher *et al.*, 2015)].

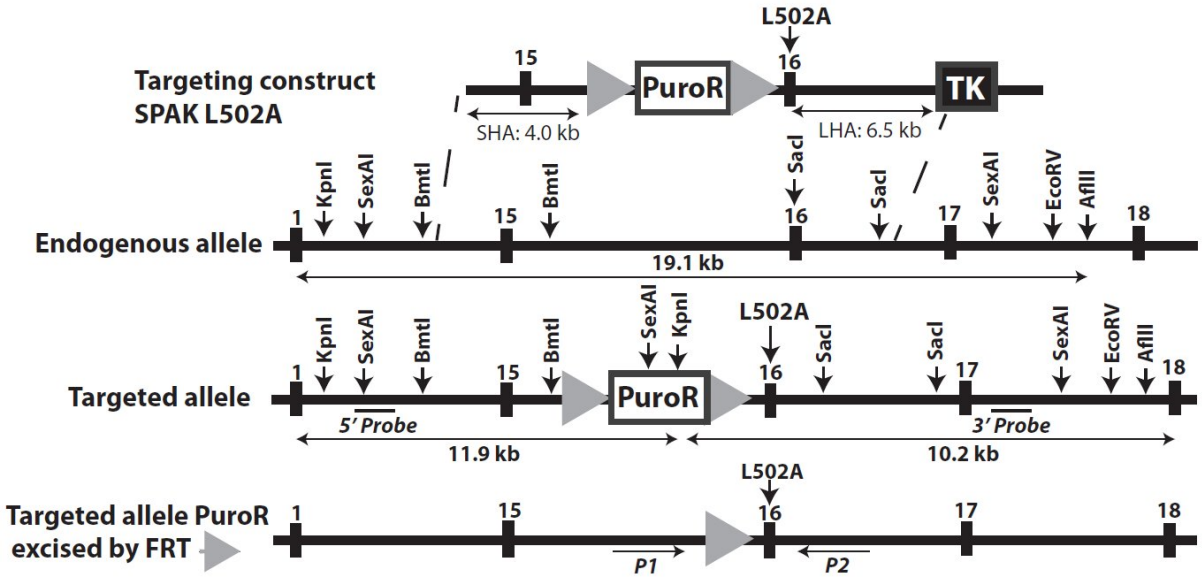

Figure 2.2: SPAK mouse model generation.

Diagram depicting the knock-in construct, the endogenous SPAK allele containing exons 15–16 and the targeted allele with the puromycin cassette removed by Flp recombinase. The black rectangles represent exons, and the grey triangles represent FRT sites. Black lines with arrowheads are used to indicate the positions of the probes used for Southern analysis. The knock-in allele containing the Leu502Ala mutation in exon 16 is illustrated as a grey rectangle. The knock-in allele can be detected

by genotyping using PCR primers (P1 and P2), which are represented by short black lines with arrowheads. [Taken from (Zhang *et al.*, 2015)].

2.1.2 Genotyping

Genomic DNA (gDNA) from ear and tail biopsies were isolated from samples collected at 3-4 weeks of age for initial genotyping and again post-mortem for genotype confirmation. Genotyping was achieved by standard PCR amplification of gDNA and gel-electrophoresis analysis to identify bp lengths of products produced by specific alleles; performed by Gail Gilmour and Elaine Forsyth (MRC Protein Phosphorylation and Ubiquitylation Unit, University of Dundee). The PCR program consisted of 2 min at 95 °C; 30 s at 95 °C, 1 min at 60 °C and 1 min at 72 °C: 35 cycles; 10 min at 72 °C. The following primers were used for CUL3 mice (Figure 2.1), primer 1: (oligo 1: AAA CTT ACC CAC TTG TTT GCC) and primer 2: (oligo 2: AGA CAT CTC AGG TTA CTA TGG GC). The $CUL3^{WT}$ allele generate a 683 bp product and $CUL3^{\Delta 403\text{-}459}$ allele generates a shorter 395 bp product. For the SPAK (Figure 2.2), Forward Primer (P1: GTC TAG GAC ATG ATG GTA TGG) and Reverse Primer (P2: CCA ACA TGG GGT ACC AAC AAA TGC) were used to detect the wild-type and knock-in alleles. The $SPAK^{WT}$ generates a 587 bp product whereas the $SPAK^{L502A}$ generates a 679 bp product. The larger knock-in allele product is due to the presence of the FRT site and flanking region, which remains in an intronic region following Flp-mediated excision of the puromycin resistance (PuroR) selection cassette. The genotypes MO25β mice were identified by utilising forward primer (ACA CCC CTC CCA ACT TTG TA), reverse primer (GGC CAC TAC GTG CTA AGA GG), and a second reverse primer targeting the pU-21W elements (CCT GGC CTC CAG ACA AGT AG) to detect the presence of the $MO25\beta^{+}$ (larger product) or $MO25\beta^{-}$ (smaller product) alleles.

Additionally, to confirm correct amino acid substitution for SPAK founder mice the resultant PCR products were ligated into the pCR-Topo 2.1 vector and transformed into *E. coli*, and clones were sequenced. DNA sequencing was performed by The Sequencing Service, College of Life Sciences, University of Dundee.

2.1.3 Animal Care and Husbandry

Mice were maintained under specific pathogen-free (SPF) conditions in individually ventilated cages (IVC) at Temp: 19-23 ºC, Humidity: 40-70%, Air Changes: 12-15 per h, Daylight: 12 h daily. All mice were group housed 2-6 per cage, food and water was given *ad libitum* (unless otherwise stated) and cages were changed regularly by animal technicians (Biological Services, Wellcome Building Resource Unit, University of Dundee).

$CUL3^{WT/\Delta 403-459}$ heterozygote X $CUL3^{WT/WT}$ wildtype breeding pairs were established for generating heterozygote experimental group $CUL3^{WT/\Delta 403-459}$ and wild-type control group $CUL3^{WT/WT}$ littermates. $MO25\beta^{+/-}$ X $MO25\beta^{+/-}$ heterozygote breeding pairs were established for generating homozygote experimental group $MO25\beta^{-/-}$ and wild-type control group $MO25\beta^{+/+}$ littermates. $SPAK^{+/L502A}$ X $SPAK^{+/L502A}$ heterozygote breeding pairs were established for generating homozygote experimental group $SPAK^{L502A/L502A}$ and wild-type control group $SPAK^{WT/WT}$ littermates. Excess $SPAK^{+/L502A}$ and $MO25\beta^{+/-}$ heterozygotes were either culled or used for establishing new breeding pairs.

2.2 Physiology and Anatomy

Data collection and analyses were carried out in a blinded fashion throughout, where possible.

2.2.1 Body Fluid Analysis

2.2.1.1 Creatinine Assay

Plasma and urine (non-acidified) creatinine levels were assayed by standard Jaffe reaction or enzymatic method performed by Keith Burling, Peter Barker and Ashley Clarke (Core Biochemical Assay Laboratory, Addenbrooke's Hospital, Cambridge, UK).

2.2.1.2 Fasting Blood Gases and Electrolytes

To reduce variability introduced by dietary potassium ingestion, animals were fasted for a 4 h minimum before being anaesthetised with isoflurane on 100% O_2 (induction: 3% v/v, maintenance: 1.75% v/v) and placed on a self-regulating rectal probe-coupled heat mat (TC-1000; CWE) to maintain a body temperature of 37 °C. To minimise air contact of arterial bloods during measurements, the right carotid artery was cannulated with a mouse arterial catheter (MAC-02; SAI Infusion Technologies) pre-flushed with 10 U heparin-0.9% w/v saline to prevent clots. Blood was released via the catheter into the EC8+ cartridge for analysis on the iSTAT (Abaxsis).

2.2.1.3 Diet Manipulations and Longitudinal Electrolyte Measurements

To determine baseline plasma and urine electrolyte homeostasis animals were placed on a normal diet containing either 0.25% or 0.3% w/w Na for 2 weeks with urine and plasma time-matched samples collected between days 7-10 for normal Na (NNa) diet baseline. On day 14 mice were switched onto a 0.03% w/w Na diet with sampling repeated on days 7-10 for low Na (LNa) diet measurements.

To provide a physiological challenge for renal salt handling some animals were sodium loaded on a 3% w/w Na diet for 14 days with urine and plasma samples collected between days 7-10 for High Na (HNa) diet measurements. On day 14 mice were switched onto a 0.03% w/w Na diet (LNa) with urine samples collected at 0, 3, 6, 12, 24 h after Na-diet switch to investigate the rapid renal adaptive response to salt restriction.

Spot urine was collected from awake mice following spontaneous micturition upon handling over a sheet of Saran wrap or Parafilm. Samples were then divided and one sample received acidification with HNO_3 to a final concentration of 1% v/v to prevent precipitation of electrolytes, before both were stored at -80 °C. Blood was collected with heparin-coated Microvette CB 300 LH (Sarstedt) by saphenous venepuncture in awake restrained animals or in the case of MO25β mice, by post-operative exsanguination via cardiac puncture in animals under terminal anaesthesia. Plasma was separated by centrifuged at 2,000 g for 5 min and collected for storage at -80 °C. To avoid affecting blood pressure or electrolyte homeostasis in longitudinal studies, blood collection intervals were spaced such that no more than 10% of total

blood volume was taken on any single occasion or 25% of total blood volume in any 28 day period.

Where sample volumes permitted, MO25β samples were analysed using the Siemens Dimension RxL Max Integrated Chemistry System, performed by Keith Burling, Peter Barker and Ashley Clarke (Core Biochemical Assay Laboratory, Addenbrooke's Hospital, Cambridge, UK). Otherwise, plasma or urine electrolytes were determined using an inductively coupled plasma – optical emission spectrometer (ICP-OES Analyser; Perkin Elmer) at the Cambridge Geography Science Laboratories (coordinated by Chris Rolfe, Steve Boreham and Samantha Smith).

Prior to ICP-OES analysis, plasma and urine (acidified) samples were defrosted, vortexed and centrifuged for dilution at 1:1000 using ultra-pure polished water containing 1% v/v HNO_3 in new unopened 15 mL conical centrifuge tubes (Falcon) with the same pipette to reduce error. Fresh acid-washed glassware was rinsed three times with ultrapure polished water and new unopened pipette tips were used to minimise possible contaminants. Cations were then measured by an ICP-OES Analyser equipped with an argon plasma torch and programmable autosampler. Optima blank nitric acid solution and concentration standards in Table 2.1 were used to zero the device and generate calibration curves.

Element	Calcium	Potassium	Magnesium	Sodium	Phosphorous
Wavelength (nm)	317.933	766.490	285.213	589.592	213.617
Standard (mg/L)	1	1	1	1	5

Table 2.1: ICP-OES element wavelength detection peaks and standards.

Three consecutive measurements were taken per analyte for all 5 elements, followed by a nitric acid flush between samples to prevent cross contamination. Samples to be compared were analysed in the same session, with urines and plasmas grouped according to dietary manipulation. To quantify detector drift, sample groups were bookended with confirmatory measurements of the same optima blank and concentration standards used for calibration. A sample blank containing 1% v/v of the original HNO_3 used to acidify the urine was diluted 1:1000 in the same solution and tubes as above. This was used to quantify trace contamination

from the HNO_3 sources, ultra-pure polished water system and leaching from plastic and glassware.

The average and relative standard deviation the three readings are automatically calculated and exported into an Excel spreadsheet (Microsoft) for data processing. Samples that had abnormally high relative standard deviation, evidence of haemolysis, evaporation or insufficient volume were excluded from the analysis. Assuming detector drift is linear, a correction factor can be applied using the following formula: (raw values between A and B) x (known concentration of standards / average of measures for bookend standards A and B) – (average of Optima blanks A and B). The drift corrected sample blank measurements can then be subtracted from all drift corrected values to account for trace contaminants. Sample blank corrected values are then adjusted for dilution factors (from acidification of urine and sample preparation for ICP-OES analysis) converted from mg/L to mMol/L. Urinary electrolytes were then normalised against creatinine levels determined in section 2.2.1.1.

2.2.1.4 Aldosterone Assay

Post-surgery, additional blood samples were collected using heparin-coated Microvette CB 300 LH (Sarstedt) from animals used in section 2.2.1.2. Samples were centrifuged at 2,000 g for 5 min to extract plasma before storage at -80 °C.

Plasma aldosterone was calculated by HTRF (homogeneous time-resolved fluorescence) aldosterone assay (cisbio Codolet, France), performed according to manufacturer's protocol using the PheraStar FS (BMG labtech) plate reader by Irish Hardege (University of Cambridge).

2.2.2 Cardiovascular Assessment

When groups of animals were being compared, the order of animals selected for procedures was randomised.

2.2.2.1 Experimental Setup and Animal Preparation

In order to record and monitor physiological parameters in real-time, custom LabChart version 6/7/8 pro (AD Instruments) settings template files were created to display 3 raw data channels - Blood pressure, ECG, body temperature and 5 calculate channels - mean arterial pressure, systolic blood pressure maximum, diastolic blood pressure maximum, BP first derivative maximum and heart rate. For vasopressor experiments a separate settings template file was created that had additional windows to monitor and analyse dose responses in real-time.

At the start of each recording session the 1F Mikro-Tip pressure transducer (SPR-1000; Millar) was soaked in 0.9% w/v saline solution to allow for equilibration. A two-point calibration was performed by securing the catheter in a sealed water filled chamber connected to an aneroid sphygmomanometer with 10 s recordings taken at 0 mmHg and 100 mmHg. Between animals the pressure transducer two-point calibration was confirmed and adjusted to account for drift if necessary.

For MO25β blood pressure recordings a polyurethane mouse arterial catheter (MAC-2B; SAI Infusion Technologies) attached to a physiological pressure transducer (MLT844, AD Instruments) was used. The transducer received the pressure signal through a disposable clip-on BP Dome (MLA844, AD Instruments), which in turn was connected to 3-way stopcocks on the front and back ports. The front end 3-way stopcock was connected to the catheter and a 5 mL syringe filled with 500 U/mL heparin solution used to prime and clear the catheter between uses, while the back port 3-way stopcock was connected to an air filled 60 mL syringe and mercury sphygmomanometer used for calibration. To avoid air bubbles in the fluid column that may dampen the pressure signal, the set-up was assembled under water. A two-point calibration was performed by opening the back port 3-way stopcock to connect the air filled syringe and sphygmomanometer to the system for 10 s recordings at 0 mmHg and 140 mmHg. Between animals the pressure transducer two-point calibration was confirmed and adjusted to account for drift if necessary.

Animals (at least 2 months old) were anaesthetised by gas inhalation of isoflurane (chamber induction: 3% v/v with 4 L/min 100% oxygen / nose-cone maintenance: 1.75% v/v with 1.5 L/min 100% oxygen). To minimise stress, animals scheduled for surgery were placed in a separate holding room and the surgical space was cleaned between uses to avoid sight, sound and smell exposure to urine, blood or carcasses, whilst anaesthetic induction was performed in a small red-tinted chamber which was cleaned and voided with 100% oxygen

between animals. Once transferred to the nose-cone and depth of anaesthesia was confirmed by the absence of self-righting, blinking and pain-withdrawal reflexes. Using surgical tape mice were secured with limbs extended in the supine position on a self-regulating rectal probe-coupled heat mat (TC-1000; CWE) which maintained a body temperature of 37 °C. ECG Lead II was recorded using an animal bio amp (FE136; AD Instruments) with needle electrodes inserted subcutaneously into fore and hind limbs (MLA1213; AD Instruments). Fur around the neck area was shaved with an electric trimmer, and under a dissecting microscope the right carotid artery was catheterised (Figure 2.3) with either a 1F Mikro-Tip pressure transducer (SPR-1000; Millar) or 1F polyurethane mouse arterial catheter (MAC-2B; SAI Infusion Technologies) attached to a physiological pressure transducer (MLT844, AD Instruments), which were connected to a bridge amp (FE221 or ML221; AD Instruments) and powerlab system (PL3504/P or ML866; AD Instruments). When the animals had acclimated and stabilised, recordings of body temperature, ECG and blood pressure pulse waveforms were captured at 2000 samples/s using LabChart version 6/7/8 pro (AD Instruments).

For vasopressor experiments, a length of polyurethane tubing suitable for a 25G needle (MAC-02; SAI Infusion Technologies) was measured and cut to ensure its internal volume was < 10 µL. After baseline measurements were recorded the right external jugular vein was cannulated with a saline filled length of tubing attached to a 10 µL Hamilton syringe. Once secure, the cannula was cleared by flushing three times with 10 µL of saline using pre-filled 10 µL Hamilton syringes and the animals was left to acclimate and stabilise before administering vasopressors.

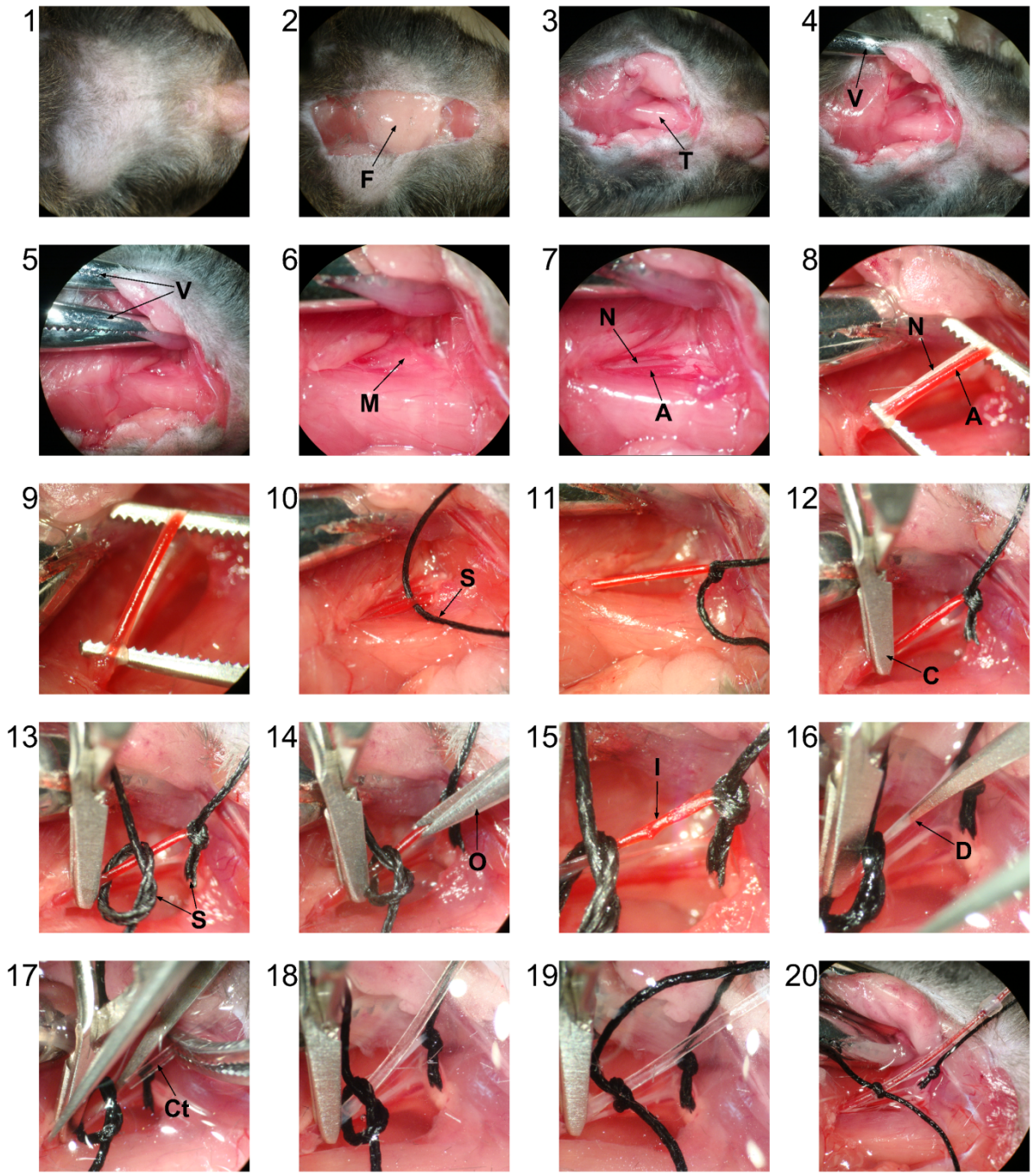

Figure 2.3: Surgical catheterisation of major blood vessels.

[1] Mice were anaesthetised, shaved and secured to the heat mat; **[2]** A midline incision was made to expose subcutaneous (F) fatty tissue and salivary glands; **[3]** The tissue was then blunt dissected away to reveal the trachea (T); **[4]** A haemostat vice (V) is then used to hold the subcutaneous tissue clear of the site; **[5]** Another haemostat vice holds back skeletal muscles away from the carotid artery to provide more working space; **[6]** A thin layer of muscle and connective tissues (M) obscures access to the artery; **[7]** The carotid artery (A) and vagus nerve (N) are exposed by blunt dissection; **[8]** Care is taken to clean the artery and nerve from surrounding tissues with forceps; **[9]** The carotid artery is then separated from the vagus nerve so as to avoid crush injury during the procedure, which would alter blood pressure measurements; **[10]** Silk suture (S) is manoeuvred under the carotid; **[11]** The suture is then tied off distal to the heart to occlude blood flow and extend the artery; **[12]** A temporary clamp (C) is then placed proximal to the heart to occlude blood flow; **[13]** Another silk suture is loosely tied proximal to

the heart; **[14]** With a fine ophthalmic scissors (O) a small incision is made into the artery, distal to the clamp and loose suture knot; **[15]** The incision (I) should ideally be at a 30-45 ° angle, and any excess blood removed by cotton cue tip; **[16]** The area is then bathe in saline solution to avoid drying, and a Dumont forceps (D) is used to pry open the slit created by the incision; **[17]** The catheter (Ct) is then guided into the opening with the aid of the Dumont forceps, and care must be taken to ensure no air bubbles enter; **[18]** once inside the catheter is guided down the artery as far as the temporary clip; **[19]** The loose suture is then tightened to fasten the artery over the catheter; **[20]** The temporary clamp is released allow pressure measurements.

2.2.2.2 Blood Pressure and Heart Rate

Data processing and analysis was performed in LabChart 8 pro. After the stabilisation period, a representative 10 min selection of the trace was analysed using the blood pressure add-on in arterial signal mode with cycle detection set to a minimum height peak of 5 mmHg, no cycle averaging and dicrotic notch minimum height at 0.1% of peak height. Identified beats were then processed in the classifier view and cross-referenced with the chart view to exclude "bad" beats affected by excessive intra-thoracic negative pressure artefact resulting from anaesthetic-induced changes in respiration. Blood pressure parameters (e.g. systolic, diastolic, dicrotic notch pressure) are exported from table view to Excel (Microsoft) and further processing. Mean arterial pressure was calculated as (1/3 peak systolic pressure + 2/3 end diastolic pressure) and pulse pressure as (peak systolic pressure – end diastolic pressure). Heart rate was measured from the R-R wave interval of ECG limb lead II. For measurements taken with the physiological pressure transducer (MLT844, AD Instruments) it was only possible to determine mean arterial pressure and heart rate based on cycle detection of the pressure trace.

2.2.2.3 Pulse Waveform Analysis

A combination of in-built tools and custom designed macros (see appendix 5), scripted by Paula Croft (AD Instruments, UK), were used to perform pulse waveform analysis on beats analysed in Section 2.2.2.1.

To assess arterial stiffness, a method was developed to calculate pulse wave velocity from two pulse arrival time (PAT_{Foot}) measurements separated by a known distance using a single catheter. In brief, after baseline measurements the sampling rate was increased to 10,000 samples/s and recorded for 5 min to obtain the distal PAT_{Foot}. From the point of the securing suture knot, 5 mm was measured and marked with a sharpie pen distal to the knot on the

catheter cable. The catheter was then advanced proximal to the heart until the 5 mm ink mark was at the base of the securing knot, and measurements were recorded for minutes to obtain the proximal PAT_{Foot}. A macro was scripted to calculate the PAT_{Foot} (Figure 2.4) as the difference between the ECG R-wave peak (approximating the aortic valve opening and pressure wave leaving the heart) and the peak of the second derivative blood pressure waveform (approximating the foot "onset" of the pressure wave arriving at the transducer). Pulse wave velocity was calculated for each beat using the following formula: 0.5 mm / (distal – proximal PAT_{Foot}). However, due to unacceptable experimental error and poor reproducibility this technique was not deemed sensitive enough to detect pulse wave velocity differences between genotypes and alternative strategies to determine arterial stiffness were explored.

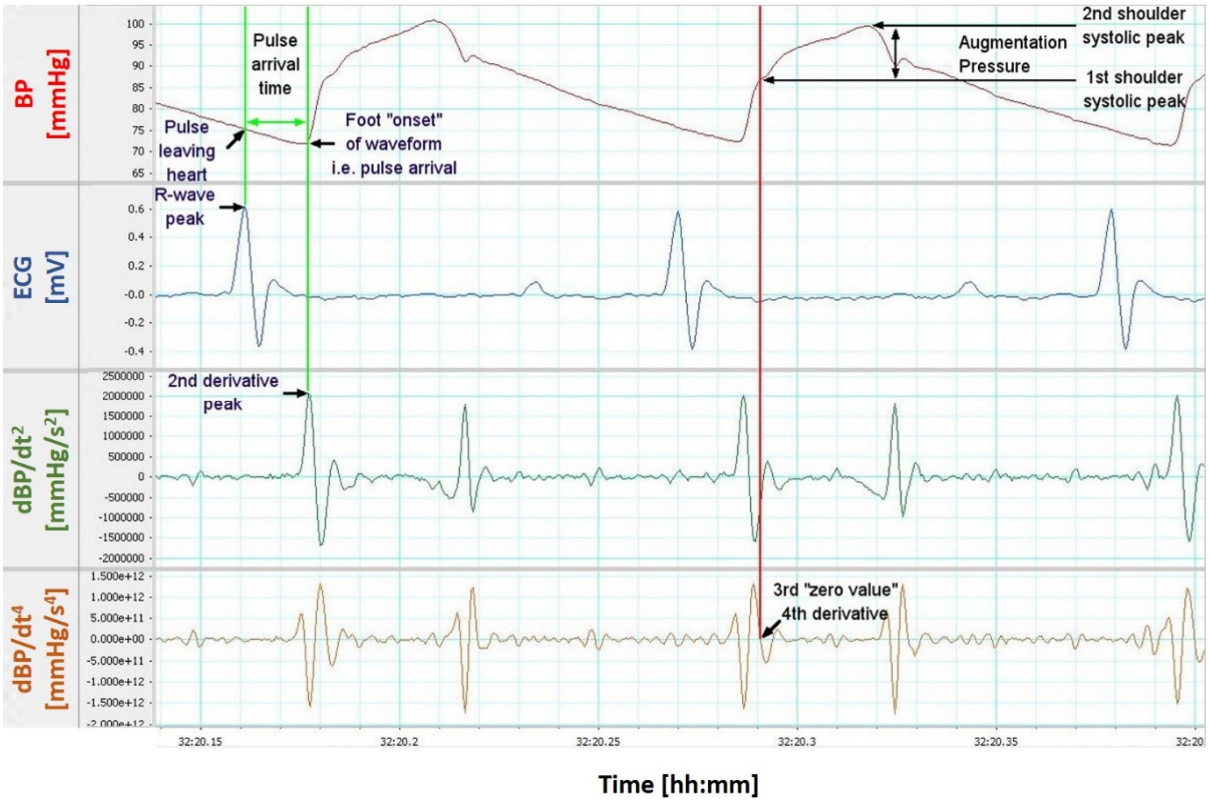

Figure 2.4: Strategies to determine augmentation pressure and pulse arrival time.

1st shoulder systolic peak (anacrotic notch) is identified using the 3rd zero-crossing point of blood pressure (BP) 4th derivative (dBP/dt^4). Augmentation pressure is calculated as the difference between 1st and 2nd systolic peak pressures, and is expressed as a percentage of pulse pressure to obtain augmentation index; a marker of arterial stiffness. Pulse arrival time (PAT_{Foot}) can be calculated from peak of ECG R-wave (approximating aortic valve opening) to peak of blood pressure 2nd derivative (dBP/dt^2) (approximating arrival of pressure wave at the transducer location).

The augmentation index was subsequently selected as a well-established indicator of arterial stiffness, and was determined using a macro developed to detect the anacrotic notch (1st shoulder systolic peak) using the third zero value crossing the fourth derivative of the blood pressure waveform (Figure 2.4), as described in (Kelly *et al.*, 1989). The augmentation pressure was calculated as (peak systolic pressure – anacrotic notch pressure) and augmentation index as (augmentation pressure/pulse pressure).

To assess a marker of vascular resistance, a macro was designed to measure the slope of the log of the diastolic pressure decay (Figure 2.5), 30 ms after the dicrotic notch and 20 ms before the end diastolic pressure (to avoid perturbations caused by aortic valve opening/closing). The reciprocal of this slope (ignoring the +/- sign and calculated from the 20% trimmed mean values) was used to determine the time decay constant of the diastolic pressure decay ($\tau_{Bourgeois}$) which correlates with vascular resistance (i.e. higher resistance increases "emptying" time of blood from large to small vessels), as described previously (Bourgeois *et al.*, 1974). Beats with no identifiable or a misplaced dicrotic notch were excluded from the analysis.

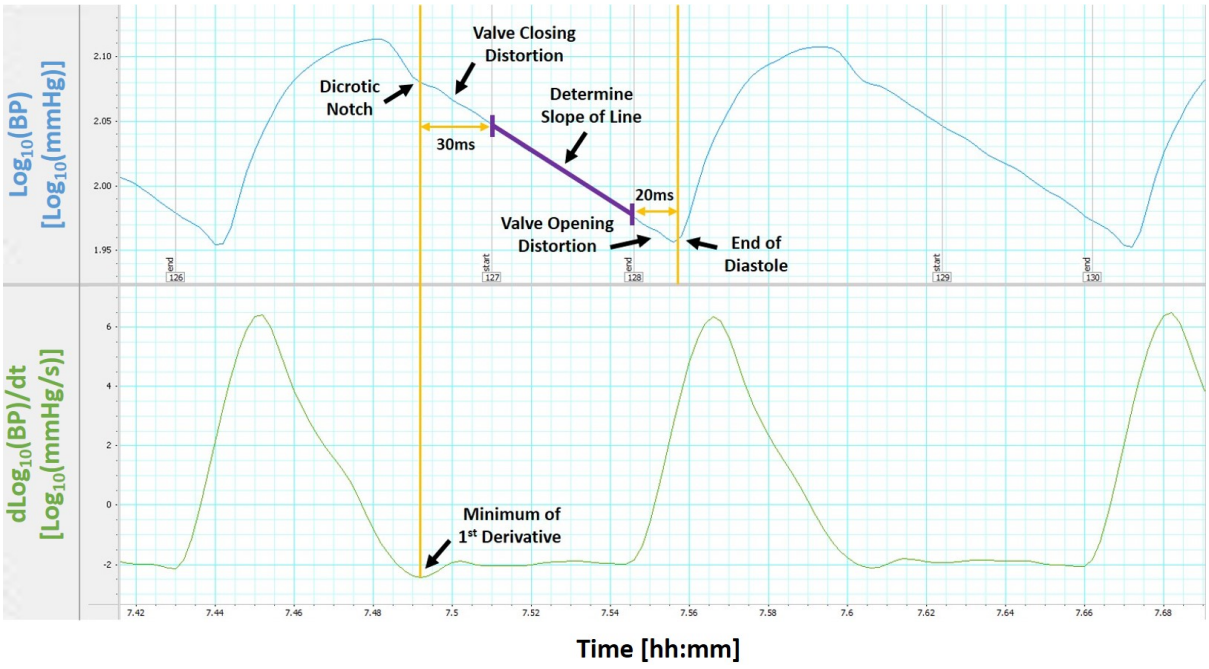

Figure 2.5: Strategy to determine slope of diastolic pressure decay.

The diastolic pressure decay time constant ($\tau_{Bourgeois}$) is calculated from the reciprocal of the slope of the line of the log of the diastolic pressure decay (ignoring the +/- sign) and is used as a surrogate marker of vascular resistance. To avoid aortic value closing/opening waveform artefacts, "start" comments are placed 30 ms after the dicrotic notch and 20 ms before the end of diastole.

2.2.2.4 Vasopressor Dose-Response

In vivo dose-responses to vasopressor agents were taken after baseline blood pressure traces were obtained from mice. The right external jugular vein was cannulated for administration of bolus doses in increasing half-log steps of µg/kg bodyweight (bw) until a plateau in response was reached (Figure 2.6). Initially phenylephrine was administered and after washout and return to baseline, angiotensin II was administered in a similar fashion. Each dose concentration was made up as a half-log serial dilution in sterile 0.9% w/v saline and administered at a volume of 0.2 mL/kg.bw with an accompanying 20 µL 0.9% w/v saline cannula flush between doses. Peak systolic blood pressure responses were measured for each dose and dose-response curves generated and analysed (GraphPad Prism 5 and LabChart 8 Pro dose-response add-on) using a 4-parameter logistical function to determine the estimated dose producing maximum response (E_{max}) and half maximal response (ED_{50}).

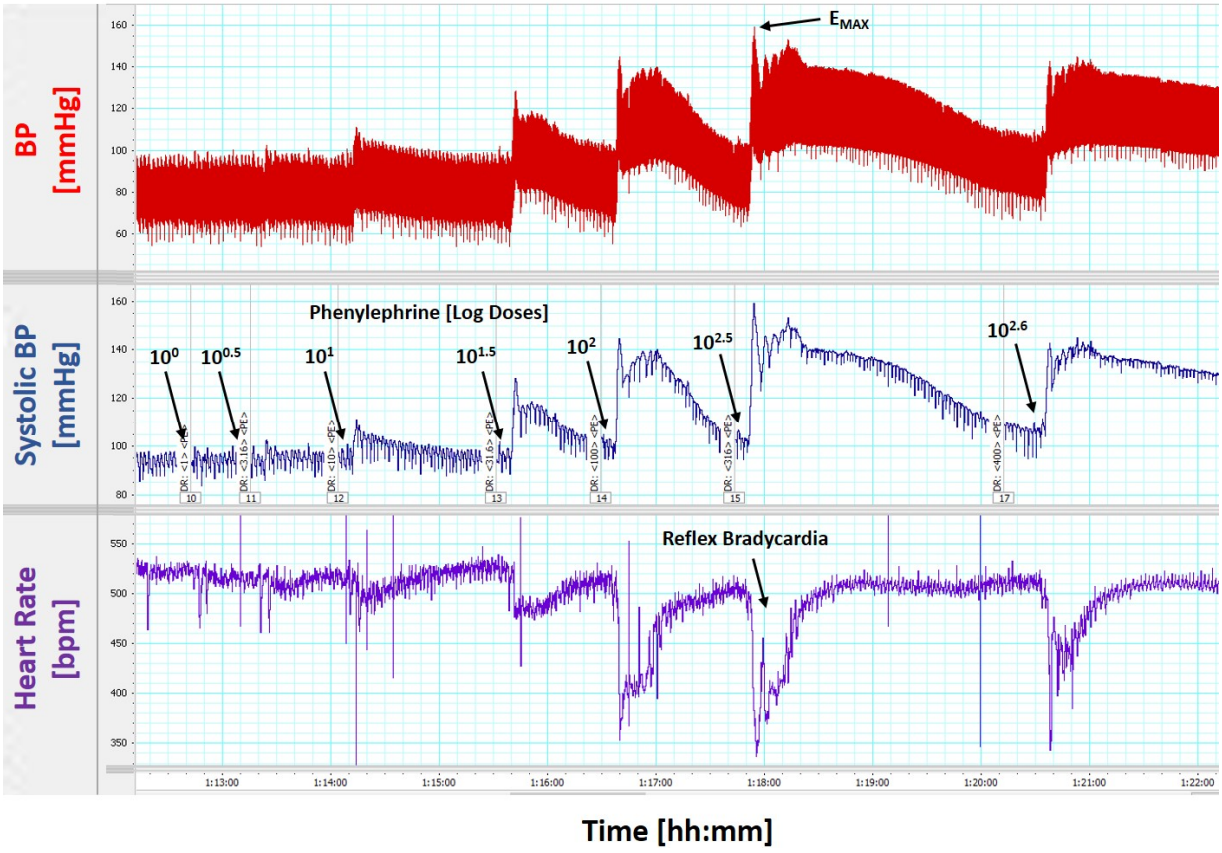

Figure 2.6: Representative *in vivo* vasopressor dose-response.

Bolus doses were administered in increasing half-log steps of µg/kg.bw until a plateau was reached. Consecutive doses were administered once blood pressure and heart rate had approximately returned to baseline. Delivery of drugs and saline flushes were confirmed by transient reflex bradycardia.

2.2.3 Morphometry

2.2.3.1 Gross Morphology

Bodyweight was regularly measured two times per week throughout the study to determine differences in mass in age-matched mice. Body length was also recorded using photographs of mice post-mortem with a reference scale. Fully body length was determined as well as tail:body length ratio using FIJI image analysis software with the set scale and measuring tools.

2.2.3.2 Cardiac Ventricular Mass

Post-mortem the left ventricle and septum were separated from the heart and wet weight measurements were taken. The combined weights of the left ventricle and septum were then normalised against bodyweight to compare between genotypes.

2.2.3.3 Vascular Microanatomy

Three 5 μm sections of thoracic aorta taken at upper (proximal to the heart), mid and lower (nearest the diaphragm) segments per mouse. These were de-paraffinised, rehydrated and stained with haematoxylin and eosin, dehydrated and mounted by Nichola Figg (Division of Cardiovascular Medicine, University of Cambridge). Each section was imaged under brightfield illumination and halogen lamp epifluorescent imaging of autofluorescent elastin laminae with a GFP filter set. Using FIJI image analysis software, macros were scripted (see appendix 5) to draw eight lines at ~22.5 ° to one another that intersect the aortic ring at a total of 16 points. At the point of intersection on the outer circumference the distance from the external lamina to the inner lumen was measured. The average of the three rings (max of 16 points per ring, with points excluded if they fell on an arterial branching point or incomplete portion of a ring) was used to calculate the average thoracic aorta intima-media wall thickness. The above step was repeated to count the average number of elastic laminae in the thoracic aorta of each mouse. Data collection and analysis was carried out in a blinded fashion throughout by a supervised operator, James Ferryman (University of Cambridge).

2.3 Histology

2.3.1 Light Microscopy

2.3.1.1 Sample Preparation

Excess tissues from harvested mouse organs were carefully removed (e.g. kidney decapsulation) prior to immersion fixation in fresh 4% w/v formaldehyde-PBS pH 6.9 for 16 h at 37 °C, followed by three washes in PBS and storage at 4 °C. Samples were then paraffin embedded and microtome sectioned to 5 μm thickness by Nichola Figg (Division of Cardiovascular Medicine, University of Cambridge) and stored in darkness at room temperature for later histochemical and immunofluorescent analysis.

Readily available glass slides of formalin-fixed paraffin embedded human tissue pre-sectioned to 5 μm thickness were obtained from anonymised male and female donors through the Cambridge Human Research Tissue Bank for immunohistochemistry.

2.3.1.2 Antigen Retrieval and Immunostaining

Sections were deparaffinised in Histoclear (National Diagnostics) and rehydrated in graded steps from 100% to 70% methanol. An antigen retrieval step was performed with R-Universal buffer in the 2100 antigen retriever for a single heat-pressure cycle (Aptum Biologics). Sections were permeabilised with 0.05% v/v Triton-X100-PBS for 20 min and blocked for 1 h at 37 °C with sterile-filtered (0.22 μm) 2% v/v donkey serum in 0.05% v/v Triton-X100-PBS. Primary antibodies were diluted in sterile-filtered (0.22 μm) 0.05% v/v Triton-X100-PBS with 1% v/v donkey serum at the concentrations listed in Table 2.2 and incubated overnight in humidity chambers for 16 h at 4 °C. To prevent non-specific staining, phospho-specific antibodies included the addition of 10 μg/mL of the non-phospho form of the immunogenic peptide per 2 μg/mL of antibody used. Negative controls for secondary antibody specificity and autofluorescence omitted the primary antibody and were processed in parallel. Slides were then washed for 20 min in 0.05% v/v Triton-X100-PBS and incubated in secondary antibody for 1 h at 37 °C light-shielded humidity chambers. Cross-absorbed donkey IgG conjugated Alexa

Fluor 488, 568, 633 and 647 secondary antibodies (Life Technologies/Abcam) were used at 1:200 diluted in sterile-filtered (0.22 μm) 1% v/v donkey serum in 0.05% v/v Triton-X100-PBS for immunofluorescent labelling of mouse tissues. Slides were washed as above, and in some cases counterstained using Sytox orange nucleic acid stain (S11368 – Life Technologies) before being mounted using Prolong gold antifade (P36930 - Life Technologies) and shielded from light. Human immunohistochemistry DAB staining was performed by Nichola Figg (Division of Cardiovascular Medicine, University of Cambridge) with ImmPRESS Reagent peroxidase Universal anti-mouse/rabbit IgG (MP-7500, Vector) kit, after which slides were then dehydrated through graded methanol steps and mounted with DPX.

Target	Immunogen [Residues]	Conc.	Host	Code	Source
CUL3	Peptide [Hu: 681-704]	2 µg/mL	Rb	-	(Sumara *et al.*, 2007)
KLHL3 [Mo]	Peptide [Mo: 1-21]	4 µg/mL	Sh	S740D	MRC-PPU
KLHL3 [Hu]	Peptide [Hu: 1-32]	4 µg/mL	Rb	HPA051291	Atlas Antibodies
LAMP1	Peptide [Hu: 350-CT]*	1 µg/mL	Rb	ab24170	Abcam
NCC	Peptide [Rt: 74-95]	2 µg/mL	Rb	ab95302	Abcam
pNCC T44	Peptide [Mo: 38-52]	2 µg/mL	Sh	S242C	MRC-PPU
NKCC2	Protein-GST [Hu: 1-174]	2 µg/mL	Sh	S838B	MRC-PPU
NKCC2 pS91	Peptide [Hu: 86-97]	2 µg/mL	Sh	S451C	MRC-PPU
PVALB	Protein-HPLC [Rt: FL]	1:2000	Rb	PV25	Swant
SPAK	Protein-GST [Mo: 424-556]	4 µg/mL	Sh	S669D	MRC-PPU
SPAK pT233	Peptide [Hu: 226-238]	4 µg/mL	Sh	S668D	MRC-PPU
Ubiquitin	Protein-KLH [Hu: FL]	1:500	Mo	ab7254	Abcam
MO25β	Protein-GST [Hu: FL]	2 µg/mL	Sh	S082B	MRC-PPU
ROMK	PrEST [Hu: 303-387]	1 µg/mL	Rb	HPA026962	Atlas Antibodies
OSR1	Peptide [Mo: 333-352]	2 µg/mL	Sh	S149C	MRC-PPU
FTCD	Protein [Rt: FL]	5 µg/mL	Mo	ab27043	Abcam
Calnexin	Peptide [Hu: 550-CT]*	2 µg/mL	Rb	ab22595	Abcam
EEA1	Peptide [Hu: 1350-CT]*	2 µg/mL	Rb	ab2900	Abcam
LC3	Peptide [Hu: 1-100]*	5 µg/mL	Rb	NB100-2220	Novus Biologicals
WNK1	Protein [1079-1293]*	2 µg/mL	Rb	ab137687	Abcam
WNK4	Peptide [Mo: 1-14]	4 µg/mL	Sh	S726D	MRC-PPU

Table 2.2: Primary antibodies used in immunostaining.

Antibodies were used for both mouse and human immunostaining unless otherwise stated. Abbreviations: Phosphorylated amino acid (p), C-terminal (CT), Full-length (FL), Human (Hu), Mouse (Mo), Rabbit (Rb), Rat (Rt), Sheep (Sh), Recombinant Protein Epitope Signature Tag (PrEST), * indicates proprietary immunogens where the exact peptide sequence is unknown, but lies within the given range.

2.3.1.3 Image Acquisition and Processing

Immunofluorescent images were acquired using a Leica TCS SP2 laser-scanning confocal microscope mounted on an upright Leica DM RXA fluorescent microscope body. Argon 488 nm, HeNe 543 nm and HeNe 633 nm excitation laser lines were used with a triple dichroic filter 488/543/633 and a Leica HC PL FLUOTAR 20X/0.5 NA dry or Leica HCX PL APO 63X/1.40 NA oil objective to acquire images. Acquisition Parameters: 12-bit, 1024x1024 pixels, digital zoom 2.0X (with 20X objective) or 2.6X (with 63X objective), pinhole 1 airy disk, 800 Hz scan speed, 4-line Kalman filtering, sequential (by line) channel imaging, 10 slice z-stack of 5 µm. Laser power intensity, spectral detectors, offset (set to zero) and PMT gain settings were kept uniform for all samples to be compared. Images were saved as uncompressed TIFF files.

Immunohistochemically stained specimens were imaged in brightfield with white light source set to Köhler illumination on an Olympus BX51 upright epifluorescent microscope using a UPLANFL 20X 0.5 NA objective with the Infinity3 (Lumenera) CCD set to 1936x1456 pixels. Exposure times and light source intensity were kept uniform for all samples to be compared.

Post-acquisition image processing was performed in FIJI image analysis software (64-bit). Macros were scripted and developed to automate batch processing of image data sets (see appendix 5) of multicolour channel confocal z-stacks. Fluorescent z-stacks underwent background subtraction (1000 pixel radius rolling ball, no smoothing) and either average or maximum intensity z-projection. Brightness and contrast were adjusted by linear histogram stretching to enhance visibility. Any images to be compared to one another were processed evenly across the whole image in parallel, the exception to this were nuclei images where brightness and contrast were performed on each image independently to ensure the best visibility. Similarly brightfield images underwent linear histogram stretching to increase visibility uniformly across the image.

2.3.2 Electron Microscopy

2.3.2.1 Sample Preparation

A subset of tissues from animal used in section 2.2.1.1 were selected for exploratory electron microscopy. Samples were hemisected prior to paraffin embedding and one half was impregnated with sucrose in graded steps (10%, 30%, 60% w/v) until the tissue no longer floated and was then stored long term at 4 °C until needed.

Follow-up studies were performed on samples prepared by perfusion fixation. Mice were fasted for approximately 4 h before being placed under deep non-recoverable anaesthesia. First, an incision was made along the midline to expose the diaphragm and abdominal viscera. To access the heart the ribcage was retracted by using surgical scissors to cut along the sides of the ribs and diaphragm. Next, a small incision was made into the left ventricle to allow placement of a gavage needle which was secured with a haemostat. The right atrium was cut for drainage, and the gavage needle connected to the Perfusion One Sacrifice System (Leica Biosystems). Blood and extracellular fluids were rapidly removed by flushing 20-50 mL of pre-wash solution containing 9.25% w/v sucrose, 0.1% w/v Na Nitrite and 50 IU/mL Heparin; this should prevent clotting, tissue shrinkage and preserve the extracellular space. Once the solution from the heart ran clear and the liver and kidneys had become pale, 100-150 mL of perfusion fixative containing 0.05 M Na Cacodylate, 2% v/v gluataraldehyde, 3% w/v formaldehyde and 2 mM $CaCl_2$ at pH 7.4 was run through until the animal was completely fixed and stiff (i.e. rigid tail). All solutions were perfused at a constant pressure of 120 mmHg at ~37 °C to prevent temperature shock induced translocation of membrane proteins. Tissues were then removed and sectioned by slicing cross-sections of 1-2 mm with a fresh razor blade, whilst taking care to avoid compression artefact. Sections were further immersion fixed in perfusion fixative solution overnight at 4 °C, washed 3 times in 0.05 M Na Cacodylate pH 7.2 and stored at 4 °C.

2.3.2.2 Block Face Scanning Electron Microscopy

Immersion-fixed sucrose impregnated samples were subsequently trimmed to 1 mm thick slices and further fixed in perfusion fixation solution at 4 °C for 6 h, washed 5 times in cold

0.05 M Na Cacodylate pH 7.2 containing 2 mM $CaCl_2$. Right before use, a solution containing 3% w/v potassium ferricyanide in 0.3 M Na Cacodylate with 4 mM $CaCl_2$ was combined with an equal volume of 4% w/v aqueous osmium tetroxide (EMS). Immersion or perfusion fixed tissue slices were incubated in this solution for 48 h at 4 °C, rinsed 5 times with deionised water at room temperature and then placed in filtered freshly made 1% w/v thiocarbohydrazide (Sigma Aldrich) solution for 20 - 30 min at room temperature and protected from light. Wash steps were repeated, followed by incubation in 4% aqueous, osmium tetroxide for 60 min at room temperature and more washing steps as before. To increase contrast, samples were incubated in 1% w/v uranyl acetate (Maleate buffered to pH 5.5) at 4 ° for 4 days and washed 5 times. Followed by incubation at 60 ◦C for 30 min in freshly made Walton's lead aspartate solution containing 0.02 M lead nitrate and 0.03 M aspartic acid adjusted pH to 5.5; repeat rinse steps. Samples were then dehydrated through 2 times each of 50%, 70%, 90%, and 100% ethanol. 2 time dried ethanol, 2 times dry acetone and 2 times dry acetonitrile. 50/50 acetonitrile/Quetol 651(no BDMA) overnight, 3 days in Quetol 651(no BDMA), 3 days Quetol 651 with BDMA and a final incubation at 60 °C for 48 h minimum.

Tissue blocks up to 4 x 4 mm attached to 13 mm Cambridge SEM stubs were sectioned with a Leica Ultracut UCT to produce 1 μm sections. These were stained with methylene blue, cover-slipped and imaged with either a high resolution flat-bed scanner or a macro-scanner. The block faces were polished to an ultra-smooth finish with a histo-diamond knife. They were coated with 15 nm of carbon and imaged in a FEI Verios 460 operated in Back Scattered Electron mode at 4kV with a probe current of 200 – 400 pA.

Block Face Scanning Electron Microscopy protocols and imaging were performed by Jeremy Skepper (Cambridge Advanced Imaging Centre, University of Cambridge). Images of the entire 4 x 4 mm block face were obtained at high resolution and stitched together using the FEI MAPS software or FIJI stitching plugins for qualitative analysis of cell ultrastructure. Distal convoluted tubule (DCT) cells in the renal cortex were identified for the focus of analysis by the high degree of basolateral membrane infolding and adjacent high density of columnar mitochondria.

2.4 Molecular Biology and Biochemistry

Protocols in sections 2.4 were performed or supervised by either Jinwei Zhang, Frances-Rose Schumacher or Paola de los Heros (MRC PPU, University of Dundee), unless otherwise stated.

2.4.1 CUL3 Study

2.4.1.1 Plasmids and protein purification

The following plasmids and/or protein purifications have been described elsewhere in (Ohta *et al.*, 2013): KLHL3 (DU23218), DAC-TEV-CUL3-RBX1 (DU23291), His-UBE1 (DU32888), His-TEV-UBE2D3 (DU15703), and (Kelsall *et al.*, 2013): Nedd8 (DU20689), UBE2M (DU15804), APPBP1/UBA3 heterodimer (Nedd8 activating E1) (DU21784).

DAC-TEV- CUL3$^{\Delta 403\text{-}459}$-RBX1 (DU23292) was cloned in a comparable way to DAC-TEV-CUL3^{WT}-RBX1 (DU23291). Specifically, the pFastBac Dual DAC-TEV expression system was created by subcloning a BglII-BamHI-flanked PCR product encoding the full length DAC-tag followed by a TEV protease site into a pFastBacTM Dual (Life Technologies, UK). Human Cullin3 (Δ403-459; Genbank NM_003590.4) was codon optimised for expression in insect cells and custom synthesised (GenScript USA Inc) before being subcloned downstream of the DAC-tag in cassette two of this vector. Human RBX1 (Genbank NM_014248.2) was amplified from an EST IMAGE clone 3138751 and subcloned into cassette one (untagged). Human CAND1 (Genbank NM_018448.3) was amplified as a Not1 flanked ORF from EST IMAGE clone 5265409 and sub-cloned into pGEX6P-2 (GE Healthcare LifeSciences UK) for bacterial expression with an N-terminal GST tag. All PCR reactions were carried out using KOD Hot Start DNA Polymerase (Merck Millipore, Germany). All full-length products or fragments were cloned into pSc-B (Agilent) and sequenced in full prior to further subcloning or manipulation. DNA sequencing was performed by the Sequencing Service at the College of Life Sciences, University of Dundee (www.dnaseq.co.uk)

Human recombinant CUL3$^{\Delta 403\text{-}459}$-RBX1 or CUL3^{WT}-RBX1 was expressed in a multibac vector with a Dac-TEV-fusion tag on the CUL3 and untagged RBX1 (Lee *et al.*, 2012*b*). Proteins were expressed in the baculovirus system in Sf21 cells cultured in Insect-

Protein-free Insect Cell Medium (Lonza). The fusion protein was captured from the lysate by incubation with ampicillin-Sepharose. After washing, the protein was recovered from the solid phase by incubation with C-terminally His-tagged TEV-protease (10 μg per 1 mg substrate). The protease and any free Dac-tag were removed with Ni-agarose and ampicillin-Sepharose. The protein was then concentrated and further purified by size-exclusion chromatography (SEC) in 50 mM HEPES pH 7.5, 150 mM NaCl, 10% glycerol.

Human recombinant CAND1 was expressed as an N-terminally GST-tagged fusion protein in BL21 cells. Expression was induced with 50 μM IPTG at 15 °C for 16 h. Following cell lysis, GST-CAND1 was captured on Glutathione resin, washed and then eluted from the resin with 10 mM reduced glutathione in 50 mM HEPES pH 7.5, 150 mM NaCl, 10% glycerol w/v, and 1 mM DTT. The protein was then dialysed to remove glutathione.

Nedd8 was expressed as an untagged protein in BL21 cells, and following induction with 1 mM IPTG at 16 °C cells were lysed and frozen. Upon thawing benzonase and 2 mM $Mg(C_2H_3O_2)_2$ were added and cells were disrupted by sonication. Insoluble material was pelleted and this pellet was resuspended in 50 mM Tris pH 7.5, 150 mM NaCl, and washed thrice. To extract Nedd8, the pellet was resuspended in 8 M Urea and mixed overnight. Following clarification by centrifugation the supernatant was diluted four-fold with MQ water and dialyzed thrice to remove Urea and enable Nedd8 refolding. Contaminants were removed by depletion using a Q-Sepharose column. The Nedd8 was concentrated prior to a final purification by SEC in 20 mM HEPES pH 7.5, 150 mM NaCl, and 0.03% Brij 35.

2.4.1.2 Antibodies

The following antibodies were raised in sheep and affinity purified on the appropriate antigen by the Division of Signal Transduction Therapy Unit at the University of Dundee: WNK1-total antibody (residues 2360-2382 of human WNK1, S62B), WNK4 N-terminal antibody (residues 1-14 of mouse WNK4, S726D), SPAK-mouse N-terminal antibody (2–76 of mouse SPAK, S668D), SPAK-mouse C-terminal antibody (424-556 of mouse SPAK, S669D), SPAK/OSR1 (T-loop) phospho-Thr233/Thr185 antibody (226–238 of human SPAK or residues 178–190 of human OSR1, TRNKVRKpTFVGTP, S204C), SPAK phospho-Thr233 antibody (226–238 of human SPAK, TRNKVRKpTFVGTP, S668B and S668D), NKCC1-total antibody (residues 1-260 of shark NKCC1, S841B), NCC phospho-Thr60 antibody (residues 54–66 of human

NCC phosphorylated at Thr60, RTFGYNpTIDVVPT, S995B), NCC phospho-Thr44 antibody (residues 38–52 of mouse NCC phosphorylated at Thr44, SQPSHLTpHGSTLYMRRR, S242C), KLHL3 N-terminal mouse (1-21 of mouse KLHL3, S740D). The anti-ERK1/2 antibody (9102) was purchased from Cell Signaling Technology. The anti-FLAG antibody (F1804), anti-β-actin antibody and anti-His antibody were purchased from Sigma-Aldrich. The rabbit anti-human CUL3 antibody was a kind gift from Izabela Sumara at the IGBMC, Strasbourg (Sumara *et al.*, 2007). The following commercial rabbit anti-human antibodies were obtained and used for immunodetection: KLHL3 antibody (HPA051291) from Atlas Antibodies, KLHL3 (AB196776) (~14% immunogen peptide homology with KLHL2), NCC-total [SLC12A3] (AB95302) and LAMP1 (AB24170) from Abcam, PV25 (PVALB) from Swant. The goat anti-GFP (AB5450) and the mouse monoclonal anti-ubiquitin (AB7254) were purchased from Abcam. The MYPT1 phospho-Thr696 mouse monoclonal antibody (MAB0001) was obtained from Abnova. Secondary antibodies coupled to horseradish peroxidase used for immunoblotting were obtained from Pierce. Secondary antibodies conjugated to fluorochromes for LiCor odessey western blot scanning were obtained from Licor (www.licor.com) and Life Technologies.

2.4.1.3 *In vitro* assays

Ubiquitin-E2 discharge assays were performed based on the method described (Plechanovová *et al.*, 2011). Firstly, His-UBE2D2 (150 μM) was incubated in the presence of 2 mM ATP, 5 mM $MgCl_2$, 200 μM ubiquitin and 0.25 μM UBE1 in 50 mM HEPES pH 7.5, 150 mM NaCl, 10% glycerol, 1 mM DTT at 16 °C for 15 min. To stop the reaction ATP was depleted by incubating the charging mixture with Apyrase (4.5 U/mL; New England Biolabs) at 16 °C for 10 min. To this, 1 μM E3 was added and discharge reactions were then allowed to proceed for the time indicated in the figure, at 30 °C. Reactions were stopped by the addition of non-reducing SDS-Laemmli sample buffer. 16 % Bis-Acrylaminde non-reducing SDS PAGE, followed by immunodetection with anti-His antibody allowed visualisation of ubiquitin discharge. E3 ubiquitin-ligase activity assays were based on those described previously in (Ohta *et al.*, 2013). When used as a substrate in assays, full-length WNK kinases were purified from HEK-293 cells, either 5 μL of immunoprecipated endogenous WNK1 protein derived from 0.5 mg of HEK-293 cells, or 5 μL of immunoprecipated over-expressed FLAG-WNK4 from 0.05 mg of HEK-293 cells was used for each assay reaction. Ubiquitylation assays

typically contained 20 mM HEPES/HCl (pH 7.5), 150 mM NaCl, 2 M DTT, 10% w/v glycerol, 8 μM CUL3-RBX1 complex (WT or mutant), 7 μM KLHL3, 7 μM UBE1, 60 μM UBE2D3, and 3000 μM ubiquitin. The concentrations of some components were altered on occasion (e.g. Fig. 3b) to best illustrate a given point. Reactions were initiated by adding ATP and $MgCl_2$ to a final concentration of 1 mM and samples were incubated for the times indicated at 30 °C. Reactions were stopped by the addition of SDS sample buffer and samples were analysed after SDS-PAGE followed by immunoblotting or Coomassie blue gel staining. For the N8-ligase activity assays: 1 μM E3 was incubated at 30 °C with 68 μM Nedd8, 8 μM UBE2M, and 0.2 μM NAE in the presence of 0.15 mM ATP, 1.5 mM $MgCl_2$ 50 mM HEPES pH 7.5, 150 mM NaCl, 20% w/v glycerol for the time indicated. Reactions were stopped by the addition of SDS sample buffer and samples were analysed following SDS-PAGE separation and Coomassie blue staining.

2.4.1.4 *In vitro* protein interaction pull downs

For KLHL3-CUL3: anti-KLHL3 resin was made by covalently coupling anti-KLHL3 antibody (S377D) to Protein-G-Sepharose utilising dimethyl pimelimidate. Anti-KLHL3 resin, or control resin (prepared in the absence of any antibody) was incubated with saturating amounts of purified KLHL3, and washed thrice, resulting in KLHL3-resin. This resin was then incubated with $CUL3^{WT}$ or $CUL3^{\Delta 403-459}$ at 4 °C for 1 h, before being washed thrice with PBS 0.02% Tween20. For CAND1-CUL3: Purified GST-CAND1 or GST was incubated in excess with resin at 4 °C resulting in GSH-resin-GST or GSH-GST-CAND1 resin. Each resin was then incubated with purified $CUL3^{WT}$ or $CUL3^{\Delta 403-459}$ for 1 h at 4 °C before being washed once with PBS 0.02% Tween20, then twice with PBS in the absence of detergent. Following washing, volumes were reduced to a minimum and proteins were eluted from the resin by the addition of SDS sample buffer, prior to analysis by SDS-PAGE and immunoblotting.

2.4.1.5 Cell culture

HEK (human embryonic kidney)-293 cells were cultured in 14-cm-dishes in DMEM (Dulbecco's modified Eagle's medium; Life Technologies) supplemented with 10% v/v foetal bovine serum, 2 mM L-glutamine, 100 units/mL penicillin and 0.1 mg/mL streptomycin.

Protein expression was induced for 24 h with 1 μg/mL tetracycline (Life Technologies). To obtain endogenous WNK1 for activity assays the immunoprecipitation protocol was followed as described in (Ohta *et al.*, 2013). To obtain wild type FLAG-WNK4 cell lines were utilised from (Ohta *et al.*, 2013; Schumacher *et al.*, 2014). When FLAG-WNK4 was to be used for in vitro ubiquitylation assays, a 14 cm plate of confluent cells was lysed in 0.5 mL ice cold Mammalian lysis buffer A (Mammalian lysis buffer A: 50 mM Tris/HCl (pH 7.5), 0.15 M NaCl, 1 mM EGTA, 1 mM EDTA, 1 mM Na_3VO_4, 50 mM NaF, 5 mM $Na_4P_2O_7$, 0.27 M sucrose, 1% w/v Nonidet P40, 1 mM benzamidine, 0.1 mM PMSF, 0.1% 2-mercaptoethanol, Roche protease inhibitor mix (1 tablet in 50 mL) for M2 affinity purification). Lysates were clarified by centrifugation and to this 10 μL M2-resin per 100 μL lysate was added. Incubation of the resin with the cellular lysate for 1 h at 4 °C was followed by two-washes with Mammalian lysis buffer A, and two further washes with 1x PBS to give a pure M2-Flag-WNK4 slurry. For interaction studies with FLAG-CUL3^{WT} and FLAG-CUL3$^{\Delta 403-459}$, the same method was followed as above, with an alternative mammalian lysis buffer B (50 mM HEPES/KOH pH 7.2, 5 mM $Mg(C_2H_3O_2)_2$, 70 mM $KC_2H_3O_2$, 0.2 % w/v Triton X-100, 10% w/v glycerol, 0.2 mM EDTA, 1 mM Na_3VO_4, 50 mM NaF, 5 mM $Na_4P_2O_7$ and Roche protease inhibitor mix (1 tablet in 50 mL). When it was desirable to prevent deneddylation, buffers were supplemented with 50 μM 1,10-phenanthrolin.

2.4.1.6 Mass spectrometry analysis

Prior to SDS PAGE samples were reduced and alkylated in the following way. Reactions were stopped at the time shown and incubated at 95 °C in 1x LDS (Invitrogen) 5 mM DTT for 1 min. Alkylation occurred at room temperature for 30 min by addition of 20 mM iodoacetamide (20 mM) to the samples. To quench the reaction DTT was added to a final concentration of 20 mM and the sample then process on precast 4-12% gradient gel (Invitrogen). Gel pieces were excised as shown by the boxed areas in the figure and in gel digestion of the proteins with 5 μg/mL trypsin and subsequent analysis.

Mass spectrometric analysis was performed by LC-MS-MS on a Linear ion trap-orbitrap hybrid mass spectrometer (Orbitrap-VelosPro, Thermo) coupled to a U3000 RSLC Hplc (Thermo). Peptides were trapped on a nanoViper Trap column, 2 cm x 100 mm C18 5 mm 100 Å (Thermo, 164564) then separated on a 15 cm Thermo EasySpray column (ES800) equilibrated with a flow of 300 nL/min of 3% Solvent B [Solvent A: 2% Acetonitrile, 0.1%

formic acid, 3% DMSO in H2O; Solvent B: 80% acetonitrile, 0.08% formic acid, 3% DMSO in H2O]. The elution gradient was as follows, Time(min):Solvent B(%); 0:3, 5:3, 45:35, 47:99, 52:99, 55:3, 60:3. The instrument was operated with the "lock mass" option to improve the mass accuracy of precursor ions and data were acquired in the data-dependent mode, automatically switching between MS and MS-MS acquisition. Full scan spectra (m/z 400-1600) were acquired in the orbitrap with resolution R = 60,000 at m/z 400 (after accumulation to an FTMS Full AGC Target; 1,000,000; FTMS MSn AGC Target; 50,000). The 20 most intense ions, above a specified minimum signal threshold (2,000), based upon a low resolution (R = 15,000) preview of the survey scan, were fragmented by collision induced dissociation and recorded in the linear ion trap, (Full AGC Target; 30,000. MSn AGC Target; 5,000). Data files were analysed by Proteome Discoverer 1.4-SP1 (Thermo), using Mascot 2.4.1 (www.matrixscience.com), and searching an in-house database containing the relevant sequences. Scaffold (www.ProteomeSoftware.com) was also used to examine the Mascot result files. Allowance was made for the following fixed, Carbamidomethyl (C), and variable modifications, Oxidation (M), Dioxidation (M), GlyGly (K), LeuArgGlyGly (K) and Phospho (ST). Error tolerances were 10 ppm for MS1 and 0.6 Da for MS2.

2.4.1.7 Mouse kidney & testes lysates

Mice tissues were rapidly harvested and either; snap frozen in liquid nitrogen and stored at -80 °C, or incubated in 1 mL RNAlater solution (Sigma-Aldrich) at 4 °C for 16-30 h before being removed from this buffer, patted dry with clean tissue and then stored dry at -80 °C. Lysates were prepared by homogenising tissue on ice using a Polytron PT1200C homogeniser (Kinematica) in 2 mL ice-cold Mammalian lysis buffer and then clarified by centrifugation at 13,000 rpm for 30 min. The clarified supernatant was then quantified and used immediately. Any excess sample was snap-frozen in liquid nitrogen in single-use aliquots for use as required.

The lysates to be used for immunoprecipitation were prepared in the same way, with the following exceptions, all designed to promote deneddylation of the cullin proteins. Detergent was not included in the lysis buffer. Following homogenisation samples were incubated on ice for 4 h. Following clarification by centrifugation at 13,000 rpm for 30 min, samples were aliquoted into fractions and either frozen in liquid nitrogen and stored at -80 °C, or used immediately. Clarified supernatant was incubated at room temperature for 1 h to enable further deneddylation, samples were then cooled on ice and centrifuged a second time to ensure

any precipitate was removed. Anti-CUL3 antibody (S067D) cross-linked (DMP) to Protein G agarose was mixed with saturating amount of lysate and incubated rotating overnight at 4 °C. The next morning, the agarose beads were washed thrice with mammalian lysis buffer B and twice with 1x PBS. Proteins were eluted from beads by SDS-sample buffer addition and boiling at 95 °C for 10 min prior to centrifugation and SDS-PAGE and immunodetection.

2.4.1.8 Immunoblotting

Lysates, or protein mixes were boiled at 95 °C with 1x SDS Laemmli sample buffer, for 5 min before being subject to SDS-PAGE (8 or 10% Tris-Glycine gel, or 4-10% Gradient Gels (Life Technologies) or self-prepared 16% bis-acrylamide. Gels were transferred to nitrocellulose membrane using the standard wet transfer method (15% MeOH Towbin transfer buffer). Following blocking of the membranes (TBST 5% w/v dried skimmed milk) they were then incubated overnight at 4 °C with the primary antibody indicated. All DSTT produced sheep antibodies were used at 2 µg/mL, and phospho-specific antibodies included the addition of 10 µg/mL of the dephospho-peptide used to raise the antibody. Commercial antibodies were diluted 1 in 1000. Membranes were then washed in TBST five times and incubated with the appropriate secondary-HRP antibody at room temperature at 1:5000 dilution. Membranes were subsequently washed five times and the HRP-signal was detected using chemiluminescence reagent (Pierce). Immunoblots were developed using an automatic film processor (SRX-101, Konica Minolta Medical).

2.4.1.9 CUL3 structural docking

Cullin3 was modelled using Phyre2 server (Kelley & Mje, 2009) using human CUL3$^{\Delta 403\text{-}459}$ as the sequence input and Cullin1 chosen for the docking model (Q13616, PDB:1LDK) (Zheng *et al.*, 2002). A coil was predicted in place of the missing structural elements. UBE2D~UB was docked to RBX1 using PDB: 4AP4. Images were modified and made in UCSF Chimera (http://www.cgl.ucsf.edu/chimera) (Pettersen *et al.*, 2004).

2.4.1.10 Immunoprecipitation (mouse tissue and cell extracts)

Lysates of cellular preparations (buffer B) from FLAG-tagged CUL3 were mixed with M2 resin in the presence of 50 μM 1,10-phenanthrolin to prevent deneddylation, and were incubated rotating at 4 °C for 1 h. Resins were washed twice with Mammalian buffer B and twice with 1xPBS the volume was then reduced to ~15 μL and following the addition of SDS-gel sample buffer to 1x, samples were boiled and the entire sample was loaded to allow analysis by SDS-PAGE and immunodetection with the antibodies indicated.

2.4.1.11 Human and mouse aorta sample preparation

Human aortic tissue were collected from donors through transplant coordinators at Addenbrooke's Hospital, Cambridge. All samples were handled in accordance with the policies and procedures of the Human Tissue Act and with the approval of the Local and Regional Ethics Committees. Mouse tissues were rapidly harvested, perivascular fat and residual blood were removed and the samples incubated in 1 mL RNAlater solution at 4 °C for 16-30 h before being removed from this buffer and stored dry at -80 °C. Frozen aortic tissue were homogenised using TissueLyser LT (Qiagen #85600) and protein lysates were extracted in NE-PER (Life Technologies #78833) lysis buffers containing protease and phosphatase inhibitors (Roche #11836170001 & #04906845001). All steps were carried out at 4 °C. Protein concentrations were determined with the PierceTM BCA protein assay (Life Technologies #23225). These experiments were performed by Iris Hardege and Raya Al Maskari (University of Cambridge).

2.4.1.12 Human and mouse aorta immunoblotting

10 μg of aortic protein lysates were separated by SDS-PAGE. Prior to loading, samples were heated at 70 °C for 10 min in 1 x LDS sample buffer and 1X reducing agent (Life Technologies #B0007 & # B0009) to a total volume of 20 μL/well. Samples and 5μL of Precision Plus molecular weight ladder (Biorad #161-0374) were then loaded onto a Bolt 4-12% Bis-Tris Plus Gel (Novex #BG04125BOX) and run at 165 V in 1X MES running buffer (Novex #B0001), for 35 min or until the dye front reached the end of the gel. Resolved proteins were then transferred to 0.22 μM nitrocellulose membrane (Life Technologies #IB23001) using the iblot2

(Life Technologies) at 20 V for 7 min. Antibodies were incubated in 5% milk. Membranes were incubated in 5% in milk or BSA in TBS for 1 h at room temperature. Primary antibodies were incubated overnight at 4 °C in 5% Milk or BSA in TBS-Tween (0.1% v/v Tween), then washed 6X in TBS-Tween. Secondary antibodies were incubated in TBS-Tween for 1h at room temperature in the dark, then washed 6X in TBS-Tween. Membranes were imaged and integrated intensity values quantified (bands were normalised against β-actin) using the LiCor odessey system (www.licor.com). These experiments were performed by Iris Hardege and Raya Al Maskari (University of Cambridge).

2.4.2 MO25 Study

2.4.2.1 Antibodies

The following antibodies were raised in sheep and affinity purified on the appropriate antigen by the Division of Signal Transduction Therapy Unit at the University of Dundee: MO25β antibody (GST-MO25β human protein, S082B) and MO25α antibody (GST-MO25α human protein, S898A). Secondary antibodies coupled to horseradish peroxidase used for immunoblotting were obtained from Pierce.

2.4.2.2 Tissue Lysates

Tissues were rapidly harvested and either; snap frozen in liquid nitrogen and stored at -80 °C, or incubated in 1 mL RNAlater solution (Sigma-Aldrich) at 4 °C for 16-30 h before being removed from this buffer, patted dry with clean tissue and then stored dry at -80 °C. Lysates were prepared by homogenising tissue on ice using a Polytron PT1200C homogeniser (Kinematica) in 2 mL ice-cold Mammalian lysis buffer and then clarified by centrifugation at 13,000 rpm for 30 min. The clarified supernatant was then quantified and used immediately. Any excess sample was snap-frozen in liquid nitrogen in single-use aliquots for use as required.

2.4.2.3 Immunoprecipitation

2 mg aliquots of clarified tissue extract were incubated with 15 µg of the indicated total antibodies conjugated to 15 µl of protein-G–Sepharose. Incubation was for 2 h at 4 °C with gentle agitation, and the immunoprecipitates were washed three times with 1 ml of lysis buffer containing 0.15 M NaCl and twice with 1 ml of buffer A. Bound proteins were eluted with 1x lithium dodecyl sulfate (LDS) sample buffer.

2.4.2.4 Immunoblotting

Lysates, or protein mixes in SDS sample buffer were subjected to electrophoresis on polyacrylamide gels and transferred to nitrocellulose membranes. The membranes were incubated for 30 min with TBS-T containing 5% w/v skim milk. The membranes were then immunoblotted in 5% w/v skim milk in TBS-T with the indicated primary antibodies overnight at 4 °C. Sheep antibodies were used at a concentration of 1-2 µg/ml. The blots were then washed six times with TBS-T and incubated for 1 h at room temperature with secondary HRP-conjugated antibodies diluted 5000-fold in 5% w/v skim milk in TBS-T. After repeating the washing steps, the signal was detected with enhanced chemiluminescence reagent. Immunoblots were developed using a film automatic processor (SRX-101; Konica Minolta Medical) and films were scanned with a 600-dpi resolution on a scanner (PowerLook 1000; UMAX). Figures were generated using Photoshop/Illustrator (Adobe).

2.4.3 SPAK Study

2.4.3.1 Materials

Lumio Green, Colloidal Blue staining kit and precast SDS polyacrylamide BisTris gels were from Invitrogen. GL Biochem synthesised all peptides to a purity of > 95%; peptide sequences were determined by MS. Tissue-culture reagents were from Life Technologies. P81 phospho-cellulose paper was from Whatman and [γ-^{32}P]-ATP was from Perkin Elmer.

2.4.3.2 Plasmids and primers

C-terminal human SPAK, full length, N-, C-terminal mouse SPAKs were amplified employing SuperScript III (Invitrogen) from placenta total RNA (Stratagene) using appropriate oligonucleotides. The RT-PCR products were ligated into pCR2.1-TOPO vector and sequenced. The sequence-verified SPAKs were sub-cloned into bacterial (pGEX-6P-1) and mammalian (pCMV5) expression vectors using BamHI and NotI. Required amino acid mutations were introduced into the pCR2.1-TOPO clone using site-directed mutagenesis by QuikChange method (Stratagene) but substituting the Taq enzyme with KOD Hot Start DNA polymerase (Novagen). Oligonucleotides were obtained from Invitrogen Life Sciences. DNA sequencing was performed by The Sequencing Service, College of Life Sciences, University of Dundee (www.dnaseq.co.uk). All recombinant proteins, plasmids, and antibodies generated for the present study are available on request and are described in additional detail on the reagents website (https://mrcppureagents.dundee.ac.uk/).

Symbol	Protein	Use	Sense primer (5`-3`)	Antisense primer (5`-3`)
SPAK	SPAK	PCR	TCTGTAAGCTCATTTATGTAGTCACC P1: STK39 6062_39	CAAGTGAGTGAGTGAATACAGCC P1: STK39 6062_40
SPAK	SPAK	q-PCR	GTCTAGGACATGATGGTATGG	CCAACATGGGGTACCAACAAATGC
OSR1	OSR1	q-PCR	CGCTGCAGTCTCCTGTCATCTG	CAGAGTGAGGTCTAGGACAGCCAGG
SLC12A1	NKCC2	q-PCR	TTGGATATAACCCACGCCTTTACG	GCCATGCCGCTGTTCATCTC
SLC12A2	NKCC1	q-PCR	GCAGATCCTCAGTCAGCCATAC	TCCCGAACAACACACGAACC
SLC12A3	NCC	q-PCR	CGGGGTTTGTGTCATGAGGATG	TTGTATCAATGCCTCTGGGGTTG
18S	18S rRNA	q-PCR	GTAACCCGTTGAACCCCATT	CCATCCAATCGGTAGTAGCG

Table 2.3: Primer sequences used for quantitative PCR.

[Taken from (Zhang *et al.*, 2015)].

2.4.3.3 Expression and purification of proteins

All pGEX-6P-1 constructs encoding expression of recombinant with N-terminal Glutathione-S-Transferase (GST) tags were transformed into BL21 *E. coli* cells and 1-litre cultures were grown at 37 °C in Luria Broth containing 100 µg/ml ampicillin until the absorbance at 600 nm was 0.8. Isopropyl ß-D-thiogalactopyranoside (30 µM) was then added and the cells were cultured for a further 18 h at 26 °C. Cells were isolated by centrifugation, re-suspended in 40 ml of ice-cold lysis buffer and lysed in one round of freeze/thawing, followed by sonication

(Branson Digital Sonifier; ten 15-second pulses with a setting of 45% amplitude) to fragment DNA. Lysates were centrifuged at 4 °C for 15 minutes at 26,000 g. The GST-SPAK recombinant proteins were affinity-purified on 0.5 ml glutathione-Sepharose and eluted in buffer A containing 0.27 M sucrose and 20 mM glutathione.

Kinase/protein	DU number	Expression system	Affinity tag
GST-SPAK 452 – 545 (end)	DU41572	Bacteria	GST
GST-SPAK 452-end L491A	DU41619	Bacteria	GST
GST-mSPAK 2-74	DU44920	Bacteria	GST
GST-mSPAK 424-556	DU44891	Bacteria	GST
MBP-mSPAK 2-74	DU48033	Bacteria	MBP
MBP-mSPAK 424-556	DU48034	Bacteria	MBP
FLAG-mSPAK	DU48072	HEK293	FLAG
FLAG-mSPAK Opt L502A	DU48455	HEK293	FLAG

Table 2.4: Summary of purified proteins.

The division of signal transduction therapy (DSTT), University of Dundee - DU number, purification system and affinity tags for purified proteins used in Figure 5.1 and Figure 5.3. [Taken from (Zhang *et al.*, 2015)].

2.4.3.4 Fluorescence polarisation

Fluorescence polarisation measurements were performed at 25 °C with purified SPAK proteins in 50 mM Tris/HCl, pH 7.5, 150 mM NaCl and 2 mM DTT. The concentration of the SPAK proteins determined by measuring their absorbance at 280 nm and calculated using the molar absorption coefficient determined by the ProtParam Online tool (Gasteiger *et al.*, 2001). All peptides (SEEGKPQLVGRFQVTSSK [EP4543] and SEEGKPQLVGAFQVTSSK [EP4544) contained an N-terminal linker required for conjugating to the Lumio Green fluorophore (CCPGCCGGGG) and were initially resuspended in 50 mM ammonium bicarbonate, pH 8. Peptide labelling was achieved by incubating 10 nM of each peptide in a 0.5 ml reaction

mixture of 20 µM Lumio Green in 25 mM Tris/HCl, pH 7.5, 200 mM NaCl and 5 mM 2-mercaptoethanol. Reactions were left to proceed in the dark for 2 h. The peptides were dialysed for 4 h into 25 mM Tris/HCl, pH 7.5, 200 mM NaCl and 5 mM 2-mercaptoethanol using a Micro DispoDIALYZER with a 100 Da molecular-mass cut-off (Harvard Apparatus), and then for another 12 h with changed buffer. For fluorescence polarisation, mixtures were set up containing the indicated concentration of protein, 10 nM Lumio-Green-labelled peptide in a final volume of 30 µl. All individual bindings were performed in duplicate with at least 12 data points per curve. Fluorescence polarisation measures were made using a BMG PheraStar plate reader, with an excitation wavelength of 485 nm and an emission wavelength of 538 nm, and measurements were corrected to the fluorescent probe alone. Data analysis and graphing were then performed in GraphPad Prism6; a one-site specific binding model was assumed (Y=Bmax*X/[Kd+X]) and the fitted dissociation constant computed. All experimental bindings were repeated at least twice and comparable results to those shown in the present study were obtained.

2.4.3.5 Cell culture and transfections

HEK293 (human embryonic kidney 293) cells were cultured on 10-cm-diameter dishes in DMEM supplemented with 10% v/v foetal bovine serum, 2 mM L-glutamine, 100 U/ml penicillin and 0.1 mg/ml streptomycin. For transfection experiments, each dish of adherent HEK293 cells was transfected with 20 µl of 1 mg/ml polyethylenimine (Polysciences) and 5-10 µg of plasmid DNA as described previously (Durocher, 2002). 36 h post-transfection cells were lysed in 0.3 ml of ice-cold lysis buffer/dish, lysates were clarified by centrifugation at 4 °C for 15 minutes at 26,000 g and the supernatants were frozen in aliquots in liquid nitrogen and stored at –20 °C. Protein concentrations were determined using the Bradford method.

2.4.3.6 Buffers

Lysis buffer was 50 mM Tris/HCl, pH 7.5, 1 mM EGTA, 1 mM EDTA, 50 mM sodium fluoride, 5 mM sodium pyrophosphate, 1 mM sodium orthovanadate, 1% w/v NP-40 or 1% w/v Triton X-100, 0.27 M sucrose, 0.1% v/v 2-mercaptoethanol, and protease inhibitors (1 tablet per 50 ml). Buffer A was 50 mM Tris/HCl, pH 7.5, 0.1 mM EGTA, and 0.1% v/v 2-

mercaptoethanol. TBS-Tween buffer (TTBS) was Tris/HCl, pH 7.5, 0.15 M NaCl, and 0.2% v/v Tween-20. SDS sample buffer was 1 × NuPAGE LDS sample buffer (Invitrogen), containing 1% v/v 2-mercaptoethanol.

2.4.3.7 Antibodies

The following antibodies were raised in sheep and affinity purified on the appropriate antigen by the Division of Signal Transduction Therapy Unit at the University of Dundee: WNK1-total antibody (residues 2360-2382 of human WNK1, S62B), WNK4-total antibody (residues 1221-1243 of human WNK4, S064B), WNK4 N-terminal antibody (residues 1-14 of mouse WNK4, S726D), SPAK-mouse antibody (2–76 of mouse SPAK, S668D), OSR1 mouse antibody (389–408 of mouse OSR1, SAHLPQPAGQMPTQPAQVSL, S149C), SPAK/OSR1 (T-loop) phospho-Thr233/Thr185 antibody (226–238 of human SPAK or residues 178–190 of human OSR1, TRNKVRKpTFVGTP, S204C), SPAK/OSR1 (S-motif) phospho-Ser373/Ser325 antibody (367–379 of human SPAK, RRVPGSpSGHLHKT, which is highly similar to residues 319–331 of human OSR1 in which the sequence is RRVPGSpSGRLHKT, S670B), SPAK phospho-Thr233 antibody (226–238 of human SPAK, TRNKVRKpTFVGTP, S668B), NKCC1 phospho-Thr203+Thr207+Thr212 (residues 198-217 of human NKCC1, HYYYDpTHTNpTYYLRpTFGHNT, S763B), NKCC1 phospho-Thr 212+Thr 217 (residues 208-223 of human NKCC1, YYLRpTFGHNpTMDAVPR, S063D), NKCC1-total antibody (residues 1-260 of shark NKCC1, S841B), NCC phospho-Thr46+Thr50+Thr55 antibody (residues 41–60 of human NCC phosphorylated at Thr46+Thr50+Thr55, HPSHLpTHSSpTFCMRpTFGYNT, S908B), NCC phospho-Thr46 antibody (residues 40–54 of human NCC phosphorylated at Thr46, SHPSHLpTHSSTFCMRRR, S241C), NCC phospho-Thr60 antibody (residues 54–66 of human NCC phosphorylated at Thr60, RTFGYNpTIDVVPT, S995B), NCC phospho-Ser91 antibody (residues 85–97 of human NCC phosphorylated at Ser91, CTLADLHpSFLKQEGRR, S996B), NCC-total antibody (residues 906–925 of human NCC, CHTKRFEDMIAPFRLNDGFKD, S965B), NKCC2 phospho-Thr100 (residues 94-106 of human NKCC2, NTYYLQpTFGHNTM, S431C), NKCC2 phospho-Ser130 (residues 123-137 of human NKCC2, GPKVNRPpSLLEIHEQ, S888C), NKCC2 phospho-Ser91 (residues 86-97 of human NKCC2, RRFHAYDpSHTNTYYRR, S451C), NKCC2-total antibody (residues 1–174 of human NKCC2, S838B), GST-total antibody (raised against the glutathione S-transferase protein, S902A), ERK1 total antibody (

full-length human ERK1 protein, S221B). The anti-GAPDH antibody (ab8245), anti-NCC-total [SLC12A3] (AB95302) and the anti-parvalbumin antibody (ab11427) were purchased from Abcam. Anti-PVALB (Parvalbumin PV25) from Swant. Anti-NKCC2-total (LS-C313275) from LifeSpan BioSciences. The anti-ERK1/2 antibody (9102) was purchased from Cell Signalling Technology. The anti-FLAG antibody (F1804) was purchased from Sigma-Aldrich. Secondary antibodies coupled to horseradish peroxidase used for immunoblotting were obtained from Pierce. Preimmune IgG used in control immunoprecipitation experiments were affinity purified from pre-immune serum using protein G-Sepharose.

2.4.3.8 Immunoprecipitation and assay of SPAK

One milligram of clarified cell lysate was incubated with 5 µg of the SPAK/OSR1 (total) antibody conjugated to 5 µl of protein G-Sepharose and incubated for 2 h at 4 °C with gentle agitation. The immunoprecipitates were washed twice with 1 ml of lysis buffer containing 0.5 M NaCl and twice with 1 ml of buffer A. The SPAK/OSR1 immunoprecipitates were assayed with the CATCHtide peptide substrate (RRHYYYDTHTNTYYLRTFGHNTRR) that encompasses the SPAK/OSR1 phosphorylation sites on NKCC1 (3). Assays were set up in a total volume of 50 µl in buffer A containing 10 mM $MgCl_2$, 0.1 mM [γ^{32}P]ATP and 300 µM CATCHtide (37). After incubation for 30 min at 30 °C, the reaction mixture was applied onto P81 phosphocellulose paper, the papers were washed in phosphoric acid, and incorporation of ^{32}P-radioactivity in CATCHtide was quantified by Cerenkov counting.

2.4.3.9 Immunoblotting and total-antibody immunoprecipitation

Cell lysates (15 µg) in SDS sample buffer were subjected to electrophoresis on polyacrylamide gels and transferred to nitrocellulose membranes. The membranes were incubated for 30 min with TBS-T containing 5% w/v skim milk. The membranes were then immunoblotted in 5% w/v skim milk in TBS-T with the indicated primary antibodies overnight at 4 °C. Sheep antibodies were used at a concentration of 1-2 µg/ml. The incubation with phospho-specific sheep antibodies was performed with the addition of 10 µg/ml of the dephospho-peptide antigen used to raise the antibody. The blots were then washed six times with TBS-T and incubated for 1 h at room temperature with secondary HRP-conjugated antibodies diluted

5000-fold in 5% w/v skim milk in TBS-T. After repeating the washing steps, the signal was detected with enhanced chemiluminescence reagent. Immunoblots were developed using a film automatic processor (SRX-101; Konica Minolta Medical) and films were scanned with a 600-dpi resolution on a scanner (PowerLook 1000; UMAX). Figures were generated using Photoshop/Illustrator (Adobe). For total-antibody immunoprecipitation NCC, NKCC1 and NKCC2 were immunoprecipitated from indicated kidney extracts. A 2 mg aliquot of the indicated clarified kidney extract were incubated with 15 µg of the indicated total NCC, NKCC1 and NKCC2 antibodies conjugated to 15 µl of protein-G–Sepharose. Incubation was for 2 h at 4 °C with gentle agitation, and the immunoprecipitates were washed three times with 1 ml of lysis buffer containing 0.15 M NaCl and twice with 1 ml of buffer A. Bound proteins were eluted with 1x lithium dodecyl sulfate (LDS) sample buffer.

2.5 Phenotype and Histology Database Mining

2.5.1 Data Sourcing

To discover potential mouse models targeting MO25β, SPAK and CUL3 with open data, searches were initially conducted on the International Mouse Strain Resource (IMSR) (http://www.findmice.org/) and Mouse Genome Informatics (MGI) (http://www.informatics.jax.org/) websites. Identified strains were then further investigated for phenotypic data on these databases and at the International Mouse Phenotyping Consortium (IMPC) - Release 5.0 (http://www.mousephenotype.org/) (Koscielny *et al.*, 2014). Searches for protein expression and localisation information were done on the Human Protein Atlas - Version 17 (www.proteinatlas.org) in various organ tissues and cell lines (Uhlen *et al.*, 2015; Thul *et al.*, 2017).

2.5.2 Data Assessment and Extraction

Data from the IMPC has been gathered in core facilities at participating institutes using standardised protocols and procedures from the IMPReSS (International Mouse Phenotyping Resource of Standardised Screens) core phenotype pipeline (Figure 2.7). Phenotype associations for the genes of interest were viewed in ontological heatmap mode with a p-value

threshold set to <0.05. Raw data for selected parameters was then downloaded in XLS format for analysis, interpretation and graphical/tabular representation. Expression data and images from the Human Protein Atlas were downloaded and processed with FIJI image analysis software (64-bit).

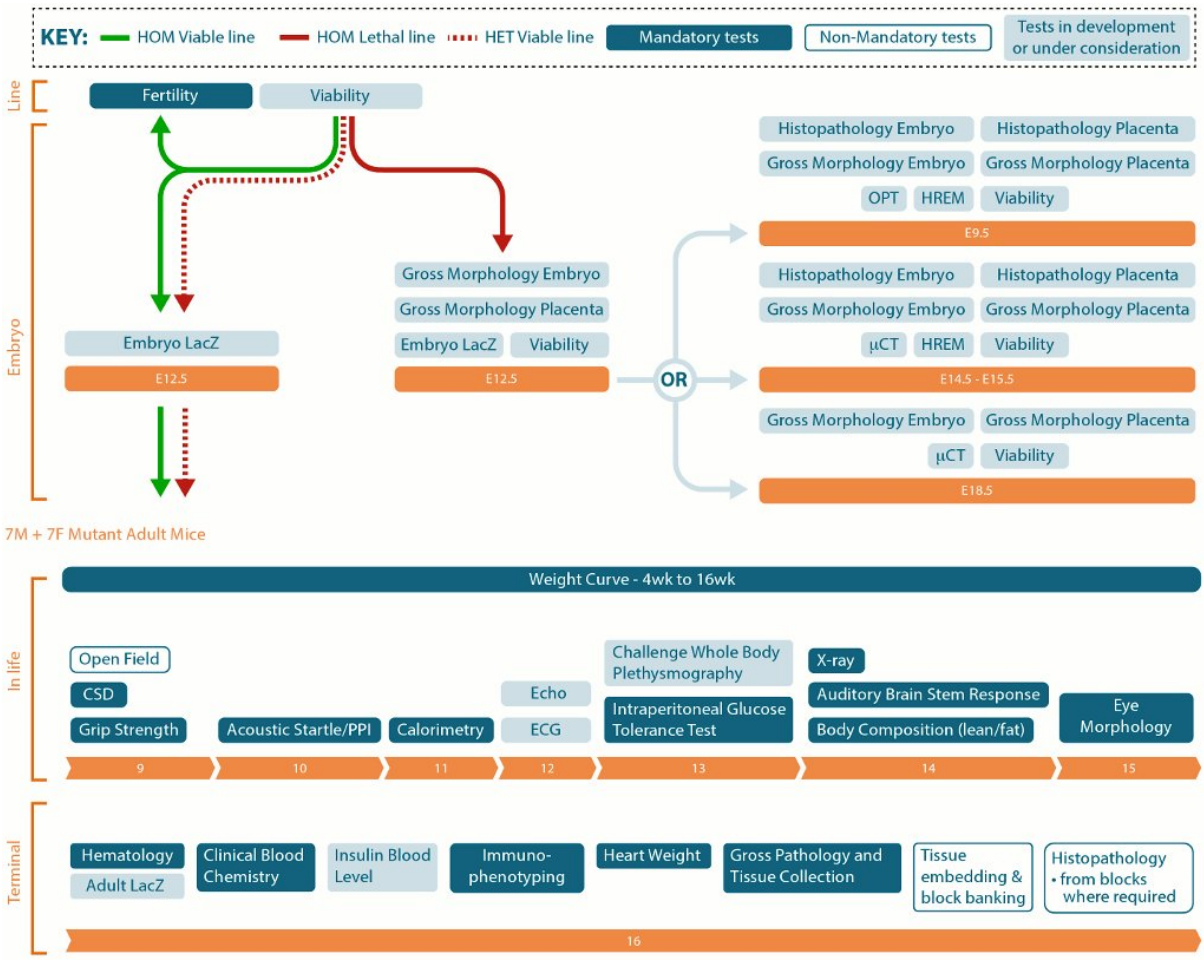

Figure 2.7: Core IMPC adult and embryonic phenotype pipeline.

The pipeline schematic details the decision tree used in phenotyping new mouse models. Orange sections detail animal age and the periods in which experimental procedures are conducted by either embryonic day or postpartum week. For protocols and parameters see the IMPReSS website (www.mousephenotype.org/impress).

2.5.2.1 MO25β Study

The European Conditional Mouse Mutagenesis Program (EUCOMM) as part of the International Knockout Mouse Consortium (IKMC) created the mouse strain

Cab39l$^{tm1b(EUCOMM)Wtsi}$ on a C57BL/6NTac background at the Wellcome Trust Sanger Institute (WTSI) (Figure 2.8), which produces viable homozygous MO25β null mice (referred to hereafter as CAB39L$^{-/-}$). To investigate the phenotype, the mice underwent the IMPC mandatory tests (Figure 2.7) at the Medical Research Council Harwell centre with the exception of immunophenotyping, and additionally undertook the viability, open field and adult LacZ expression tests.

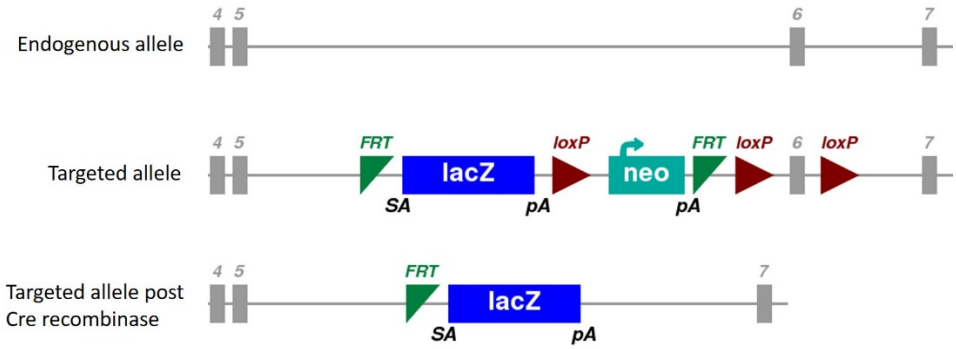

Figure 2.8: Cab39l$^{tm1b(EUCOMM)Wtsi}$ mouse model generation.

The tm1b knock-out strategy of endogenous MO25β/CAB39L. The endogenous allele is represented and the tm1a target allele with the neomycin cassette (neo) and exon 6 flanked by loxP sites, which are then removed by Cre recombinase to create a tm1b model. The cassette expresses LacZ in tissues where the gene is knocked out. Beta-gaslactosidase staining can be used to follow the tissue expression of the gene. The grey rectangles represent exons, the flippase-recognition target (FRT) sites, splice acceptor (SA) and polyadenylation (pA) sequences are also indicated.

2.5.2.2 SPAK Study

The EUCOMM as part of the IKMC created the mouse strain Stk39$^{tm1a(EUCOMM)Wtsi}$ on a C57BL/6NTac background at the WTSI (Figure 2.9), which produces viable homozygous SPAK knock-out mice (referred to hereafter as STK39$^{-/-}$). However it should be noted that for some genes skipping over the LacZ cassette can restore gene expression to some extent and the tm1a strategy can also result in hypomorphs. To investigate the phenotype, the mice underwent the following tests at the WTSI: clinical blood chemistry, haematology, body weight, heart weight, hot plate, calorimetry, body composition, eye morphology, X-ray and histopathology.

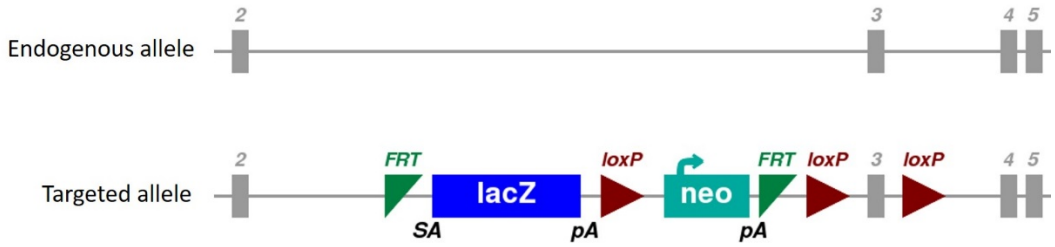

Figure 2.9: Stk39$^{tm1a(EUCOMM)Wtsi}$ mouse model generation.

The tm1a knock-out strategy of endogenous STK39 (which codes for the SPAK protein). The endogenous allele is represented and the tm1a target allele with the neomycin cassette (neo) and exon 3 flanked by loxP sites. The cassette expresses LacZ in tissues where the gene is knocked out. Beta-galactosidase staining can be used to follow the tissue expression of the gene. The grey rectangles represent exons, the flippase-recognition target (FRT) sites, splice acceptor (SA) and polyadenylation (pA) sequences are also indicated.

2.6 Statistical Analyses and Power Calculations

Data presented are mean ± standard error of the mean (SEM), unless otherwise stated. Data were tabulated and processed in Microsoft Office Professional Plus 2013 – Excel, with statistical analyses performed on either SPSS version 22 or GraphPad Prism 5 (http://www.graphpad.com/scientific-software/prism/) software. Two-tail student t-tests tests were performed either paired or unpaired where appropriate. $P < 0.05$ was taken as statistically significant throughout.

For myosin phosphatase target subunit 1 (MYPT1) phosphorylation quantification, ratiometric expression was calculated for CUL3$^{WT/\Delta 403-459}$ vs CUL3^{WT} on each western blot of independent biological replicates. The mean of the ratios and bounds of the 95% confidence interval were calculated, where ratio = 1 represents no change in phosphorylation and ratio > 1 represents an increase in the phosphorylation status of CUL3$^{WT/\Delta 403-459}$ mice. Statistical significance was determined by the ratio t-test <Available at http://www.wormbook.org/chapters/www_statisticalanalysis/statisticalanalysis.html>.

Unless otherwise stated, experiments were performed with an approximately even divide of males and females. Power calculations were performed in G*Power to ensure experiments, where possible, had a sufficient sample size to provide at least 80% power at a 5% alpha to measure the desired effect size.

Chapter 3 : Gordon Syndrome Reveals CUL3 as a Potent Regulator of Blood Pressure

[*This chapter is principally based on and expands upon the content from the abstracts in Appendix 1 and paper in Appendix 3* (Schumacher *et al.*, 2015)]

3.1 Abstract

Deletion of exon-9 from Cullin-3 (CUL3, residues 403-459: $CUL3^{\Delta 403-459}$) causes pseudohypoaldosteronism type IIE (PHA2E), a severe form of Familial Hyperkalaemia and Hypertension (FHHt). CUL3 binds the RING protein RBX1 and various substrate-adaptors to form Cullin-RING-ubiquitin-ligase complexes. Bound to KLHL3, CUL3-RBX1 ubiquitylates WNK kinases, promoting their ubiquitin-mediated proteasomal degradation. Since WNK kinases activate Na^+/Cl^- cotransporters to promote salt retention, CUL3 regulates blood pressure. Mutations in both KLHL3 and WNK kinases cause PHA2 by disrupting Cullin-RING-Ligase formation. We report here that the PHA2E mutant, $CUL3^{\Delta 403-459}$, is severely compromised in its ability to ubiquitylate WNKs, possibly due to altered structural flexibility. Instead, $CUL3^{\Delta 403-459}$ auto-ubiquitylates and loses interaction with two important Cullin regulators: the COP9-Signalosome and CAND1. A novel knock-in mouse model of $CUL3^{WT/\Delta 403-459}$ closely recapitulates the human PHA2E phenotype. These mice also show changes in the arterial pulse waveform, suggesting a vascular contribution to their hypertension not reported in previous FHHt models. These findings may explain the severity of the FHHt phenotype caused by CUL3 mutations compared to those reported in KLHL3 or WNK kinases.

3.2 Introduction

Blood pressure is controlled in part by the WNK kinase pathway, which acts to modulate the activity of key cation-chloride cotransporters in the kidney (Kahle *et al.*, 2008; Alessi *et al.*, 2014). Considerable insight into this pathway has come from exploring the molecular basis for mutations described in patients with a rare monogenic form of hypertension called Familial Hypertension and Hyperkalaemia (FHHt, also known as Gordon syndrome or

pseudohypoaldosteronism type II, PHA2, OMIM #145260). Mutations in the genes encoding WNK kinases have been shown to increase protein levels of WNK1 and WNK4 in the kidney, leading to increased activation of this pathway (Wilson *et al.*, 2001; Kahle *et al.*, 2008). When activated by phosphorylation, the WNK kinases phosphorylate and activate the downstream kinases, SPAK (SPS1-related proline/alanine-rich kinase) and OSR1 (oxidative stress–responsive kinase 1), which in turn phosphorylate and activate cation-chloride cotransporters in the kidney, such as NCC (Na^+/Cl^- cotransporter), which leads to increased sodium ion reabsorption (Vitari *et al.*, 2005; Delpire & Gagnon, 2008; Richardson *et al.*, 2008). It is this up-regulation of the WNK signalling pathway that is responsible for the salt retention that drives the hypertension in FHHt. These patients also present with disturbed plasma electrolytes especially hyperkalaemia and a metabolic acidosis, partly driven by NCC activation (Boyden *et al.*, 2012; Tsuji *et al.*, 2013; Osawa *et al.*, 2013; McCormick *et al.*, 2014; Glover *et al.*, 2014). As FHHt patients are salt-loaded through NCC activation, the hypertension and electrolyte disturbance responds to either salt-restriction or low doses of thiazide diuretics (Gordon & Hodsman, 1986; Mayan *et al.*, 2002).

More recently, the Ubiquitin Proteasome System (UPS) was shown to have a critical upstream role in regulating blood pressure by modulating WNK kinase levels (Mori *et al.*, 2013*b*; Wu & Peng, 2013; Wakabayashi *et al.*, 2013; Ohta *et al.*, 2013). This was first suggested when patients with severe forms of FHHt were described with mutations in Cullin-3 (CUL3; PHA2E), and one of its substrate adaptors, KLHL3 (PHA2D) (Boyden *et al.*, 2012; Louis-Dit-Picard *et al.*, 2012). CUL3 belongs to the Cullin-RING ligase (CRL) family that form the largest class of ubiquitin E3 ligases in the cell. Cullins are elongated proteins, which confer an extended structure to active CRL complexes (Zheng *et al.*, 2002; Duda *et al.*, 2011). Through their C-terminus, Cullins constitutively bind to a small really interesting new gene (RING) finger domain protein, either RING-box protein (RBX) 1 or 2, which forms the catalytic core of the ligase complex. The binding to various substrate-adaptor proteins at the N-terminal domain enables CUL3-RBX1 to appropriately ubiquitylate a plethora of cellular substrates (Wee *et al.*, 2005; Harper & M-km, 2012). In this way, CUL3 acts as an active scaffold to direct ubiquitylation, as C-terminally bound RBX1 binds ubiquitin-conjugating E2 enzymes that are charged with ubiquitin, while simultaneously binding to the substrate adaptor, in this instance KLHL3 (Figure 3.1). The overall structural rigidity of the Cullin, in particular between the elongated N-terminus and the globular C-terminus, is important for the ubiquitin E3 ligase function of the complex. Alterations in the connecting sequence between the Cullin N- and C-

terminus are thought to change the relative positioning of the RING domain towards the bound substrate, which can prevent substrate modification (Zheng *et al.*, 2002; Liu & Nussinov, 2011).

For efficient CRL-dependent ubiquitylation of its targets, a conserved C-terminal lysine residue (Lys 721 in CUL3) must be modified by the addition of a single molecule of a ubiquitin-like protein, namely neural precursor cell expressed developmentally down-regulated protein 8 (Nedd8) (Pintard *et al.*, 2003). This modification process, also known as neddylation, is auto-catalysed by CUL3-RBX1 and aided by Nedd8-E3 ligases (Kurz *et al.*, 2005; Rabut *et al.*, 2011), and serves to alter the flexibility of the C-terminal Cullin-RBX1 module to activate E3 ligase activity (Duda *et al.*, 2008; Scott *et al.*, 2014). While neddylation is required for efficient ubiquitylation, studies show that the cycling between a neddylated and deneddylated state is crucial in a cellular context (Cope *et al.*, 2002; Pintard *et al.*, 2003). As such, Cullin interactions with the deneddylation complex constitutive photomorphogenesis 9 (COP9)-signalosome (CSN), a metalloprotease, are also required for activity. Another regulator of CRLs, cullin-associated nedd8-dissociated protein 1 (CAND1), interacts with the N- and C-terminus of Cullins only in their deneddylated state to promote the exchange of substrate-adaptors (Figure 3.1) (Liu *et al.*, 2002; Goldenberg *et al.*, 2004; Pierce *et al.*, 2013; Wu & Peng, 2013; Zemla *et al.*, 2013).

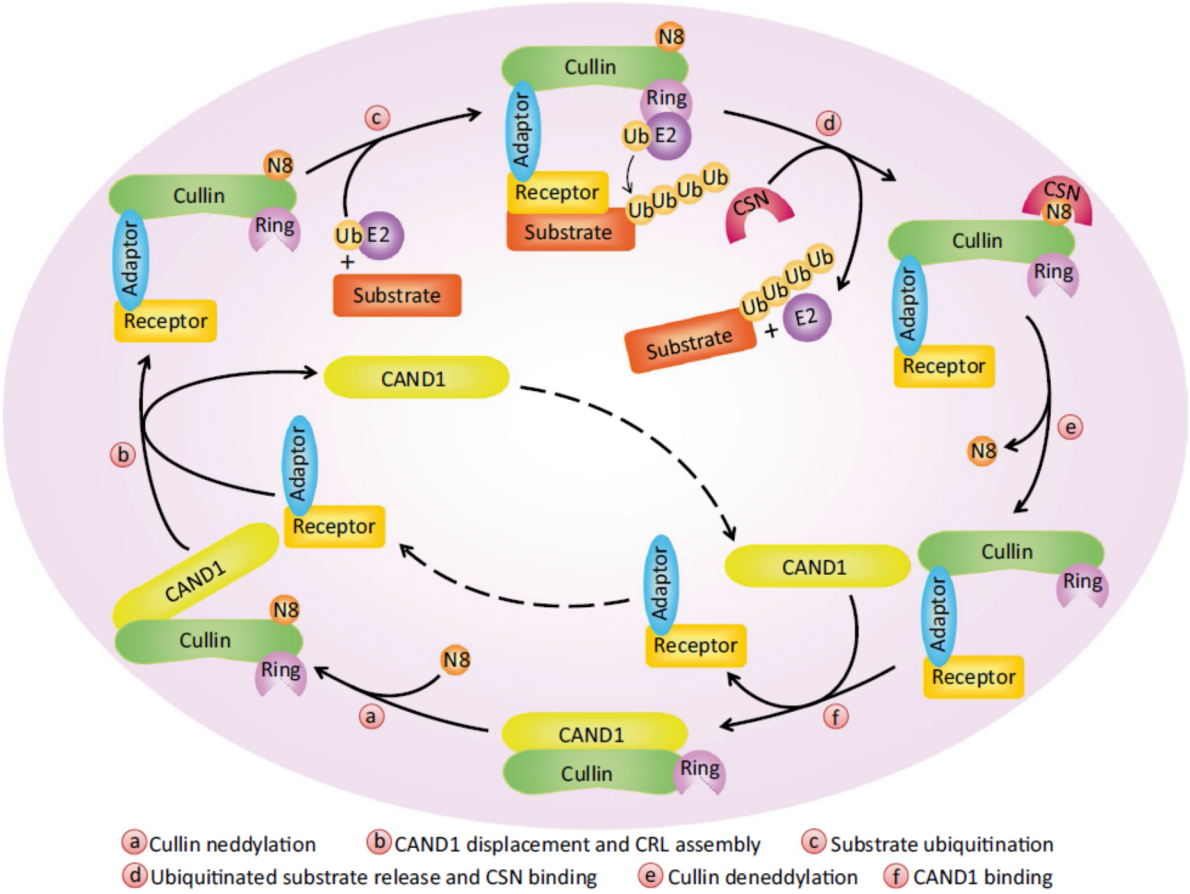

Figure 3.1: Illustration of substrate ubiquitylation through Cullin-RING ligase activity.

For the Cullin-RING ligase (CRL) complexes to become activated they must be **[A]** neddylated through the addition of nedd8 (N8) to a lysine residue on Cullin to promote an active conformation and dissociate from CAND1, and **[B]** recruit a substrate adaptor to the CRL assembly. **[C]** The RING protein of the CRL then binds ubiquitin-conjugating E2 enzymes that are charged with ubiquitin (Ub), to direct ubiquitylation of the substrate bound to the adaptor protein. **[D]** Subsequent COP9-Signalosome (CSN) binding promotes removal of the "empty" E2 enzyme and **[E]** deneddylation of CRL, which allows for multiple rounds of neddylation/deneddylation cycling and "new" ubiquitin-charged E2 enzymes recruitment for multi-ubiquitylation of the same substrate molecule and/or release of the ubiquitylated substrate and recruitment of a new substrate molecule. **[F]** Deneddylated CRL then binds to CAND1 to inactivate it and promote dissociation of the adaptor protein for recycling. [Taken from (Cui *et al.*, 2016)].

In the context of PHA2, KLHL3 is the critical adaptor that links the WNK kinases to CUL3-RBX1, enabling CUL3 to directly ubiquitylate the bound WNK kinase. Earlier work showed the KLHL3 mutations described in FHHt (PHA2D) patients disrupt the formation of

the complex and prevent WNK ubiquitylation, leading to WNK stabilisation and increased electrolyte flux mediated by the WNK kinase pathway (Mori *et al.*, 2013*b*; Shibata *et al.*, 2013; Wu & Peng, 2013; Wakabayashi *et al.*, 2013; Ohta *et al.*, 2013; Susa *et al.*, 2014; Schumacher *et al.*, 2014). Some patients with FHHt have mutations in WNK kinases, which promote WNK stabilisation by disrupting WNK-KLHL3 interactions (Akhtar & Hafeez, 2009; Pathare *et al.*, 2012; Ali *et al.*, 2013; Schumacher *et al.*, 2014) or, in some cases, by the increased expression of WNK mRNA (Wilson *et al.*, 2001).

While FHHt patients with CUL3, KLHL3 or WNK mutations present with the same disease, those with mutations in CUL3 display a more severe phenotype, evident both in terms of an earlier age-of-onset and the degree of hypertension and electrolyte disturbance reported (Boyden *et al.*, 2012; Tsuji *et al.*, 2013; Osawa *et al.*, 2013). To date, all the reported CUL3 PHA2E mutations are heterozygous, transmit as autosomal dominant traits and result in the deletion of the amino acids encoded for by exon-9 of the CUL3 mRNA (residues 403-459) (Boyden *et al.*, 2012; Grimm *et al.*, 2012; Tsuji *et al.*, 2013; Osawa *et al.*, 2013; Glover *et al.*, 2014). Nevertheless, precisely why and how this truncated form of CUL3 (hereafter referred to as $CUL3^{\Delta 403\text{-}459}$) causes a more severe phenotype is currently unclear. To investigate this question a biochemical *in vitro* approach to understand the molecular defects caused by the mutation and a mouse model of PHA2E to better understand the physiological basis of the effects of $CUL3^{\Delta 403\text{-}459}$ was used.

3.3 Results

3.3.1 CUL3$^{\Delta 403-459}$ forms an active Cullin-RING ligase complex

To investigate the molecular defect of CUL3$^{\Delta 403-459}$ it was determined if this form of CUL3 was able to build a CRL complex. First, it was established that CUL3$^{\Delta 403-459}$ binds RBX1 similar to CUL3^{WT}, by showing that both versions of CUL3 form a stable complex with RBX1 when co-expressed in insect cells (Figure 3.2 A). A second critical interaction for a functional CRL is the ability to bind substrate-adaptor proteins, and in the context of WNK kinase modification, CUL3 must interact with KLHL3 (Lamark & Johansen, 2012; Ji & Privé, 2013; Canning & Bullock, 2014). The 57-residue deletion in CUL3$^{\Delta 403-459}$ lies in a structurally distinct domain of CUL3 and would not be expected to perturb binding to substrate adaptors. It was confirmed that CUL3$^{\Delta 403-459}$ indeed retains the ability to bind KLHL3 by *in vitro* pull-down assays with purified proteins (Figure 3.2 B). It was also shown this interaction is maintained in a cellular system, using ectopically expressed FLAG-tagged CUL3 to co-precipitate endogenous KLHL3 in FLAG immunoprecipitates (Figure 3.6 A). Thus, CUL3$^{\Delta 403-459}$ maintains crucial interactions important for ubiquitin ligase function. Given this, whether CUL3$^{\Delta 403-459}$-RBX1 also maintains the ability to hydrolyse the thioester bond between the catalytic cysteine residue of a recruited E2 enzyme and ubiquitin (E2~UB), a critical step in ubiquitylation and a measure for catalytic activity, was tested. Using ubiquitin-release assays from charged E2 enzymes, it was shown that CUL3$^{\Delta 403-459}$ hydrolyses E2~UB more efficiently than CUL3^{WT}, demonstrating a functionally intact CUL3$^{\Delta 403-459}$-RBX1 catalytic core, while also suggesting potential hyper-activity (Figure 3.2 C). Together, these results demonstrate that CUL3$^{\Delta 403-459}$ maintains interactions and basic functionality critical for CRL activity.

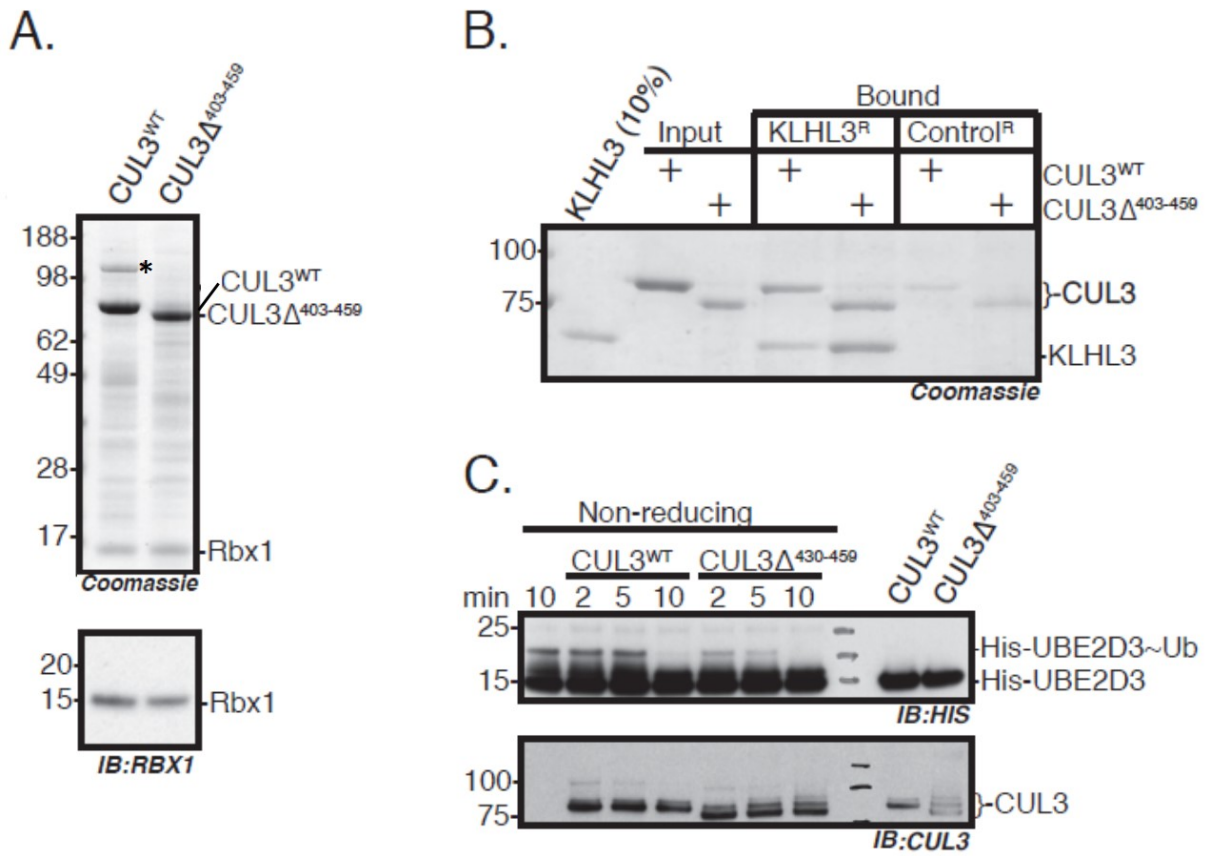

Figure 3.2: CUL3$^{\Delta 403-459}$ forms a functional Cullin-RING ligase with altered activity.

[A] Shows the proteins which interact with purified CUL3^{WT} and CUL3$^{\Delta 403-459}$ as analysed by SDS–PAGE and Coomassie blue staining, following expression in SF21 cells. Bands migrating between 62- and 98-kDa protein markers are CUL3^{WT} and CUL3$^{\Delta 403-459}$, respectively, while the band below 17-kDa is RBZ1, which was confirmed by immunoblot (shown in the lower panel). The band in CUL3^{WT} denoted with * is co-purified insect cell CAND1. All protein identities were confirmed by mass spectrometry. **[B]** KLHL3 binding to CUL3^{WT} and CUL3$^{\Delta 403-459}$ is comparable as shown by pull-down assays with anti-KLHL3 resin (KLHL^{R}) and the protein G sepharose control resin (Control^{R}). **[C]** UBE2D3~ubiquitin-release assays analysed by non-reducing SDS–PAGE and immunodetection shows that CUL3$^{\Delta 403-459}$ more efficiently hydrolyses the ubiquitin-charged E2 enzyme as shown by lower levels of UBE2D3~Ub over time. The lower panel is an immunoblot for CUL3 confirming equivalent amounts of CUL3^{WT} and CUL3$^{\Delta 403-459}$ were used; the appearance of higher molecular weight bands over time represents the modification of CUL3 by covalent attachment of ubiquitin. The first lane is the negative control with no CUL3 added, and the right two lanes are positive control lanes incubated for 10 min with E2~Ub but then treated with reducing agent prior to SDS–PAGE to remove ubiquitin from UBE2D3. "~" denotes thioester bond. [Taken from (Schumacher *et al.*, 2015)].

3.3.2 Structural modelling suggests CUL3$^{\Delta 403-459}$ is more flexible than CUL3^{WT}

To better understand how the deletion in CUL3$^{\Delta 403-459}$ may affect the CRL, the structure of CUL3 was predicted, using closely related Cullin1 (CUL1) (Figure 3.3). The region deleted in CUL3$^{\Delta 403-459}$ likely forms a three-helical bundle juxtaposed to the globular C-terminal domain.

Removal of these helices would fuse together two short unstructured regions to create a longer loop, which, as well as shortening the elongated structure of the CRL complex, may increase the flexibility between the two domains. If correct, this model explains how RBX1 and KLHL3 binding is maintained (Munir *et al.*, 2007; Calabrese *et al.*, 2011), while also suggesting the function of the ligase may be compromised due to the altered relative orientation of the CRL components towards each other. Studies investigating the structure of CUL1 demonstrated the importance of a rigid Cullin conformation for substrate ubiquitylation, as increasing the flexibility of CUL1, in an area that corresponds to the CUL3 deletion, led to strongly decreased substrate ubiquitylation (Zheng *et al.*, 2002) (Figure 3.3). It is therefore possible that due to the presence of a predicted unstructured flexible loop, $CUL3^{\Delta 403\text{-}459}$ may similarly sample non-productive conformations.

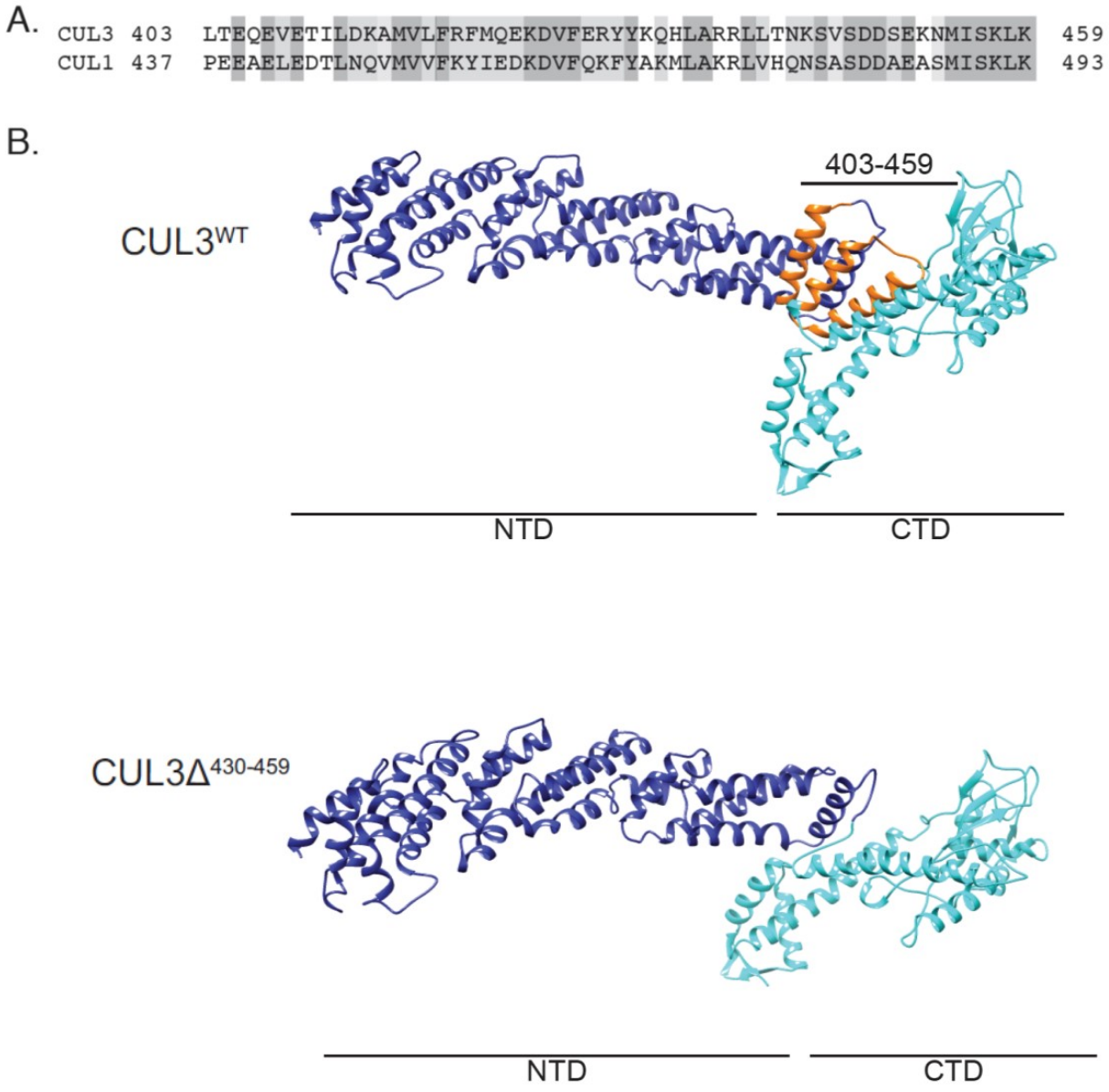

Figure 3.3: Cullin homology and structural predictions.

[A] Clustal-Omega alignment of full length Cullin1 and Cullin3 shows the highly conserved nature of the region equating to exon-9 of Cullin3, with ~81% of the residues either the same (dark grey) or functionally similar substitutions (light grey). **[B]** Structural model of $CUL3^{WT}$ and $CUL3^{\Delta 403-459}$ made based on the structure of full length Cullin1 (PDB: 1LDK), highlighting the residues deleted in the PHA2E mutant which (orange) are located close to the N-terminal domain (NTD; in dark blue) and C-terminal domain (CTD; in cyan) border. [Taken from (Schumacher *et al.*, 2015)].

3.3.3 CUL3$^{\Delta 403-459}$ has altered Nedd8-ligase activity and is unable to interact with the CRL regulators COP9-Signalosome and CAND1

Available structural data of CRL proteins bound to Cullin regulators suggest the deleted region in CUL3$^{\Delta 403-459}$ may also influence neddylation and binding of the COP9-Signalosome (CSN) (Lingaraju *et al.*, 2014) and of CAND1 (Figure 3.4) (Goldenberg *et al.*, 2004). This prompted further examination to see if these interactions are affected by the PHA2E mutation.

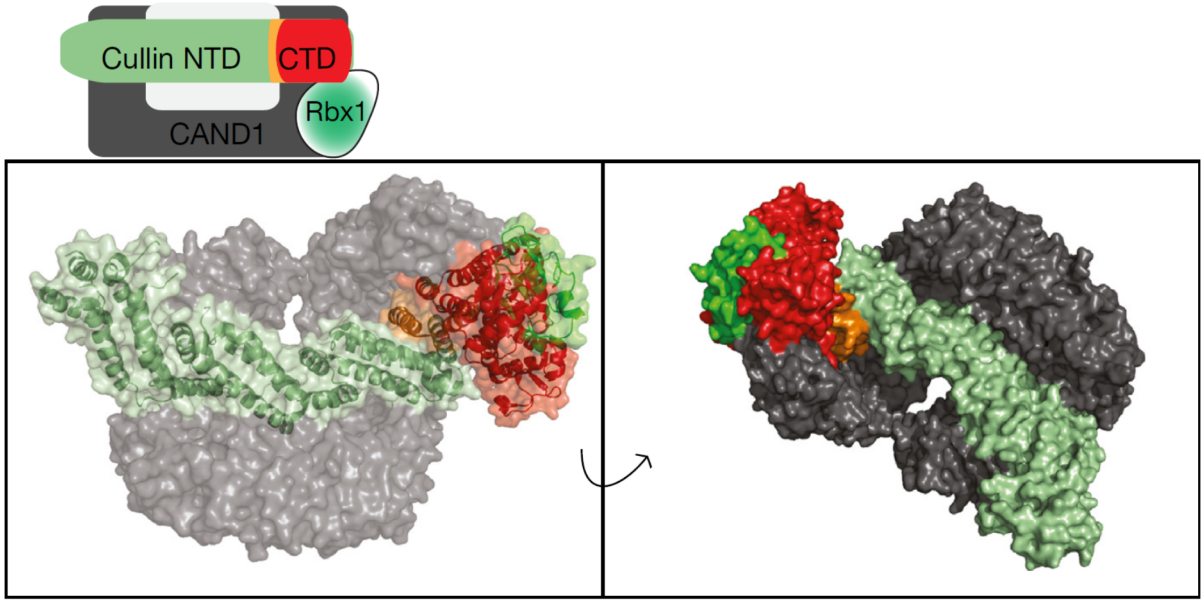

Figure 3.4: Structural context of the area deleted by the disease-causing mutation in CUL3.

[Top] Schematic representation of the interactions between CRL and CAND1. **[Bottom]** Representation of CAND1 in complex with CUL1-RBX1 (PDB: 1U6G) (Goldenberg *et al.*, 2004). Coloured as shown in the schematic representation. Residues 437–493 of CUL1 (equivalent to 403–459 of CUL3) are coloured orange. [Taken from (Schumacher *et al.*, 2015)].

To investigate the ability of CUL3$^{\Delta 403-459}$ to be auto-modified with Nedd8, *in vitro* neddylation assays with purified CUL3, Nedd8 activating enzyme (NAE), Nedd8 E1 (APPBP1-UBA3), Nedd8 E2 (UBE2M) and Nedd8 were used. As Nedd8 forms a covalent isopeptide bond with CUL3, neddylation can be visualised as a slower-migrating band on SDS PAGE. CUL3$^{\Delta 403-459}$ was found to retain the ability to auto-neddylate (Figure 3.5 A). However unlike CUL3^{WT}, CUL3$^{\Delta 403-459}$ appears less efficient at transferring Nedd8 as some unmodified CUL3$^{\Delta 403-459}$ remained even 45 min after neddylation was initiated. Moreover, while CUL3^{WT}

was only mono-neddylated, multiple Nedd8 molecules were attached to CUL3$^{\Delta 403-459}$ (Figure 3.5 A). Both of these differences in neddylation are consistent with increased structural flexibility of CUL3$^{\Delta 403-459}$.

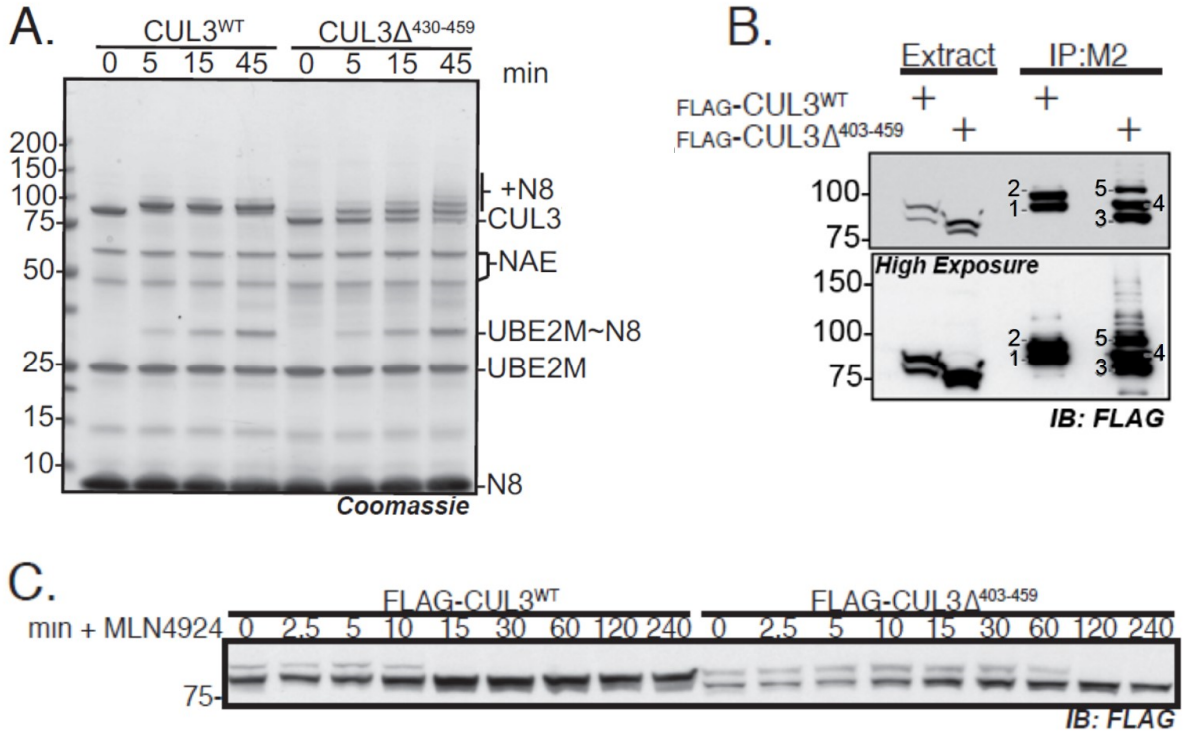

Figure 3.5: CUL3$^{\Delta 403-459}$ has altered Nedd8-ligase activity.

[A] Time course study of *in vitro* neddylation reactions shows a band shift for CUL3^{WT} (0 vs 5,15,45 mins) that is representative of a single Nedd8 modification, while multiple bands represent CUL3$^{\Delta 403-459}$ hyperneddylation with attachment of up to three Nedd8 (N8) molecules. Additionally, the continued presence of unmodified CUL3$^{\Delta 403-459}$ suggests it is less efficient at transferring Nedd8. **[B]** Overexpression experiments in HEK293 cells also show hyperneddylation of CUL3$^{\Delta 403-459}$. Bands are labelled as follows: **1**. CUL3^{WT} // **2**. CUL3^{WT}-N8 // **3**. CUL3$^{\Delta 403-459}$ // **4**. CUL3$^{\Delta 403-459}$-N8 // **5**. CUL3$^{\Delta 403-459}$-2(N8). **[C]** Overexpression experiments in HEK293 cells treated with the neddylation inhibitor, MLN4924, show that CUL3$^{\Delta 403-459}$ has a decreased rate of deneddylation. [Adapted from (Schumacher *et al.*, 2015) with changes to labels].

As previously reported (McCormick *et al.*, 2014), elevated CUL3$^{\Delta 403-459}$ neddylation in cells was also noticed (Figure 3.5 B). CRLs cycle between neddylated and deneddylated states to maintain activity (Pintard *et al.*, 2003). Therefore, the increased cellular neddylation of CUL3$^{\Delta 403-459}$ could reflect a decrease in deneddylation by the isopeptidase CSN. The structure of the CSN bound to CUL1 supports this idea, as the Cullin C-terminal domain, including the

region equivalent to residue 403-459 in CUL3, contacts the CSN subunits directly (Lingaraju *et al.*, 2014). To investigate this possibility, neddylation was blocked using an inhibitor of the Nedd8-E1 enzyme (MLN4924, Millennium pharmaceuticals) and monitored CUL3 deneddylation over time. Consistent with decreased rates of deneddylation, CUL3$^{\Delta 403\text{-}459}$ remained neddylated for longer than CUL3^{WT} (Figure 3.5 C) and also showed markedly reduced binding to CSN subunits (Figure 3.6 A). As such, the observed elevated Nedd8 modification of CUL3$^{\Delta 403\text{-}459}$ in cells is likely due to a combination of Nedd8 ligation to non-physiological lysine residues and of reduced CSN deneddylation.

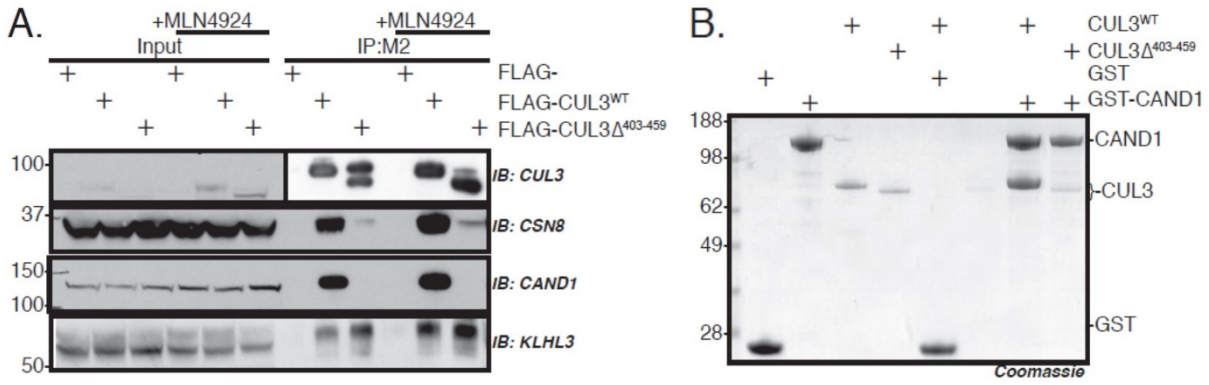

Figure 3.6: CUL3$^{\Delta 403\text{-}459}$ is unable to interact with CRL regulators.

[A] HEK293 overexpression pull-down assays revealed reduced CUL3$^{\Delta 403\text{-}459}$ binding to the COP9-Signalsome subunit CSN8. Additionally, there was a complete absence of CUL3$^{\Delta 403\text{-}459}$ binding to CAND1, even in the presences of MLN4924 which would be expected to increase the abundance of non-neddylated CUL3 for CAND1 to associate with. **[B]** *In vitro* pull-down assays using purified proteins confirms that CUL3^{WT} but not CUL3$^{\Delta 403\text{-}459}$ interacts with CAND1. [Taken from (Schumacher *et al.*, 2015)].

CRLs must be deneddylated for a productive interaction with the substrate-adaptor exchange factor CAND1. Furthermore, the structure of CUL1 bound to CAND1 suggests that, regardless of neddylation state, CUL3$^{\Delta 403\text{-}459}$ may be unable to form the required critical interactions (Goldenberg *et al.*, 2004; Pierce *et al.*, 2013; Wu & Peng, 2013; Zemla *et al.*, 2013). Therefore the next step was to investigate whether CUL3$^{\Delta 403\text{-}459}$ was indeed defective in binding to CAND1. Cells expressing either FLAG-CUL3^{WT} or FLAG-CUL3$^{\Delta 403\text{-}459}$ were treated with the neddylation inhibitor MLN4924 to force all of CUL3 into the non-neddylated state and then determined interaction with CAND1 by immunoprecipitation. While CUL3^{WT} strongly bound to CAND1 in these assays, CUL3$^{\Delta 403\text{-}459}$ was unable to interact with CAND1

(Figure 3.6 A). These findings were confirmed using *in vitro* assays with purified proteins (Figure 3.6 B). These data advocate that structural perturbations prevent CUL3$^{\Delta 403\text{-}459}$ from binding to CAND1. In combination with the impairment of CSN binding, such defects suggest the regulation of CUL3$^{\Delta 403\text{-}459}$ in cells is likely to be severely disrupted.

3.3.4 CUL3$^{\Delta 403\text{-}459}$ displays enhanced auto-ubiquitylation

The data suggests the regulation of CUL3$^{\Delta 403\text{-}459}$ is disrupted in cells, and it made sense to test whether its ubiquitylation activity is similarly affected. The Ellison group suggested that CUL3$^{\Delta 403\text{-}459}$ may stabilise WNK kinases by ectopically degrading the substrate adaptor KLHL3; preventing the formation of functional CUL3-KLHL3 complexes (McCormick *et al.*, 2014). Some CRLs are known to ubiquitylate bound substrate-adaptors (Wee *et al.*, 2005) and it is feasible that altering the CUL3 backbone structure could indeed lead to erroneous ubiquitylation of KLHL3. In the *in vitro* system, it was confirmed that CUL3$^{\Delta 403\text{-}459}$ directly modified KLHL3 with a greater efficiency than CUL3^{WT} (Figure 3.7 A). Interestingly, CUL3$^{\Delta 403\text{-}459}$ also exhibited markedly increased auto-ubiquitylation (Figure 3.7 B).

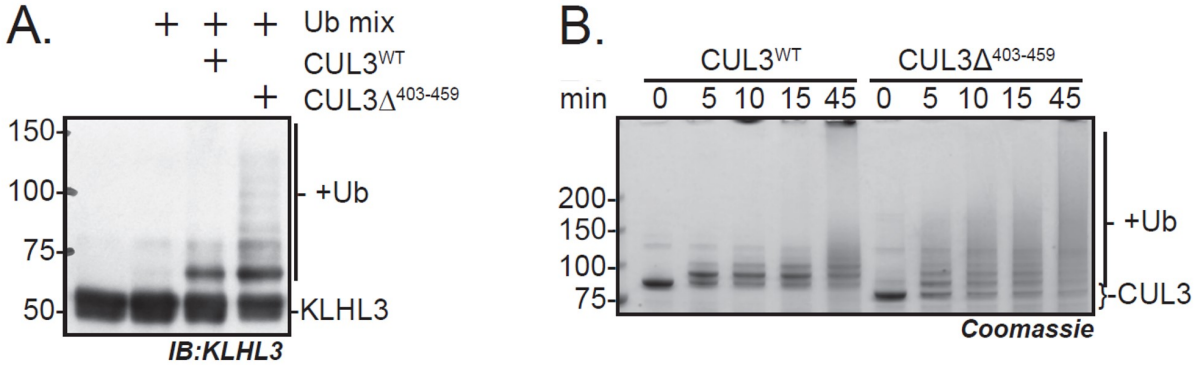

Figure 3.7: CUL3$^{\Delta 403\text{-}459}$ displays increased auto-ubiquitylation and ubiquitylation of KLHL3.

In vitro ubiquitylation assays with purified proteins. As ubiquitin is covalently attached to the substrate lysine residue, the appearance of higher molecular weight protein bands reflects the modification of the protein with ubiquitin. **[A]** Even at 2× molar concentration of KLHL3 over CUL3, CUL3$^{\Delta 403\text{-}459}$ was capable of much higher levels of KLHL3 ubiquitylation. **[B]** Time course measurements of basal auto-ubiquitylation reveal significantly higher levels of CUL3$^{\Delta 403\text{-}459}$ auto-ubiquitylation. [Taken from (Schumacher et al., 2015)].

Auto-ubiquitylation is often utilised as a read-out for ubiquitin ligase activity. In a cellular context, self-modification can lead to auto-degradation of the ligase (Silke *et al.*, 2005). If $CUL3^{\Delta 403-459}$ modifies lysine residues inaccessible to $CUL3^{WT}$, this could explain the increased auto-ubiquitylation. Alternatively, $CUL3^{\Delta 403-459}$ could build longer ubiquitin chains on the same lysine residues that are also targeted by $CUL3^{WT}$. To explore these possibilities, *in vitro* ubiquitylation assays were performed with methylated ubiquitin, a form of ubiquitin unable to build ubiquitin-chains (Kirisako *et al.*, 2006). In these assays $CUL3^{\Delta 403-459}$ was auto-modified on multiple lysine residues, while $CUL3^{WT}$ only mono-ubiquitylated one residue (Figure 3.8 A). Therefore the observed increase in auto-ubiquitylation is most likely due to erroneous modification of multiple lysine residues on $CUL3^{\Delta 403-459}$, which is consistent with an increase in structural flexibility as suggested by the model proposed here. Alternatively, the mutation may change the active site environment of CUL3, exposing more lysine residues close to the E2~UB binding site. To distinguish between these possibilities, the lysine residues modified in the *in vitro* assay system were mapped using mass spectrometry. *In vitro* auto-ubiquitylation reactions of CUL3 were performed with methylated ubiquitin for either five or 45 min and the ubiquitylated lysine residues were determined by analysing which lysine residue(s) carry di-Glycine remnants after trypsin digest (Kim *et al.*, 2011). Using this approach it was found that after five min $CUL3^{WT}$ was only auto-ubiquitylated on a single lysine residue (K336), while ten lysine residues on $CUL3^{\Delta 403-459}$ were modified (Figure 3.8 B-C). After running the reaction for 45 min, the modification sites on $CUL3^{WT}$ had increased to five, all of which were C-terminal to the original site and contained within the globular C-terminal Cullin domain. The ubiquitylation sites on $CUL3^{\Delta 403-459}$, however, had increased to 25 sites distributed along the entire length of the protein (most N-terminal: K47; most C-terminal: K743) (Figure 3.8 B-C).

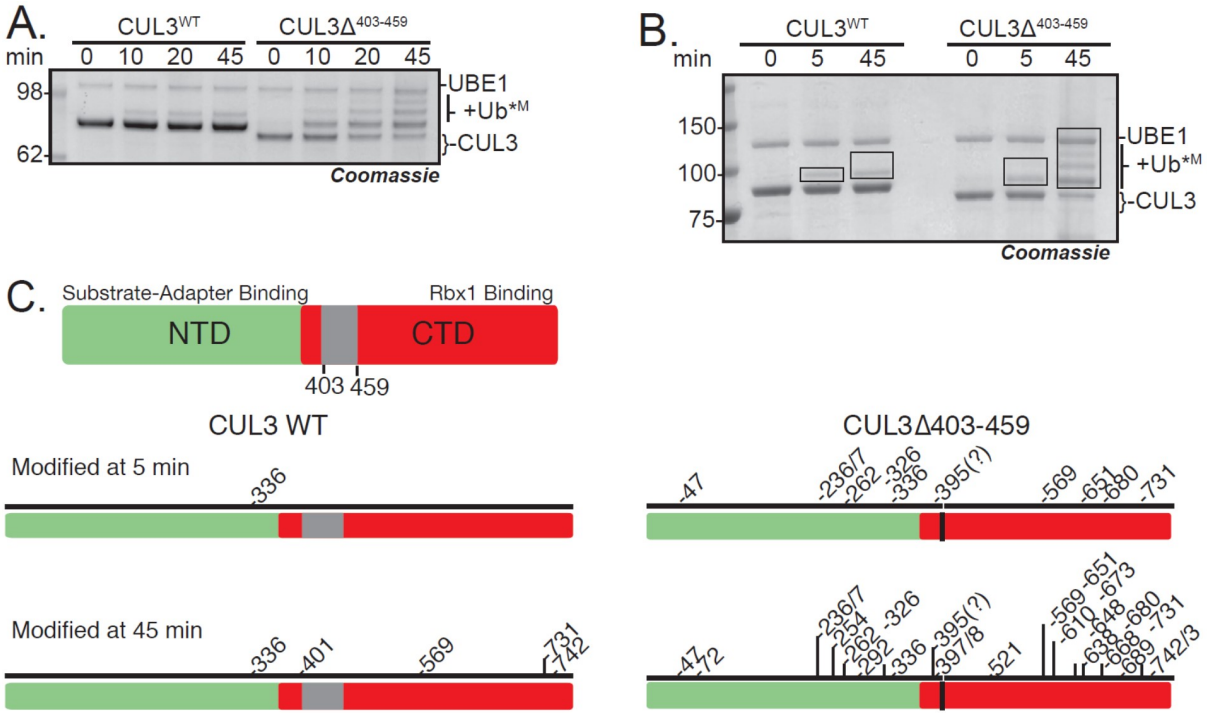

Figure 3.8: CUL3$^{\Delta 403-459}$ is auto-ubiquitylated at multiple residues.

[A] *In vitro* activity assays containing methylated ubiquitin, a form of ubiquitin incapable of forming ubiquitin chains, show that CUL3$^{\Delta 403-459}$ is ubiquitylated at more lysine residues than CUL3^{WT} as evidenced by the higher bands in CUL3$^{\Delta 403-459}$. **[B]** Activity assay performed as in **[A]** with methyl-ubiquitin, the boxes shown on the gel are indicative of the gel pieces excised for mass spectrometry analysis in **[C]**. **[C]** Schematic representation (to linear residue scale) highlighting the domains of CUL3 and schematic representation of the lysine residues of CUL3^{WT} or CUL3$^{\Delta 403-459}$, modified at 5 and 45 min, as determined by mass spectrometry. [Taken from (Schumacher et al., 2015)].

These results support the model that the CUL3 exon-9 deletion induces increased structural flexibility, leading to the erroneous auto-ubiquitylation of sites normally not accessible to CUL3^{WT} (Figure 3.9).

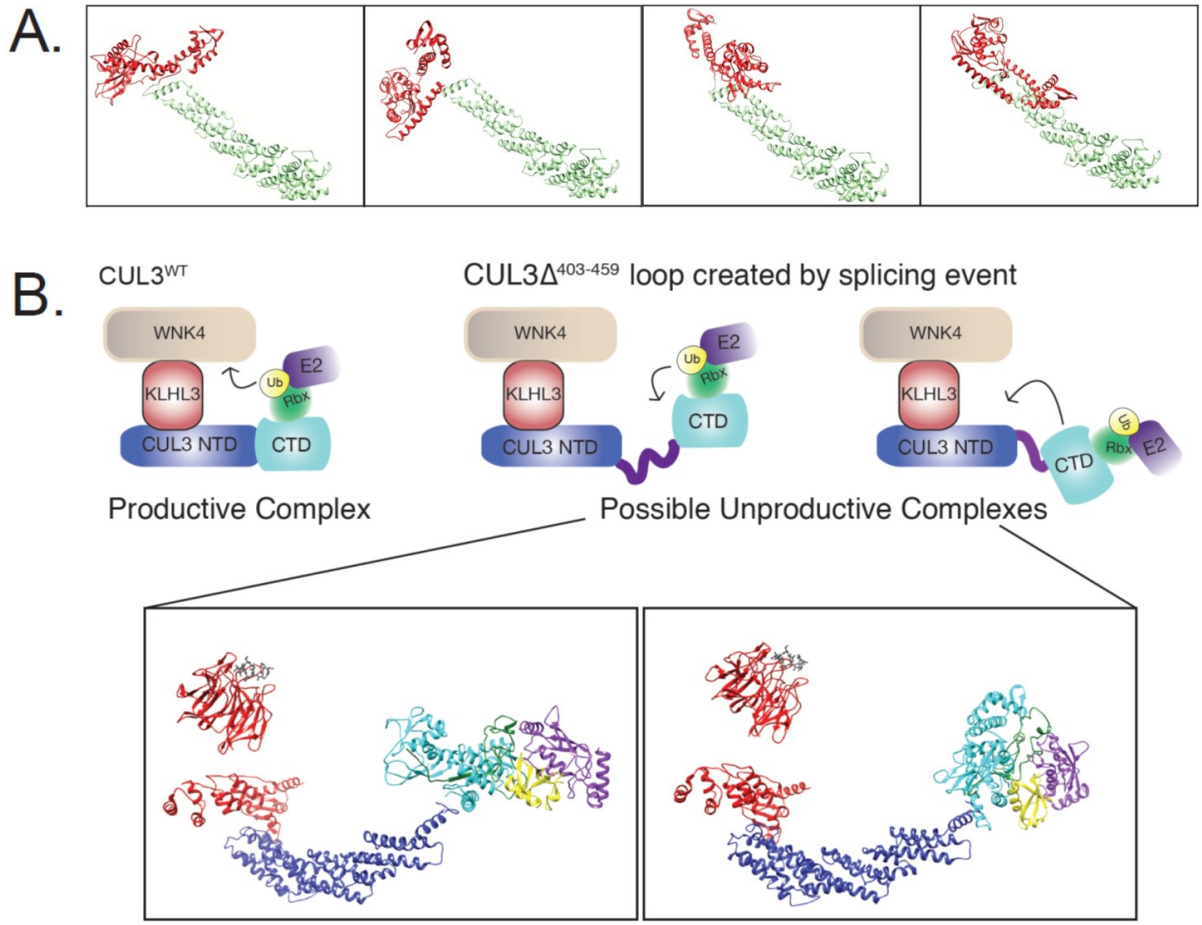

Figure 3.9: Schematic representation of the possible structural effects of the mutation.

[A] Structural docking model of CUL3$^{\Delta 403-459}$ based on the structure of full-length CUL1 (PDB: 1LDK) using Chimera. The NTD is coloured green, while the CTD is red, and the four panels sample possible positioning of the CTD relative to the NTD in CUL3$^{\Delta 403-459}$, assuming full flexibility of the linker after deletion of three helices encoded by exon-9. **[B]** The schematics represent a functional CUL3^{WT} complex and show two contrasting positions for an active CUL3$^{\Delta 403-459}$ that is unable to modify the WNK kinases. The structural representations (bottom) correspond to the schematics above. These were generated in Chimera, and known structures were utilised as docking references to enable the possible orientations to be explored. KLHL3-KELCH domain (red) bound to a WNK peptide (grey) (PDB: 4CH9). KLHL3-BTB domain (red) bound to CUL3-N-terminal domain (blue), CUL3-C-terminal domain (cyan) (based on CUL1 CTD) (PDB: 1LDK). RBX1 (green), UBE2D (purple) and ubiquitin (yellow) were docked based on the complex RNF4-E2-UB structure (PBD: 4AP4). [Taken from (Schumacher et al., 2015)].

3.3.5 CUL3$^{\Delta 403-459}$ cannot ubiquitylate WNK kinases

As CUL3$^{\Delta 403-459}$ is able to more efficiently auto-ubiquitylate itself and KLHL3, the next question asked was whether it similarly shows increased ubiquitylation towards a bound WNK substrate in *in vitro* ubiquitylation assays using purified components. As previously shown, CUL3^{WT} efficiently ubiquitylates WNK kinases *in vitro* (Ohta *et al.*, 2013) (Figure 3.10).

$CUL3^{\Delta 403\text{-}459}$, however, while maintaining the ability to efficiently modify itself and KLHL3, was not able to modify either WNK1 or WNK4 (Figure 3.10 A-B). As described for CUL1 (Zheng *et al.*, 2002), increasing the flexibility of the Cullin backbone, can lead to a decrease in substrate modification, while promoting excessive modification of other CRL components (Zheng *et al.*, 2002). Thus, increased structural flexibility of $CUL3^{\Delta 403\text{-}459}$ may lead to similar defects. If so, then it becomes important to understand how this *in vitro* finding can explain the increased WNK stabilisation found *in vivo*. It is possible that only one of the three defects, the lack of substrate ubiquitylation, the increased Cullin auto-ubiquitylation or the increased KLHL3 ubiquitylation, is the major driver for the observed phenotypes. Decisively, KLHL3 levels are not decreased in the kidney of $CUL3^{WT/\Delta 403\text{-}459}$ mice, while the overall CUL3 levels are lower (Figure 3.11 A). This suggests that KLHL3 degradation is unlikely to contribute to the observed PHA2E phenotype and instead proposes that $CUL3^{\Delta 403\text{-}459}$ stabilises WNK levels in the following ways: firstly, $CUL3^{\Delta 403\text{-}459}$ excessively auto-ubiquitylates, leading to its own degradation, and secondly, any $CUL3^{\Delta 403\text{-}459}$ protein that escapes degradation cannot promote the ubiquitylation of the WNK kinases. Importantly, all PHA2E patients are heterozygous for the mutation, suggesting that with respect to blood pressure regulation $CUL3^{\Delta 403\text{-}459}$ behaves either as a dominant-negative or $CUL3^{WT}$ is haploinsufficient. These data demonstrate that the mutation causes a loss-of-function, so a dominant-negative effect seemed less likely. It was also found that *in vitro*, equimolar amounts of $CUL3^{\Delta 403\text{-}459}$ do not appear to inhibit $CUL3^{WT}$ ubiquitylation of WNK4 (Figure 3.10 C), which further supported the concept of haploinsufficiency.

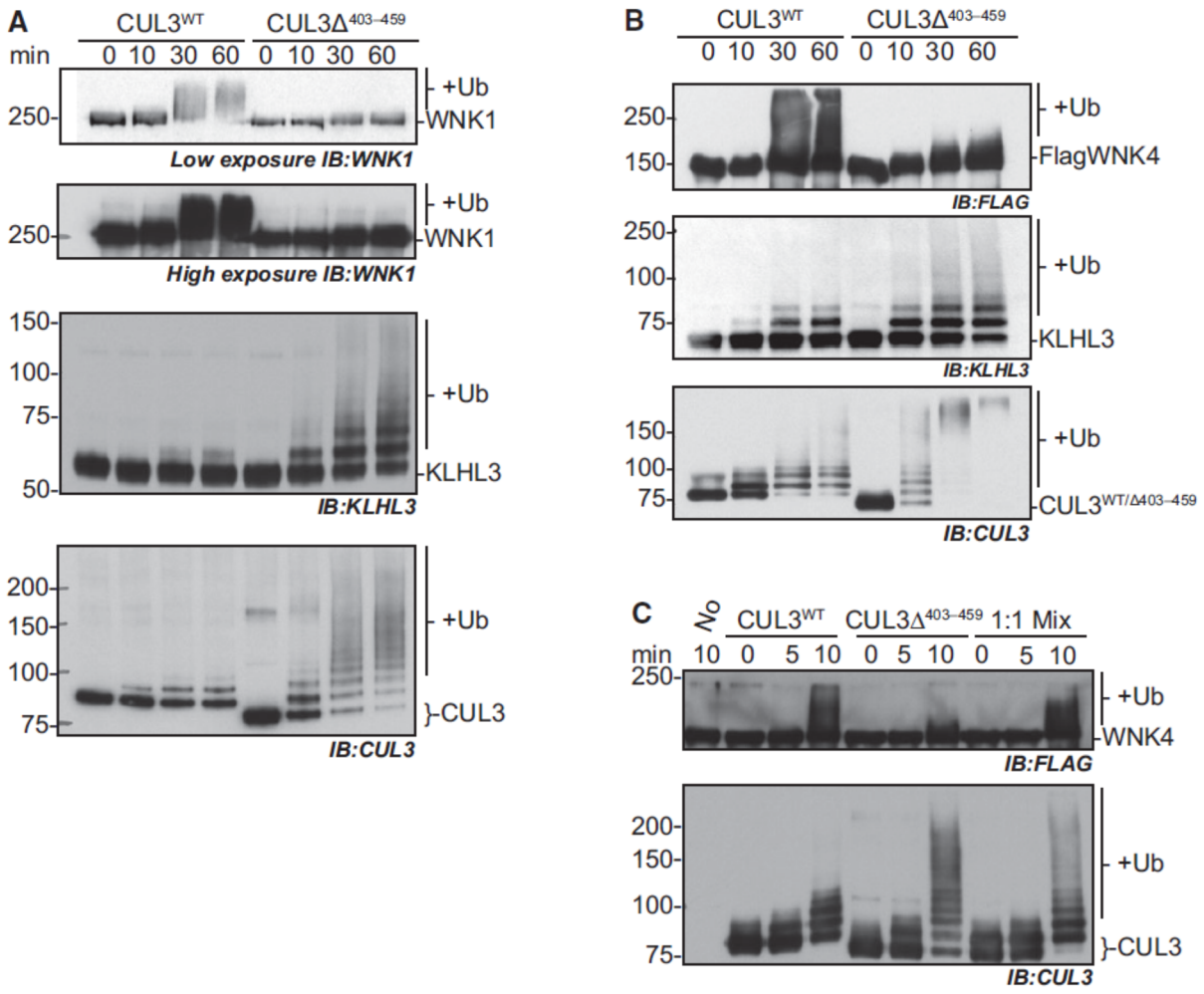

Figure 3.10: CUL3 $^{\Delta 403\text{-}459}$ is unable to ubiquitylate WNK1 or WNK4 kinases in an *in vitro* system.

In vitro ubiquitylation assays using immunoprecipitated proteins show **[A]** CUL3 $^{\Delta 403\text{-}459}$ has lost the ability to modify either **[A]** WNK1 or **[B]** with ubiquitin (Ub), and instead has increased ubiquitylation activity directed towards itself and KLHL3. **[C]** In an equimolar solution of CUL3^{WT}:CUL3$^{\Delta 403\text{-}459}$ (1:1 Mix) also containing KLHL3 and WNK4, the presence of CUL3$^{\Delta 403\text{-}459}$ did not appear to inhibit WNK ubiquitylation by CUL3^{WT}. [Taken from (Schumacher et al., 2015)].

3.3.6 CUL3$^{WT/\Delta 403\text{-}459}$ mice have increased WNK kinase pathway signalling with typical FHHt phenotypic features of electrolyte imbalance and growth retardation

To complement the *in vitro* findings and to determine more accurately what occurs in PHA2E patients, a knock-in mouse carrying the same exon-9 deletion of CUL3 as reported in PHA2E pedigrees (CUL3$^{\Delta 403\text{-}459}$) was engineered. Despite setting up heterozygous mating pairs, no homozygous knock-in mice were born suggesting that, like deletion of the entire coding region of CUL3, the homozygous deletion of residues 403-459 is lethal (Singer *et al.*, 1999).

Nevertheless, all the reported PHA2E pedigrees are heterozygous, so the heterozygous knock-in mice were phenotyped. Utilising both immunoblotting of whole kidney lysates and immunofluorescence confocal microscopy of kidney sections the relative abundance and distribution of proteins involved in the WNK signalling pathway was determined. Whole kidney lysate was analysed by immunoblotting confirming the expression of CUL3 and the presence of an additional band corresponding to the expected PHA2E form, $CUL3^{\Delta 403-459}$, in the heterozygous mice (Figure 3.11 A). In the context of the *in vitro* data, examining the levels of KLHL3 and CUL3 in the mouse kidney was especially warranted, and the expression of KLHL3 and CUL3 in normal human kidney lysates was confirmed to support inferences about the human condition (Figure 3.11 B). Definitively, the overall level of KLHL3 was comparable between $CUL3^{WT/WT}$ and $CUL3^{WT/\Delta 403-459}$ mice (Figure 3.11 A). In contrast, $CUL3^{\Delta 403-459}$ appears to be less abundant than $CUL3^{WT}$ in the heterozygous mice. These observations suggest that $CUL3^{\Delta 403-459}$ does not promote KLHL3 degradation *in vivo* and moreover, that the lower levels of $CUL3^{\Delta 403-459}$ may be due to the propensity of $CUL3^{\Delta 403-459}$ to self-modify presumably causing degradation through the UPS. The lower level of observable $CUL3^{\Delta 403-459}$ may also be due to non-proteolytic hyper-modification of $CUL3^{\Delta 403-459}$ with either Nedd8 or ubiquitin. Indeed, this may in part be the case, as incubation of kidney extract at room temperature to promote de-conjugation of Nedd8 or ubiquitin, increased the abundance of the faster migrating $CUL3^{\Delta 403-459}$ band, but did not restore it to $CUL3^{WT}$ levels (Figure 3.11 A, lower panel). Regardless of precisely why, increased levels of WNK4 and downstream signalling of the WNK kinase pathway, reported in other mouse models of FHHt, were also observed (Figure 3.11 C-D) and consistent with a PHA2E model. Specifically, there were striking increases in phospho-SPAK as well as total and phosphorylated forms of NCC (Figure 3.11 C). A decrease in the level of total and active ENaC was also noted, without changes in its regulator, Nedd4-2 (Figure 3.11 D). This finding is supported by the McCormick group who found a blunted natriuretic response to amiloride (Ferdaus *et al.*, 2017), suggesting impaired electrogenic Na^+ reabsorption through ENaC to provide the drive for potassium secretion, and therefore contributing to hyperkalaemia.

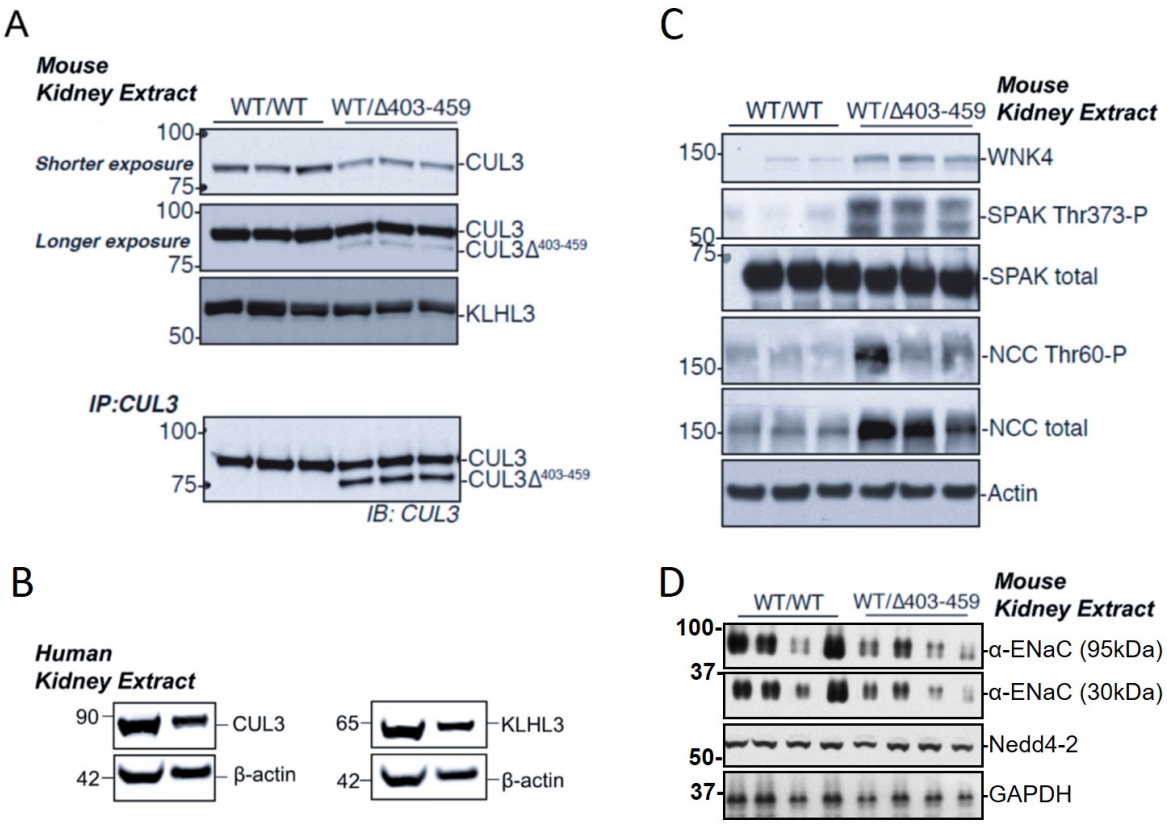

Figure 3.11: CUL3$^{WT/\Delta 403-459}$ mice have over-activation of the renal WNK pathway.

Western blot of whole kidney lysates from mice culled after a minimum 4-h fast. **[A]** Immunodetection reveals KLHL3 levels do not differ between groups, however levels of CUL3 are significantly decreased in CUL3$^{\Delta 403-459}$ mice. (Lower panel) Deneddylation of immunoprecipitated CUL3 reveals that CUL3$^{\Delta 403-459}$ is indeed present within the kidney lysate, and suggests that neddylated CUL3$^{\Delta 403-459}$ likely overlaps with the non-neddylated CUL3^{WT} band. **[B]** Western blot analysis confirmed the expression of KLHL3 and CUL3 in normal healthy human kidneys. **[C]** Immunodetection highlights elevated signalling through the WNK kinase pathway in CUL3$^{WT/\Delta 403-459}$ versus CUL3$^{WT/WT}$ mice. **[D]** CUL3$^{WT/\Delta 403-459}$ mice have reduced expression of the inactive uncleaved α-ENaC subunit (95kDa) and activated cleaved portion of the α-ENaC subunit (30kDa), but unaltered Nedd4-2 expression. [Adapted from (Schumacher et al., 2015)].

Over-activation of the WNK pathway would be expected to perturb electrolyte homeostasis. This was confirmed by measuring urine electrolytes, blood biochemistries and aldosterone levels in the mice (Figure 3.12, Figure 3.13, Figure 3.14). The CUL3$^{WT/\Delta 403-459}$ mice showed typical features of FHHt with hyperkalaemia, hyperchloraemia and a compensated metabolic acidosis; with the pH maintained by an increased respiratory drive to increase CO_2 removal, hence reduced total CO_2 and pCO_2 levels (Figure 3.12). Detailed electrolyte analysis of plasma and urine revealed several disturbances in mice fed a normal-

sodium diet, in particular hypermagnesaemia and hyperphosphataemia, which are the converse of the abnormalities reported in Gitelman syndrome/Gitelman-like animal models with several of the disturbances partially corrected on a low-sodium diet (Akhtar & Hafeez, 2009; Rafiqi *et al.*, 2010; Pathare *et al.*, 2012; Ali *et al.*, 2013) (Figure 3.13, Figure 3.14). The mice also had elevated aldosterone levels driven by the hyperkalaemia without pronounced hypervolaemia as evidenced by similar haematocrit levels (Figure 3.12, lower panel). Additionally, the $CUL3^{WT/\Delta 403\text{-}459}$ mice have significantly lower body weight and body length relative to the WT mice (Figure 3.15). This is consistent with Gordon's original observation that children with PHA2 may present with a low percentile body weight and height for their age (Gordon, 1986) and more recent reports that $CUL3^{WT/\Delta 403\text{-}459}$ patients are growth retarded (Tsuji *et al.*, 2013; Osawa *et al.*, 2013).

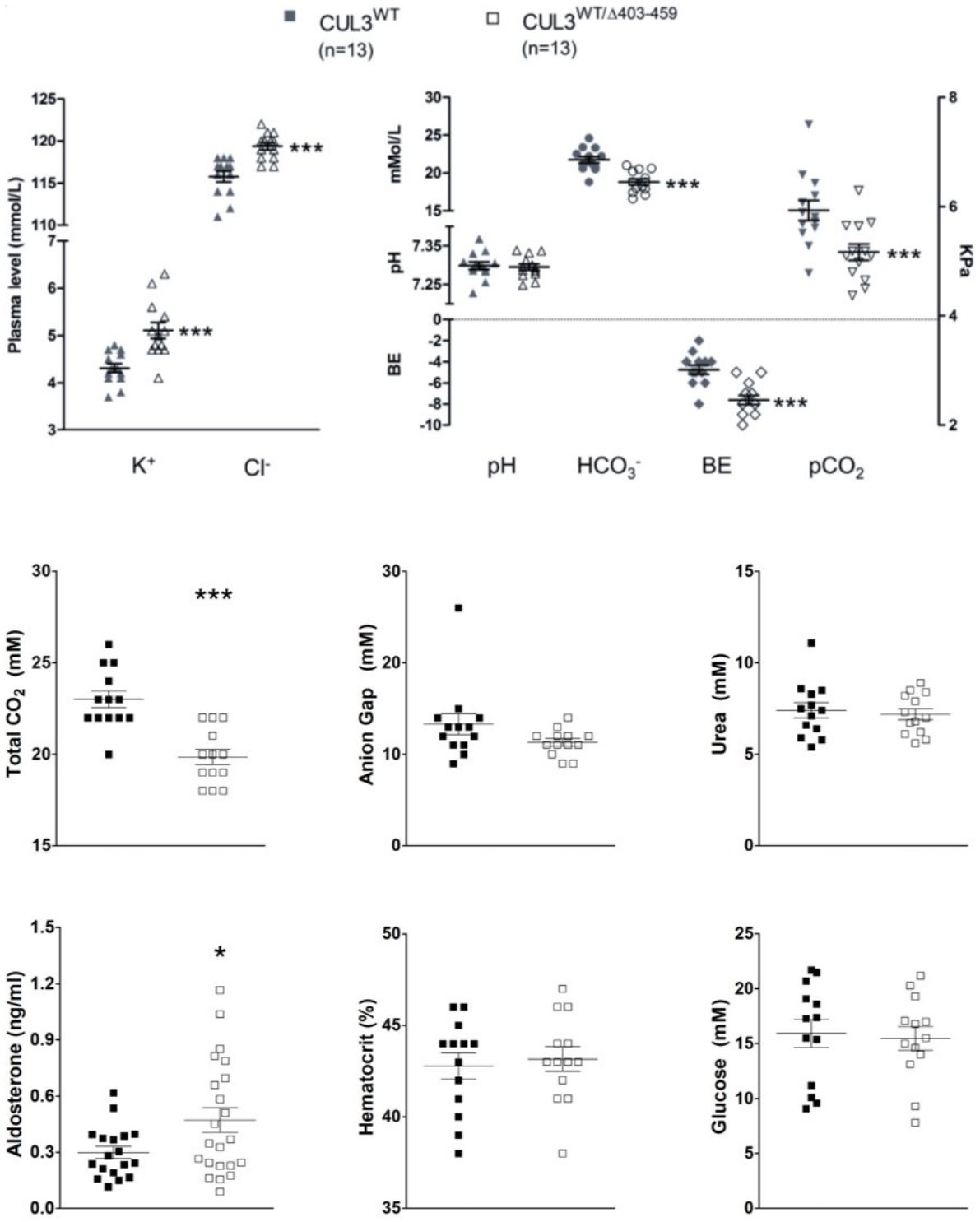

Figure 3.12: CUL3$^{WT/\Delta 403-459}$ mice have hyperkalaemia, hyperchloraemia with compensated metabolic acidosis.

Arterial blood biochemistries after a minimum 4-h fast. CUL3$^{WT/\Delta 403-459}$ mice present with abnormal electrolyte homoeostasis compared to CUL3$^{WT/WT}$ mice, exhibiting hyperkalaemia (***P = 0.0004) and hyperchloraemia (***P = 9.5×10^{-5}) with a compensated metabolic acidosis (P = 0.7766), marked by decreases in bicarbonate (HCO_3^-) (***P = 3.4×10^{-5}), base excess (BE) (***P = 9.1×10^{-5}), partial pressure of carbon dioxide (pCO_2) (***P = 0.0038), total CO_2 (***P = $3.7x10^{-5}$) with normal anion gap (P = 0.1022) and urea levels (P = 0.8914). A 58% increase in aldosterone was detected in CUL3$^{WT/\Delta 403-459}$ (n=22) versus CUL3$^{WT/WT}$ (n=18) mice (*P = 0.0245) with no significant changes in haematocrit (P

= 0.8757), a volaemic status marker, or glucose homeostasis (P = 0.8757). Two-tailed unpaired Student's t-test; data are mean ± SEM. [Adapted from (Schumacher et al., 2015) with changes to data presentation].

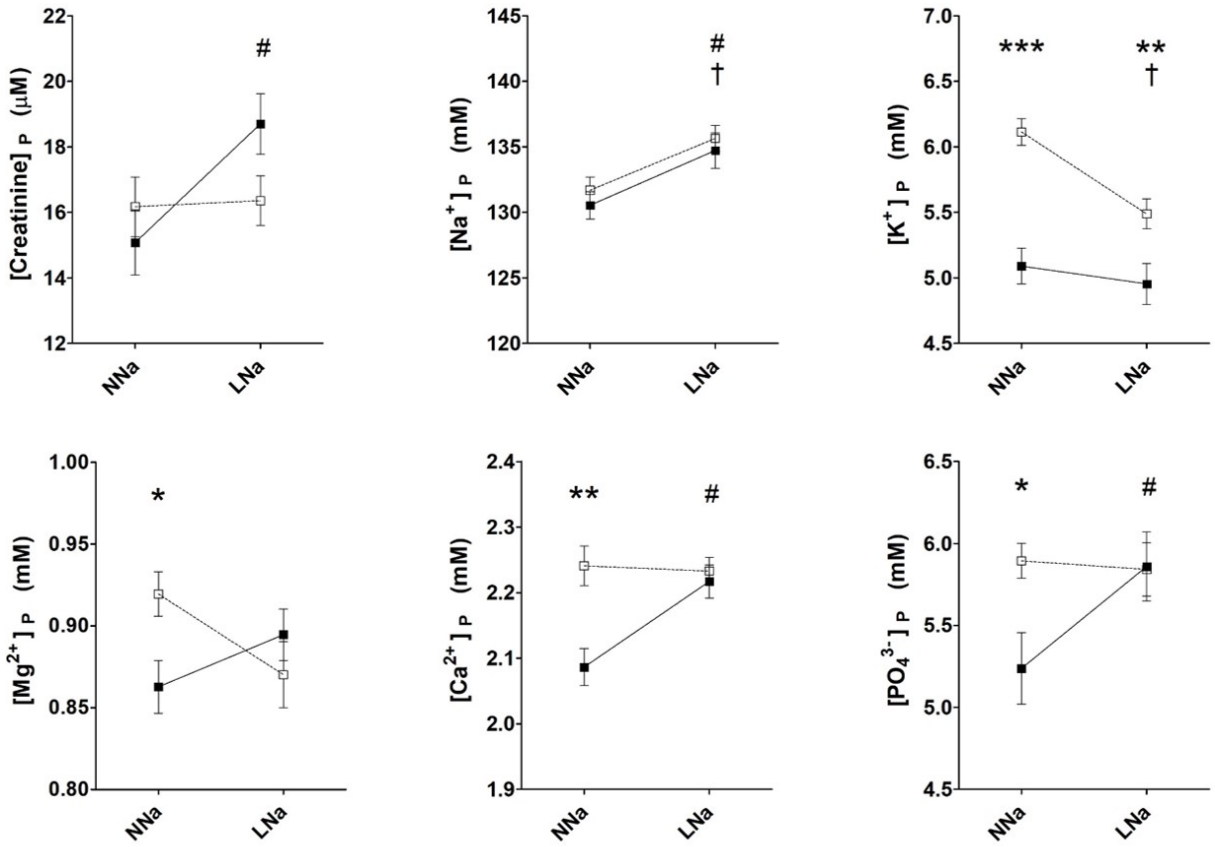

P-Values

Plasma	Creatinine	Na^+	K^+	Mg^{2+}	Ca^{2+}	PO_4^{3-}
NNa: $CUL3^{WT}$ vs $CUL3^{WT/\Delta403-459}$	0.4326	0.4459	$4.1x10^{-7}$	0.0110	0.0015	0.0129
LNa: $CUL3^{WT}$ vs $CUL3^{WT/\Delta403-459}$	0.0550	0.8120	0.0078	0.3749	0.8195	0.9470
$CUL3^{WT}$: NNa vs LNa	0.0072	0.0478	0.6643	0.4043	0.0083	0.0493
$CUL3^{WT/\Delta403-459}$: NNa vs LNa	0.9714	0.0194	0.0004	0.0755	0.4859	0.9757

Figure 3.13: Plasma electrolyte homeostasis in response to normal-to-low sodium diet switch.

Plasma (P) electrolytes on either a 0.3% w/w normal-sodium (NNa) or 0.03% w/w low-sodium (LNa) diet measured by ICP-OES analysis. The differences between genotypes that are significantly different are shown as *, the differences between NNa and LNa for $CUL3^{WT/WT}$ that are significantly different are shown as #, and the differences between NNa and LNa for $CUL3^{WT/\Delta403-459}$ that are significantly different are shown as † (n-values as follows: $CUL3^{WT/WT}$: NNa = 16; LNa = 17 // $CUL3^{WT/\Delta403-459}$: NNa = 23; LNa = 23). Two-tailed unpaired Student's t-test for comparisons between genotypes and two-tailed paired Student's t-test for comparisons between diets within the same genotype; data are mean ± SEM. [Adapted from (Schumacher et al., 2015) with changes to table order].

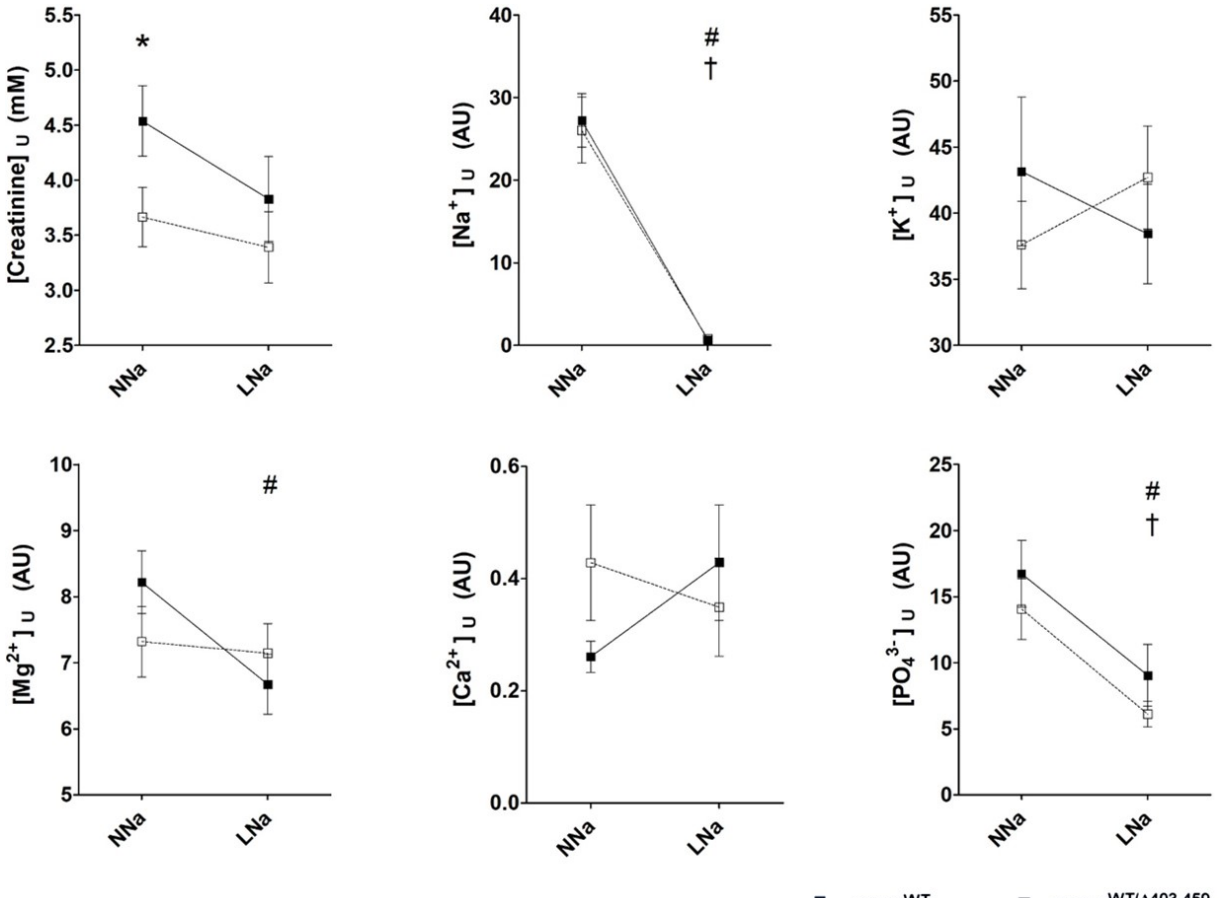

P-Values

Urine	Creatinine	Na^+	K^+	Mg^{2+}	Ca^{2+}	PO_4^{3-}
NNa: $CUL3^{WT}$ vs $CUL3^{WT/\Delta403-459}$	0.0424	0.8236	0.3852	0.2191	0.0633	0.4370
LNa: $CUL3^{WT}$ vs $CUL3^{WT/\Delta403-459}$	0.3864	0.8700	0.4400	0.4714	0.5574	0.2602
$CUL3^{WT}$: NNa vs LNa	0.2503	$2.5x10^{-6}$	0.6864	0.0126	0.1545	0.0395
$CUL3^{WT/\Delta403-459}$: NNa vs LNa	0.5435	0.0001	0.4127	0.5515	0.0671	0.0031

Figure 3.14: Urine electrolyte homeostasis in response to normal-to-low sodium diet switch.

Urinary (U) electrolytes on either a 0.3% w/w normal-sodium (NNa) or 0.03% w/w low-sodium (LNa) diet measured by ICP-OES analysis. The urinary electrolyte values (arbitrary units; AU) are calculated as a ratio of the urinary concentration of creatinine ($[analyte]_U/[creatinine]_U$). The differences between genotypes that are significantly different are shown as *, the differences between NNa and LNa for $CUL3^{WT/WT}$ that are significantly different are shown as #, and the differences between NNa and LNa for $CUL3^{WT/\Delta403-459}$ that are significantly different are shown as † (n-values as follows: $CUL3^{WT/WT}$: NNa = 18; LNa = 16 // $CUL3^{WT/\Delta403-459}$: NNa = 21; LNa = 19). Two-tailed unpaired Student's t-test for comparisons between genotypes and two-tailed paired Student's t-test for comparisons between diets within the same genotype; data are mean ± SEM. [Adapted from (Schumacher et al., 2015) with changes to table order].

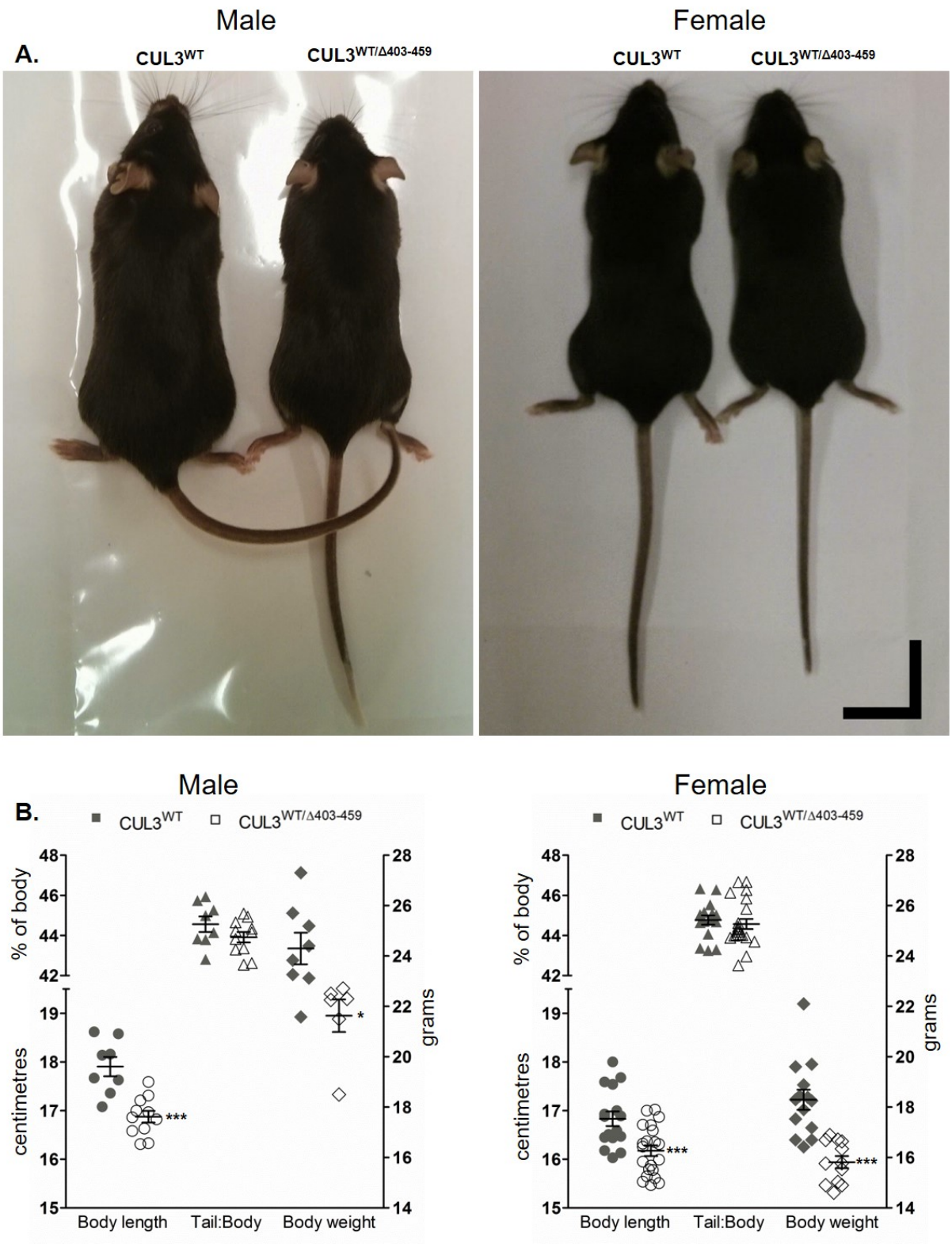

Figure 3.15: CUL3$^{WT/\Delta 403-459}$ mice have growth retardation.

[A] Illustrative side-by-side size comparisons of male and female CUL3$^{WT/\Delta 403-459}$ and CUL3$^{WT/WT}$ littermates. Scale bar = 2cm. **[B]** CUL3$^{WT/\Delta 403-459}$ exhibit features of growth retardation when compared with CUL3$^{WT/WT}$ mice. The CUL3$^{WT/\Delta 403-459}$ have lower body weight (male: * P=0.0128 // female: *** P=3.3x10^{-5}) and length [measured nose-to-anus] (male: *** P=0.0002 // female: *** P=0.0009), although with no changes in proportionality as measured by tail-to-body ratio (male: P=0.1654 // female

P=0.5817). Data are mean ± SEM (male n-values: $CUL3^{WT/WT}$ = 8, $CUL3^{WT/\Delta403-459}$ = 11 for body length; $CUL3^{WT/WT}$ = 8, $CUL3^{WT/\Delta403-459}$ = 6 for body weight // female n-values: $CUL3^{WT/WT}$ = 16, $CUL3^{WT/\Delta403-459}$ = 21 for body length; $CUL3^{WT/WT}$ = 14, $CUL3^{WT/\Delta403-459}$ = 12 for body weight). Two-tail unpaired student t-test; data are mean ± SEM. [Taken from (Schumacher et al., 2015)].

3.3.7 WNKs accumulate and form puncta with SPAK and OSR1 in the distal tubule of $CUL3^{WT/\Delta403-459}$ mice

Using immunofluorescence confocal microscopy of kidney sections, the distribution of proteins involved in the WNK kinase cascade in both $CUL3^{WT/WT}$ and $CUL3^{WT/\Delta403-459}$ mice was studied (Figure 3.16 A). $CUL3^{WT/\Delta403-459}$ mice showed a similar CUL3 distribution compared to both the WT mice, and to the WT human kidney (Figure 3.16 A-B). Increases were seen in the levels of WNK4 and pSPAK along the length of the distal tubule, which led to a rise in total and phospho-NCC levels in the early and late DCT, which was in keeping with the levels observed in the kidney immunoblots (Figure 3.11 A). There were no discernible changes in ROMK (which was more extensively studied in (Murthy *et al.*, 2016)) or total NKCC2 in the thick ascending limb (TAL; Figure 3.16 A), which was verified by the McCormick group but also shown to be hyperphosphorylated (Ferdaus *et al.*, 2017). This would be expected to increase potassium reabsorption and in combination with overactive NCC, decrease delivery of sodium to the ENaC expressing distal segments thereby impeding potassium excretion via ROMK. Although, new data is emerging to suggest that nephron remodelling underlies the hyperkalaemia in FHHt rather than reduced sodium delivery to ROMK-expressing distal tubules (Mccormick & Ellison, 2017).

In contrast, staining for WNK4, WNK1, SPAK and OSR1 in the $CUL3^{WT/\Delta403-459}$ mice revealed these proteins to have a striking punctate appearance in the early and late DCT (Figure 3.16 A, Figure 3.17), but not in the adjacent thick ascending limb (Figure 3.16 A). Recent reports also suggested the presence of these puncta in tubular segments downstream of the DCT (Boyd-Shiwarski *et al.*, 2017; Ferdaus *et al.*, 2017), and on further inspection of the data in this study a handful of connecting tubules (CNT) were discovered to have puncta which were smaller than those seen in the DCT (Figure 3.18 A).

While WNK1 and OSR1 puncta have been reported in the DCT of SPAK knock-out mice, these were smaller in size and far less numerous (Grimm *et al.*, 2012) and resemble the WNK1 puncta observed in our $CUL3^{WT/WT}$ mice (Figure 3.18 B). It was therefore hypothesised that the enlarged puncta of $CUL3^{WT/\Delta403-459}$ mice might represent an accumulation of WNK-

SPAK/OSR1 proteins within a protein-processing compartment, such as the trans-Golgi network or activation of secondary protein degradation pathways or storage compartments, due to failed proteasomal clearance (D'Urso *et al.*, 1998; Lamark & Johansen, 2012; Wolff *et al.*, 2014), however these puncta did not colocalise with several common markers of subcellular compartments (Figure 3.17). These enlarged puncta appear to represent a previously uncharacterised population distinct from that seen in WT mice. In particular, these puncta are electron-lucent, membraneless, 1-4 μm structures with preferential basolateral/juxta-nuclear localisation in the cytosol, commonly surrounded by dilated Golgi and numerous mitochondria (Figure 3.18 C).

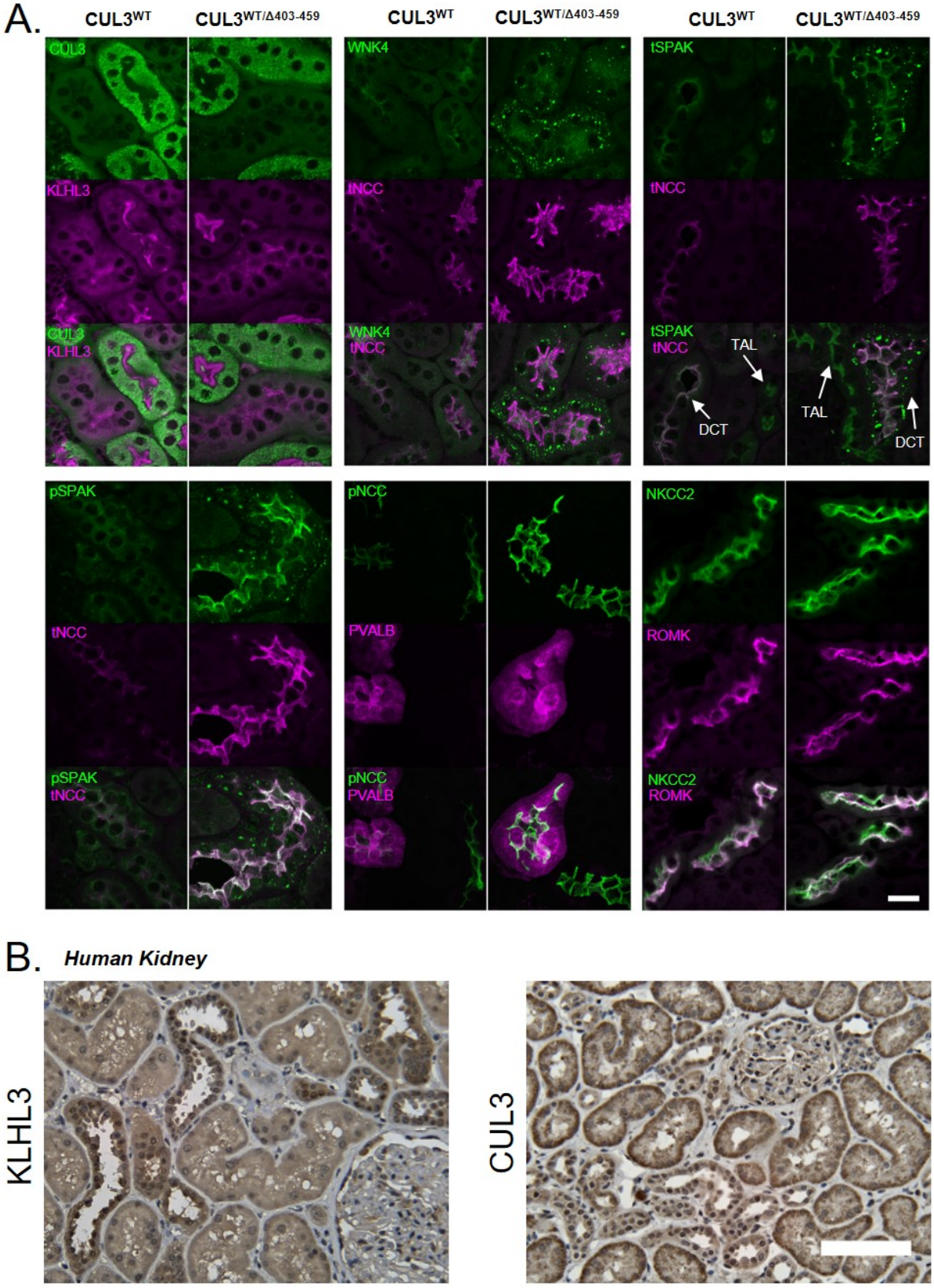

Figure 3.16: WNK4 accumulates and forms puncta in the distal convoluted tubule of CUL3$^{WT/\Delta 403-459}$

[A] Representative pseudocoloured maximum-intensity z projections of immunofluorescently stained kidney sections showing the distribution of the WNK/SPAK pathway components between CUL3$^{WT/\Delta 403-459}$ and CUL3$^{WT/WT}$ mice at a minimum 4-h fasting baseline (n = 4 per genotype). CUL3 and KLHL3 are comparable between genotypes, with significantly higher levels of CUL3 in the proximal convoluted tubule (PCT) compared to the weaker staining in the distal tubules, while KLHL3 shows higher expression in the cytosol of the distal tubules with staining of the PCT more prominent in the apical membrane. The increase in WNK4 abundance promotes phosphorylation (p) of NCC Thr44 and SPAK Thr243 and their localisation at the apical membrane of the parvalbumin (PVALB)-positive early and late (PVALB-negative) distal convoluted tubule (DCT) of CUL3$^{WT/\Delta 403-459}$ mice. This increases total (t) NCC levels but with no changes in total SPAK or NKCC2 and ROMK1 in the thick ascending limb (TAL) of the loop of Henle. Unexpectedly, the stabilisation of WNK4 and SPAK resulted in the formation of discrete puncta in the DCT of CUL3$^{WT/\Delta 403-459}$ mice, but not in the TAL. Scale bar, 20 µm. **[B]** Representative immunohistochemical staining of KLHL3 and CUL3 in human kidney sections (n = 6). KLHL3 shows preferential cytosolic staining in the distal tubules similar to the mouse despite no evidence of PCT apical staining as seen in **[A]**. CUL3 exhibits preferential basolateral cytosolic staining of the PCT with similarly low levels of diffuse staining in the distal tubules to that of the mouse. Scale bar, 100 µm. [Taken from (Schumacher et al., 2015)].

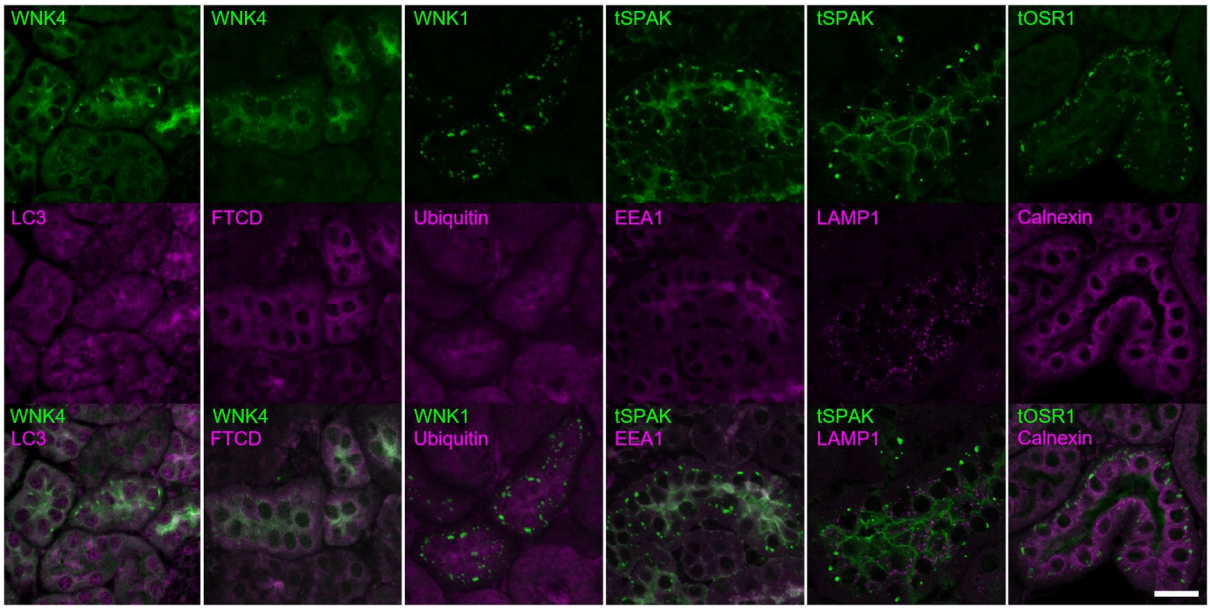

Figure 3.17: WNK4 puncta colocalise with other components of the WNK pathway and do not localises to any known subcellular compartments.

Representative pseudocoloured average-intensity z projections of immunofluorescently stained CUL3$^{WT/\Delta 403-459}$ mouse kidney sections (n = 4). Immunolocalisation of total (t) WNK4, WNK1, SPAK and OSR1showed they colocalise and form discrete punctate structures in the distal convoluted tubule at a 4-h fasting baseline. Surprisingly, these puncta do not colocalise with either autophagosome (LC3), Golgi apparatus (FTCD), ubiquitylated aggregate (Ubiquitin), endosome (EEA1), lysosome (LAMP1) or endoplasmic reticulum (Calnexin) markers. Scale bar, 20 µm. [Adapted from (Schumacher et al., 2015)].

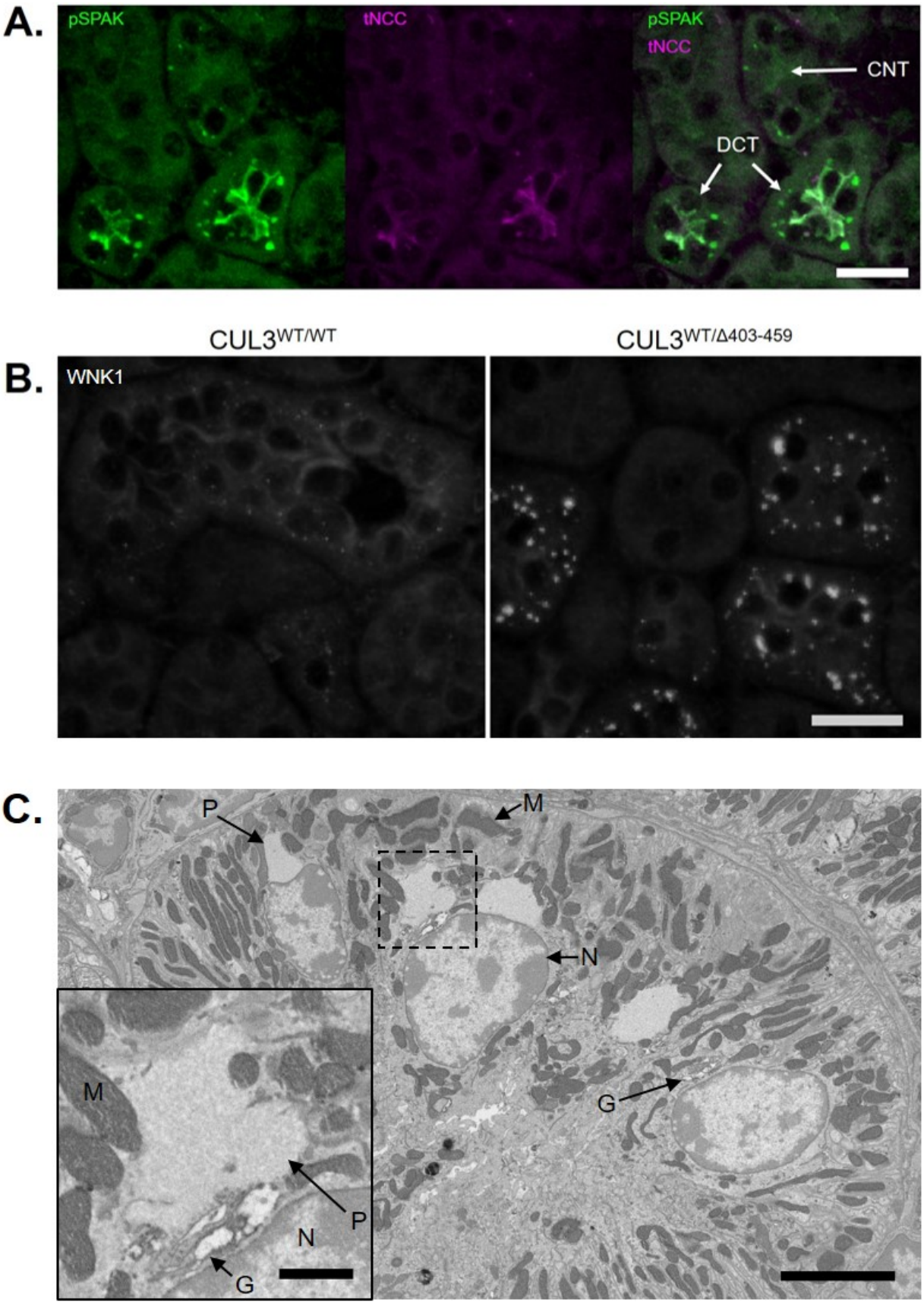

Figure 3.18: The enlarged WNK pathway puncta seen in CUL3$^{WT/\Delta403-459}$ mice represent a previously uncharacterised population of subcellular structures.

[A] Representative pseudocoloured average-intensity z projections of phospho-SPAK (pSPAK) and total NCC (tNCC) immunofluorescently stained CUL3$^{WT/\Delta403-459}$ mouse kidney sections (n = 4). While the puncta were not observed in the thick ascending limb of the loop of Henle, a very small population of these puncta were observed adjacent to the NCC-positive distal convoluted tubules (DCT) in the NCC-negative early connecting tubules (CNT). Scale bar, 20 μm. **[B]** Representative epifluorescent kidney sections (n = 4 per genotype) immunostained for WNK1 at a 4-h fasting baseline. A population of tiny WNK1 puncta can be seen in CUL3$^{WT/WT}$ mice, whereas puncta in CUL3$^{WT/\Delta403-459}$ mice appear to have two populations, one resembling that seen in CUL3$^{WT/WT}$ and a second population of enlarged puncta with a predominantly basolateral or juxta-nuclear preference. Scale bar, 20 μm. **[C]** Block-face scanning electron microscopy of osmium, uranium and lead stained DCT of a CUL3$^{WT/\Delta403-459}$ mouse, revealed the enlarged puncta (P) to be electron-lucent, membraneless structures that generally abut the nucleus (N) and are surrounded by mitochondria (M) and dilated Golgi (G). Scale bar, 5 μm. **[Inset]** Scale bar, 1 μm.

3.3.8 CUL3$^{WT/\Delta403-459}$ mice have hypertension and a novel vascular phenotype

Over-activation of the WNK pathway as observed in our CUL3$^{WT/\Delta403-459}$ mice (Figure 3.11 A, Figure 3.16 A) should lead to salt retention and elevated blood pressure. Therefore the blood pressure (BP) of the CUL3$^{WT/\Delta403-459}$ mice was measured using a pressure-transducer catheter in the common carotid artery under general anaesthesia. Both male and female CUL3$^{WT/\Delta403-459}$ mice exhibited significantly higher BP relative to CUL3$^{WT/WT}$ littermates (Figure 3.19 A).

Strikingly, a previously unreported haemodynamic change in the blood pressure trace of the CUL3$^{WT/\Delta403-459}$ mice was also observed. The systolic aortic pressure wave of the heterozygous mice is augmented while the diastolic pressure decay time constant (τ) is significantly slowed, a surrogate marker of increased vascular resistance (Munir *et al.*, 2007) (Figure 3.19 B). These changes suggest early wave reflection of the pressure wave and compliance changes consistent with a stiffened vascular tree. This stiffening could reflect a primary change in the contractile state of vascular smooth muscle, so to explore this the *in vivo* vasoconstrictor responses to intravenous administration of phenylephrine and angiotensin II was studied (Bergaya *et al.*, 2011) (Figure 3.19 C). The resulting dose-response curves showed that the maximal constrictor response to both vasopressor agents was substantially higher in the CUL3$^{WT/\Delta403-459}$ mice.

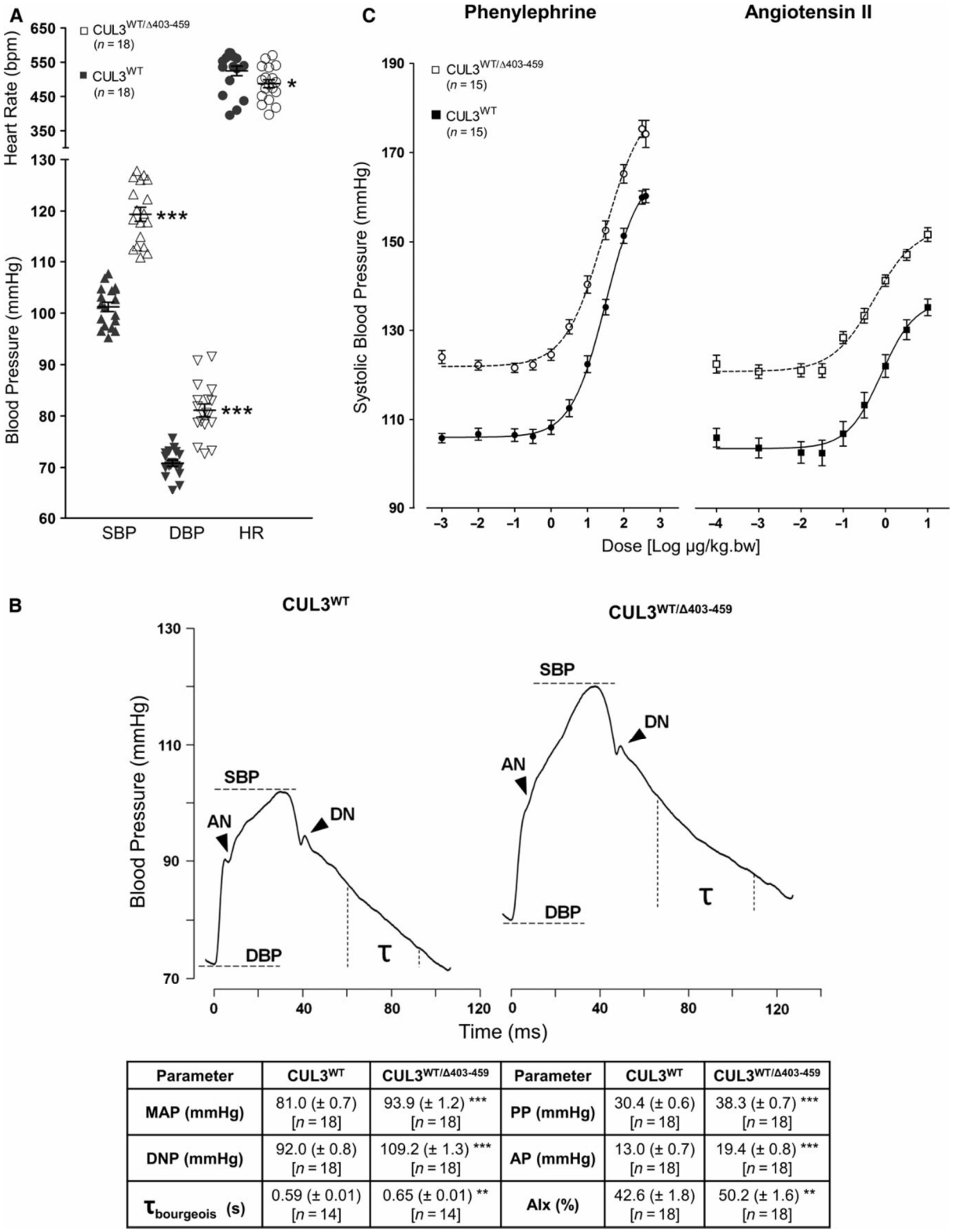

Parameter	CUL3^{WT}	CUL3$^{WT/\Delta403-459}$	Parameter	CUL3^{WT}	CUL3$^{WT/\Delta403-459}$
MAP (mmHg)	81.0 (± 0.7) [*n* = 18]	93.9 (± 1.2) *** [*n* = 18]	PP (mmHg)	30.4 (± 0.6) [*n* = 18]	38.3 (± 0.7) *** [*n* = 18]
DNP (mmHg)	92.0 (± 0.8) [*n* = 18]	109.2 (± 1.3) *** [*n* = 18]	AP (mmHg)	13.0 (± 0.7) [*n* = 18]	19.4 (± 0.8) *** [*n* = 18]
$\tau_{bourgeois}$ (s)	0.59 (± 0.01) [*n* = 14]	0.65 (± 0.01) ** [*n* = 14]	AIx (%)	42.6 (± 1.8) [*n* = 18]	50.2 (± 1.6) ** [*n* = 18]

Figure 3.19: Increased arterial stiffness contributes towards the hypertension of CUL3$^{WT/\Delta403-459}$ mice.

[A] CUL3$^{WT/\Delta403-459}$ mice have elevated systolic (SBP) (***P = 1 × 1012) and diastolic (DBP) blood pressure (***P = 8.5 × 108), although they also present with 7% lower heart rates (*P = 0.0485) when compared to CUL3$^{WT/WT}$ mice. Two-tailed unpaired Student's t-test; data are mean ± SEM. **[B]** Pulse waveform analysis of blood pressure traces obtained in **[A]** reveals that CUL3$^{WT/\Delta403-459}$ mice have an

increased pulse pressure (PP) [SBP – DBP] (***P = 2.1 × 1010), augmentation pressure (AP) [SBP – anacrotic notch (AN) pressure] (***P = 3.5 × 106), dicrotic notch (DN) pressure (***P = 4.7 × 1013) and mean arterial pressure (MAP) [1/3 × SBP + 2/3 × DBP] (***P = 1.3 × 109). This hypertensive phenotype is in part due to changes in vascular contractility in $CUL3^{WT/\Delta 403-459}$ mice as evidenced by their higher augmentation index (AIx) [AP/PP] (**P = 0.0096), a marker of arterial stiffness, and is further supported by an increase in their diastolic pressure decay time constant ($\tau_{bourgeois}$) [1/slope of diastolic pressure decay; measured 30 ms after DN and 20 ms before end DBP] (**P = 0.0083), a surrogate marker of increased vascular resistance. Two-tailed unpaired Student's t-test; data are mean ± SEM. **[C]** *In vivo* dose–responses to phenylephrine and angiotensin II, after baseline measurements were obtained from mice in **[A].** The fitted E_{max} for phenylephrine was increased in $CUL3^{WT/\Delta 403-459}$ versus $CUL3^{WT/WT}$ (183.9 ± 2.5 versus 164.9 ± 1.4 mmHg) (***P = 1 × 10^{-}6) indicating an increased vasoconstrictor response to adrenergic stimulation elevating systolic blood pressure substantially above the $CUL3^{WT/WT}$ maximum. Similarly, the fitted E_{max} for angiotensin II stimulation was higher in $CUL3^{WT/\Delta 403-459}$ versus $CUL3^{WT/WT}$ (155.5 ± 1.8 versus 138.3 ± 2.2 mmHg) (***P = 1.7 × 10^{-}6). However, there was no change between $CUL3^{WT/\Delta 403-459}$ versus $CUL3^{WT/WT}$ sensitivity (as measured by ED_{50}) to phenylephrine (36.6 ± 5.1 versus 31.4 ± 2.8 µg/kg.bw) (P = 0.3778) or angiotensin II (0.77 ± 0.16 versus 0.93 ± 0.13 µg/kg.bw) (P = 0.4401). Two-tailed unpaired Student's t-test; data are mean ± SEM. [Taken from (Schumacher et al., 2015)].

3.3.9 CUL3 and KLHL3 is expressed in the mouse and human aorta, and $CUL3^{WT/\Delta 403-459}$ mice have aortic wall thickening

We also looked for evidence of biochemical changes in the vasculature and confirmed the expression of CUL3 and KLHL3 in mouse and human aorta by immunoblot analysis (Figure 3.20). Similar to the kidneys (Figure 3.11 A), no differences were seen in KLHL3 expression between $CUL3^{WT/\Delta 403-459}$ and $CUL3^{WT/WT}$ mice, while the levels of CUL3 WT protein were lower in $CUL3^{WT/\Delta 403-459}$ aorta.

Image analysis of mouse and human aortae confirmed that both have strong CUL3 and KLHL3 staining of the vascular endothelium and smooth muscle cells of the intimal and medial layers of the vessel wall (Figure 3.21 A). To address the altered contractility in the vessel wall *in vivo,* the level of phospho-myosin phosphatase target subunit 1 (pMYPT1) in aortic vessel lysates was also measured and showed a significant 1.7-fold increase, indicative of stimulation of the myosin-actin contractile machinery (Figure 3.21 B) (Feng *et al.*, 1999; Somlyo & Somlyo, 2003).

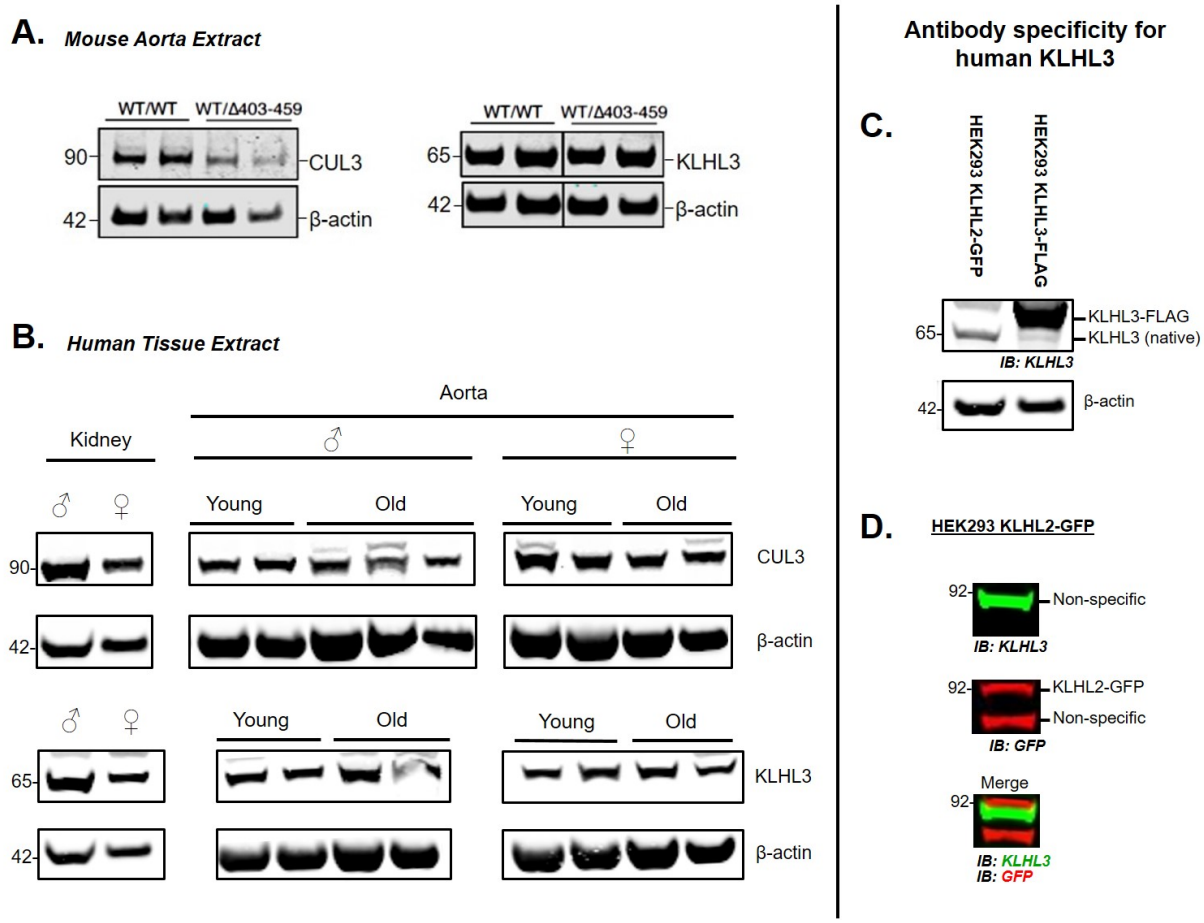

Figure 3.20: CUL3 and KLHL3 are present in mouse and human aorta.

[A] Western blot of tunica media-intima thoracic aorta lysates from mice culled after a minimum 4-h fast confirmed the expression of KLHL3 and CUL3. Similar to the kidney, the aorta of CUL3 $^{WT/\Delta403-459}$ showed slightly lower levels of CUL3 compared to CUL3$^{WT/WT}$ without any change in KLHL3 levels. **[B]** Western blot analysis confirmed the expression of KLHL3 and CUL3 in normal healthy human aorta. No obvious sex or age differences were observed. Human kidneys were used as positive controls. **[C]** Western blot of HEK-293 cell lysates over-expressing KLHL2-GFP or KLHL3-FLAG. The anti-KLHL3 antibody shows an intense band at the predicted molecular weight of FLAG modified KLHL3, confirming its ability to detect KLHL3. **[D]** Dual channel multiplex western blot of HEK-293 cell lysates over-expressing KLHL2-GFP showing a band at the predicted molecular weight for GFP modified KLHL2 with an anti-GFP antibody (red). The anti-KLHL3 antibody (green) detects a non-specific higher weight band that does not overlap with KLHL2-GFP, therefore confirming specificity for KLHL3 with no cross-reactivity for KLHL2. [Adapted from (Schumacher et al., 2015) with changes to labels].

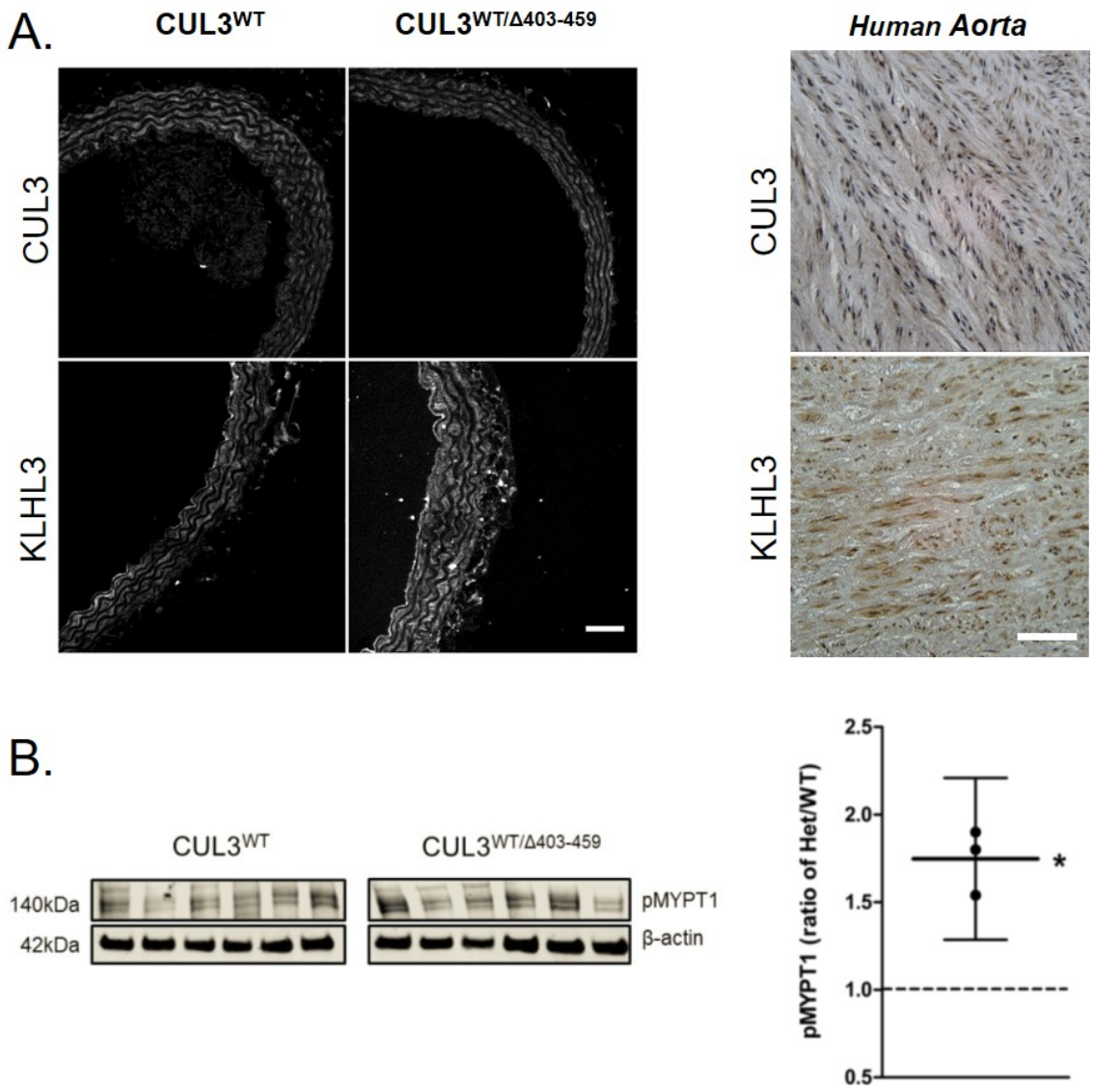

Figure 3.21: Biochemical evidence for increased aortic contractility.

[A, left] Representative maximum-intensity z projections of immunofluorescently stained thoracic aorta sections showing the distribution of CUL3 and KLHL3 between CUL3 $^{WT/\Delta403-459}$ and CUL3$^{WT/WT}$ mice at a minimum 4-h fasting baseline (n = 4 per genotype). CUL3 and KLHL3 localisation is comparable between genotypes. The highest levels were detected in the vascular smooth muscle cells and endothelium, with a minimal expression in the perivascular adipose tissue of the adventitia. Scale bar, 50 µm. **[A, right]** Representative immunohistochemical staining of KLHL3 and CUL3 in human thoracic aorta sections (n = 6). Similar to the mouse staining, vascular smooth muscle cells in the tunica media of the human aortic wall are positive for KLHL3 and CUL3. Scale bar, 50 µm. **[B, left]** A representative western blot of thoracic aorta MYPT1 phospho-Thr696 isoforms and β-actin expression from CUL3$^{WT/\Delta403-459}$ and CUL3$^{WT/WT}$ mice run on the same gel. **[B, right]** CUL3$^{WT/\Delta403-459}$ thoracic aorta have increased phosphorylation of MYPT1 isoforms. Ratiometric expression of quantified MYPT1 phospho-T696 isoforms (normalised against β-actin) were calculated for CUL3$^{WT/\Delta403-459}$ vs CUL3$^{WT/WT}$ on each western blot. The mean of the ratios and bounds of the 95% confidence interval are >1, confirming significantly increased phosphorylation (where ratio = 1 represents no change in phosphorylation). Results are from three separate blots containing independent biological replicates of aortic lysates from both genotypes (total n-values across three blots: CUL3$^{WT/WT}$ = 19 / CUL3$^{WT/\Delta403-459}$ = 21). Statistical significance was determined by the ratio t-test (see methods for more information); * P = 0.02. [Adapted from (Schumacher et al., 2015) with changes to labels].

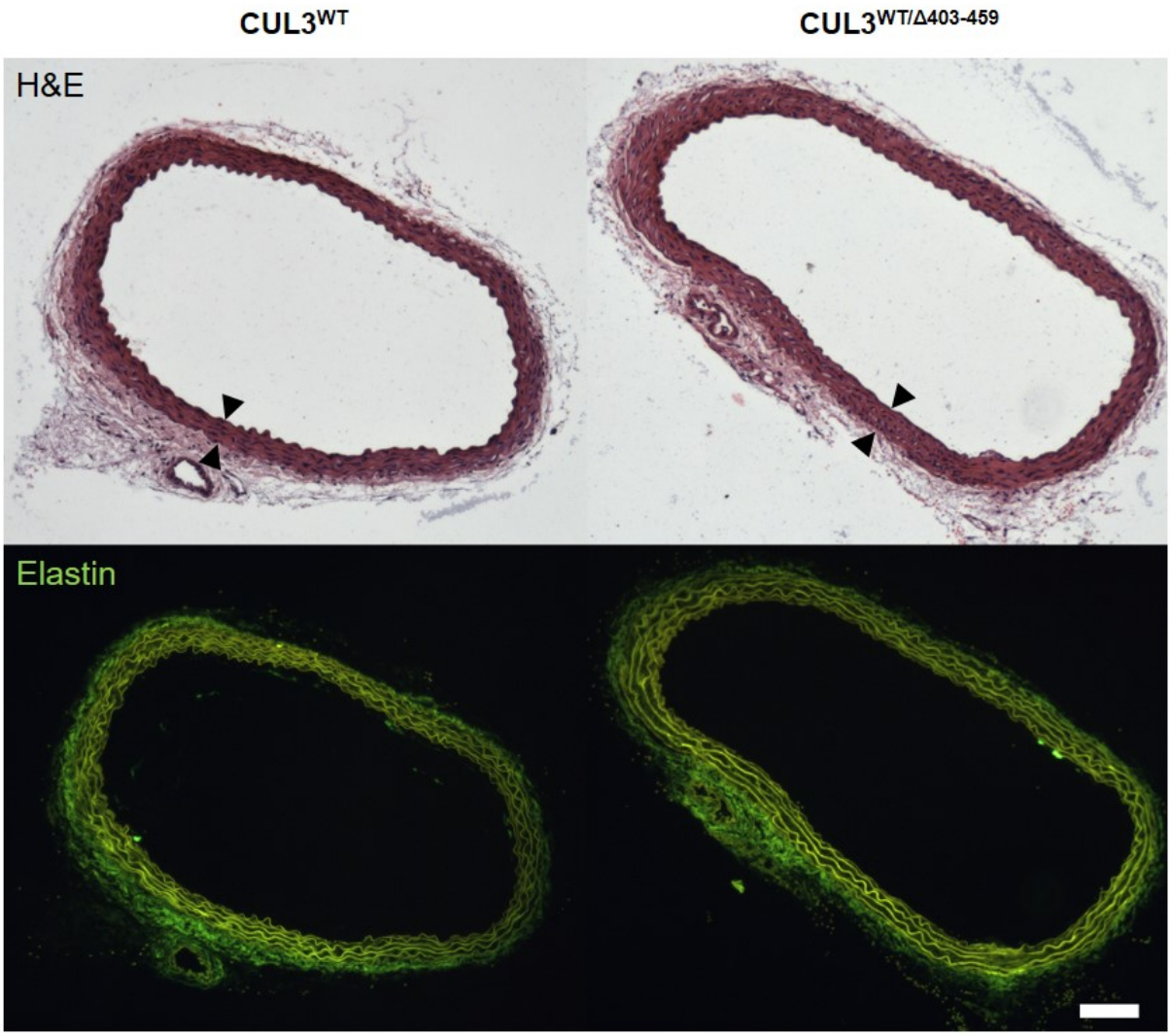

Parameter	CUL3^{WT} (n=10)	CUL3$^{WT/\Delta 403-459}$ (n=11)
Wall thickness (µm)	99.6 (± 3.5)	120.8 (± 3.3) ***
No. of elastic laminae	5.3 (± 0.1)	5.4 (± 0.1)

Figure 3.22: CUL3$^{WT/\Delta 403-459}$ mice undergo aortic vascular remodelling.

Morphometric analysis of thoracic aortae reveals vascular remodelling in CUL3$^{WT/\Delta 403-459}$ mice. There is an increase of ~21% in the vessel wall intima-media thickness (demarcated by arrows) of CUL3$^{WT/\Delta 403-459}$ compared to CUL3$^{WT/WT}$ mice (***P = 0.0003). However, there is no change in the number of elastin laminae (P = 0.1458) and therefore no increase in the number of medial muscle layers between genotypes. Two-tailed unpaired Student's t-test; data are mean ± SEM. [Taken from (Schumacher et al., 2015)]

Finally, to explore further the vascular phenotype a morphometric analysis of the aortas of CUL3 mice was performed that confirmed significant thickening of the vessel wall in the heterozygote mice (Figure 3.22). This probably reflects hyperplasia/hypertrophy of the

vascular smooth muscle cells in the medial layer, as the numbers of elastic laminae were not significantly different (Figure 3.22).

3.4 Discussion

This study describes the first successful PHA2E mouse model involving CUL3 and highlights the molecular differences and defects of the mutant CUL3 protein. The deletion of 57 amino acids in $CUL3^{\Delta 403\text{-}459}$ does not affect the ability of the bound RING domain to hydrolyse E2~UB, and as such $CUL3^{\Delta 403\text{-}459}$ is still an active E3 ligase, although, the Sigmund group also showed impaired $CUL3^{\Delta 403\text{-}459}$ binding to RBX1 suggesting a mechanism for decreased ubiquitylation efficiency of bound substrates. Additionally, the structural predictions and experimental findings provide a second mechanism, suggesting that the $CUL3^{\Delta 403\text{-}459}$ CRL scaffold lacks a level of rigidity required for substrate ubiquitylation. These results are consistent with a previous report that demonstrated ubiquitylation of the Cullin1 substrate (p27) was abrogated when a linker was inserted between the NTD and CTD of the closely related CUL1 protein (Zheng *et al.*, 2002). Thus the $CUL3^{\Delta 403\text{-}459}$ mutation is a novel physiological example of the importance of this CRL rigidity and to our knowledge the first example of a human mutation that impedes the scaffolding function of a Cullin, and these data are consistent with the working hypothesis that the $CUL3^{\Delta 403\text{-}459}$ mutation has increased structural flexibility. The deletion of three helices fuses together two unstructured regions, which likely allows greater movement between the N-terminal and C-terminal domains of the Cullin. This prevents the complex from successfully directing ubiquitin towards a bound substrate, and instead, leads to increased auto-ubiquitylation of CUL3. Importantly, it appears as if *in vivo* this auto-ubiquitylation triggers degradation of the mutant form of the Cullin, as only relatively low amounts of $CUL3^{\Delta 403\text{-}459}$ are detectable in tissue from the mouse model.

Initially, it was suspected that the auto-degradation of CUL3 is likely to be the major driver for the associated phenotype in patients, and while some $CUL3^{\Delta 403\text{-}459}$ remains in cells, the data shows that this remaining protein is unable to ubiquitylate WNK substrates. Taken together, the data in this study suggested that the disease-associated deletion of exon-9 from CUL3 is a loss-of-function mutation with respect to substrate-ubiquitylation. Importantly, all PHA2E patients are heterozygotes, so they retain a functioning copy of $CUL3^{WT}$. Thus the $CUL3^{\Delta 403\text{-}459}$ mutation either behaves as a dominant-negative to inhibit $CUL3^{WT}$ or is haploinsufficient in the context of blood pressure regulation with the single functional copy of

CUL3 unable to sustain the physiological need for WNK ubiquitylation. These data supported a haploinsufficiency model (Figure 3.23), as a large proportion of the mutant protein is removed from the cell by auto-degradation and *in vitro* the data did not show $CUL3^{\Delta 403\text{-}459}$ to inhibit $CUL3^{WT}$. However, two recent studies have provided strong evidence that a reduction in CUL3 levels alone is not sufficient to develop FHHt. The Uchida group generated constitutive $CUL3^{G(-1)A/+}$ knock-in mice containing the same pathogenic mutation of the C-terminus of intron 8 found in human PHA2E pedigrees (Araki *et al.*, 2015). Although instead of disrupting activity at splice site to produce an exon-9 skipped mRNA transcript as seen in PHA2E patients (Glover *et al.*, 2014), the mutation unexpectedly acted like a knock-out allele. These mice had approximately half the CUL3 mRNA and protein levels of wildtype mice and had no changes in WNK pathway protein abundance or activity, blood pressure or electrolyte homeostasis (Araki *et al.*, 2015). The McCormick group sought to directly test our haploinsufficiency model and produced an inducible renal epithelial–specific mouse heterozygous for $CUL3^{WT}$ ($CUL3^{Het}$), which had approximately half the CUL3 protein abundance of wildtype controls and similar phenotype to wildtype mice (Ferdaus *et al.*, 2017). Notably, they directly compared the levels of CUL3 protein between $CUL3^{Het}$ and $CUL3^{Het/\Delta 9}$ mice, and while $CUL3^{Het}$ levels were more variable overall they found a remarkable similarity in the average CUL3 protein abundance between the mice (Ferdaus *et al.*, 2017). Taken together these studies imply that a model of substrate-ubiquitylation loss-of-function due to CUL3 haploinsufficiency cannot alone fully explain the aetiology of $CUL3^{\Delta 403\text{-}459}$ mutants.

Figure 3.23: The haploinsufficiency model of dysregulated cullin ring ligase activity by the PHA2E-causing CUL3 $^{\Delta 403-459}$ mutant.

The haploinsufficiency model proposes that the underlying mechanism is a simple reduction in the total levels of functional CUL3 protein available to ubiquitylate WNKs, due to auto-ubiquitylation and degradation of CUL3$^{\Delta 403-459}$. [Taken from (Ferdaus & McCormick, 2018)].

In vitro the BTB-BACK substrate adaptor, KLHL3, is ubiquitylated by CUL3^{WT} and with even greater efficiency by CUL3$^{\Delta 403-459}$, which has been reported to enhance KLHL3 degradation in cells (McCormick *et al.*, 2014) leading to the proposal by several groups of a KLHL3 degradation model (Figure 3.24) to explain PHA2E aetiology (McCormick *et al.*, 2014; Ferdaus *et al.*, 2017; Yoshida *et al.*, 2017; Ferdaus & McCormick, 2018). In contrast with the *in vitro* data, the *in vivo* levels of KLHL3 appear unaffected in our model; a finding replicated by the McCormick group's inducible renal epithelial–specific CUL3$^{Het/\Delta 9}$ mice with an identical mutation (Ferdaus *et al.*, 2017). This was disputed by the Uchida group, who's CUL3$^{WT/\Delta 403-259}$ mouse had a 75% reduction in KLHL3 abundance compared to wildtypes (Yoshida *et al.*, 2017) which was detected by immunoblot using a KLHL3 antibody validated in KLHL3 knock-out mice (Sasaki *et al.*, 2017). However, the McCormick group could not successfully immunoblot kidney lysates with the same antibody, and instead showed no significant difference in KLHL3 levels by immunofluorescence with this antibody (Ferdaus *et al.*, 2017). Similar to the McCormick group the mouse kidney lysates were immunoblotted

using anti-KLHL3 antibodies that may also detect KLHL2 (mouse KLHL2 and KLHL3 have 87.4% similarity), which is known to interact with and ubiquitylate WNKs in the kidney (Takahashi *et al.*, 2013; Kasagi *et al.*, 2017), and so it can't be rule out that the results may reflect a compensatory rise in renal KLHL2 levels in the face of decreased KLHL3. The discrepancies between the *in vitro* and *in vivo* data of these studies might simply be attributed to the inappropriate use of overexpression studies in *Xenopus* oocytes and HEK293 cells (N.B. – The HEK293 line is suspected to be neuronal in origin – www.hek293.com), which would result in supraphysiological levels of CUL3 in a context that poorly reflects the *in vivo* DCT (McCormick *et al.*, 2014). In HEK293T cells (a line derived from HEK293), there is evidence for enhanced KLHL3 degradation by p62/SQSTM1-mediated selective autophagy when proteasomal degradation of WNK 4 is inhibited (Mori *et al.*, 2015), a phenomenon which may not occur in the DCT. Furthermore, CUL3 auto-ubiquitylation possibly precedes ubiquitylation of KLHL3 *in vivo*, leading to rapid proteasomal degradation of $CUL3^{\Delta 403\text{-}459}$ leaving KLHL3 untouched. It is also known that neddylation/deneddylation cycling is required for CUL3 activity *in vivo*, whereby: 1) CUL3 neddylation promotes recruitment of a ubiquitin charged E2 enzyme for ubiquitin transfer, 2) the CSN then deneddylates CUL3 to release the "empty" E2 enzyme, and 3) subsequent rounds of neddylation/deneddylation cycling allows recruitment of "new" E2 enzymes conjugated to ubiquitin to repeat the process (Figure 3.1) (Pintard *et al.*, 2003). This allows multi-ubiquitylation of the same target molecule and formation of chains of ubiquitin moieties, with four to eight moieties necessary for recognition and subsequent proteasomal degradation of ubiquitylated substrates (Piotrowski *et al.*, 1997). Therefore, the poly-neddylation of $CUL3^{\Delta 403\text{-}459}$ and loss of CSN-dependent deneddylation would be expected to halt neddylation/deneddylation cycling leaving "empty" E2 enzymes stuck within the CRL complex. If this is considered in combination with the increased structural flexibility of $CUL3^{\Delta 403\text{-}459}$, the ubiquitylation of KLHL3 may be constituted of smaller sub-threshold ubiquitin moieties at multiple sites not normally accessible to CUL^{WT}, that do not lead to proteasomal degradation *in vivo*. Importantly, heterozygous KLHL3 knock-out ($KLHL3^{+/-}$) mice do not manifest the phenotypic hallmarks of FHHt (Sasaki *et al.*, 2017), and taking the above into consideration, these data argue against KLHL3 degradation as the primary driver for FHHt development in $CUL3^{\Delta 403\text{-}459}$ mutants. Ultimately, further investigation will be necessary to provide unequivocal confirmation that KLHL3 levels are unchanged *in vivo* to rule out augmented KLHL3 degradation as a contributing factor in mutant $CUL3^{\Delta 403\text{-}259}$ PHA2E aetiology. Indeed, it would be interesting to cross $CUL3^{Het}$ and $KLHL3^{+/-}$ mice to see

if a hybrid CUL3 haploinsufficiency-KLHL3 degradation model provides a viable explanation for PHA2E.

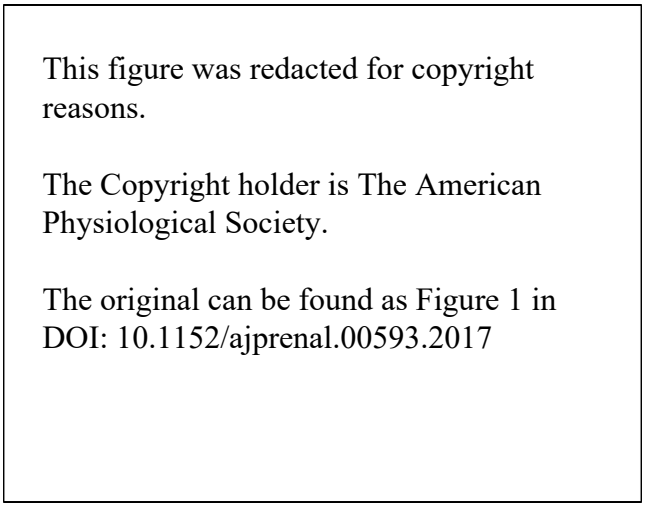

Figure 3.24: The KLHL3 degradation model of dysregulated cullin ring ligase activity by the PHA2E-causing CUL3$^{\Delta 403\text{-}459}$ mutant.

The KLHL3 degradation model proposes that increased ubiquitylation and degradation of KLHL3 by CUL3$^{\Delta 403\text{-}459}$ is the primary driver of the disease. [Taken from (Ferdaus & McCormick, 2018)].

A third model was proposed by the Sigmund group, in which CUL3$^{\Delta 403\text{-}459}$ acts in gain-of-function dominant-negative fashion by sequestering substrate adaptors and disrupting CUL3^{WT} complexes through the formation of CUL3^{WT}-CUL3$^{\Delta 403\text{-}459}$ heterodimers (Figure 3.25) (Ibeawuchi *et al.*, 2015). Like the Sigmund and Ellison groups, an increased binding between CUL3$^{\Delta 403\text{-}459}$ and KLHL3 was noted (McCormick *et al.*, 2014; Ibeawuchi *et al.*, 2015), and a reduced affinity for CAND1 which would be predicted to prevent the release of KLHL3 from the non-functional CUL3$^{\Delta 403\text{-}459}$ complexes (Figure 3.6 A). This would reduce the amount of unbound KLHL3 available to CUL3^{WT} without necessarily leading to a change in the overall abundance of the protein. An issue that may be compounded by a simultaneous increase in the amount of CAND1 available to CUL3^{WT}, which would lead to exaggerated removal of KLHL3 from CUL3^{WT} and prolonged sequestration of CUL3^{WT} by CAND1 thereby inhibiting subsequent re-binding of KLHL3 to CUL3^{WT} (Lo & Hannink, 2006; Kim *et al.*, 2010). Additionally, certain substrates require the formation of dimerised active CRL complexes to ubiquitylate their substrates (McMahon *et al.*, 2006; Kigoshi *et al.*, 2011). This may also be true for WNKs, with a stoichiometry for the association of CUL3 and KLHL3 measured as 1:1, but crystal structure data revealing a 2:2 complex is formed made up of two CUL3 monomers

independently bound to two equivalent and non-overlapping surfaces of a KLHL3 homodimer (Ji & Privé, 2013). *In vitro*, KLHL3 has been shown to dimerise in HEK293T cells, with the dominant negative effect of the KLHL3 R528 mutant demonstrated to be dependent on dimer formation, suggesting it acts by forming an excess of non-productive heterodimers to hinder its wildtype counterpart (Sasaki *et al.*, 2017). Furthermore, Nedd8 has been shown to mediate the formation of an active CUL3 dimer comprised of one neddylated and one unneddylated CUL3. The arrangement in this dimer positions the substrate of one CUL3 so that it is closer to the ubiquitin-conjugating E2 enzymes of its partner CUL3 than that of its own, which may be necessary for effective ubiquitylation of specific sets of protein substrates, but is unlikely to be useful for WNK ubiquitylation, as the distance between the CUL3 binding sites for substrate adaptors is increased and may limit the binding of KLHL3 homodimers to a single CUL3 arm in this CUL3 dimer arrangement (Wimuttisuk & Singer, 2007). Interestingly, coexpression of $CUL3^{\Delta 403\text{-}459}$ with $CUL3^{WT}$ in HEK293T cells showed that while $CUL3^{\Delta 403\text{-}459}$-$CUL3^{\Delta 403\text{-}459}$ homodimers were highly unstable and almost undetectable at baseline, heterodimers of $CUL3^{WT}$-$CUL3^{\Delta 403\text{-}459}$ could be formed although were less stable than $CUL3^{WT}$-$CUL3^{WT}$ homodimers. Of particular note, was the finding that cotransfection of $HEK293T^{CUL3KO}$ cells with either 1µg $CUL3^{\Delta 403\text{-}459}$ and 1µg $CUL3^{WT}$ plasmids or 0.5µg empty vector, 0.5µg $CUL3^{\Delta 403\text{-}459}$ and 1µg $CUL3^{WT}$ plasmids yielded the same reduction in the levels of "active" neddylated $CUL3^{WT}$ (Ibeawuchi *et al.*, 2015). These data suggest $CUL3^{\Delta 403\text{-}459}$ impairs $CUL3^{WT}$ activity, and while intact WNK4 ubiquitylation was observed in equimolar mixtures of $CUL3^{\Delta 403\text{-}459}$ and $CUL3^{WT}$ *in vitro* (Figure 3.10 C), the experiment in our study was not performed in live cells with an intact UPS nor was WNK4 degradation quantified, so this possibility cannot be ruled out. It is conceivable that the same scenario described above for KLHL3 may apply here, whereby the observed WNK4 ubiquitylation is a combination of normal $CUL3^{WT}$-$CUL3^{WT}$ homodimer activity and smaller sub-threshold ubiquitin moieties placed by $CUL3^{WT}$-$CUL3^{\Delta 403\text{-}459}$ heterodimers. The reduction in neddylated $CUL3^{WT}$ may be attributed to the absence of $CUL3^{\Delta 403\text{-}459}$ competition for CSN and CAND1, which would increase their availability for $CUL3^{WT}$ binding to enhance and maintain deneddylation (Kim *et al.*, 2010). In conjunction with this, the increased structural flexibility and loss of CSN affinity for $CUL3^{\Delta 403\text{-}459}$ results in chronic hyperneddylation at potentially non-physiological residues, which may cause $CUL3^{\Delta 403\text{-}459}$ to preferential sequester unneddylated $CUL3^{WT}$ to form inherently unstable $CUL3^{WT}$-$CUL3^{\Delta 403\text{-}459}$ heterodimers that trap $CUL3^{WT}$ in an unneddylated state rendering it unable to ubiquitylate WNKs (Wimuttisuk & Singer, 2007). However, the major caveat of this dominant negative sequestration model is the relatively low levels of

$CUL3^{\Delta 403\text{-}459}$ detectable *in vivo* and the uncertainty surrounding the *in vivo* dependence of WNK ubiquitylation and degradation on dimerised active CRL complexes. Nonetheless, strong evidence for this model has emerged from the McCormick group which produced a mouse with two $CUL3^{WT}$ alleles and inducible renal epithelial–specific expression of a third $CUL3^{\Delta 403\text{-}459}$ allele ($CUL3^{WT/WT/\Delta 9}$) reported to have increased WNK4 abundance, pNCC and pNKCC2 levels despite similar quantities of $CUL3^{WT}$ when compared to kidneys of $CUL3^{WT/WT}$ mice (Ferdaus *et al.*, 2017). Similarly, the Sigmund group produced a mouse with two $CUL3^{WT}$ alleles and inducible smooth muscle–specific expression of a third $CUL3^{\Delta 403\text{-}459}$ allele ($CUL3^{S\text{-}\Delta 9}$), which presented with increases in another CUL3 substrate, RhoA, and surprisingly decreases in both the neddylated and total levels of $CUL3^{WT}$ when compared with the aortae of non-transgenic mice (Agbor *et al.*, 2016).

Figure 3.25: The sequestration model of dysregulated cullin ring ligase activity by the PHA2E-causing $CUL3^{\Delta 403\text{-}459}$ mutant.

The dominant negative model suggestions that $CUL3^{\Delta 403\text{-}459}$ sequesters KLHL3 and/or impairs dimer functions necessary for WNK ubiquitylation and degradation. [Adapted from (Ferdaus & McCormick, 2018) with modification to the schematic].

The $CUL3^{WT/\Delta 403\text{-}459}$ mice have high blood pressure and up-regulated signalling in the context of the WNK-kinase pathway, which parallels the WNK4 D565E (Chowdhury *et al.*, 2013), WNK4 D561A/+ (Yang *et al.*, 2007*b*) and KLHL3 R528H (Susa *et al.*, 2014) PHA2 mouse models previously described. Mechanistically, the data in our study suggest $CUL3^{\Delta 403\text{-}459}$ promotes its own degradation, as it has a heightened propensity to self-ubiquitylate and is

less abundant in mouse kidney extract. Hence it would be predicted that PHA2E CUL3$^{WT/\Delta 403-459}$ patients would similarly have lower overall CUL3 levels. As CUL3 ubiquitylates a number of other proteins, it seems remarkable then that PHA2E patients do not have a plethora of other phenotypic manifestations. However this may not be surprising if considered in the context of either the dominant negative sequestration model or a hybrid CUL3 haploinsufficiency-KLHL3 degradation model. The Sigmund and Ellison groups showed that compared to CUL3^{WT}, CUL3$^{\Delta 403-459}$ has an approximately 2-fold increased binding to various substrate adaptors, namely, Bacurd1, RhoBTB1, BTBD1 and KCTD6, whereas KLHL3 binding is as least 3.5-fold higher (McCormick *et al.*, 2014; Ibeawuchi *et al.*, 2015). But the most surprising finding was that the *in vitro* expression of CUL3$^{\Delta 403-459}$ either did not affect or actually increased abundance of these substrate adaptors in cells (McCormick *et al.*, 2014; Ibeawuchi *et al.*, 2015), which was not always true for KLHL3 (McCormick *et al.*, 2014). These studies imply CUL3$^{\Delta 403-459}$ directed degradation or sequestration of substrate adaptors may be preferentially targeted towards KLHL3, and in a similar vein, the requirement for functional CUL3 dimers to facilitate substrate ubiquitylation may be a phenomenon relatively specific to WNKs, however these possibilities need to be tested directly *in vivo*. Additionally, BP homeostasis requires reactive and precise control of vascular tone and of ion fluxes in the distal nephron, especially the DCT, as changes in intake and output of salt are constantly balanced. The phosphorylation of the NCC/NKCC ion transporters by WNK kinases appears to be regulated by two complementary systems: the regulation of total WNK protein levels by CUL3-KLHL3, and the level of WNK activation by phosphorylation. Currently our understanding of the sensing-mechanisms that leads to WNK-phosphorylation or the degradation of the WNK kinases by CUL3-KLHL3 is limited. Only recently have DCT cells been discovered to sense changes in extracellular potassium via membrane voltage, effectively coupling serum potassium levels with DCT intracellular chloride concentration to direct WNK activity, achieved through increased chloride ion binding to WNKs which inhibits WNK autophosphorylation necessary for activation (Terker *et al.*, 2015*b*, 2015*a*). Another recent breakthrough was the discovery that WNK interactions with KLHL3 are impaired by phosphorylation of KLHL3 at serine 433 (Wang & Peng, 2017), which can be induced *in vivo* and *in vitro* by angiotensin II, vasopressin, insulin and potassium depletion to prevent WNK degradation (Shibata *et al.*, 2014; Yoshizaki *et al.*, 2015; Ishizawa *et al.*, 2016). Hence, while most other CUL3 substrates may be unaffected in the CUL3$^{WT/\Delta 403-459}$ mice, the rapid and signal-dependent switching of WNK ubiquitylation may require a larger complement of functional CUL3-KLHL3 CRL complexes within blood vessel and kidney cells for the system

to respond adequately. The lack of a gross phenotype in either heterozygous CUL3 or KLHL3 knock-out mice support this concept of redundancy with respect to most CUL3 substrates (Araki *et al.*, 2015; Ferdaus *et al.*, 2017; Sasaki *et al.*, 2017), with the threshold for CUL3 insufficiency-induced cell lethality previously demonstrated to lie somewhere between 45% and 50% CUL3 expression in mouse embryonic fibroblasts (McEvoy *et al.*, 2007).

Another intriguing finding from our study was the discovery of WNK-SPAK/OSR1 containing puncta in the DCT/CNT of CUL3$^{WT/\Delta403\text{-}459}$ mice. Subcellular structures containing WNK-SPAK/OSR1 have been reported *in vitro* in a various cell lines and *in vivo* rodent models, often referred to as either puncta, foci or 'WNK bodies' (Boyd-Shiwarski *et al.*, 2017), with the latter description perhaps the most apt. While there are now numerous reports of WNK bodies in animals undergoing dietary potassium manipulations or Gitelman-like genetic knock-out mice (Grimm *et al.*, 2012; Mori *et al.*, 2015; Terker *et al.*, 2015*b*), this is to our knowledge the first report of a FHHt model exhibiting these structures. A running theme for the appearance of WNK bodies seems to be perturbations of serum potassium concentration, with both high and low levels triggering their DCT/CNT restricted formation. However, the two stimuli create morphologically different populations of WNK bodies; low potassium produces bodies with a basolateral preference averaging 2μm in diameter, while high potassium results in a significantly lower number of sub-apical bodies averaging 1μm in diameter (Boyd-Shiwarski *et al.*, 2017). Interestingly, the bodies associated with low serum potassium in wildtype animals (Terker *et al.*, 2015*b*; Boyd-Shiwarski *et al.*, 2017) bear a closer resemblance to that of our and the McCormick group's CUL3$^{WT/\Delta403\text{-}459}$ mice despite the presence of pronounced hyperkalaemia (Ferdaus *et al.*, 2017), which may suggest that this population of bodies plays a role in promoting WNK-SPAK/OSR1 pathway activity. This is supported by the presence of phospho-SPAK T243 and autophosphorylated WNK1 S382 in WNK bodies of our CUL3$^{WT/\Delta403\text{-}459}$ mice and animals fed a low potassium high sodium diet (Terker *et al.*, 2015*b*), respectively, while the opposite is true for high potassium-induced WNK bodies that were noted to have an absence of phospho-WNK1 T60 (Boyd-Shiwarski *et al.*, 2017). The Subramanya lab also bolstered the argument for WNK bodies having an important functional role by demonstrating that they are kidney-specific WNK1 (KS-WNK1) dependent, and that formation requires an evolutionary conserved cysteine-rich hydrophobic motif in the unique exon-4a of the KS-WNK1 isoform, which may have emerged to facilitate the transition of life from water to land (Boyd-Shiwarski *et al.*, 2017). This would mean that KS-WNK1 abundance would be expected to rise in CUL3$^{WT/\Delta403\text{-}459}$ mice due failed ubiquitylation, which may be

sufficient to drive activity-promoting WNK body formation even in the face of hyperkalaemia. In fact the extreme hyperkalaemia and overactivation of the WNK pathway in PHA2E presents a paradox, as the currently accepted model for potassium-dependent WNK activation predicts that hyperkalaemia would increase intracellular chloride to a concentration capable of totally inhibiting the activating-autophosphorylation of WNKs, irrespective of their increased abundance. WNK bodies may offer a solution to this FHHt paradox, by serving to recruit components of the WNK pathway into densely packed compartments which effectively occludes the chloride ion binding sites of WNKs through a process known as 'macromolecular crowding' (Parker, 1993; Kuznetsova *et al.*, 2014), permitting them to autophosphorylate regardless of the intracellular chloride levels in the rest of the cytosol. As the WNK pathway is known to also be activated by decreases in cell volume, it was proposed by the Goldsmith team who discovered the chloride binding site, that this response might be mediated by crowding effects which could compete with chloride to promote an autophosphorylation-competent conformation (Piala *et al.*, 2014). To support this, Goldsmith has demonstrated *in vitro* that macromolecular surrogates such as polyethylene glycol can activate WNK1/3 in a manner which is opposed by chloride (Goldsmith *et al.*, 2017), and Subramanya has shown in FRAP and supernatant-pellet assays that KS-WNK1 movement is confined to a biochemically distinct fraction of the cell when compared to full-length 'long' WNK1 (L-WNK1), leading them to propose that WNK bodies are demixed hydrophobic microdomains of the cytosol designed to partition signalling processes (Boyd-Shiwarski *et al.*, 2017). Originally, it was suspected WNK bodies in CUL3$^{WT/\Delta 403-459}$ DCT cells may represent deployment of secondary protein degradation pathways to manage excess WNK proteins, such as the autophagy-lysosomal system, aggresome or juxta-nuclear quality control compartment (JUNQ) in an attempt to compensate for loss of proteasomal degradation (Lamark & Johansen, 2012; Wolff *et al.*, 2014). However, as these WNK bodies have not been found to colocalise with any known subcellular organelle, quality control compartment or pathogenic aggregations, this concept was abandoned (Boyd-Shiwarski *et al.*, 2017). Instead, a surprising discovery was made linking WNK bodies to the seemingly unrelated 60s ribosomal subunit L22 (RPL22), with high potassium colocalising with ~35% of RPL22 that then dramatically increases to >80% in low potassium (Boyd-Shiwarski *et al.*, 2017). In animals suspected to have hypokalaemia induced by chronic administration of aldosterone, RPL22 formed puncta which were morphologically similar to WNK bodies. Interestingly, these bodies were also found to have an almost the 80% colocalisation with the 20s proteasome (Cheema *et al.*, 2014), which can degrade damaged and misfolded proteins via an ubiquitin-independent pathway (Ben-Nissan & Sharon, 2014).

Therefore, it is attractive to postulate that WNK bodies simultaneously recruit these additional proteins to ensure the integrity of WNK signalling by degrading and replacing worn out WNK-SPAK/OSR1 complexes during low potassium stimulation. Although it remains to be seen if WNK-SPAK/OSR1 signalling is contingent on WNK body formation or if the 20s proteasome colocalises with WNK bodies *in vivo*.

Mutations in CUL3, KLHL3, WNK1 and WNK4 are known to cause FHHt with constitutive activation of the NCC cotransporter (Boyden *et al.*, 2012; Tsuji *et al.*, 2013; Osawa *et al.*, 2013; Glover *et al.*, 2014; Alessi *et al.*, 2014). What has been less clear is why the mutation of CUL3 has resulted in a more severe form of FHHt (PHA2E). The unexpected discovery of a vascular phenotype in the $CUL3^{WT/\Delta 403-459}$ mice, led to speculation that their hypertension may not be driven by salt-retention in the DCT alone. It is possible that part of their hypertension originates from an increased contractile state in their vasculature tree. If a similar phenomenon occurs in PHA2E, this may explain the early-onset and severity of the blood pressure that occurs in these patients. The $CUL3^{WT/\Delta 403-459}$ mice have an altered aortic pulse-wave form and slowed diastolic relaxation that is consistent with stiffening of their arterial tree. These changes have been reported before in humans with hypertension (Kaess *et al.*, 2012), but not previously in a hypertensive mouse model. It is also worth noting that augmentation of the aortic pressure wave is often not detected by brachial cuff BP measurements, so it could have gone unnoticed in the routine clinical assessment of PHA2E patients. The increase in pMYPT1 in the aortas from the $CUL3^{WT/\Delta 403-459}$ mice and the increase in their *in vivo* pressor responses to phenylephrine and angiotensin-II further suggest that the altered contractile state could be a primary phenomenon rather than simply a secondary response to hypertension. If this is the case, the contraction could occur by at least two distinct pathways. Firstly the WNK1/WNK3/SPAK/OSR1 pathway is thought to be important for regulating vascular tone by controlling the phosphorylation state of the NKCC1 cotransporter and hence the membrane potential of vascular smooth muscle (VSM) cells (Zeniya *et al.*, 2013). So if either WNK1 or WNK3 accumulates in the vessel wall of the $CUL3^{WT/\Delta 403-459}$ mice, the contractile tone would be expected to rise through depolarisation of VSM and increased calcium entry. Alternatively, the mutant Cullin-3 protein may directly affect the phosphorylation state of myosin light chain by regulating RhoA/RhoA kinase (ROCK) levels (Ibeawuchi *et al.*, 2015). RhoA protein levels in the VSM are thought to be regulated by CUL3 in complex with the substrate adaptor RhoBTB1 (Pelham *et al.*, 2012). Indeed the Sigmund group's $CUL3^{S-\Delta 9}$ mouse model with smooth muscle-specific ectopic expression of $CUL3^{\Delta 403-}$

^{459} on a CUL3$^{WT/WT}$ background provides the strongest evidence that the hypercontractile state is a primary phenomenon. Isolated blood vessel work with basilar arteries showed that CUL3$^{S-\Delta9}$ have a higher contractile response to phenylephrine, angiotensin II and endothelin-1, and impaired vasodilation in response to acetylcholine, angiotensin 1-7, cromakalim and sodium nitroprusside, but surprisingly nifedipine-induced vasodilatation was normal (Agbor *et al.*, 2016). Similarly, acetylcholine-induced relaxation of the aorta was impaired due to higher levels of RhoA and pMYPT1 caused by increased ROCK activity, which could by inhibited by Y27632 to restore normal acetylcholine-dependent vasodilatation in basilar arteries/aortae. These vascular defects lead to sleep-period systolic hypertension and increased pulse wave velocity, the gold standard measurement for increased arterial stiffness (Agbor *et al.*, 2016), all of which confirms our own finding in CUL3$^{WT/\Delta403-459}$ mice. Though it appears as if vascular story does not end here, and additional endothelia mechanisms may contribute to the altered vascular tone in CUL3$^{\Delta403-459}$ mutants. The Sigmund group developed an additional model similar to CUL3$^{S-\Delta9}$, but this time with endothelial-specific inducible promotor to produce E-CUL3Δ9 mice. The basilar and carotid arteries of these mice exhibited impaired endothelium-dependent relaxation in response acetylcholine without a change in VSM function, and similar to CUL3$^{S-\Delta9}$ mice, the E-CUL3Δ9 manifested nocturnal hypertension and elevated pulse wave velocity (Wu *et al.*, 2017*b*, 2017*a*). The underlying mechanism for this appeared to be impaired turnover of Cullin-3 substrate protein phosphatase 2A (PP2A), a marked decrease in phosphorylated endothelial nitric oxide synthase (eNOS), and reduced nitric oxide (NO) bioavailability, which could be rescued by PP2A inhibitors Calyculin A and Okacaic acid (Wu *et al.*, 2017*b*, 2017*a*).

If these same pathways are operational in human PHA2E, then they suggest that treatment with a thiazide diuretic or dietary sodium restriction while effective in reversing the electrolyte disturbances, may be less effective in reversing any central aortic pressure changes in PHA2E. Given the overactivation of the RhoA/ROCK pathway and impairment of eNOS function, a direct arterial vasodilator or a specific ROCK inhibitor (Liao *et al.*, 2007) might be the most appropriate drug of choice. The contribution of WNK/SPAK/OSR1 to this vascular phenotype has yet to be determined, and a loop diuretic such as bumetanide may be more effective than a thiazide, as it would target both NKCC1 and NKCC2. Central aortic pressure elevation is now widely accepted to be an important and independent cardiovascular risk factor (Liao & Farmer, 2014), so if it is elevated in patients with PHA2E it will be important to show that it is normalised by appropriate pharmacotherapy.

Chapter 4 : MO25 as a Master Regulator of SPAK/OSR1 *in vivo*

[*This chapter is principally based on and expands upon the content from the abstracts in Appendix 1*]

4.1 Abstract

Recently mouse protein-25 (MO25) isoforms were discovered to be master regulators of SPAK/OSR1; which form a cascade with WNKs to regulate the Cation–Cl Cotransporters involved in cell volume, blood pressure and electrolyte homeostasis. MO25α (also known as calcium-binding protein 39; CAB39) colocalises with renal NCC, increases SPAK/OSR1 activity up to 100-fold independent of WNKs, facilitates SPAK/OSR1 monomer interactions and stabilises their active conformations, which in turn would promote an increase in NCC activity and Na^+ reabsorption. The paralog MO25β (also known as calcium-binding protein 39-like; CAB39L) shares 79% sequence identity with MO25α, has high renal expression and interacts similarly with substrates such as the tumour suppressor liver kinase B1 (LKB1) which phosphorylates adenosine monophosphate-activated protein kinase (AMPK). However, the embryonic lethality of MO25α knock-out mice has limited *in vivo* data gathering, and MO25β knock-out mice were selected as an alternative model to test the hypothesis that MO25 deficiency would produce a hypotensive salt-wasting phenotype. It was found that MO25β knock-out mice do not recapitulate the expected Gitelman syndrome phenotype (salt-wasting hypotension), with few electrolyte abnormalities and were normotensive even in the face of prolonged salt restriction. With the exception of slight differences in haematology and body composition the mice otherwise appeared to be healthy. It was therefore concluded that mammalian MO25β does not play a significant role in blood pressure or electrolyte homoeostasis *in vivo*.

4.2 Introduction

MO25α (also known as Calcium-binding protein 39; CAB39) is part of a protein scaffold with STRAD (STE20-Related ADaptor protein) isoforms that binds and activates members of the

STE20 (Sterile 20) family of serine/threonine kinases (Filippi *et al.*, 2011). The C-terminus of STRAD binds through a conserved WEF motif to MO25 and this conformation increases the catalytic activity of the bound STK (Serine-Threonine Kinase) (Figure 1.9). The STE20 family includes both SPAK and OSR1 kinases that act through well-defined WNK/SPAK/OSR1 signalling pathways to regulate members of the SLC12A (solute carrier family 12) family of electroneutral CCCs (cation-chloride cotransporters) in the kidney and elsewhere (Richardson *et al.*, 2008, 2011; Richardson & Alessi, 2008; Rafiqi *et al.*, 2010). The role of SLC12A transporters is to regulate intracellular chloride concentration that is critical for controlling cell volume and ultimately blood pressure (Rafiqi *et al.*, 2010; Yang *et al.*, 2010*c*; Filippi *et al.*, 2011). SPAK/OSR1 protein kinases drive chloride influx by phosphorylation and activation of sodium-driven CCC members. These include the NCC (Na–Cl Cotransporter) in the distal convoluted tubule (DCT) of the kidney (Yang *et al.*, 2010*c*; Zeniya *et al.*, 2013), the NKCC2 (Na–K–2Cl Cotransporter 2) in the thick ascending limb (TAL) of the kidney (Giménez & Forbush, 2003; Ponce-Coria *et al.*, 2008) and the ubiquitously expressed NKCC1 (Vitari *et al.*, 2006; Zeniya *et al.*, 2013).

The MO25 protein is highly conserved in evolutionary terms across humans, mice, zebrafish, flies and yeast (Miyamoto *et al.*, 1993; Nozaki *et al.*, 1996; Zhang *et al.*, 2013), but in mammals it exists as closely related isoforms, MO25α and MO25β (also known as Calcium-binding protein 39-like; CAB39L), that share 79% of their amino acid sequence (Boudeau *et al.*, 2003). They are both widely expressed in tissues, although MO25β has a more restricted pattern of expression than MO25α. SPAK is one of a subgroup of members of the STE20 family that are unusual in having four conserved WEW motifs that can bind to MO25 (Figure 1.6). Using *in vitro* phosphorylation assays the MO25 isoforms stimulate the activity of SPAK 100-fold and silencing the gene in HEK293 cells reduces NKCC1 phosphorylation (Filippi *et al.*, 2011). As the putative interaction model predicts (Filippi *et al.*, 2011), MO25 has its action without affecting the key phosphorylation site in the T–loop of SPAK.

Study of growth and development in *Drosophila melanogaster*, led to the initial discovery that dMo25 and Fray (orthologs of mammalian MO25α/β and SPAK/OSR1, respectively) work together in the same pathway (Yamamoto *et al.*, 2008), and later purified proteins were used to show that dMo25 can stimulate Fray phosphorylation of the fly NKCC *in vitro* (Rodan *et al.*, 2017). In these flies, neither overexpression of a chloride-insensitive

WNK^{L421F} (predicted to be constitutively active), nor knockdown/overexpression of dMo25 in the fly renal tubule *in vivo* altered transepithelial potassium flux under isotonic conditions. However, simultaneous overexpression of dMo25 and WNK^{L421F} increased potassium flux under isotonic conditions, while dMo25 knockdown prevented any increase in potassium flux in response to a hypotonic stimulus (Rodan *et al.*, 2017). Taken together, these data and the highly conserved nature of MO25, would predict that mammalian MO25 isoforms have an active role in electrolyte homeostasis and therefore blood pressure control.

The aim of this study was to explore the roles of mammalian MO25 isoforms *in vivo*. Initial attempts were made to knock-out MO25α to explore its functions directly (Alessi *et al*. unpublished data), however, in our hands knock-out of MO25α proved to be lethal *in utero*. In contrast MO25β knock-out embryos are viable to adulthood, allowing the investigation of the role of this isoform in the adult kidney.

4.3 Results

4.3.1 Expression and Localisation of MO25β

Database mining revealed the existence of a phenotyped $Cab39l^{tm1b(EUCOMM)Wtsi}$ heterozygous ($CAB39L^{+/-}$) mouse model with a β-galactosidase (LacZ) reporter in the MO25β null allele. X-gal staining indicated that MO25β gene expression was strongest in cartilaginous tissues, bladder mucosa, renal papilla, adrenal medulla and parathyroid glands. Gene expression was also detected in the heart, lungs, thyroid, brain ventricles and spinal cord central canal (Figure 4.1). Of particular interest, moderate to high levels of gene expression were detected in small blood vessels (Figure 4.1 B) and the renal cortex and inner medulla (Figure 4.1 A).

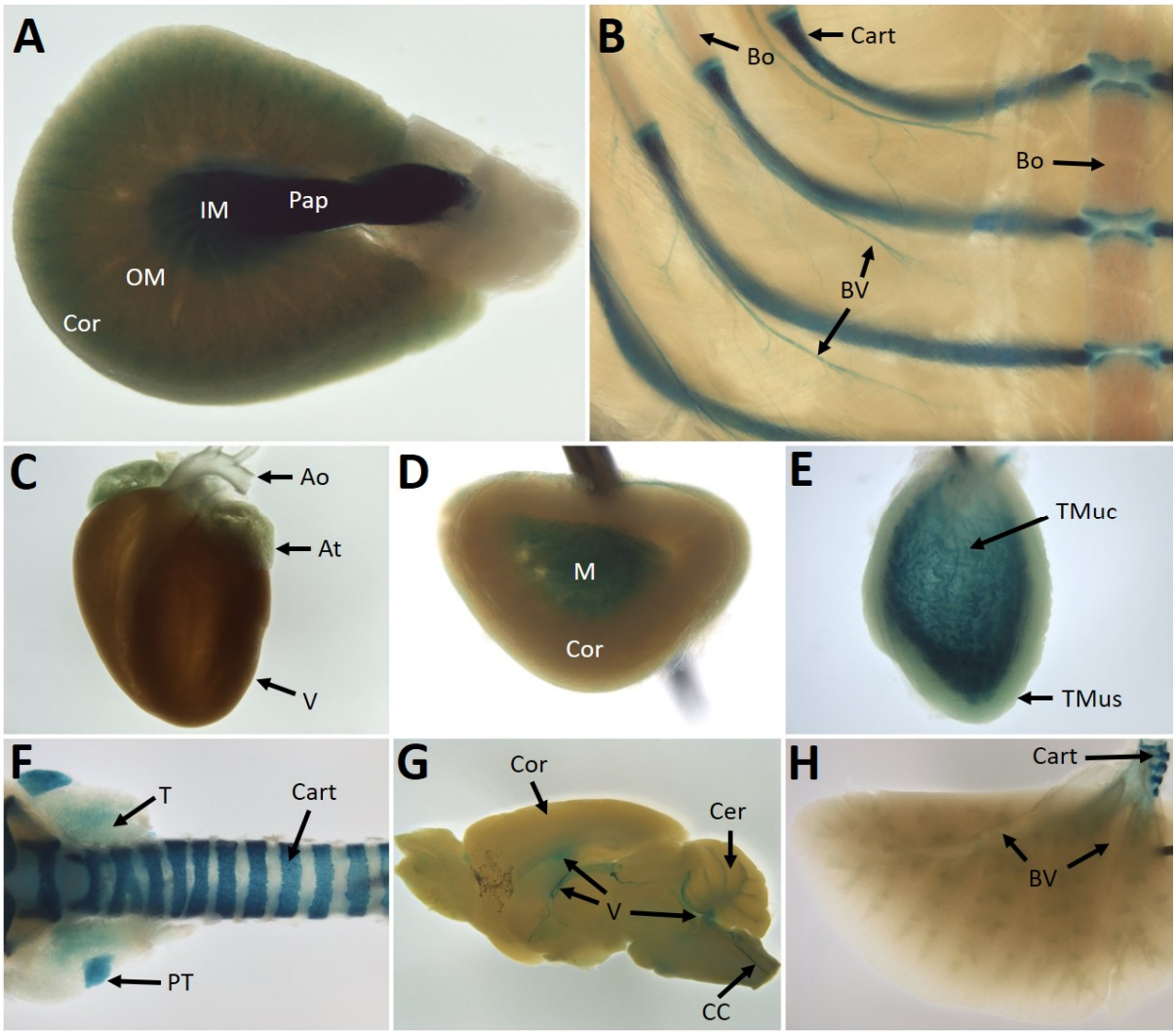

Figure 4.1: MO25β gene expression and distribution in mouse tissues.

X-gal staining was performed in various whole-mount organs and tissues of male and female Cab39l$^{tm1b(EUCOMM)Wtsi}$ heterozygous (CAB39L$^{+/-}$) mice, which have a β-galactosidase (LacZ) reporter in the MO25β null allele. Blue staining indicates gene expression. **[A]** Kidney, axial section; **[B]** Ribcage and sternum; **[C]** Heart and aortic arch; **[D]** Adrenal gland, transverse section; **[E]** Bladder; **[F]** Trachea, thyroid and parathyroid glands; **[G]** Brain, sagittal section; **[H]** Lung. Abbreviations: Cortex (Cor), Outer Medulla (OM), Inner Medulla (IM), Papilla (Pap), Cartilage (Cart), Bone (Bo), Blood Vessels (BV), Aorta (Ao), Atria (At), Ventricle (V), Medulla (M), Tunica Mucosa (TMuc), Tunica Muscularis (TMus), Thyroid (T), Parathyroid (PT), Cerebellum (Cer), Central Canal (CC). Images by IMPC [http://www.mousephenotype.org/data/genes/MGI:1914081], copyright by © 2016 IMPC.

Our MO25β knock-out heterozygous (MO25β$^{+/-}$) and homozygous (MO25β$^{-/-}$) embryos proved to be viable and produced fertile adult mice. MO25α/β proteins expression was detected in the heart, lungs and kidneys by immunoblot of wildtype mice, with confirmation of successful MO25β knock-out by immunoprecipitation and immunoblotting of tissue lysates. Interestingly, there was no marked compensatory upregulation of MO25α protein expression (Figure 4.2).

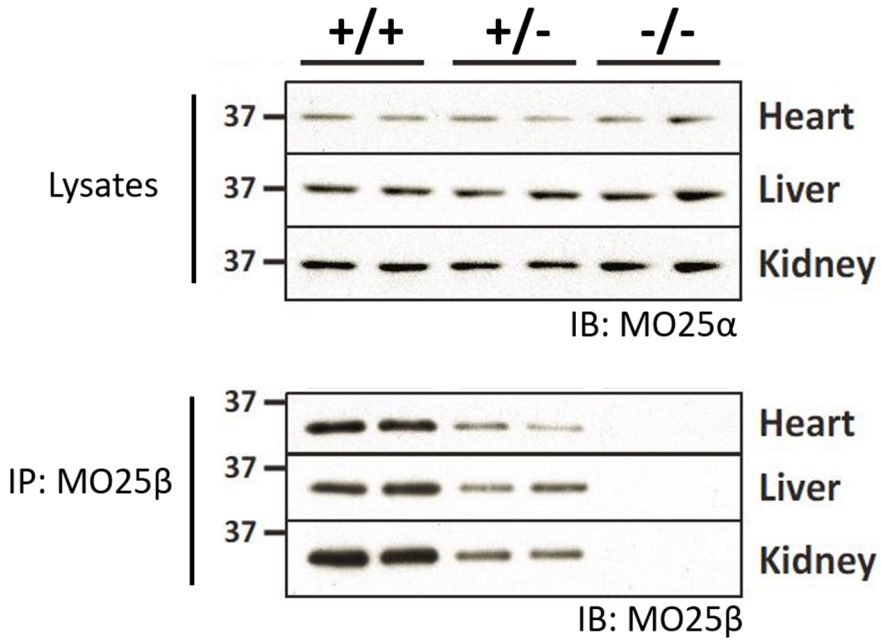

Figure 4.2: Protein expression of MO25 isoforms in mice.

Immunoblot (IB) of MO25α and MO25β from either immunoprecipitates (IP) or lysates from tissue homogenates of MO25β$^{+/+}$, MO25β$^{+/-}$, and MO25β$^{-/-}$ mice. The complete knock-out of MO25β was confirmed, with no compensatory overexpression of MO25α detected.

To explore the distribution of MO25β in the kidney, clues were first sought from the Human Protein Atlas. In the human renal cortex, MO25β immunohistochemistry shows diffuse staining within the cytosol of the distal tubules which is totally absent from proximal tubules and glomeruli (Figure 4.3). This suggests a potential role in renal distal tubular salt transport.

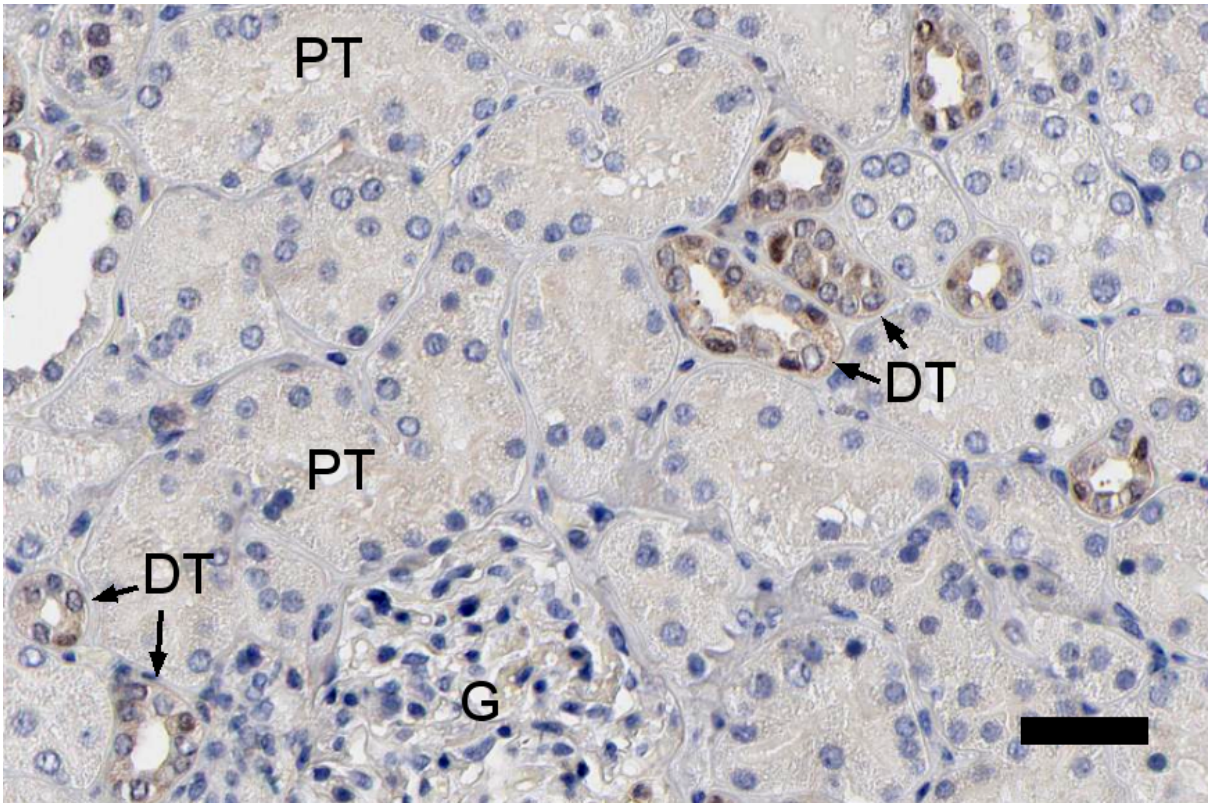

Figure 4.3: Localisation of MO25β in the human kidney.

Representative immunohistochemically-stained wildtype kidney section (n = 3) showing the distribution of MO25β in the renal cortex, as identified by the presence of glomeruli (G). MO25β is absent from human proximal tubules (PT) and is generally confined to the cytosol of the distal tubules (DT). Sections were stained with a mouse monoclonal antibody (H00081617-M01; Abnova) raised against full length recombinant MO25β protein. Scale bar = 50μm. This image of CAB003686 (Patient ID1943) is from the Human Protein Atlas [https://v17.proteinatlas.org/ENSG00000102547-CAB39L/tissue/kidney], used under CC BY-SA 4.0. Brightness and contrast were adjusted from original by linear histogram stretching to enhance visibility.

Immunofluorescent staining of the mouse renal cortex showed a similar pattern of distribution to that seen in human kidneys. MO25β exhibited minimal or no staining in the proximal tubules and glomeruli, and was generally confined to the cytosol of distal tubules (Figure 4.4). MO25β has a diffuse staining with the basolateral preference unlike MO25α which is concentrated at the apical membrane of distal tubules (Grimm *et al.*, 2012). Further exploration of the Human Protein Atlas revealed that at the subcellular level MO25β associated with cytosolic vesicles in both mouse and human cell lines (Figure 4.5).

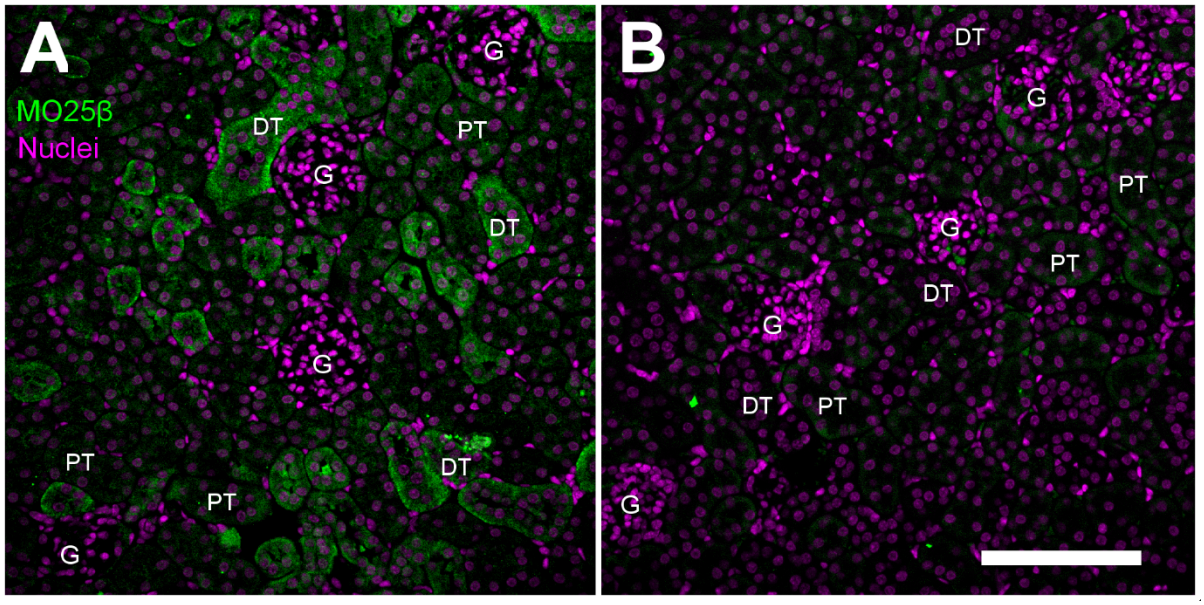

Figure 4.4: Localisation of MO25β in the mouse kidney.

Representative pseudocoloured maximum-intensity z projections of immunofluorescent-stained wildtype kidney sections (n = 4) showing the distribution of MO25β in the renal cortex, as identified by the presence of glomeruli (G). **[A]** Based on the absence of a brush border and the high density of nuclei, MO25β generally mimics human localisation and is confined to the cytosol of the distal tubules (DT) with a basolateral preference, and is very low or non-existent in proximal tubules (PT); **[B]** Primary antibody negative control (i.e. secondary antibody only). Scale bar = 50µm.

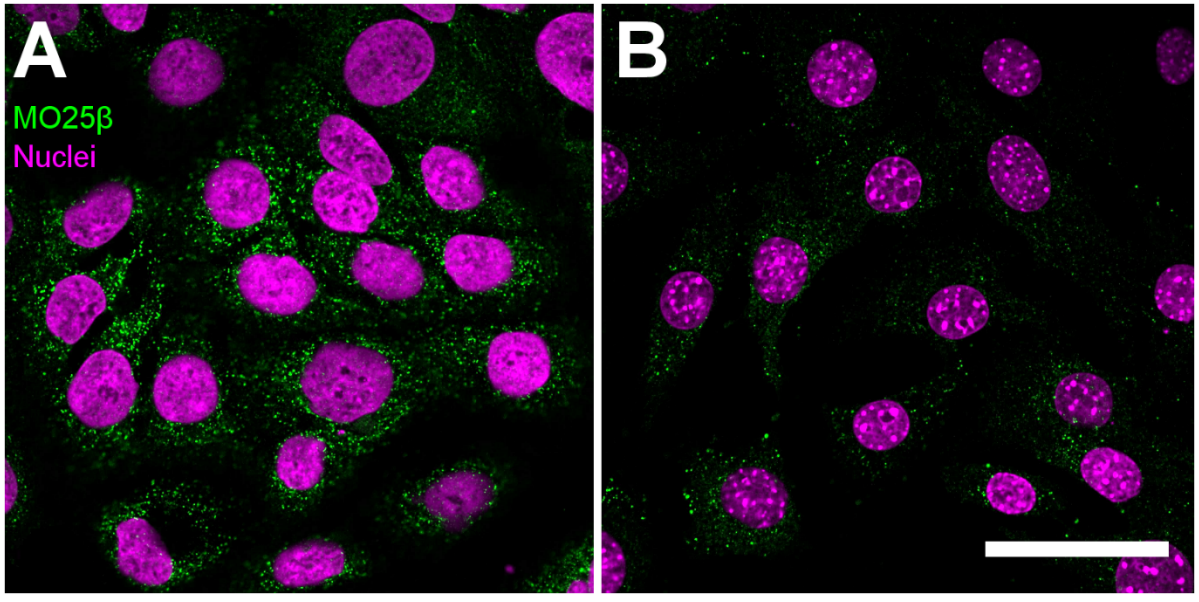

Figure 4.5: Subcellular localisation of MO25β.

Representative pseudocoloured immunofluorescent-stained cells (n = 2) showing the sub-cellular distribution of MO25β in human and mouse cell lines. **[A]** In the CACO-2 (human colon adenocarcinoma) cell line, MO25β is localised to vesicles in the cytosol. **[B]** In the NIH 3T3 (mouse embryonal fibroblast) cell line, MO25β is similarly localised to cytosolic vesicles, although at lower

abundance than CACO-2 cells. Cells were stained with a rabbit polyclonal antibody (HPA045954; Atlas Antibodies) raised against a recombinant protein epitope signature tag (PrEST) MO25β antigen sequence. Scale bar = 50μm. HPA045954 stained CACO-2 and NIH 3T3 images are from the Human Protein Atlas [https://v17.proteinatlas.org/ENSG00000102547-CAB39L/cell], used under CC BY-SA 4.0. Re-pseudocolouring, brightness and contrast were adjusted from original by linear histogram stretching to enhance visibility.

4.3.2 Morphometry

Neither of the MO25β$^{-/-}$ or CAB39L$^{-/-}$ mice models presented with developmental issues or exhibited gross morphological abnormalities in the adult. However, CAB39L$^{-/-}$ male mice did have a higher percentage of body fat despite no differences in body weight or bone mineral density. Additionally, an enlarged heart was found in one male CAB39L$^{-/-}$ mouse, although no significant difference was found in heart weights between the sexes of each genotype (Table 4.1).

Parameter	CAB39L$^{+/+}$		CAB39L$^{-/-}$		P-value
♂ **Bodyweight (g)**	29.93 ± 0.06	(n=1388)	30.50 ± 0.60	(n=12)	0.3803
♀ **Bodyweight (g)**	24.37 ± 0.05	(n=1628)	25.53 ± 0.29	(n=12)	0.1384
♂ **BMD (g/cm^2)**	0.0549 ± 0.0001	(n=1452)	0.0559 ± 0.0008	(n=7)	0.4630
♀ **BMD (g/cm^2)**	0.0545 ± 0.0001	(n=1438)	0.0534 ± 0.0005	(n=8)	0.2498
♂ **Body Fat (%)**	18.48 ± 0.12	(n=1452)	22.17 ± 1.05	(n=7)	*0.0294
♀ **Body Fat (%)**	18.23 ± 0.09	(n=1438)	17.83 ± 0.94	(n=8)	0.7525
♂ **Heart (mg)**	137.4 ± 0.5	(n=1407)	144.1 ± 4.1	(n=8)	0.3609
♀ **Heart (mg)**	113.2 ± 0.4	(n=1382)	116 ± 2.1	(n=8)	0.5665
♂ **Enlarged Heart**	-		1 of 4		-

Table 4.1: Morphometry and body composition.

DEXA scans for bone mineral density (BMD) and body composition were performed at age 14 weeks. Terminal bodyweight and organ wet weights were taken at age 16 weeks. Cab39l$^{tm1b(EUCOMM)Wtsi}$ homozygous knock-out (CAB39L$^{-/-}$) mice showed no significant differences from the wildtype CAB39L$^{+/+}$ with the exception of male percentage body fat and a single male with an enlarged heart. *(P<0.05). Data from IMPC [http://www.mousephenotype.org/data/genes/MGI:1914081] and copyright © 2016 IMPC.

4.3.3 Haematology

IMPC database records indicate that CAB39L$^{-/-}$ mice have several significant differences in a complete blood count analysis. Females have a higher white blood cell count, although overall CAB39L$^{-/-}$ mice have a lower mean corpuscular volume, accompanied by increased red blood cell count, haematocrit and haemoglobin, despite no change in mean corpuscular haemoglobin concentration (Table 4.2).

Parameter	CAB39L$^{+/+}$		CAB39L$^{-/-}$		P-value
♂ **Platelets (10^3/μL)**	1472.7 ± 13.5	(n=128)	1465.4 ± 38.3	(n=8)	0.8946
♀ **Platelets (10^3/μL)**	1189.4 ± 10.0	(n=145)	1128.0 ± 37.9	(n=7)	0.1880
♂ **WBC (10^3/μL)**	9.049 ± 0.217	(n=128)	8.0413 ± 0.660	(n=8)	0.2566
♀ **WBC (10^3/μL)**	6.346 ± 0.128	(n=145)	8.090 ± 0.587	(n=7)	**0.0040
RBC (10^6/μL)	10.184 ± 0.025	(n=273)	10.784 ± 0.110	(n=15)	***1.4x10^{-7}
Haematocrit (%)	49.06 ± 0.12	(n=273)	50.51 ± 0.40	(n=15)	**0.0060
Haemoglobin	15.00 ± 0.03	(n=272)	15.56 ± 0.08	(n=15)	***4.0x10^{-6}
MCV (fL)	48.19 ± 0.07	(n=273)	46.86 ± 0.24	(n=15)	***1.7x10^{-5}
MCHC (d/dL)	30.61 ± 0.07	(n=272)	30.83 ± 0.22	(n=15)	0.4765

Table 4.2: Complete blood count.

Cab39l$^{tm1b(EUCOMM)Wtsi}$ homozygous knock-out (CAB39L$^{-/-}$) mice have decreased mean corpuscular volume (MCV) and increased haematocrit, haemoglobin and red blood cell (RBC) counts with no changes in mean corpuscular haemoglobin concentration (MCHC) or platelet counts, however only females have a higher white blood cell (WBC) count. *(P<0.05), **(P<0.01), ***(P<0.001). Copyright data (© 2016 IMPC) is from IMPC [http://www.mousephenotype.org/data/genes/MGI:1914081].

4.3.4 Electrolyte Homeostasis

To determine a potential role for MO25β in salt homeostasis *in vivo*, plasma and urine electrolytes were analysed on various sodium diets. At baseline, CAB39L$^{-/-}$ mice had a lower plasma creatinine level (Table 4.3) which might be reflective of their higher body fat percentage (Table 4.2). CAB39L$^{-/-}$ also have roughly 1 mmol/L higher plasma sodium (Table 4.3) despite no significant differences observed in sodium handling for MO25β$^{-/-}$ on a normal Na diet, however these mice do have excess magnesium excretion (Table 4.4).

Parameter	CAB39L$^{+/+}$		CAB39L$^{-/-}$		P-value
[Creat]$_P$ (µmol/L)	9.51 ± 0.03	(n=2785)	8.69 ± 0.57	(n=16)	*0.0454
[Na^+]$_P$ (mmol/L)	147.11 ± 0.04	(n=2804)	148.25 ± 0.50	(n=16)	*0.0217
[K^+]$_P$ (mmol/L)	4.47 ± 0.01	(n=2802)	4.36 ± 0.11	(n=16)	0.3266
[Cl^-]$_P$ (mmol/L)	110.65 ± 0.04	(n=2803)	110.75 ± 0.34	(n=16)	0.8349
[Ca^{2+}]$_P$ (mmol/L)	2.31 ± 0.00	(n=2804)	2.30 ± 0.01	(n=16)	0.7006
[PO_4^{3-}]$_P$ (mmol/L)	1.76 ± 0.01	(n=2804)	1.80 ± 0.06	(n=16)	0.6116

Table 4.3: Baseline Plasma Electrolytes.

Cab39l$^{tm1b(EUCOMM)Wtsi}$ homozygous knock-outs (CAB39L$^{-/-}$) have lower creatinine (Creat) and higher sodium plasma levels compared to CAB39L$^{+/+}$ mice. *(P<0.05). Please note data for baseline plasma Mg^{2+} was not available. Data from IMPC [http://www.mousephenotype.org/data/genes/MGI:1914081] and copyright by © 2016 IMPC.

Parameter	MO25β$^{+/+}$		MO25β$^{-/-}$		P-value
[Creat]$_U$ (mmol/L)	5.00 ± 0.39	(n=10)	4.17 ± 0.24	(n=10)	0.0877
[Na^+]$_U$ / [Creat]$_U$ ratio	8.06 ± 1.18	(n=10)	10.31 ± 0.68	(n=10)	0.1159
[K^+]$_U$ / [Creat]$_U$ ratio	13.22 ± 1.23	(n=10)	15.96 ± 1.43	(n=10)	0.1649
[Cl^-]$_U$ / [Creat]$_U$ ratio	17.85 ± 1.12	(n=10)	21.01 ± 1.68	(n=10)	0.1345
[Ca^{2+}]$_U$ / [Creat]$_U$ ratio	0.95 ± 0.15	(n=7)	1.59 ± 0.26	(n=8)	0.0625
[Mg^{2+}]$_U$ / [Creat]$_U$ ratio	22.41 ± 1.46	(n=7)	28.46 ± 2.15	(n=8)	*0.0416
[PO_4^{3-}]$_U$ / [Creat]$_U$ ratio	4.15 ± 0.97	(n=7)	1.94 ± 0.63	(n=8)	0.0735

Table 4.4: Baseline urine electrolytes.

On a normal Na diet (0.25% w/w) MO25β$^{-/-}$ have a higher excretion of magnesium compared to MO25β$^{+/+}$ mice. Normalised electrolyte values were expressed as ratios (electrolyte concentration divided by creatinine concentration). *(P<0.05).

To exaggerate differences or reveal a compensated phenotype, the sodium intake of MO25β$^{-/-}$ mice was modified via dietary manipulation in order to assess homeostatic responses to physiological extremes. This was achieved by sodium loading mice on a high Na diet (3% w/w) for several days before switching to a low Na (0.03% w/w) diet to provide a sodium restriction; a strategy which proved to be successful in elucidating the SPAK kinase inactive mouse phenotype (Rafiqi *et al.*, 2010). However, despite the presence of small difference in plasma and urine electrolytes at baseline, no significant differences were observed in sodium restricted plasma electrolytes (Table 4.5) or urine electrolytes for the time-course sodium diet switch (Figure 4.6).

Parameter	MO25β$^{+/+}$		MO25β$^{-/-}$		P-value
[Creat]$_P$ (µmol/L)	45.33 ± 1.76	(n=6)	40.91 ± 2.16	(n=11)	0.1898
[Na^+]$_P$ (mmol/L)	124.50 ± 0.85	(n=6)	124.45 ± 1.49	(n=11)	0.9833
[K^+]$_P$ (mmol/L)	5.17 ± 0.60	(n=6)	4.86 ± 0.19	(n=11)	0.6479
[Cl^-]$_P$ (mmol/L)	91.00 ± 1.13	(n=6)	92.18 ± 1.10	(n=11)	0.5017
[Ca^{2+}]$_P$ (mmol/L)	2.50 ± 0.03	(n=6)	2.47 ± 0.03	(n=11)	0.5521
[Mg^{2+}]$_P$ (mmol/L)	0.97 ± 0.10	(n=6)	0.96 ± 0.04	(n=11)	0.8964
[PO_4^{3-}]$_P$ (mmol/L)	1.89 ± 0.09	(n=6)	2.00 ± 0.09	(n=11)	0.4551

Table 4.5: Plasma electrolytes on a low Na^+ diet.

No significant difference were found in plasma electrolytes between MO25β$^{-/-}$ and MO25β$^{+/+}$ mice after sodium restriction. *($P<0.05$).

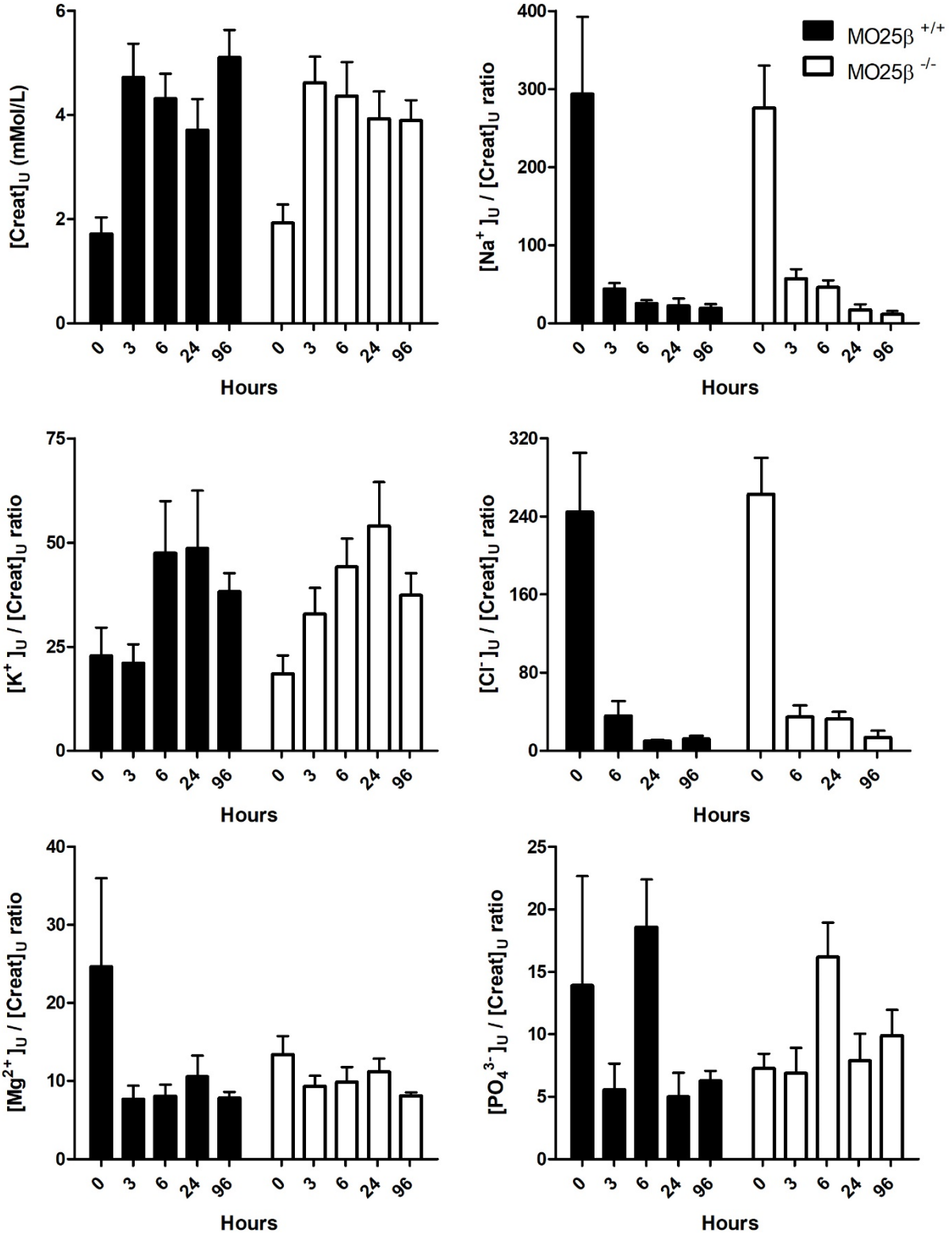

Figure 4.6: Urine electrolyte homeostasis during a time-course sodium diet switch.

Normalised urinary electrolyte excretion expressed as ratios (electrolyte concentration divided by creatinine concentration) at various time points after sodium loaded animals were switched from a high (3% w/w) to a low (0.03% w/w) Na diet. Please note data for 3h Cl^- was not available. No significant differences were observed between MO25β$^{-/-}$ and MO25β$^{+/+}$ mice at any time point. [Creatinine] n = 7-14; [Na^+] n = 5-13; [K^+] n = 5-13; [Cl^-] n = 3-10; [Mg^{2+}] n = 5-13; [PO_4^{3-}] n = 5-13; *($P<0.05$).

4.3.5 Cardiovascular Function

To assess the impact of MO25β knock-out on blood pressure maintenance, direct invasive blood pressure measurements were recorded in MO25β$^{-/-}$ and MO25β$^{+/+}$ mice on various Na diets. Low Na diet was expected to exaggerate any potential phenotypic difference as per previous studies with mouse models of Gitelman syndrome (Rafiqi *et al.*, 2010). However, no significant differences in blood pressure or heart rate were observed between MO25β$^{-/-}$ and MO25β$^{+/+}$ mice on either normal or low Na diets (Figure 4.7).

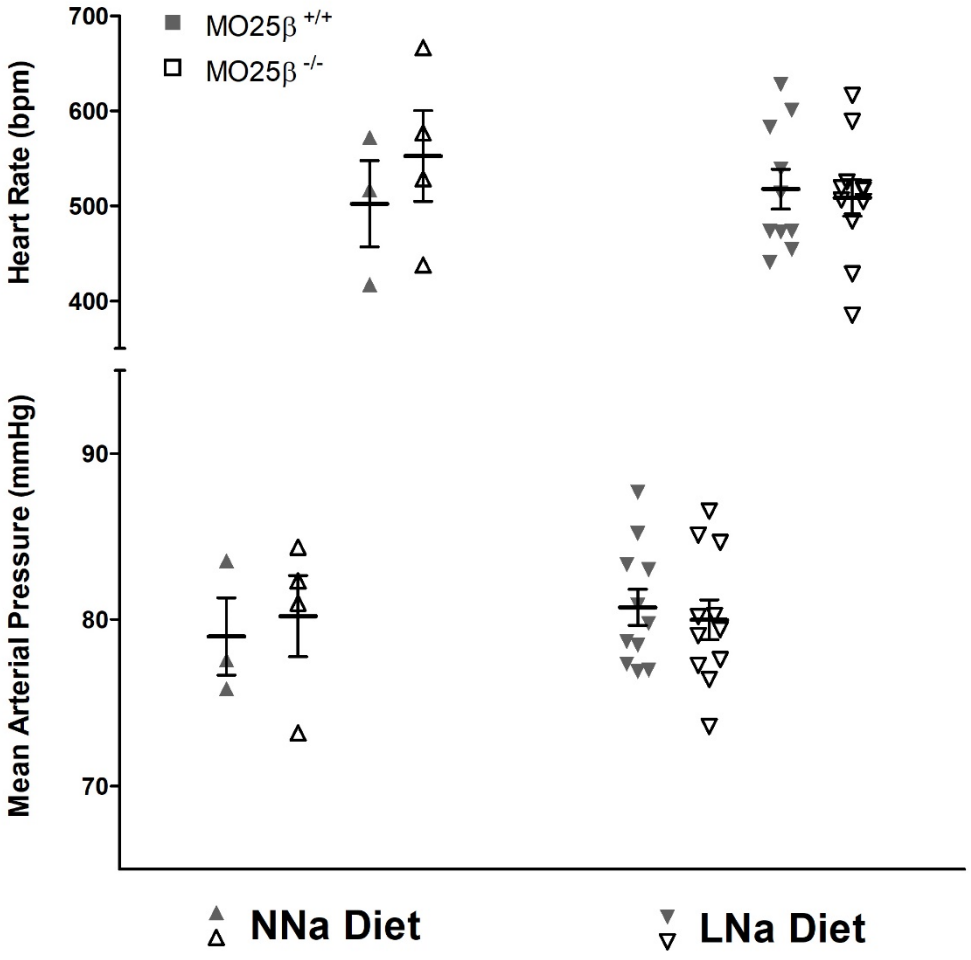

Figure 4.7: Cardiovascular function in response to Na diet manipulations.

Invasive carotid blood pressure measurements did not reveal any differences in systemic blood pressure or heart rate between MO25β$^{-/-}$ and MO25β$^{+/+}$ mice on either salt diet. Normal Na (NNa), n= 3-4 per genotype; Low Na (LNa), n = 10-11 per genotype; *($P<0.05$).

4.4 Discussion

Our study was designed to investigate the role of MO25 in blood pressure and electrolyte homeostasis. For *in vivo* studies, attempts were originally made to obtain a MO25α knock-out mouse model, although this genotype did not produce viable offspring and a MO25β knock-out model was developed instead. In hindsight this should not have come as a surprise given that the MO25 gene was first cloned from mouse cleavage-stage embryos and discovered to be one of the first genes to be transcribed in the 2-cell stage mouse embryo, implying it serves an essential general function in embryological development (Miyamoto *et al.*, 1993). Additionally, dMo25 is expressed in Drosophila embryogenesis and was mapped to left arm of the third chromosome at the 73AB interval, which was known to harbour several uncharacterised genes that when mutated were recessively lethal in the embryonic or early larval stages (Nozaki *et al.*, 1996). Definitive evidence for this was provided when dMo25 and Fray were discovered in a screen of maternal effect lethal mutations to identify genes regulating neuroblast asymmetric division, with knock-out of dMO25 shown to result in mislocalisation of cell-fate determinants and improper embryo development (Yamamoto *et al.*, 2008). Similarities in our approach to study MO25α/β can be drawn with the SPAK/OSR1 story, where a constitutive homozygote OSR1 knock-out proved embryonically lethal, and the alternative strategy of disrupting the closely related SPAK protein was opted for to infer OSR1 functions (Rafiqi *et al.*, 2010; Yang *et al.*, 2010*c*; Lin *et al.*, 2011), while alternative conditional OSR1 knock-outs were under development.

Relatively little information exists in the literature on the roles of MO25β/CAB39L and this work represents the first study to directly explore the gene's functions *in vivo*. Other than the odd study linking MO25β to coffee drinking (Amin *et al.*, 2012) or male infertility (Garrido *et al.*, 2009), the only two areas of MO25β which have garnered attention are in cancer biology and energy metabolism.

So far MO25β has been purported to have anti-tumoural activity primarily through its actions on LKB1 and STK24, with frameshift mutations in MO25β implicated as drivers of gastric and colorectal cancers (Choi *et al.*, 2016), and higher MO25β transcript and protein expression identified in the early stage of oral cancer but not correlated with tumour progression (Lo *et al.*, 2012). Interestingly, MO25β has been implicated in the anti-cancer mechanism of actions of metformin, a first-line medication for the treatment of overweight type 2 diabetes patients, with particularly promising results as an adjunctive therapy in breast

(Pulito *et al.*, 2017) and endometrial cancers (Meireles *et al.*, 2017). Metformin-induces downregulation of microRNA 21-5p to increase MO25β expression which leads to AMPK activation and inhibition of mammalian target of rapamycin (mTOR), which significantly reduces clonogenicity, migration and invasion of cancer cells (Pulito *et al.*, 2017). Additionally, a splice variant of CAB39L has been linked with acute monocytic leukaemia (Zhang *et al.*, 2009), which appears to promote cancer by inhibition of apoptosis (Zhang, 2012; Zhang *et al.*, 2017), with high levels of this novel acute monocytic leukaemia (M5)-associated antigen 34 (MLAA-34) independently associated with a poorer relapse-free and overall survivability (Zhao *et al.*, 2011). Our study did not test for this, however, findings in the literature suggest that MO25β$^{-/-}$ and CAB39L$^{-/-}$ mouse models would be more susceptible to these forms of cancer, while counterintuitively specifically resistant to acute monocytic leukaemia. The only phenotypic findings on this front relate to changes in whole blood counts where white blood cell counts were elevated only in female CAB39L$^{-/-}$ mice (Table 4.2).

Morphologically CAB39L$^{-/-}$ male mice also exhibit increased body fat percentage, although there appears to be no overall difference in body weights (Table 4.1). This may in part be explained by the role of AMPK in the modulation of energy balance, where MO25β has been associated with bodyweight and food intake in chickens (Zhang *et al.*, 2011; Lei & Lixian, 2012; Yuan *et al.*, 2015), and bodyweight and obesity in humans (Rahmioglu *et al.*, 2015). Additionally, out of the four CAB39L$^{-/-}$ male mice examined post-mortem, one was found to have an enlarged heart (Table 4.1). Elevated levels of microRNAs which target MO25α have been implicated in the development of cardiac hypertrophy through suppression of LKB1/AMPK pathway, which suggests that loss of MO25β-dependent LKB1/AMPK signalling may have a similar effect (Chen *et al.*, 2012; Kuwabara *et al.*, 2015). These same microRNAs are strongly induced in during erythropoiesis and their ablation in mice leads to mild anaemia (Fang *et al.*, 2017). The subsequent loss of MO25β-dependent LKB1/AMPK/mTOR pathway activation promotes red cell precursor survival and offers an explanation for the increases in red blood cell counts, haematocrit, haemoglobin, and perhaps decreased mean corpuscular volume observed in CAB39L$^{-/-}$ mice (Table 4.2), athough further investigation would be required to confirm this phenotype and the underlying mechanisms.

Electrolyte homeostasis appears almost identical between the genotypes with only slight, although statistically significant differences between the baseline plasma creatinine and sodium of CAB39L$^{-/-}$ and wild types (Table 4.3), which either retained a non-statistically

significant trend or normalised in MO25β$^{-/-}$ mice on a low salt diet (Table 4.5). A near total absence of any meaningful alterations in renal excretory functions provides no clear explanation for the changes seen in plasma (Table 4.4). Similarly the increased renal excretion of magnesium in MO25β$^{-/-}$ mice at baseline (Table 4.5) is hard to account for without any signs of hypomagnesaemia (Table 4.3) and with normalisation of renal excretion on high and low salt diets (Figure 4.6). Interpretation of this result is further hampered by the generally poor understanding of renal magnesium homeostasis, with TRPM6 being the only identified apical transcellular magnesium-selective channel in the DCT and currently not known to be regulated by the WNK pathway (Blaine *et al.*, 2015).

These data suggest that MO25β has a limited role in electrolyte homeostasis, whereas recent *w*ork has provided evidence for a role of MO25α in electrolyte homeostasis. In *Xenopus laevis* oocyte studies it was revealed that the sodium-driven CCCs can also be activated by a SPAK-independent pathway involving MO25α and WNK4 (Ponce-Coria *et al.*, 2014). The importance of this novel pathway was highlighted by the enhanced MO25α/WNK/NKCC1 signalling observed in spontaneously hypertensive rats which was found to increase their susceptibility to ischaemic brain damage (Bhuiyan *et al.*, 2016). However, the *in vivo* role of MO25α in the mammalian kidney is largely unexplored. MO25α is expressed in the DCT and TAL where it co-localises with NCC and NKCC2, but unlike OSR1 its expression and localisation does not change in a SPAK knock-out mouse (Grimm *et al.*, 2012). This is striking as NCC phosphorylation in SPAK knock-out and loss-of-function knock-in mouse models is only reduced and not completely absent (Rafiqi *et al.*, 2010; Yang *et al.*, 2010*c*). A possible explanation for this is a putative MO25α/WNK/NCC pathway which partially compensates for the loss of WNK/SPAK/NCC signalling and disrupted MO25α stabilisation and activation of OSR1 monomers and dimers due to displacement of OSR1 from the apical membrane to cytosolic puncta in the DCT (Gagnon *et al.*, 2011; Grimm *et al.*, 2012; Ponce-Coria *et al.*, 2012, 2014; Li *et al.*, 2014). This may also help to explain the divergent nature of NKCC2 hyperphosphorylation in SPAK knock-out models (Yang *et al.*, 2010*c*; Grimm *et al.*, 2012) and NKCC2 hypophosphorylation in loss-of-function SPAK knock-in models (Rafiqi *et al.*, 2010). In the DCT of wildtype animals SPAK is predominantly full length, whereas most SPAK isoforms in the TAL are truncated splice variants, KS-SPAK and SPAK2 (Mccormick *et al.*, 2011), which lack intact kinase domains and can inhibit NKCC2 phosphorylation by competing for binding sites (Park *et al.*, 2013). Therefore, in SPAK knock-out models with no isoforms to compete for NKCC2 binding sites, the uninhibited activity of the MO25α/WNK/NKCC2,

MO25α/OSR1/NKCC2 and WNK/OSR1/NKCC2 signalling pathways would lead to hyperphosphorylation in the TAL. While in the TAL of loss-of-function SPAK knock-in models, the hypophosphorylation of NKCC2 may be explained by inactive mutant full length SPAK acting as a third inhibitory isoform, working alongside the intact KS-SPAK and SPAK2 isoforms to further compete for binding sites, thus preventing any compensation for the loss of SPAK activity by other MO25α, WNK or OSR1 dependent pathways (Gagnon *et al.*, 2011; Grimm *et al.*, 2012; Ponce-Coria *et al.*, 2012, 2014; Li *et al.*, 2014).

Similarly the data in this study suggests that MO25β has a limited role in blood pressure maintenance (Figure 4.7). However, in the case of MO25α, preliminary reports show that mice with renal tubule-specific overexpression MO25α result in seemingly phenotypically normal animals with elevated phosphorylation of SPAK, NKCC2 and NCC. Although when these mice are subjected to salt loading they develop marked hypertension with slight hyperkalaemia, reminiscent of familial hyperkalaemia hypertension syndrome (FHHt) (Yang *et al.*, 2013). Additionally, when these mice are crossed with WNK4 knock-out mice with a Gitelman-like phenotype, they can partially rescue the hypotension, hypokalaemia, hypomagnesaemia, hypocalciuria and reduced abundance of phosphorylated SPAK/OSR1 and NCC (Yang *et al.*, 2014), most likely through enhanced WNK-independent MO25α activation of SPAK/OSR1 (Gagnon *et al.*, 2011; Filippi *et al.*, 2011; Ponce-Coria *et al.*, 2012; Li *et al.*, 2014). This makes MO25α a potential anti-hypertensive target, and a recent small-molecule compound library screening identified HK01 as a promising candidate for indirect SPAK/OSR1 kinase inhibition. In live cell assays, HK01 reduced NKCC1 phosphorylation in a dose-dependent manner by binding to the hydrophobic site of MO25 and competing with the WEW motifs of SPAK/OSR1 (Kadri *et al.*, 2017).

In conclusion, the *in vivo* data gathered from the MO25β knock-out mice suggest that either MO25β has no role in blood pressure or electrolyte homeostasis or has a limited redundant role where MO25α is the physiologically dominant isoform and normal levels are sufficient to compensate for MO25β loss. Though this model may be useful in exploring the role of the MO25β in cancer biology.

Chapter 5 : Gitelman Syndrome Validates SPAK as a Novel Anti-Hypertensive Target

[*This chapter is principally based on and expands upon the content from the abstracts in Appendix 1 and paper in Appendix 4* (Zhang *et al.*, 2015)]

5.1 Abstract

The STE20/SPS1-related proline/alanine-rich kinase (SPAK) controls blood pressure by phosphorylating and stimulating the Na-Cl (NCC) and Na-K-2Cl (NKCC2) cotransporters, which regulate salt reabsorption in the kidney. SPAK possesses a conserved carboxy-terminal (CCT) domain, which recognises RFxV/I motifs present in its upstream activator (isoforms of the With-No-lysine (K) kinases [WNKs]) as well as its substrates (NCC and NKCC2). To define the physiological importance of the CCT domain, knock-in mice were generated in which the critical CCT domain Leu502 residue required for high affinity recognition of the RFxI/V motif was mutated to Alanine. The SPAK CCT domain defective knock-in animals are viable, and the Leu502Ala mutation abolished co-immunoprecipitation of SPAK with WNK1, NCC and NKCC2. The CCT domain defective animals displayed markedly reduced SPAK activity and phosphorylation of NCC and NKCC2 cotransporters at the residues phosphorylated by SPAK. This was also accompanied by a reduction in the expression of NCC and NKCC2 protein without changes in mRNA levels. The SPAK CCT domain knock-in mice showed typical features of Gitelman Syndrome with mild hypokalaemia, hypomagnesaemia, hypocalciuria and displayed salt-wasting on switching to a low Na-diet. These observations establish that the CCT domain plays a crucial role in controlling SPAK activity and blood pressure. Our results indicate that CCT domain inhibitors would be effective at reducing blood pressure by lowering phosphorylation as well as expression of NCC and NKCC2.

5.2 Introduction

SPAK (SPS1-related proline/alanine rich kinase) and OSR1 (oxidative stress-responsive kinase 1) are closely related protein kinases, which play key roles in regulating cellular ion

homeostasis and blood pressure (BP) (Delpire & Gagnon, 2008; Richardson & Alessi, 2008). SPAK and OSR1 are activated following the phosphorylation of their T-loop residue (SPAK Thr233 and OSR1 Thr185) by one of the four isoforms of the WNK [With No lysine (K) kinase] protein kinase (Moriguchi *et al.*, 2005; Vitari *et al.*, 2005). The activity of SPAK and OSR1 is further enhanced following interaction with the scaffolding protein termed MO25 (Filippi *et al.*, 2011). The best-characterised SPAK/OSR1 substrates comprise the SLC12A (solute carrier family 12) family of electroneutral CCCs (cation–chloride cotransporters) (Piechotta *et al.*, 2002; Anselmo *et al.*, 2006; Gagnon *et al.*, 2006; Richardson *et al.*, 2008, 2011; de Los Heros *et al.*, 2014). These transporters regulate intracellular chloride concentration critical in controlling blood pressure and cell volume homoeostasis (Gagnon & Delpire, 2013). SPAK/OSR1 protein kinases drive chloride influx by phosphorylation and activating sodium-driven CCC members. These include the NCC (Na^+–Cl^- Cotransporter) in the distal convoluted tubule of the kidney (Richardson *et al.*, 2008), the NKCC2 (Na^+–K^+–$2Cl^-$ Cotransporter 2) in the thick ascending limb of the kidney (Richardson *et al.*, 2011) and the ubiquitously expressed NKCC1 (Piechotta *et al.*, 2002; Anselmo *et al.*, 2006; Gagnon *et al.*, 2006). SPAK/OSR1 also phosphorylate and inhibit potassium-driven CCCs that drive chloride efflux (de Los Heros *et al.*, 2014), which comprise four different K^+–Cl^- cotransporters (KCC1–KCC4) (Kahle *et al.*, 2010; Gagnon & Delpire, 2013). This reciprocal regulation of Na^+- and K^+-driven CCCs by SPAK and OSR1 ensures that cellular $Cl^–$ influx and efflux is tightly co-ordinated (Kahle *et al.*, 2010; Gagnon & Delpire, 2013).

The importance of the WNK signalling pathway is exemplified by its evolutionary conservation from worms to humans and that several Mendelian hypertension disorders in humans are caused by mutations in WNK pathway components (Kahle *et al.*, 2008; Alessi *et al.*, 2014). These include various mutations that lead to increased expression of the WNK1 and WNK4 genes causing PHAII (PseudoHypoAldosteronism type II, OMIM #145260) (Wilson *et al.*, 2001; Boyden *et al.*, 2012; Louis-Dit-Picard *et al.*, 2012; Shibata *et al.*, 2013; Wakabayashi *et al.*, 2013; Ohta *et al.*, 2013; Schumacher *et al.*, 2014). Conversely, loss-of-function mutations in NCC and NKCC2 cause familial forms of hypotension and hypokalaemia termed Gitelman (OMIM #263800) and Bartter type 1 syndrome (OMIM #601678) respectively (Simon *et al.*, 1996). A mutation that ablates the key activating WNK-regulated SPAK/OSR1 phosphorylation site on NCC (T60M (Richardson *et al.*, 2008)) also causes Gitelman syndrome (Lin *et al.*, 2005; Shao *et al.*, 2008). Moreover, SPAK-knock-out mice (Yang *et al.*, 2010*c*; Mccormick *et al.*, 2011; Grimm *et al.*, 2012), or knock-in mice expressing

a form of SPAK that cannot be activated by WNK kinase isoforms (Rafiqi *et al.*, 2010), exhibit low blood pressure and are resistant to hypertension when crossed to animals bearing a PHAII-causing knock-in mutation that enhances WNK4 expression (Chiga *et al.*, 2011). Genome-wide association studies have also identified intronic SNPs within the SPAK gene (*STK39*) that correlate with increased blood pressure in humans (Wang *et al.*, 2009) and have been shown to increase SPAK-CCC activity in cells expressing these SNPs (Mandai *et al.*, 2015). Two common types of drugs used in the treatment of high blood pressure also target SPAK sodium-driven CCC substrates, namely thiazide diuretics (such as bendroflumethiazide) that inhibit NCC and the loop diuretics (such as furosemide) that inhibits NKCC2 (Gordon & Hodsman, 1986; Gordon *et al.*, 1995).

These data suggest that chemical agents that inhibit SPAK would have the potential to treat hypertension, but without the off-target effects of agents like thiazide diuretics (Glover & O'Shaughnessy, 2011; Alessi *et al.*, 2014). One approach would be to elaborate small molecule compounds that directly inhibit SPAK/OSR1 protein kinase activity (Cohen & Alessi, 2013). However, to our knowledge no highly selective and potent kinase inhibitors of SPAK and OSR1 have been reported. There is also concern whether sufficiently selective SPAK/OSR1 kinase inhibitors could be synthesised for the management of a chronic largely asymptomatic condition, without them inhibiting other protein kinases or ATP binding enzymes and causing intolerable off-target effects. An alternative strategy to suppress SPAK/OSR1 function would be to target the docking domain within the non-catalytic C-terminal region of SPAK/OSR1 called the CCT (Conserved C-Terminal) domain. *In vitro* and overexpression studies indicate that the CCT domain binds to conserved RFxV/I motifs present on WNK isoforms and that these interactions facilitate phosphorylation and activation of SPAK/OSR1 (Vitari *et al.*, 2006; Gagnon *et al.*, 2007). Furthermore, the sodium-driven CCC members also possess conserved RFxI/V motifs at their N-terminus which experimental data indicate are critical for enabling SPAK/OSR1 to interact with, phosphorylate and stimulate activity of these transporters (Gagnon *et al.*, 2007; Richardson *et al.*, 2008, 2011; Mori *et al.*, 2013*a*).

This study sought to define the role that the CCT domain plays *in vivo* by generating and characterising SPAK knock-in mice in which function of the CCT domain has been ablated by a mutation of the critical Leu502 residue required for high affinity binding of the RFxI/V motif.

5.3 Results

5.3.1 Characterisation of a mutation that inhibits the CCT domain of SPAK

Previous crystallographic analysis of the human OSR1 CCT domain complexed to an RFxI motif containing peptide derived from WNK4 (Villa *et al.*, 2007), revealed that the highly conserved Leu473 CCT residue lying at the base of a deep hydrophobic pocket, formed critical hydrophobic contacts with the Phe residue of the RFxI motif (Figure 5.1 A). Consistent with this, mutation of Leu473 to Ala reduced binding of OSR1 to RFxI WNK4 peptide over 100-fold (Villa *et al.*, 2007). Mutation of the equivalent residue (Leu502) in mouse SPAK also prevented full-length mouse SPAK co-immunoprecipitating with endogenously expressed WNK1 and NKCC1 in HEK293 cells (Figure 5.1 B). Moreover, *in vitro* fluorescence polarisation studies confirmed that mutation of this Leu residue in the SPAK CCT domain reduced binding to an RFxV-motif possessing peptide derived from WNK4 by ~100-fold (Figure 5.1 C).

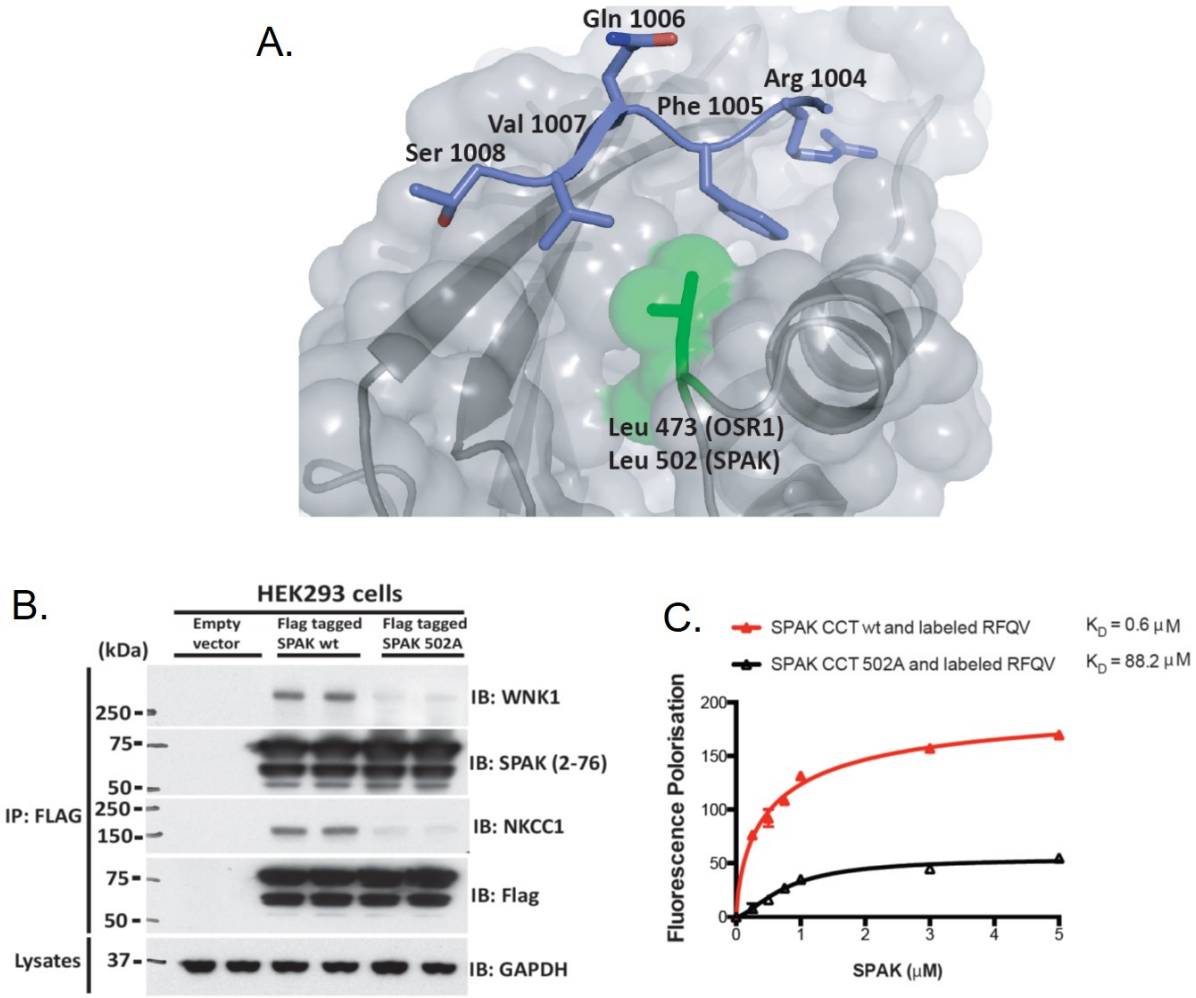

Figure 5.1: Evidence that SPAK associates with WNK1 and interaction is disrupted by SPAK CCT mutation.

[A] Molecular interaction of the RFxV peptide with the conserved carboxy-terminal domain of OSR1 based on (PDB: 2V3S) CCT domain of OSR1 (residues 434–527) coloured in grey (β-strands and α-helices) bound to the GRFQVT WNK4-derived peptide coloured in blue. **[B]** Pull-down assays of transfected HEK293 cells show that SPAK L502A has significantly reduced interactions with WNK1 and NKCC1 compared to WT. Similar results were obtained in three separate experiments. **[C]** Analysis of SPAK–WNK interaction confirmed impaired binding of the SPAK CCT mutant to the WNK docking motif, as evidenced by reduced fluorescence polarisation. [Taken from (Zhang *et al.*, 2015)].

5.3.2 Characterisation of CCT domain deficient SPAK$^{L502A/L502A}$ mice

We exploited these observations to explore the impact that mutation of the CCT domain Leu502 residue had, by generating knock-in mice on an inbred C57BL/6J background, in which the Leu502 CCT domain residue was changed to Ala (Figure 5.2 A). Homozygous SPAK$^{L502A/L502A}$ mice were born at the expected Mendelian frequency (Table 5.1), were of normal size and appearance, and did not display any overt phenotype, at least up to 1 year of age (the oldest animals analysed in this study).

Cross	Genotype		Number Born (%)	Expected Mendelian Frequency (%)
SPAK (+/502A) OSR1 (+/+)	SPAK (+/+)	OSR1 (+/+)	94 (30%)	25
SPAK (+/502A) OSR1 (+/+)	SPAK (+/502A)	OSR1 (+/+)	180 (57%)	50
	SPAK (502A/502A)	OSR1 (+/+)	42 (13%)	25

Table 5.1: Breeding of ratios SPAK knock-in mice.

Mating pairs for SPAK were set up as outlined above and the progeny were genotyped as described in the methods. The percentage of each genotype observed is indicated in parenthesis followed by its expected Mendelian frequency. [Taken from (Zhang *et al.*, 2015)].

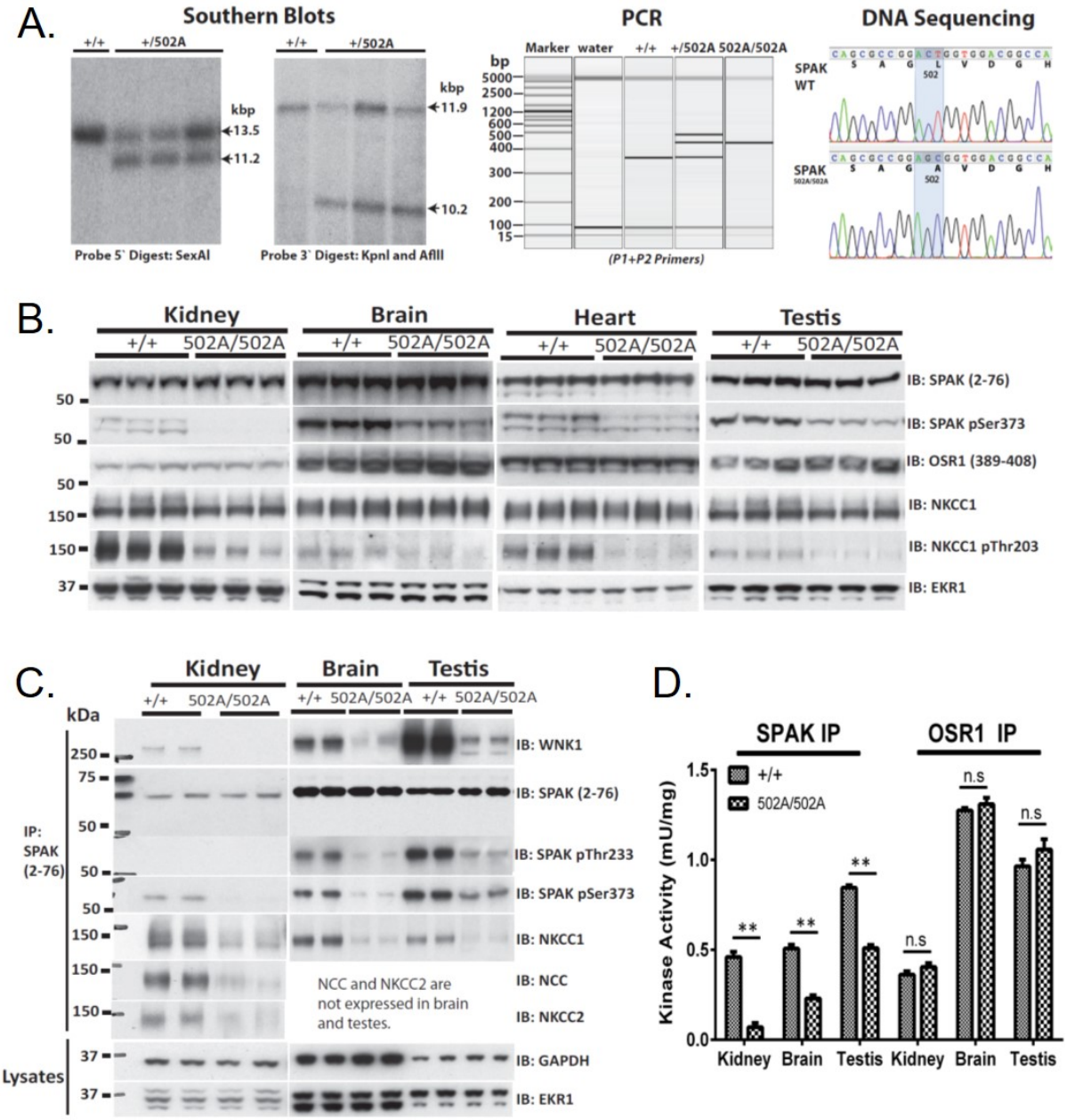

Figure 5.2: Targeting strategy used to generate SPAK knock-in mutations.

[A, left] Southern blot analysis of genomic DNA purified from the targeted ES cells and subjected to enzymatic digestion permitted the identification the wild-type and knock-in alleles for genotyping. **[A, middle]** PCR amplification of genomic DNA can be used to determine genotype with the knock-in allele producing a larger product than WT allele due to the presence of a FRT site and flanking region, which remains in an intronic region following Flp-mediated excision of the puromycin resistance (PuroR) selection cassette. **[A, right]** DNA sequencing of PCR products encompassing the knock-in mutation region show successful point mutation of the target site. **[B]** Total levels of SPAK, OSR1 NKCC1 in various tissues was unaltered in knock-in versus wildtype mice, although phosphorylation of SPAK and NKCC1 was markedly reduced. Similar results were obtained in three separate experiments. **[C]** Pull-down assays of SPAK from kidney, testis and brain lysates from wild-type and knock-in mice confirm impaired SPAK-WNK and SPAK-CCC binding *in vivo*. **[D]** Immunoprecipitates subjected to activity measurements using the CATCHtide peptide substrate show

that SPAK L502A is dramatically reduced without any impact on OSR1 activity (Moriguchi *et al.*, 2005). [Taken from (Zhang *et al.*, 2015)].

Immunoblot analysis of tissues (kidney, brain, heart and testis) derived from littermate wild type and $SPAK^{L502A/L502A}$ homozygous animals of 2 months of age employing a novel mouse SPAK antibody that was generated which does not recognise mouse OSR1 (Figure 5.3), revealed that the L502A mutation did not influence expression of SPAK in these tissues. In all tissues analysed deriving from $SPAK^{L502A/L502A}$ mice, a significant reduction of the phosphorylation of SPAK at a key WNK phosphorylation site (Ser373) (Moriguchi *et al.*, 2005) was observed in comparison to wild type mice (Figure 5.2 B). This is consistent with the L502A mutation suppressing the ability of WNK isoforms to phosphorylate SPAK. Furthermore, the $SPAK^{L502A/L502A}$ knock-in animals displayed markedly reduced phosphorylation of NKCC1, in agreement with the CCT domain being required for SPAK to bind to and phosphorylate NKCC1 (Figure 5.2 B).

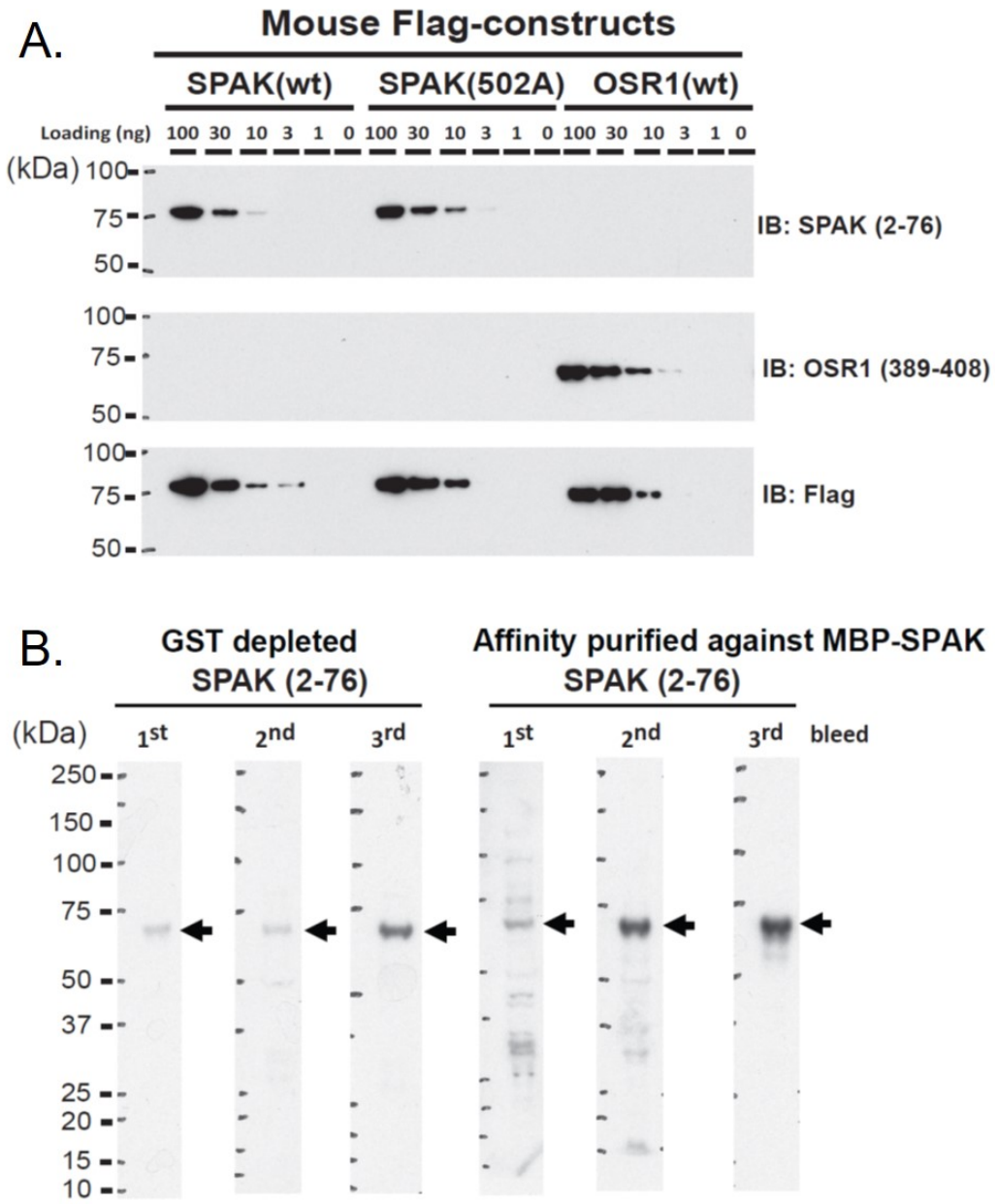

Figure 5.3: Generation and characterisation of specific SPAK antibodies.

Immunoblots of HEK293 cell lysates **[A]** and kidney lysates **[B]** with the newly generated SPAK and OSR1 mouse antibodies. The N-terminal SPAK antibody was generated by ligating cDNA corresponding to amino acids 2–76 of mouse SPAK downstream of the GST open reading frame in the pGEX-6P-1 vector. The resulting fusion protein was injected into sheep to produce polyclonal antibodies. HEK293 cells were transfected with the constructs encoding the full-length mouse FLAG-tagged $SPAK^{WT}$ and $SPAK^{L502A}$. [Taken from (Zhang *et al.*, 2015)].

To obtain further evidence that the L502A mutation impacted on the ability of SPAK to bind WNK1 and NKCC1, SPAK was immunoprecipitated from kidney, brain and testis, derived from littermate wild type and $SPAK^{L502A/L502A}$ homozygous animals of 2 months of

age and tested how CCT domain mutation effected association with WNK1 and NKCC1. This revealed that in the SPAK$^{L502A/L502A}$ knock-in animals co-immunoprecipitation of WNK1 and NKCC1 with SPAK was markedly reduced in all tissues analysed (Figure 5.2 C). In the kidney it was also observed that mutation of the CCT domain inhibited co-immunoprecipitation of NCC and NKCC2 with SPAK (Figure 5.2 C). Further immunoblot analysis of SPAK immunoprecipitates confirmed that the L502A mutation inhibited phosphorylation of SPAK at the two key residues that WNK isoforms phosphorylate (Thr243 and Ser373) (Figure 5.2 C) (Vitari *et al.*, 2005). SPAK as well as OSR1 immunoprecipitates from tissues (kidney, brain and testis) were also subjected to a protein kinase assay activity assay employing the previously described CATCHtide peptide that encompasses the NKCC1 phosphorylation sites (Vitari *et al.*, 2006). This revealed that SPAK immunoprecipitated from all tissues derived from SPAKL$^{502A/L502A}$ knock-in mice displayed significantly reduced activity compared to wild type animals (Figure 5.2 D). As expected, activity of OSR1 was not affected in SPAK$^{L502A/L502A}$ knock-in mice (Figure 5.2 D).

5.3.3 SPAK$^{L502A/L502A}$ mice display reduced phosphorylation of NCC and NKCC2 in kidney

We next compared the relative levels of phosphorylation of NCC in total kidney extracts derived from male and female 2-month-old wild type and SPAK$^{L502A/L502A}$ knock-in littermate animals (Figure 5.4 A-D). Phosphorylation of NCC was monitored by employing different previously characterised phosphospecific antibodies recognising major SPAK NCC phosphorylation sites (Thr46, Thr50, Thr55, Thr60 and Ser91) (Richardson *et al.*, 2011). This revealed that in both male and female mice the phosphorylation of NCC at all residues analysed was drastically reduced in kidney derived from SPAK$^{L502A/L502A}$ knock-in mice compared to wild type (Figure 5.4 B). Similar to what was previously observed in SPAK kinase inactive (SPAK$^{T243A/T243A}$) knock-in mice (Rafiqi *et al.*, 2010) as well as SPAK knock-out mice (Yang *et al.*, 2010*c*; Mccormick *et al.*, 2011; Grimm *et al.*, 2012), ~2-fold reduction in total levels of NCC protein in kidney extracts of SPAK$^{L502A/L502A}$ knock-in mice was also observed when compared to wild type (Figure 5.4 B). In contrast, kidney mRNA levels of NCC were similar in wild type and of SPAKL$^{502A/L502A}$ knock-in mice (Figure 5.5).

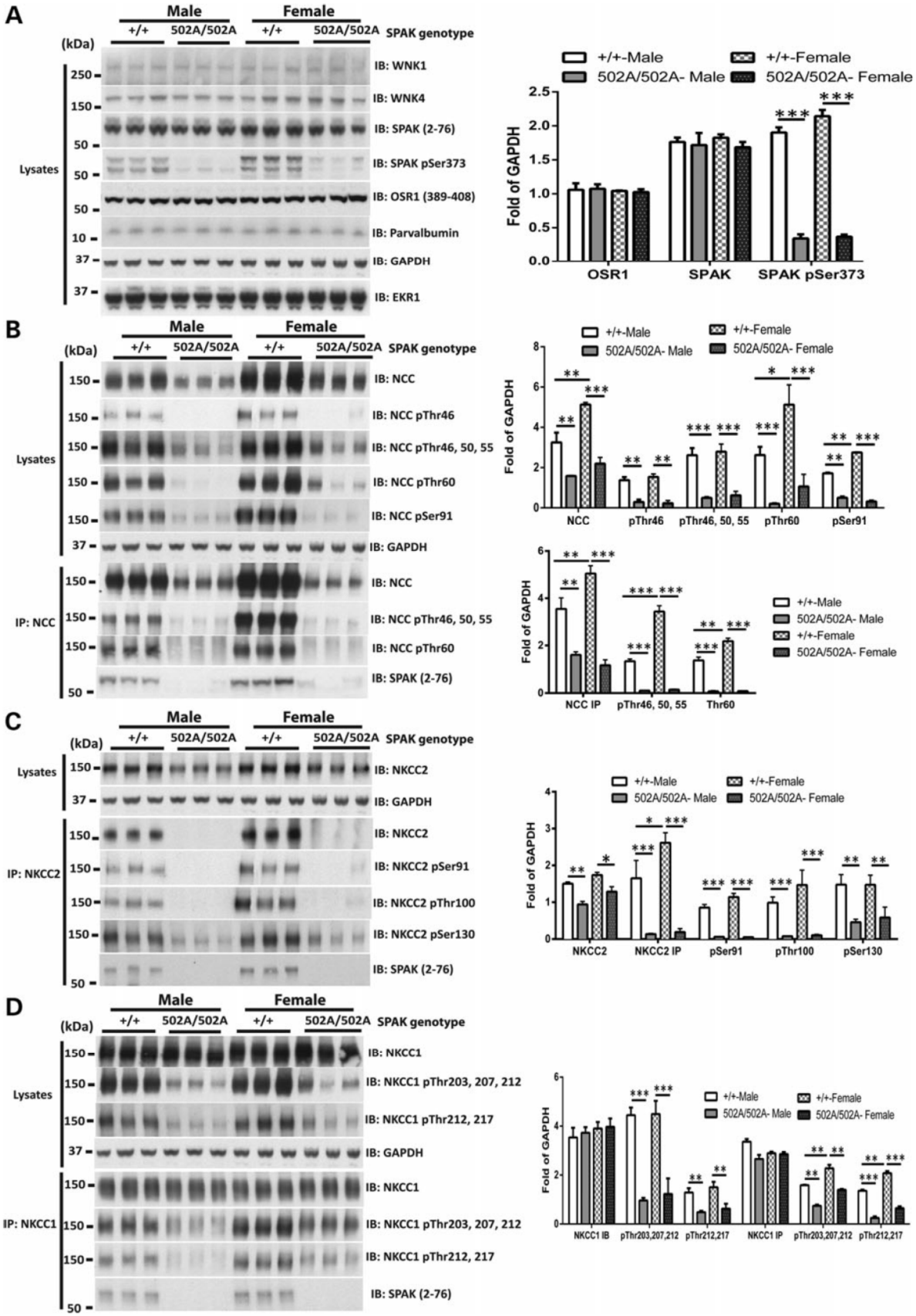

Figure 5.4: Reduced phosphorylation of SPAK, NCC, NKCC1, NKCC2 and expression of NCC and NKCC2 in both male and female SPAK$^{L502A/L502A}$.

Immunoblot analysis of immunoprecipitates and lysates from kidneys of wild-type and knock-in male and female mice. This study has been repeated over three times each with kidney extracts derived from different animals on each occasion with consistent results. The right-hand side panels show quantification of the results of the blots (n = 6, mean ± SEM). **[A]** Expression of WNK1, WNK4, SPAK, OSR1 and Parvalbumin is unaltered, however phosphorylation of SPAK is significantly reduced in knock-in mice. **[B]** Analysis of NCC protein levels and phosphorylation reveal that wildtype females have higher levels of total NCC and increased phosphorylation compared to males. SPAK CCT mutation dramatically reduced NCC protein and phosphorylation at multiple residues, abolishing the sex differences. **[C]** Similar to NCC, immunoprecipitated total NKCC2 protein levels were higher in female vs male wildtypes, although there were no significant differences in NKCC2 phosphorylation between sexes. SPAK CCT mutation markedly reduced NKCC2 protein levels, phosphorylation and abolished the sex differences. **[D]** While NKCC1 protein levels were not different between sexes, immunoprecipitated NKCC1 had greater levels of phosphorylation in female versus male wildtype mice. SPAK CCT mutation did not alter NKCC1 levels but decreased phosphorylation and abolished sex differences. *P < 0.05; **P < 0.01; ***P < 0.001. [Taken from (Zhang *et al.*, 2015)].

We next monitored NKCC2 expression and similarly to NCC observed that levels were reduced ~2-fold in the kidney of $SPAK^{L502A/L502A}$ knock-in male and female mice compared to wild type animals (Figure 5.4 C). NKCC2 was immunoprecipitated and analysed its phosphorylation at 3 residues that SPAK phosphorylates (Ser91, Thr100 and Ser130) (Richardson *et al.*, 2011), and found that phosphorylation of each of these residues was substantially reduced in both male and female kidney derived from $SPAK^{L502A/L502A}$ knock-in animals (Figure 5.4 C). Kidney mRNA levels of NKCC2 were similar in wild type and of $SPAK^{L502A/L502A}$ knock-in mice (Figure 5.5).

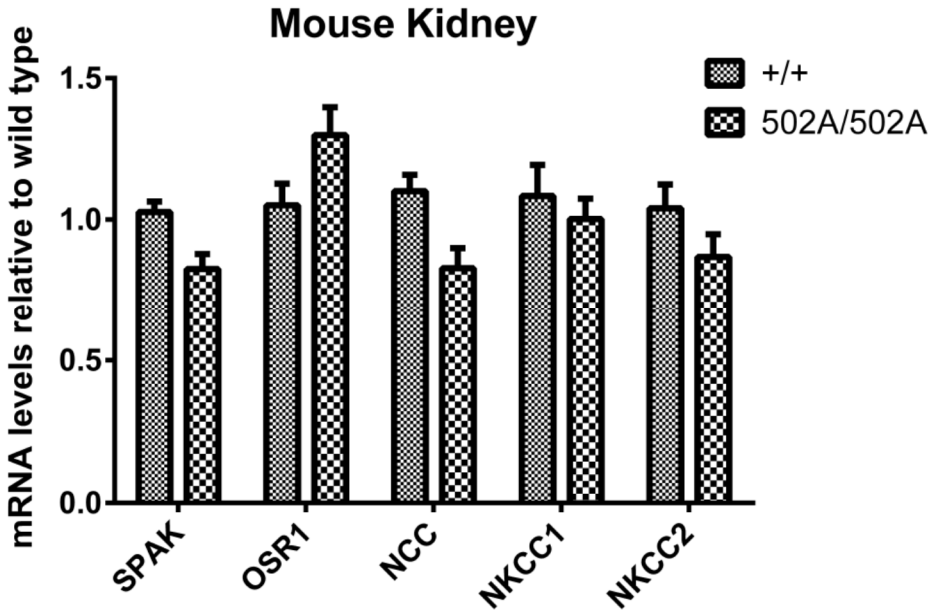

Figure 5.5: Quantitative real-time PCR analysis of sodium ion cotransporter expression in the kidney.

Quantitative real-time PCR analysis of mRNA levels quantified from five separate mice, each PCR performed in triplicate, results normalised to 18S rRNA expression with levels presented relative to wild type expression. No significant differences were found.[Taken from (Zhang *et al.*, 2015)].

We also analysed NKCC1 and found that the levels of this cotransporter were unaffected in kidney extracts derived from wild type and SPAK$^{L502A/L502A}$ knock-in male and female mice (Figure 5.4 D). NKCC1 was immunoprecipitated and analysed its phosphorylation at 4 sites that SPAK phosphorylates (Thr203, Thr207, Thr212 and Thr217 (Vitari *et al.*, 2005; Filippi *et al.*, 2011)) and found that phosphorylation of these sites was markedly diminished in both male and female kidney extracts derived from SPAK$^{L502A/L502A}$ knock-in animals compared to wild type. Kidney mRNA levels of NKCC1 were similar in wild type and of SPAK$^{L502A/L502A}$ knock-in mice (Figure 5.5).

5.3.4 SPAK$^{L502A/L502A}$ mice show a marked reduction in immunostaining for phosphorylated NCC and NKCC2 without remodelling of kidney tubules

Confocal imaging of kidney sections from the SPAK$^{L502A/L502A}$ mice confirmed the modest reduction in total NCC and NKCC2 in the tubules of the distal convoluted (DCT) and thick ascending limb (TAL) tubules compared to wild type mice, with no obvious changes in the

morphology and numbers of tubules or the intracellular protein distribution between genotypes (Figure 5.6). In striking contrast, staining for the phosphorylated forms of NCC and NKCC2 in the same tubules was almost completely lost in the SPAK$^{L502A/L502A}$ mice in keeping with the immunoblots from whole kidney lysates (Figure 5.4). Additionally no changes were observed in the intracellular localisation of WNK4 in the DCT or TAL (Figure 5.7).

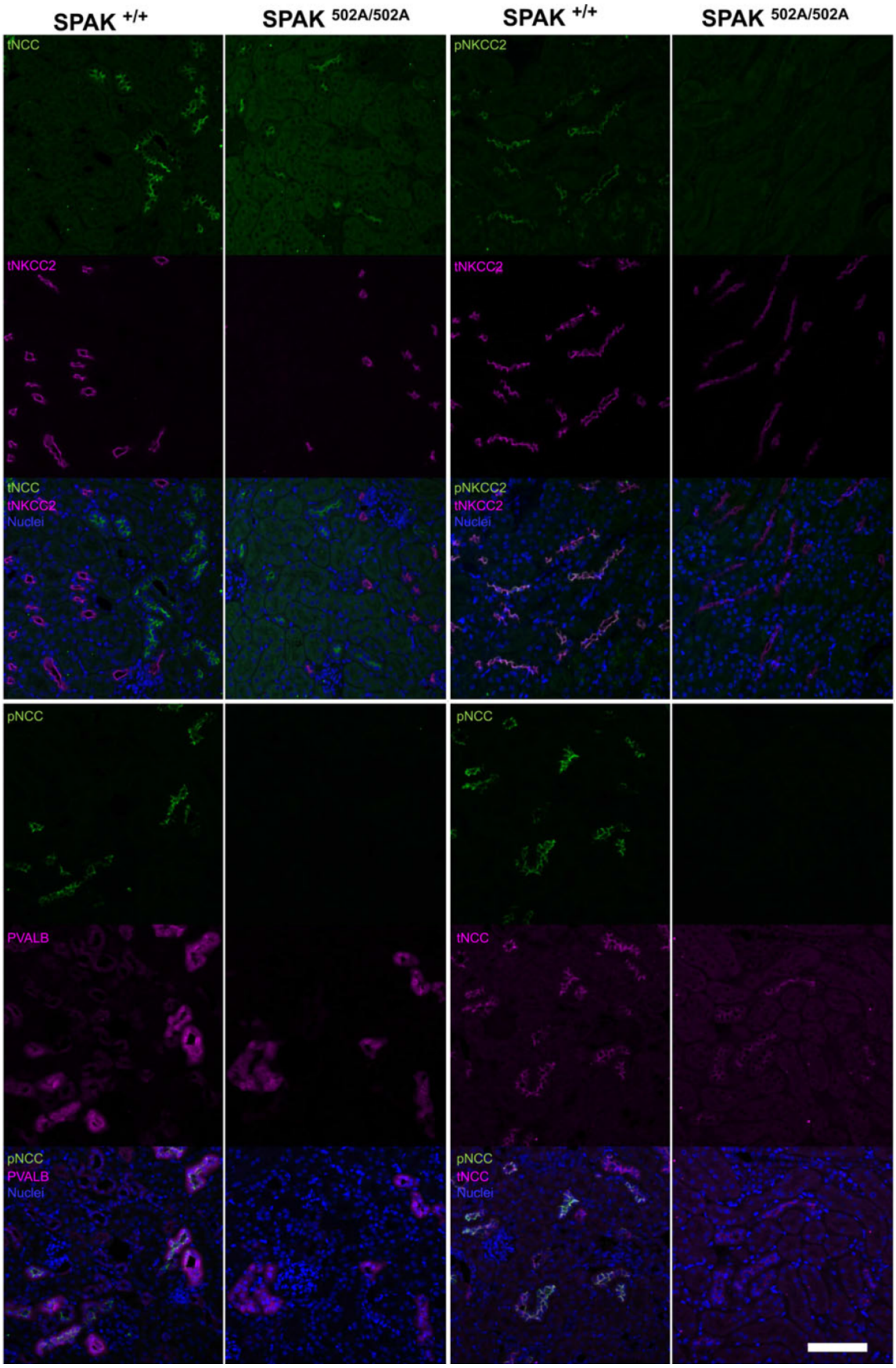

Figure 5.6: Immunolocalisation of NCC and NKCC2 in the renal tubules of SPAK$^{L502A/L502A}$ mice.

Representative pseudocoloured average intensity z projections of immunofluorescent-stained kidney sections (n = 4 per genotype) showing the distribution of total and phospho proteins in the TAL marked by total NKCC2 (tNKCC2), early distal convoluted tubule (DCT1) marked by parvalbumin (PVALB) and whole distal convoluted tubule (DCT1/2) marked by total NCC (tNCC). Phospho-NCC T46 (pNCC) and phospho-NKCC2 S91 (pNKCC2) are virtually undetectable in the SPAKL$^{502A/L502A}$ mice. Scale bar = 100 µm. [Taken from (Zhang *et al.*, 2015)].

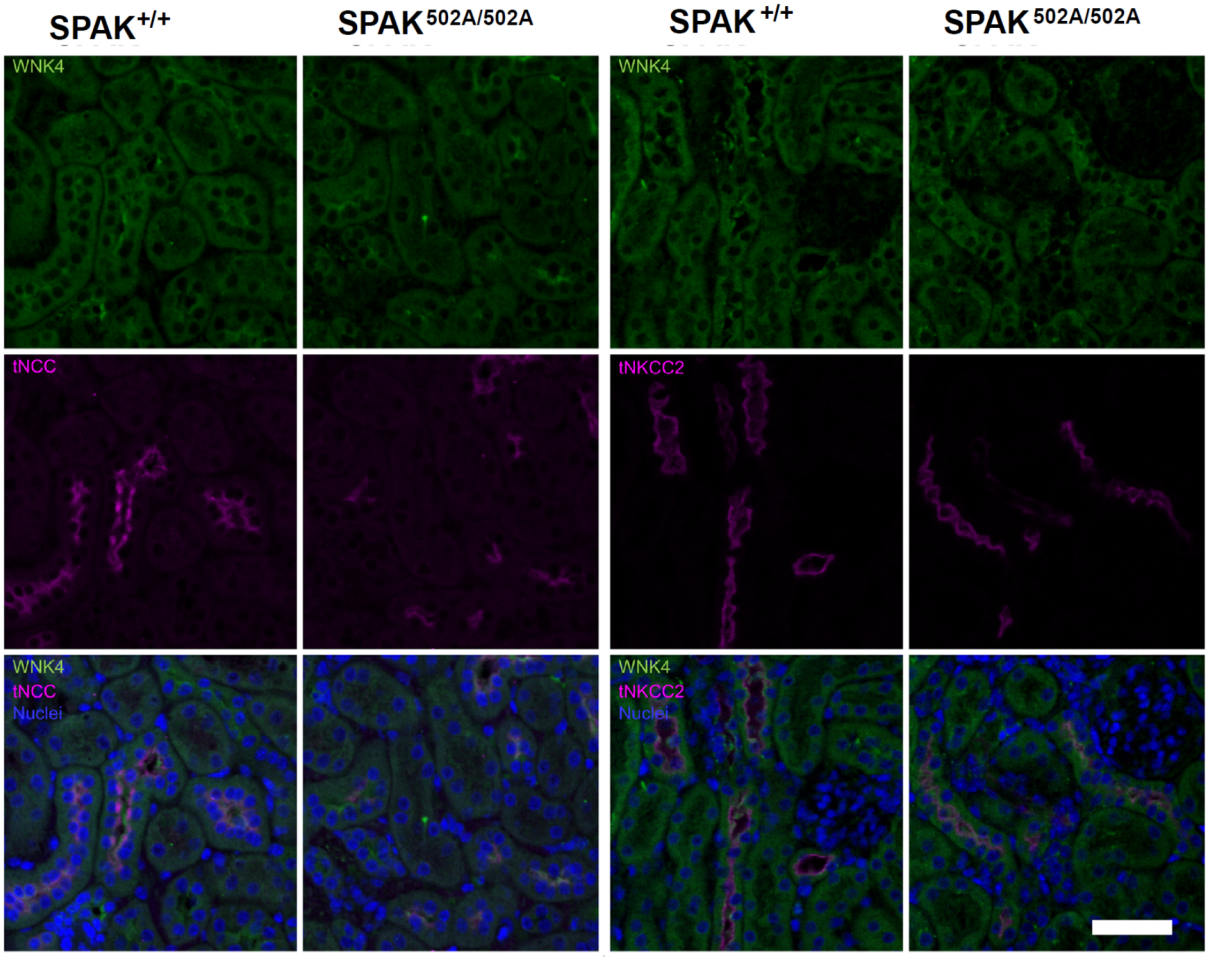

Figure 5.7: Immunolocalisation of WNK4 in the renal tubules of SPAK$^{L502A/L502A}$ mice.

Immunolocalisation of WNK4 appears unaltered between groups in the DCT marked by tNCC and TAL marked by NKCC2 (n=4 per genotype. Scale bar = 50µm). [Taken from (Zhang *et al.*, 2015)].

5.3.5 SPAKL$^{502A/L502A}$ mice display reduced blood pressure and augmentation index.

To study the cardiovascular phenotype of these mice, the arterial blood pressure (BP) was measured in the SPAK$^{L502A/L502A}$ knock-in animals by carotid artery cannulation under general anaesthesia, which showed that their systolic, diastolic and mean arterial BPs were ~20mmHg

lower than wild type littermates (Figure 5.8 A). *In vivo* dose-response to phenylephrine, suggested that vascular tone may be altered, however due to scatter in the data this did not reach statistical significance (Figure 5.8 B). Although, the lower BP of the SPAKL502A/L502A knock-in animals was also reflected in a significantly lower left ventricular mass in these animals (Figure 5.8 C).

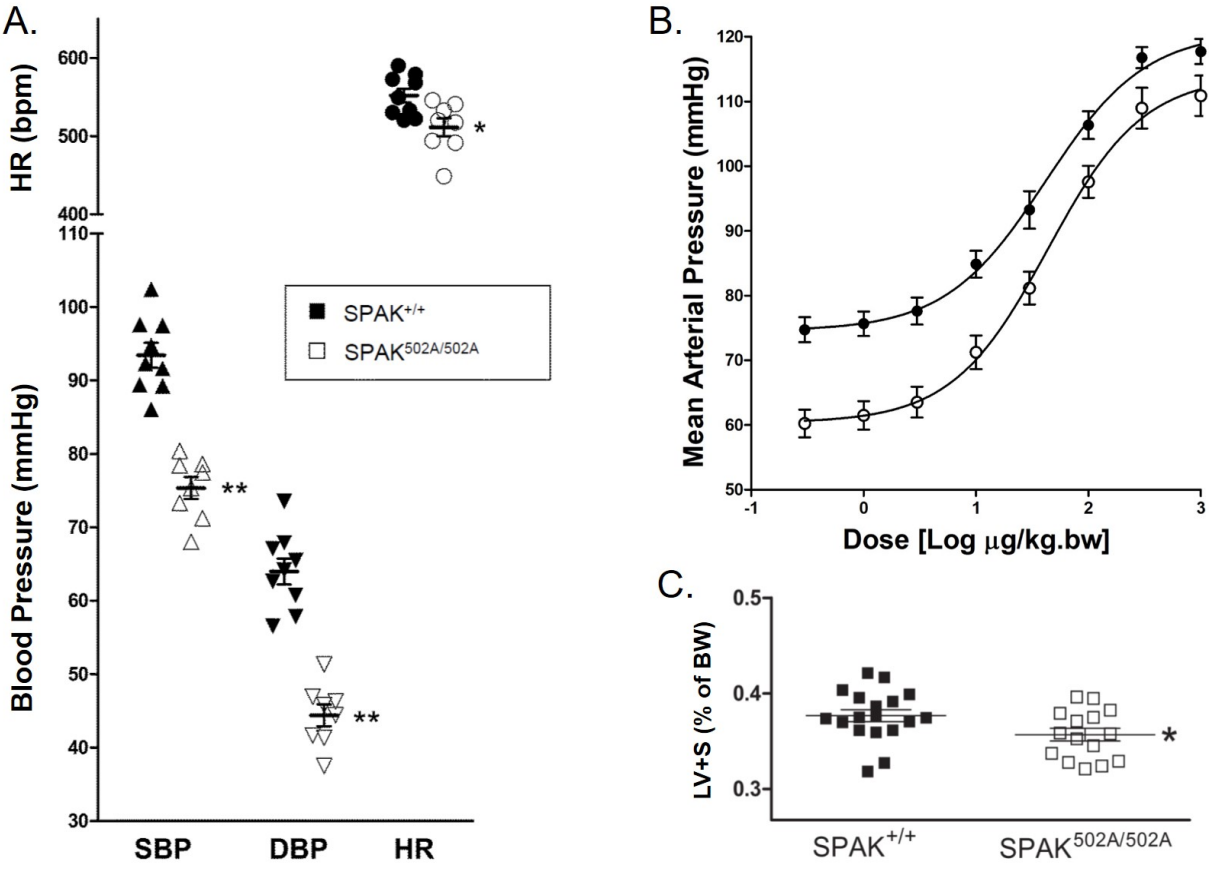

Figure 5.8: Blood pressure, vasopressor response and cardiac ventricular mass of SPAK$^{L502A/L502A}$ mice.

[A] SPAK$^{L502A/L502A}$ have significantly lower systemic systolic blood pressure (SBP), diastolic blood pressure (DBP), and heart rate (HR) compared to wildtypes. **[B]** For *in vivo* phenylephrine dose–responses, no significant differences between SPAK$^{L502A/L502A}$ versus SPAK$^{+/+}$ mice were detected for the estimated dose producing half-maximal response (ED_{50}) (45.6 ± 3.7 vs 45.6 ± 6.3 μg/kg.bw) (P = 0.9964) and fitted maximum response (E_{max}) (114.4 ± 3.7 vs 121.3 ± 2.7 mmHg) (P = 0.1552). Two-tailed unpaired Student's t-test; data are mean ± SEM, n = 9 per genotype **[C]** The wet weights of the left ventricle and septum combined (LV+S) expressed as a % of bodyweight (BW) are significantly lower for SPAK$^{L502A/L502A}$ mice. Bars are mean ± SEM, n=14-16. * P<0.05; ** P<0.01. [Adapted from (Zhang *et al.*, 2015)].

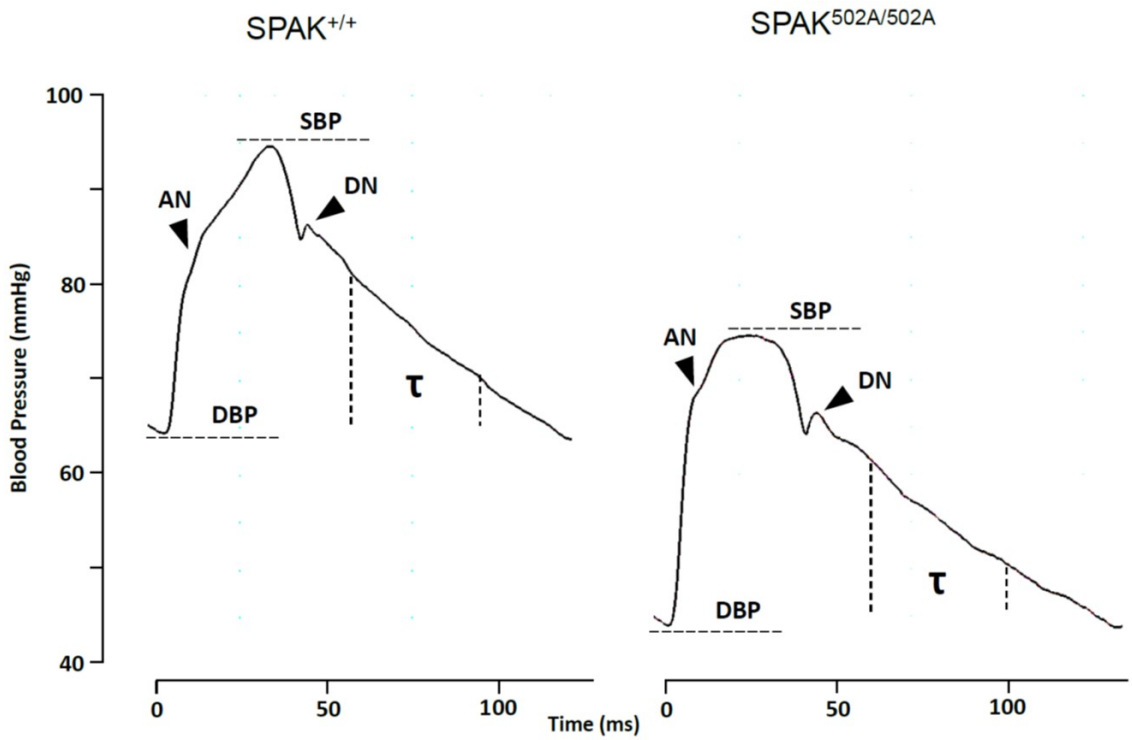

Parameter	+/+	502A/502A	Parameter	+/+	502A/502A
MAP (mmHg)	73.7 (± 1.8)	54.0 (± 1.6) **	PP (mmHg)	29.5 (± 0.5)	31.0 (± 0.6)
DNP (mmHg)	82.6 (± 1.9)	62.9 (± 1.5) **	AP (mmHg)	10.4 (± 0.7)	6.6 (± 0.3) **
$\tau_{bourgeois}$ (s)	0.56 (±0.02)	0.44 (±0.01) **	AIx (%)	35.0 (± 2.1)	21.1 (± 1.0) **

Figure 5.9: Arterial pressure waveform analysis of SPAK$^{L502A/L502A}$ mice.

Pulse waveform analysis reveals no change in pulse pressure (PP) [SBP–DBP] but does show decreased augmentation pressure (AP) [SBP–anacrotic notch (AN) pressure], dicrotic notch (DN) pressure and MAP [1/3 SBP + 2/3 DBP] in the SPAKL$^{502A/L502A}$ versus SPAK$^{+/+}$. This hypotensive phenotype is in part owing to changes in vascular contractility in SPAKL$^{502A/L502A}$ mice as evidenced by their lower augmentation index (AIx) [AP/PP], a marker of arterial stiffness, and is further supported by a decrease in their diastolic pressure decay time constant ($\tau_{bourgeois}$) [1/slope of diastolic pressure decay; measured 30 ms after DN and 20 ms before end DBP], a surrogate marker of decreased vascular resistance. Bars are mean ± SEM, n= 8–9. Significant differences from the SPAK wild type are shown by: *P < 0.02, **P < 0.001. [Taken from (Zhang *et al.*, 2015)].

Further analysis of the BP traces from the mice also showed that the shape of the arterial pressure wave was significantly different (Figure 5.9). The SPAK$^{L502A/L502A}$ knock-in animals have a lower diastolic pressure time decay constant ($\tau_{bourgeois}$), an index of vascular resistance (Bourgeois *et al.*, 1974), suggesting decreased vascular tone compared to wild type littermates (Figure 5.9). Specifically, the SPAK$^{L502A/L502A}$ knock-in animals had lower augmentation of the peak systolic pressure (AIx) with no change in pulse pressure consistent with a reduction in arterial stiffness (Figure 5.9) (Safar, 2001).

5.3.6 SPAK$^{L502A/L502A}$ mice show a Gitelman Syndrome pattern of plasma and urinary electrolytes and salt-wasting

Analysis of the plasma electrolytes showed that the SPAK$^{L502A/L502A}$ mice had a typical Gitelman pattern of plasma electrolytes with hypokalaemia and mild hypomagnesaemia compared to the wild-type animals (Figure 5.10 A). This is consistent with reduced WNK pathway signalling caused by inactivation of the SPAK CCT domain. The urinary electrolytes also showed a Gitelman-like pattern of electrolytes with marked hypocalciuria compared to the wild-type mice (Figure 5.10 B). The salt wasting expected of a Gitelman-like phenotype was also confirmed by salt restricting the SPAKL$^{502A/L502A}$ knock-in animals after salt loading by switching to a 100-fold lower Na-diet (Figure 5.10 C).

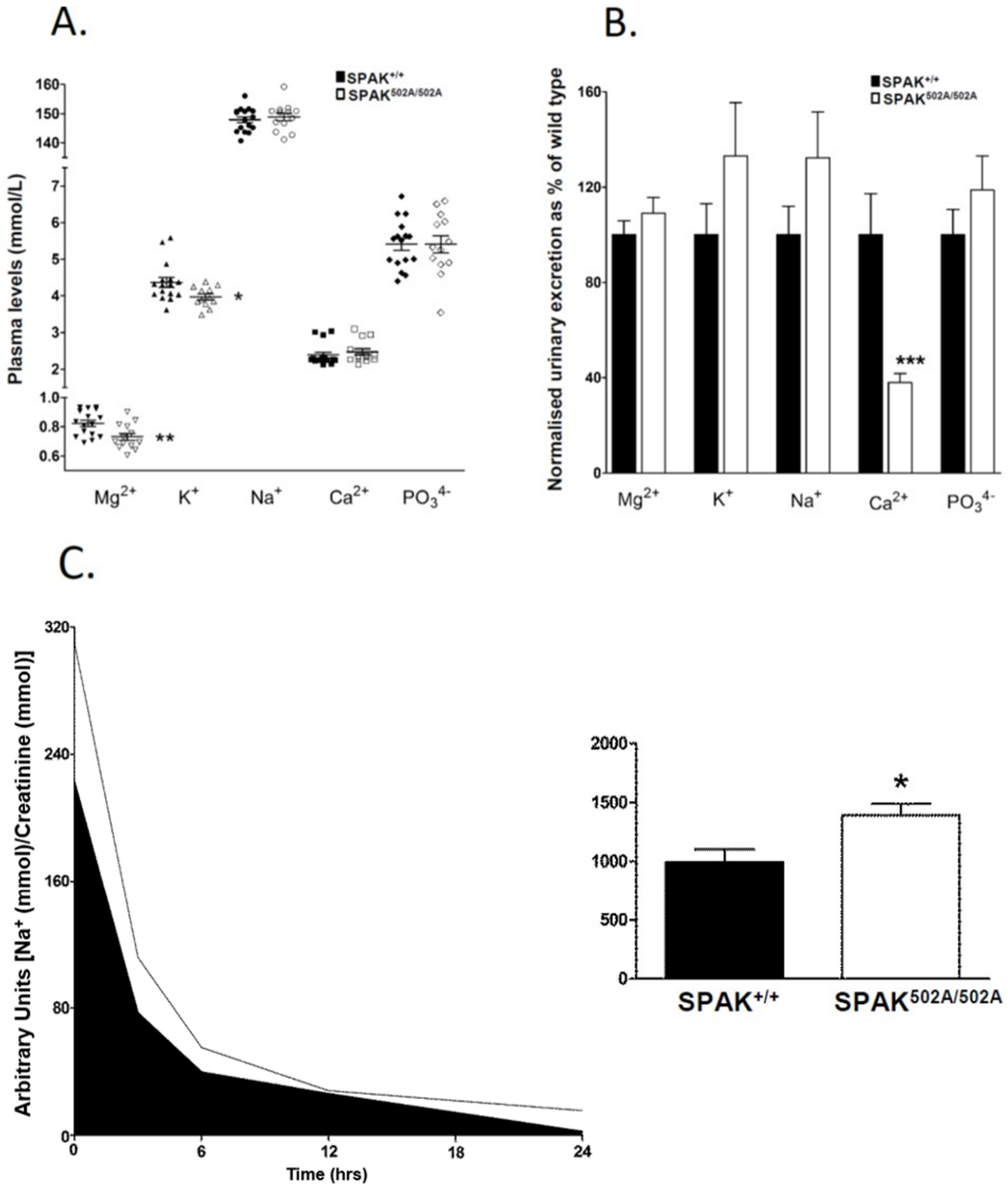

Figure 5.10: Plasma and urine electrolyte levels of SPAK$^{L502A/L502A}$ mice.

[A] Plasma electrolytes analysis shows SPAK$^{L502A/L502A}$ mice have hypokalaemia and hypomagnesaemia (n= 12–16 per genotype per electrolyte) and **[B]** creatinine normalised urinary electrolyte analysis reveals SPAK$^{L502A/L502A}$ mice have hypocalciuria (n = 16–18 per genotype per electrolyte). **[C, left]** Urinary Na^+ excretion expressed as Na^+ (mmol)/creatinine (mmol) at various time points after switching from a 3% w/w to a 0.03% w/w salt diet. **[C, right]** area under the curve (AUC) analysis demonstrates that SPAK$^{L502A/L502A}$ mice are sodium wasting in the face of adaptation to physiological extremes (n = 16 per genotype). Bars are mean ± SEM. Significant differences from the SPAK wild type are shown by: *P < 0.02, **P < 0.01, ***P < 0.005. [Adapted from (Zhang *et al.*, 2015)].

5.3.7 STK39$^{-/-}$ Gitelman syndrome mouse model has altered body composition

Stk39$^{tm1a(EUCOMM)Wtsi}$ SPAK homozygous knock-out (STK39$^{-/-}$) mice on a normal diet present with increased bone mineral density (BMD) which is consistent with reports of increased BMD in Gitelman patients and mouse models (Table 5.2) (Nicolet-Barousse *et al.*, 2005; Pathare *et al.*, 2012; Hsu *et al.*, 2015), which is primarily due to hypocalciuria that was also observed in the SPAK$^{L502A/L502A}$ mice (Figure 5.10 B). Interestingly, STK39$^{-/-}$ mice also have decreased fat mass with no changes in lean mass, which leads to a lower bodyweight in age-matched female STK39$^{-/-}$ but not male mice on a normal diet (Table 5.2). The difference in male bodyweight did not likely reach significance due to the larger magnitude of difference in BMD in males versus females, which may offset the decreased fat mass.

Parameter	STK39$^{+/+}$		STK39$^{-/-}$		P-value
♂ Bodyweight (g)	38.50 ± 0.13	(n=644)	36.50 ± 1.66	(n=7)	0.1144
♀ Bodyweight (g)	32.52 ± 0.13	(n=613)	28.71 ± 1.24	(n=7)	**0.0026
♂ BMD (g/cm^2)	0.0493 ± 0.0001	(n=634)	0.0528 ± 0.0007	(n=7)	***0.0004
♀ BMD (g/cm^2)	0.0495 ± 0.0000	(n=604)	0.0506 ± 0.0011	(n=7)	*0.0116
♂ Fat mass (g)	17.17 ± 0.10	(n=635)	14.25 ± 1.44	(n=7)	**0.0031
♀ Fat mass (g)	14.13 ± 0.12	(n=603)	11.52 ± 1.03	(n=7)	*0.0161
♂ Lean mass (mg)	21.80 ± 0.07	(n=635)	22.52 ± 0.68	(n=7)	0.3096
♀ Lean mass (mg)	18.71 ± 0.05	(n=603)	17.80 ± 0.34	(n=7)	0.0524

Table 5.2: Body composition analysis.

DEXA scans for bone mineral density (BMD) and body composition were performed at age 14 weeks. Stk39$^{tm1a(EUCOMM)Wtsi}$ homozygous knock-out (STK39$^{-/-}$) mice have increased bone mineral density (BMD) and lower fat mass compared to wildtypes (STK39$^{+/+}$) with no change in lean mass, although only females have a significant difference in bodyweight. *(P<0.05), **(P<0.01), **(P<0.001). Data from IMPC [http://www.mousephenotype.org/data/genes/MGI:1858416] and copyright © 2016 IMPC.

5.4 Discussion

Our results define the importance that the CCT docking domain plays in regulating the ability of WNK isoforms to control the activation as well as function of SPAK in regulating NCC/NKCC2 ion cotransporters and hence blood pressure. Most importantly these findings establish that a single point mutation ablating the ability of the CCT domain to interact with RFxI motifs on its WNK activators or ion cotransporters substrates, is sufficient to markedly

reduce phosphorylation and levels of NCC/NKCC2 resulting in a ~20mmHg reduction in blood pressure. Strikingly, impact of the CCT domain mutation is similar to that observed previously by ablating SPAK kinase activity in $SPAK^{T243A/T243A}$ knock-in mice (Rafiqi *et al.*, 2010) or by complete knock-out of SPAK protein in mice (Yang *et al.*, 2010*c*; Mccormick *et al.*, 2011; Grimm *et al.*, 2012), and recent work suggests that inhibition of SPAK activity can even attenuate angiotensin II-induced hypertension (Cervantes-Perez *et al.*, 2018). The $SPAKL^{502A/L502A}$ animals still possess OSR1, which is activated normally by WNK isoforms (Figure 5.2 D), emphasising that inhibiting SPAK without effecting OSR1 is sufficient to markedly lower blood pressure. This is consistent with previous analysis indicating that SPAK in mammals evolved as a result of a gene duplication of OSR1, to undertake more specialised roles such as control of NCC/NKCC2 in the kidney and regulation of blood pressure (Delpire & Gagnon, 2008).

Intriguingly, in the $SPAK^{L502A/L502A}$ knock-in animals in addition to a reduced phosphorylation of NCC/NKCC2, had levels of NCC and NKCC2 protein that were significantly reduced (Figure 5.4), under conditions which mRNA levels were unaffected (Figure 5.5). Similar results were also observed when analysing catalytically inactive SPAK knock-in mice (Rafiqi *et al.*, 2010). In converse, in mouse models in which the WNK signalling pathway is activated by introducing knock-in mutations that inhibit the ubiquitylation of and proteasomal degradation of WNK4 (i.e. WNK4 [D561A] knock-in mice (Yang *et al.*, 2007*a*; Chiga *et al.*, 2011) or KLHL3[R528H] knock-in mice (Susa *et al.*, 2014)), NCC and NKCC2 protein levels are markedly elevated. Taken together these results provide strong genetic evidence that phosphorylation of NCC/NKCC2 by SPAK in addition to regulating cotransporter activity; also promote the stability of these critical cotransporters. Further work is required to unravel the mechanism, by which NCC and NKCC2 expression is controlled by SPAK phosphorylation.

The plasma and urinary electrolyte pattern of the $SPAK^{L502A/L502A}$ knock-in mice resembles Gitelman Syndrome. In fact, it recapitulates closely the phenotype of the previously reported $SPAK^{T243A/T243A}$ kinase-dead knock-in mouse (Rafiqi *et al.*, 2010). The extensive loss of NKCC2 and phospho-NKCC2 from the TAL tubules could be expected to produce a more extensive or even Bartter-like Syndrome (Kemter *et al.*, 2010). Levels of NKCC2 were also reduced in the kinase-dead SPAK knock-in mouse, but the reduction was modest in comparison to almost complete loss of phosphorylated NKCC2 from the $SPAK^{L502A/L502A}$ mouse kidney (Figure 5.4; Figure 5.6). Nevertheless, the presence of both hypocalciuria and

hypomagnesaemia in the SPAK$^{L502A/L502A}$ mice is in keeping with a predominant loss of NCC function, since the loss of NKCC2 function in the mouse is associated with the opposite phenotype of hypermagnesaemia and hypercalciuria (Kemter *et al.*, 2010). In fact, plasma magnesium levels and urinary calcium excretion are clinical measures used routinely to distinguish between Gitelman and the related Bartter syndrome (Knoers *et al.*, 2003). The finding that the total level and phosphorylation of NKCC2 is reduced in the kidneys of the SPAK$^{L502A/L502A}$ mouse is also notable because previous SPAK knock-out models reported hypophosphorylated NCC in the DCT, but markedly hyperphosphorylated NKCC2 in the TAL with increases in total NKCC2 levels (Yang *et al.*, 2010*c*) or without a change in total NKCC2 levels (Mccormick *et al.*, 2011; Grimm *et al.*, 2012). The authors suggested this was due to removal of inhibitory isoforms of SPAK (SPAK2 and KS-SPAK), which are a product of alternative splice variants and enzymatic cleavage (Koumangoye & Delpire, 2017), and assumed to compete with full-length SPAK/OSR1 in the TAL to prevent overactivation of NKCC2 (Park *et al.*, 2013). Alternatively, as yet unidentified kinases may act to phosphorylate SPAK/OSR1-dependent sites as a compensatory mechanism (Ferdaus *et al.*, 2016). Another intriguing finding in these models was that the hypophosphorylation of NCC was accompanied by physical reduction in numbers of DCT1 tubular segments. In particular, the Welling group found that mice expressing a constitutively active form of SPAK$^{T243E/S383D}$ (CA-SPAK) restricted to the DCT1 on a background of global SPAK knock-out was sufficient to reproduce the salient PHAII electrolyte abnormalities. When these mice were treated with thiazides the subsequent restoration of sodium was not immediately followed by potassium excretion and instead took 2-3 days. On closer inspection they found CA-SPAK mice to have remodelling of the aldosterone-sensitive distal nephron, specifically and increase in DCT1 and decrease in connecting tubule (CNT) masses (Grimm *et al.*, 2017). Conversely, other studies with mouse models of NCC genetic ablation (Loffing *et al.*, 2004), knock-out of the DCT1 specific calcium binding protein, parvalbumin (Belge *et al.*, 2007), and SPAK knock-outs have shown atrophy of the DCT1 with CNT hypertrophy and CCD remodelling, partially attributed to increased α-ketoglutarate paracrine signalling (Grimm *et al.*, 2015, 2017; Mccormick & Ellison, 2017; Lazo-Fernandez *et al.*, 2018). SPAK has been reported to be directly involved with stabilisation of OSR1 at the apical membrane in the DCT and SPAK knock-out results in a significant reduction of parvalbumin expression (Grimm *et al.*, 2012). However, unlike the knock-out models used in these studies the SPAK scaffolding functions in all tubular segments remained intact in the point-mutant knock-in SPAK$^{L502A/L502A}$ and SPAK$^{T243A/T243A}$ mice. This may explain why no changes were observed in the levels or staining of parvalbumin (Figure 5.4 A;

Figure 5.6) or gross changes in DCT morphology. It is therefore, possible to postulate that these remodelling phenomena may largely be due to loss of key components of regulatory pathways which maintain normal tubular structure, rather than simply due to changes in NCC activity.

The altered shape of the arterial pressure waveform in the $SPAK^{L502A/L502A}$ mice (Figure 5.9) is consistent with increased vascular compliance and reduced wave reflection in the periphery as compared to the wild type animals. Although this may be explained in part by a diminished cardiac output arising from possible reductions in cardiac contractility due to loss of NKCC1 activity in the heart (Prasad *et al.*, 2008) (Figure 5.2 B) and the lower heart rates of the $SPAK^{L502A/L502A}$ mice (Figure 5.8 A), since augmentation is negatively correlated with heart rate in humans (Crilly, 2014). It has also been previously shown that intracranial administration of bumetanide can be used to inhibit the over activity of NKCC1 in the hypothalamic paraventricular nucleus of spontaneously hypertensive rats. The inhibition of NKCC1 in these hypertensive animals acts to reduce sympathetic vasomotor tone and lower their heart rates (Ye *et al.*, 2012). A similar phenomenon may be occurring in the $SPAK^{L502A/L502A}$ mice due to reductions in brain phospho-NKCC1 (Figure 5.2), thus providing a potential neurological explanation for their lower heart rate and reduced vascular tone.

However, SPAK directly affects vascular smooth muscle contraction through WNK1 (Bergaya *et al.*, 2011) and WNK3 (Zeniya *et al.*, 2013) signalling and NKCC1 (Yang *et al.*, 2010*c*), the activity of which is necessary for maintaining vascular smooth muscle tone (Meyer *et al.*, 2002), so it is likely that reduced augmentation also reflects hypophosphorylation of NKCC1 in blood vessels in a parallel fashion to ther findings in the kidney and other tissues (Figure 5.2; Figure 5.4). This is further supported by the shorter $\tau_{bourgeois}$ found in $SPAK^{L502A/L502A}$ mice, which implies reduced vascular resistance consistent with a reduction in vascular contractility. This suggests that targeting the CCT domain of SPAK may have an additional effect on blood pressure through a direct reduction in vascular tone. It also suggests a reduced arterial stiffness without a change in pulse pressure (Figure 5.9), and both are importantly independent risk factors for cardiovascular mortality (Safar, 2001).

There is increasing interest in targeting the WNK-SPAK/OSR1 signalling pathway as a new therapeutic strategy to treat hypertension (Glover & O'Shaughnessy, 2011; Alessi *et al.*, 2014). The finding that ablation of the CCT domain function is sufficient to reduce blood pressure to the same extent as a kinase ablating knock-in mutation (Rafiqi *et al.*, 2010),

suggests that the CCT domain of SPAK plays a similarly important role as the kinase domain in controlling blood pressure. Thus inhibitors that prevent the CCT domain recognising RFxV motifs should be as effective as compounds that target the protein kinase domain of SPAK in lowering blood pressure. Structural analysis reveals that CCT domain recognises RFxV/I motifs by adopting a unique fold not observed on other proteins (Villa *et al.*, 2007). This may indicate that CCT domain inhibitors might be inherently more specific than ATP competitive kinase inhibitors that would have the potential to target other protein kinases and/or ATP binding enzymes. For the treatment of a chronic largely asymptomatic condition such as hypertension, it is particularly important that therapies are as specific as possible in order to reduce poorly tolerated off-target side effects. Although, owing to the high degree of homology between the CCT domain of SPAK and OSR1 it may be impossible to develop drugs that selectively inhibit SPAK. However, even a drug that partially inhibited both SPAK and OSR1 isoforms might reduce phosphorylation and expression of NCC and NKCC1/2 enough to lower blood pressure without significant adverse effects.

On the other hand, not all off-target effects are undesirable. Chronic thiazide users and Gitelman syndrome patients are noted to have increased bone mineral density (BMD) which results in a reduced rate of fractures, primarily attributed to hypocalciuria (Aung & Htay, 2011; Santos *et al.*, 2016); an electrolyte abnormality that was also observed in $SPAK^{L502A/L502A}$ mice. This strongly suggests that like $STK39^{-/-}$ (Table 5.2) and $SPAK^{T243A/T243A}$ mice (Pathare *et al.*, 2012), disruptors of SPAK binding would also increase BMD, making them particularly attractive for treating hypertension in elderly or osteoporotic patients. However, Gitelman syndrome is also known to be associated with poorer glucose homeostasis and insulin responsiveness (Ren *et al.*, 2013; Yuan *et al.*, 2017), while chronic thiazide users have a well-documented higher risk of new-onset diabetes mellitus (Agarwal, 2008). Yet, surprisingly no reports of mice deficient in SPAK activity have ever reported glucose or insulin homeostatic abnormalities. Recently, some exciting new work from the Gamba group on $SPAK^{T243A/T243A}$ mice has shed some light on this discrepancy between SPAK Gitelman syndrome-like animal models and thiazide users/Gitelman syndrome patients. They demonstrated that inhibition of SPAK activity actually led to greatly improved whole body glucose tolerance and insulin sensitivity compared to wildtypes on both control and high-fat diets, specifically showing that these animals were capable of increasing insulin-dependent AKT phosphorylation in the liver and skeletal muscles (Torre-Villalvazo *et al.*, 2017). Another astounding finding of their study was that $SPAK^{T243A/T243A}$ mice fed a high-fat diet had lower circulating levels of cholesterol,

triglycerides and leptin, in addition to being resistant to obesity due to higher energy expenditure by brown adipose tissue and mitochondrial activity in skeletal muscle which prevented white adipocyte hypertrophy (Torre-Villalvazo *et al.*, 2017). Interestingly, a higher degree of epigenetic silencing of STK39 through DNA methylation has been associated with increasing body mass index in humans (Wilson *et al.*, 2017), which was also supported by the discovery of reduced fat mass without a change in lean mass in $STK39^{-/-}$ mice at baseline (Table 5.2). If these findings can be replicated in $SPAK^{T243A/T243A}$ mice, it could have profound implications for the treatment of metabolic syndrome and obesity-related disorders.

In conclusion, these results establish that the SPAK CCT domain plays a major role in regulating blood pressure. These data suggest that the SPAK CCT domain regulates blood pressure via SPAK activation by WNK isoforms that in turn enhance both activity and expression of the renal sodium cotransporters NCC and NKCC2 with potential concomitant effects on NKCC1 in the nervous and cardiovascular systems. The hypotensive phenotype of the $SPAK^{L502A/L502A}$ mice, validate the CCT domain as a promising new target for future anti-hypertensive agents, while $SPAK^{T243A/T243A}$ and SPAK KO mice suggest CCT binding disruptors may also have the added benefit of increasing BMD, insulin sensitivity and obesity resistance, potentially representing a long-awaited panacea for metabolic syndrome. Importantly, the lack of an overt phenotype in these mice also indicates that CCT domain inhibitors may be well tolerated. Thus far a CCT domain inhibitor termed STOCK 1S-50699 has been reported that has an IC_{50} of ~ 3 μM, that is capable of inhibiting WNK-SPAK phosphorylation of NKCC1 and NCC in mammalian cell lines (Mori *et al.*, 2013*a*; de Los Heros *et al.*, 2014). STOCK 1S-50699 is highly hydrophobic, displays poor solubility and cannot be used in animal models, but the data obtained so far provides evidence that the development of CCT domain inhibitors is feasible.

Chapter 6 : Conclusions

6.1 Monogenic diseases in drug target identification and validation

The cloning and characterisation of NCC and WNKs occurred in 1990's (Gamba *et al.*, 1993, 1994; Mastroianni *et al.*, 1996) and 2000's (Xu *et al.*, 2000; Veríssimo & Jordan, 2001; Nakamichi *et al.*, 2002), respectively, but it was the study of the monogenic diseases, FHHt and Gitelman syndrome, a few years later that provided the first genetic confirmation that these genes are major players in blood pressure control (Simon *et al.*, 1996; Lemmink *et al.*, 1998; Wilson *et al.*, 2001; Achard *et al.*, 2003). Effectively serving as nature's knock-out experiments, their intense study and modelling over the past two decades have revealed the existence of an evolutionarily ancient pathway compromised of opposing phosphorylation and ubiquitylation cascades to control ion fluxes and regulate cell volume, and later the electrolyte and blood pressure homeostasis of more complex lifeforms (Choe & Strange, 2007).

With this in mind, the study set out to investigate the most severe form of FHHt (PHA2E) to probe the physiological extremes of WNK pathway perturbation, in the hopes of developing new anti-hypertensive strategies. This led to discovery that there may be non-renal contributions to the FHHt phenotype, further highlighting the importance of WNKs for blood pressure regulation and finally confirming increased WNK abundance to be the common endpoint for FHHt-causing mutations. While thiazides and dietary salt restriction appears to alleviate the symptoms of FHHt, our findings imply that current treatment strategies inadequately address the abnormal vascular activity that underlies the arterial stiffness in these patients, which if left untreated could increase a plethora of cardiovascular and cognitive risk factors despite blood pressure and electrolyte normalisation (Liao & Farmer, 2014; Acampa *et al.*, 2017; Tanaka *et al.*, 2017).

Spurred on by this, the next step was to begin looking for ways to inhibit the WNK pathway-dependent activation of CCCs as means to lower blood pressure. As MO25 can activate SPAK/OSR1 independent of WNKs (Gagnon *et al.*, 2011; Filippi *et al.*, 2011; Ponce-Coria *et al.*, 2012; Li *et al.*, 2014) and MO25 can complex with WNKs to activate CCCs in a SPAK/OSR1-independent manner (Ponce-Coria *et al.*, 2014; Bhuiyan *et al.*, 2016), the first approach was to try knock-out of MO25 isoforms to investigate their potential as druggable targets. However, to our disappointment complete knock-out of MO25α proved embryonically

lethal and MO25β knock-outs did not present with a blood pressure phenotype. In hindsight, the embryonic lethality of MO25α homozygous knock-outs might have been anticipated, as the evolutionarily conserved gene was originally discovered in the cleavage stages of mouse embryos (Miyamoto *et al.*, 1993; Nozaki *et al.*, 1996). For this reason our work with constitutive MO25 knock-outs does not completely preclude MO25α as viable drug target in adults, and a more elegant study design would seek to create an animal model with inducible knock-out or knockdown of MO25α to better assess its potential.

In light of this stumbling block, it was logical to target areas of the WNK pathway that might result in fewer off-target effects. So far, study of SPAK-KO and $SPAK^{T243A/T243A}$ Gitelman-like mouse models suggests that SPAK would make for an attractive drug target with a reduced profile of adverse side-effects (Rafiqi *et al.*, 2010; Yang *et al.*, 2010*c*; Mccormick *et al.*, 2011; Grimm *et al.*, 2012). However, drug-induced knockdown of SPAK proteins, direct antagonism of its kinase domain, or SPAK-activating phosphorylation and ATP site blockade seemed impractical approaches and with unacceptable potential for non-specific activity directed towards other kinases. Consequently, disruption of SPAK binding to its regulators and substrates was investigated as an alternative approach, and given the highly conserved nature of this binding mechanism it was predicted to have a higher probability of being specific to the WNK pathway. To our delight, this approach proved successful and suggests this it is the most viable strategy for targeting WNK-SPAK-CCC signalling. Therefore, SPAK binding disruptors would serve as a new class of anti-hypertensives that simultaneously act on the kidneys, heart, blood vessels and sympathetic nervous system to lower blood pressure, effectively duplicating the combined actions of diuretics, vasodilators, ionotropes and chronotropes in a monotherapy without their adverse effects. Another exciting aspect of these novel anti-hypertensives would be their implications for the treatment of co-morbidities such as obesity, diabetes type 2 and osteoporosis, representing a potential silver bullet for metabolic syndrome.

6.2 Drug discovery and development of WNK pathway based therapeutics

Almost a decade ago, the first compounds with activity towards the WNK pathways were identified. Using an novel screening assay the Alessi group had submitted for patent, revealed Hypericin, an extract of Saint John's wort, to have an IC_{50} of 1.5 μM at 20 μM ATP for inhibition of OSR1 phosphorylation by WNK1 (Alessi & Vitari, 2006). Using a similar assay,

the Sode group screened a commercially available library of 86 kinase inhibitors and identified the following compounds to have IC_{50} values ranging from 1.9-32 μM at 25 μM ATP for inhibition of OSR1 phosphorylation by WNK1: Staurosporine (PKA, PKG, CaMK, tyrosine kinases, and phosphorylase kinase inhibitor), Tyrophostin 47 (EGF receptor kinase inhibitor), PP1 (Hck, Lck and Src inhibitor), PP2 (Hck, Lck and Src inhibitor) (Yagi *et al.*, 2009). However, all of these appeared to rely on ATP-competitive kinase inhibition and were by their very nature of discovery non-specific for the WNK pathways and not pursued further. It is only within the last 5 years that new agents have been discovered or developed with relatively specific activity for the WNK pathway, which are detailed in the following sections.

6.2.1 WNK kinase inhibition

A classic strategy for targeting WNKs would be to directly inhibit their kinase activity, typically through an ATP-competitive mechanism. A group led by Yamada *et al* at Novartis introduced the first orally bioavailable pan-WNK kinase inhibitor, WNK463, that exploits the unusual structure of the WNK kinase domain to bind the hinge portion of the ATP pocket (Yamada *et al.*, 2016*a*). WNK463 is a low nanomolar binder of both WNK1 and WNK4, regardless of activation state with incredible selectivity for the WNK kinase family. At 10 μM, 2,500-fold higher than the binding K_D for human WNK1/4, WNK463 showed >50% inhibition against 2 out of 442 human kinases tested. When tested in spontaneously hypertensive rats, WNK463 decreased blood pressure in a dose-dependent manner with simultaneous increases in heart rate, urinary volume, sodium and potassium excretion. Similarly, FHHt mice overexpressing WNK1 also had a significant drop in blood pressure after oral administration of WNK463, accompanied by dose-dependent reduction in renal levels of phospho-SPAK/OSR1. Unfortunately as WNK463 acts on a conserved site within the WNK family it functions as a pan-WNK inhibitor, and given the essential roles of WNKs throughout the body, development of it as a therapeutic was discontinued due to an unacceptable preclinical safety profile (Yamada *et al.*, 2016*a*).

Novartis also sought an ATP-noncompetitive means of WNK kinase inhibition. To identify compounds that bind outside of the ATP pocket, they performed screening at high ATP concentrations. This led to the discovery of Compound 2, an allosteric inhibitor with an exquisite specificity for members of the WNK family, and operating with an ATP and substrate noncompetitive mode of inhibition. When tested in HeLa and HT29 cells, Compound 2 was

capable of inhibiting the bumetanide-sensitive NKCC1-mediated rubidium uptake (Yamada *et al.*, 2016*b*). Although potent, the pharmacokinetic profile of compound 2 was inadequate for *in vivo* efficacy testing of this mode of WNK inhibition. To overcome this, several modifications were made to the compound 2 to create compound 11 which had a 150-fold improvement in potency and significantly higher lipophilic efficiency (Yamada *et al.*, 2017). Interestingly, even after modification the new compound still retained the ATP noncompetitive mode of inhibition with few significant off-targets, though curiously it now had a nearly 1,000-fold selectivity for WNK1 vs WNK4. In rat pharmacokinetic studies compound 11 showed moderate clearance but low oral bioavailability and absolute exposure, so another modification was made to create compound 12 which had lower clearance, improved absolute exposure and double the oral bioavailability. Similar to WNK463, compound 12 reduced blood pressure in WNK1 FHHt mice and dose-dependent increases in urinary volume, sodium and potassium excretion in spontaneously hypertensive rats (Yamada *et al.*, 2017). A particularly exciting advantage of allosteric vs ATP-site WNK inhibition, is the ability to achieve selectivity among the WNK family members, this suggests that it might be possible to develop allosteric inhibitors with a high affinity for WNK4 which would be a more useful target for blood pressure control.

6.2.2 SPAK kinase inhibition

The Uchida group has been quite active on the drug discovery front and has developed several screening systems to find novel SPAK inhibitors. Using an ELISA-based system that looks at SPAK-dependent phosphorylation of NKCC2 *in vitro*, STOCK 1S-14279 was found to bind to SPAK and potently inhibit phosphorylation of NKCC2 in an ATP-noncompetitive way (IC_{50} of 0.26 μM). A drug repositioning strategy was then utilised to reveal existing drugs that may also inhibit SPAK activity, and this led to the identification of closantel, an oral antiparasitic agent commonly used in livestock. In mpkDCT and MOVA cells both drugs reduced NCC and NKCC1 phosphorylation, respectively, in a dose-dependent manner. This was replicated in mouse aorta and kidneys, without a change in NKCC2 status following acute *in vivo* administration. Unfortunately, repeated doses of STOCK 1S-14279 proved lethal and it could not be taken forward for further *in vivo* testing, although closantel was confirmed to produce decreases in blood pressure and heart rate (Kikuchi *et al.*, 2015).

Until recently the exact mechanism of inhibition for both STOCK 1S-14279 and closantel have been unclear. New work by the Mehellou group has identified the highly conserved secondary pocket in the C-terminal domain of SPAK/OSR1 as a site of allosteric inhibition of SPAK kinase activity. Modelling shows that the majority of documented SPAK inhibitor agents (STOCK 1S-14279, STOCK 1S-50699, STOCK 2S-26016, closantel and rafoxanide) dock with this secondary pocket, and surprisingly show minimal if any interaction with the primary pocket which is involved in binding to the conserved RFxI/V motif present in WNKs, NKCC1/2 and NCC. Interestingly, STOCK 1S-50699, closantel and rafoxanide were capable of inhibiting constitutively active $OSR1^{T185E}$ *in vitro* but this effect was abolished if the $OSR1^{T185E}$ was truncated and lacking a C-terminal. Additionally, closantel and rafoxanide do not show see changes in either HEK293 phospho-SPAK S373 levels or WNK RFQV motif – endogenous SPAK pulldowns assays but have a decrease in phospho-NKCC1 across a range of doses, suggesting that allosteric binding to the secondary pocket does not affect interactions between WNK-SPAK/OSR1 but rather hinders the capability of SPAK to phosphorylate CCCs (AlAmri *et al.*, 2017).

6.2.3 SPAK binding disruption

An alternative strategy to indirectly inhibit SPAK function is to disrupt its binding to regulators and substrates. Using a newly developed *in vitro* WNK4 RFQV motif and SPAK CCT binding inhibition assay, the Uchida group identified the first agents discovered to have this potential, namely STOCK 1S-50699 and STOCK 2S-26016, which showed clinically relevant IC_{50} values in the micromolar range. In mpkDCT and MOVA cells, these agents were also cable of decreasing phosphorylation of CCCs in a dose dependent fashion (Mori *et al.*, 2013*a*). An intriguing possibility is that these drugs may actually have dual mechanisms of action, in which they bind and inhibit SPAK/OSR1 activation of CCCs via allosteric interaction with the secondary pocket of the CCT, while at higher concentrations inhibiting the interactions with WNKs through the CCT as evidenced by the decreases in phospho-SPAK levels (Mori *et al.*, 2013*a*; Austin *et al.*, 2015; AlAmri *et al.*, 2017).

However, STOCK 1S-50699 and STOCK 2S-26016 do not represent true primary pocket CCT binding inhibitors and due to their hydrophobic nature and poor solubility, they are not suitable for *in vivo* testing. To get around this issue the Uchida group, redeployed its screening assay and discovered viable compound that was subsequently altered to produce

compound 10 and compound 20, which have high potency, low cytotoxicity and increased solubility. These compounds are suspected to be true CCT binding disruptors and their acute testing *in vivo* produced marked dose-dependent decreases in the phosphorylation of SPAK and NCC, with slight but noticeable changes in NKCC1/2 phosphorylation (Ishigami-yuasa *et al.*, 2017).

6.2.4 MO25 binding disruption

A unique strategy adopted by the Mehellou group was to side-step perturbations of WNK-SPAK/OSR1 and instead target the MO25-dependent amplification of SPAK/OSR1 activity. To screen for potential candidates they developed a fluorescent polarisation assay using MO25 and the WEW motif of SPAK/OSR1. Out of a library of ~4,000 compounds they identified one small-molecule inhibitor, HK01, which is capable of inhibiting the activity of $OSR1^{T185E}$ dose-dependent manner. Based on the evidence from the competition experiment for MO25 binding to the SPAK WEW motif peptide by HK01 and subsequent pulldown assay, the authors believe the drug binds directly binds to MO25 to deny access to the SPAK/OSR1 WEW motif to prevent interaction. In HEK293 cells, HK01 inhibits the phospho-NKCC1 response to hypotonic solution, in a dose-dependent manner without changes in phospho-SPAK. Although the authors express their desire to direct efforts towards structural optimisation of HK01 to achieve better binding affinity before moving to animal tests.

6.3 WNKs as signal transducers – a new paradigm

In recent years the field of WNK biology has seen an explosion of interest. Many labs, funding bodies and pharma now recognise that importance of the WNK pathway in blood pressure maintenance and its potential for discovering new drug targets. Importantly, a new body of work has emerged which has caused a paradigm shift in the understanding of the physiological relevance of WNKs, suggesting that they are in fact the long awaited chloride/pressure sensing kinases.

The Goldsmith group identified a chloride binding site within WNK1, that through prevention of autophosphorylation results in inhibition of WNK activity in the presence of high chloride concentrations (Piala *et al.*, 2014). Two key leucine residues (L369/L371) of WNK1,

which are conserved in WNK3 (L295/L297) and WNK4 (L322/L324), were demonstrated to be essential for mediating the inhibitory effects of chloride on WNK autophosphorylation. However, the Ellison group showed that the WNKs are not equally sensitive to chloride. *In vitro* WNK4 is inhibited at the physiological ranges of DCT cell intracellular chloride concentration, with most potent effects between 0-40 mmol/L. While WNK1 was inhibited between 60-150 mmol/L and WNK3 between 100-150mmol/L (Terker *et al.*, 2015*a*). Mutation of these leucines to phenylalanines (i.e. LLFF) blocked chloride binding, but unexpectedly expression in mammalian cells led to differing effects between the WNKs. Phospho-NCC (pNCC) levels in HEK293 cells did not differ between $WNK3^{LLFF}$ and $WNK3^{WT}$, supporting the notion WNK3 is the least chloride sensitive of the WNKs. On the other hand, $WNK1^{LLFF}$ increased pNCC by 140% compared $WNK1^{LLFF}$, confirming the findings of the Goldsmith group (Terker *et al.*, 2015*a*), whereas $WNK4^{LLFF}$ increased pNCC by a dramatic 339% compared to $WNK4^{WT}$, which has led to the interesting proposition by the Goldsmith group that while WNK4 is key chloride sensor, WNK1 and WNK3 may instead be primarily osmotic/hydrostatic pressure sensors, as they can be activated by macromolecular crowding mechanisms and that this regulation is opposed by chloride (Goldsmith *et al.*, 2017).

Previous reports have reported that $WNK4^{WT}$ decreases pNCC when expressed in HEK293 and *Xenopus* oocytes, suggesting that the intracellular chloride concentrations of these cells is greater than the physiological levels found in DCT cells *in vivo* (Terker *et al.*, 2015*a*). This may provide an explanation for a long standing controversy between *in vitro* data which purports a negative regulation of NCC by WNK4 (Golbang *et al.*, 2006; Zhou *et al.*, 2010), and *in vivo* data which suggests that WNK4 is the major WNK positively regulating NCC in the kidney (Takahashi *et al.*, 2014). WNKs are capable of dimerising with one another via a HQ motif in their conserved C-terminal (Thastrup *et al.*, 2012), in particular stimulation of NCC activity by WNK1 was shown to be antagonised by WNK4 and dependent on their interactions via their HQ motif (Chávez-Canales *et al.*, 2014). Although, seeing as $WNK4^{LLFF}$ stimulates and $WNK4^{WT}$ inhibits SPAK-NCC activity in these cells, it suggests that chloride acts as a switch between these two actions, and is dependent on WNK4 kinase activity as evidenced by the fact that inactivation of the WNK^{LLFF} kinase domain returned SPAK-NCC activity to WNK^{WT} levels (Terker *et al.*, 2015*a*). Therefore, at the concentrations of chloride in the DCT *in vivo* WNK4 would be expected to provide tonic activation of NCC through its kinase activity directed at activating SPAK, but should this level rise it would cause WNK4

kinase inactivation whilst simultaneously antagonising WNK1 stimulation of NCC by the formation of heterodimers.

Another major breakthrough by the Ellison group is that DCT cells can sense and respond to changes in serum potassium via alterations in cell voltage, effectively coupling intracellular chloride to extracellular potassium concentration through Kir4.1 (encoded by *KCNJ10*), Kir5.1 (encoded by *KCNJ16*) and CLC-K2 (also known as CLC-Kb, and encoded by *CLCNKB*) voltage-gated channels to modulate WNK activity (Terker *et al.*, 2015*b*), thereby transducing serum potassium levels into changes in electrolyte and blood pressure homeostasis. Not unlike the zona glomerulosa cells of the adrenal glands which release aldosterone, the DCT cells appear capable of responding to changes in serum potassium levels, and thereby dietary potassium intake (Figure 6.1**Error! Reference source not found.**). A particularly noteworthy finding was that a diet deficient in potassium activates NCC, even when coupled with high sodium diet (i.e. a western diet), resulting in salt loading and elevated blood pressure (Terker *et al.*, 2015*b*).

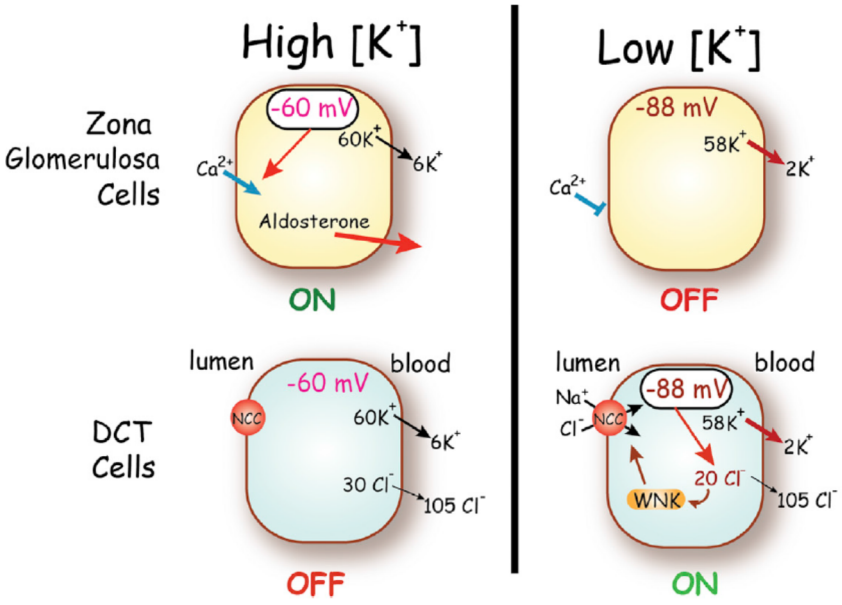

Figure 6.1: Effects of serum potassium concentration on cells of the adrenal and kidney.

Similar changes in membrane voltage due to alterations in extracellular K^+ result in opposite effects on cellular activity/inhibition of the kidneys and adrenal glands. [Taken from (Terker *et al.*, 2015*b*)].

Interestingly, this suggested an explanation for the blood pressure lowering effects of a diet rich in potassium (i.e. DASH diet), and indeed animals fed a high potassium diet had reduced pNCC. Additionally, extracellular potassium concentration was confirmed to be inversely related to the levels of pNCC in *ex vivo* models. Using kidney slices bathe in solutions of varying potassium concentration allowed the assessment of the effects on NCC phosphorylation without hormonal or neural confounding factors, while isolated microperfused tubules were used to verify that the extracellular potassium concentration is detected on the basolateral side of DCT cells (Penton *et al.*, 2016). However, the first holes began to emerge in the Ellison group's model on closer inspection of the effects of high extracellular potassium on NCC dephosphorylation by the Loffing group. The hypothesis states that decreases in extracellular potassium will cause a change in DCT membrane potential to drive chloride out of the cell, thereby lowering intracellular chloride concentration to increase WNK-dependent SPAK and NCC phosphorylation. While this was verified to be the case in *ex vivo* kidney slices under standard conditions of 110 mmol/L of extracellular chloride, the effect was abolished when extracellular chloride was lowered to 5 mmol/L by replacing NaCl with Na gluconate in the buffer solution, suggesting that SPAK-NCC was already at higher level of activation in the 5 mmol/L chloride buffer and that decreasing potassium in this buffer did little to meaningfully lower intracellular chloride to activate them further. In contrast, increasing extracellular potassium in both 110 and 5 mmol/L chloride buffers actually promoted NCC dephosphorylation to a similar degree, surprisingly without any significant change in SPAK phosphorylation from control potassium levels. To confirm this finding the Loffing group also used a chloride channel blocker DID, and found that it too did not prevent NCC dephosphorylation in response to rising extracellular potassium levels, contradictory to the Ellison hypothesis. Given the rapid SPAK-independent nature of dephosphorylation in response to high extracellular potassium, they investigated if this effect might be mediated by protein phosphatases. However, pharmacological inhibition of PP1, PP2A and PP3 had no effect on dephosphorylation of NCC in response to high extracellular potassium (Penton *et al.*, 2016). This suggests that NCC phosphorylation is under the control of a chloride-dependent involving the WNK-SPAK pathway, whereas NCC dephosphorylation is likely governed by a chloride-independent pathway which may include other signalling cascades or phosphatases, such as PP4 (Glover *et al.*, 2010).

Furthermore, work involving WNK4 knock-out (WNK4-KO) mice has confirmed that WNK4 is the primary chloride sensor and its ablation abolishes the phosphorylation of NCC

in response to low potassium intake (Yang *et al.*, 2018). Notwithstanding this, the Ellison group hypothesis presents another conundrum, in that high NCC activity would be expected to increase intracellular chloride, effectively creating a negative feedback loop in the WNK-SPAK-NCC pathway if the apical NaCl entry is not sufficiently coupled to basolateral exit. While conditions of low extracellular potassium may be sufficient to keep intracellular chloride low in the face of high NCC activity, it is not the case for increased luminal NaCl delivery to the DCT which is also known to increase NCC activity. To test the effects of increase luminal NaCl delivery, the Huang group chose to avoid using loop diuretics which may induce compensatory upregulation of NCC resulting from loop diuretic-induced diuresis and volume loss. Instead they administered subcutaneous injections of 0.5mL normal saline twice daily until the mice reached a new steady-state sodium balance with no volume expansion and the entire injected quantity of sodium excreted in the urine, therefore confirming increased luminal delivery of sodium. As expected, NaCl loaded wildtype animals had dramatically increased thiazide-induced sodium excretion and NCC phosphorylation, but surprisingly so did the WNK4-KO mice despite no differences in serum potassium or renin mRNA (Yang *et al.*, 2018). Taken together the Loffing and Huang studies suggest that the Ellison hypothesis cannot be generalised to all physiological circumstances, and there are many as of yet unidentified pathways regulating NCC activity that warrant further investigation. A current working model of the integrated signalling pathways is summarised in Figure 6.2.

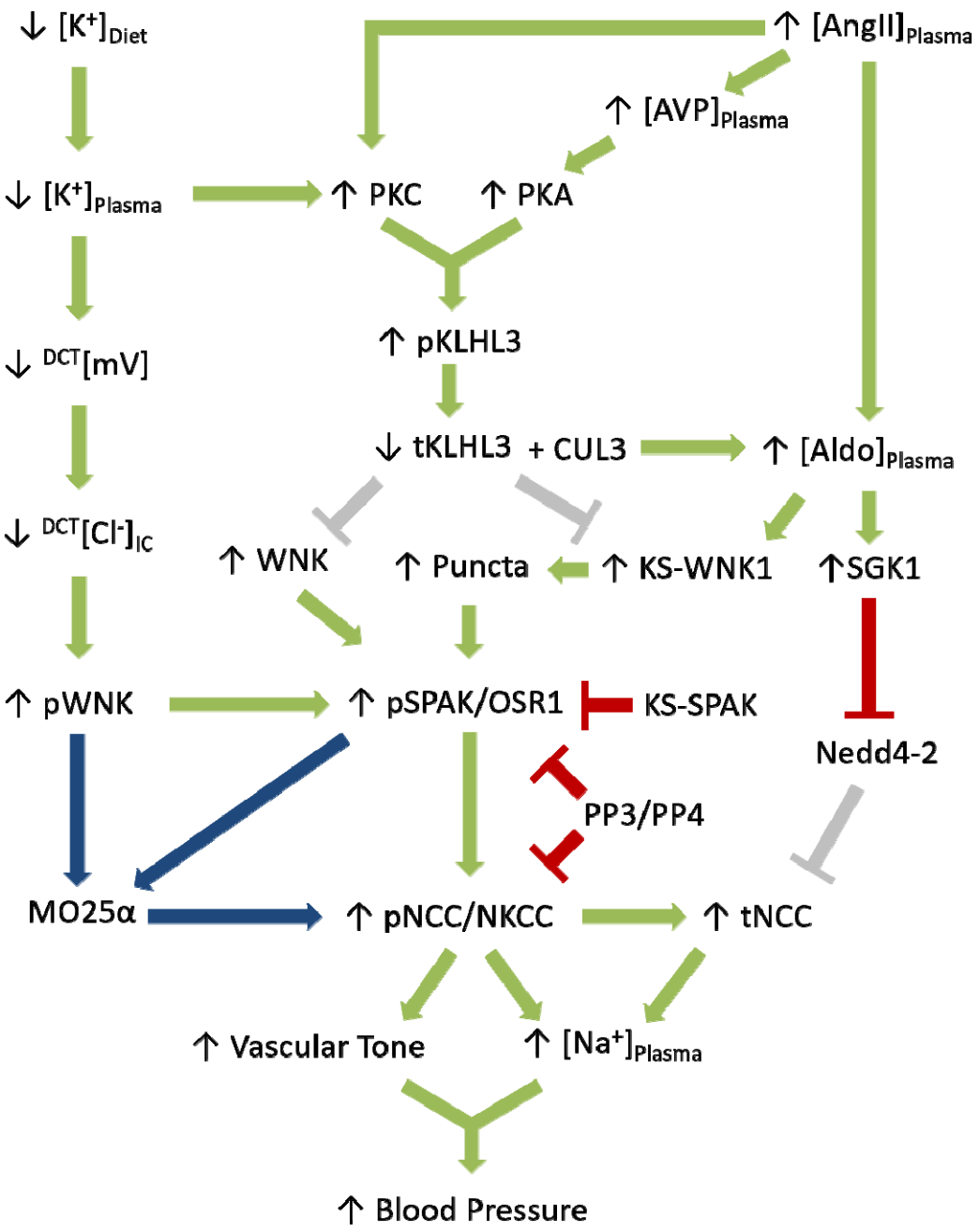

Figure 6.2: Diagram of integrated CUL3-KLHL3-MO25α-WNK-SPAK/OSR1 signalling.

In response to a low potassium diet, decreases in plasma K^+ levels are detected by changes in DCT membrane voltage (mV) which lowers intracellular Cl^- levels promoting WNK auto-phosphorylation and activation. Angiotensin II (AngII), vasopressin (AVP) and K^+ depletion stimulate phosphorylation of KLHL3 via PKC and PKA signalling. This simultaneously destabilises KLHL3 levels and blocks the ability of CUL3-KLHL3 to bind and ubiquitylate WNKs, leading to their accumulation. Aldosterone (Aldo) also promotes transcription of KS-WNK1 which is essential for puncta formation and is believed to promote WNK-SPAK/OSR1 phosphorylation through macromolecular crowding mechanisms. Together these actions stimulate phosphorylation of SPAK/OSR1 to increase NCC/NKCC transporter activity via phosphorylation, with additional modulation provided by KS-SPAK and PP3/PP4 negative regulation or MO25α-dependent amplification of WNK and SPAK/OSR signalling. Phosphorylation of NCC along with aldosterone/SGK1- dependent inhibition of Nedd4-2 activity, increases NCC apical abundance to promote salt retention, which in addition to NKCC1-dependent increases in vascular tone

contributes to a rise in blood pressure. Green pointed arrows indicate a positive effect; blue pointed arrows indicate positive effects that are dependent on a secondary component; Red flat-head arrows indicate an inhibitory effect; grey flat-head arrows indicate inhibitory effect that has been removed.

6.4 Future work

Although FHHt is a rare disease, the discovery of a vascular phenotype in our animal model of PHA2E has worrying implications for current treatment strategies. A useful follow-up study would be to compare various pharmacological treatments of PHA2E to assess the best strategy for tackling the drivers of arterial stiffness in this disease. This would look at the following therapies as standalones or in combination:

- Hydrochlorothiazide; an NCC-inhibiting diuretic and classic therapy of choice for treating FHHt.
- Fasudil; a potent Rho-kinase inhibitor and vasodilator used in the treatment of stroke victims.
- Furosemide, an NKCC2-inhibiting loop diuretic often deployed in the treatment of hyperkalaemia, but with potential vascular effects via NKCC1 inhibition.

Following this evaluation of therapies, it would necessary to perform non-invasive arterial pulse wave velocity (aPWV) measurements in thiazide-treated PHA2E patients and unaffected family members to determine if PHA2E patients have persistent arterial stiffness even when blood pressure is normalised. However, given the rarity of these patients, it might be more useful to determine Z-score of aPWV against age-matched blood pressure-matched healthy populations. If the same $CUL3^{WT/\Delta 403\text{-}459}$ vascular phenotype exists in human patients, it would be advisable to adjust the treatment guidelines based on the outcomes of the $CUL3^{WT/\Delta 403\text{-}459}$ pharmacotherapies comparison.

Given that MO25α overexpression has been demonstrated to predispose mice to salt-sensitive hypertension (Yang *et al.*, 2013), it is worth revisiting genetic animal models to validate MO25α as a viable anti-hypertensive target. In particular, the growing evidence for MO25α-WNK3-SPAK-NKCC1 signalling affecting the susceptibility and outcomes of ischaemic brain injury and post-haemorrhagic hydrocephalus (Bhuiyan *et al.*, 2016; Zhang *et al.*, 2016; Karimy *et al.*, 2017), implies that MO25α inhibitors may have relevance in the

treatment of stroke injury. An improved study design employing inducible homozygous and heterozygous MO25α knock-outs would be useful not only in assessing blood pressure changes, but also recovery outcomes from surgical animal models of ischaemic and haemorrhagic stroke. However, should knockdown/knock-out strategies still result in a more extreme phenotype due to pleiotropic effects, animal models homozygous and heterozygous for inducible dual alanine mutations in the WEW motif of SPAK (W382A/W374A) and OSR1 (W336A/W338A) required for MO25α-SPAK/OSR1 interactions, could provide an alternative for validating MO25α binding inhibition, which would be expected to have a less severe off-target profile (Kadri *et al.*, 2017).

Similarly, it may be worth revisiting the $SPAK^{L502A/L502A}$ animal models to establish if the same bone mineral density, metabolic and endocrine features observed in $SPAK^{T243A/T243A}$ mice can be recapitulated. Building on the previous work, as SPAK CCT inhibiting agents would be expected to also affect OSR1 due to their highly conserved nature, it would be important to generate, characterise and cross mice with the equivalent mutation in the CCT OSR1 (i.e. L473A), to ensure that the additional inhibition of OSR1 does not significantly expand the adverse side effect profile. Arguably the best study design to address CCT inhibition would be to generate inducible animal models, heterozygous and homozygous for $SPAK^{L502A}$ and $OSR1^{L473A}$ to investigate any dose depended effects and bypass the issue of embryonic lethality associated with OSR1 homozygous knock-out (Lin *et al.*, 2011).

Many unanswered questions still remain in WNK biology. In particular, the transduction of dietary/serum potassium into electrolyte and blood pressure changes has yet to be fully validated in an intact living animal. Also to date, there has been no adequate explanation for the paradox that FHHt presents to the model of serum potassium-intracellular chloride coupling regulating WNK activity in the DCT, which would predict that hyperkalaemia and hyperchloraemia would inhibit WNK activity irrespective of protein abundance. Conversely, it might be expected that the hypokalaemia seen in SPAK activity-deficient models of Gitelman syndrome would trigger overactivation of WNK-OSR1 signalling, yet there is limited evidence to support this either. Resolving these issues will be essential to underpin our understanding of WNK based signal transduction and provide a sound basis for therapeutics targeting the WNK pathway.

Bibliography

Abriel H & Staub O (2005). Ubiquitylation of Ion Channels. *Physiology* **20,** 398–407.

Acampa M, Camarri S, Lazzerini PE, Guideri F, Tassi R, Valenti R, Cartocci A & Martini G (2017). Increased arterial stiffness is an independent risk factor for hemorrhagic transformation in ischemic stroke undergoing thrombolysis. *Int J Cardiol* **243,** 466–470.

Achard J-M, Warnock DG, Disse-Nicodème S, Fiquet-Kempf B éatric., Corvol P, Fournier A & Jeunemaitre X (2003). Familial hyperkalemic hypertension: phenotypic analysis in a large family with the WNK1 deletion mutation. *Am J Med* **114,** 495–498.

Agarwal R (2008). Hypertension, hypokalemia, and thiazide-induced diabetes: A 3-way connection. *Hypertension* **52,** 1012–1013.

Agbor LN, Ibeawuchi S-RC, Hu C, Wu J, Davis DR, Keen HL, Quelle FW & Sigmund CD (2016). Cullin-3 mutation causes arterial stiffness and hypertension through a vascular smooth muscle mechanism. *JCI Insight* **1,** 1–11.

Ahlstrom R & Yu ASL (2009). Characterization of the kinase activity of a WNK4 protein complex. *Am J Physiol Renal Physiol* **297,** F685--F692.

Akar F, Jiang G, Paul RJ & O'Neill WC (2001). Contractile regulation of the Na+-K+2Cl- cotransporter in vascular smooth muscle. *Am J Physiol Physiol* **281,** C579–C584.

Akhtar N & Hafeez F (2009). A rare case of Gitelman's syndrome with hypophosphatemia. *J Coll Physicians Surg Pak* **19,** 257–259.

AlAmri MA, Kadri H, Alderwick LJ, Simpkins NS & Mehellou Y (2017). Rafoxanide and Closantel Inhibit SPAK and OSR1 Kinases by Binding to a Highly Conserved Allosteric Site on Their C-terminal Domains. *ChemMedChem* **12,** 639–645.

Alessi DR & Vitari AC (2006). Methods for modulating a wnk isoform protein kinase activity. Patent No: WO 2007/010219 A2.

Alessi DR, Zhang J, Khanna A, Hochdörfer T, Shang Y & Kahle KT (2014). The WNK-SPAK/OSR1 pathway: Master regulator of cation-chloride cotransporters. *Sci Signal* **7,** re3.

Ali A, Masood Q, Yaqub S & Kashif W (2013). A case of Gitelman syndrome with severe hyponatraemia and hypophosphataemia. *Singapore Med J* **54,** e18-20.

Amin N et al. (2012). Genome-wide association analysis of coffee drinking suggests association with CYP1A1/CYP1A2 and NRCAM. *Mol Psychiatry* **17,** 1116–1129.

Amirlak I & Dawson KP (2000). Bartter syndrome: an overview. *QJM* **93,** 207–215.

Anfinogenova YJ, Baskakov MB, Kovalev I V., Kilin AA, Dulin NO & Orlov SN (2004). Cell-volume-dependent vascular smooth muscle contraction: Role of Na +, K+, 2Cl-cotransport, intracellular Cl - and L-type Ca2+ channels. *Pflügers Arch - Eur J Physiol* **449,** 42–55.

Anselmo AN, Earnest S, Chen W, Juang Y-C, Kim SC, Zhao Y & Cobb MH (2006). WNK1 and OSR1 regulate the Na+, K+, 2Cl- cotransporter in HeLa cells. *Proc Natl Acad Sci U S A* **103,** 10883–10888.

Araki Y, Rai T, Sohara E, Mori T, Inoue Y, Isobe K, Kikuchi E, Ohta A, Sasaki S & Uchida S (2015). Generation and analysis of knock-in mice carrying pseudohypoaldosteronism type II-causing mutations in the cullin 3 gene. *Biol Open* **4,** 1509–1517.

Arion D & Lewis DA (2011). Altered expression of regulators of the cortical chloride transporters NKCC1 and KCC2 in schizophrenia. *Arch Gen Psychiatry* **68,** 21.

Arroyo JP et al. (2011). Nedd4-2 Modulates Renal Na+-Cl- Cotransporter via the Aldosterone-SGK1-Nedd4-2 Pathway. *J Am Soc Nephrol* **22,** 1707–1719.

Aubin R, Ménard P & Lajeunesse D (1996). Selective effect of thiazides on the human osteoblast-like cell line MG-63. *Kidney Int* **50,** 1476–1482.

Aung K & Htay T (2011). Thiazide diuretics and the risk of hip fracture. *Cochrane Database Syst Rev* **10,** CD005185.

Austin T, Deluca S, Meiler J & Delpire E (2015). Computational Modeling Suggests a Mechanism of Inhibition of SPAK/OSR1 by a known RFxV Pocket Inhibitor. *FASEB J* **29,** 2017.

Barry EL, Gesek FA, Kaplan MR, Hebert SC & Friedman PA (1997). Expression of the sodium-chloride cotransporter in osteoblast-like cells: effect of thiazide diuretics. *Am J*

Physiol Physiol **272,** C109–C116.

Bastians H, Krebber H, Hoheisel J, Ohl S, Lichter P, Ponstingl H & Joos S (1997). Assignment of the Human Serine/Threonine Protein Phosphatase 4 Gene (PPP4C) to Chromosome 16p11–p12 by Fluorescencein SituHybridization. *Genomics* **42,** 181–182.

Bazzini C (2005). Thiazide-sensitive NaCl-cotransporter in the Intestine: possible role of hydrochlorothiazide in the intestinal Ca2+ uptake. *J Biol Chem* **280,** 19902–19910.

Belge H & Devuyst O (2010). Parvalbumine et régulation du transport ionique dans le tube contourné distal du rein. *Med Sci* **26,** 566–568.

Belge H, Gailly P, Schwaller B, Loffing J, Debaix H, Riveira-Munoz E, Beauwens R, Devogelaer J-P, Hoenderop JG, Bindels RJ & Devuyst O (2007). Renal expression of parvalbumin is critical for NaCl handling and response to diuretics. *Proc Natl Acad Sci U S A* **104,** 14849–14854.

Ben-Nissan G & Sharon M (2014). Regulating the 20S Proteasome Ubiquitin-Independent Degradation Pathway. *Biomolecules* **4,** 862–884.

Bercier V, Brustein E, Liao M, Dion PA, Lafrenière RG, Rouleau GA & Drapeau P (2013). WNK1/HSN2 mutation in human peripheral neuropathy deregulates KCC2 expression and posterior lateral line development in zebrafish (*Danio rerio*). *PLoS Genet* **9,** e1003124.

Bergaya S, Faure S, Baudrie V, Rio M, Escoubet B, Bonnin P, Henrion D, Loirand G, Achard JM & Jeunemaitre X et al. (2011). WNK1 regulates vasoconstriction and blood pressure response to alpha 1-adrenergic stimulation in mice. *Hypertension* **58,** 439–445.

Bhuiyan MIH, Song S, Yuan H, Begum G, Kofler J, Kahle KT, Yang S-S, Lin S-H, Alper SL, Subramanya AR & Sun D (2016). WNK-Cab39-NKCC1 signaling increases the susceptibility to ischemic brain damage in hypertensive rats. *J Cereb Blood Flow {&} Metab*0271678X16675368.

Blaine J, Chonchol M & Levi M (2015). Renal Control of Calcium, Phosphate, and Magnesium Homeostasis. *Clin J Am Soc Nephrol* **10,** 1257–1272.

Bolívar JJ (2013). Essential hypertension: An approach to its etiology and neurogenic pathophysiology. *Int J Hypertens*; DOI: 10.1155/2013/547809.

Boudeau J, Baas AF, Deak M, Morrice NA, Kieloch A, Schutkowski M, Prescott AR, Clevers HC & Alessi DR (2003). MO25α/β interact with STRADα/β enhancing their ability to bind, activate and localize LKB1 in the cytoplasm. *EMBO J* **22,** 5102–5114.

Bourgeois MJ, Gilbert BK, Donald DE & Wood EH (1974). Characteristics of aortic diastolic pressure decay with application to the continuous monitoring of changes in peripheral vascular resistance. *Circ Res* **35,** 56–66.

Boyd-Shiwarski CR, Shiwarski DJ, Roy A, Nkashama LJ, Namboodiri HN, Xie J, McClain KL, Marciszyn A, Kleyman TR, Tan RJ, Stolz DB, Puthenveedu MA, Huang C-L & Subramanya AR (2017). Potassium-Regulated Distal Tubule WNK Bodies are Kidney-Specific WNK1 Dependent. *Mol Biol Cell* **1,** mbc.E17-08-0529.

Boyden LM et al. (2012). Mutations in kelch-like 3 and cullin 3 cause hypertension and electrolyte abnormalities. *Nature* **482,** 98–102.

Calabrese MF, Scott DC, Duda DM, Crr G, Kurinov I, Kriwacki RW & Schulman BA (2011). A RING E3-substrate complex poised for ubiquitin-like protein transfer: structural insights into cullin-RING ligases. *Nat Struct Mol Biol* **18,** 947–949.

Câmpean V, Kricke J, Ellison D, Luft FC, Bachmann S, Gamba G, Bailey MA, Paterson JM, Hadoke PWF, Wrobel N, Christopher OC, Brownstein DG, Seckl JR, Mullins JJ, Grimm PR, Foutz RM, Brenner R & Sansom SC (2001). Localization of thiazide-sensitive Na(+)-Cl(-) cotransport and associated gene products in mouse DCT. *Am J Physiol Renal Physiol* **281,** F1028--F1035.

Canning P & Bullock AN (2014). New strategies to inhibit KEAP1 and the Cul3-based E3 ubiquitin ligases. *Biochem Soc Trans* **42,** 103–107.

Cantone A, Yang X, Yan Q, Giebisch G, Hebert SC & Wang T (2008). Mouse model of type II Bartter's syndrome. I. Upregulation of thiazide-sensitive Na-Cl cotransport activity. *Am J Physiol Physiol* **294,** F1366–F1372.

Carretero OA & Oparil S (2000). Essential hypertension. Part I: definition and etiology. *Circulation* **101,** 329–335.

Cervantes-Perez LG, Castaneda-Bueno M, Jimenez J V., Vazquez N, Rojas-Vega L, Alessi DR, Bobadilla NA & Gamba G (2018). Disruption of the with no lysine kinase-STE20-

proline alanine-rich kinase pathway reduces the hypertension induced by angiotensin II. *J Hypertens* **36,** 361–367.

Chávez-Canales M, Zhang C, Soukaseum C, Moreno E, Pacheco-Alvarez D, Vidal-Petiot E, Castañeda-Bueno M, Vázquez N, Rojas-Vega L, Meermeier NP, Rogers S, Jeunemaitre X, Yang CL, Ellison DH, Gamba G & Hadchouel J (2014). WNK-SPAK-NCC cascade revisited: WNK1 stimulates the activity of the Na-Cl cotransporter via SPAK, an effect antagonized by WNK4. *Hypertension* **64,** 1047–1053.

Cheema MU, Damkier HH, Nielsen J, Poulsen ET, Enghild JJ, Fenton RA & Praetorius J (2014). Distal Renal Tubules Are Deficient in Aggresome Formation and Autophagy upon Aldosterone Administration. ; DOI: 10.1371/journal.pone.0101258.

Chen H, Untiveros GM, McKee LAK, Perez J, Li J, Antin PB & Konhilas JP (2012). Micro-RNA-195 and -451 regulate the LKB1/AMPK signaling axis by targeting MO25. *PLoS One* **7,** 1–11.

Chiga M, Rafiqi FH, Alessi DR, Sohara E, Ohta A, Rai T, Sasaki S & Uchida S (2011). Phenotypes of pseudohypoaldosteronism type II caused by the WNK4 D561A missense mutation are dependent on the WNK-OSR1/SPAK kinase cascade. *J Cell Sci* **124,** 1391–1395.

Choe KP & Strange K (2007). Evolutionarily conserved WNK and Ste20 kinases are essential for acute volume recovery and survival after hypertonic shrinkage in Caenorhabditis elegans. *AJP Cell Physiol* **293,** C915--C927.

Choi MR, An CH, Yoo NJ & Lee SH (2016). Frameshift Mutations of CAB39L, an Activator of LKB1 Tumor Suppressor, in Gastric and Colorectal Cancers. *Pathol Oncol Res* **22,** 225–226.

Chowdhury JAA, Liu C-HH, Zuber AMM, O'Shaughnessy KM & O'Shaughnessy KM (2013). An inducible transgenic mouse model for familial hypertension with hyperkalaemia (Gordon's syndrome or pseudohypoaldosteronism type II). *Clin Sci* **124,** 701–708.

Cohen P & Alessi DR (2013). Kinase drug discovery--what's next in the field? *ACS Chem Biol* **8,** 96–104.

Cohen PTW, Philp A, Va C & Vázquez-Martin C (2005). Protein phosphatase 4 - From

obscurity to vital functions. *FEBS Lett* **579,** 3278–3286.

Condon JR & Nassim R (1970). Hypophosphataemia and hypokalaemia. *BMJ* **1,** 110.

Cope G, Golbang A & O'Shaughnessy KM (2005). WNK kinases and the control of blood pressure. *Pharmacol Ther* **106,** 221–231.

Cope GA, Gsb S, Aravind L, Schwarz SE, Zipursky SL, Koonin E V & Deshaies RJ (2002). Role of predicted metalloprotease motif of Jab1/Csn5 in cleavage of Nedd8 from Cul1. *Science (80-)* **298,** 608–611.

Crilly MA (2014). Adjusting the aortic augmentation index for the resting heart rate. *J Atheroscler Thromb* **21,** 378–380.

Cui D, Xiong X & Zhao Y (2016). Cullin-RING ligases in regulation of autophagy. *Cell Div* **11,** 8.

D'Urso D, Prior R, Greiner-Petter R, Gabreëls-Festen a a & Müller HW (1998). Overloaded endoplasmic reticulum-Golgi compartments, a possible pathomechanism of peripheral neuropathies caused by mutations of the peripheral myelin protein PMP22. *J Neurosci* **18,** 731–740.

Delaloy C, Hadchouel J, Imbert-Teboul M, Clemessy M, Houot AM & Jeunemaitre X (2006). Cardiovascular expression of the Mouse WNK1 gene during development and adulthood revealed by a BAC reporter assay. *Am J Pathol* **169,** 105–118.

Delpire E & Gagnon KBE (2008). SPAK and OSR1: STE20 kinases involved in the regulation of ion homoeostasis and volume control in mammalian cells. *Biochem J* **409,** 321–331.

Dimke H (2011). Exploring the intricate regulatory network controlling the thiazide-sensitive NaCl cotransporter (NCC). *Pflügers Arch - Eur J Physiol* **462,** 767–777.

Duarte JD & Cooper-DeHoff RM (2010). Mechanisms for blood pressure lowering and metabolic effects of thiazide and thiazide-like diuretics. *Expert Rev Cardiovasc Ther* **8,** 793–802.

Duda DM, Borg LA, Scott DC, Hunt HW, Hammel M & Schulman BA (2008). Structural insights into NEDD8 activation of cullin-RING ligases: conformational control of conjugation. *Cell* **134,** 995–1006.

Duda DM, Scott DC, Calabrese MF, Zimmerman ES, Zheng N & Schulman BA (2011). Structural regulation of cullin-RING ubiquitin ligase complexes. *Curr Opin Struct Biol* **21,** 257–264.

Durocher Y (2002). High-level and high-throughput recombinant protein production by transient transfection of suspension-growing human 293-EBNA1 cells. *Nucleic Acids Res* **30,** 9e.

Dvorak MM, De Joussineau C, Carter DH, Pisitkun T, Knepper MA, Gamba G, Kemp PJ & Riccardi D (2007). Thiazide Diuretics Directly Induce Osteoblast Differentiation and Mineralized Nodule Formation by Interacting with a Sodium Chloride Co-Transporter in Bone. *J Am Soc Nephrol* **18,** 2509–2516.

Fang X, Shen F, Lechauve C, Xu P, Zhao G, Itkow J, Wu F, Hou Y, Wu X, Yu L, Xiu H, Wang M, Zhang R, Wang F, Zhang Y, Wang D, Weiss MJ & Yu D (2017). miR-144/451 represses the LKB1/AMPK/mTOR pathway to promote red cell precursor survival during recovery from acute anemia. *Haematologica*haematol.2017.177394.

Farrow EG, Davis SI, Summers LJ & White KE (2009). Initial FGF23-Mediated Signaling Occurs in the Distal Convoluted Tubule. *J Am Soc Nephrol* **20,** 955–960.

Feng J, Ito M, Ichikawa K, Isaka N, Nishikawa M, Hartshorne DJ & Nakano T (1999). Inhibitory phosphorylation site for Rho-associated kinase on smooth muscle myosin phosphatase. *J Biol Chem* **274,** 37385–37390.

Ferdaus MZ, Barber KW, López-Cayuqueo KI, Terker AS, Argaiz ER, Gassaway BM, Chambrey R, Gamba G, Rinehart J & McCormick JA (2016). SPAK and OSR1 play essential roles in potassium homeostasis through actions on the distal convoluted tubule. *J Physiol* **594,** 4945–4966.

Ferdaus MZ & McCormick JA (2018). Mechanisms and controversies in mutant Cul3-mediated Familial Hyperkalemic Hypertension. *Am J Physiol Physiol*ajprenal.00593.2017.

Ferdaus MZ, Miller LN, Agbor LN, Saritas T, Singer JD, Sigmund CD & McCormick JA (2017). Mutant Cullin 3 causes familial hyperkalemic hypertension via dominant effects. *JCI Insight*; DOI: 10.1172/jci.insight.96700.

Filippi BM, de los Heros P, Mehellou Y, Navratilova I, Gourlay R, Deak M, Plater L, Toth R, Zeqiraj E & Alessi DR (2011). MO25 is a master regulator of SPAK/OSR1 and MST3/MST4/YSK1 protein kinases. *EMBO J* **30,** 1730–1741.

Fu Y (2006). WNK kinases influence TRPV4 channel function and localization. *AJP Ren Physiol* **290,** F1305--F1314.

Gagnon KB & Delpire E (2010). Multiple pathways for protein phosphatase 1 (PP1) regulation of Na-K-2Cl cotransporter (NKCC1) function: The N-terminal tail of the Na-K-2Cl cotransporter serves as a regulatory scaffold for Ste20-related proline/alanine-rich kinase (SPAK) and PP1. *J Biol Chem* **285,** 14115–14121.

Gagnon KB & Delpire E (2013). Physiology of SLC12 transporters: lessons from inherited human genetic mutations and genetically engineered mouse knockouts. *Am J Physiol - Cell Physiol* **304,** C693–C714.

Gagnon KB, Rios K & Delpire E (2011). Functional insights into the activation mechanism of Ste20-related kinases. *Cell Physiol Biochem* **28,** 1219–1230.

Gagnon KBE, England R & Delpire E (2006). Volume sensitivity of cation-Cl- cotransporters is modulated by the interaction of two kinases: Ste20-related proline-alanine-rich kinase and WNK4. *Am J Physiol Cell Physiol* **290,** C134–C142.

Gagnon KBE, England R & Delpire E (2007). A single binding motif is required for SPAK activation of the Na-K-2Cl cotransporter. *Cell Physiol Biochem* **20,** 131–142.

Gamba G (2005). Role of WNK kinases in regulating tubular salt and potassium transport and in the development of hypertension. *AJP Ren Physiol* **288,** F245--F252.

Gamba G, Miyanoshita A, Lombardi M, Lytton J, Lee W Sen, Hediger MA & Hebert SC (1994). Molecular cloning, primary structure, and characterization of two members of the mammalian electroneutral sodium-(potassium)-chloride cotransporter family expressed in kidney. *J Biol Chem* **269,** 17713–17722.

Gamba G, Saltzberg SN, Lombardi M, Miyanoshita A, Lytton J, Hediger MA, Brenner BM & Hebert SC (1993). Primary structure and functional expression of a cDNA encoding the thiazide-sensitive, electroneutral sodium-chloride cotransporter. *Proc Natl Acad Sci U S A* **90,** 2749–2753.

Garrido N, Martínez-Conejero JA, Jauregui J, Horcajadas JA, Simón C, Remohí J & Meseguer M (2009). Microarray analysis in sperm from fertile and infertile men without basic sperm analysis abnormalities reveals a significantly different transcriptome. *Fertil Steril* **91,** 1307–1310.

Gasteiger E, Jung E & Bairoch A (2001). SWISS-PROT: connecting biomolecular knowledge via a protein database. *Curr Issues Mol Biol* **3,** 47–55.

Geng Y, Hoke A & Delpire E (2009). The Ste20 Kinases Ste20-related proline-alanine-rich kinase and oxidative-stress response 1 regulate NKCC1 function in sensory neurons. *J Biol Chem* **284,** 14020–14028.

Giménez I & Forbush B (2003). Short-term stimulation of the renal Na-K-Cl cotransporter (NKCC2) by vasopressin involves phosphorylation and membrane translocation of the protein. *J Biol Chem* **278,** 26946–26951.

Glover M, Mercier Zuber A, Figg N & O'Shaughnessy KM (2010). The activity of the thiazide-sensitive Na(+)-Cl(-) cotransporter is regulated by protein phosphatase PP4. *Can J Physiol Pharmacol* **88,** 986–995.

Glover M & O'Shaughnessy KM (2011). SPAK and WNK kinases: A new target for blood pressure treatment? *Curr Opin Nephrol Hypertens* **20,** 16–22.

Glover M, Ware JS, Henry A, Wolley M, Walsh R, Wain L V., Xu S, Van't Hoff WG, Tobin MD, Hall IP, Cook S, Gordon RD, Stowasser M & O'Shaughnessy KM (2014). Detection of mutations in KLHL3 and CUL3 in families with FHHt (familial hyperkalaemic hypertension or Gordon's syndrome). *Clin Sci* **126,** 721–726.

Glover M, Zuber AM & O'Shaughnessy KM (2009). Renal and brain isoforms of WNK3 have opposite effects on NCCT expression. *J Am Soc Nephrol* **20,** 1314–1322.

Golbang AP, Cope G, Hamad A, Murthy M, Liu CH, Cuthbert AW & O'Shaughnessy KM (2006). Regulation of the expression of the Na/Cl cotransporter by WNK4 and WNK1: evidence that accelerated dynamin-dependent endocytosis is not involved. *Am J Physiol Renal Physiol* **291,** F1369--76.

Goldenberg SJ, Cascio TC, Shumway SD, Garbutt KC, Liu J, Xiong Y & Zheng N (2004). Structure of the Cand1-Cul1-Roc1 complex reveals regulatory mechanisms for the

assembly of the multisubunit cullin-dependent ubiquitin ligases. *Cell* **119,** 517–528.

Goldsmith EJ, Akella R & Jiou J (2017). Structural Basis of Activation of WNK Kinases by Hydrostatic Pressure. *Acta Cryst* **A73,** a312.

Gordon RD (1986). Syndrome of hypertension and hyperkalemia with normal glomerular filtration rate. *Hypertension* **8,** 93–102.

Gordon RD & Hodsman GP (1986). The syndrome of hypertension and hyperkalaemia without renal failure: long term correction by thiazide diuretic. *Scott Med J* **31,** 43–44.

Gordon RD, Klemm SA, Tunny TJ & Stowasser M (1995). Gordon's syndrome: A sodium-volume-dependent form of hypertension with a genetic basis. In *Hypertension: pathophysiology, diagnosis, and management*, ed. Laragh JH & Brenner BM, pp. 2111–2123. Raven Press, New York.

Grimm PR, Coleman R, Delpire E & Welling PA (2017). Constitutively Active SPAK Causes Hyperkalemia by Activating NCC and Remodeling Distal Tubules. 1–10.

Grimm PR, Lazo-Fernandez Y, Delpire E, Wall SM, Dorsey SG, Weinman EJ, Coleman R, Wade JB & Welling PA (2015). Integrated compensatory network is activated in the absence of NCC phosphorylation. *J Clin Invest* **125,** 2136–2150.

Grimm PR, Taneja TK, Liu J, Coleman R, Chen YY, Delpire E, Wade JB & Welling PA (2012). SPAK isoforms and OSR1 regulate sodium-chloride co-transporters in a nephron-specific manner. *J Biol Chem* **287,** 37673–37690.

Hadchouel J, Soukaseum C, Busst C, Zhou X -o., Baudrie V, Zurrer T, Cambillau M, Elghozi J-L, Lifton RP, Loffing J & Jeunemaitre X (2010). Decreased ENaC expression compensates the increased NCC activity following inactivation of the kidney-specific isoform of WNK1 and prevents hypertension. *Proc Natl Acad Sci* **107,** 18109–18114.

Hall TJ & Schaueblin M (1994). Hydrochlorothiazide inhibits osteoclastic bone resorption In vitro. *Calcif Tissue Int* **55,** 266–268.

Harper JW & M-km T (2012). Ubiquitin Pathway Proteomics. *Mol Cell Proteomics* **11,** 1541–1550.

Hastie CJ & Cohen PTW (1998). Purification of protein phosphatase 4 catalytic subunit:

Inhibition by the antitumour drug fostriecin and other tumour suppressors and promoters. *FEBS Lett* **431,** 357–361.

Hebert SC, Mount DB & Gamba G (2004). Molecular physiology of cation-coupled Cl- cotransport: The SLC12 family. *Pflugers Arch Eur J Physiol* **447,** 580–593.

Hong C, Moorefield KS, Jun P, Aldape KD, Kharbanda S, Phillips HS & Costello JF (2007). Epigenome scans and cancer genome sequencing converge on WNK2, a kinase-independent suppressor of cell growth. *Proc Natl Acad Sci* **104,** 10974–10979.

Hoorn EJ, Walsh SB, McCormick JA, Fürstenberg A, Yang C-L, Roeschel T, Paliege A, Howie AJ, Conley J, Bachmann S, Unwin RJ & Ellison DH (2011). The calcineurin inhibitor tacrolimus activates the renal sodium chloride cotransporter to cause hypertension. *Nat Med* **17,** 1304–1309.

Hottenga JJ, Boomsma DI, Kupper N, Posthuma D, Snieder H, Willemsen G & De Geus EJC (2005). Heritability and stability of resting blood pressure. *Twin Res Hum Genet* **8,** 499–508.

Hsu YJ, Yang S Sen, Cheng CJ, Liu ST, Huang SM, Chau T, Chu P, Salter DM, Lee HS & Lin SH (2015). Thiazide-Sensitive Na+-Cl- Cotransporter (NCC) Gene Inactivation Results in Increased Duodenal Ca2+ Absorption, Enhanced Osteoblast Differentiation and Elevated Bone Mineral Density. *J Bone Miner Res* **30,** 116–127.

Hu MC, Shui JW, Mihindukulasuriya KA & Tan TH (2001). Genomic structure of the mouse PP4 gene: a developmentally regulated protein phosphatase. *Gene* **278,** 89–99.

Hu MC, Tang-Oxley Q, Qiu WR, Wang YP, Mihindukulasuriya KA, Afshar R & Tan TH (1998). Protein phosphatase X interacts with c-Rel and stimulates c-Rel/nuclear factor kappaB activity. *J Biol Chem* **273,** 33561–33565.

Hyde TM, Lipska BK, Ali T, Mathew S V, Law AJ, Metitiri OE, Straub RE, Ye T, Colantuoni C, Herman MM, Bigelow LB, Weinberger DR & Kleinman JE (2011). Expression of GABA signaling molecules KCC2, NKCC1, and GAD1 in cortical development and schizophrenia. *J Neurosci* **31,** 11088–11095.

Ibeawuchi S-RC, Agbor LN, Quelle FW & Sigmund CD (2015). Hypertension-causing Mutations in Cullin3 Protein Impair RhoA Protein Ubiquitination and Augment the

Association with Substrate Adaptors. *J Biol Chem* **290,** 19208–19217.

Ishigami-yuasa M, Watanabe Y, Mori T, Masuno H, Fujii S, Kikuchi E, Uchida S & Kagechika H (2017). Development of WNK Signaling Inhibitors as a New Class of Antihypertensive Drugs. *Bioorg Med Chem*; DOI: 10.1016/j.bmc.2017.05.034.

Ishizawa K, Xu N, Loffing J, Lifton RP, Fujita T, Uchida S & Shibata S (2016). Potassium depletion stimulates Na-Cl cotransporter via phosphorylation and inactivation of the ubiquitin ligase Kelch-like 3. *Biochem Biophys Res Commun* **480,** 745–751.

Ji AX & Privé GG (2013). Crystal Structure of KLHL3 in Complex with Cullin3. *PLoS One* **8,** e60445.

Jiang Y, Cong P, Williams SR, Zhang W, Na T, Ma H-P & Peng J-B (2008). WNK4 regulates the secretory pathway via which TRPV5 is targeted to the plasma membrane. *Biochem Biophys Res Commun* **375,** 225–229.

Jiang Y, Ferguson WB & Peng J-B (2006). WNK4 enhances TRPV5-mediated calcium transport: potential role in hypercalciuria of familial hyperkalemic hypertension caused by gene mutation of WNK4. *AJP Ren Physiol* **292,** F545--F554.

Jing H, Na T, Zhang W, Wu G, Liu C & Peng J-B (2011). Concerted actions of NHERF2 and WNK4 in regulating TRPV5. *Biochem Biophys Res Commun* **404,** 979–984.

Kadri H, Alamri MA, Navratilova IH, Alderwick LJ, Simpkins NS & Mehellou Y (2017). Towards the Development of Small-Molecule MO25 Binders as Potential Indirect SPAK/OSR1 Kinase Inhibitors. *ChemBioChem* **18,** 460–465.

Kaess BM, Rong J, Larson MG, Hamburg NM, Vita JA, Levy D, Benjamin EJ, Vasan RS & Mitchell GF (2012). Aortic stiffness, blood pressure progression, and incident hypertension. *JAMA* **308,** 875–881.

Kahle KT, Gimenez I, Hassan H, Wilson FH, Wong RD, Forbush B, Aronson PS & Lifton RP (2004). WNK4 regulates apical and basolateral Cl- flux in extrarenal epithelia. *Proc Natl Acad Sci U S A* **101,** 2064–2069.

Kahle KT, Rinehart J & Lifton RP (2010). Phosphoregulation of the Na-K-2Cl and K-Cl cotransporters by the WNK kinases. *Biochim Biophys Acta - Mol Basis Dis* **1802,** 1150–1158.

Kahle KT, Rinehart J, de los Heros P, Louvi A, Meade P, Vazquez N, Hebert SC, Gamba G, Gimenez I & Lifton RP (2005). WNK3 modulates transport of Cl- in and out of cells: Implications for control of cell volume and neuronal excitability. *Proc Natl Acad Sci* **102,** 16783–16788.

Kahle KT, Ring AM & Lifton RP (2008). Molecular physiology of the WNK kinases. *Annu Rev Physiol* **70,** 329–355.

Kalkman HO (2011). Alterations in the expression of neuronal chloride transporters may contribute to schizophrenia. *Prog Neuro-Psychopharmacology Biol Psychiatry* **35,** 410–414.

Karimy JK, Zhang J, Kurland DB, Theriault BC, Duran D, Stokum JA, Furey CG, Zhou X, Mansuri MS, Montejo J, Vera A, Diluna ML, Delpire E, Alper SL, Gunel M, Gerzanich V, Medzhitov R, Simard JM & Kahle KT (2017). Inflammation-dependent cerebrospinal fluid hypersecretion by the choroid plexus epithelium in posthemorrhagic hydrocephalus. *Nat Med* **23,** 997–1003.

Kasagi Y, Takahashi D, Aida T, Nishida H, Nomura N, Zeniya M, Mori T, Sasaki E, Ando F, Rai T, Uchida S & Sohara E (2017). Impaired degradation of medullary WNK4 in the kidneys of KLHL2 knockout mice. *Biochem Biophys Res Commun* **487,** 368–374.

Katopodis K, Elisaf M & Siamopoulos KC (1996). Hypophosphataemia in a patient with Gitelinan's syndrome. *Nephrol Dial Transplant* **11,** 2090–2092.

Kelley LA & Mje S (2009). Protein structure prediction on the Web: a case study using the Phyre server. *Nat Protoc* **4,** 363–371.

Kelly R, Hayward C, Avolio A, O'Rourke M & Kelly, R ; Hayward, C ; Avolio, A ; O'rourke M (1989). Noninvasive determination of age-related changes in the human arterial pulse. *Circ (New York, NY)* **80,** 1652–1659.

Kelsall IR, Duda DM, Olszewski JL, Hofmann K, Knebel A, Feder L, Wood N, Wightman M, Schulman BA & Alpi AF (2013). TRIAD1 and HHARI bind to and are activated by distinct neddylated Cullin-RING ligase complexes. *EMBO J* **32,** 2848–2860.

Kemter E, Rathkolb B, Bankir L, Schrewe A, Hans W, Landbrecht C, Klaften M, Ivandic B, Fuchs H, Gailus-Durner V, Hrabé de Angelis M, Wolf E, Wanke R & Aigner B (2010).

Mutation of the Na+-K+-2Cl- cotransporter NKCC2 in mice is associated with severe polyuria and a urea-selective concentrating defect without hyperreninemia. *Am J Physiol - Ren Physiol* **298,** F1405–F1415.

Kigoshi Y, Tsuruta F & Chiba T (2011). Ubiquitin Ligase Activity of Cul3-KLHL7 Protein Is Attenuated by Autosomal Dominant Retinitis Pigmentosa Causative Mutation. *J Biol Chem* **286,** 33613–33621.

Kikuchi E, Mori T, Zeniya M, Isobe K, Ishigami-Yuasa M, Fujii S, Kagechika H, Ishihara T, Mizushima T, Sasaki S, Sohara E, Rai T & Uchida S (2015). Discovery of novel SPAK inhibitors that block WNK kinase signaling to cation chloride transporters. *Nihon Jinzo Gakkai Shi* **57,** 1319–1322.

Kim S-H, Kim H-J, Kim S & Yim J (2010). Drosophila Cand1 regulates Cullin3-dependent E3 ligases by affecting the neddylation of Cullin3 and by controlling the stability of Cullin3 and adaptor protein. *Dev Biol* **346,** 247–257.

Kim W, Bennett EJ, Huttlin EL, Guo A, Li J, Possemato A, Sowa ME, Rad R, Rush J, Comb MJ, Harper JW & Gygi SP (2011). Systematic and quantitative assessment of the ubiquitin-modified proteome. *Mol Cell* **44,** 325–340.

Kirisako T, Kamei K, Murata S, Kato M, Fukumoto H, Kanie M, Sano S, Tokunaga F, Tanaka K & Iwai K (2006). A ubiquitin ligase complex assembles linear polyubiquitin chains. *EMBO J* **25,** 4877–4887.

Knoers NVAM, De Jong JC, Meij IC, Van Den Heuvel LPWJ & Bindels RJM (2003). Genetic renal disorders with hypomagnesemia and hypocalciuria. In *Journal of Nephrology*, pp. 293–296.

Ko B, Joshi LM, Cooke LL, Vazquez N, Musch MW, Hebert SC, Gamba G & Hoover RS (2007). Phorbol ester stimulation of RasGRP1 regulates the sodium-chloride cotransporter by a PKC-independent pathway. *Proc Natl Acad Sci U S A* **104,** 20120–20125.

Ko B, Kamsteeg E-J, Cooke LL, Moddes LN, Deen PMT & Hoover RS (2010). RasGRP1 stimulation enhances ubiquitination and endocytosis of the sodium-chloride cotransporter. *Am J Physiol Renal Physiol* **299,** F300--9.

Koscielny G et al. (2014). The International Mouse Phenotyping Consortium Web Portal, a

unified point of access for knockout mice and related phenotyping data. *Nucleic Acids Res* **42,** 802–809.

Koumangoye R & Delpire E (2017). DNPEP is not the only peptidase that produces SPAK fragments in kidney. *Physiol Rep* **5,** 1–9.

Kurz T, Özlü N, Rudolf F, O'Rourke SM, Luke B, Hofmann K, Hyman AA, Bowerman B & Peter M (2005). The conserved protein DCN-1/Dcn1p is required for cullin neddylation in C. elegans and S. cerevisiae. *Nature* **435,** 1257–1261.

Kuwabara Y, Horie T, Baba O, Watanabe S, Nishiga M, Usami S, Izuhara M, Nakao T, Nishino T, Otsu K, Kita T, Kimura T & Ono K (2015). MicroRNA-451 exacerbates lipotoxicity in cardiac myocytes and high-fat diet-induced cardiac hypertrophy in mice through suppression of the LKB1/AMPK pathway. *Circ Res* **116,** 279–288.

Kuznetsova IM, Turoverov KK & Uversky VN (2014). *What macromolecular crowding can do to a protein*.

Lalande A, Roux S, Denne M-A, Stanley ER, Schiavi P, Guez D & De Vernejoul M-C (2001). Indapamide, a thiazide-like diuretic, decreases bone resorption *in vitro*. *J Bone Miner Res* **16,** 361–370.

Lamark T & Johansen T (2012). Aggrephagy: Selective disposal of protein aggregates by macroautophagy. *Int J Cell Biol* **2012,** 5.

Lazo-Fernandez Y, Welling PA & Wall SM (2018). α-ketoglutarate stimulates pendrin-dependent Cl^- absorption in the mouse CCD through protein kinase C. *Am J Physiol Physiol*ajprenal.00576.2017.

Lee A-Y, Chen W, Stippec S, Self J, Yang F, Ding X, Chen S, Juang Y-C & Cobb MH (2012*a*). Protein kinase WNK3 regulates the neuronal splicing factor Fox-1. *Proc Natl Acad Sci* **109,** 16841–16846.

Lee DW, Peggie M, Deak M, Toth R, Gage ZO, Wood N, Schilde C, Kurz T & Knebel A (2012*b*). The Dac-tag, an affinity tag based on penicillin-binding protein 5. *Anal Biochem* **428,** 64–72.

Lee K-Z, Kniazeva M, Han M, Pujol N & Ewbank J (2010). The fatty acid synthase fasn-1 acts upstream of WNK and Ste20/GCK-VI kinases to modulate antimicrobial peptide

expression in C. elegans epidermis. *Virulence* **1,** 113–122.

Lee SJ, Cobb MH & Goldsmith EJ (2009). Crystal structure of domain-swapped STE20 OSR1 kinase domain. *Protein Sci* **18,** 304–313.

Lei L & Lixian Z (2012). Effect of 24 h fasting on gene expression of AMPK, appetite regulation peptides and lipometabolism related factors in the hypothalamus of broiler chicks. *Asian-Australasian J Anim Sci* **25,** 1300–1308.

Lemmink HH, Knoers NVAM, Karolyi L, Van Dijk H, Niaudet P, Antignac C, Guay-Woodford LM, Goodyer PR, Carel JC, Hermes A, Seyberth HW, Monnens LAH & Van Den Heuvel LPWJ (1998). Novel mutations in the thiazide-sensitive NaCl cotransporter gene in patients with Gitelman syndrome with predominant localization to the C- terminal domain. *Kidney Int* **54,** 720–730.

Lemonnier E & Ben-Ari Y (2010). The diuretic bumetanide decreases autistic behaviour in five infants treated during 3 months with no side effects. *Acta Paediatr* **99,** 1885–1888.

Li C, Feng M, Shi Z, Hao Q, Song X, Wang W, Zhao Y, Jiao S & Zhou Z (2014). Structural and biochemical insights into the activation mechanisms of germinal center kinase OSR1. *J Biol Chem* **289,** 35969–35978.

Liao J & Farmer J (2014). Arterial stiffness as a risk factor for coronary artery disease. *Curr Atheroscler Rep* **16,** 387.

Liao JK, Seto M & Noma K (2007). Rho kinase (ROCK) inhibitors. *J Cardiovasc Pharmacol* **50,** 17–24.

Licht JH, Amundson D, Hsueh WA & Lombardo J V (1985). Familiar hyperkalaemic acidosis. *QJM An Int J Med* **54,** 161–176.

Lieben L & Carmeliet G (2012). The involvement of TRP channels in bone homeostasis. *Front Endocrinol (Lausanne)* **3,** 99.

Liedtke CM, Wang X & Smallwood ND (2005). Role for protein phosphatase 2A in the regulation of calu-3 epithelial Na+-K+-2Cl-, type 1 co-transport function. *J Biol Chem* **280,** 25491–25498.

Lin S-WS-H, Yu I-S, Jiang S-T, Lin S-WS-H, Chu P, Chen A, Sytwu H-K, Sohara E, Uchida

S, Sasaki S & Yang S-S (2011). Impaired phosphorylation of Na+-K+-2Cl- cotransporter by oxidative stress-responsive kinase-1 deficiency manifests hypotension and Bartter-like syndrome. *Proc Natl Acad Sci* **108,** 17538–17543.

Lin SH, Shiang JC, Huang CC, Yang S Sen, Hsu YJ & Cheng CJ (2005). Phenotype and genotype analysis in Chinese patients with Gitelman's syndrome. *J Clin Endocrinol Metab* **90,** 2500–2507.

Lingaraju GM, Bunker RD, Cavadini S, Hess D, Hassiepen U, Renatus M, Fischer ES & Thomä NH (2014). Crystal structure of the human COP9 signalosome. *Nature* **512,** 161–165.

Little R, Muimo R, Robson L, Harris K & Grabowski PS (2011). The transient receptor potential ion channel TRPV6 is expressed at low levels in osteoblasts and has little role in osteoblast calcium uptake. *PLoS One* **6,** e28166.

Liu J, Furukawa M, Matsumoto T & Xiong Y (2002). NEDD8 Modification of CUL1 Dissociates p120CAND1, an Inhibitor of CUL1-SKP1 Binding and SCF Ligases. *Mol Cell* **10,** 1511–1518.

Liu J & Nussinov R (2011). Flexible Cullins in Cullin-RING E3 Ligases Allosterically Regulate Ubiquitination. *J Biol Chem* **286,** 40934–40942.

Liu S & Quarles LD (2007). How fibroblast growth factor 23 works. *J Am Soc Nephrol* **18,** 1637–1647.

Lo S-C & Hannink M (2006). CAND1-Mediated Substrate Adaptor Recycling Is Required for Efficient Repression of Nrf2 by Keap1. *Mol Cell Biol* **26,** 1235–1244.

Lo WY, Wang HJ, Chiu CW & Chen SF (2012). MiR-27b-regulated TCTP as a novel plasma biomarker for oral cancer: From quantitative proteomics to post-transcriptional study. *J Proteomics* **77,** 154–166.

Loffing J, Loffing-cueni D, Valderrabano V, Kläusli L, Hebert SC, Rossier BC, Hoenderop JGJ, Bindels RJM, Kaissling B, Kla L, Rossier C & Bindels JM (2001). Distribution of transcellular calcium and sodium transport pathways along mouse distal nephron. *Am J Physiol - Ren Physiol* **281,** F1021--F1027.

Loffing J, Vallon V, Loffing-Cueni D, Aregger F, Richter K, Pietri L, Bloch-Faure M,

Hoenderop JGJ, Shull GE, Meneton P & Kaissling B (2004). Altered Renal Distal Tubule Structure and Renal Na+ and Ca2+ Handling in a Mouse Model for Gitelman's Syndrome. *J Am Soc Nephrol* **15,** 2276–2288.

Loggia ML, Bushnell MC, Tetreault M, Thiffault I, Bherer C, Mohammed NK, Kuchinad AA, Laferriere A, Dicaire M-J, Loisel L, Mogil JS & Brais B (2009). Carriers of recessive WNK1/HSN2 mutations for hereditary sensory and autonomic neuropathy type 2 (HSAN2) are more sensitive to thermal stimuli. *J Neurosci* **29,** 2162–2166.

de Los Heros P, Alessi DR, Gourlay R, Campbell DG, Deak M, Macartney TJ, Kahle KT & Zhang J (2014). The WNK-regulated SPAK/OSR1 kinases directly phosphorylate and inhibit the K+-Cl- co-transporters. *Biochem J* **458,** 559–573.

Louis-Dit-Picard H et al. (2012). KLHL3 mutations cause familial hyperkalemic hypertension by impairing ion transport in the distal nephron. *Nat Genet* **44,** 456–460.

Mandai S, Mori T, Sohara E, Rai T & Uchida S (2015). Generation of Hypertension-Associated STK39 Polymorphism Knockin Cell Lines With the Clustered Regularly Interspaced Short Palindromic Repeats/Cas9 System. *Hypertension* **66,** 1199–1206.

Mastroianni N, De Fusco M, Zollo M, Arrigo G, Zuffardi O, Bettinelli A, Ballabio A & Casari G (1996). Molecular cloning, expression pattern, and chromosomal localization of the human Na-Cl thiazide-sensitive cotransporter (SLC12A3). *Genomics* **35,** 486–493.

Mayan H, Munter G, Shaharabany M, Mouallem M, Pauzner R, Holtzman EJ & Farfel Z (2004). Hypercalciuria in familial hyperkalemia and hypertension accompanies hyperkalemia and precedes hypertension: Description of a large family with the Q565E WNK4 mutation. *J Clin Endocrinol Metab* **89,** 4025–4030.

Mayan H, Vered I, Mouallem M, Tzadok-Witkon M, Pauzner R & Farfel Z (2002). Pseudohypoaldosteronism type II: marked sensitivity to thiazides, hypercalciuria, normomagnesemia, and low bone mineral density. *J Clin Endocrinol Metab* **87,** 3248–3254.

McCormick JA et al. (2014). Hyperkalemic hypertension-associated cullin 3 promotes WNK signaling by degrading KLHL3. *J Clin Invest* **124,** 4723–4736.

Mccormick JA & Ellison DH (2017). Nephron Remodeling Underlies Hyperkalemia in

Familial Hyperkalemic Hypertension. 1–3.

McCormick JA & Ellison DH (2011). The WNKs: Atypical Protein Kinases With Pleiotropic Actions. *Physiol Rev* **91,** 177–219.

Mccormick JA, Mutig K, Nelson JH, Saritas T, Hoorn EJ, Yang CL, Rogers S, Curry J, Delpire E, Bachmann S & Ellison DH (2011). A SPAK isoform switch modulates renal salt transport and blood pressure. *Cell Metab* **14,** 352–364.

McEvoy JD, Kossatz U, Malek N & Singer JD (2007). Constitutive Turnover of Cyclin E by Cul3 Maintains Quiescence. *Mol Cell Biol* **27,** 3651–3666.

McMahon M, Thomas N, Itoh K, Yamamoto M & Hayes JD (2006). Dimerization of Substrate Adaptors Can Facilitate Cullin-mediated Ubiquitylation of Proteins by a "Tethering" Mechanism: A TWO-SITE INTERACTION MODEL FOR THE Nrf2-Keap1 COMPLEX . *J Biol Chem* **281,** 24756–24768.

Meireles CG, Pereira SA, Valadares LP, Rêgo DF, Simeoni LA, Guerra ENS & Lofrano-Porto A (2017). Effects of metformin on endometrial cancer: Systematic review and meta-analysis. *Gynecol Oncol*; DOI: 10.1016/j.ygyno.2017.07.120.

Melnikov S, Mayan H, Uchida S, Holtzman EJ & Farfel Z (2011). Cyclosporine metabolic side effects: Association with the WNK4 system. *Eur J Clin Invest* **41,** 1113–1120.

Mendes AI, Mascarenhas MR, Matos S, Sousa I, Ferreira J, Barbosa AP, Bicho M & Jordan P (2011). A WNK4 gene variant relates to osteoporosis and not to hypertension in the Portuguese population. *Mol Genet Metab* **102,** 465–469.

Messerli FH, Williams B & Ritz E (2007). Essential hypertension. *Lancet* **370,** 591–603.

Meyer JW, Flagella M, Sutliff RL, Lorenz JN, Nieman ML, Weber CS, Paul RJ & Shull GE (2002). Decreased blood pressure and vascular smooth muscle tone in mice lacking basolateral Na(+)-K(+)-2Cl(-) cotransporter. *Am J Physiol Hear Circ Physiol* **283,** H1846-1855.

Milburn CC, Boudeau J, Deak M, Alessi DR & van Aalten DMF (2004). Crystal structure of MO25α in complex with the C terminus of the pseudo kinase STE20-related adaptor. *Nat Struct Mol Biol* **11,** 193–200.

Miyamoto H, Matsushiro A & Nozaki M (1993). Molecular Cloning of a Novel messenger RNA Sequence Expressed in Cleavage Stage Mouse Embryos. *Mol Reprod Dev* **34,** 1–7.

Moniz S & Jordan P (2010). Emerging roles for WNK kinases in cancer. *Cell Mol Life Sci* **67,** 1265–1276.

Mori T, Kikuchi E, Watanabe Y, Fujii S, Ishigami-Yuasa M, Kagechika H, Sohara E, Rai T, Sasaki S & Uchida S (2013*a*). Chemical library screening for WNK signalling inhibitors using fluorescence correlation spectroscopy. *Biochem J* **455,** 339–345.

Mori Y, Mori T, Wakabayashi M, Yoshizaki Y, Zeniya M, Sohara E, Rai T & Uchida S (2015). Involvement of selective autophagy mediated by p62/SQSTM1 in KLHL3-dependent WNK4 degradation. *Biochem J* **472,** 33–41.

Mori Y, Wakabayashi M, Mori T, Araki Y, Sohara E, Rai T, Sasaki S & Uchida S (2013*b*). Decrease of WNK4 ubiquitination by disease-causing mutations of KLHL3 through different molecular mechanisms. *Biochem Biophys Res Commun* **439,** 30–34.

Moriguchi T, Urushiyama S, Hisamoto N, Iemura S, Uchida S, Natsume T, Matsumoto K & Shibuya H (2005). WNK1 regulates phosphorylation of cation-chloride-coupled cotransporters via the STE20-related kinases, SPAK and OSR1. *J Biol Chem* **280,** 42685–42693.

Munir S, Guilcher A, Kamalesh T, Clapp B, Redwood S, Marber M & Chowienczyk P (2007). Peripheral Augmentation Index Defines the Relationship Between Central and Peripheral Pulse Pressure. *Hypertension* **51,** 112–118.

Murthy M, Kurz T & O'Shaughnessy KM (2016). ROMK expression remains unaltered in a mouse model of familial hyperkalemic hypertension caused by the CUL3??403-459 mutation. *Physiol Rep*; DOI: 10.14814/phy2.12850.

Na T, Wu G & Peng J-B (2012). Disease-causing mutations in the acidic motif of WNK4 impair the sensitivity of WNK4 kinase to calcium ions. *Biochem Biophys Res Commun* **419,** 293–298.

Nakamichi N, Murakami-Kojima M, Sato E, Kishi Y, Yamashino T & Mizuno T (2002). Compilation and characterization of a novel WNK family of protein kinases in Arabiodpsis thaliana with reference to circadian rhythms. *Biosci Biotechnol Biochem* **66,**

2429–2436.

Nicolet-Barousse L, Blanchard A, Roux C, Pietri L, Bloch-Faure M, Kolta S, Chappard C, Geoffroy V, Morieux C, Jeunemaitre X, Shull GE, Meneton P, Paillard M, Houillier P & De Vernejoul MC (2005). Inactivation of the Na-Cl Co-transporter (NCC) gene is associated with high BMD through both renal and bone mechanisms: Analysis of patients with Gitelman syndrome and Ncc null mice. *J Bone Miner Res* **20,** 799–808.

Nozaki M, Onishi Y, Togashi S & Miyamoto H (1996). Molecular characterization of the Drosophila Mo25 gene, which is conserved among Drosophila, mouse, and yeast. *DNA Cell Biol* **15,** 505–509.

O'Reilly M, Marshall E, Speirs HJL & Brown RW (2003). WNK1, a gene within a novel blood pressure control pathway, tissue-specifically generates radically different isoforms with and without a kinase domain. *J Am Soc Nephrol* **14,** 2447–2456.

O'Shaughnessy KM & Karet FE (2004). Salt handling and hypertension. *J Clin Invest* **113,** 1075–1081.

O'Shaughnessy KM & Karet FE (2006). Salt Handling and Hypertension. *Annu Rev Nutr* **26,** 343–365.

Ohta A, Schumacher F-RR, Mehellou Y, Johnson C, Knebel A, Macartney TJ, Wood NT, Alessi DR & Kurz T (2013). The CUL3-KLHL3 E3 ligase complex mutated in Gordon's hypertension syndrome interacts with and ubiquitylates WNK isoforms: disease-causing mutations in KLHL3 and WNK4 disrupt interaction. *Biochem J* **451,** 111–122.

Olmos JM, Hernández JL, Martínez J, Castillo J, Valero C, Pérez Pajares I, Nan D & González-Macías J (2010). Bone turnover markers and bone mineral density in hypertensive postmenopausal women on treatment. *Maturitas* **65,** 396–402.

Orlov SN, Koltsova S V., Tremblay J, Baskakov MB & Hamet P (2012). NKCC1 and hypertension: Role in the regulation of vascular smooth muscle contractions and myogenic tone. *Ann Med* **44,** S111--S118.

Orlov SN & Mongin AA (2007). Salt-sensing mechanisms in blood pressure regulation and hypertension. *Am J Physiol Circ Physiol* **293,** H2039–H2053.

Osawa M, Ogura Y, Isobe K, Uchida S, Nonoyama S & Kawaguchi H (2013). CUL3 gene

analysis enables early intervention for pediatric pseudohypoaldosteronism type II in infancy. *Pediatr Nephrol* **28,** 1881–1884.

Park HJ, Curry JN & Mccormick JA (2013). Regulation of NKCC2 activity by inhibitory SPAK isoforms: KS-SPAK is a more potent inhibitor than SPAK2. *Am J Physiol - Ren Physiol* **305,** F1687--F1696.

Park HW, Kim JY, Choi S-K, Lee Y-H, Zeng W, Kim KH, Muallem S & Lee MG (2011). Serine-threonine kinase with-no-lysine 4 (WNK4) controls blood pressure via transient receptor potential canonical 3 (TRPC3) in the vasculature. *Proc Natl Acad Sci* **108,** 10750–10755.

Parker JC (1993). In defense of cell volume? *Am J Physiol* **265,** C1191-200.

Pasham V, Pathare G, Fajol A, Rexhepaj R, Michael D, Pakladok T, Alesutan I, Rotte A, Foller M, Lang F, Föller M & Lang F (2012*a*). OSR1-sensitive small intestinal Na+ transport. *AJP Gastrointest Liver Physiol* **303,** G1212--G1219.

Pasham V, Rotte A, Yang W, Zelenak C, Bhandaru M, Föller M & Lang F (2012*b*). OSR1-sensitive regulation of Na+/H+ exchanger activity in dendritic cells. *Am J Physiol Physiol* **303,** C416–C426.

Pathare G, Föller M, Michael D, Walker B, Hierlmeier M, Mannheim JG, Pichler BJ & Lang F (2012). Enhanced FGF23 serum concentrations and phosphaturia in gene targeted mice expressing WNK-resistant SPAK. *Kidney Blood Press Res* **36,** 355–364.

Pelham CJ, Ketsawatsomkron P, Groh S, Grobe JL, De Lange WJ, Ibeawuchi SRC, Keen HL, Weatherford ET, Faraci FM & Sigmund CD (2012). Cullin-3 regulates vascular smooth muscle function and arterial blood pressure via PPARγ and RhoA/Rho-kinase. *Cell Metab* **16,** 462–472.

Penton D, Czogalla J, Wengi A, Himmerkus N, Loffing-Cueni D, Carrel M, Rajaram RD, Staub O, Bleich M, Schweda F & Loffing J (2016). Extracellular K {<}sup{>}+{<}/sup{>} rapidly controls NaCl cotransporter phosphorylation in the native distal convoluted tubule by Cl {<}sup{>}−{<}/sup{>} -dependent and independent mechanisms. *J Physiol* **594,** 6319–6331.

Pettersen EF, Goddard TD, Huang CC, Couch GS, Greenblatt DM, Meng EC & Ferrin TE

(2004). UCSF Chimera--a visualization system for exploratory research and analysis. *J Comput Chem* **25,** 1605–1612.

Piala AT, Moon TM, Akella R, He H, Cobb MH, May EJG & Goldsmith EJ (2014). Chloride Sensing by WNK1 Involves Inhibition of Autophosphorylation. *Sci Signal* **7,** ra41--ra41.

Pichlmair A et al. (2012). Viral immune modulators perturb the human molecular network by common and unique strategies. *Nature* **487,** 486–490.

Piechotta K, Garbarini N, England R & Delpire E (2003). Characterization of the interaction of the stress kinase SPAK with the Na+-K+-2Cl- cotransporter in the nervous system: Evidence for a scaffolding role of the kinase. *J Biol Chem* **278,** 52848–52856.

Piechotta K, Lu J & Delpire E (2002). Cation chloride cotransporters interact with the stress-related kinases Ste20-related proline-alanine-rich kinase (SPAK) and oxidative stress response 1 (OSR1). *J Biol Chem* **277,** 50812–50819.

Pierce NW, Lee JE, Liu X, Sweredoski MJ, Rlj G, Larimore EA, Rome M, Zheng N, Clurman BE, Hess S, S-o S & Deshaies RJ (2013). Cand1 Promotes Assembly of New SCF Complexes through Dynamic Exchange of F Box Proteins. *Cell* **153,** 206–215.

Pintard L, Kurz T, Glaser S, Willis JH, Peter M & Bowerman B (2003). Neddylation and deneddylation of CUL-3 is required to target MEI-1/Katanin for degradation at the meiosis-to-mitosis transition in C. elegans. *Curr Biol* **13,** 911–921.

Piotrowski J, Beal R, Hoffman L, Wilkinson KD, Cohen RE & Pickart CM (1997). Inhibition of the 26 S Proteasome by Polyubiquitin Chains Synthesized to Have Defined Lengths. *J Biol Chem* **272,** 23712–23721.

Plechanovová A, Jaffray EG, McMahon SA, Johnson KA, Navratilova I, Naismith JH & Hay RT (2011). Mechanism of ubiquitylation by dimeric RING ligase RNF4. *Nat Struct Mol Biol* **18,** 1052–1059.

Ponce-Coria J et al. (2008). Regulation of NKCC2 by a chloride-sensing mechanism involving the WNK3 and SPAK kinases. *Proc Natl Acad Sci U S A* **105,** 8458–8463.

Ponce-Coria J, Gagnon KB & Delpire E (2012). Calcium-binding protein 39 facilitates molecular interaction between Ste20p proline alanine-rich kinase and oxidative stress response 1 monomers. *Am J Physiol Physiol* **303,** C1198–C1205.

Ponce-Coria J, Markadieu N, Austin TM, Flammang L, Rios K, Welling PA & Delpire E (2014). A novel Ste20-related Proline/Alanine-rich Kinase (SPAK)-independent pathway involving Calcium-binding Protein 39 (Cab39) and Serine Threonine Kinase with No Lysine Member 4 (WNK4) in the activation of Na-K-Cl cotransporters. *J Biol Chem* **289,** 17680–17688.

Potulska-Chromik A, Kabzińska D, Lipowska M, Kostera-Pruszczyk A & Kochański A (2012). A novel homozygous mutation in the WNK1/HSN2 gene causing hereditary sensory neuropathy type 2. *Acta Biochim Pol* **59,** 413–415.

Prasad V, Bodi I, Meyer JW, Wang Y, Ashraf M, Engle SJ, Doetschman T, Sisco K, Nieman ML, Miller ML et al., Lorenz JN & Shull GE (2008). Impaired Cardiac Contractility in Mice Lacking Both the AE3 Formula Exchanger and the NKCC1 Na+-K+-2Cl-Cotransporter: Effects on Ca2+ handling and protein phosphatases. *J Biol Chem* **283,** 31303–31314.

Pulito C, Mori F, Sacconi A, Goeman F, Ferraiuolo M, Pasanisi P, Campagnoli C, Berrino F, Fanciulli M, Ford RJ, Levrero M, Pediconi N, Ciuffreda L, Milella M, Steinberg GR, Cioce M, Muti P, Strano S & Blandino G (2017). Metformin-induced ablation of microRNA 21-5p releases Sestrin-1 and CAB39L antitumoral activities. *Cell Discov* **3,** 17022.

Qiao Y, Liu X, Harvard C, Hildebrand MJ, Rajcan-Separovic E, Holden JJA & Lewis MES (2008). Autism-associated familial microdeletion of Xp11.22. *Clin Genet* **74,** 134–144.

Quinn SJ, Thomsen ARB, Pang JL, Kantham L, Brauner-Osborne H, Pollak M, Goltzman D & Brown EM (2012). Interactions between calcium and phosphorus in the regulation of the production of fibroblast growth factor 23 in vivo. *AJP Endocrinol Metab* **304,** E310--E320.

Rabut G, Le Dez G, Verma R, Makhnevych T, Knebel A, Kurz T, Boone C, Deshaies RJ & Peter M (2011). The TFIIH subunit Tfb3 regulates cullin neddylation. *Mol Cell* **43,** 488–495.

Rafiqi FH et al. (2010). Role of the WNK-activated SPAK kinase in regulating blood pressure. *EMBO Mol Med* **2,** 63–75.

Rahmioglu N, MacGregor S, Drong AW, Hedman ÅK, Harris HR, Randall JC, Prokopenko I,

Nyholt DR, Morris AP, Montgomery GW, Missmer SA, Lindgren CM & Zondervan KT (2015). Genome-wide enrichment analysis between endometriosis and obesity-related traits reveals novel susceptibility loci. *Hum Mol Genet* **24,** 1185–1199.

Ramoz N, Cai G, Reichert JG, Silverman JM & Buxbaum JD (2008). An analysis of candidate autism loci on chromosome 2q24-q33: Evidence for association to the STK39 gene. *Am J Med Genet Part B Neuropsychiatr Genet* **147,** 1152–1158.

Rejnmark L, Vestergaard P, Pedersen AR, Heickendorff L, Andreasen F & Mosekilde L (2003). Dose-effect relations of loop- and thiazide-diuretics on calcium homeostasis: a randomized, double-blinded Latin-square multiple cross-over study in postmenopausal osteopenic women. *Eur J Clin Invest* **33,** 41–50.

Ren H, Qin L, Wang W, Ma J, Zhang W, Shen PY, Shi H, Li X & Chen N (2013). Abnormal glucose metabolism and insulin sensitivity in Chinese patients with Gitelman syndrome. *Am J Nephrol* **37,** 152–157.

Richardson C & Alessi DR (2008). The regulation of salt transport and blood pressure by the WNK-SPAK/OSR1 signalling pathway. *J Cell Sci* **121,** 3293–3304.

Richardson C, Rafiqi FH, Karlsson HKR, Moleleki N, Vandewalle A, Campbell DG, Morrice NA & Alessi DR (2008). Activation of the thiazide-sensitive Na+-Cl- cotransporter by the WNK-regulated kinases SPAK and OSR1. *J Cell Sci* **121,** 675–684.

Richardson C, Sakamoto K, de los Heros P, Deak M, Campbell DG, Prescott AR & Alessi DR (2011). Regulation of the NKCC2 ion cotransporter by SPAK-OSR1-dependent and -independent pathways. *J Cell Sci* **124,** 789–800.

Rinehart J, Kahle KT, de Los Heros P, Vazquez N, Meade P, Wilson FH, Hebert SC, Gimenez I, Gamba G, Lifton RP, Heros PDL, Vazquez N, Meade P, Wilson FH, Hebert SC, Gimenez I, Gamba G & Lifton RP (2005). WNK3 kinase is a positive regulator of NKCC2 and NCC, renal cation-Cl- cotransporters required for normal blood pressure homeostasis. *Proc Natl Acad Sci U S A* **102,** 16777–16782.

Rinehart J, Vázquez N, Kahle KT, Hodson CA, Ring AM, Gulcicek EE, Louvi A, Bobadilla NA, Gamba G & Lifton RP (2011). WNK2 kinase is a novel regulator of essential neuronal cation-chloride cotransporters. *J Biol Chem* **286,** 30171–30180.

Riveira-Munoz E, Devuyst O, Belge H, Jeck N, Strompf L, Vargas-Poussou R, Jeunemaître X, Blanchard A, Knoers N V., Konrad M & Dahan K (2008). Evaluating PVALB as a candidate gene for SLC12A3-negative cases of Gitelman's syndrome. *Nephrol Dial Transplant* **23,** 3120–3125.

Rodan A, Wu Y, Sun Q, Humphreys J, Schellinger J & Goldsmith E (2017). Intracellular Cl− and the Scaffold Protein Mo25/Cab39 Regulate WNK-SPAK/OSR1 Signaling in Transepithelial Ion Transport. *FASEB J* **31,** 856.13-856.13.

Rodriguez-Ortiz ME, Lopez I, Munoz-Castaneda JR, Martinez-Moreno JM, Ramirez AP, Pineda C, Canalejo A, Jaeger P, Aguilera-Tejero E, Rodriguez M, Felsenfeld A & Almaden Y (2012). Calcium deficiency reduces circulating levels of FGF23. *J Am Soc Nephrol* **23,** 1190–1197.

Rotin D & Staub O (2012). Nedd4-2 and the regulation of epithelial sodium transport. *Front Physiol* **3,** 212.

Rozansky DJ, Cornwall T, Subramanya AR, Rogers S, Yang YF, David LL, Zhu X, Yang CL & Ellison DH (2009). Aldosterone mediates activation of the thiazide-sensitive Na-Cl cotransporter through an SGK1 and WNK4 signaling pathway. *J Clin Invest* **119,** 2601–2612.

Safar ME (2001). Systolic blood pressure, pulse pressure and arterial stiffness as cardiovascular risk factors. *Curr Opin Nephrol Hypertens* **10,** 257–261.

Santos F, Gil-Peña H, Blázquez C & Coto E (2016). Gitelman syndrome: a review of clinical features, genetic diagnosis and therapeutic management. *Expert Opin Orphan Drugs* **4,** 1005–1009.

Sasaki E, Susa K, Mori T, Isobe K, Araki Y, Inoue Y, Yoshizaki Y, Ando F, Mori Y, Mandai S, Zeniya M, Takahashi D, Nomura N, Rai T, Uchida S & Sohara E (2017). KLHL3 knockout mice reveal the physiological role of KLHL3 and the pathophysiology of PHAII caused by mutant KLHL3. *Mol Cell Biol* **37,** e00508-16.

Schneeberger PR & Heizmann CW (1986). Parvalbumin in rat kidney. Purification and localization. *FEBS Lett* **201,** 51–56.

Schumacher F-R, Sorrell FJ, Alessi DR, Bullock AN & Kurz T (2014). Structural and

biochemical characterization of the KLHL3–WNK kinase interaction important in blood pressure regulation. *Biochem J* **460,** 237–246.

Schumacher F-RF-R et al. (2015). Characterisation of the Cullin-3 mutation that causes a severe form of familial hypertension and hyperkalaemia. *EMBO Mol Med* **7,** 1285–1306.

Scott DC, Sviderskiy VO, Monda JK, Lydeard JR, Cho SE, Harper JW & Schulman BA (2014). Structure of a RING E3 Trapped in Action Reveals Ligation Mechanism for the Ubiquitin-like Protein NEDD8. *Cell* **157,** 1671–1684.

Seyberth HW & Schlingmann KP (2011). Bartter- and Gitelman-like syndromes: salt-losing tubulopathies with loop or DCT defects. *Pediatr Nephrol* **26,** 1789–1802.

Shao L, Ren H, Wang W, Zhang W, Feng X, Li X & Chen N (2008). Novel SLC12A3 mutations in Chinese patients with Gitelman's syndrome. *Nephron - Physiol*; DOI: 10.1159/000117815.

Shekarabi M, Girard N, Rivière J, Dion P, Houle M, Toulouse A, Lafrenière RG, Vercauteren F, Hince P, Laganiere J, Rochefort D, Faivre L, Samuels M & Rouleau GA (2008). Mutations in the nervous system - specific HSN2 exon of WNK1 cause hereditary sensory neuropathy type II. *J Clin Invest* **118,** 2496–2505.

Shibata S et al. (2014). Angiotensin II signaling via protein kinase C phosphorylates Kelch-like 3, preventing WNK4 degradation. *Proc Natl Acad Sci* **111,** 15556–15561.

Shibata S, Zhang J, Puthumana J, Stone KL & Lifton RP (2013). Kelch-like 3 and Cullin 3 regulate electrolyte homeostasis via ubiquitination and degradation of WNK4. *Proc Natl Acad Sci USA* **110,** 7838–7843.

Shui J-W, Hu MC-T & Tan T-H (2007). Conditional knockout mice reveal an essential role of protein phosphatase 4 in thymocyte development and pre-T-cell receptor signaling. *Mol Cell Biol* **27,** 79–91.

Siew K & O'Shaughnessy KM (2013). Extrarenal roles of the with-no-lysine[K] kinases (WNKs). *Clin Exp Pharmacol Physiol* **40,** 885–894.

Silke J, Kratina T, Chu D, Ekert PG, Day CL, Pakusch M, Dcs H & Vaux DL (2005). Determination of cell survival by RING-mediated regulation of inhibitor of apoptosis (IAP) protein abundance. *Proc Natl Acad Sci USA* **102,** 16182–16187.

Simon DB, Nelson-Williams C, Johnson Bia M, Ellison D, Karet FE, Morey Molina A, Vaara I, Iwata F, Cushner HM, Koolen M, Gainza FJ, Gitelman HJ & Lifton RP (1996). Gitelman's variant of Barter's syndrome, inherited hypokalaemic alkalosis, is caused by mutations in the thiazide-sensitive Na–Cl cotransporter. *Nat Genet* **12,** 24–30.

Singer JD, Gurian-West M, Clurman B & Roberts JM (1999). Cullin-3 targets cyclin E for ubiquitination and controls S phase in mammalian cells. *Genes Dev* **13,** 2375–2387.

Somlyo AP & Somlyo A V (2003). Ca2+ sensitivity of smooth muscle and nonmuscle myosin II: modulated by G proteins, kinases, and myosin phosphatase. *Physiol Rev* **83,** 1325–1358.

Subramanya AR, Liu J, Ellison DH, Wade JB & Welling PA (2009). WNK4 diverts the thiazide-sensitive NaCl cotransporter to the lysosome and stimulates AP-3 interaction. *J Biol Chem* **284,** 18471–18480.

Subramanya AR, Yang C, Zhu X & Ellison DH (2006). Dominant-negative regulation of WNK1 by its kidney-specific kinase-defective isoform. *AJP Ren Physiol* **290,** F619--24.

Sumara I, Quadroni M, Frei C, Olma MH, Sumara G, Ricci R & Peter M (2007). A Cul3-Based E3 Ligase Removes Aurora B from Mitotic Chromosomes, Regulating Mitotic Progression and Completion of Cytokinesis in Human Cells. *Dev Cell* **12,** 887–900.

Susa K, Sohara E, Isobe K, Chiga M, Rai T, Sasaki S & Uchida S (2012). WNK-OSR1/SPAK-NCC signal cascade has circadian rhythm dependent on aldosterone. *Biochem Biophys Res Commun* **427,** 743–747.

Susa K, Sohara E, Rai T, Zeniya M, Mori Y, Mori T, Chiga M, Nomura N, Nishida H, Takahashi D, Isobe K, Inoue Y, Takeishi K, Takeda N, Sasaki S & Uchida S (2014). Impaired degradation of WNK1 and WNK4 kinases causes PHAII in mutant KLHL3 knock-in mice. *Hum Mol Genet* **23,** 5052–5060.

Takahashi D, Mori T, Nomura N, Khan MZH, Araki Y, Zeniya M, Sohara E, Rai T, Sasaki S & Uchida S (2014). WNK4 is the major WNK positively regulating NCC in the mouse kidney. *Biosci Rep* **34,** 195–206.

Takahashi D, Mori T, Wakabayashi M, Mori Y, Susa K, Zeniya M, Sohara E, Rai T, Sasaki S & Uchida S (2013). KLHL2 interacts with and ubiquitinates WNK kinases. *Biochem*

Biophys Res Commun **437,** 457–462.

Tanaka K, Kitagawa M, Onishi A, Yamanari T, Ogawa-Akiyama A, Mise K, Inoue T, Morinaga H, Uchida HA, Sugiyama H & Wada J (2017). Arterial Stiffness is an Independent Risk Factor for Anemia after Percutaneous Native Kidney Biopsy. *Kidney Blood Press Res* **42,** 284–293.

Terker AS, Zhang C, Erspamer KJ, Gamba G, Yang C-L & Ellison DH (2015*a*). Unique chloride-sensing properties of WNK4 permit the distal nephron to modulate potassium homeostasis. *Kidney Int* **89,** 1–8.

Terker AS, Zhang CC, McCormick JA, Lazelle RA, Zhang CC, Meermeier NP, Siler DA, Park HJ, Fu Y, Cohen DM, Weinstein AM, Wang WH, Yang CL & Ellison DH (2015*b*). Potassium modulates electrolyte balance and blood pressure through effects on distal cell voltage and chloride. *Cell Metab* **21,** 39–50.

Thastrup JO, Rafiqi FH, Vitari AC, Pozo-Guisado E, Deak M, Mehellou Y & Alessi DR (2012). SPAK/OSR1 regulate NKCC1 and WNK activity: analysis of WNK isoform interactions and activation by T-loop trans-autophosphorylation. *Biochem J* **441,** 325–337.

Thul PJ et al. (2017). A subcellular map of the human proteome. *Science (80-)* **356,** eaal3321.

Torre-Villalvazo I, Cervantes-Perez LG, Noriega LG, Jimenez J V, Uribe N, Chavez-Canales M, Tovar-Palacio C, Marfil-Garza BA, Torres N, Bobadilla NA, Tovar AR & Gamba G (2017). Inactivation of SPAK kinase reduces body weight gain in mice fed a High-fat diet by improving energy expenditure and insulin sensitivity. *Am J Physiol - Endocrinol Metab*ajpendo.00108.2017.

Tsuji S, Yamashita M, Unishi G, Takewa R, Kimata T, Isobe K, Chiga M, Uchida S & Kaneko K (2013). A young child with pseudohypoaldosteronism type II by a mutation of Cullin 3. *BMC Nephrol* **14,** 166.

Uhlen M et al. (2015). Tissue-based map of the human proteome. *Science (80-)* **347,** 1260419–1260419.

Unwin RJ & Capasso G (2006). Bartter's and Gitelman's syndromes: Their relationship to the actions of loop and thiazide diuretics. *Curr Opin Pharmacol* **6,** 208–213.

Veríssimo F & Jordan P (2001). WNK kinases, a novel protein kinase subfamily in multi-cellular organisms. *Oncogene* **20,** 5562–5569.

Vidal-Petiot E, Cheval L, Faugeroux J, Malard T, Doucet A, Jeunemaitre X & Hadchouel J (2012). A New Methodology for Quantification of Alternatively Spliced Exons Reveals a Highly Tissue-Specific Expression Pattern of WNK1 Isoforms. *PLoS One* **7,** e37751.

Vidal-petiot E, Elvira-matelot E, Mutig K, Soukaseum C & Baudrie V (2013). WNK1 -related Familial Hyperkalemic Hypertension results from an increased expression of L-WNK1 speci fi cally in the distal nephron. ; DOI: 10.1073/pnas.1304230110/-/DCSupplemental.www.pnas.org/cgi/doi/10.1073/pnas.1304230110.

Viganò C, Amoruso C, Barretta F, Minnici G, Albisetti W, Syrèn M-L, Bianchetti MG & Bettinelli A (2012). Renal phosphate handling in Gitelman syndrome—the results of a case–control study. *Pediatr Nephrol* **28,** 65–70.

Villa F, Goebel J, Rafiqi FH, Deak M, Thastrup J, Alessi DR & van Aalten DMF (2007). Structural insights into the recognition of substrates and activators by the OSR1 kinase. *EMBO Rep* **8,** 839–845.

Vinck WJ Loos R, Vlietinck R. FRH (2001). The impact of genetic and environmental influences on blood pressure variance across age-groups. *J Hypertens* **19,** 1007–1013.

Vitari AC, Deak M, Morrice NA & Alessi DR (2005). The WNK1 and WNK4 protein kinases that are mutated in Gordon's hypertension syndrome phosphorylate and activate SPAK and OSR1 protein kinases. *Biochem J* **391,** 17–24.

Vitari AC, Thastrup J, Rafiqi FH, Deak M, Morrice NA, Karlsson HKR & Alessi DR (2006). Functional interactions of the SPAK/OSR1 kinases with their upstream activator WNK1 and downstream substrate NKCC1. *Biochem J* **397,** 223–231.

Wagner CA, Loffing-Cueni D, Yan Q, Schulz N, Fakitsas P, Carrel M, Wang T, Verrey F, Geibel JP, Giebisch G, Hebert SC & Loffing J (2008). Mouse model of type II Bartter's syndrome. II. Altered expression of renal sodium- and water-transporting proteins. *Am J Physiol Physiol* **294,** F1373–F1380.

Wakabayashi M, Mori T, Isobe K, Sohara E, Susa K, Araki Y, Chiga M, Kikuchi E, Nomura N, Mori Y et al., Matsuo H, Murata T, Nomura S, Asano T, Kawaguchi H, Nonoyama S,

Rai T, Sasaki S & Uchida S (2013). Impaired KLHL3-mediated ubiquitination of WNK4 causes human hypertension. *Cell Rep* **3,** 858–868.

Walsh AH, Cheng A & Honkanen RE (1997). Fostriecin, an antitumor antibiotic with inhibitory activity against serine/threonine protein phosphatases types 1 (PP1) and 2A (PP2A), is highly selective for PP2A. *FEBS Lett* **416,** 230–234.

Wang DD & Kriegstein AR (2011). Blocking early GABA depolarization with bumetanide results in permanent alterations in cortical circuits and sensorimotor gating deficits. *Cereb Cortex* **21,** 574–587.

Wang L & Peng J-B (2017). Phosphorylation of KLHL3 at serine 433 impairs its interaction with the acidic motif of WNK4: a molecular dynamics study. *Protein Sci* **26,** 163–173.

Wang Y et al. (2009). Whole-genome association study identifies STK39 as a hypertension susceptibility gene. *Proc Natl Acad Sci U S A* **106,** 226–231.

Wee S, Geyer RK, Toda T & Wolf DA (2005). CSN facilitates Cullin-RING ubiquitin ligase function by counteracting autocatalytic adapter instability. *Nat Cell Biol* **7,** 387–391.

Wilson FH, Disse-Nicodème S, Choate KA, Ishikawa K, Nelson-Williams C, Desitter I, Gunel M, Milford D V., Lipkin GW, Achard JM, Feely MP, Dussol B, Berland Y, Unwin RJ, Mayan H, Simon DB, Farfel Z, Jeunemaitre X & Lifton RP (2001). Human hypertension caused by mutations in WNK kinases. *Science (80-)* **293,** 1107–1112.

Wilson LE, Harlid S, Xu Z, Sandler DP & Taylor JA (2017). An epigenome-wide study of body mass index and DNA methylation in blood using participants from the Sister Study cohort. *Int J Obes* **41,** 194–199.

Wimuttisuk W & Singer JD (2007). The Cullin3 Ubiquitin Ligase Functions as a Nedd8-bound Heterodimer. *Mol Biol Cell* **18,** 899–909.

Wolff S, Weissman JS & Dillin A (2014). Differential scales of protein quality control. *Cell* **157,** 52–64.

World Health Organisation (2007). WHO | Prevention of cardiovascular disease. *WHO*. Available at: http://www.who.int/cardiovascular_diseases/publications/Prevention_of_Cardiovascular_Disease/en/.

World Health Organisation (2012). WHO | World Health Statistics 2012. *WHO*. Available at: http://www.who.int/gho/publications/world_health_statistics/2012/en/.

World Health Organisation (2016). WHO | Fact Sheets: Salt reduction. *WHO*. Available at: http://www.who.int/news-room/fact-sheets/detail/salt-reduction.

Wu G & Peng J Bin (2013). Disease-causing mutations in KLHL3 impair its effect on WNK4 degradation. *FEBS Lett* **587,** 1717–1722.

Wu J, Agbor LN, Fang S, Hu C, Lu K-T, Liu X, Mukohda M, Nair AR & Sigmund CD (2017*b*). Endothelial Cullin3 Mutation Causes Vascular Dysfunction, Arterial Stiffening, and Hypertension. *FASEB J* **31,** 1015.20.

Wu J, Agbor LN, Fang S, Hu C, Lu K-T, Liu X, Mukohda M, Nair AR & Sigmund CD (2017*a*). Endothelial Cullin3 Mutation Causes Vascular Dysfunction, Arterial Stiffening, and Hypertension. *Hypertension* **70,** AP189.

Xiao P, Chen Y, Jiang H, Liu YZ, Pan F, Yang TL, Tang ZH, Larsen JA, Lappe JM, Recker RR & Deng HW (2008). *In vivo* genome-wide expression study on human circulating B cells suggests a novel ESR1 and MAPK3 network for postmenopausal osteoporosis. *J Bone Miner Res* **23,** 644–654.

Xie J, Wu T, Xu K, Huang IK, Cleaver O & Huang CL (2009). Endothelial-specific expression of WNK1 kinase is essential for angiogenesis and heart development in mice. *Am J Pathol* **175,** 1315–1327.

Xu B, Stippec S, Chu PY, Lazrak A, Li XJ, Lee BH, English JM, Ortega B, Huang CL & Cobb MH (2005). WNK1 activates SGK1 to regulate the epithelial sodium channel. *Proc Natl Acad Sci* **102,** 10315–10320.

Xu BE, English JM, Wilsbacher JL, Stippec S, Goldsmith EJ & Cobb MH (2000). WNK1, a novel mammalian serine/threonine protein kinase lacking the catalytic lysine in subdomain II. *J Biol Chem* **275,** 16795–16801.

Yagi YI, Abe K, Ikebukuro K & Sode K (2009). Kinetic mechanism and inhibitor characterization of WNK1 kinase. *Biochemistry* **48,** 10255–10266.

Yamada K et al. (2016*a*). Small-molecule WNK inhibition regulates cardiovascular and renal function. *Nat Chem Biol* **12,** 896–898.

Yamada K et al. (2016*b*). Discovery and Characterization of Allosteric WNK Kinase Inhibitors. *ACS Chem Biol* **11,** 3338–3346.

Yamada K et al. (2017). Optimization of Allosteric With-No-Lysine (WNK) Kinase Inhibitors and Efficacy in Rodent Hypertension Models. *J Med Chem* **60,** 7099–7107.

Yamamoto Y, Izumi Y & Matsuzaki F (2008). The GC kinase Fray and Mo25 regulate Drosophila asymmetric divisions. *Biochem Biophys Res Commun* **366,** 212–218.

Yang C-LL, Zhu X, Wang Z, Subramanya AR & Ellison DH (2005). Mechanisms of WNK1 and WNK4 interaction in the regulation of thiazide-sensitive NaCl cotransport. *J Clin Invest* **115,** 1379–1387.

Yang CL, Angell J, Mitchell R & Ellison DH (2003). WNK kinases regulate thiazide-sensitive Na-Cl cotransport. *J Clin Invest* **111,** 1039–1045.

Yang CL, Zhu X & Ellison DH (2007*a*). The thiazide-sensitive Na-Cl cotransporter is regulated by a WNK kinase signaling complex. *J Clin Invest* **117,** 3403–3411.

Yang S-S, Fang Y, Tseng M, Cheng H & Lin S-HP (2013). Augmented Calcium-Binding Protein 39 (Cab39) Expression in Renal Tubule Contributes to Salt-Sensitive Hypertension through Activating N(K)CC. *J Am Soc Nephrol* **24Abstract,** 532A.

Yang S-S, Lin S-HP & Cheng C-J (2014). Increased Calcium-Binding Protein 39 (Cab39) Expression in Renal Tubule Recuses the Gitelman-Like Phenotype in Wnk4 Knockout Mice. *J Am Soc Nephrol* **25Abstract,** 28A.

Yang S-S Sen et al. (2007*b*). Molecular Pathogenesis of Pseudohypoaldosteronism Type II: Generation and Analysis of a Wnk4D561A/+ Knockin Mouse Model. *Cell Metab* **5,** 331–344.

Yang S Sen, Hsu YJ, Chiga M, Rai T, Sasaki S, Uchida S & Lin SH (2010*a*). Mechanisms for hypercalciuria in pseudohypoaldosteronism type II-causing WNK4 knock-in mice. *Endocrinology* **151,** 1829–1836.

Yang S Sen, Lo YF, Yu IS, Lin SW, Chang TH, Hsu YJ, Chao TK, Sytwu HK, Uchida S, Sasaki S & Lin SH (2010*b*). Generation and analysis of the thiazide-sensitive Na+-Cl- cotransporter (Ncc/Slc12a3) Ser707X knockin mouse as a model of Gitelman syndrome. *Hum Mutat* **31,** 1304–1315.

Yang SS et al. (2010*c*). SPAK-Knockout Mice Manifest Gitelman Syndrome and Impaired Vasoconstriction. *J Am Soc Nephrol* **21,** 1868–1877.

Yang Y, Xie J, Yang S, Lin S, Huang C, Drive H & Gh E (2018). Differential roles of WNK4 in regulation of NCC in vivo Division of Nephrology , Department of Medicine , UT Southwestern Medical Center , Graduate Institute of Biomedical Sciences , Academia Sinica , Taipei , Taiwan University of Iowa Carver College of M.

Yasin A, Liu D, Chau L, Madrenas J & Filler G (2013). Fibroblast growth factor-23 and calcium phosphate product in young chronic kidney disease patients: A cross-sectional study. *BMC Nephrol* **14,** 39.

Ye ZY, Li DP, Byun HS, Li L & Pan HL (2012). NKCC1 upregulation disrupts chloride homeostasis in the hypothalamus and increases neuronal activity-sympathetic drive in hypertension. *J Neurosci* **32,** 8560–8568.

Yoshida S, Araki Y, Mori T, Sasaki E, Kasagi Y, Isobe K, Susa K, Inoue Y, Rai T, Uchida S & Sohara E (2017). Decreased Protein Expression of KLHL3 Is Involved in the Pathogenesis of PHAII Caused by CUL3 Mutation In Vivo. *J Am Soc Nephrol* **28Abstract,** 946.

Yoshida T, Kato K, Yokoi K, Oguri M, Watanabe S, Metoki N, Yoshida H, Satoh K, Aoyagi Y, Nozawa Y & Yamada Y (2010). Association of genetic variants with hemorrhagic stroke in Japanese individuals. *Int J Mol Med* **25,** 649–656.

Yoshizaki Y et al. (2015). Impaired degradation of WNK by Akt and PKA phosphorylation of KLHL3. *Biochem Biophys Res Commun* **467,** 229–234.

Yu ASL (2006). WNK signaling in the distal tubule: an inhibitory cascade regulating salt transport. *Am J Physiol Renal Physiol* **290,** F617--8.

Yuan J, Wang K, Yi G, Ma M, Dou T, Sun C, Qu L-J, Shen M, Qu L & Yang N (2015). Genome-wide association studies for feed intake and efficiency in two laying periods of chickens. *Genet Sel Evol* **47,** 82.

Yuan T, Jiang L, Chen C, Peng X, Nie M, Li X, Xing X, Li X & Chen L (2017). Glucose tolerance and insulin responsiveness in Gitelman syndrome patients. *Endocr Connect* **6,** 243–252.

Zacchia M & Capasso G (2008). Parvalbumin: A key protein in early distal tubule NaCl reabsorption. *Nephrol Dial Transplant* **23,** 1109–1111.

Zambrowicz BP et al. (2003). Wnk1 kinase deficiency lowers blood pressure in mice: A gene-trap screen to identify potential targets for therapeutic intervention. *Proc Natl Acad Sci* **100,** 14109–14114.

Zemla A, Thomas Y, Kedziora S, Knebel A, Wood NT, Rabut G & Kurz T (2013). CSN- and CAND1-dependent remodelling of the budding yeast SCF complex. *Nat Commun* **4,** 1641.

Zeniya M, Sohara E, Kita S, Iwamoto T, Susa K, Mori T, Oi K, Chiga M, Takahashi D & Yang SS et al. (2013). Dietary salt intake regulates WNK3-SPAK-NKCC1 phosphorylation cascade in mouse aorta through angiotensin II. *Hypertension* **62,** 872–878.

Zeqiraj E, Filippi BM, Deak M, Alessi DR & Van Aalten DMF (2009*a*). Structure of the LKB1-STRAD-MO25 complex reveals an allosteric mechanism of kinase activation. *Science (80-)* **326,** 1707–1711.

Zeqiraj E, Filippi BM, Goldie S, Navratilova I, Boudeau J, Deak M, Alessi DR & Van Aalten DMF (2009*b*). ATP and MO25α regulate the conformational state of the STRADα pseudokinase and activation of the LKB1 tumour suppressor. *PLoS Biol* **7,** e1000126.

Zhang H, Liu SH, Zhang Q, Zhang YD, Wang SZ, Wang QG, Wang YX, Tang ZQ & Li H (2011). Fine-mapping of quantitative trait loci for body weight and bone traits and positional cloning of the RB1 gene in chicken. *J Anim Breed Genet* **128,** 366–375.

Zhang J, Gao G, Begum G, Wang J, Khanna AR, Shmukler BE, Daubner GM, De Los Heros P, Davies P, Varghese J, Bhuiyan MIH, Duan J, Duran D, Alper SL, Sun D, Elledge SJ, Alessi DR & Kahle KT (2016). Functional kinomics establishes a critical node of volume-sensitive cation-Cl-cotransporter regulation in the mammalian brain. *Sci Rep* **6,** 1–19.

Zhang J, Siew K, Macartney T, O'Shaughnessy KM & Alessi DR (2015). Critical role of the SPAK protein kinase CCT domain in controlling blood pressure. *Hum Mol Genet* **24,** 4545–4558.

Zhang P-Y, Zhang W-G, He A-L, Wang J-L & Li W-B (2009). Identification and functional characterization of the novel acute monocytic leukemia associated antigen MLAA-34. *Cancer Immunol Immunother* **58,** 281–290.

Zhang P, Zhao X, Zhang W, He A, Lei B, Zhang W & Chen Y (2017). Leukemia-associated gene MLAA-34 reduces arsenic trioxide-induced apoptosis in HeLa cells via activation of the Wnt/β-catenin signaling pathway. *PLoS One* **12,** e0186868.

Zhang W-G (2012). The expression and functional characterization associated with cell apoptosis and proteomic analysis of the novel gene MLAA-34 in U937 cells. *Oncol Rep*491–506.

Zhang W, Na T & Peng J-B (2008). WNK3 positively regulates epithelial calcium channels TRPV5 and TRPV6 via a kinase-dependent pathway. *AJP Ren Physiol* **295,** F1472--F1484.

Zhang Z, Wang Y, Shi Z & Zhang M (2013). Structure of zebrafish MO25. *Acta Crystallogr Sect F Struct Biol Cryst Commun* **69,** 989–993.

Zhao J, He A, Zhang W, Meng X & Gu L (2011). Quantitative assessment of MLAA-34 expression in diagnosis and prognosis of acute monocytic leukemia. *Cancer Immunol Immunother* **60,** 587–597.

Zheng N, Schulman BA, Song L, Miller JJ, Jeffrey PD, Wang P, Chu C, Koepp DM, Elledge SJ, Pagano M, Conaway RC, Conaway JW, Harper JW & Pavletich NP (2002). Structure of the Cul1-Rbx1-Skp1-F boxSkp2 SCF ubiquitin ligase complex. *Nature* **416,** 703–709.

Zhou B, Wang D, Feng X, Zhang Y, Wang Y, Zhuang J, Zhang X, Chen G, Delpire E, Gu D & Cai H (2012). WNK4 inhibits NCC protein expression through MAPK ERK1/2 signaling pathway. *Am J Physiol Renal Physiol* **302,** F533--9.

Zhou B, Zhuang J, Gu D, Wang H, Cebotaru L, Guggino WB & Cai H (2010). WNK4 enhances the degradation of NCC through a sortilin-mediated lysosomal pathway. *J Am Soc Nephrol* **21,** 82–92.

Appendices

Appendix 1 Published Abstracts

Appendix 2 Siew K and O'Shaughnessy KM (2013). 'Extra-renal Roles of WNKs'. *Clinical and Experimental Pharmacology and Physiology* 40:885-894

Appendix 3 Schumacher FR, Siew K, Zhang J, Johnson C, Wood N, Cleary SE, Al Maskari RS, Ferryman JT, Hardege I, Yasmin, Figg NL, Enchev R, Knebel A, O'Shaughnessy KM, Kurtz T (2015). Characterisation of the Cullin-3 mutation that causes a severe form of familial hypertension and hyperkalaemia. *EMBO Molecular Medicine* 7:1285-1306

Appendix 4 Zhang J, Siew K, Macartney T, O'Shaughnessy KM, Alessi DR (2015). Critical role of the SPAK protein kinase CCT domain in controlling blood pressure. *Human Molecular Genetics* 24:4545-4558

Appendix 5 Macro scripts used in data analysis

APPENDIX 1

Published Abstracts:

Siew K, Schumacher FR, Kurtz T, O'Shaughnessy KM (2015). Characterisation of the Cullin-3 Mutation That Causes a Severe Form of Familial Hypertension and Hyperkalaemia. *Journal of the American Society of Nephrology* 26 (Abstract Edition): 2015:188A, TH-PO444

Siew K, Zhang J, Schumacher FR, Alessi DR, Kurtz T, O'Shaughnessy KM (2015). Pulse waveform analysis reveals vascular contributions to Gordon Syndrome and Gitelman Syndrome blood pressure homeostasis. *Proceedings of The Physiological Society* 34, PC267

Siew K, Zhang J, Alessi DR, O'Shaughnessy KM (2014). Disruption of STE20/SPS1-related proline/alanine-rich kinase (SPAK) targeted mouse model of Gitelman Syndrome. *Journal of the American Society of Nephrology* 25 (Abstract Edition): 2014:375A, FR-P0012.

Siew K, Zhang J, Alessi DR, O'Shaughnessy KM (2014). Disruption of STE20/SPS1-related proline/alanine-rich kinase (SPAK) targeted mouse model of Gitelman Syndrome. *Journal of Human Hypertension* 28:617-48, OA1

Siew K, Glover M, O'Shaughnessy KM (2014). Sex differences in bone mineral density of the STE20/SPS1-related proline/alanine-rich kinase (SPAK) targeted mouse model of Gitelman Syndrome. *Proceedings of The Physiological Society* 31, PCB109

Siew K, Glover M, O'Shaughnessy KM (2014). Sex differences in bone mineral density of the STE20/SPS1-related proline/alanine-rich kinase (SPAK) binding lowers blood pressure and recapitulates Gitelman Syndrome in Mice. *The FASEB Journal* 28 (1 Suppl), 1083.4

Siew K, Maguire JJ, Davenport AP, O'Shaughnessy KM (2014). Vascular phenotype of STE20/SPS1-related proline/alanine-rich kinase targeted hypotensive mouse model of Gitelman Syndrome. *The FASEB Journal* 28 (1 Suppl), 697.6

Siew K, Maguire JJ, Davenport AP, O'Shaughnessy KM (2013). Vascular Phenotype of STE20/SPS1-related Proline/Alanine-rich Kinase (SPAK) Targeted Mouse Model of Gitelman Syndrome. *pA2 Online* 11 (3), 136P

Siew K, de los Heros P, Alessi DR and O'Shaughnessy KM (2013). MO25β has no physiological role in electrolyte homeostasis or systemic blood pressure maintenance in the mouse. *Journal of Human Hypertension* 27:635-55, PD1

Siew K, de los Heros P, Alessi DR and O'Shaughnessy KM (2013). MO25β has no physiological role in electrolyte homeostasis or systemic blood pressure maintenance. *Proceedings of the 37th IUPS*, PCD227

The original can be found in:

Siew K, Schumacher FR, Kurtz T, O'Shaughnessy KM (2015). Characterisation of the Cullin-3 Mutation That Causes a Severe Form of Familial Hypertension and Hyperkalaemia. *Journal of the American Society of Nephrology* 26 (Abstract Edition): 2015:188A, TH-PO948

https://www.asn-online.org/api/download/?file=/education/kidneyweek/archives/KW15Abstracts.pdf

The original can be found in:

Siew K, Zhang J, Alessi DR, O'Shaughnessy KM (2014). Disruption of STE20/SPS1-related proline/alanine-rich kinase (SPAK) targeted mouse model of Gitelman Syndrome. *Journal of the American Society of Nephrology* 25 (Abstract Edition): 2014:375A, FR-P0012.

https://www.asn-online.org/api/download/?file=/education/kidneyweek/archives/KW14Abstracts.pdf

This page was redacted for the same reasons as the previous page

APPENDIX 2

WNK Review:

Siew K and O'Shaughnessy KM (2013). 'Extra-renal Roles of WNKs'. *Clinical and Experimental Pharmacology and Physiology* 40:885-894

This page was redacted for the same reasons as the previous page

This page was redacted for the same reasons as the previous page

This page was redacted for the same reasons as the previous page

This page was redacted for the same reasons as the previous page

This page was redacted for the same reasons as the previous page

This page was redacted for the same reasons as the previous page

This page was redacted for the same reasons as the previous page

This page was redacted for the same reasons as the previous page

This page was redacted for the same reasons as the previous page

APPENDIX 3

CUL3 Paper:

Schumacher FR, Siew K, Zhang J, Johnson C, Wood N, Cleary SE, Al Maskari RS, Ferryman JT, Hardege I, Yasmin, Figg NL, Enchev R, Knebel A, O'Shaughnessy KM, Kurtz T (2015). Characterisation of the Cullin-3 mutation that causes a severe form of familial hypertension and hyperkalaemia. *EMBO Molecular Medicine* 7:1285-1306

Published online: August 18, 2015

Research Article

SOURCE DATA | TRANSPARENT PROCESS | OPEN ACCESS

EMBO Molecular Medicine

Characterisation of the Cullin-3 mutation that causes a severe form of familial hypertension and hyperkalaemia

Frances-Rose Schumacher[1,*,†,‡], Keith Siew[2,†], Jinwei Zhang[1], Clare Johnson[1], Nicola Wood[1], Sarah E Cleary[2], Raya S Al Maskari[2], James T Ferryman[2], Iris Hardege[2], Yasmin[2], Nichola L Figg[3], Radoslav Enchev[4], Axel Knebel[1], Kevin M O'Shaughnessy[2,**] & Thimo Kurz[1,***]

Abstract

Deletion of exon 9 from Cullin-3 (CUL3, residues 403–459: CUL3$^{\Delta 403–459}$) causes pseudohypoaldosteronism type IIE (PHA2E), a severe form of familial hyperkalaemia and hypertension (FHHt). CUL3 binds the RING protein RBX1 and various substrate adaptors to form Cullin-RING-ubiquitin-ligase complexes. Bound to KLHL3, CUL3-RBX1 ubiquitylates WNK kinases, promoting their ubiquitin-mediated proteasomal degradation. Since WNK kinases activate Na/Cl co-transporters to promote salt retention, CUL3 regulates blood pressure. Mutations in both KLHL3 and WNK kinases cause PHA2 by disrupting Cullin-RING-ligase formation. We report here that the PHA2E mutant, CUL3$^{\Delta 403–459}$, is severely compromised in its ability to ubiquitylate WNKs, possibly due to altered structural flexibility. Instead, CUL3$^{\Delta 403–459}$ auto-ubiquitylates and loses interaction with two important Cullin regulators: the COP9-signalosome and CAND1. A novel knock-in mouse model of CUL3$^{WT/\Delta 403–459}$ closely recapitulates the human PHA2E phenotype. These mice also show changes in the arterial pulse waveform, suggesting a vascular contribution to their hypertension not reported in previous FHHt models. These findings may explain the severity of the FHHt phenotype caused by CUL3 mutations compared to those reported in KLHL3 or WNK kinases.

Keywords cullin; CUL3; monogenic hypertension syndromes; proteasome; ubiquitin; WNK/SPAK/OSR1 pathway

Subject Categories Genetics, Gene Therapy & Genetic Disease; Post-translational Modifications, Proteolysis & Proteomics; Urogenital System

DOI 10.15252/emmm.201505444 | Received 18 May 2015 | Revised 17 July 2015 | Accepted 21 July 2015 | Published online 18 August 2015

EMBO Mol Med (2015) 7: 1285–1306

See also: **FC Luft** (October 2015)

Introduction

Blood pressure is controlled in part by the WNK kinase pathway, which acts to modulate the activity of key cation–chloride co-transporters in the kidney (Kahle *et al*, 2008; Alessi *et al*, 2014). Considerable insight into this pathway has come from exploring the molecular basis for mutations described in patients with a rare monogenic form of hypertension called familial hypertension and hyperkalaemia [FHHt, also known as pseudohypoaldosteronism (PHA2); OMIM: 145260]. Mutations in the genes encoding WNK kinases have been shown to increase protein levels of WNK1 and WNK4 in the kidney, leading to increased activation of this pathway (Wilson *et al*, 2001; Kahle *et al*, 2008). When activated by phosphorylation, the WNK kinases phosphorylate and activate the downstream kinases, SPAK (SPS1-related proline/alanine-rich kinase) and OSR1 (oxidative stress–responsive kinase 1), which in turn phosphorylate and activate cation–chloride co-transporters in the kidney, such as NCC (Na^+/Cl^- co-transporter), which leads to increased sodium ion reabsorption (Vitari *et al*, 2005; Delpire & Gagnon, 2008; Richardson *et al*, 2008, 2011). It is this up-regulation of the WNK signalling pathway that is responsible for the salt retention that drives the hypertension in FHHt. These patients also present with disturbed plasma electrolytes especially hyperkalaemia and a metabolic acidosis, partly driven by NCC activation (Boyden *et al*, 2012; Osawa *et al*, 2013; Tsuji *et al*, 2013; Glover *et al*, 2014; McCormick *et al*, 2014). As FHHt patients are salt-loaded through NCC activation, the hypertension and electrolyte disturbance respond to either salt restriction or low doses of thiazide diuretics (Gordon & Hodsman, 1986; Mayan *et al*, 2002).

More recently, the ubiquitin–proteasome system (UPS) was shown to have a critical upstream role in regulating blood pressure by modulating WNK kinase levels (Mori *et al*, 2013; Ohta *et al*,

1 MRC Protein Phosphorylation and Ubiquitylation Unit, College of Life Sciences, University of Dundee, Dundee, UK
2 Division of Experimental Medicine and Immunotherapeutics, University of Cambridge, Cambridge, UK
3 Division of Cardiovascular Medicine, Department of Medicine, University of Cambridge, Cambridge, UK
4 Institute of Biochemistry, ETH Zürich, Zürich, Switzerland
*Corresponding author. Tel: +44 1382 384241; E-mail: francesrose.schumacher@gmail.com
**Corresponding author. Tel: +44 1223 762578; E-mail: kmo22@medschl.cam.ac.uk
***Corresponding author. Tel: +44 1382 388371; E-mail: t.kurz@dundee.ac.uk
† These authors contributed equally to this work
‡ Current address: Proteomics and Biological Resource Management, Department of Protein Chemistry, Genentech, 1 DNA Way, South San Francisco, CA, USA

2013; Wakabayashi *et al*, 2013; Wu & Peng, 2013). This was first suggested when patients with severe forms of FHHt were described with mutations in Cullin-3 (CUL3; PHA2E), and one of its substrate adaptors, KLHL3 (PHA2D) (Boyden *et al*, 2012; Louis-Dit-Picard *et al*, 2012; OMIM:145260). CUL3 belongs to the Cullin-RING ligase (CRL) family that form the largest class of ubiquitin E3 ligases in the cell. Cullins are elongated proteins, which confer an extended structure to active CRL complexes (Zheng *et al*, 2002; Duda *et al*, 2011). Through their C-terminus, Cullins constitutively bind to a small RING finger protein, either RBX1 or RBX2, which forms the catalytic core of the ligase complex. The binding to various substrate-adaptor proteins at the N-terminal domain enables CUL3-RBX1 to appropriately ubiquitylate a plethora of cellular substrates (Wee *et al*, 2005; Harper & Tan, 2012). In this way, CUL3 acts as an active scaffold to direct ubiquitylation, as C-terminally bound RBX1 binds ubiquitin-conjugating E2 enzymes that are charged with ubiquitin, while simultaneously binding to the substrate adaptor, in this instance KLHL3. The overall structural rigidity of the Cullin, in particular between the elongated N-terminus and the globular C-terminus, is important for the ubiquitin E3 ligase function of the complex. Alterations in the connecting sequence between the Cullin N- and C-terminus are thought to change the relative positioning of the RING domain towards the bound substrate, which can prevent substrate modification (Zheng *et al*, 2002; Liu & Nussinov, 2011). Efficient CRL ubiquitylation also requires the modification of a conserved C-terminal lysine residue (Lys 721 in CUL3) by a single molecule of the ubiquitin-like protein Nedd8 (Pintard *et al*, 2003). This modification, auto-catalysed by CUL3-RBX1, is aided by Nedd8-E3 ligases (Kurz *et al*, 2005; Rabut *et al*, 2011) and alters the flexibility of the C-terminal Cullin-RBX1 module to activate E3 ligase activity (Duda *et al*, 2008; Scott *et al*, 2014). While neddylation is required for efficient ubiquitylation, studies show that the cycling between a neddylated and deneddylated state is crucial in a cellular context (Cope *et al*, 2002; Pintard *et al*, 2003). As such, Cullin interactions with the deneddylation complex COP9-signalosome (CSN), a metalloprotease, are also required for activity. Another regulator of CRLs, CAND1, interacts with the N- and C-terminus of Cullins only in their deneddylated state to promote the exchange of substrate adaptors (Liu *et al*, 2002; Goldenberg *et al*, 2004; Pierce *et al*, 2013; Wu *et al*, 2013; Zemla *et al*, 2013).

In the context of PHA2, KLHL3 is the critical adaptor that links the WNK kinases to CUL3-RBX1, enabling CUL3 to directly ubiquitylate the bound WNK kinase. In earlier work, we and others showed the KLHL3 mutations described in FHHt (PHA2D) patients disrupt the formation of the complex and prevent WNK ubiquitylation, leading to WNK stabilisation and increased flux through the WNK kinase pathway (Mori *et al*, 2013; Ohta *et al*, 2013; Shibata *et al*, 2013; Wakabayashi *et al*, 2013; Wu & Peng, 2013; Schumacher *et al*, 2014; Susa *et al*, 2014). Some patients with FHHt have mutations in WNK kinases, which promote WNK stabilisation by disrupting WNK-KLHL3 interactions (Wakabayashi *et al*, 2013; Schumacher *et al*, 2014) or, in some cases, by the increased expression of WNK mRNA (Wilson *et al*, 2001).

While FHHt patients with CUL3, KLHL3 or WNK mutations present with the same disease, those with mutations in CUL3 display a more severe phenotype, evident in terms of both an earlier age-of-onset and the degree of hypertension and electrolyte disturbance reported (Boyden *et al*, 2012; Osawa *et al*, 2013; Tsuji *et al*, 2013). To date, all the reported CUL3 PHA2E mutations are heterozygous, transmit as autosomal dominant traits and result in the deletion of the amino acids encoded for by exon 9 of the CUL3 mRNA (residues 403–459) (Boyden *et al*, 2012; Grimm *et al*, 2012; Osawa *et al*, 2013; Tsuji *et al*, 2013; Glover *et al*, 2014). Nevertheless, precisely why and how this truncated form of CUL3 (hereafter referred to as $CUL3^{\Delta 403–459}$) causes a more severe phenotype is currently unclear. We have investigated this question using a biochemical *in vitro* approach to understand the molecular defects caused by the mutation and a mouse model of PHA2E to better understand the physiological basis of the effects of $CUL3^{\Delta 403–459}$. This has uncovered a number of critical molecular and physiological factors that enhance our understanding of Cullin-RING ligase mechanisms, the physiology of CUL3, and importantly its pathophysiology in FHHt patients.

Results

$CUL3^{\Delta 403–459}$ forms an active Cullin-RING ligase complex

To investigate the molecular defect of $CUL3^{\Delta 403–459}$, we determined whether this form of CUL3 was able to build a CRL complex. First, we established that $CUL3^{\Delta 403–459}$ binds RBX1 similar to $CUL3^{WT}$, by showing that both versions of CUL3 form a stable complex with RBX1 when co-expressed in insect cells (Fig 1A). A second critical interaction for a functional CRL is the ability to bind substrate-adaptor proteins, and in the context of WNK kinase modification, CUL3 must interact with KLHL3 (Lamark & Johansen, 2012; Ji & Privé, 2013; Canning & Bullock, 2014). The 57-residue deletion in $CUL3^{\Delta 403–459}$ lies in a structurally distinct domain of CUL3 and would not be expected to perturb binding to substrate adaptors. We confirmed that $CUL3^{\Delta 403–459}$ indeed retains the ability to bind KLHL3 by *in vitro* pull-down assays with purified proteins (Fig 1B). We also showed this interaction is maintained in a cellular system, using ectopically expressed FLAG-tagged CUL3 to co-precipitate endogenous KLHL3 in FLAG immunoprecipitates (Fig 1H, lower panel). Thus, $CUL3^{\Delta 403–459}$ maintains crucial interactions important for ubiquitin-ligase function. Given this, we tested whether $CUL3^{\Delta 403–459}$-RBX1 also maintains the ability to hydrolyse the thioester bond between the catalytic cysteine residue of a recruited E2 enzyme and ubiquitin (E2~UB), a critical step in ubiquitylation and a measure for catalytic activity. Using ubiquitin-release assays from charged E2 enzymes, we show that $CUL3^{\Delta 403–459}$ hydrolyses E2~UB more efficiently than $CUL3^{WT}$, demonstrating a functionally intact $CUL3^{\Delta 403–459}$-RBX1 catalytic core, while also suggesting potential hyper-activity (Fig 1C). Together, these results demonstrate that $CUL3^{\Delta 403–459}$ maintains interactions and basic functionality critical for CRL activity.

Structural modelling suggests $CUL3^{\Delta 403–459}$ is more flexible than $CUL3^{WT}$

To better understand how the deletion in $CUL3^{\Delta 403–459}$ may affect the CRL, we predicted the structure of CUL3, using closely related Cullin-1 (CUL1; Fig 1D; Appendix Fig S1). The region deleted in $CUL3^{\Delta 403–459}$ likely forms a three-helical bundle juxtaposed to the globular C-terminal domain. Removal of these helices would fuse together two short unstructured regions to create a longer loop,

which, as well as shortening the elongated structure of the CRL complex, may increase the flexibility between the two domains. If correct, this model explains how RBX1 and KLHL3 binding is maintained (Munir *et al*, 2007; Calabrese *et al*, 2011), while also suggesting the function of the ligase may be compromised due to the altered relative orientation of the CRL components towards each other. Studies investigating the structure of CUL1 demonstrated the importance of a rigid Cullin conformation for substrate ubiquitylation, as increasing the flexibility of CUL1, in an area that corresponds to the CUL3 deletion, led to strongly decreased substrate ubiquitylation (Zheng *et al*, 2002; Appendix Fig S1). It is therefore possible that due to the presence of a predicted unstructured flexible loop, CUL3$^{\Delta 403–459}$ may similarly sample non-productive conformations.

CUL3$^{\Delta 403–459}$ has altered Nedd8-ligase activity and is unable to interact with the CRL regulators COP9-signalosome and CAND1

Available structural data of CRL proteins bound to Cullin regulators suggest the deleted region in CUL3$^{\Delta 403–459}$ may also influence neddylation and binding of the CSN (Lingaraju *et al*, 2014) and of CAND1 (Goldenberg *et al*, 2004; Fig EV1). This prompted us to examine whether these interactions are affected by the PHA2E mutation.

To investigate the ability of CUL3$^{\Delta 403–459}$ to be auto-modified with Nedd8, we used *in vitro* neddylation assays with purified CUL3, Nedd8 E1 (APPBP1-UBA3), Nedd8 E2 (UBE2M) and Nedd8. As Nedd8 forms a covalent isopeptide bond with CUL3, neddylation can be visualised as a slower-migrating band on SDS–PAGE. We found CUL3$^{\Delta 403–459}$ retains the ability to auto-neddylate (Fig 1E, Appendix Fig S2A). However, CUL3$^{\Delta 403–459}$ appears less efficient at transferring Nedd8, as unlike for CUL3^{WT}, some unmodified CUL3$^{\Delta 403–459}$ remained even 45 min after neddylation was initiated. Moreover, while CUL3^{WT} was only mono-neddylated, multiple Nedd8 molecules were attached to CUL3$^{\Delta 403–459}$ (Fig 1E). Both of these differences in neddylation are consistent with increased structural flexibility of CUL3$^{\Delta 403–459}$.

As reported (McCormick *et al*, 2014), we also noticed that CUL3$^{\Delta 403–459}$ neddylation is elevated in cells (Fig 1F). CRLs cycle between neddylated and de-neddylated states to maintain activity (Pintard *et al*, 2003). Therefore, the increased cellular neddylation of CUL3$^{\Delta 403–459}$ could reflect a decrease in de-neddylation by the isopeptidase CSN. The structure of the CSN bound to

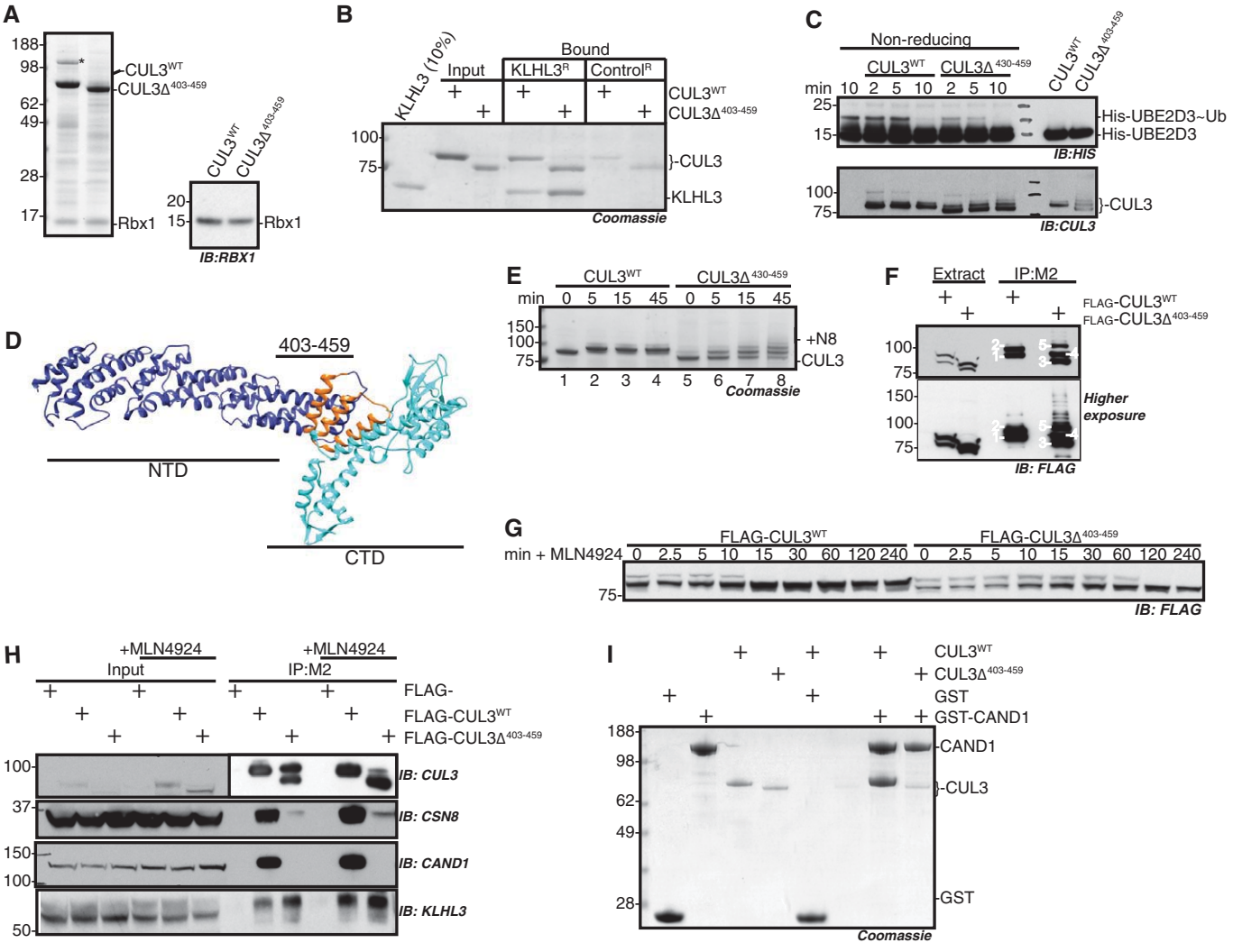

Figure 1.

CUL1 supports this idea, as the Cullin C-terminal domain, including the region equivalent to residue 403–459 in CUL3, contacts the CSN subunits directly (Lingaraju *et al*, 2014). To investigate this possibility, we blocked neddylation using an inhibitor of the Nedd8-E1 enzyme (MLN4924; Millennium Pharmaceuticals) and monitored CUL3 de-neddylation over time. Consistent with decreased rates of deneddylation, $CUL3^{\Delta403–459}$ remained neddylated for longer than $CUL3^{WT}$ (Fig 1G) and also showed markedly reduced binding to CSN subunits (Fig 1H, Appendix Fig S2B). As such, the observed elevated Nedd8 modification of $CUL3^{\Delta403–459}$ in cells is likely due to a combination of Nedd8 ligation to non-physiological lysine residues and of reduced CSN de-neddylation.

CRLs must be de-neddylated for a productive interaction with the substrate-adaptor exchange factor CAND1. Furthermore, the structure of CUL1 bound to CAND1 suggests that, regardless of neddylation state, $CUL3^{\Delta403–459}$ may be unable to form the required critical interactions (Goldenberg *et al*, 2004; Pierce *et al*, 2013; Wu *et al*, 2013; Zemla *et al*, 2013). We therefore investigated whether $CUL3^{\Delta403–459}$ was indeed defective in binding to CAND1. We treated cells expressing either FLAG-$CUL3^{WT}$ or FLAG- $CUL3^{\Delta403–459}$ with the neddylation inhibitor MLN4924 to force all of CUL3 into the non-neddylated state and then determined interaction with CAND1 by immunoprecipitation. While $CUL3^{WT}$ strongly bound to CAND1 in these assays, $CUL3^{\Delta403–459}$ was unable to interact with CAND1 (Fig 2H, Appendix Fig S2B). We confirmed these findings using *in vitro* assays with purified proteins (Fig 1I). These data advocate that structural perturbations prevent $CUL3^{\Delta403–459}$ from binding to CAND1. In combination with the impairment of CSN binding, such defects suggest that the regulation of $CUL3^{\Delta403–459}$ in cells is likely severely disrupted.

$CUL3^{\Delta403–459}$ displays enhanced auto-ubiquitylation

Our data indicate that the regulation of $CUL3^{\Delta403–459}$ is defective in cells, and we wanted to test whether its ubiquitylation activity is similarly affected. McCormick *et al* suggested that $CUL3^{\Delta403–459}$ may stabilise WNK kinases by ectopically degrading the substrate adaptor KLHL3, preventing the formation of functional CUL3-KLHL3 complexes (McCormick *et al*, 2014). Some CRLs are known to ubiquitylate bound substrate adaptors (Wee *et al*, 2005), and it is feasible that altering the CUL3 backbone structure could indeed lead to erroneous ubiquitylation of KLHL3. In our *in vitro* system, we confirmed that $CUL3^{\Delta403–459}$ directly modified KLHL3 with a greater efficiency than $CUL3^{WT}$ (Fig 2A, Appendix Fig S2C). Interestingly, we observed that $CUL3^{\Delta403–459}$ also exhibited markedly increased auto-ubiquitylation (Fig 2B, Appendix Fig S2D).

Auto-ubiquitylation is often utilised as a read-out for ubiquitin-ligase activity. In a cellular context, self-modification can lead to auto-degradation of the ligase (Silke *et al*, 2005). If $CUL3^{\Delta403–459}$

Figure 1. $CUL3^{\Delta403–459}$ forms a functional Cullin-RING ligase with altered activity and is unable to interact with CRL regulators.

A Purified $CUL3^{WT}$ and $CUL3^{\Delta403–459}$ analysed by SDS–PAGE and Coomassie blue staining, following expression in SF21 cells, and DAC-tag-affinity purification and tag cleavage (see Materials and Methods). Bands migrating between 62- and 98-kDa protein markers are $CUL3^{WT}$ and $CUL3^{\Delta403–459}$, respectively, while the band below 17 kDa is Rbx1. The immunoblot for RBX1 is shown on the right. The band in $CUL3^{WT}$ denoted with * is co-purified insect cell CAND1, which was later removed by SEC. All protein identities were confirmed by mass spectrometry.

B KLHL3 binding to $CUL3^{WT}$ and $CUL3^{\Delta403–459}$ is comparable as shown by pull-down assays with a KLHL3 resin generated from cross-linking anti-KLHL3 antibody to Protein G sepharose, and then binding saturating amounts of KLHL3 to the anti-KLHL3 resin (denoted $KLHL3^{R}$), the control resin ($Control^{R}$) is Protein G sepharose (see Materials and Methods for further detail). $CUL3^{WT}$ or $CUL3^{\Delta403–459}$ was incubated with either $KLHL3^{R}$ or $Control^{R}$ at 4°C for 1 h and then washed thrice with 1× PBS, resin volumes were minimised, and SDS–Laemmli buffer was used to elute protein from resin prior to analysis by SDS–PAGE and staining with colloidal blue.

C UBE2D3~ubiquitin-release assays analysed by non-reducing SDS–PAGE and immunodetection. His-tagged UBE2D3 was charged with ubiquitin by incubation with ATP and UAE, and charging was stopped by ATP depletion with apyrase. No CUL3 (negative control, lane 1), $CUL3^{WT}$ or $CUL3^{\Delta403–459}$ was then added to the charged E2 and the activity of the RING domain, RBX1, monitored by the hydrolysis of ubiquitin from UBE2D3, visualised by immunodetection with anti-His antibody (upper panel, "~" denotes thioester bond). The lower panel is an immunoblot for CUL3, showing equivalent amount of both $CUL3^{WT}$ and $CUL3^{\Delta403–459}$ was added to the reaction mix; over time, the appearance of higher molecular weight bands represents the modification of CUL3 by covalent attachment of ubiquitin. The right two lanes are control lanes incubated for 10 min with E2~Ubi but then treated with reducing agent prior to SDS–PAGE.

D Structural model of $CUL3^{WT}$ based on the structure of CUL1 (PDB:1LDK), highlighting the residues deleted in the PHA2E mutant which are located close to the N-terminal domain (NTD) and C-terminal domain (CTD) border, using Phyre2 and Chimera (see Materials and Methods). The NTD is coloured purple, the CTD cyan, and residues 403–459 orange.

E Time course of *in vitro* neddylation reactions. Purified NAE, UBE2M and Nedd8 were mixed with either $CUL3^{WT}$ or $CUL3^{\Delta403–459}$ and incubated at 30°C for the time indicated. Due to the covalent attachment of Nedd8 (8.6 kDa), modified proteins have decreased mobility. The band shift observed for $CUL3^{WT}$ (lane 1 versus lane 2) is representative of a single Nedd8 modification, while the multiple bands in the $CUL3^{\Delta403–459}$ reaction reflect the attachment of up to three Nedd8 molecules (lane 5 versus lane 8).

F HEK-293 cells over-expressing either FLAG-$CUL3^{WT}$ or FLAG-$CUL3^{\Delta403–459}$ were immunoprecipitated with M2 Flag-binding sepharose, in the presence of a deneddylase inhibitor (OPT). Extract, cells were lysed in the presence of OPT and clarified by centrifugation. IP:M2, clarified supernatant samples were incubated for 1 h at 4°C with M2 (anti-Flag) sepharose, then washed with PBS and eluted with SDS–Laemmli buffer, prior to SDS–PAGE and immunodetection with anti-FLAG antibody. Bands are labelled as follows: 1. $CUL3^{WT}$, 2. $CUL3^{WT}$-N8, 3. $CUL3^{\Delta403–459}$, 4. $CUL3^{\Delta403–459}$-N8, 5. $CUL3^{\Delta403–459}$-2(N8).

G Neddylation in HEK-293 cells over-expressing FLAG-$CUL3^{WT}$ or FLAG-$CUL3^{\Delta403–459}$ was blocked by treatment with a Nedd8-E1-enzyme inhibitor, 3 μM MLN4924 (Millennium Pharmaceuticals), in cells over-expressing FLAG-$CUL3^{WT}$ and FLAG-$CUL3^{\Delta403–459}$ respectively. Cell extracts were sampled over time in the presence of OPT to prevent de-neddylation and subjected to SDS–PAGE and immunodetection of the FLAG tag.

H FLAG-$CUL3^{WT}$ or FLAG-$CUL3^{\Delta403–459}$ was immunoprecipitated with M2-sepharose as described in (F). +MLN4924 indicates cell culture media supplementation with 3 μM MLN4924 for 5 h prior to cell lysis to achieve complete deneddylation of CUL3. Following SDS–PAGE, immunoblotting with COP9 Signalosome (CSN) or CAND1 antibodies determined the interaction between these Cullin regulators and FLAG-$CUL3^{WT}$ and FLAG-$CUL3^{\Delta403–459}$, respectively.

I GST-CAND1 pull-down assays with CUL3 proteins. Purified GST or GST-CAND1 immobilised on glutathione–sepharose was mixed with either purified $CUL3^{WT}$ or $CUL3^{\Delta403–459}$ and incubated at 4°C for 1 h. The sepharose was then washed thrice and eluted from the resin by incubation with SDS–Laemmli buffer prior to SDS–PAGE and Coomassie staining. $CUL3^{WT}$ but not $CUL3^{\Delta403–459}$ interacts with CAND1.

Source data are available online for this figure.

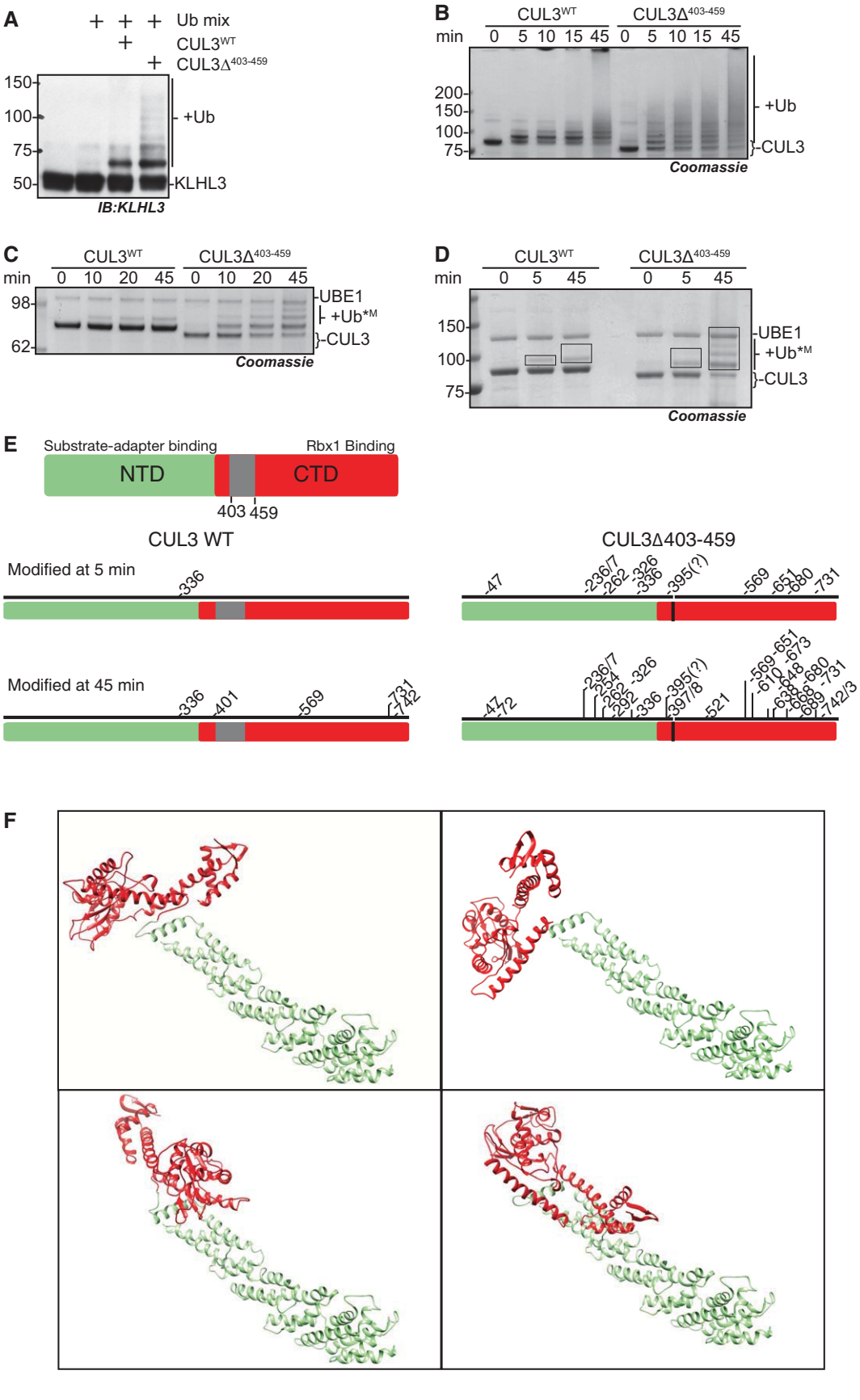
A
Ub mix
CUL3WT
CUL3Δ403-459
150
100
75
50
+Ub
KLHL3
IB:KLHL3
B
CUL3WT
CUL3Δ403-459
min
0 5 10 15 45 0 5 10 15 45
200
150
100
75
+Ub
CUL3
Coomassie
C
CUL3WT
CUL3Δ403-459
min
0 10 20 45 0 10 20 45
98
62
UBE1
+Ub*M
CUL3
Coomassie
D
CUL3WT
CUL3Δ403-459
min
0 5 45 0 5 45
150
100
75
UBE1
+Ub*M
CUL3
Coomassie
E
Substrate-adapter binding
Rbx1 Binding
NTD
CTD
403 459
CUL3 WT
Modified at 5 min
336
Modified at 45 min
336
401
569
731
742
CUL3Δ403-459
47
236/7
262
326
336
395(?)
569
651
680
731
47
72
236/7
254
262
292
326
336
395(?)
397/8
521
569-651
610
648-673
638-680
688-731
742/3
F

Figure 2.

Figure 2. $CUL3^{\Delta 403–459}$ displays increased auto-ubiquitylation and ubiquitylation of KLHL3.

A–D *In vitro* ubiquitylation assays with purified proteins. As ubiquitin is covalently attached to the substrate lysine residue, the appearance of higher molecular weight protein bands reflects the modification of the protein with ubiquitin. All assays contain purified UBE1, UBE2D3, ubiquitin, 0.1 mM ATP, 1 mM $MgCl_2$ and were buffered in 50 mM HEPES, 150 mM NaCl and incubated at 30°C for the time indicated. Reactions were stopped by the addition of SDS–Laemmli buffer to a concentration of 1×. SDS–PAGE, staining with Coomassie blue, or detection with the indicated antibody following immunoblotting enabled the visualisation of ubiquitylation. (A) to determine the relative modification of KLHL3 by $CUL3^{WT}$ and $CUL3^{\Delta 403–459}$, KLHL3 was included into the reaction at 2× molar concentration over $CUL3^{WT}$ and $CUL3^{\Delta 403–459}$. (B, C) Reactions serve to determine basal auto-ubiquitylation of $CUL3^{WT}$ or $CUL3^{\Delta 403–459}$ and do not contain KLHL3 or other potential substrate proteins. Lysine residues on $CUL3^{WT}$ or $CUL3^{\Delta 403–459}$ act as the substrate. (B) High molecular weight bands reflect ubiquitin chain linkages on CUL3 or the multiple mono-ubiquitylation of a number of CUL3 lysine residues. (C) Activity assays contain methylated ubiquitin, a form of ubiquitin incapable of forming ubiquitin chains; as such, higher band shifts reflect the attachment of mono-ubiquitin to one more lysine residue on $CUL3^{WT}$ or $CUL3^{\Delta 403–459}$, respectively. (D) Activity assay performed as in (C) with methyl-ubiquitin, the boxes shown on the gel are indicative of the gel pieces excised for mass spectrometry analysis in (F).

E Schematic representation (to linear residue scale) highlighting the domains of CUL3 and schematic representation of the lysine residues of $CUL3^{WT}$ or $CUL3^{\Delta 403–459}$, modified at 5 and 45 min, respectively, in the *in vitro* ubiquitylation assay shown in (D) and as determined by mass spectrometry.

F Structural docking model of $CUL3^{\Delta 403–459}$ based on the structure of full-length CUL1 (1LDK) using Chimera (see Materials and Methods). The NTD is coloured green, while the CTD is red, and the four panels sample possible positioning of the CTD relative to the NTD in $CUL3^{\Delta 403–459}$, assuming full flexibility of the linker after deletion of three helices encoded by exon 9.

Source data are available online for this figure.

modifies lysine residues inaccessible to $CUL3^{WT}$, this could explain the increased auto-ubiquitylation. Alternatively, $CUL3^{\Delta 403–459}$ could build longer ubiquitin chains on the same lysine residues that are also targeted by $CUL3^{WT}$. To explore these possibilities, we performed *in vitro* ubiquitylation assays with methylated ubiquitin, a form of ubiquitin unable to build ubiquitin chains (Kirisako *et al*, 2006). In these assays, $CUL3^{\Delta 403–459}$ was auto-modified on multiple lysine residues, while $CUL3^{WT}$ only mono-ubiquitylated one residue (Fig 2C). Therefore, the observed increase in auto-ubiquitylation is most likely due to erroneous modification of multiple lysine residues on $CUL3^{\Delta 403–459}$, which is consistent with an increase in structural flexibility as suggested by our model. Alternatively, the mutation may change the active site environment of CUL3, exposing more lysine residues close to the E2~UB binding site. To distinguish between these possibilities, we mapped the lysine residues modified in our *in vitro* assay system using mass spectrometry. We performed *in vitro* auto-ubiquitylation reactions of CUL3 with methylated ubiquitin for either 5 or 45 min and determined the ubiquitylated lysine residues by analysing which lysine residue(s) carry di-glycine remnants after trypsin digest (Fig 2D and E; Kim *et al*, 2011). Using this approach, we found that after 5 min, $CUL3^{WT}$ was only auto-ubiquitylated on a single lysine residue (K336), while ten lysine residues on $CUL3^{\Delta 403–459}$ were modified (Fig 2D and E). After running the reaction for 45 min, the modification sites on $CUL3^{WT}$ had increased to five, all of which were C-terminal to the original site and contained within the globular C-terminal Cullin domain. The ubiquitylation sites on $CUL3^{\Delta 403–459}$, however, had increased to 25 sites distributed along the entire length of the protein (most N-terminal: K47; most C-terminal: K743). These results support our model that the CUL3 deletion induces increased structural flexibility, leading to the erroneous auto-ubiquitylation of sites normally not accessible to $CUL3^{WT}$ (Figs 2E and F and EV2).

$CUL3^{\Delta 403–459}$ cannot ubiquitylate WNK kinases

As $CUL3^{\Delta 403–459}$ is able to more efficiently auto-ubiquitylate itself and KLHL3, we next asked whether it similarly shows increased ubiquitylation towards a bound WNK substrate in *in vitro* ubiquitylation assays using purified components. As we previously showed, $CUL3^{WT}$ efficiently ubiquitylates WNK kinases *in vitro* (Fig 3; Ohta *et al*, 2013). $CUL3^{\Delta 403–459}$, however, while maintaining the ability to efficiently modify itself and KLHL3, was not able to modify either WNK1 or WNK4 (Fig 3A and B). As described for CUL1 (Zheng *et al*, 2002), increasing the flexibility of the Cullin backbone can lead to a decrease in substrate modification, while promoting excessive modification of other CRL components (Zheng *et al*, 2002). Thus, increased structural flexibility of $CUL3^{\Delta 403–459}$ may lead to similar defects. If so, then it becomes important to understand how this *in vitro* finding can explain the increased WNK stabilisation found *in vivo*. It is possible that only one of the three defects, the lack of substrate ubiquitylation, the increased Cullin auto-ubiquitylation or the increased KLHL3 ubiquitylation, is the major driver for the observed phenotypes. Decisively, KLHL3 levels are not decreased in the kidney of $CUL3^{WT/\Delta 403–459}$ mice, while the overall CUL3 levels are lower. This suggests that KLHL3 degradation does not contribute to the observed PHA2E phenotype, and instead, we propose that $CUL3^{\Delta 403–459}$ stabilises WNK levels in two ways: firstly, $CUL3^{\Delta 403–459}$ excessively auto-ubiquitylates, leading to its own degradation; and secondly, any $CUL3^{\Delta 403–459}$ protein that escapes degradation cannot promote the ubiquitylation of the WNK kinases. Importantly, all PHA2E patients are heterozygous for the mutation, suggesting that with respect to blood pressure regulation either $CUL3^{\Delta 403–459}$ behaves as a dominant-negative or $CUL3^{WT}$ is haploinsufficient. Our data demonstrate that the mutation causes a loss-of-function, so a dominant-negative effect seems less likely. We also find that *in vitro*, equimolar amounts of $CUL3^{\Delta 403–459}$ do not inhibit $CUL3^{WT}$ (Fig 3C), further supporting the concept of haploinsufficiency.

$CUL3^{WT/\Delta 403–459}$ mice have increased flux through the WNK kinase pathway and typical FHHt phenotypic features of electrolyte imbalance

To complement our *in vitro* findings and to determine more accurately what occurs in PHA2E patients, we engineered a knock-in (KI) mouse carrying the same exon 9 deletion of CUL3 as reported in PHA2E pedigrees ($CUL3^{\Delta 403–459}$; Appendix Fig S3). Despite setting up heterozygous mating pairs, no homozygous KI mice were born suggesting that, like deletion of the entire coding region of CUL3, the homozygous deletion of residues 403–459 is lethal (Singer *et al*, 1999). Nevertheless, all the reported PHA2E pedigrees are heterozygous, so we phenotyped the heterozygous KI mice. Utilising both immunoblotting of whole kidney lysates and immunofluorescence

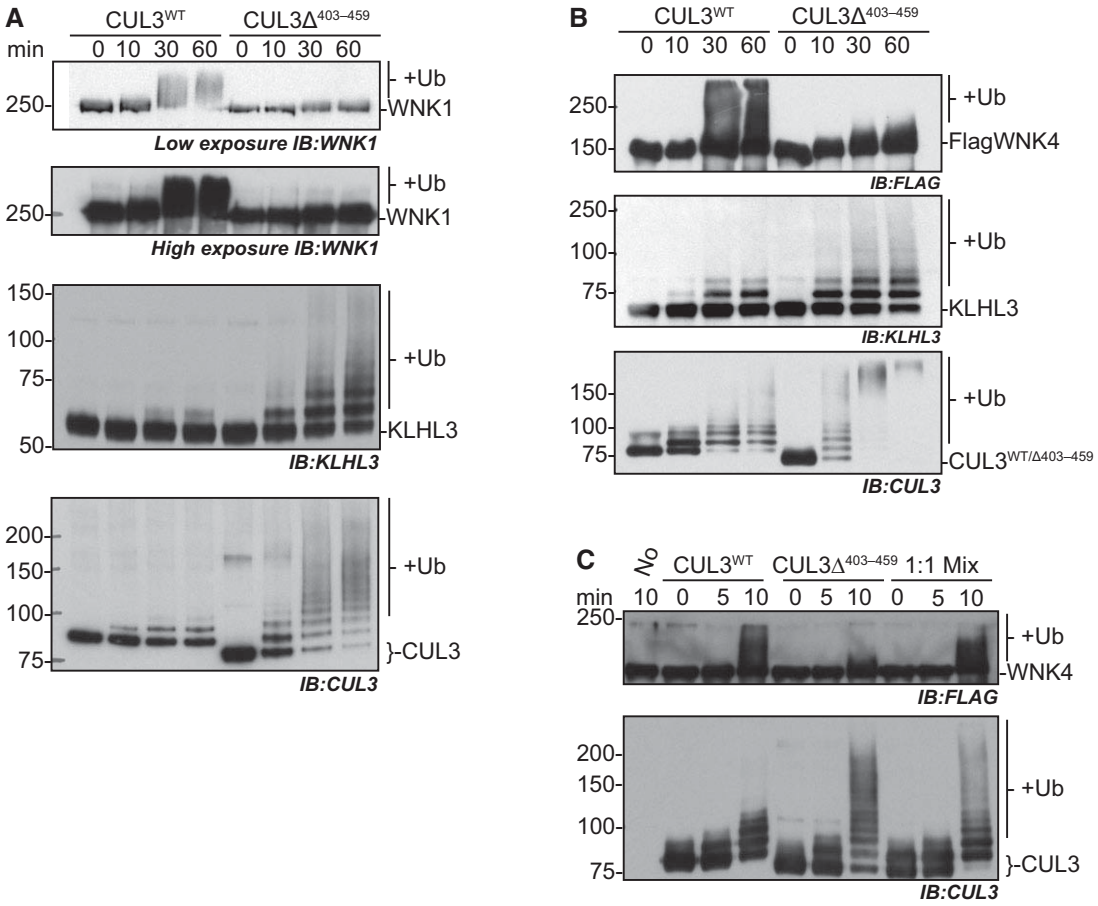

Figure 3. CUL3$^{\Delta 403–459}$ is unable to ubiquitylate WNK1 or WNK4 kinases in an *in vitro* system, and this deficiency cannot be rescued by the presence of CUL3^{WT}.

A–C *In vitro* ubiquitylation assays were performed as described in Figure 2, but with the addition of immunoprecipitated WNK1 in (A), or immunoprecipitated over-expressed FLAG-WNK4 in (B, C) (see Materials and Methods). The WNK kinases are modified by CUL3^{WT}-KLHL3, with the higher molecular weight smear observed in anti-WNK1 and anti-FLAG panels representative of multiple ubiquitin molecules being covalently attached to the WNK protein. CUL3$^{\Delta 403–459}$ is unable to modify WNKs. Samples from the same assay reactions were divided to allow immunodetection of the different protein components modified within the same assay reaction. (C) CUL3^{WT}, CUL3$^{\Delta 403–459}$ and an equimolar solution CUL3^{WT}:CUL3$^{\Delta 403–459}$ (1:1 Mix) were incubated with KLHL3 and immunoprecipitated FLAG-WNK4 in ubiquitylation reactions to determine the influence of CUL3$^{\Delta 403–459}$ on the ubiquitylation activity of CUL3^{WT}. Notably, the presence of CUL3$^{\Delta 403–459}$ does not inhibit WNK ubiquitylation by CUL3^{WT}.

confocal microscopy of kidney sections, we determined the relative abundance and distribution of proteins involved in the WNK signalling pathway. Whole kidney lysate was analysed by immunoblotting confirming the expression of CUL3 and the presence of an additional band corresponding to the expected PHA2E form, CUL3$^{\Delta 403–459}$, in the heterozygous mice (Fig 4A). Increased levels of WNK4 and the downstream components of the WNK kinase pathway, reported in other mouse models of FHHt, were also observed (Fig 4A). Specifically, there were striking increases in both total and phosphorylated forms of SPAK and NCC (Fig 4A). We also confirmed the expression of KLHL3 and CUL3 in normal human kidney lysates (Fig 4B). In the context of our *in vitro* data, we were especially interested in examining the levels of KLHL3 and CUL3 in the mouse kidney (Fig 4A). Definitively, the overall level of KLHL3 was comparable between CUL3$^{WT/WT}$ and CUL3$^{WT/\Delta 403–459}$ mice. In contrast, CUL3$^{\Delta 403–459}$ appears to be less abundant than CUL3^{WT} in the heterozygous mice. These observations suggest that CUL3$^{\Delta 403–459}$ does not promote KLHL3 degradation *in vivo* and, moreover, that the lower levels of CUL3$^{\Delta 403–459}$ may be due to the propensity of CUL3$^{\Delta 403–459}$ to self-modify presumably causing degradation through the UPS. The lower level of observable CUL3$^{\Delta 403–459}$ may also be due to non-proteolytic hyper-modification of CUL3$^{\Delta 403–459}$ with either Nedd8 or ubiquitin. Indeed, this may in part be the case, as incubation of kidney extract at room temperature to promote de-conjugation of Nedd8 or ubiquitin increased the abundance of the faster migrating CUL3$^{\Delta 403–459}$ band, but did not restore it to CUL3^{WT} levels (Fig 4A, lower panel). Regardless of precisely why, the stabilisation of WNK4 and increased signalling through the WNK cascade is consistent with a PHA2E model.

Over-activation of the WNK pathway would be expected to perturb electrolyte homoeostasis. We confirmed this by measuring urine electrolytes, blood biochemistries and aldosterone levels in the mice (Figs 4C and D and EV3). The CUL3$^{WT/\Delta 403–459}$ mice showed the typical electrolyte disturbance of FHHt with hyperkalaemia, hyperchloraemia and a compensated metabolic acidosis, with the pH maintained by an increased respiratory drive to increase

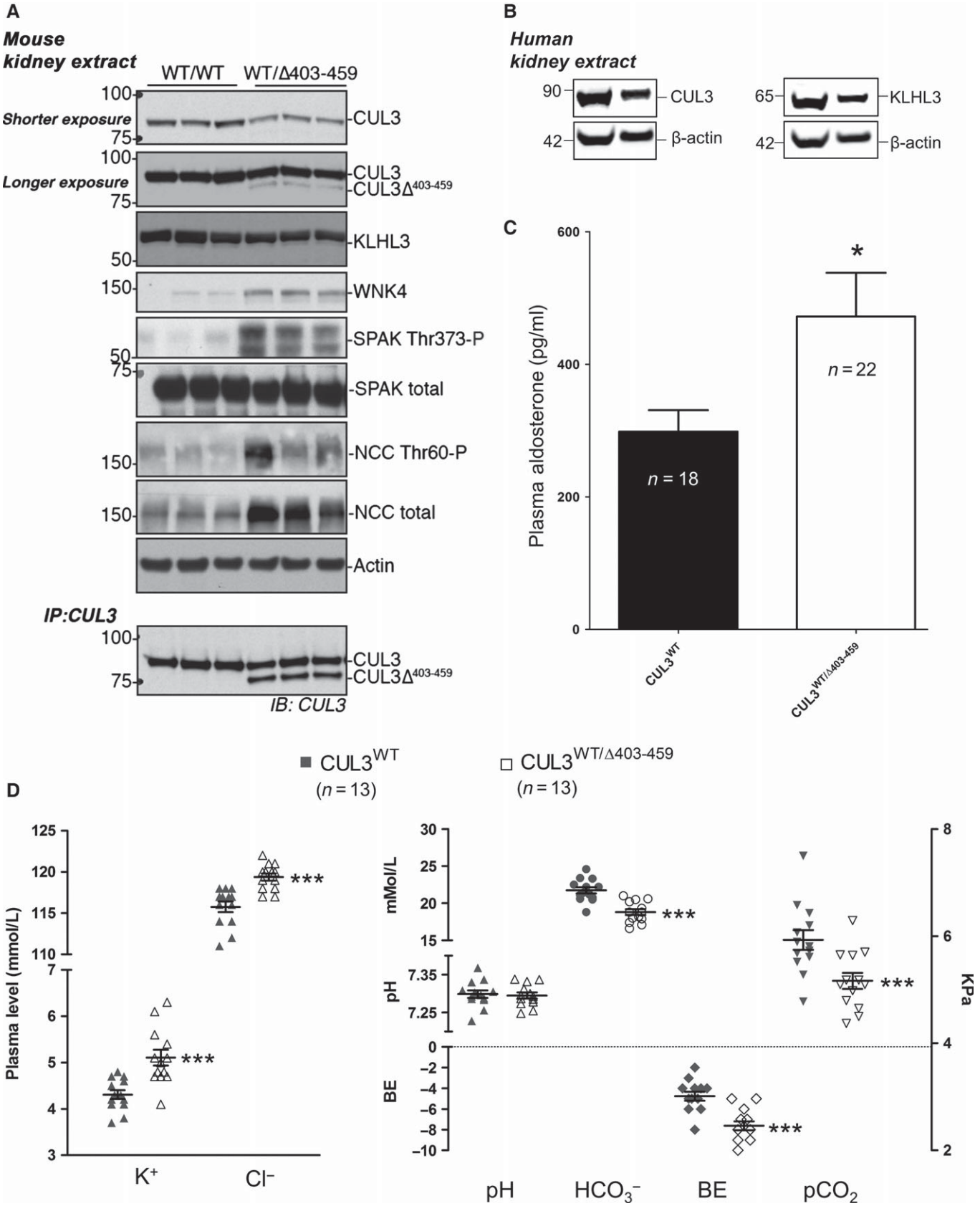

Figure 4.

Figure 4. $CUL3^{WT/\Delta 403–459}$ mice recapitulate PHAII electrolyte imbalances due to over-activation of the renal WNK4-SPAK pathway.

A Western blot of whole kidney lysates from mice culled after a minimum 4-h fast. Following exsanguination after surgery, mouse tissues were rapidly harvested and stored, samples were then homogenised, clarified and quantified prior to SDS–PAGE. Immunodetection with the antibodies shown highlights elevated signalling through the WNK kinase pathway in $CUL3^{WT/\Delta 403–459}$ versus $CUL3^{WT}$ mice. The lowest panel is an anti-CUL3 immunoprecipitation of the kidney lysate samples, whereby the CUL3 antibody was cross-linked to Protein G sepharose and used to affinity purify $CUL3^{WT}$ and $CUL3^{\Delta 403–459}$ from kidney lysates. The samples were incubated together overnight to allow deneddylation of CUL3 proteins to occur and maximise CUL3 binding to the anti-CUL3 resin. Samples were thoroughly washed and eluted from the resin prior to SDS–PAGE and immunodetection for CUL3. The IP highlights that $CUL3^{\Delta 403–459}$ is indeed present within the kidney lysate.

B Fresh frozen kidney tissues from transplant patient and donor cadavers were homogenised, clarified and quantified prior to SDS–PAGE. Western blot analysis confirmed the expression of KLHL3 and CUL3 in normal healthy human kidneys.

C Plasma aldosterone after a minimum 4-h fast was calculated by HTRF (homogeneous time-resolved fluorescence) aldosterone assay. The average aldosterone level per mouse was calculated from duplicate samples run in parallel on the assay. Blood was rapidly harvested in heparin-coated plasma extraction tubes following exsanguination after surgery, and samples were snap-frozen for storage. A 58% increase in aldosterone was detected in $CUL3^{WT/\Delta 403–459}$ versus $CUL3^{WT}$ mice ($^{*}P = 0.0245$). Two-tailed unpaired Student's *t*-test; data are mean ± SEM.

D Arterial blood biochemistries after a minimum 4-h fast. Under anaesthesia, the right carotid artery was cannulated to minimise atmospheric exposure of samples collected for iSTAT blood gas and electrolyte measurements. $CUL3^{WT/\Delta 403–459}$ mice present with abnormal electrolyte homoeostasis compared to $CUL3^{WT}$ mice, exhibiting hyperkalaemia ($^{***}P = 0.0004$) and hyperchloraemia ($^{***}P = 9.5 \times 10^{-5}$) with a compensated metabolic acidosis ($P = 0.7766$), marked by a decrease in bicarbonate (HCO_3^-) ($^{***}P = 3.4 \times 10^{-5}$), base excess (BE) ($^{***}P = 9.1 \times 10^{-5}$) and partial pressure of carbon dioxide (pCO_2) ($^{***}P = 0.0038$). Two-tailed unpaired Student's *t*-test; data are mean ± SEM.

Source data are available online for this figure.

CO_2 removal and hence reduced total CO_2 and pCO_2 levels. The mice also had elevated aldosterone levels (Fig 4C) driven by the hyperkalaemia without pronounced hypervolaemia as evidenced by similar haematocrit levels (Fig EV3). Hypermagnesaemia and hyperphosphataemia were noted on detailed electrolyte analysis of plasma and urine, which are the converse of the abnormalities reported in Gitelman syndrome (Fig EV3; Akhtar & Hafeez, 2009; Rafiqi *et al*, 2010; Pathare *et al*, 2012; Ali *et al*, 2013; Zhang *et al*, 2015). Additionally, we also found that the $CUL3^{WT/\Delta 403–459}$ mice have significantly lower body weight and body length relative to the WT mice (Appendix Fig S4). This is consistent with Gordon's original observation that children with PHA2 may present with a low percentile body weight and height for their age (Gordon, 1986) and more recent reports that $CUL3^{WT/\Delta 403–459}$ patients are growth retarded (Osawa *et al*, 2013; Tsuji *et al*, 2013).

WNK4 and SPAK accumulate and form puncta in the distal convoluted tubule of $CUL3^{WT/\Delta 403–459}$ mice

Using immunofluorescence confocal microscopy of kidney sections, we studied the distribution of proteins involved in the WNK kinase cascade in both $CUL3^{WT/WT}$ and $CUL3^{WT/\Delta 403–459}$ mice (Fig 5A). $CUL3^{WT/\Delta 403–459}$ mice showed a similar CUL3 distribution compared to both the WT mice, and to the WT human kidney (Fig 5A and B). This was in keeping with the abundance observed in the kidney immunoblots (Fig 4A). In contrast, staining for WNK4 and SPAK in the $CUL3^{WT/\Delta 403–459}$ mice revealed these proteins to have a striking punctate appearance in the DCT, but not in adjacent segments of the nephron including the thick ascending limb (TAL; Figs 5A and EV4). While WNK1 and OSR1 puncta have been reported in the DCT of SPAK knockout mice, these were smaller in size and far less numerous (Grimm *et al*, 2012). As these puncta do not co-localise with the lysosomal marker LAMP1 or form ubiquitin-containing aggregates (Figs 5A and EV4), they may represent an accumulation of WNK and SPAK proteins within a protein-processing compartment, such as the trans-Golgi network or activation of secondary protein degradation pathways or storage compartments, due to failed proteasomal clearance (D'Urso *et al*, 1998; Lamark & Johansen, 2012; Wolff *et al*, 2014).

$CUL3^{WT/\Delta 403–459}$ mice have hypertension and a novel vascular phenotype

Over-activation of the WNK pathway as observed in our $CUL3^{WT/\Delta 403–459}$ mice (Figs 4 and 5) should lead to salt retention and elevated blood pressure. We therefore measured the blood pressure (BP) of the $CUL3^{WT/\Delta 403–459}$ mice using a carotid pressure transducer catheter under general anaesthesia. Both male and female $CUL3^{WT/\Delta 403–459}$ mice exhibited significantly higher BP relative to $CUL3^{WT/WT}$ littermates (Fig 6A).

Strikingly, we also observed a previously unreported haemodynamic change in the blood pressure trace of the $CUL3^{WT/\Delta 403–459}$ mice. The systolic aortic pressure wave of the heterozygous mice is augmented, while the diastolic relaxation (τ) is significantly slowed (Munir *et al*, 2007; Fig 6B). These changes suggest early wave reflection of the pressure wave and compliance changes consistent with a stiffened vascular tree. This stiffening could reflect a primary change in the contractile state of vascular smooth muscle, so to explore this we studied the *in vivo* vasoconstrictor responses to intravenous administration of phenylephrine and angiotensin II (Fig 6C; Bergaya *et al*, 2011). The resulting dose–response curves showed that the maximal constrictor response to both vasopressor agents was substantially higher in the $CUL3^{WT/\Delta 403–459}$ mice.

CUL3 and KLHL3 are expressed in the mouse and human aorta, and $CUL3^{WT/\Delta 403–459}$ mice have aortic wall thickening

We also looked for evidence of biochemical changes in the vasculature and confirmed the expression of CUL3 and KLHL3 in mouse and human aorta by immunoblot analysis (Fig 7A and B, Appendix Fig S5). Similar to the kidneys (Fig 4A), no differences were seen in KLHL3 expression between $CUL3^{WT/\Delta 403–459}$ and $CUL3^{WT}$ mice, while the levels of CUL3 WT protein were lower in $CUL3^{WT/\Delta 403–459}$ aorta. To address the altered contractility in the vessel wall *in vivo*, we also measured the level of pMYPT1 in aortic vessel lysates and showed a significant 1.7-fold increase (Feng *et al*, 1999; Somlyo & Somlyo, 2003; Appendix Fig S6). Image analysis of mouse and human aortae confirmed that both have strong CUL3 staining of the vascular endothelium and smooth muscle cells of the intimal and medial layers of the vessel wall (Fig 7C and D). Finally, to explore

Published online: August 18, 2015
EMBO Molecular Medicine

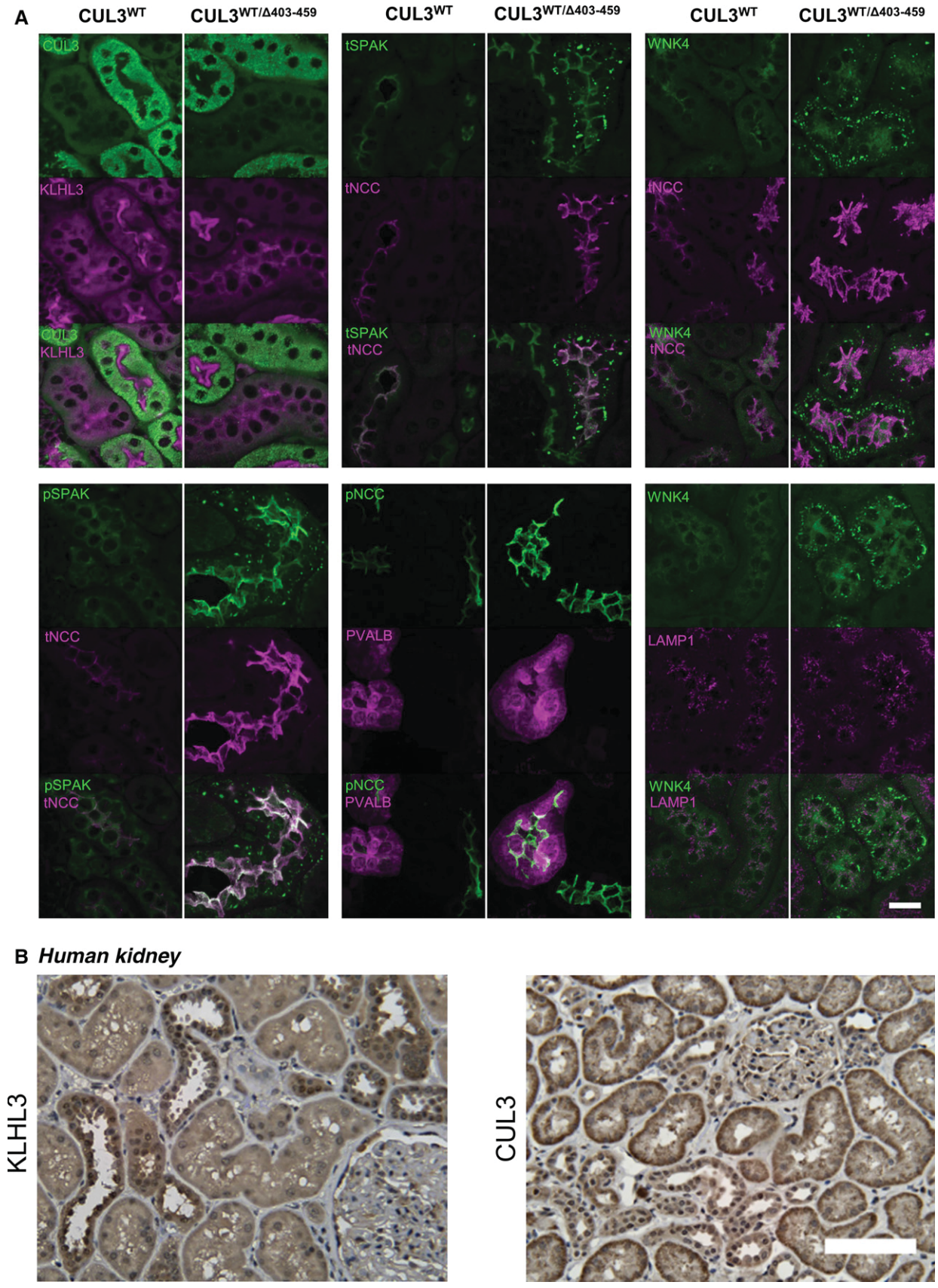

Figure 5.

Figure 5. WNK4 and SPAK specifically accumulate and form puncta in the distal convoluted tubule of CUL3$^{WT/\Delta403–459}$ mice.

A Representative pseudocoloured maximum-intensity *z* projections of immunofluorescently stained kidney sections showing the distribution of the WNK/SPAK pathway components between CUL3$^{WT/\Delta403–459}$ and CUL3^{WT} mice at a minimum 4-h fasting baseline (n = 4 per genotype). CUL3 and KLHL3 are comparable between genotypes, with significantly higher levels of CUL3 in the proximal convoluted tubule (PCT) compared to the weak staining in distal convoluted tubule (DCT) and thick ascending limb of the loop of Henle (TAL), while KLHL3 shows higher expression in the DCT/TAL cytosol with staining of the PCT confined to the apical membrane. Total (t) and phospho (p) NCC Thr44 and SPAK Thr243 show increased apical membrane expression in the parvalbumin (PVALB)-positive early and late (PVALB-negative) DCT of CUL3$^{WT/\Delta403–459}$ mice. Unexpectedly, the increased levels of WNK4 and SPAK resulted in the formation of discrete puncta specifically in the DCT of CUL3$^{WT/\Delta403–459}$ mice. It is possible that the autophagy–lysosomal system may attempt to compensate and degrade these excess proteins although the WNK4 puncta do not colocalise with the lysosomal marker LAMP1. Scale bar, 20 μm.

B Representative immunohistochemical staining of KLHL3 and CUL3 in human kidney sections (n = 6). KLHL3 shows preferential DCT/TAL cytosolic staining similar to the mouse despite no evidence of PCT apical staining as seen in (A). CUL3 exhibits preferential basolateral cytosolic staining of the PCT with similarly low levels of diffuse staining in the DCT/TAL to that of the mouse. Scale bar, 100 μm.

further the vascular phenotype, we performed a morphometric analysis of the aortae of CUL3 mice that confirmed significant thickening of the vessel wall in the heterozygote mice (Fig 7E). This probably reflects hyperplasia/hypertrophy of the vascular smooth muscle cells in the medial layer, as the numbers of elastic laminae were not significantly different (Fig 7E).

Discussion

This study describes the first successful PHA2E mouse model involving CUL3 and highlights the molecular differences and defects of the mutant CUL3 protein. The deletion of 57 amino acids in CUL3$^{\Delta403–459}$ does not affect the ability of the bound RING domain to hydrolyse E2~UB, and as such CUL3$^{\Delta403–459}$ is still an active E3 ligase. Instead, our structural predictions and experimental findings suggest that the CUL3$^{\Delta403–459}$ CRL scaffold lacks a level of rigidity required for substrate ubiquitylation. Our results are consistent with a previous report that demonstrated ubiquitylation of the Cullin-1 substrate (p27) was abrogated when a linker was inserted between the NTD and CTD of the closely related CUL1 protein (Zheng *et al*, 2002). Thus, the CUL3$^{\Delta403–459}$ mutation is a novel physiological example of the importance of this CRL rigidity and to our knowledge the first example of a human mutation that impedes the scaffolding function of a Cullin. Our data are consistent with the working hypothesis that the CUL3$^{\Delta403–459}$ mutation has increased structural flexibility. The deletion of three helices fuses together two unstructured regions, which likely allows greater movement between the N-terminal and C-terminal domains of the Cullin. This prevents the complex from successfully directing ubiquitin towards a bound substrate, and instead, leads to increased auto-ubiquitylation of CUL3 and KLHL3. Importantly, it appears as if *in vivo* this auto-ubiquitylation triggers degradation of the mutant form of the Cullin, as only relatively low amounts of CUL3$^{\Delta403–459}$ are detectable in tissue from the mouse model, while the levels of KLHL3 are unaffected. *In vivo*, CUL3 auto-ubiquitylation possibly precedes ubiquitylation of KLHL3, leading to rapid proteasomal degradation of CUL3$^{\Delta403–459}$ leaving KLHL3 untouched. The auto-degradation of CUL3 is likely to be the major driver for the associated phenotype in patients. While, some CUL3$^{\Delta403–459}$ remains in cells, we show that this remaining protein is unable to ubiquitylate WNK substrates. Taken together, our data suggest that the disease-associated deletion of exon 9 from CUL3 is a loss-of-function mutation with respect to substrate ubiquitylation. Importantly, all PHA2E patients are heterozygotes, so they retain a functioning copy of CUL3^{WT}. Thus, the CUL3$^{\Delta403–459}$ mutation either behaves as a dominant-negative to inhibit CUL3^{WT} or is haploinsufficient in the context of blood pressure regulation with the single functional copy of CUL3 unable to sustain the physiological need for WNK ubiquitylation. Our data support a haploinsufficiency model, as a large proportion of the mutant protein is removed from the cell by auto-degradation and *in vitro* CUL3$^{\Delta403–459}$ does not inhibit CUL3^{WT}. However, it is possible that *in vivo* the remaining CUL3$^{\Delta403–459}$ may still sequester KLHL3 from CUL3^{WT} in a dominant-negative fashion, as in cells we observed increased binding between CUL3$^{\Delta403–459}$ and KLHL3 (Fig 1H) and the reduced affinity for CAND1 may prevent the release of KLHL3 from non-functional CUL3$^{\Delta403–459}$ complexes. These two possibilities could be addressed in a heterozygous mouse model carrying a full-length CUL3 deletion; under the haploinsufficiency model, it should show WNK stabilisation.

The CUL3$^{WT/\Delta403–459}$ mice have high blood pressure and up-regulated signalling in the context of the WNK kinase pathway, which parallels the WNK4 (D568E; Yang *et al*, 2007; Chowdhury *et al*, 2013) and KLHL3 (R528H; Mori *et al*, 2013) PHA2 mouse models previously described. Mechanistically, our data suggest CUL3$^{\Delta403–459}$ promotes its own degradation, as it has a heightened propensity to self-ubiquitylate and is less abundant in mouse kidney extract. Hence, we would predict that PHA2E CUL3$^{WT/\Delta403–459}$ patients would similarly have lower overall CUL3 levels. As CUL3 ubiquitylates a number of other proteins, it seems remarkable then that PHA2E patients do not have other phenotypic manifestations. However, this may not be surprising if considered in the context of a haploinsufficiency model. BP homoeostasis requires reactive and precise control of ion fluxes in the distal nephron, especially the DCT, as changes in intake and output of salt are constantly balanced. The phosphorylation of the NCC/NKCC ion transporters by WNK kinases appears to be regulated by two complementary systems: the regulation of total WNK protein levels by CUL3-KLHL3, and the level of WNK activation by phosphorylation. Currently, the sensing mechanisms that lead to WNK phosphorylation or the degradation of the WNK kinases by CUL3-KLHL3 are largely unknown. However, sufficient amounts of CUL3 must be available for signalling-dependent ubiquitylation of the WNK kinases. It is possible that having only half the amount of functional CUL3 within kidney cells is not enough for the system to respond rapidly. The presence in our knock-in mice of WNK4 puncta *in vivo* also suggests that DCT cells may deploy secondary protein degradation pathways to manage excess WNK proteins, such as the autophagy–lysosomal system. However, the nuclear proximity of the large puncta and the absence of lysosomal staining or formation of ubiquitylated aggregates suggest that these excess WNK proteins are shunted to protein quality control compartments such as the aggresome or

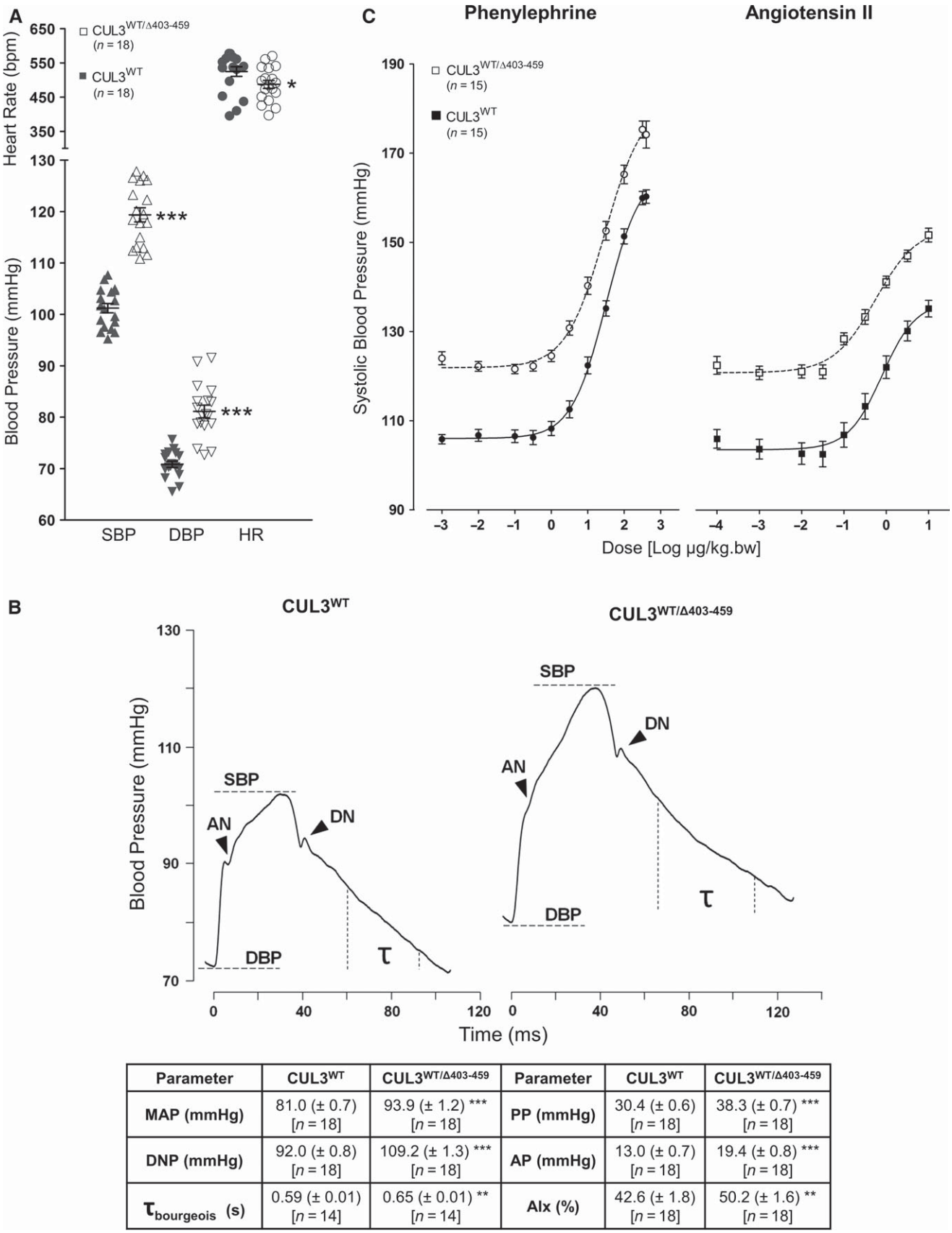

Parameter	CUL3^{WT}	CUL3$^{WT/\Delta 403-459}$	Parameter	CUL3^{WT}	CUL3$^{WT/\Delta 403-459}$
MAP (mmHg)	81.0 (± 0.7) [*n* = 18]	93.9 (± 1.2) *** [*n* = 18]	PP (mmHg)	30.4 (± 0.6) [*n* = 18]	38.3 (± 0.7) *** [*n* = 18]
DNP (mmHg)	92.0 (± 0.8) [*n* = 18]	109.2 (± 1.3) *** [*n* = 18]	AP (mmHg)	13.0 (± 0.7) [*n* = 18]	19.4 (± 0.8) *** [*n* = 18]
$\tau_{bourgeois}$ (s)	0.59 (± 0.01) [*n* = 14]	0.65 (± 0.01) ** [*n* = 14]	AIx (%)	42.6 (± 1.8) [*n* = 18]	50.2 (± 1.6) ** [*n* = 18]

Figure 6.

Figure 6. Increased arterial stiffness contributes towards the hypertension of CUL3$^{WT/\Delta403-459}$ mice.

A Continuous blood pressure measurements were taken in mice under general anaesthesia with thermostatically controlled body temperature, right carotid artery pressure transducer catheterisation and ECG Lead II heart rate monitoring. CUL3$^{WT/\Delta403-459}$ mice have elevated systolic (SBP) (***$P = 1 \times 10^{-12}$) and diastolic (DBP) blood pressure (***$P = 8.5 \times 10^{-8}$), although they also present with 7% lower heart rates (*$P = 0.0485$) when compared to CUL3^{WT} mice. Two-tailed unpaired Student's *t*-test; data are mean ± SEM.

B Pulse waveform analysis of blood pressure traces obtained in (A) reveals that CUL3$^{WT/\Delta403-459}$ mice have an increased pulse pressure (PP) [SBP − DBP] (***$P = 2.1 \times 10^{-10}$), augmentation pressure (AP) [SBP − anacrotic notch (AN) pressure] (***$P = 3.5 \times 10^{-6}$), dicrotic notch (DN) pressure (***$P = 4.7 \times 10^{-13}$) and mean arterial pressure (MAP) [1/3 × SBP + 2/3 × DBP] (***$P = 1.3 \times 10^{-9}$). This hypertensive phenotype is in part due to changes in vascular contractility in CUL3$^{WT/\Delta403-459}$ mice as evidenced by their higher augmentation index (AIx) [AP/PP] (**$P = 0.0096$), a marker of arterial stiffness, and is further supported by an increase in their diastolic pressure decay time constant ($\tau_{bourgeois}$) [1/slope of diastolic pressure decay; measured 30 ms after DN and 20 ms before end DBP] (**$P = 0.0083$), a surrogate marker of increased vascular resistance. Two-tailed unpaired Student's *t*-test; data are mean ± SEM

C *In vivo* dose–responses to phenylephrine and angiotensin II. After baseline measurements were obtained from mice in (A), the right external jugular vein was cannulated for administration of bolus doses of vasopressors in increasing half-log steps. Dose–response curves were generated and data analysed using a logistical function to determine the estimated dose producing half-maximal response (ED_{50}) and maximum response (E_{max}). The fitted E_{max} for phenylephrine was increased in CUL3$^{WT/\Delta403-459}$ versus CUL3^{WT} (183.9 ± 2.5 versus 164.9 ± 1.4 mmHg) (***$P = 1 \times 10^{-6}$) indicating an increased vasoconstrictor response to adrenergic stimulation elevating systolic blood pressure substantially above the CUL3^{WT} maximum. Similarly, the fitted E_{max} for angiotensin II stimulation was higher in CUL3$^{WT/\Delta403-459}$ versus CUL3^{WT} (155.5 ± 1.8 versus 138.3 ± 2.2 mmHg) (***$P = 1.7 \times 10^{-6}$). However, there was no change between CUL3$^{WT/\Delta403-459}$ versus CUL3^{WT} sensitivity (as measured by ED_{50}) to phenylephrine (36.6 ± 5.1 versus 31.4 ± 2.8 μg/kg bw) ($P = 0.3778$) or angiotensin II (0.77 ± 0.16 versus 0.93 ± 0.13 μg/kg bw) ($P = 0.4401$). Two-tailed unpaired Student's *t*-test; data are mean ± SEM.

Source data are available online for this figure.

juxta-nuclear quality control compartment (JUNQ) in an attempt to compensate for loss of proteasomal degradation (Lamark & Johansen, 2012; Wolff *et al*, 2014). Hence, while other CUL3 substrates may be unaffected in the CUL3$^{WT/\Delta403-459}$ mice, the rapid and signal-dependent switching of WNK ubiquitylation may be executed abnormally in these mice and PHA2E patients.

Mutations in CUL3, KLHL3, WNK1 and WNK4 are known to cause FHHt with constitutive activation of the NCC co-transporter (Boyden *et al*, 2012; Osawa *et al*, 2013; Tsuji *et al*, 2013; Alessi *et al*, 2014; Glover *et al*, 2014). What has been less clear is why the mutation of CUL3 has resulted in a more severe form of FHHt (PHA2E). Our unexpected discovery of a vascular phenotype in the CUL3$^{WT/\Delta403-459}$ mice leads us to speculate that their hypertension may not be driven by salt retention in the DCT alone. It is possible that part of their hypertension originates from an increased contractile state in their vasculature tree. If a similar phenomenon occurs in PHA2E, this may explain the early onset and severity of the blood pressure that occurs in these patients. The CUL3$^{WT/\Delta403-459}$ mice have an altered aortic pulse waveform and slowed diastolic relaxation that is consistent with stiffening of their arterial tree. These changes have been reported before in humans with hypertension (Kaess *et al*, 2012), but not previously in a hypertensive mouse model. It is also worth noting that augmentation of the aortic pressure wave is often not detected by brachial cuff BP measurements, so it could have gone unnoticed in the routine clinical assessment of PHA2E patients. The increase in pMYPT1 in the aortae from the CUL3$^{WT/\Delta403-459}$ mice and the increase in their *in vivo* pressor responses to phenylephrine and angiotensin II further suggest that the altered contractile state could be a primary phenomenon rather than simply a secondary response to hypertension. If this is the case, the contraction could occur by at least two distinct pathways. Firstly, the WNK1/WNK3/SPAK/OSR1 pathway is thought to be important for regulating vascular tone by controlling the phosphorylation state of the NKCC1 co-transporter and hence the membrane potential of vascular smooth muscle (VSM) cells (Yang *et al*, 2010; Bergaya *et al*, 2011; Zeniya *et al*, 2013). So if either WNK1 or WNK3 accumulates in the vessel wall of the CUL3$^{WT/\Delta403-459}$ mice, the contractile tone would be expected to rise through depolarisation of VSM and increased calcium entry. Alternatively, the mutant Cullin-3 protein may directly affect the phosphorylation state of myosin light chain by regulating RhoA/RhoA kinase (ROCK) levels (Ibeawuchi *et al*, 2015). RhoA protein levels in the VSM are thought to be regulated by CUL3 in complex with the substrate adaptor RhoBTB1 (Pelham *et al*, 2012). If these pathways are operational in PHA2E, then they suggest that treatment with a thiazide diuretic or dietary sodium restriction, while effective in reversing the electrolyte disturbances, may be less effective in reversing any central aortic pressure changes in PHA2E. If WNK/SPAK/OSR1 is the predominant pathway causing disease, a loop diuretic such as bumetanide may be more effective than a thiazide, while for the RhoA/ROCK pathway a direct arterial vasodilator or a specific ROCK inhibitor (Liao *et al*, 2007) may be the more appropriate drug of choice. Central aortic pressure elevation is now widely accepted to be an important and independent cardiovascular risk factor (Liao & Farmer, 2014), so if it is elevated in patients with PHA2E, it will be important to show that it is normalised by appropriate pharmacotherapy.

Materials and Methods

All plasmids, antibodies and recombinant proteins that we have generated for this study are available on request from the MRC-PPU reagents website (http://mrcppureagents.dundee.ac.uk/).

Plasmids and protein purification

The following plasmids and/or protein purifications have been described elsewhere in Ohta *et al* (2013): KLHL3 (DU23218), DAC-TEV-CUL3-RBX1 (DU23291), His-UBE1 (DU32888) and His-TEV-UBE2D3 (DU15703); and in Kelsall *et al* (2013): Nedd8 (DU20689), UBE2M (DU15804) and APPBP1/UBA3 heterodimer (Nedd8 activating E1) (DU21784).

DAC-TEV-CUL3$^{\Delta403-459}$-RBX1 (DU23292) was cloned in a comparable way to DAC-TEV-CUL3^{WT}-RBX1 (DU23291). Specifically, the pFastBac Dual DAC-TEV expression system was created by subcloning a BglII-BamHI-flanked PCR product encoding the full-length DAC-tag followed by a TEV protease site into a

Published online: August 18, 2015
EMBO Molecular Medicine

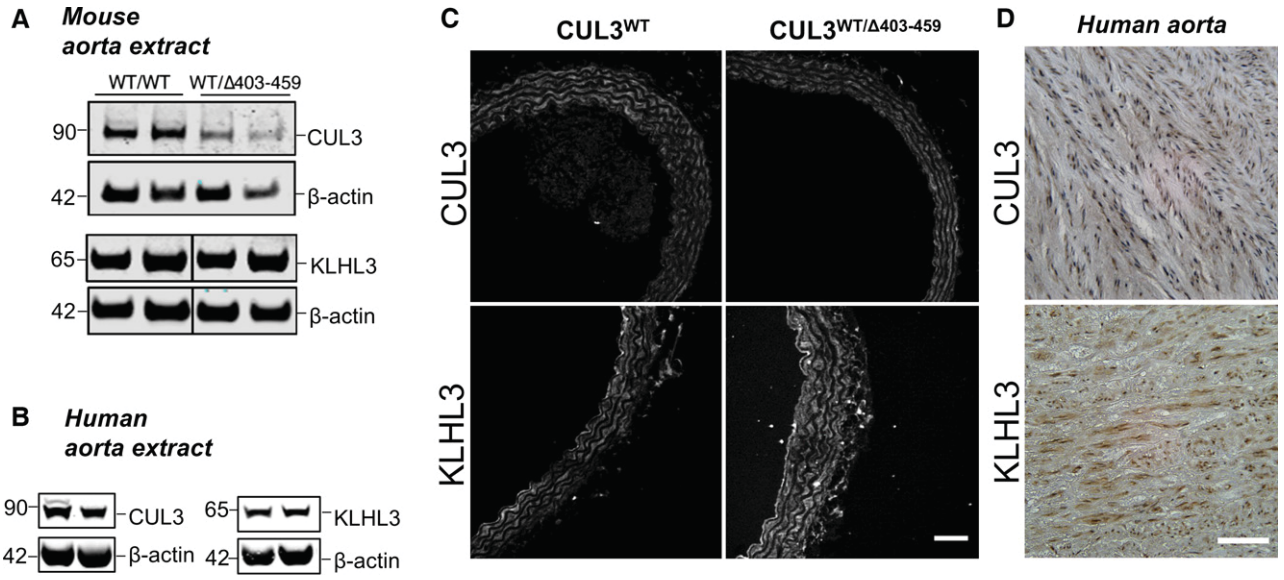

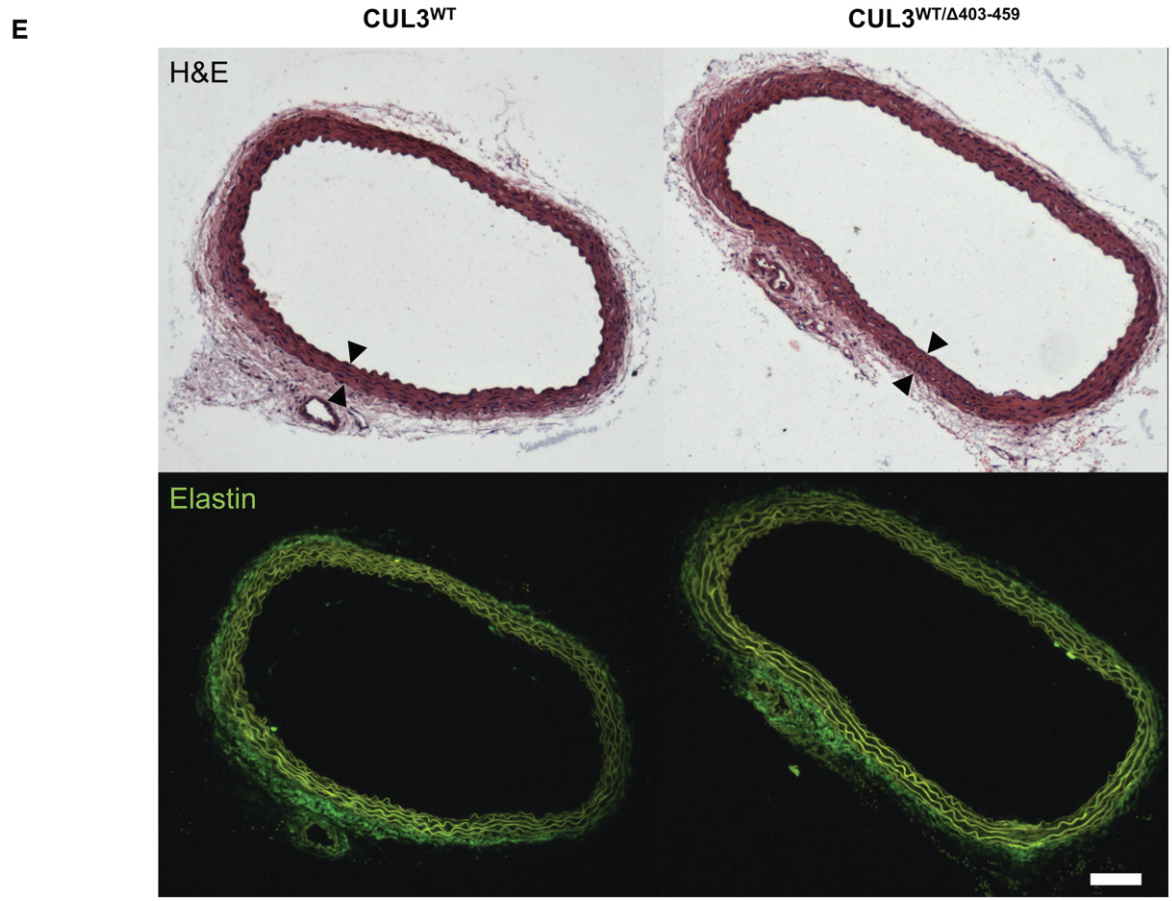

Parameter	CUL3^{WT} (n = 10)	CUL3$^{WT/\Delta 403-459}$ (n = 11)
Wall thickness (μm)	99.6 (± 3.5)	120.8 (± 3.3) ***
No. of elastic laminae	5.3 (± 0.1)	5.4 (± 0.1)

Figure 7.

Figure 7. CUL3 and KLHL3 are present in mouse and human aorta, and CUL3$^{WT/\Delta 403–459}$ mice undergo aortic vascular remodelling.

A Western blot of tunica media-intima thoracic aorta lysates from mice culled after a minimum 4-h fast. Following exsanguination after surgery, mouse tissues were rapidly harvested and the tunica adventitia removed before storage, and later, the samples were homogenised, clarified and quantified prior to SDS–PAGE. Western blot analysis confirmed the expression of KLHL3 and CUL3. Similar to the kidney, the aorta of CUL3$^{WT/\Delta 403–459}$ showed slightly lower levels of CUL3 compared to CUL3^{WT} without any change in KLHL3 levels.

B Fresh frozen thoracic aorta tissues from donor cadavers were homogenised, clarified and quantified prior to SDS–PAGE. Western blot analysis confirmed the expression of KLHL3 and CUL3 in normal healthy human aorta.

C Representative maximum-intensity *z* projections of immunofluorescently stained thoracic aorta sections showing the distribution of CUL3 and KLHL3 between CUL3$^{WT/\Delta 403–459}$ and CUL3^{WT} mice at a minimum 4-h fasting baseline (n = 4 per genotype). CUL3 and KLHL3 localisation is comparable between genotypes. The highest levels were detected in the vascular smooth muscle cells and endothelium, with a minimal expression in the perivascular adipose tissue of the adventitia. Scale bar, 50 μm.

D Representative immunohistochemical staining of KLHL3 and CUL3 in human thoracic aorta sections (n = 6). Similar to the mouse staining seen in (C), vascular smooth muscle cells in the tunica media of the aortic wall are positive for KLHL3 and CUL3. Scale bar, 50 μm.

E Morphometric analysis of thoracic aortae reveals vascular remodelling in CUL3$^{WT/\Delta 403–459}$ mice. There is an increase of ~21% in the vessel wall intima-media thickness (demarcated by arrows) of CUL3$^{WT/\Delta 403–459}$ compared to CUL3^{WT} mice (***P = 0.0003). However, there is no change in the number of elastin laminae (P = 0.1458) and therefore no increase in the number of medial muscle layers between genotypes. Two-tailed unpaired Student's *t*-test; data are mean ± SEM.

Source data are available online for this figure.

pFastBac™ Dual (Life Technologies, UK). Human Cullin-3 (Δ403–459; GenBank NM_003590.4) was codon-optimised for expression in insect cells and custom synthesised (GenScript USA Inc.) before being subcloned downstream of the DAC-tag in cassette two of this vector. Human RBX1 (GenBank NM_014248.2) was amplified from an EST IMAGE clone 3138751 and subcloned into cassette one (untagged). Human CAND1 (GenBank NM_018448.3) was amplified as a Not1 flanked ORF from EST IMAGE clone 5265409 and subcloned into pGEX6P-2 (GE Healthcare LifeSciences UK) for bacterial expression with an N-terminal GST tag. All PCRs were carried out using KOD Hot Start DNA Polymerase (Merck Millipore, Germany). All full-length products or fragments were cloned into pSc-B (Agilent) and sequenced in full prior to further subcloning or manipulation. DNA sequencing was performed by the Sequencing Service at the College of Life Sciences, University of Dundee (www.dnaseq.co.uk).

Human recombinant CUL3$^{\Delta 403–459}$-RBX1 or CUL3^{WT}-RBX1 was expressed in a multibac vector with a Dac-TEV-fusion tag on the CUL3 and untagged RBX1 (Lee *et al*, 2012). Proteins were expressed in the baculovirus system in Sf21 cells cultured in Insect-Protein-free Insect Cell Medium (Lonza). The fusion protein was captured from the lysate by incubation with ampicillin-sepharose. After washing, the protein was recovered from the solid phase by incubation with C-terminally His-tagged TEV protease (10 μg per 1 mg substrate). The protease and any free Dac-tag were removed with Ni-agarose and ampicillin–sepharose. The protein was then concentrated and further purified by size-exclusion chromatography (SEC) in 50 mM HEPES pH 7.5, 150 mM NaCl and 10% glycerol.

Human recombinant CAND1 was expressed as an N-terminally GST-tagged fusion protein in BL21 cells. Expression was induced with 50 μM IPTG at 15°C for 16 h. Following cell lysis, GST-CAND1 was captured on glutathione resin, washed and then eluted from the resin with 10 mM reduced glutathione in 50 mM HEPES pH 7.5, 150 mM NaCl, 10% glycerol (w/v) and 1 mM DTT. The protein was then dialysed to remove glutathione.

Nedd8 was expressed as an untagged protein in BL21 cells, and following induction with 1 mM IPTG at 16°C, cells were lysed and frozen. Upon thawing, benzonase and 2 mM $Mg(C_2H_3O_2)_2$ were added and cells were disrupted by sonication. Insoluble material was pelleted, and this pellet was resuspended in 50 mM Tris pH 7.5 and 150 mM NaCl and washed thrice. To extract Nedd8, the pellet was resuspended in 8 M urea and mixed overnight. Following clarification by centrifugation the supernatant was diluted fourfold with MQ water and dialysed thrice to remove urea and enable Nedd8 refolding. Contaminants were removed by depletion using a Q-sepharose column. The Nedd8 was concentrated prior to a final purification by SEC in 20 mM HEPES pH 7.5, 150 mM NaCl and 0.03% Brij 35.

Antibodies

The following antibodies were raised in sheep and affinity-purified on the appropriate antigen by the Division of Signal Transduction Therapy Unit at the University of Dundee: WNK1-total antibody (residues 2,360–2,382 of human WNK1, S62B), WNK4 N-terminal antibody (residues 1–14 of mouse WNK4, S726D), SPAK-mouse N-terminal antibody (2–76 of mouse SPAK, S668D), SPAK-mouse C-terminal antibody (424–556 of mouse SPAK, S669D), SPAK/OSR1 (T-loop) phospho-Thr233/Thr185 antibody (226–238 of human SPAK or residues 178–190 of human OSR1, TRNKVRKpTFVGTP, S204C), SPAK phospho-Thr233 antibody (226–238 of human SPAK, TRNKVRKpTFVGTP, S668B and S668D), NKCC1-total antibody (residues 1–260 of shark NKCC1, S841B), NCC phospho-Thr60 antibody (residues 54–66 of human NCC phosphorylated at Thr60, RTFGYNpTIDVVPT, S995B), NCC phospho-Thr44 antibody (residues 38–52 of mouse NCC phosphorylated at Thr44, SQPSHLTpHGSTLYMRRR, S242C) and KLHL3 N-terminal mouse (1–21 of mouse KLHL3, S740D). The anti-ERK1/2 antibody (9102) was purchased from Cell Signaling Technology. The anti-FLAG antibody (F1804), anti-β-actin antibody and anti-His antibody were purchased from Sigma-Aldrich. The rabbit anti-human CUL3 antibody was a kind gift from Izabela Sumara at the IGBMC, Strasbourg (Sumara *et al*, 2007). The following commercial rabbit anti-human antibodies were obtained and used for immunodetection: KLHL3 antibody (HPA051291) from Atlas Antibodies; KLHL3 (AB196776) (~14% immunogen peptide homology with KLHL2), NCC-total [SLC12A3] (AB95302) and LAMP1 (AB24170) from Abcam; and PV25 (PVALB) from Swant. The goat anti-GFP (AB5450) and the mouse monoclonal anti-ubiquitin (AB7254) were purchased from Abcam. The MYPT1 phospho-Thr696 mouse monoclonal antibody (MAB0001) was obtained from Abnova. Secondary antibodies coupled to horseradish peroxidase used for immunoblotting were obtained from

Pierce. Secondary antibodies conjugated to fluorochromes for LiCor Odyssey Western blot scanning were obtained from Licor (www.licor.com) and Life Technologies. Fluorochrome-conjugated secondary antibodies for immunofluorescent confocal microscopy were obtained from Life Technologies and Abcam.

In vitro assays

Ubiquitin E2 discharge assays were performed based on the method described (Plechanovová *et al*, 2011). Firstly, His-UBE2D2 (150 μM) was incubated in the presence of 2 mM ATP, 5 mM $MgCl_2$, 200 μM ubiquitin and 0.25 μM UBE1 in 50 mM HEPES pH 7.5, 150 mM NaCl, 10% glycerol and 1 mM DTT at 16°C for 15 min. To stop the reaction, we depleted ATP by incubating the charging mixture with apyrase (4.5 U/ml; New England Biolabs) at 16°C for 10 min. To this, 1 μM E3 was added and discharge reactions were then allowed to proceed for the time indicated in the figure, at 30°C. Reactions were stopped by the addition of non-reducing SDS–Laemmli sample buffer. 16% bis-acrylamide non-reducing SDS–PAGE, followed by immunodetection with anti-His antibody, allowed visualisation of ubiquitin discharge. E3 ubiquitin-ligase activity assays were based on those described previously in Ohta *et al* (2013). When used as a substrate in assays, full-length WNK kinases were purified from HEK-293 cells, and either 5 μl of immunoprecipitated endogenous WNK1 protein derived from 0.5 mg of HEK-293 cells or 5 μl of immunoprecipitated over-expressed FLAG-WNK4 from 0.05 mg of HEK-293 cells was used for each assay reaction. Ubiquitylation assays typically contained 20 mM HEPES/HCl (pH 7.5), 150 mM NaCl, 2 M DTT, 10% (w/v) glycerol, 8 μM CUL3-RBX1 complex (WT or mutant), 7 μM KLHL3, 7 μM UBE1, 60 μM UBE2D3 and 3,000 μM ubiquitin. The concentrations of some components were altered on occasion (e.g. Fig 3B) to best illustrate a given point. Reactions were initiated by adding ATP and $MgCl_2$ to a final concentration of 1 mM, and samples were incubated for the times indicated at 30°C. Reactions were stopped by the addition of SDS sample buffer, and samples were analysed after SDS–PAGE followed by immunoblotting or Coomassie blue gel staining. For the N8-ligase activity assays, 1 μM E3 was incubated at 30°C with 68 μM Nedd8, 8 μM UBE2M and 0.2 μM NAE in the presence of 0.15 mM ATP, 1.5 mM $MgCl_2$ 50 mM HEPES pH 7.5, 150 mM NaCl and 20% (w/v) glycerol for the time indicated. Reactions were stopped by the addition of SDS sample buffer, and samples were analysed following SDS–PAGE separation and Coomassie blue staining.

In vitro protein interaction pull downs

For KLHL3-CUL3, anti-KLHL3 resin was made by covalently coupling anti-KLHL3 antibody (S377D) to Protein G sepharose utilising dimethyl pimelimidate. Anti-KLHL3 resin, or control resin (prepared in the absence of any antibody), was incubated with saturating amounts of purified KLHL3 and washed thrice, resulting in KLHL3 resin. This resin was then incubated with $CUL3^{WT}$ or $CUL3^{\Delta 403–459}$ at 4°C for 1 h, before being washed thrice with PBS 0.02% Tween-20. For CAND1-CUL3, purified GST-CAND1 or GST was incubated in excess with resin at 4°C resulting in GSH-resin-GST or GSH-GST-CAND1 resin. Each resin was then incubated with purified $CUL3^{WT}$ or $CUL3^{\Delta 403–459}$ for 1 h at 4°C before being washed once with PBS 0.02% Tween-20 and then twice with PBS in the absence of detergent. Following washing, volumes were reduced to a minimum and proteins were eluted from the resin by the addition of SDS sample buffer, prior to analysis by SDS–PAGE and immunoblotting.

Cell culture

HEK (human embryonic kidney)-293 cells were cultured in 14-cm dishes in DMEM (Dulbecco's modified Eagle's medium; Life Technologies) supplemented with 10% (v/v) foetal bovine serum, 2 mM L-glutamine, 100 units/ml penicillin and 0.1 mg/ml streptomycin. Protein expression was induced for 24 h with 1 μg/ml tetracycline (Life Technologies). To obtain endogenous WNK1 for activity assays, we followed the immunoprecipitation protocol described in Ohta *et al* (2013). To obtain wild-type FLAG-WNK4, we utilised the cell lines from Schumacher *et al* (2014) and Ohta *et al* (2013). When FLAG-WNK4 was to be used for *in vitro* ubiquitylation assays, a 14-cm plate of confluent cells was lysed in 0.5 ml ice-cold mammalian lysis buffer A (mammalian lysis buffer A: 50 mM Tris/HCl (pH 7.5), 0.15 M NaCl, 1 mM EGTA, 1 mM EDTA, 1 mM Na_3VO_4, 50 mM NaF, 5 mM $Na_4P_2O_7$, 0.27 M sucrose, 1% (w/v) Nonidet P-40, 1 mM benzamidine, 0.1 mM PMSF, 0.1% 2-mercaptoethanol, and Roche protease inhibitor mix (1 tablet in 50 ml) for M2 affinity purification). Lysates were clarified by centrifugation, and to this, 10 μl M2 resin per 100 μl lysate was added. Incubation of the resin with the cellular lysate for 1 h at 4°C was followed by two washes with mammalian lysis buffer A, and two further washes with 1× PBS to give a pure M2-Flag-WNK4 slurry. For interaction studies with FLAG-$CUL3^{WT}$ and FLAG-$CUL3^{\Delta 403–459}$, the same method was followed as above, with an alternative mammalian lysis buffer B (50 mM HEPES/KOH pH 7.2, 5 mM $Mg(C_2H_3O_2)_2$, 70 mM $KC_2H_3O_2$, 0.2% (w/v) Triton X-100, 10% (w/v) glycerol, 0.2 mM EDTA, 1 mM Na_3VO_4, 50 mM NaF, 5 mM $Na_4P_2O_7$ and Roche protease inhibitor mix (1 tablet in 50 ml)). When it was desirable to prevent deneddylation, buffers were supplemented with 50 μM 1,10-phenanthrolin.

Mass spectrometry analysis

Prior to SDS–PAGE, samples were reduced and alkylated in the following way. Reactions were stopped at the time shown and incubated at 95°C in 1× LDS (Invitrogen) 5 mM DTT for 1 min. Alkylation occurred at room temperature for 30 min by the addition of 20 mM iodoacetamide (20 mM) to the samples. To quench the reaction, DTT was added to a final concentration of 20 mM, and the sample was then processed on precast 4–12% gradient gel (Invitrogen). Gel pieces were excised as shown by the boxed areas in the figure and in gel digestion of the proteins with 5 μg/ml trypsin and subsequent analysis. Mass spectrometric analysis was performed by LC-MS-MS on a linear ion trap–orbitrap hybrid mass spectrometer (Orbitrap-VelosPro; Thermo) coupled to a U3000 RSLC HPLC (Thermo). Peptides were trapped on a NanoViper trap column, 2 cm × 100 mm C18 5 mm 100 Å (Thermo, 164564) and then separated on a 15-cm Thermo EasySpray column (ES800) equilibrated with a flow of 300 nl/min of 3% solvent B [solvent A: 2% acetonitrile, 0.1% formic acid and 3% DMSO in H_2O; solvent B: 80% acetonitrile, 0.08% formic acid and 3% DMSO in H_2O]. The elution

gradient was as follows: time (min): solvent B (%): 0:3, 5:3, 45:35, 47:99, 52:99, 55:3 and 60:3. The instrument was operated with the "lock mass" option to improve the mass accuracy of precursor ions, and data were acquired in the data-dependent mode, automatically switching between MS and MS-MS acquisition. Full-scan spectra (m/z 400–1,600) were acquired in the orbitrap with resolution $R = 60{,}000$ at m/z 400 (after accumulation to an FTMS Full AGC Target, 1,000,000; FTMS MSn AGC Target, 50,000). The 20 most intense ions, above a specified minimum signal threshold (2,000), based upon a low-resolution ($R = 15{,}000$) preview of the survey scan, were fragmented by collision-induced dissociation and recorded in the linear ion trap (Full AGC Target, 30,000; MSn AGC Target, 5,000). Data files were analysed by Proteome Discoverer 1.4-SP1 (Thermo), using Mascot 2.4.1 (www.matrixscience.com), and searching an in-house database containing the relevant sequences. Scaffold (www.ProteomeSoftware.com) was also used to examine the Mascot result files. Allowance was made for the following fixed, Carbamidomethyl (C), and variable modifications, Oxidation (M), Dioxidation (M), GlyGly (K), LeuArgGlyGly (K) and Phospho (ST). Error tolerances were 10 ppm for MS1 and 0.6 Da for MS2.

Generation and genotyping of WT and CUL3$^{\Delta 403–459}$ mice

Standard housing conditions were used to maintain the mice. Taconic Artemis generated the CUL3$^{\Delta 403–459}$ mice on a C57BL/6N background, which were backcrossed onto C57BL/6J to maintain the colony. All experiments were performed using littermates that were backcrossed at least once onto C57BL/6J. Genomic DNA from ear biopsies was isolated and used to genotype all mice in the study. Genotyping by PCR utilising primer 1: AAACTTACCCACTTGTT TGCC, and primer 2: AGACATCTCAGGTTACTATGGGC detected the presence of the CUL3^{WT} (683 bp) or CUL3$^{\Delta 403–459}$ (395 bp) allele. Studies were conducted on groups of approximately equal ratios of male-to-female mice with the exception of *in vivo* cardiovascular phenotyping in which a 1:2 ratio of male-to-female mice was used. All animal studies and breeding were approved by the University of Dundee ethical committee and performed under a UK Home Office-approved licence.

Mouse kidney and testes lysates

Mouse tissues were rapidly harvested and either snap-frozen in liquid nitrogen and stored at −80°C or incubated in 1 ml RNAlater® solution (Sigma-Aldrich) at 4°C for 16–30 h before being removed from this buffer, patted dry with clean tissue and then stored dry at −80°C. Lysates were prepared by homogenising tissue on ice using a Polytron PT1200C homogenizer (Kinematica) in 2 ml ice-cold mammalian lysis buffer and then clarified by centrifugation at 18,000 *g* for 30 min. The clarified supernatant was then quantified and used immediately. Any excess sample was snap-frozen in liquid nitrogen in single-use aliquots for use as required.

The lysates to be used for immunoprecipitation were prepared in the same way, with the following exceptions, all designed to promote deneddylation of the cullin proteins. Detergent was not included in the lysis buffer. Following homogenisation, samples were incubated on ice for 4 h. Following clarification by centrifugation at 18,000 *g* for 30 min, samples were aliquoted into fractions and either frozen in liquid nitrogen and stored at −80°C or used immediately. Clarified supernatant was incubated at room temperature for 1 h to enable further deneddylation, and samples were then cooled on ice and centrifuged a second time to ensure any precipitate was removed. Anti-CUL3 antibody (S067D) cross-linked (DMP) to Protein G agarose was mixed with saturating amount of lysate and incubated rotating overnight at 4°C. The next morning, the agarose beads were washed thrice with mammalian lysis buffer B and twice with 1× PBS. Proteins were eluted from beads by SDS sample buffer addition and boiling at 95°C for 10 min prior to centrifugation and SDS–PAGE and immunodetection.

Immunoblotting

Lysates or protein mixes were boiled at 95°C with 1× SDS–Laemmli sample buffer, for 5 min before being subject to SDS–PAGE (8 or 10% Tris–glycine gel, or 4–10% gradient gels (Life Technologies) or self-prepared 16% bis-acrylamide). Gels were transferred to nitrocellulose membrane using the standard wet transfer method (15% MeOH Towbin transfer buffer). Following blocking of the membranes (TBST 5% (w/v) dried skimmed milk), they were then incubated overnight at 4°C with the primary antibody indicated. All DSTT-produced sheep antibodies were used at 2 μg/ml, and phospho-specific antibodies included the addition of 10 μg/ml of the dephospho-peptide used to raise the antibody. Commercial antibodies were diluted 1 in 1,000. Membranes were then washed in TBST five times and incubated with the appropriate secondary HRP antibody at room temperature at 1:5,000 dilution. Membranes were subsequently washed five times, and the HRP signal was detected using chemiluminescence reagent (Pierce). Immunoblots were developed using an automatic film processor (SRX-101; Konica Minolta Medical).

CUL3 structural docking

Cullin-3 was modelled using Phyre2 server (Kelley & Sternberg, 2009) using human CUL3$^{\Delta 403–459}$ as the sequence input and Cullin-1 chosen for the docking model (Q13616, PDB:1LDK; Zheng *et al*, 2002). A coil was predicted in place of the missing structural elements. UBE2D~UB was docked to RBX1 using PDB: 4AP4. Images were modified and made in UCSF Chimera (Pettersen *et al*, 2004; http://www.cgl.ucsf.edu/chimera).

Immunoprecipitation (mouse tissue and cell extracts)

Lysates of cellular preparations (buffer B) from FLAG-tagged CUL3 were mixed with M2 resin in the presence of 50 μM 1,10-phenanthrolin to prevent deneddylation and were incubated rotating at 4°C for 1 h. Resins were washed twice with mammalian buffer B and twice with 1× PBS, the volume was then reduced to ~15 μl, and following the addition of SDS gel sample buffer to 1×, samples were boiled and the entire sample was loaded to allow analysis by SDS–PAGE and immunodetection with the antibodies indicated.

Human and mouse aorta sample preparation

Human aortic tissues were collected from donors through transplant coordinators at Addenbrooke's Hospital, Cambridge. All samples were handled in accordance with the policies and

procedures of the Human Tissue Act and with the approval of the Local and Regional Ethics Committees. Mouse tissues were rapidly harvested, perivascular fat and residual blood were removed, and the samples were incubated in 1 ml RNAlater® solution at 4°C for 16–30 h before being removed from this buffer and stored dry at −80°C. Frozen aortic tissues were homogenised using TissueLyser LT (Qiagen #85600), and protein lysates were extracted in NE-PER (Life Technologies #78833) lysis buffers containing protease and phosphatase inhibitors (Roche #11836170001 and #04906845001). All steps were carried out at 4°C. Protein concentrations were determined with the Pierce™ BCA protein assay (Life Technologies #23225).

Human and mouse aorta immunoblotting

A total of 10 μg of aortic protein lysates was separated by SDS–PAGE. Prior to loading, samples were heated at 70°C for 10 min in 1× LDS sample buffer and 1× reducing agent (Life Technologies #B0007 and # B0009) to a total volume of 20 μl/well. Samples and 5 μl of Precision Plus molecular weight ladder (Biorad #161-0374) were then loaded onto a Bolt® 4–12% Bis–Tris Plus Gel (Novex® #BG04125BOX) and run at 165 V in 1× MES running buffer (Novex® #B0001), for 35 min or until the dye front reached the end of the gel. Resolved proteins were then transferred to 0.22 μM nitrocellulose membrane (Life Technologies #IB23001) using the iblot2 (Life Technologies) at 20 V for 7 min. Antibodies were incubated in 5% milk. Membranes were incubated in 5% in milk or BSA in TBS for 1 h at room temperature. Primary antibodies were incubated overnight at 4°C in 5% milk or BSA in TBS–Tween (0.1% v/v Tween) and then washed 6× in TBS–Tween. Secondary antibodies were incubated in TBS–Tween for 1 h at room temperature in the dark and then washed 6× in TBS–Tween. Membranes were imaged and integrated intensity values quantified (bands were normalised against β-actin) using the LiCor Odyssey system (www.licor.com).

Sample preparation and immunostaining for imaging

Formal-fixed, paraffin-embedded human tissue sections were obtained from the Cambridge Human Research Tissue Bank. Harvested mouse tissues were immersion-fixed in fresh 4% w/v formaldehyde–PBS pH 6.9 for 16 h at 37°C and washed 3× in PBS and stored at 4°C until paraffin embedding. Five-micrometre sections were deparaffinised in Histoclear (National Diagnostics) and rehydrated in graded methanol steps. An antigen retrieval step was performed with R-Universal buffer in the 2100 antigen retriever for a single heat–pressure cycle (Aptum Biologics). Sections were permeabilised with 0.05% v/v Triton X-100–PBS for 20 min and blocked for 1 h at 37°C with 2% v/v donkey serum in 0.05% v/v Triton X-100–PBS. Primary antibodies were incubated overnight for 16 h at 4°C at the following concentrations diluted in 1% v/v donkey serum in 0.05% v/v Triton X-100–PBS: 2 μg/ml for pNCC T44, tNCC, CUL3 (Sumara *et al*, 2007); 4 μg/ml for KLHL3 N-terminal, WNK4 N-terminal, SPAK C-terminal and pSPAK T233 (to detect mouse pSPAK T243); and 1 μg/ml for LAMP1, 1:500 for ubiquitin and 1:2,000 for PVALB. Phospho-specific antibodies included the addition of 10 μg/ml of the non-phospho form of the peptide used to raise the antibody per 2 μg/ml of antibody used. Slides were then washed for 20 min in 0.05% v/v Triton X-100–PBS and incubated in secondary antibody for 1 h at 37°C. Pre-absorbed donkey IgG-conjugated Alexa Fluor 488, 568, 633 and 647 secondary antibodies (Life Technologies/Abcam) were used at 1:200 dilution in 1% v/v donkey serum in 0.05% v/v Triton X-100–PBS for immunofluorescent labelling. Slides were washed as described above, mounted using Prolong Gold Antifade (P36930; Life Technologies) and shielded from light. Human IHC DAB staining was performed with ImmPRESS Reagent peroxidase universal anti-mouse/rabbit IgG (MP-7500, Vector) kit, after which slides were then dehydrated through graded methanol steps and mounted with DPX.

Image acquisition and processing

Immunofluorescence images were acquired on the Leica TCS SP2 laser scanning confocal microscope with 488-, 543- and 633-nm laser lines mounted on an upright Leica DM RXA fluorescence microscope using a HCX PL APO 63×/1.40NA oil immersion objective. Acquisition parameters were as follows: 12-bit, 1,024 × 1,024 pixels, 2.6× digital zoom, 800 Hz scan speed, 4-line Kalman filtering, sequential (by line) channel imaging, and 10-slice *z*-stack of 5 μm. Immunohistochemically stained specimens were imaged in brightfield on an Olympus BX51 upright epifluorescent microscope using a UPLANFL 20×/0.5NA dry objective with the Infinity3 (Lumenera) CCD set to 1,936 × 1,456 pixels.

In FIJI image analysis software (http://fiji.sc/Fiji), fluorescent *z*-stacks underwent background subtraction (1,000-pixel-radius rolling ball, no smoothing) and maximum-intensity *z*-projection. Brightness and contrast were adjusted by linear histogram stretching to enhance visibility. Any images to be compared to one another were processed in parallel. Similarly, brightfield images underwent linear histogram stretching to increase visibility uniformly across the image.

Morphometric analysis

Body weight was regularly measured two times per week throughout the study to determine differences in mass in age-matched mice. Body length was measured using photographs of mice post-mortem with a reference scale. Full body length was determined as well as tail:body length ratio. Three 5-μm sections of thoracic aorta were taken at upper (heart), mid and lower (near diaphragm) segments per mouse. These were deparaffinised, rehydrated and stained with haematoxylin and eosin, and then dehydrated and mounted. Each section was imaged under brightfield illumination and epifluorescent imaging of autofluorescent elastin laminae with a GFP filter set. Using FIJI image analysis software, macros were scripted to draw eight lines at ~22.5° to one another that intersect the aortic ring at a total of 16 points. At the point of intersection on the outer circumference, the distance from the external lamina to the inner lumen was measured. The average of the three rings (max of 16 points per ring, with points excluded if they fell on an arterial branching point or incomplete portion of a ring) was used to calculate the average thoracic aorta intima-media wall thickness. The above step was repeated to count the average number of elastic laminae in the thoracic aorta of each mouse. Data collection and analysis were carried out in a blinded fashion throughout.

In vivo cardiovascular physiology

Animals were anaesthetised with isoflurane on 100% O_2 (induction: 3%, maintenance: 1.75%) and placed on a self-regulating rectal probe-coupled heat mat (TC-1000; CWE) to maintain a body temperature of 37°C. Heart rate was measured by the R-R wave interval from ECG Lead II using an animal bio amp (FE136; AD Instruments) with needle electrodes inserted into fore and hind limbs (MLA1213; AD Instruments). The right carotid artery was catheterised with a 1F Mikro-Tip pressure transducer (SPR-1000; Millar) connected to a bridge amp (FE221; AD Instruments) and powerlab system (PL3504/P; AD Instruments). When the animals had stabilised, measurements were taken at 2,000 samples/s using LabChart version 7/8 Pro (AD Instruments) to record ECG and blood pressure pulse waveforms. *In vivo* dose–responses to vasopressor agents were taken after baseline blood pressure traces were obtained from mice. The right external jugular vein was cannulated for administration of bolus doses in increasing half-log steps of μg/kg body weight (bw); initially, phenylephrine was administered, and after washout and return to baseline, angiotensin II was administered in a similar fashion. Each dose concentration was made up as a half-log serial dilution in sterile 0.9% w/v saline and administered at a volume of 0.2 ml/kg.bw with an accompanying 20 μl 0.9% w/v saline cannula flush between doses.

Data processing and analysis were performed in LabChart 8 Pro. Using the blood pressure add-on, systolic, diastolic and dicrotic notch blood pressures were automatically detected per beat (beats with respiratory-induced artefact were gated out of the analysis using the beats classifier). Mean arterial pressure was calculated as (1/3 peak systolic pressure + 2/3 end diastolic pressure) and pulse pressure as (peak systolic pressure – end diastolic pressure). A macro was scripted to detect the anacrotic notch, by using the third zero value crossing the fourth derivative of the blood pressure, as described in Kelly *et al* (1989). The augmentation pressure was calculated as (peak systolic pressure – anacrotic notch pressure) and augmentation index as (augmentation pressure/pulse pressure). A macro was scripted to measure the slope of the diastolic pressure decay, 30 ms after the dicrotic notch and 20 ms before the end diastolic pressure (to avoid perturbations caused by aortic valve opening/closing). The reciprocal of this slope (ignoring the sign and calculated from the 20% trimmed mean values) was used to determine the time decay constant of the diastolic pressure decay which correlates with vascular resistance, as described previously (Bourgeois *et al*, 1974). Dose–response curves were generated and data analysed (GraphPad Prism 5 and LabChart 8 Pro) using a 4-parameter logistical function to determine the estimated dose producing half-maximal response (ED50) and maximum response (Emax). Data collection and analysis were carried out in a blinded fashion throughout. Sample sizes for the mouse work were decided based on previous experience in a related mouse model (Rafiqi *et al*, 2010). When groups of animals were being compared, procedures were performed on animals selected at random from the groups.

Blood and urine analytes

To reduce variability introduced by dietary potassium ingestion, animals were fasted for a minimum of 4 h before being anaesthetised with isoflurane on 100% O_2 (induction: 3%, maintenance: 1.75%) and placed on a self-regulating rectal probe-coupled heat mat (TC-1000; CWE) to maintain a body temperature of 37°C. To minimise air contact of arterial bloods during measurements, the right carotid artery was cannulated with a mouse arterial catheter (MAC-02; SAI Infusion Technologies) pre-flushed with 10 U heparin-0.9% w/v saline to prevent clots. Blood was released via the catheter into the EC8+ cartridge for analysis on the iSTAT (Abaxsis). Post-surgery additional blood was collected by using Microvette® CB 300 LH (Sarstedt) and centrifuged at 2,000 *g* for 5 min to extract plasma before storage at −80°C. Plasma aldosterone was calculated by HTRF (homogeneous time-resolved fluorescence) aldosterone assay (Cisbio, Codolet, France), according to the manufacturer's protocol using the PheraStar FS (BMG Labtech) plate reader.

To determine plasma and urine electrolyte homoeostasis, animals were placed on a 0.3% w/w Na diet for 2 weeks with urine and plasma time-matched samples collected between days 7 and 10 for normal Na (NNa) diet baseline. On day 14, mice were switched onto a 0.03% w/w Na diet with sampling repeated on days 7–10 for low-Na (LNa) diet measurements. Spot urine was collected from awake mice following spontaneous micturition on handling over a sheet of Saran® wrap or Parafilm®. Samples were then divided, and one sample received acidification with HNO_3 to a final concentration of 1% v/v to prevent precipitation of electrolytes, before both were stored at −80°C. Blood was collected by saphenous venepuncture in awake restrained animals, and plasma was separated and stored in a similar fashion to that described above. Plasma and urine (non-acidified) creatinine levels were assayed in the Core Biochemical Assay Laboratory, Addenbrooke's Hospital, Cambridge, UK. Plasma and urine (acidified) samples were diluted 1:1,000 using ultrapure polished water containing 1% v/v HNO3. Cations were then measured by inductively coupled plasma-optical emission spectrometry (Perkin Elmer ICP-OES Analyser) with known concentration standards and preset elemental spectra. Data collection and analysis were carried out in a blinded fashion throughout.

Statistical analysis

Data presented are mean ± standard error of the mean (SEM), unless otherwise stated. Statistical analyses were performed on either SPSS version 22 or GraphPad Prism® (http://www.graphpad.com/scientific-software/prism/) software. Two-tailed Student's *t*-tests were performed either paired or unpaired where appropriate. $P < 0.05$ was taken as statistically significant throughout.

For MYPT1 phosphorylation quantification (Appendix Fig S6), ratiometric expression was calculated for $CUL3^{WT/\Delta 403–459}$ versus $CUL3^{WT}$ on each Western blot of independent biological replicates. The mean of the ratios and bounds of the 95% confidence interval were calculated, where ratio = 1 represents no change in phosphorylation and ratio > 1 represents an increase in the phosphorylation status of $CUL3^{WT/\Delta 403–459}$ mice. Statistical significance was determined by the ratio *t*-test (http://www.wormbook.org/chapters/www_statisticalanalysis/statisticalanalysis.html).

Expanded View for this article is available online:
http://embomolmed.embopress.org

The paper explained

Problem
Mutations affecting CUL3 have been identified in patients with a syndrome of familial hypertension and hyperkalaemia. CUL3 forms a RING E3 ubiquitin ligase that controls the degradation of WNK kinases, which regulate salt homoeostasis. We wanted to understand whether and how the disease-linked CUL3 mutations (that delete residues encoded by exon 9 from the protein) affect the function of the protein and the signalling through the WNK kinase cascade.

Results
The disease-linked form of CUL3 fails to ubiquitylate WNK kinase, but retains the ability to transfer ubiquitin from a charged E2, leading to ectopic self-modification of the ligase complex. Our experiments suggest that the defect in WNK ubiquitylation is likely due to increased structural flexibility of the CUL3 scaffold. The mutant form of CUL3 also fails to bind to two of its key regulators, CAND1 and the CSN. Heterozygous mice expressing the disease-linked form of CUL3 show increased signalling through the WNK kinase pathway, high blood pressure and a pattern of deranged electrolytes that is typical of human subjects with PHA2E.

Impact
We provide the first detailed biochemical characterisation of a disease-causing CUL3 mutation involved in blood pressure regulation. We have also identified a previously unrecognised vascular phenotype in the mice expressing the mutant form of CUL3, suggesting they have increased vascular stiffness. If a similar phenotype exists in human subjects with the mutation, it may explain the severity of the PHA2E genotype. As vascular stiffness is an important and independent risk factor for cardiovascular events, it will be important to establish whether thiazides or other therapeutic interventions are able to reduce vascular stiffness in PHA2E subjects.

Acknowledgements
We thank Izabela Sumara for providing anti-CUL3 antibody for immunofluorescence. We acknowledge the technical support of the MRC Protein Phosphorylation and Ubiquitylation Unit; Elaine Forsyth for her excellent technical assistance with the mouse work; the DNA Sequencing Service (coordinated by Nicholas Helps); Thomas Macartney, Melanie Wightman and other members of the cloning team (coordinated by Rachel Toth and Mark Peggie); the Protein Purification Team and Antibody Production Team (coordinated by Hilary McLauchlan and James Hastie); the Cambridge Geography Science Laboratories (coordinated by Chris Rolfe, Steve Boreham and Samantha Smith); and Addenbrooke's Core Biochemical Assay Laboratory (coordinated by Keith Burling and Peter Barker).

This work was supported by the British Heart Foundation (a PhD studentship to KS and PG 13 89 30577), Medical Research Council, and an ERC Starting Investigator Grant (to TK), as well as the pharmaceutical companies supporting the Division of Signal Transduction Therapy Unit (AstraZeneca, Boehringer Ingelheim, GlaxoSmithKline, Merck, Janssen Pharmaceutica and Pfizer). The Human Research Tissue Bank is supported by the NIHR Cambridge Biomedical Research Centre.

Author contributions
FRS performed all biochemical analysis and experiments shown in Figs 1–3 and 4A. KS performed immunostaining and imaging in Figs 5A and 7C. KS performed surgeries, data collection and analysis of blood pressure, pressor dose–responses and pulse waveform measurements in Fig 6 with surgical support from FRS and JZ. Post-surgery KS, FRS and JZ harvested mouse tissues. KS performed dissection of aorta and kidney samples with specific experimental requirements. FRS prepared all mouse tissues and biological samples for storage as appropriate. KS performed vascular cannulations and arterial blood biochemistry data was collected with assistance from FRS; KS performed data analysis for Fig 4D. CJ and AK purified proteins used in biochemical analysis with help from FRS. RE performed structural docking and modelling shown and RE and FRS made the figures relating to this. NW performed cloning. SEC and Y collected and processed human aortic samples. RSAM and IH performed immunoblotting in Figs 4B and 7A and B with input from KS. IH performed the aldosterone assay in Fig 4C, IH and KS analysed the data. JTF performed aortic morphometric measurements in Fig 7E. NLF performed histological preparations and staining in Figs 5B and 7D and E. KS scripted macros for data extraction and processing for Figs 5A, 6B and 7C and E. KS analysed the data and generated the figures in Figs 5B and 7D and E. FRS managed the mouse study with assistance from JZ and KS. TK and KMO conceived the study and supervised the work. FRS, TK and KMO wrote the manuscript with input from KS.

For more information
All of the constructs generated in this study, and many of the purified proteins and antibodies can be purchased at the following link:
https://mrcppureagents.dundee.ac.uk
MRC-PPU Kurz webpage: http://www.ppu.mrc.ac.uk/research/?pid=1004
EMIT O'Shaughnessy webpage: http://emit.medschl.cam.ac.uk/
For more information regarding the human tissue utilised in this study please go to http://www.cuh.org.uk/tissue-bank/ about
OMIN disease database: http://www.omim.org/entry/145260
Protein structures mentioned in this study can be found under the noted PDB identifier online at http://www.rcsb.org

Conflict of interest
The authors declare that they have no conflict of interest.

References

Akhtar N, Hafeez F (2009) A rare case of Gitelman's syndrome with hypophosphatemia. *J Coll Physicians Surg Pak* 19: 257 – 259

Alessi DR, Zhang J, Khanna A, Hochdorfer T, Shang Y, Kahle KT (2014) The WNK-SPAK/OSR1 pathway: master regulator of cation-chloride cotransporters. *Sci Signal* 7: re3

Ali A, Masood Q, Yaqub S, Kashif W (2013) A case of Gitelman syndrome with severe hyponatraemia and hypophosphataemia. *Singapore Med J* 54: e18 – e20

Bergaya S, Faure S, Baudrie V, Rio M, Escoubet B, Bonnin P, Henrion D, Loirand G, Achard J-M, Jeunemaitre X *et al* (2011) WNK1 regulates vasoconstriction and blood pressure response to α 1-adrenergic stimulation in mice. *Hypertension* 58: 439 – 445

Bourgeois MJ, Gilbert BK, Donald DE, Wood EH (1974) Characteristics of aortic diastolic pressure decay with application to the continuous monitoring of changes in peripheral vascular resistance. *Circ Res* 35: 56 – 66

Boyden LM, Choi M, Choate KA, Nelson-Williams CJ, Farhi A, Toka HR, Tikhonova IR, Bjornson R, Mane SM, Colussi G *et al* (2012) Mutations in kelch-like 3 and cullin 3 cause hypertension and electrolyte abnormalities. *Nature* 482: 98 – 102

Calabrese MF, Scott DC, Duda DM, Grace CRR, Kurinov I, Kriwacki RW, Schulman BA (2011) A RING E3-substrate complex poised for ubiquitin-like

protein transfer: structural insights into cullin-RING ligases. *Nat Struct Mol Biol* 18: 947 – 949

Canning P, Bullock AN (2014) New strategies to inhibit KEAP1 and the Cul3-based E3 ubiquitin ligases. *Biochem Soc Trans* 42: 103 – 107

Chowdhury JA, Liu CH, Zuber AM, O'Shaughnessy KM (2013) An inducible transgenic mouse model for familial hypertension with hyperkalaemia (Gordon's syndrome or pseudohypoaldosteronism type II). *Clin Sci* 124: 701 – 708

Cope GA, Suh GSB, Aravind L, Schwarz SE, Zipursky SL, Koonin EV, Deshaies RJ (2002) Role of predicted metalloprotease motif of Jab1/Csn5 in cleavage of Nedd8 from Cul1. *Science* 298: 608 – 611

Delpire E, Gagnon KBE (2008) SPAK and OSR1: STE20 kinases involved in the regulation of ion homoeostasis and volume control in mammalian cells. *Biochem J* 409: 321 – 331

Duda DM, Borg LA, Scott DC, Hunt HW, Hammel M, Schulman BA (2008) Structural insights into NEDD8 activation of cullin-RING ligases: conformational control of conjugation. *Cell* 134: 995 – 1006

Duda DM, Scott DC, Calabrese MF, Zimmerman ES, Zheng N, Schulman BA (2011) Structural regulation of cullin-RING ubiquitin ligase complexes. *Curr Opin Struct Biol* 21: 257 – 264

D'Urso D, Prior R, Greiner-Petter R, Gabreëls-Festen AA, Müller HW (1998) Overloaded endoplasmic reticulum-Golgi compartments, a possible pathomechanism of peripheral neuropathies caused by mutations of the peripheral myelin protein PMP22. *J Neurosci* 18: 731 – 740

Feng J, Ito M, Ichikawa K, Isaka N, Nishikawa M, Hartshorne DJ, Nakano T (1999) Inhibitory phosphorylation site for Rho-associated kinase on smooth muscle myosin phosphatase. *J Biol Chem* 274: 37385 – 37390

Glover M, Ware JS, Henry A, Wolley M, Walsh R, Wain LV, Xu S, Van't Hoff WG, Tobin MD, Hall IP *et al* (2014) Detection of mutations in KLHL3 and CUL3 in families with FHHt (familial hyperkalaemic hypertension or Gordon's syndrome). *Clin Sci* 126: 721 – 726

Goldenberg SJ, Cascio TC, Shumway SD, Garbutt KC, Liu J, Xiong Y, Zheng N (2004) Structure of the Cand1-Cul1-Roc1 complex reveals regulatory mechanisms for the assembly of the multisubunit cullin-dependent ubiquitin ligases. *Cell* 119: 517 – 528

Gordon RD (1986) Syndrome of hypertension and hyperkalemia with normal glomerular filtration rate. *Hypertension* 8: 93 – 102

Gordon RD, Hodsman GP (1986) The syndrome of hypertension and hyperkalaemia without renal failure: long term correction by thiazide diuretic. *Scott Med J* 31: 43 – 44

Grimm PR, Taneja TK, Liu J, Coleman R, Chen Y-Y, Delpire E, Wade JB, Welling PA (2012) SPAK isoforms and OSR1 regulate sodium-chloride co-transporters in a nephron-specific manner. *J Biol Chem* 287: 37673 – 37690

Harper JW, Tan M-KM (2012) Ubiquitin pathway proteomics. *Mol Cell Proteomics* 11: 1541 – 1550

Ibeawuchi SC, Agbor LN, Quelle FW, Sigmund CD (2015) Hypertension causing mutations in Cullin3 impair RhoA ubiquitination and augment association with substrate adaptors. *J Biol Chem* 290: 19208 – 19217

Ji AX, Privé GG (2013) Crystal structure of KLHL3 in complex with Cullin3. *PLoS ONE* 8: e60445

Kaess BM, Rong J, Larson MG, Hamburg NM, Vita JA, Levy D, Benjamin EJ, Vasan RS, Mitchell GF (2012) Aortic stiffness, blood pressure progression, and incident hypertension. *JAMA* 308: 875 – 881

Kahle KT, Ring AM, Lifton RP (2008) Molecular physiology of the WNK kinases. *Annu Rev Physiol* 70: 329 – 355

Kelley LA, Sternberg MJE (2009) Protein structure prediction on the Web: a case study using the Phyre server. *Nat Protoc* 4: 363 – 371

Kelly R, Hayward C, Avolio A, O'Rourke M (1989) Noninvasive determination of age-related changes in the human arterial pulse. *Circulation* 80: 1652 – 1659

Kelsall IR, Duda DM, Olszewski JL, Hofmann K, Knebel A, Langevin FEDER, Wood N, Wightman M, Schulman BA, Alpi AF (2013) TRIAD1 and HHARI bind to and are activated by distinct neddylated Cullin-RING ligase complexes. *EMBO J* 32: 2848 – 2860

Kim W, Bennett EJ, Huttlin EL, Guo A, Li J, Possemato A, Sowa ME, Rad R, Rush J, Comb MJ *et al* (2011) Systematic and quantitative assessment of the ubiquitin-modified proteome. *Mol Cell* 44: 325 – 340

Kirisako T, Kamei K, Murata S, Kato M, Fukumoto H, Kanie M, Sano S, Tokunaga F, Tanaka K, Iwai K (2006) A ubiquitin ligase complex assembles linear polyubiquitin chains. *EMBO J* 25: 4877 – 4887

Kurz T, Ozlü N, Rudolf F, O'Rourke SM, Luke B, Hofmann K, Hyman AA, Bowerman B, Peter M (2005) The conserved protein DCN-1/Dcn1p is required for cullin neddylation in *C. elegans* and *S. cerevisiae*. *Nature* 435: 1257 – 1261

Lamark T, Johansen T (2012) Aggrephagy: selective disposal of protein aggregates by macroautophagy. *Int J Cell Biol* 2012: 736905

Lee DW, Peggie M, Deak M, Toth R, Gage ZO, Wood N, Schilde C, Kurz T, Knebel A (2012) The Dac-tag, an affinity tag based on penicillin-binding protein 5. *Anal Biochem* 428: 64 – 72

Liao JK, Seto M, Noma K (2007) Rho kinase (ROCK) inhibitors. *J Cardiovasc Pharmacol* 50: 17 – 24

Liao J, Farmer J (2014) Arterial stiffness as a risk factor for coronary artery disease. *Curr Atheroscler Rep* 16: 387

Lingaraju GM, Bunker RD, Cavadini S, Hess D, Hassiepen U, Renatus M, Fischer ES, Thomä NH (2014) Crystal structure of the human COP9 signalosome. *Nature* 512: 161 – 165

Liu J, Furukawa M, Matsumoto T, Xiong Y (2002) NEDD8 modification of CUL1 dissociates p120(CAND1), an inhibitor of CUL1-SKP1 binding and SCF ligases. *Mol Cell* 10: 1511 – 1518

Liu J, Nussinov R (2011) Flexible Cullins in Cullin-RING E3 ligases allosterically regulate ubiquitination. *J Biol Chem* 286: 40934 – 40942

Louis-Dit-Picard H, Barc J, Trujillano D, Miserey-Lenkei S, Bouatia-Naji N, Pylypenko O, Beaurain G, Bonnefond A, Sand O, Simian C *et al* (2012) KLHL3 mutations cause familial hyperkalemic hypertension by impairing ion transport in the distal nephron. *Nat Genet* 44: 456 – 460

Mayan H, Vered I, Mouallem M, Tzadok-Witkon M, Pauzner R, Farfel Z (2002) Pseudohypoaldosteronism type II: marked sensitivity to thiazides, hypercalciuria, normomagnesemia, and low bone mineral density. *J Clin Endocrinol Metab* 87: 3248 – 3254

McCormick JA, Yang C-L, Zhang C, Davidge B, Blankenstein KI, Terker AS, Yarbrough B, Meermeier NP, Park HJ, McCully B *et al* (2014) Hyperkalemic hypertension–associated cullin 3 promotes WNK signaling by degrading KLHL3. *J Clin Invest* 124: 4723 – 4736

Mori Y, Wakabayashi M, Mori T, Araki Y, Sohara E, Rai T, Sasaki S, Uchida S (2013) Decrease of WNK4 ubiquitination by disease-causing mutations of KLHL3 through different molecular mechanisms. *Biochem Biophys Res Commun* 439: 30 – 34

Munir S, Guilcher A, Kamalesh T, Clapp B, Redwood S, Marber M, Chowienczyk P (2007) Peripheral augmentation index defines the relationship between central and peripheral pulse pressure. *Hypertension* 51: 112 – 118

Ohta A, Schumacher F-R, Mehellou Y, Johnson C, Knebel A, Macartney TJ, Wood NT, Alessi DR, Kurz T (2013) The CUL3-KLHL3 E3 ligase complex mutated in Gordon's hypertension syndrome interacts with and ubiquitylates WNK isoforms: disease-causing mutations in KLHL3 and WNK4 disrupt interaction. *Biochem J* 451: 111 – 122

Osawa M, Ogura Y, Isobe K, Uchida S, Nonoyama S, Kawaguchi H (2013) CUL3 gene analysis enables early intervention for pediatric pseudohypoaldosteronism type II in infancy. *Pediatr Nephrol* 28: 1881 – 1884

Pathare G, Föller M, Michael D, Walker B, Hierlmeier M, Mannheim JG, Pichler BJ, Lang F (2012) Enhanced FGF23 serum concentrations and phosphaturia in gene targeted mice expressing WNK-resistant SPAK. *Kidney Blood Press Res* 36: 355 – 364

Pelham CJ, Ketsawatsomkron P, Groh S, Grobe JL, de Lange WJ, Ibeawuchi S-RC, Keen HL, Weatherford ET, Faraci FM, Sigmund CD (2012) Cullin-3 regulates vascular smooth muscle function and arterial blood pressure via PPARγ and RhoA/Rho-Kinase. *Cell Metab* 16: 462 – 472

Pettersen EF, Goddard TD, Huang CC, Couch GS, Greenblatt DM, Meng EC, Ferrin TE (2004) UCSF Chimera–a visualization system for exploratory research and analysis. *J Comput Chem* 25: 1605 – 1612

Pierce NW, Lee JE, Liu X, Sweredoski MJ, Graham RLJ, Larimore EA, Rome M, Zheng N, Clurman BE, Hess S *et al* (2013) Cand1 promotes assembly of new SCF complexes through dynamic exchange of f box proteins. *Cell* 153: 206 – 215

Pintard L, Kurz T, Glaser S, Willis JH, Peter M, Bowerman B (2003) Neddylation and deneddylation of CUL-3 is required to target MEI-1/Katanin for degradation at the meiosis-to-mitosis transition in *C. selegans*. *Curr Biol* 13: 911 – 921

Plechanovová A, Jaffray EG, McMahon SA, Johnson KA, Navratilova I, Naismith JH, Hay RT (2011) Mechanism of ubiquitylation by dimeric RING ligase RNF4. *Nat Struct Mol Biol* 18: 1052 – 1059

Rabut G, Le Dez G, Verma R, Makhnevych T, Knebel A, Kurz T, Boone C, Deshaies RJ, Peter M (2011) The TFIIH subunit Tfb3 regulates cullin neddylation. *Mol Cell* 43: 488 – 495

Rafiqi FH, Zuber AM, Glover M, Richardson C, Fleming S, Jovanović S, Jovanović A, O'Shaughnessy KM, Alessi DR (2010) Role of the WNK-activated SPAK kinase in regulating blood pressure. *EMBO Mol Med* 2: 63 – 75

Richardson C, Rafiqi FH, Karlsson HKR, Moleleki N, Vandewalle A, Campbell DG, Morrice NA, Alessi DR (2008) Activation of the thiazide-sensitive Na^+Cl^- cotransporter by the WNK-regulated kinases SPAK and OSR1. *J Cell Sci* 121: 675 – 684

Richardson C, Sakamoto K, de los Heros P, Deak M, Campbell DG, Prescott AR, Alessi DR (2011) Regulation of the NKCC2 ion cotransporter by SPAK-OSR1-dependent and -independent pathways. *J Cell Sci* 124: 789 – 800

Schumacher F-R, Sorrell FJ, Alessi DR, Bullock AN, Kurz T (2014) Structural and biochemical characterization of the KLHL3–WNK kinase interaction important in blood pressure regulation. *Biochem J* 460: 237 – 246

Scott DC, Sviderskiy VO, Monda JK, Lydeard JR, Cho SE, Harper JW, Schulman BA (2014) Structure of a RING E3 trapped in action reveals ligation mechanism for the ubiquitin-like protein NEDD8. *Cell* 157: 1671 – 1684

Shibata S, Zhang J, Puthumana J, Stone KL, Lifton RP (2013) Kelch-like 3 and Cullin 3 regulate electrolyte homeostasis via ubiquitination and degradation of WNK4. *Proc Natl Acad Sci USA* 110: 7838 – 7843

Silke J, Kratina T, Chu D, Ekert PG, Day CL, Pakusch M, Huang DCS, Vaux DL (2005) Determination of cell survival by RING-mediated regulation of inhibitor of apoptosis (IAP) protein abundance. *Proc Natl Acad Sci USA* 102: 16182 – 16187

Singer JD, Gurian-West M, Clurman B, Roberts JM (1999) Cullin-3 targets cyclin E for ubiquitination and controls S phase in mammalian cells. *Genes Dev* 13: 2375 – 2387

Somlyo AP, Somlyo AV (2003) Ca^{2+} sensitivity of smooth muscle and nonmuscle myosin II: modulated by G proteins, kinases, and myosin phosphatase. *Physiol Rev* 83: 1325 – 1358

Sumara I, Quadroni M, Frei C, Olma MH, Sumara G, Ricci R, Peter M (2007) A Cul3-Based E3 ligase removes aurora B from mitotic chromosomes, regulating mitotic progression and completion of cytokinesis in human cells. *Dev Cell* 12: 887 – 900

Susa K, Sohara E, Rai T, Zeniya M, Mori Y, Mori T, Chiga M, Nomura N, Nishida H, Takahashi D *et al* (2014) Impaired degradation of WNK1 and WNK4 kinases causes PHAII in mutant KLHL3 knock-in mice. *Hum Mol Genet* 23: 5052 – 5060

Tsuji S, Yamashita M, Unishi G, Takewa R, Kimata T, Isobe K, Chiga M, Uchida S, Kaneko K (2013) A young child with pseudo-hypoaldosteronism type II by a mutation of Cullin 3. *BMC Nephrol* 14: 166

Vitari AC, Deak M, Morrice NA, Alessi DR (2005) The WNK1 and WNK4 protein kinases that are mutated in Gordon's hypertension syndrome phosphorylate and activate SPAK and OSR1 protein kinases. *Biochem J* 391: 17 – 24

Wakabayashi M, Mori T, Isobe K, Sohara E, Susa K, Araki Y, Chiga M, Kikuchi E, Nomura N, Mori Y *et al* (2013) Impaired KLHL3-mediated ubiquitination of WNK4 causes human hypertension. *Cell Rep* 3: 858 – 868

Wee S, Geyer RK, Toda T, Wolf DA (2005) CSN facilitates Cullin-RING ubiquitin ligase function by counteracting autocatalytic adapter instability. *Nat Cell Biol* 7: 387 – 391

Wilson FH, Disse-Nicodème S, Choate KA, Ishikawa K, Nelson-Williams C, Desitter I, Gunel M, Milford DV, Lipkin GW, Achard JM *et al* (2001) Human hypertension caused by mutations in WNK kinases. *Science* 293: 1107 – 1112

Wolff S, Weissman JS, Dillin A (2014) Differential scales of protein quality control. *Cell* 157: 52 – 64

Wu G, Peng J-B (2013) Disease-causing mutations in KLHL3 impair its effect on WNK4 degradation. *FEBS Lett* 587: 1717 – 1722

Wu S, Zhu W, Nhan T, Toth JI, Petroski MD, Wolf DA (2013) CAND1 controls *in vivo* dynamics of the cullin 1-RING ubiquitin ligase repertoire. *Nat Commun* 4: 1642 – 1649

Yang S-S, Morimoto T, Rai T, Chiga M, Sohara E, Ohno M, Uchida K, Lin S-H, Moriguchi T, Shibuya H *et al* (2007) Molecular pathogenesis of pseudohypoaldosteronism type II: generation and analysis of a Wnk4D561A/+ knockin mouse model. *Cell Metab* 5: 331 – 344

Yang S-S, Lo Y-F, Wu C-C, Lin S-W, Yeh C-J, Chu P, Sytwu H-K, Uchida S, Sasaki S, Lin S-H (2010) SPAK-knockout mice manifest Gitelman syndrome and impaired vasoconstriction. *J Am Soc Nephrol* 21: 1868 – 1877

Zemla A, Thomas Y, Kedziora S, Knebel A, Wood NT, Rabut GEL, Kurz T (2013) CSN- and CAND1-dependent remodelling of the budding yeast SCF complex. *Nat Commun* 4: 1641

Zeniya M, Sohara E, Kita S, Iwamoto T, Susa K, Mori T, Oi K, Chiga M, Takahashi D, Yang SS *et al* (2013) Dietary salt intake regulates WNK3-SPAK-NKCC1 phosphorylation cascade in mouse aorta through angiotensin II. *Hypertension* 62: 872 – 878

Zhang J, Siew K, Macartney T, O'Shaughnessy KM, Alessi DR (2015) Critical role of the SPAK protein kinase CCT domain in controlling blood pressure. *Hum Mol Genet* 24: 4545 – 4558

Zheng N, Schulman BA, Song L, Miller JJ, Jeffrey PD, Wang P, Chu C, Koepp DM, Elledge SJ, Pagano M *et al* (2002) Structure of the Cul1-Rbx1-Skp1-F boxSkp2 SCF ubiquitin ligase complex. *Nature* 416: 703 – 709

Expanded View Figures

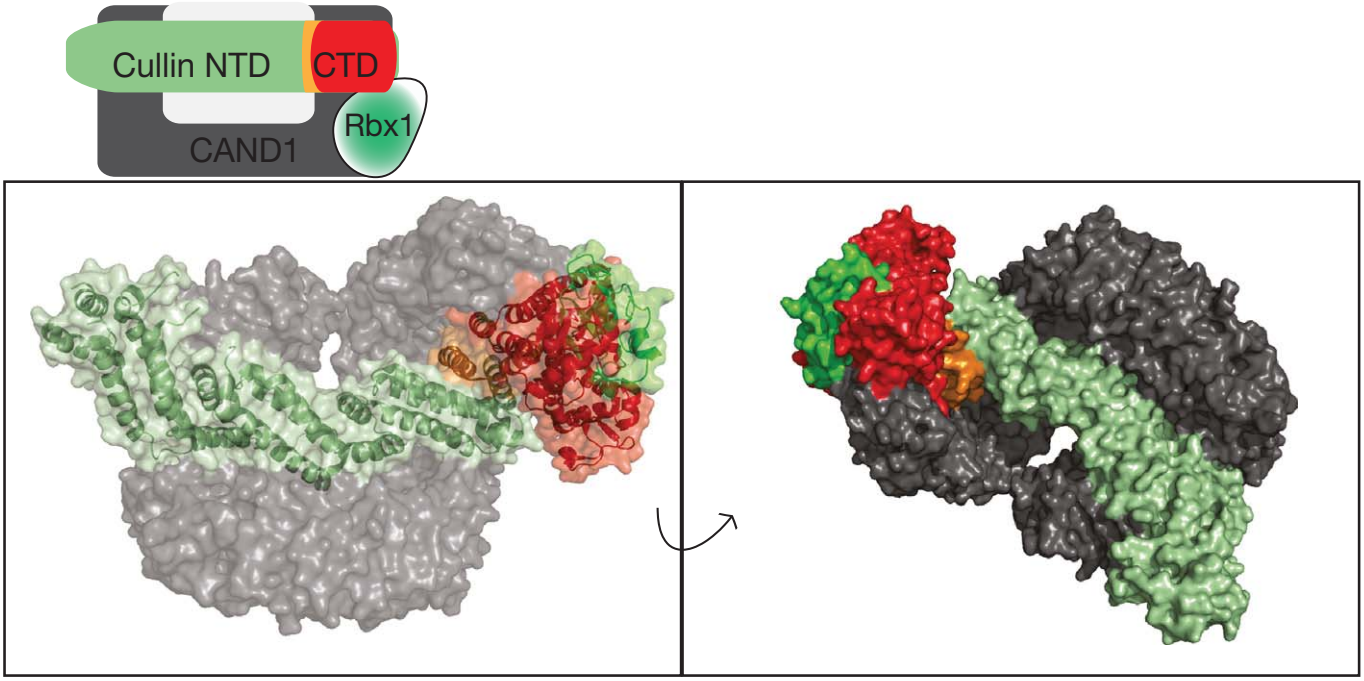

Figure EV1. Structural context of the area deleted by the disease-causing mutation in CUL3.
Top: Schematic representation of the interactions between CRL and CAND1. Bottom: Representation of CAND1 in complex with CUL1-RBX1, PDB 1u6g (Goldenberg *et al*, 2004). Coloured as shown in the schematic representation. Residues 437–493 of CUL1 (equivalent to 403–456 CUL3) are coloured orange.

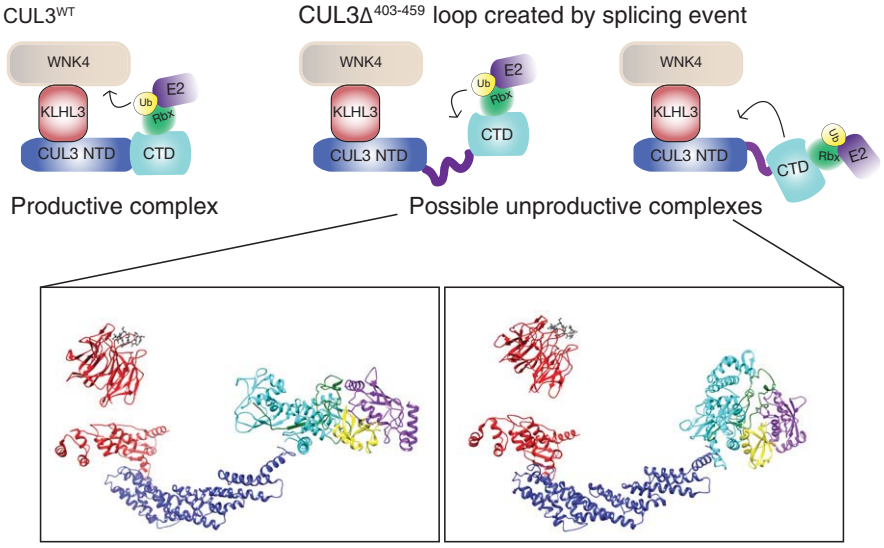

Figure EV2. Schematic representation of the possible structural effects of the mutation.
The top schematics represent a functional $CUL3^{WT}$ complex and show two contrasting positionings for an active $CUL3^{\Delta 403-456}$ that is unable to modify the WNK kinases. The lower structural representations correspond to the schematics above. These were generated in Chimera, and known structures were utilised as docking references to enable the possible orientations to be explored. KLHL3-KLECH domain (red) bound to a WNK peptide (grey) PDB: 4CH9. KLHL3-BTB domain (red) bound to CUL3-N-terminal domain (blue), CUL3-C-terminal domain (cyan) (based on CUL1 CTD) PDB: 1LDK. RBX1 (green), UBE2D (purple) and ubiquitin (yellow) were docked based on the complex RNF4-E2-UB structure PBD: 4AP4.

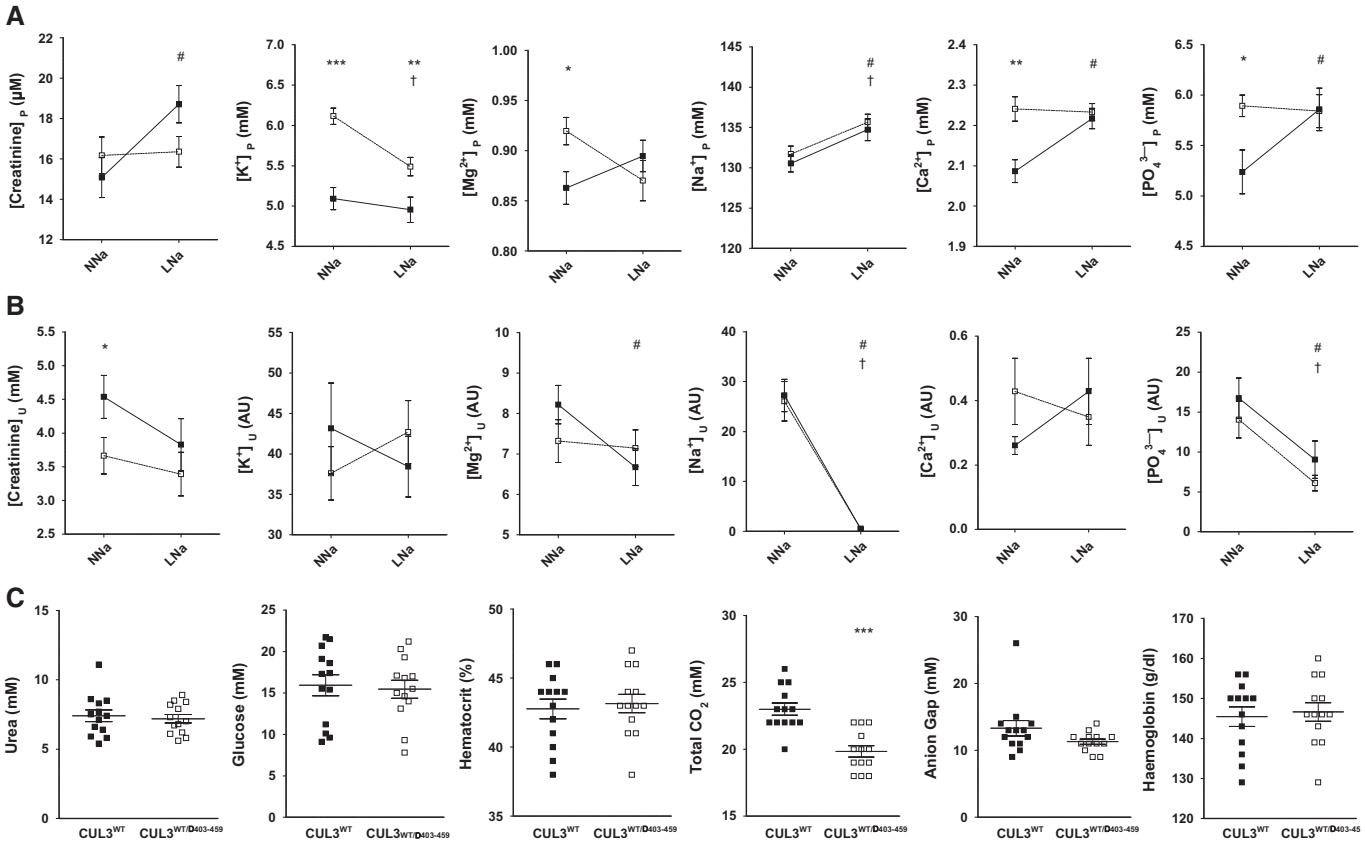

Figure EV3. Plasma and urine electrolyte response to normal and low sodium diets.

A–C The upper (A) and middle panels (B) show plasma (P) and urinary (U) electrolytes, respectively, for CUL3^{WT} mice (■) versus CUL3$^{WT/\Delta403–459}$ (□) on either a normal-salt (NNa) (0.3%) or low-salt (LNa) (0.03%) diet measured by ICP-OES analysis. The urinary values (AU) are individually ratioed to the urinary concentration of creatinine ($[analyte]_U/[creatine]_U$). The lower panel (C) shows blood biochemistries not reported in Figure 5D taken after a minimum 4-h fast by iSTAT analysis. The differences between genotypes that are significantly different are shown as *, the differences between NNa and LNa for CUL3^{WT} that are significantly different are shown as #, and the differences between NNa and LNa for CUL3$^{WT/\Delta403–459}$ that are significantly different are shown as † (*n*-values as follows: CUL3^{WT}: plasma NNa = 16; plasma LNa = 17; urine NNa = 18; urine LNa = 16; blood biochemistry = 13; CUL3$^{WT/\Delta403–459}$: plasma NNa = 23; plasma LNa = 23; urine NNa = 21; urine LNa = 19; blood biochemistry = 13). Two-tailed unpaired Student's *t*-test for comparisons between genotypes and two-tailed paired Student's *t*-test for comparisons between diets within the same genotype; data are mean ± SEM. A full table of *P*-values for this figure is shown in Appendix Table S1.

Source data are available online for this figure.

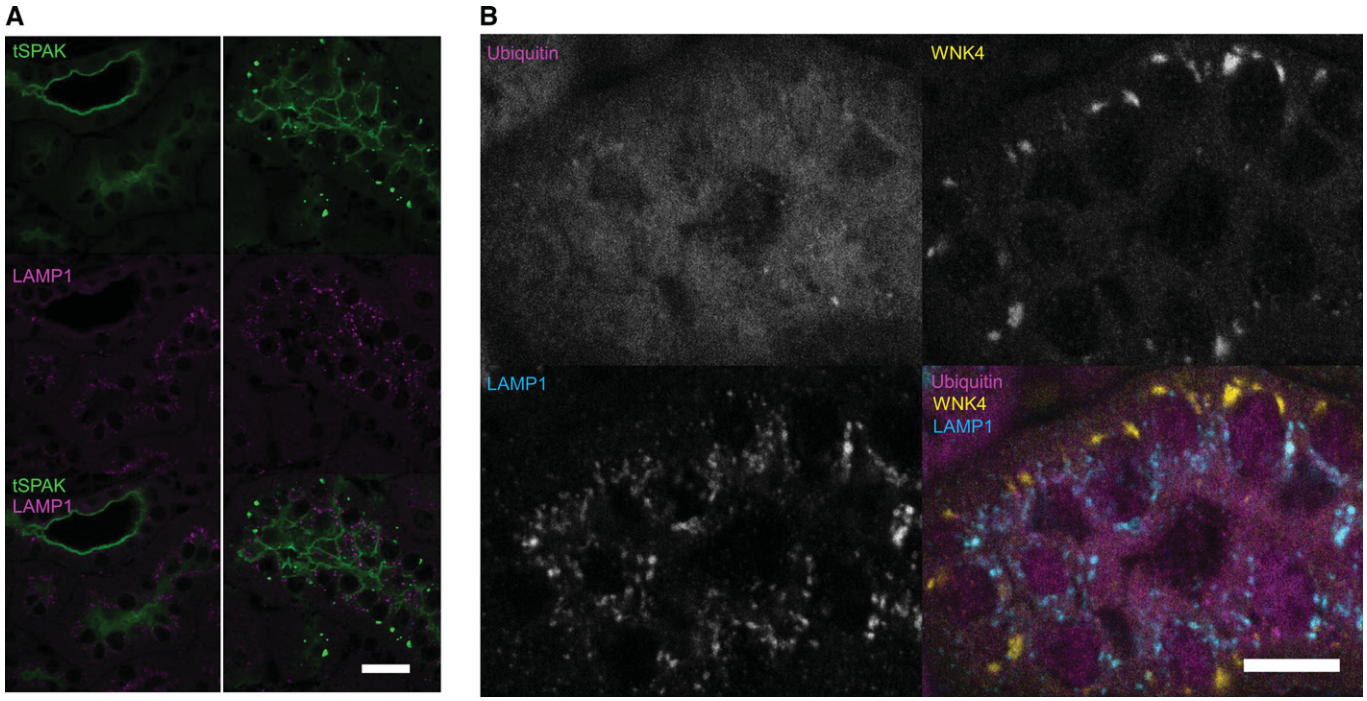

Figure EV4. WNK4 and SPAK puncta do not colocalise with LAMP1 or form ubiquitin-containing aggregates.
Representative pseudocoloured confocal single focal plane images of immunofluorescently stained kidney sections (n = 4 per genotype). WNK4 and SPAK form discrete puncta in the distal convoluted tubule of CUL3$^{WT/\Delta 403-459}$ mice. These puncta do not colocalise with lysosomes (LAMP1) or form ubiquitylated aggregates. The puncta have a predominantly basolateral preference with several large juxta-nuclear puncta per cell.

A Immunolocalisation of total SPAK protein (tSPAK) puncta and LAMP1 in the distal convoluted tubule of CUL3$^{WT/\Delta 403-459}$ versus CUL3^{WT} mice at a 4-h fasting baseline. Scale bar, 20 μm.

B Immunolocalisation of total WNK4 puncta, ubiquitin and LAMP1 in the distal convoluted tubule of CUL3$^{WT/\Delta 403-459}$ versus CUL3^{WT} mice at a 4-h fasting baseline. Scale bar, 10 μm.

Appendix

Characterisation of the Cullin-3 mutation that causes a severe form of familial hypertension and hyperkalaemia

Frances-Rose Schumacher[1*], Keith Siew[2*], Jinwei Zhang[1], Clare Johnson[1], Nicola Wood[1], Sarah E Cleary[2], Raya S Al Maskari[2], James T Ferryman[2], Iris Hardege[2], Yasmin[2], Nichola L Figg[3], Radoslav Enchev[4], Axel Knebel[1], Kevin M O'Shaughnessy[2] and Thimo Kurz[1]

[1] MRC Protein Phosphorylation and Ubiquitylation Unit, College of Life Sciences, University of Dundee, Dow Street, Dundee DD15EH, Scotland, UK.
[2] Divisions of Experimental Medicine and Immunotherapeutics and [3] Cardiovascular Medicine, Department of Medicine, University of Cambridge, Cambridge CB2 2QQ, UK.
[4] Institute of Biochemistry, ETH Zürich, Otto-Stern-Weg 3, CH-8093 Zürich, Switzerland

Content:

Appendix Figure S1.

A. Residues encoded for by exon-9 mRNA of Cullin3 are conserved in Cullin1. A Clustal-Omega alignment of full length Cullin1 and Cullin3 was performed, the region shown equates to that encoded by exon-9 mRNA in Cullin3 and highlights the similarity between these two proteins at this region.
B. Structural model of $CUL3^{WT}$ (upper) and $CUL3^{\Delta 403-459}$ (lower) made based on the structure of full length Cullin1 (1LDK) using Chimera (see methods). The NTD is coloured mauve, the CTD is coloured cyan and the region deleted in $CUL3^{\Delta 403-459}$ is coloured grey in the $CUL3^{WT}$ model.

Appendix Figure S2.

In vitro ubiquitylation assays as described in Figure 1-3**.**
A. The entire coomassie SDS PAGE (uncropped) are shown in this figure, along with additional reactions to support those in the main document.
B. Entire coomassie stained SDS PAGE of Figure 1E in main text. As described in Figure 1H, cell lines over-expressing either FLAG-$CUL3^{WT}$ or FLAG-$CUL3^{\Delta 403-459}$ were immunoprecipatated with M2 (anti-FLAG) resin. Input: Cellular extract IP: Immunoprecipated protein sample. Unbound: Protein remaining in extract following IP.
C. Coomassie SDS PAGE of reactions immunoblotted for and shown in Figure 2A.
D. Entire coomassie stained gel of Figure 2B.
E. Full commassie SDS PAGE of reactions immunoblotted for and shown in Figure 3A.

Appendix Figure S3.

The knockout strategy of exon 9 of endogenous Cullin3. The endogenous allele is represented and the target allele with the puromycin cassette (PuroR) removed by Flp recombinase. The black rectangles represent exons and the flippase-recognition target (FRT) sites are indicated.

Appendix Figure S4.

A. Illustrative side-by-side size comparisons of male and female $CUL3^{WT/\Delta 403-459}$ and $CUL3^{WT}$ littermates. Scale bar = 2cm.
B. $CUL3^{WT/\Delta 403-459}$ exhibit features of growth retardation when compared with CUL3WT mice. The CUL3WT/Δ403-459 have lower body weight (male: * P=0.0128 // female: *** $P=3.3x10^{-5}$) and length [measured nose-to-anus] (male: *** P=0.0002 // female: *** P=0.0009), although with no changes in proportionality as measured by tail-to-body ratio (male: P=0.1654 // female P=0.5817). Data are mean ± SEM (male n-values: $CUL3^{WT}$ = 8, $CUL3^{WT/\Delta 403-459}$ = 11 for body length; $CUL3^{WT}$ = 8, $CUL3^{WT/\Delta 403-459}$ = 6 for body weight // female n-values: $CUL3^{WT}$ = 16, $CUL3^{WT/\Delta 403-459}$ = 21 for body length; $CUL3^{WT}$ = 14, $CUL3^{WT/\Delta 403-459}$ = 12 for body weight). Two-tail unpaired student t-test; data are mean±SEM.

Appendix Figure S5.

A and B. Western blots showing expression of KLHL3 (**A**) or, CUL3 (**B**) in the human thoracic aorta. No obvious sex or age differences were observed. Human kidney were used as positive controls.
C. Western blot of HEK-293 cell lysates over expressing KLHL2-GFP or KLHL3-FLAG. The anti-KLHL3 antibody shows an intense band at the predicted molecular weight of FLAG modified KLHL3, confirming its ability to detect KLHL3.
D. Dual channel multiplex western blot of HEK-293 cell lysates over expressing KLHL2-GFP showing a band at the predicted molecular weight for GFP modified KLHL2 with an anti-GFP antibody (red). The anti-KLHL3 antibody (green) detects a non-specific higher weight band that does not overlap with KLHL2-GFP, therefore confirming specificity for KLHL3 with no cross-reactivity for KLHL2.

Appendix Figure S6.

A. $CUL3^{WT/\Delta 403\text{-}459}$ thoracic aorta have increased phosphorylation of MYPT1 isoforms. Ratiometric expression of quantified MYPT1 phospho-T696 isoforms (normalized against β-actin) were calculated for $CUL3^{WT/\Delta 403\text{-}459}$ vs $CUL3^{WT}$ on each western blot. The mean of the ratios and bounds of the 95% confidence interval are >1, confirming significantly increased phosphorylation (where ratio = 1 represents no change in phosphorylation). Results are from three separate blots containing independent biological replicates of aortic lysates from both genotypes (total n-values across three blots: $CUL3^{WT}$ = 19 / $CUL3^{WT/\Delta 403\text{-}459}$ = 21). Statistical significance was determined by the ratio t-test (see methods for more information); * P = 0.02.
B. A representative western blot of thoracic aorta MYPT1 phospho-Thr696 isoforms and β-actin expression from $CUL3^{WT/\Delta 403\text{-}459}$ and $CUL3^{WT}$ mice run on the same gel.

Appendix Table S1.

The full table of P-values for Fig EV3.

Appendix Figure S1.

A.

```
CUL3 403  LTEQEVETILDKAMVLFRFMQEKDVFERYYKQHLARRLLTNKSVSDDSEKNMISKLK  459
CUL1 437  PEEAELEDTLNQVMVVFKYIEDKDVFQKFYAKMLAKRLVHQNSASDDAEASMISKLK  493
```

B.

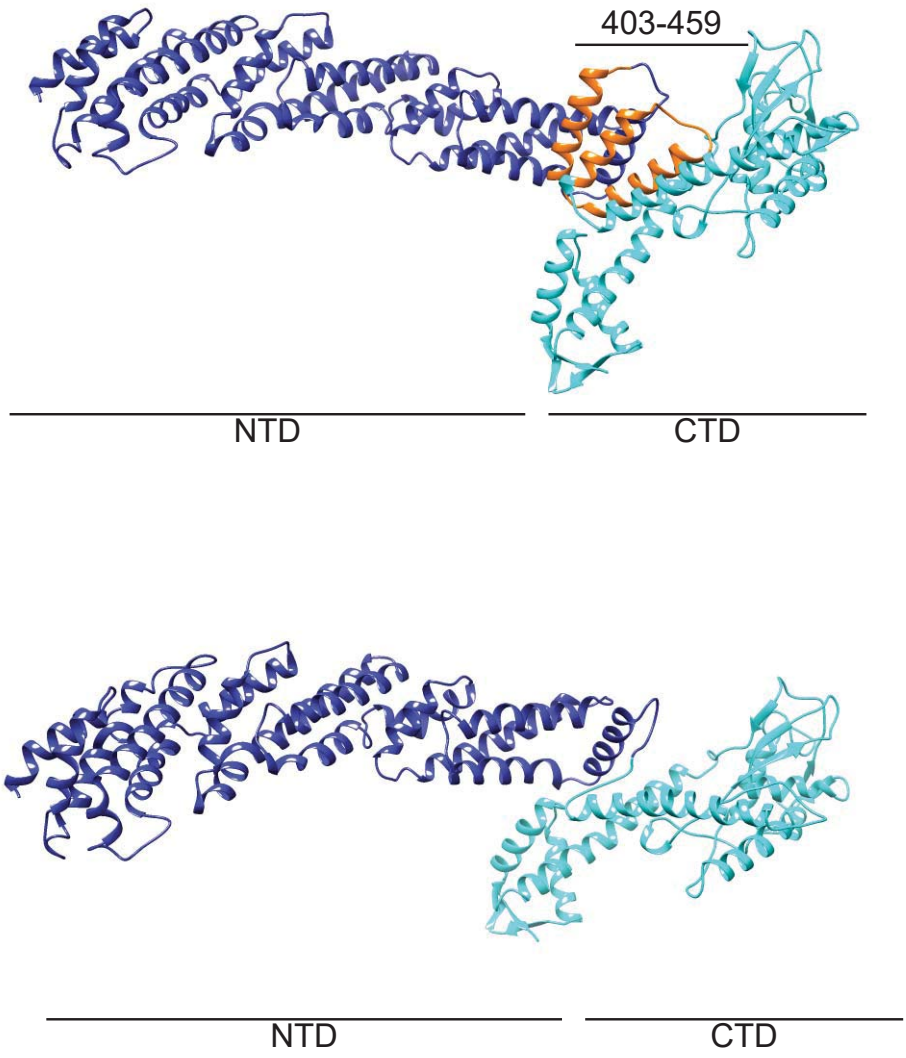

Appendix Figure S2

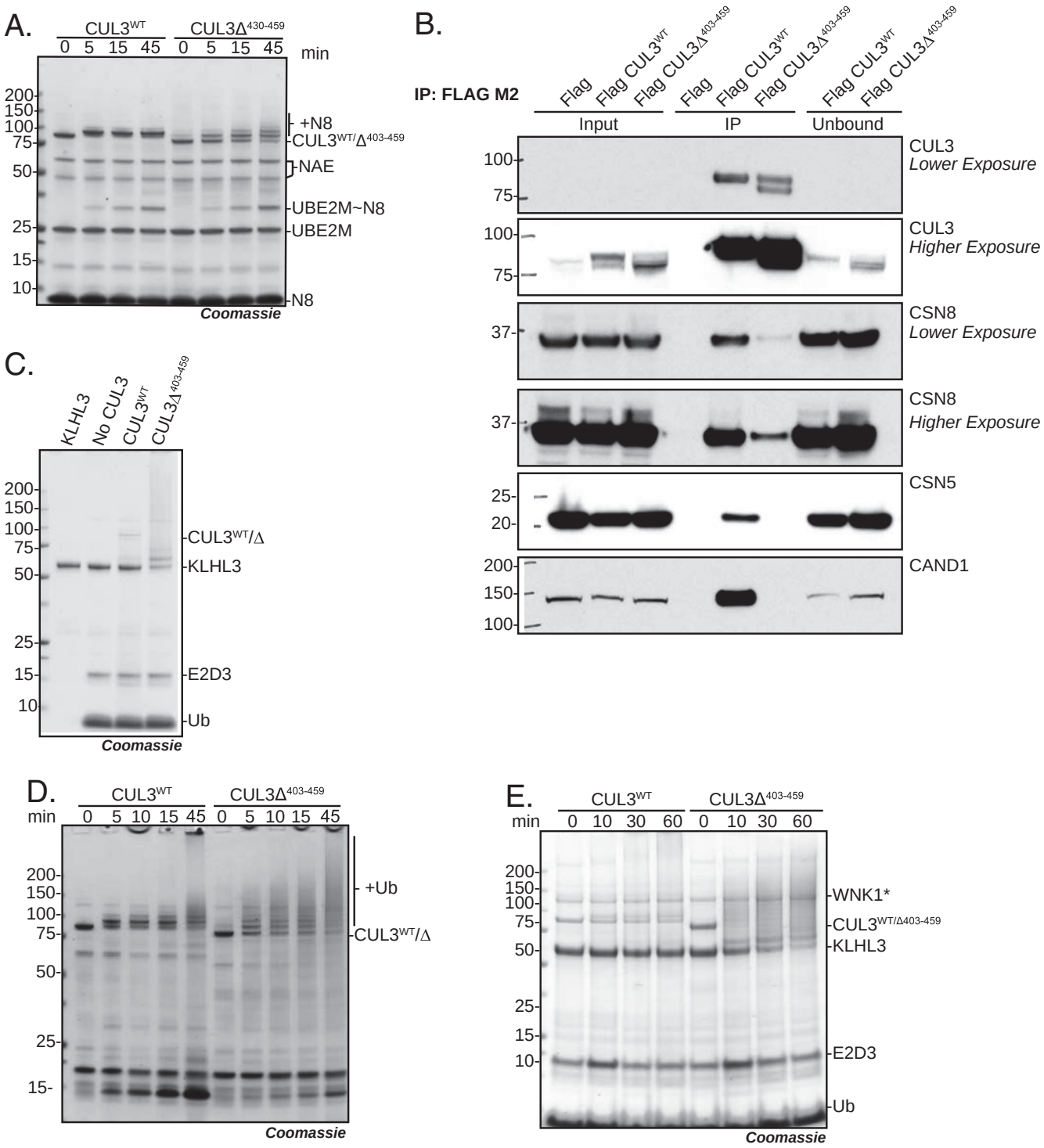

Appendix Figure S3

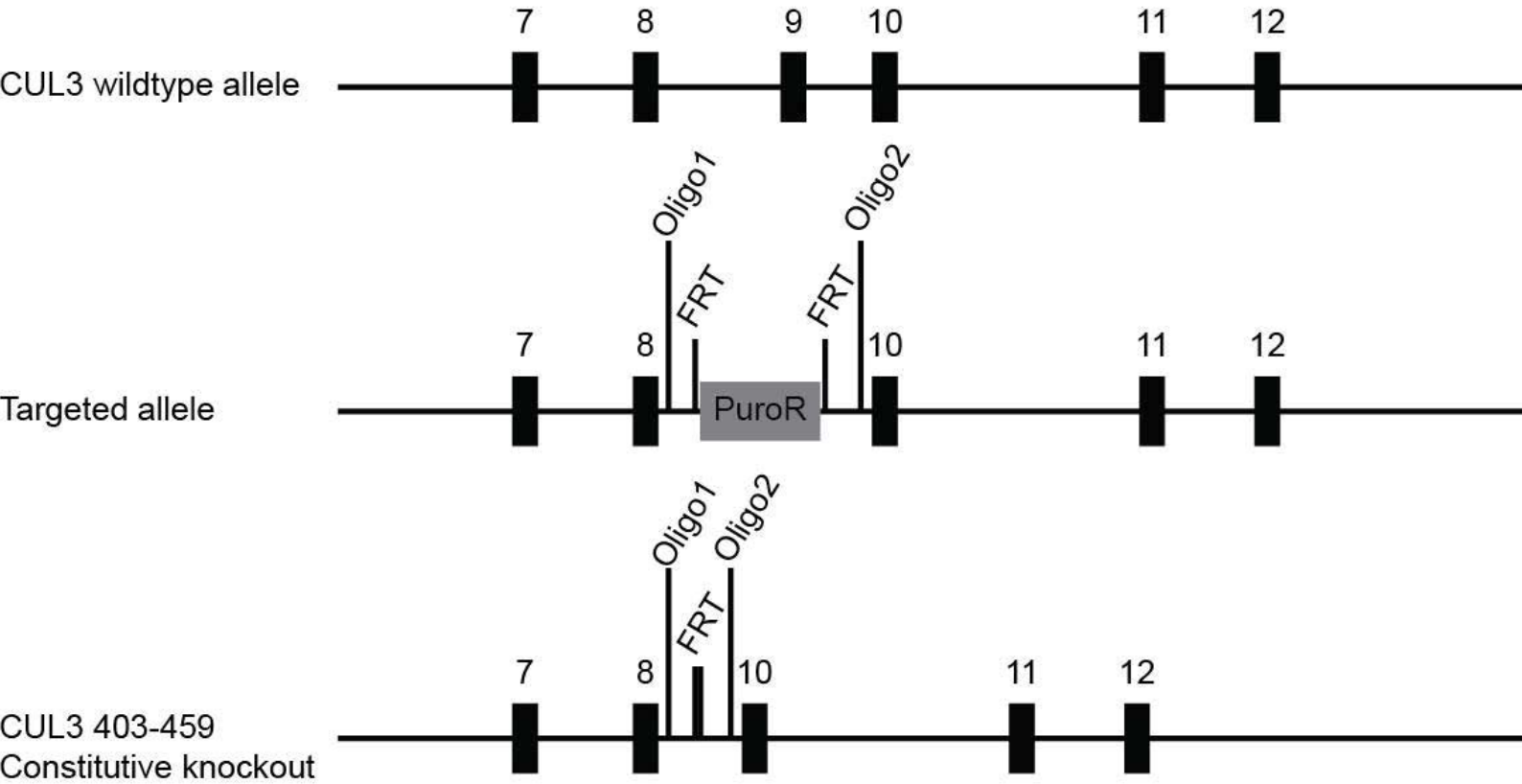

Appendix Figure S4

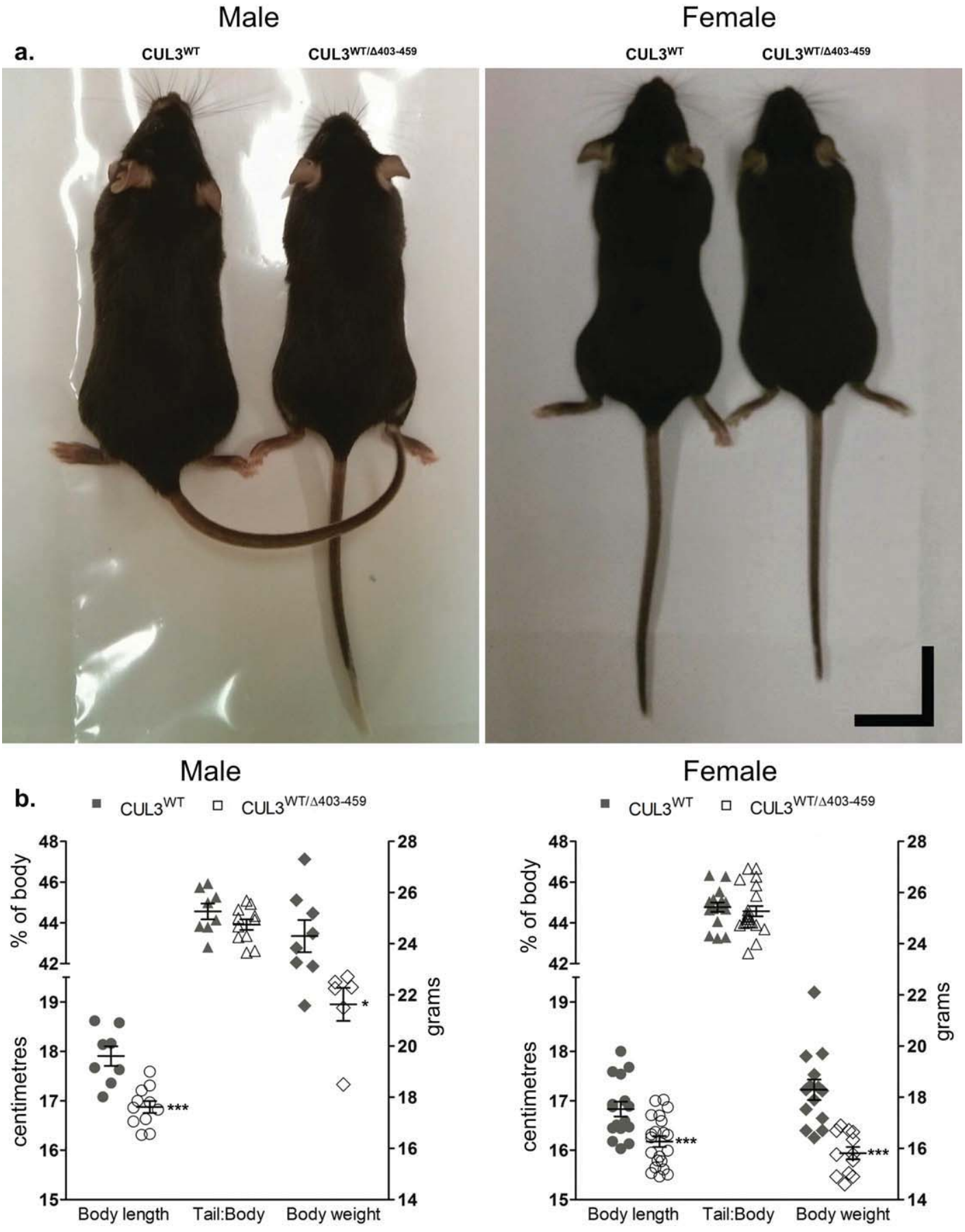

Appendix Figure S5

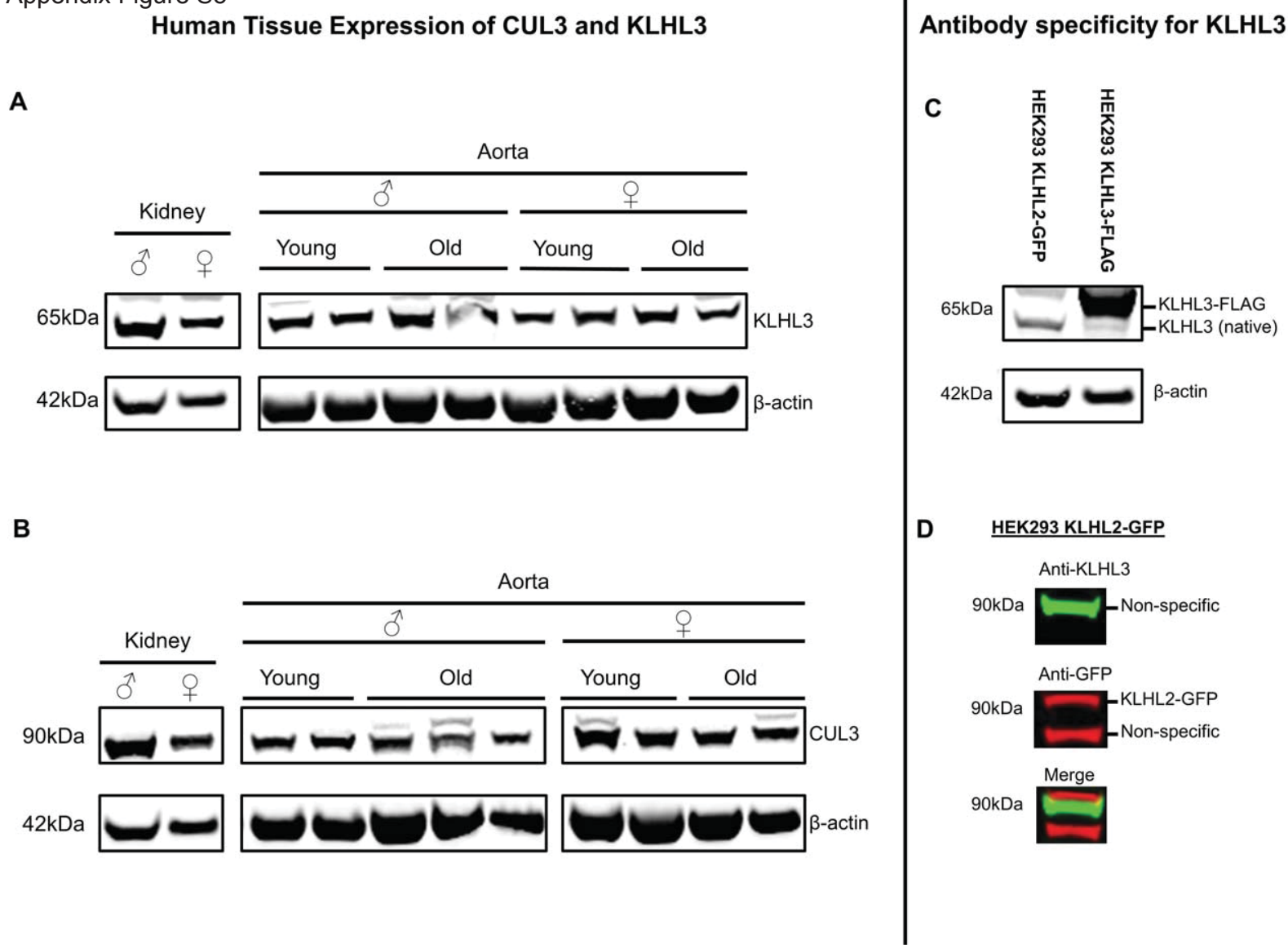

Appendix Figure S6

A.

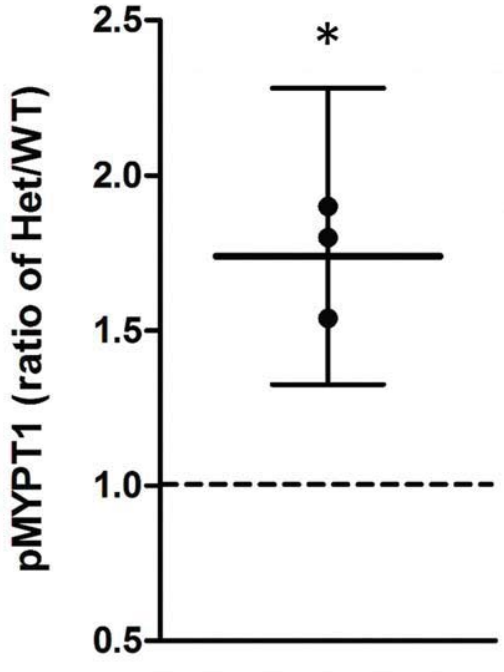

B.

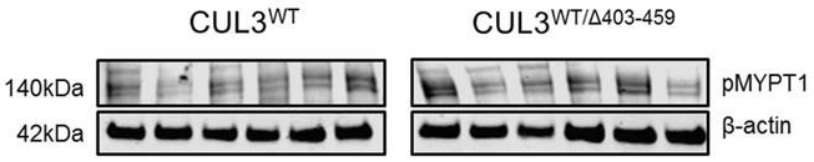

Appendix Table S1

P-values for Fig EV3

Plasma	**Cr**	**K**	**Mg**	**Na**	**Ca**	**P**
NNa $CUL3^{WT}$ vs $CUL3^{WT/\Delta 403-459}$	0.4326	$4.1x10^{-7}$	0.0110	0.4459	0.0015	0.0129
LNa $CUL3^{WT}$ vs $CUL3^{WT/\Delta 403-459}$	0.0550	0.0078	0.3749	0.8120	0.8195	0.9470
$CUL3^{WT/\Delta 403-459}$ NNa vs. LNa	0.9714	0.0004	0.0755	0.0194	0.4859	0.9757
$CUL3^{WT}$ NNa vs. LNa	0.0072	0.6643	0.4043	0.0478	0.0083	0.0493
Urine	**Cr**	**K**	**Mg**	**Na**	**Ca**	**P**
NNa $CUL3^{WT}$ vs $CUL3^{WT/\Delta 403-459}$	0.0424	0.3852	0.2191	0.8236	0.0633	0.4370
LNa $CUL3^{WT}$ vs $CUL3^{WT/\Delta 403-459}$	0.3864	0.4400	0.4714	0.8700	0.5574	0.2602
$CUL3^{WT/\Delta 403-459}$ NNa vs. LNa	0.5435	0.4127	0.5515	0.0001	0.0671	0.0031
$CUL3^{WT}$ NNa vs. LNa	0.2503	0.6864	0.0126	$2.5x10^{-6}$	0.1545	0.0395
Blood	**Urea**	**Glucose**	**Hct**	**Hb**	**Total CO_2**	**Anion Gap**
$CUL3^{WT}$ vs $CUL3^{WT/\Delta 403-459}$	0.8914	0.8757	0.8757	0.9045	$3.7x10^{-5}$	0.1022

APPENDIX 4

SPAK Paper:

Zhang J, Siew K, Macartney T, O'Shaughnessy KM, Alessi DR (2015). Critical role of the SPAK protein kinase CCT domain in controlling blood pressure. *Human Molecular Genetics* 24:4545-4558

Human Molecular Genetics, 2015, Vol. 24, No. 16 4545–4558

doi: 10.1093/hmg/ddv185
Advance Access Publication Date: 20 May 2015
Original Article

ORIGINAL ARTICLE

Critical role of the SPAK protein kinase CCT domain in controlling blood pressure

Jinwei Zhang[1,†,*], Keith Siew[2,†], Thomas Macartney[1], Kevin M. O'Shaughnessy[2,*] and Dario R. Alessi[1,*]

[1]MRC Protein Phosphorylation and Ubiquitylation Unit, College of Life Sciences, University of Dundee, Dow Street, Dundee DD1 5EH, Scotland and [2]Experimental Medicine and Immunotherapeutics, Department of Medicine, University of Cambridge, Cambridge, UK

*To whom correspondence should be addressed. Email: j.c.zhang@dundee.ac.uk (J.Z.); kmo22@medschl.cam.ac.uk (K.M.O.S.); d.r.alessi@dundee.ac.uk (D.R.A.)

Abstract

The STE20/SPS1-related proline/alanine-rich kinase (SPAK) controls blood pressure (BP) by phosphorylating and stimulating the Na-Cl (NCC) and Na-K-2Cl (NKCC2) co-transporters, which regulate salt reabsorption in the kidney. SPAK possesses a conserved carboxy-terminal (CCT) domain, which recognises RFXV/I motifs present in its upstream activator [isoforms of the With-No-lysine (K) kinases (WNKs)] as well as its substrates (NCC and NKCC2). To define the physiological importance of the CCT domain, we generated knock-in mice in which the critical CCT domain Leu502 residue required for high affinity recognition of the RFXI/V motif was mutated to Alanine. The SPAK CCT domain defective knock-in animals are viable, and the Leu502Ala mutation abolished co-immunoprecipitation of SPAK with WNK1, NCC and NKCC2. The CCT domain defective animals displayed markedly reduced SPAK activity and phosphorylation of NCC and NKCC2 co-transporters at the residues phosphorylated by SPAK. This was also accompanied by a reduction in the expression of NCC and NKCC2 protein without changes in mRNA levels. The SPAK CCT domain knock-in mice showed typical features of Gitelman Syndrome with mild hypokalaemia, hypomagnesaemia, hypocalciuria and displayed salt wasting on switching to a low-Na diet. These observations establish that the CCT domain plays a crucial role in controlling SPAK activity and BP. Our results indicate that CCT domain inhibitors would be effective at reducing BP by lowering phosphorylation as well as expression of NCC and NKCC2.

Introduction

SPAK (SPS1-related proline/alanine-rich kinase) and OSR1 (oxidative stress-responsive kinase 1) are closely related protein kinases, which play key roles in regulating cellular ion homeostasis and blood pressure (BP) (1,2). SPAK and OSR1 are activated following the phosphorylation of their T-loop residue (SPAK Thr233 and OSR1 Thr185) by one of the four isoforms of the WNK [with no lysine (K) kinase] protein kinase (3,4). The activity of SPAK and OSR1 is further enhanced following interaction with the scaffolding protein termed MO25 (5). The best-characterised SPAK/OSR1 substrates comprise the SLC12A (solute carrier family 12) family of electroneutral CCCs (cation–Cl co-transporters) (6–11). These transporters regulate intracellular chloride concentration critical in controlling BP and cell volume homoeostasis (12,13). SPAK/OSR1 protein kinases drive chloride influx by phosphorylation and activating sodium-driven CCC members. These include the NCC (Na–Cl co-transporter) in the distal convoluted tubule of the kidney (10), the NKCC2 (Na–K–2Cl co-transporter 2) in the thick ascending limb (TAL) of the kidney (9) and the ubiquitously expressed NKCC1 (6–8). SPAK/OSR1 also phosphorylate and inhibit potassium-driven CCCs that drive chloride efflux (11),

[†]J.Z. and K.S. made major contributions to the experimental work.
Received: April 29, 2015. **Revised and Accepted:** May 14, 2015

which comprise four different K–Cl– co-transporters (KCC1–KCC4) (13,14). This reciprocal regulation of Na^+- and K^+-driven CCCs by SPAK and OSR1 ensures that cellular Cl^- influx and efflux is tightly co-ordinated (13,14).

The importance of the WNK signalling pathway is exemplified by its evolutionary conservation from worms to humans and that several Mendelian hypertension disorders in humans are caused by mutations in WNK pathway components (15,16). These include various mutations that lead to increased expression of the WNK1 and WNK4 genes causing PHAII [PseudoHypoAldosteronism type II, OMIM (17–23)]. Conversely, loss-of-function mutations in NCC and NKCC2 cause familial forms of hypotension and hypokalaemia termed Gitelman (OMIM #263800) and Bartter type 1 syndrome (OMIM #601678), respectively (24). A mutation that ablates the key activating WNK-regulated SPAK/OSR1 phosphorylation site on NCC [T60M (10)] also causes Gitelman's syndrome (25,26). Moreover, SPAK-knockout mice (27–29) or knock-in mice expressing a form of SPAK that cannot be activated by WNK kinase isoforms (30) exhibit low BP and are resistant to hypertension when crossed with animals bearing a PHAII-causing knock-in mutation that enhances WNK4 expression (31). Genome-wide association studies have also identified intronic SNPs within the SPAK gene (STK39) that correlate with increased BP in humans (32). Two commonly used drugs in medicine to lower high BP also target SPAK sodium-driven CCC substrates, namely thiazide diuretics (such as bendroflumethiazide) that inhibit NCC and the loop diuretics (such as furosemide) that inhibits NKCC2 (33,34).

These data suggest that chemical agents that inhibit SPAK would have the potential to treat hypertension, but without the off-target effects of agents like thiazide diuretics (16,35). One approach would be to elaborate small molecule compounds that directly inhibit SPAK/OSR1 protein kinase activity (36). However, to our knowledge, no highly selective and potent kinase inhibitors of SPAK and OSR1 have been reported. There is also concern whether sufficiently selective SPAK/OSR1 kinase inhibitors could be synthesized for the management of a chronic largely asymptomatic condition, without them inhibiting other protein kinases or ATP-binding enzymes and causing intolerable off-target effects. An alternative strategy to suppress SPAK/OSR1 function would be to target the docking domain within the non-catalytic C-terminal region of SPAK/OSR1 called the CCT (conserved C-Terminal) domain. *In vitro* and overexpression studies indicate that the CCT domain binds to conserved RFXV/I motifs present on WNK isoforms and that these interactions facilitate phosphorylation and activation of SPAK/OSR1 (37,38). Furthermore, the sodium-driven CCC members also possess conserved RFXI/V motifs at their N-terminus which experimental data indicate are critical for enabling SPAK/OSR1 to interact with, phosphorylate and stimulate activity of these transporters (9,10,38,39).

In this study, we sought to define the role that the CCT domain plays *in vivo* by generating and characterising SPAK knock-in mice in which function of the CCT domain has been ablated by a mutation of the critical Leu502 residue required for high-affinity binding of the RFXI/V motif. Our data demonstrate that the CCT domain of SPAK does indeed play an essential role in regulating the activation and function of SPAK. Our findings establish that SPAK CCT domain knock-in mice display markedly reduced phosphorylation and expression of NCC and NKCC2 in the kidney resulting in lower BP. Our data provide genetic validation that targeting the CCT domain would be therapeutically effective in reducing BP, by lowering phosphorylation as well as expression of NCC and NKCC2 in the kidney.

Results

Characterisation of a mutation that inhibits the CCT domain of SPAK

Previous crystallographic analysis of the human OSR1 CCT domain complexed to an RFXI motif-containing peptide derived from WNK4 (40) revealed that the highly conserved Leu473 CCT residue lying at the base of a deep hydrophobic pocket formed critical hydrophobic contacts with the Phe residue of the RFXI motif (Fig. 1A). Consistent with this, mutation of Leu473 to Ala reduced binding of OSR1 to RFXI WNK4 peptide over 100-fold (40). Mutation of the equivalent residue (Leu502) in mouse SPAK also prevented full-length mouse SPAK co-immunoprecipitating with endogenously expressed WNK1 and NKCC1 in HEK293 cells (Fig. 1B). Moreover, *in vitro* fluorescence polarisation studies confirmed that mutation of this Leu residue in the SPAK CCT domain reduced binding to an RFXV-motif-possessing peptide derived from WNK4 by ~100-fold (Fig. 1C).

Characterization of CCT domain-deficient $SPAK^{L502A/L502A}$ mice

We exploited these observations to explore the impact that mutation of the CCT domain Leu502 residue had, by generating knock-in mice on an inbred C57BL/6J background, in which the Leu502 CCT domain residue was changed to Ala (Fig. 2A). Homozygous $SPAK^{L502A/L502A}$ mice were born at the expected Mendelian frequency (Supplementary Material, Table S1), were of normal size and appearance and did not display any overt phenotype, at least up to 1 year of age (the oldest animals we have analysed).

Immunoblot analysis of tissues (kidney, brain, heart and testis) derived from littermate wild-type and $SPAK^{L502A/L502A}$ homozygous animals of 2 months of age employing a novel mouse SPAK antibody that we generated that does not recognise mouse OSR1 (Supplementary Material, Fig. S1) revealed that the L502A mutation did not influence expression of SPAK in these tissues. We observed that all tissues analysed derived from $SPAK^{L502A/L502A}$ mice displayed a significant reduction of the phosphorylation of SPAK at a key WNK phosphorylation site [Ser373 (3)], compared with wild-type mice (Fig. 2B). This is consistent with the L502A mutation suppressing the ability of WNK isoforms to phosphorylate SPAK. Furthermore, the $SPAK^{L502A/L502A}$ knock-in animals displayed markedly reduced phosphorylation of NKCC1, in agreement with the CCT domain being required for SPAK to bind to and phosphorylate NKCC1 (Fig. 2B).

To obtain further evidence that the L502A mutation impacted on the ability of SPAK to bind WNK1 and NKCC1, we immunoprecipitated SPAK from kidney, brain and testis, derived from littermate wild-type and $SPAK^{L502A/L502A}$ homozygous animals of 2 months of age and tested how CCT domain mutation effected in association with WNK1 and NKCC1. This revealed that in the $SPAK^{L502A/L502A}$ knock-in animals, co-immunoprecipitation of WNK1 and NKCC1 with SPAK was markedly reduced in all tissues analysed (Fig. 2C). In the kidney, we also observed that mutation of the CCT domain inhibited co-immunoprecipitation of NCC and NKCC2 with SPAK (Fig. 2C). Further immunoblot analysis of SPAK immunoprecipitates confirmed that the L502A mutation inhibited phosphorylation of SPAK at the two key residues that WNK isoforms phosphorylate [Thr243 and Ser373 (3)] (Fig. 2C). SPAK as well as OSR1 immunoprecipitates from tissues (kidney, brain and testis) were also subjected to a protein kinase assay activity assay employing the previously

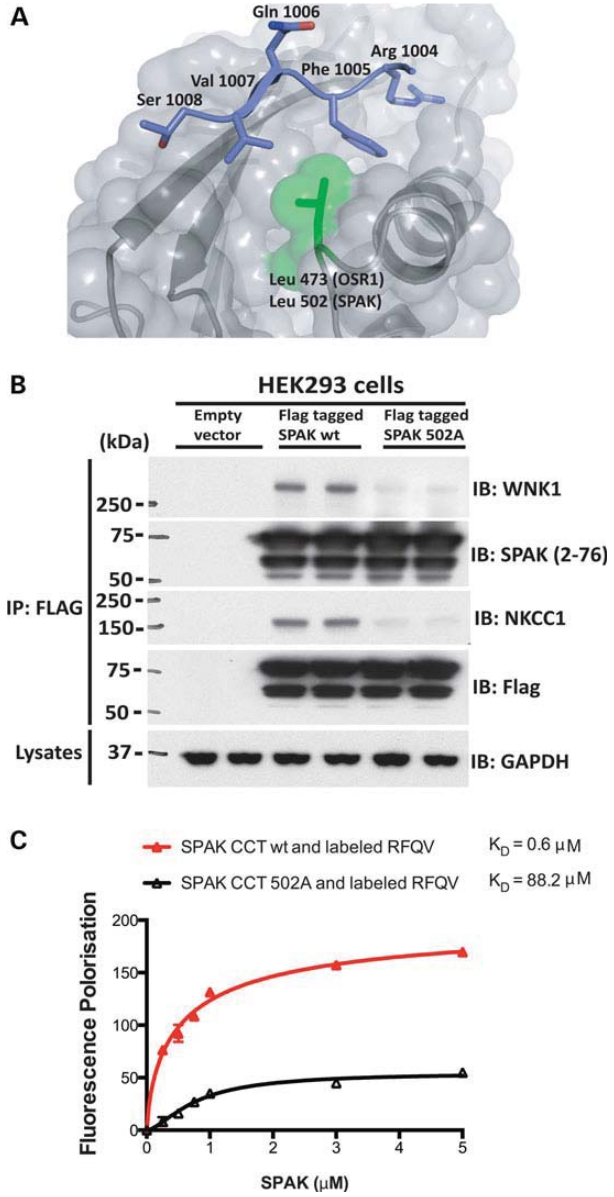

Figure 1. Evidence that SPAK associates with WNK1 and interaction is disrupted by SPAK CCT mutation. (**A**) Molecular interaction of the RFXV peptide with the conserved carboxy-terminal domain of OSR1 based on PDB 2V3S: CCT domain of OSR1 (residues 434–527) coloured in grey (β-strands and α-helices) bound to the GRFQVT WNK4-derived peptide coloured in blue. (**B**) HEK293 cells were transfected with constructs encoding a Flag empty vector or the indicated wild-type or mutant construct of N-terminal FLAG epitope-tagged full-length mouse SPAK. Thirty-six hours post-transfection, cells were lysed. Total cell extracts were subjected to immunoprecipitation (IP) with the indicated SPAK antibody, and immunoprecipitates were subjected to immunoblot (IB) analysis employing WNK1, SPAK and NKCC1 antibodies. Similar results were obtained in three separate experiments. (**C**) Analysis of SPAK–WNK interaction by fluorescence polarization. Purified human SPAK 452–547(end) and human SPAK 452–547 with L491A (equivalent to L502 in mouse) were diluted appropriately and mixed at a 1:1 volume ratio with 20 nM Lumino-Green-labelled WNK peptide to the concentration stated in the figure, with the peptide concentration consistent at 10 nM, and fluorescent polarization measurements were made. Binding curves, assuming one-site-specific binding, were then generated with Prism6 using milli-polarization (mP) units.

described CATCHtide peptide that encompasses the NKCC1 phosphorylation sites (37). This revealed that SPAK immunoprecipitated from all tissues derived from SPAK$^{L502A/L502A}$ knock-in mice displayed significantly reduced activity compared with wild-type animals (Fig. 2D). As expected, the activity of OSR1 was not affected in SPAK$^{L502A/L502A}$ knock-in mice (Fig. 2D).

SPAK$^{L502A/L502A}$ mice display reduced phosphorylation of NCC and NKCC2 in kidney

We next compared the relative levels of phosphorylation of NCC in total kidney extracts derived from male and female 2-month-old wild-type and SPAK$^{L502A/L502A}$ knock-in littermate animals (Fig. 3A–D). We monitored phosphorylation of NCC employing different previously characterised phosphospecific antibodies recognising major SPAK NCC phosphorylation sites (Thr46, Thr50, Thr55, Thr60 and Ser91) (10). This revealed that in both male and female mice, the phosphorylation of NCC at all residues analysed was drastically reduced in kidney derived from SPAK$^{L502A/L502A}$ knock-in mice compared with wild type (Fig. 3B). Similar to what was previously observed in SPAK kinase inactive (SPAK$^{T243A/T243A}$) knock-in mice (30) as well as SPAK knockout mice (27–29), we also observed ∼2-fold reduction in total levels of NCC protein in kidney extracts of SPAK$^{L502A/L502A}$ knock-in mice compared with wild type (Fig. 3B). In contrast, kidney mRNA levels of NCC were similar in wild-type and of SPAK$^{L502A/L502A}$ knock-in mice (Supplementary Material, Fig. S2).

We next monitored NKCC2 expression and similarly to NCC observed that levels were reduced ∼2-fold in the kidney of SPAK$^{L502A/L502A}$ knock-in male and female mice compared with wild-type animals (Fig. 3C). We immunoprecipitated NKCC2 and analysed its phosphorylation at three residues that SPAK phosphorylates [Ser91, Thr100 and Ser130 (9)] and found that phosphorylation of each of these residues was substantially reduced in both male and female kidney derived from SPAK$^{L502A/L502A}$ knock-in animals (Fig. 3C). Kidney mRNA levels of NKCC2 were similar in wild type and of SPAK$^{L502A/L502A}$ knock-in mice (Supplementary Material, Fig S2).

We also analysed NKCC1 and found that the levels of this co-transporter were unaffected in kidney extracts derived from wild-type and SPAK$^{L502A/L502A}$ knock-in male and female mice (Fig. 3D). We immunoprecipitated NKCC1 and analysed its phosphorylation at four sites that SPAK phosphorylates [Thr203, Thr207, Thr212 and Thr217 (3,5)] and found that phosphorylation of these sites was markedly diminished in both male and female kidney extracts derived from SPAK$^{L502A/L502A}$ knock-in animals compared with wild type. Kidney mRNA levels of NKCC1 were similar in wild-type and of SPAK$^{L502A/L502A}$ knock-in mice (Supplementary Material, Fig. S2).

SPAK$^{L502A/L502A}$ mice show a marked reduction in immunostaining for phosphorylated NCC and NKCC2 without remodelling of kidney tubules

Confocal imaging of kidney sections from the SPAK$^{L502A/L502A}$ mice confirmed the modest reduction in total NCC and NKCC2 in the tubules of the distal convoluted (DCT) and TAL tubules compared with wild-type mice, with no obvious changes in the morphology and numbers of tubules or the intracellular protein distribution between genotypes (Fig. 4). In striking contrast, staining for the phosphorylated forms of NCC and NKCC2 in the same tubules was almost completely lost in the SPAK$^{L502A/L502A}$ mice in keeping with the immunoblots from whole kidney lysates (Fig. 3). Additionally no changes were observed in the intracellular localisation of WNK4 in the DCT or TAL (Supplementary Material, Fig. S3).

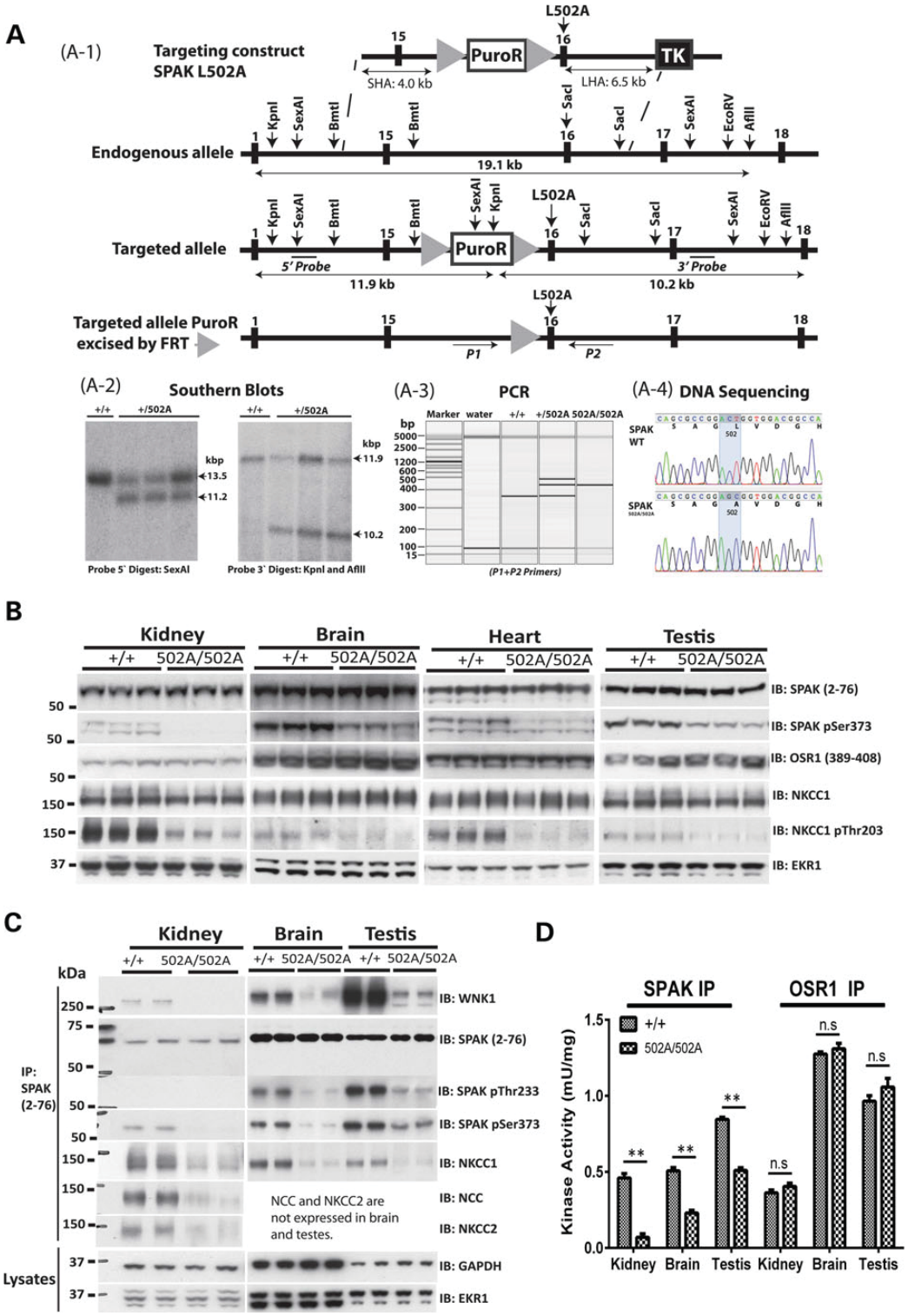

Figure 2. Targeting strategy used to generate SPAK knock-in mutations. (**A**-1) Diagram depicting the knock-in construct, the endogenous SPAK allele containing exons 15–16 and the targeted allele with the puromycin cassette removed by Flp recombinase. The black/grey rectangles represent exons, and the grey triangles represent FRT sites. Black lines with arrowheads are used to indicate the positions of the probes used for Southern analysis. The knock-in allele containing the Leu502Ala mutation in exon 16 is illustrated as a grey rectangle. The knock-in allele can be detected by genotyping using PCR primers P1 and P2, which are represented by short black lines with arrowheads. (**A**-2) Genomic DNA purified from the targeted ES cells from the indicated genotypes was digested with either the SexAI or KpnI and AflII and subjected to Southern analysis with the corresponding DNA probes. In the case of the 5′ probe, the wild-type allele generates a 13.5-kb fragment whereas the knock-in allele produces a 11.2-kb fragment. Similarly, the 3′ probe detects a fragment of 11.9 kb from the wild-type allele and 10.2 kb from the targeted knock-in allele. (**A**-3) Genomic DNA was PCR amplified with primers P1 and P2. The wild-type allele generates a 344-bp product whereas the knock-in allele generates a 419-bp product. The larger knock-in allele product is due to the presence of the 75-bp FRT site and flanking region, which remains in an intronic region following Flp-mediated excision of the puromycin resistance (PuroR) selection cassette, whereas the Thymidine kinase as a negative selection. (**A**-4) Genomic DNA purified from

SPAK$^{L502A/L502A}$ mice display reduced BP and augmentation index

To study the cardiovascular phenotype of these mice, we measured the arterial BP in the SPAK$^{L502A/L502A}$ knock-in animals by carotid artery cannulation under general anaesthesia, which showed that their systolic, diastolic and mean arterial BPs were ~20 mmHg lower than wild-type littermates (Fig. 5A). The lower BP of the SPAK$^{L502A/L502A}$ knock-in animals was also reflected in a significantly lower left ventricular mass in these animals (Supplementary Material, Fig. S4).

Further analysis of the BP traces from the mice also showed that the shape of the arterial pressure wave was significantly different (Fig. 5B). The SPAK$^{L502A/L502A}$ knock-in animals have a lower diastolic pressure time decay constant ($\tau_{bourgeois}$), an index of vascular resistance (41), suggesting decreased vascular tone compared with wild-type littermates (Fig. 5B). Specifically, the SPAK$^{L502A/L502A}$ knock-in animals had lower augmentation of the peak systolic pressure (AIx) with no change in pulse pressure consistent with a reduction in arterial stiffness (42) (Fig. 5B).

SPAK$^{L502A/L502A}$ mice show a Gitelman syndrome pattern of plasma and urinary electrolytes and are salt wasting

Analysis of the plasma electrolytes showed that the SPAK$^{L502A/L502A}$ mice had a typical Gitelman pattern of plasma electrolytes with hypokalaemia and mild hypomagnesaemia compared with the wild-type animals (Fig. 6A). This is consistent with reduced WNK pathway signalling caused by the inactivation of the SPAK CCT domain. The urinary electrolytes also showed a Gitelman-like pattern of electrolytes with marked hypocalciuria compared with the wild-type mice (Fig. 6B). The salt wasting expected of a Gitelman-like phenotype was also confirmed by salt restricting the SPAK$^{L502A/L502A}$ knock-in animals by switching to a 100-fold lower Na diet (Fig. 6C).

Discussion

Our results define the importance that the CCT-docking domain plays in regulating the ability of WNK isoforms to control the activation as well as function of SPAK in regulating NCC/NKCC2 ion co-transporters and hence BP. Most importantly, our findings establish that a single-point mutation ablating the ability of the CCT domain to interact with RFXI motifs on its WNK activators or ion co-transporters substrates is sufficient to markedly reduce phosphorylation and levels of NCC/NKCC2 resulting in a ~20 mmHg reduction in BP. Strikingly, the impact of the CCT domain mutation is similar to that observed previously by ablating SPAK kinase activity in knock-in mice (30) or by complete knockout of SPAK protein in mice (27–29). The SPAK$^{L502A/L502A}$ animals still possess OSR1, which is activated normally by WNK isoforms (Fig. 2D), emphasising that inhibiting SPAK without effecting OSR1 is sufficient to markedly lower BP. This is consistent with previous analysis indicating that SPAK in mammals evolved as a result of a gene duplication of OSR1, to undertake more specialized roles such as control of NCC/NKCC2 in the kidney and regulation of BP (1).

Intriguingly, in the SPAK$^{L502A/L502A}$ knock-in animals in addition to a reduced phosphorylation of NCC/NKCC2, we observed that the levels of NCC and NKCC2 protein were significantly reduced (Fig. 3), under conditions which mRNA levels were unaffected (Supplementary Material, Fig. S2). Similar results were also observed when analysing catalytically inactive SPAK knock-in mice (30). In converse, in mouse models in which the WNK signalling pathway is activated by introducing knock-in mutations that inhibit the ubiquitylation of and proteasomal degradation of WNK4 (i.e. WNK4 [D561A] knock-in mice (31,43) or KLHL3[R528H] knock-in mice (42)), NCC and NKCC2 protein levels are markedly elevated. Taken together results provide strong genetic evidence that phosphorylation of NCC/NKCC2 by SPAK in addition to regulating co-transporter activity also promotes the stability of these critical co-transporters. Further work is required to unravel the mechanism, by which NCC and NKCC2 expression is controlled by SPAK phosphorylation.

The plasma and urinary electrolyte pattern of the SPAK$^{L502A/L502A}$ knock-in mice resembles Gitelman Syndrome. In fact, it recapitulates closely the phenotype of our previous report with a kinase-dead SPAK knock-in mouse (30). The extensive loss of NKCC2 and phospho-NKCC2 from the TAL tubules could be expected to produce a more extensive or even Bartter-like Syndrome (44). The levels of NKCC2 were also reduced in the kinase-dead SPAK knock-in mouse, but the reduction was modest in comparison with almost complete loss of phosphorylated NKCC2 from the SPAK$^{L502A/L502A}$ mouse kidney (Figs 3 and 4). Nevertheless, the presence of both hypocalciuria and hypomagnesaemia in the SPAK$^{L502A/L502A}$ mice is in keeping with a predominant loss of NCC function, because the loss of NKCC2 function in the mouse is associated with the opposite phenotype of hypermagnesaemia and hypercalciuria (45). In fact, plasma magnesium levels and urinary calcium excretion are clinical measures used routinely to distinguish between Gitelman and the related Bartter syndrome (46). Our finding that the total level and phosphorylation of NKCC2 is reduced in the kidneys of the SPAK$^{L502A/L502A}$ mouse is also notable because previous SPAK knockout models reported hypophosphorylated NCC in the DCT, but markedly hyperphosphorylated NKCC2 in the TAL with increases in total NKCC2 levels (27) or without a change in total NKCC2 levels (28,29). The authors suggested that this was due to the removal of an inhibitory isoform of SPAK (SPAK2) and showed that the hypophosphorylation of NCC was accompanied by physical reduction in numbers of DCT1 tubular segments. Similarly, other studies with mouse models of NCC genetic ablation (47) and knockout of the DCT1-specific calcium-binding protein, parvalbumin (48), have also shown atrophy of the DCT. SPAK has been reported to be directly involved in the stabilisation of OSR1 at the apical membrane in the DCT and SPAK knockout results in a significant reduction of parvalbumin expression (29). However, unlike the knockout models used in these studies, the SPAK scaffolding functions remain intact in the point-mutant knock-in SPAK$^{L502A/L502A}$ and SPAK$^{T243A/T243A}$

mice generated through heterozygous breeding was subjected to PCR to generate a product that encompasses the knock-in mutation region. The resultant PCR products were ligated into the pCR-Topo 2.1 vector and transformed into *E. coli*, and clones were sequenced. The wild-type and knock-in sequences are presented. (**B**) Expression of SPAK in tissues (kidney, brain, heart and testis) from wild-type and knock-in mice. The indicated tissue extracts (40 µg protein) from wild-type and SPAK502A/502A mice were subjected to immunoblot analysis with the specified antibodies. Immunoblots were run in parallel and exposed for the same amount of time to ensure that signal intensities can be directly compared. Similar results were obtained in three separate experiments. (**C** and **D**) Activity of SPAK in wild-type and knock-in mouse tissues. SPAK was immunoprecipitated from the kidney, testis and brain lysates from wild-type and SPAK$^{502A/502A}$ mice using the SPAK-mouse peptide antibody. The immunoprecipitates were subjected to activity measurements using the CATCHtide peptide substrate (3). A fraction of the immunoprecipitates was also subjected to immunoblot assay with the indicated antibodies.

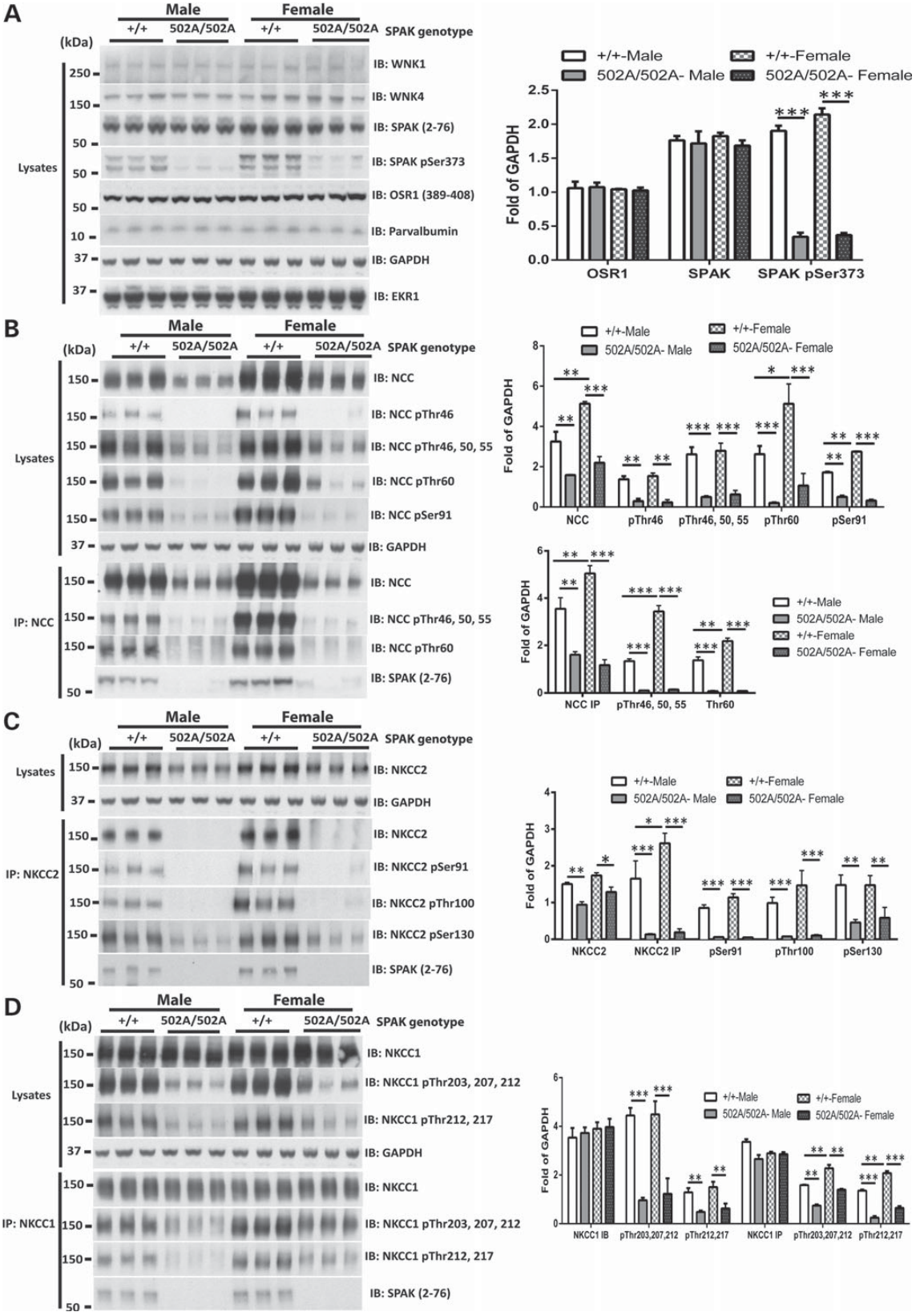

Figure 3. Reduced phosphorylation of SPAK, NCC, NKCC1, NKCC2 and expression of NCC and NKCC2 in both male and female SPAK$^{L502A/L502A}$. (**A**) Expression of WNK1, WNK4, SPAK, OSR1 and Parvalbumin and phosphorylation of SPAK in wild-type and knock-in male and female mouse kidney. Kidney extract derived from the indicated mice was subjected to immunoblot analysis with the indicated antibodies. Each sample was derived from a separate littermate animal. Band intensities were quantified using Li-Cor Odyssey, and the results are presented relative to the expression of GAPDH. This study has been repeated over three times each with kidney extracts derived from different animals on each occasion with consistent results. (**B**) The right panel shows quantification of the results of the blots ($n = 6$, mean ± SEM). *$P < 0.05$; **$P < 0.01$;

mice. This may explain why we observed no changes in the levels or staining of parvalbumin (Figs 3A and 4). It is, therefore, possible to postulate that these remodelling phenomena may largely be due to loss of key components of regulatory pathways which maintain normal tubular structure, rather than a simply loss of NCC activity.

The altered shape of the arterial pressure waveform in our $SPAK^{L502A/L502A}$ mice (Fig. 5B) is consistent with increased vascular compliance and reduced wave reflection in the periphery as compared with the wild-type animals. This may be explained in part by a diminished cardiac output arising from possible reductions in cardiac contractility owing to loss of NKCC1 activity in the heart (49) (Fig. 2B) and the lower heart rates of the $SPAK^{L502A/L502A}$ mice (Fig. 5A), because augmentation is negatively correlated with heart rate in humans (50). It has also been previously shown that intracranial administration of bumetanide can be used to inhibit the over activity of NKCC1 in the hypothalamic paraventricular nucleus of spontaneously hypertensive rats. The inhibition of NKCC1 in these hypertensive animals acts to reduce sympathetic vasomotor tone and lower their heart rates (51). A similar phenomenon may be occurring in the $SPAK^{L502A/L502A}$ mice owing to reductions in brain phospho-NKCC1 (Fig. 2), thus providing a potential neurological explanation for their lower heart rate and reduced vascular tone.

However, SPAK directly affects vascular smooth muscle contraction through WNK1 (52) and WNK3 (53) signalling and NKCC1 (27), the activity of which is necessary for maintaining vascular smooth muscle tone (54), so it is likely that reduced augmentation also reflects hypophosphorylation of NKCC1 in blood vessels in a parallel fashion to our findings in the kidney and other tissues (Figs 2 and 3). This is further supported by the shorter $\tau_{bourgeois}$ found in $SPAK^{L502A/L502A}$ mice, which implies reduced vascular resistance consistent with a reduction in vascular contractility. This suggests that targeting the CCT domain of SPAK may have an additional effect on BP through a direct reduction in vascular tone. It also suggests a reduced arterial stiffness without a change in pulse pressure (Fig. 4), and both are importantly independent risk factors for cardiovascular mortality (42).

There is increasing interest in targeting the WNK-SPAK/OSR1-signalling pathway as a new therapeutic strategy to treat hypertension (16,35). Our finding that ablation of the CCT domain function is sufficient to reduce BP to the same extent as a kinase ablating knock-in mutation (30) suggests that the CCT domain of SPAK plays a similarly important role as the kinase domain in controlling BP. Thus, inhibitors that prevent the CCT domain-recognising RFXV motifs should be as effective as compounds that target the protein kinase domain of SPAK in lowering BP. Structural analysis reveals that CCT domain recognises RFXV/I motifs by adopting a unique fold not observed on other proteins (40). This may indicate that CCT domain inhibitors might be inherently more specific than ATP competitive kinase inhibitors that would have the potential to target other protein kinases and/or ATP binding enzymes. For the treatment of a chronic largely asymptomatic condition such as hypertension, it is particularly important that therapies are as specific as possible in order to reduce poorly tolerated off-target side effects.

Owing to the high degree of homology between the CCT domain of SPAK and OSR1, it may be impossible to develop drugs that selectively inhibit SPAK. However, even a drug that partially inhibited both SPAK and OSR1 isoforms might reduce phosphorylation and expression of NCC and NKCC1/2 enough to lower BP without significant adverse effects. Thus far one CCT domain inhibitor termed STOCK 1S-50699 has been reported that has an IC50 of ~3 μM, that is capable of inhibiting WNK-SPAK phosphorylating NKCC1 and NCC in mammalian cell lines (11,39). STOCK 1S-50699 is highly hydrophobic, displays poor solubility and cannot be used in animal models, but the data obtained so far provide evidence that the development of CCT domain inhibitors is feasible.

In conclusion, our results establish that the SPAK CCT domain plays a major role in regulating BP. Our data suggest that the SPAK CCT domain regulates BP by promoting SPAK activation by WNK isoforms that in turn enhance both activity and expression of the renal sodium co-transporters NCC and NKCC2 with potential concomitant effects on NKCC1 in the vasculature. The hypotensive phenotype of the $SPAK^{L502A/L502A}$ mice validate the CCT domain as a promising new target for future anti-hypertensive agents. The lack of an overt phenotype in these mice also indicates that CCT domain inhibitors may be well tolerated.

Materials and Methods

Materials

Lumio Green, Colloidal Blue staining kit and precast SDS polyacrylamide BisTris gels were from Invitrogen. GL Biochem synthesized all peptides to a purity of >95%; peptide sequences were determined by mass spectrometry. Tissue-culture reagents were from Life Technologies. P81 phosphocellulose paper was from Whatman, and [γ-32P]-ATP was from PerkinElmer.

***$P < 0.001$. (**C**) Analysis of kidney NCC protein levels and phosphorylation in male and female wild-type and homozygous knock-in mice following NCC immunoblot and immunoprecipitation. The upper panel shows that NCC from the indicated kidney extracts was subjected to immunoblot analysis with the total NCC antibody and a phosphospecific antibodies recognizing NCC phosphorylated at Thr46, 50, 55, 60 and Ser91 (Thr60 is a key SPAK/OSR1 phosphorylation site in NCC is frequently detected in Asian patients with Gitelman's syndrome). The down panel shows that NCC was immunoprecipitated from the indicated kidney extracts and subjected to immunoblot analysis with the total NCC antibody and a phosphospecific antibodies recognizing NCC phosphorylated at Thr46, 50, 55 and 60. Band intensities were quantified using Li-Cor Odyssey, and the results are presented relative to the expression of GAPDH. This study has been repeated over three times each with kidney extracts derived from different animals on each occasion with consistent results. (**D**) The right panel shows quantification of the results of the blots ($n = 6$, mean ± SEM). *$P < 0.05$; **$P < 0.01$; ***$P < 0.001$. (**E**) Analysis of kidney NKCC2 protein levels and phosphorylation in male and female wild-type and homozygous knock-in mice following NKCC2 immunoprecipitation. NKCC2 was immunoprecipitated from the indicated kidney extracts and subjected to immunoblot analysis with the total NKCC2 antibody and a phosphospecific antibodies recognizing NKCC2 phosphorylated at Ser91, Thr100 and Ser130, a major SPAK phosphorylation site. Each sample is derived from a separate littermate animal. Band intensities were quantified using Li-Cor Odyssey, and the results are presented relative to the expression of GAPDH. The study has been repeated over three times each with kidney extracts derived from different animals on each occasion with consistent results. (**F**) The right panel shows quantification of the results of the blots ($n = 6$, mean ± SEM). *$P < 0.05$; **$P < 0.01$; ***$P < 0.001$. (**H**) Analysis of kidney NKCC1 protein levels and phosphorylation in male and female wild-type and homozygous knock-in mice following NKCC1 immunoblot and immunoprecipitation. The upper panel shows that NKCC1 from the indicated kidney extracts was subjected to immunoblot analysis with the total NKCC1 antibody and a phosphospecific antibodies recognizing NKCC1 phosphorylated at Thr203, 207, 212 and 217. The down panel shows that NKCC1 was immunoprecipitated from the indicated kidney extracts and subjected to immunoblot analysis with the total NKCC1 antibody and a phosphospecific antibodies recognizing NKCC1 phosphorylated at Thr203, 207, 212 and 217. Band intensities were quantified using Li-Cor Odyssey, and the results are presented relative to the expression of GAPDH. This study has been repeated over three times each with kidney extracts derived from different animals on each occasion with consistent results. (**I**) The right panel shows quantification of the results of the blots ($n = 6$, mean ± SEM). *$P < 0.05$; **$P < 0.01$; ***$P < 0.001$.

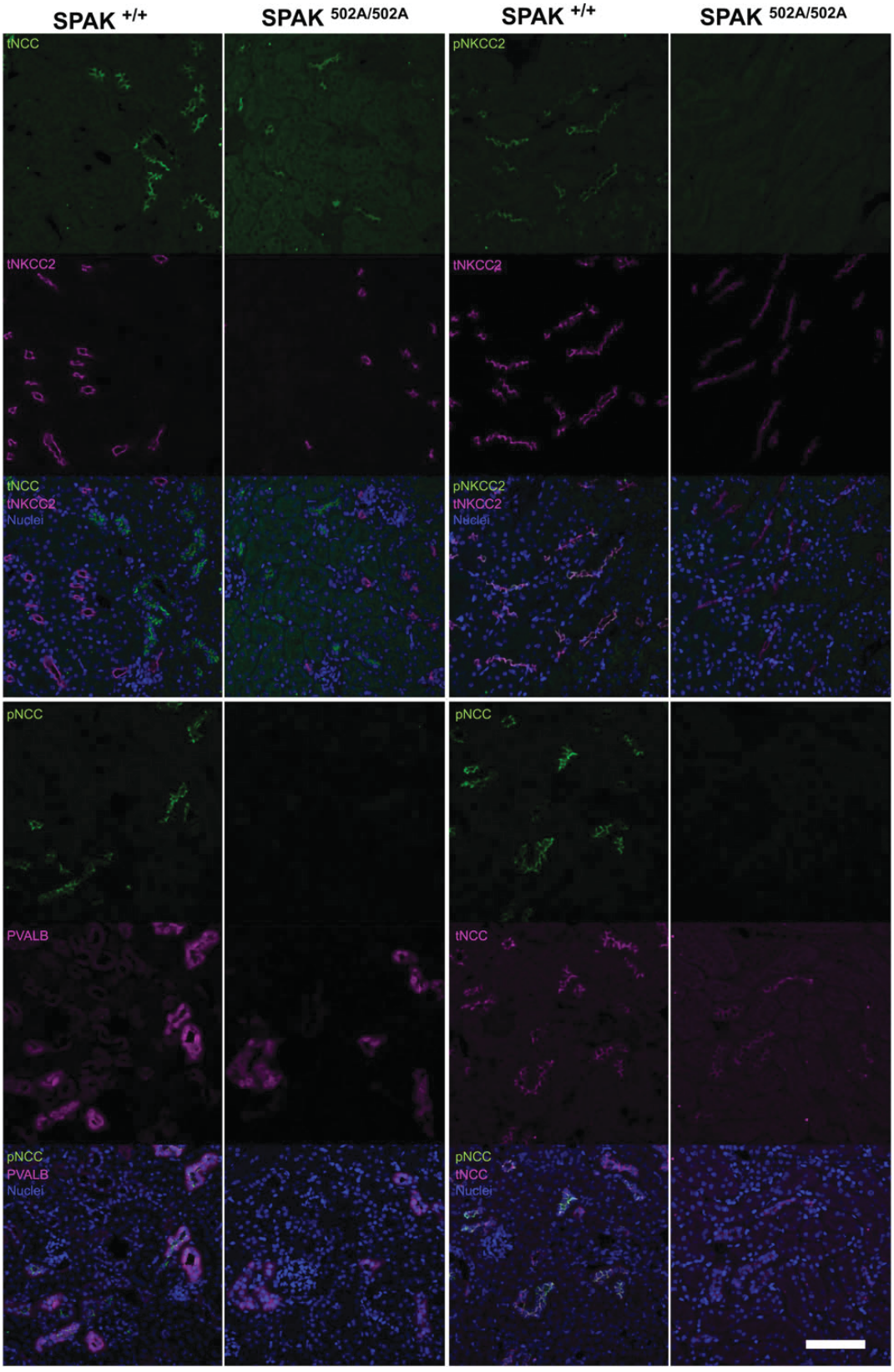

Figure 4. Immunolocalisation of NCC and NKCC2 in the renal tubules of SPAK$^{L502A/L502A}$ Mice. Representative pseudocoloured average intensity z projections of immunofluorescent-stained kidney sections ($n = 4$ per genotype) showing the distribution of total and phospho proteins in the TAL marked by total NKCC2 (tNKCC2), early distal convoluted tubule (DCT1) marked by parvalbumin (PVALB) and whole distal convoluted tubule (DCT1/2) marked by total NCC (tNCC). Phospho-NCC T46 (pNCC) and phospho-NKCC2 S91 (pNKCC2) are virtually undetectable in the SPAK$^{L502A/L502A}$ mice. Scale bar = 100 µm.

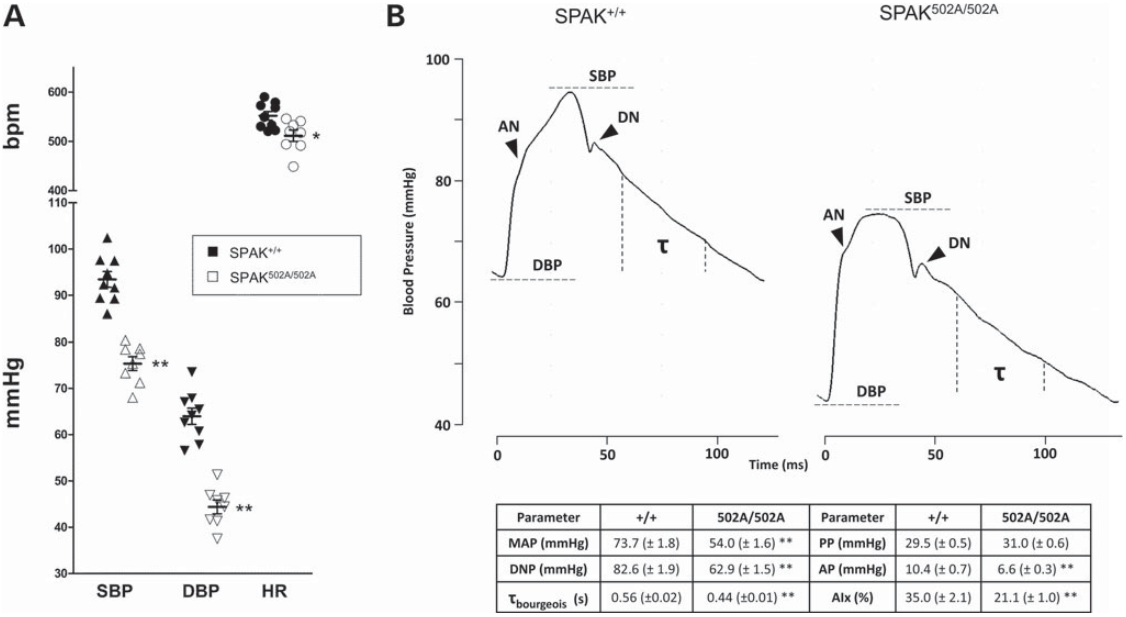

Parameter	+/+	502A/502A	Parameter	+/+	502A/502A
MAP (mmHg)	73.7 (± 1.8)	54.0 (± 1.6) **	PP (mmHg)	29.5 (± 0.5)	31.0 (± 0.6)
DNP (mmHg)	82.6 (± 1.9)	62.9 (± 1.5) **	AP (mmHg)	10.4 (± 0.7)	6.6 (± 0.3) **
$\tau_{bourgeois}$ (s)	0.56 (±0.02)	0.44 (±0.01) **	AIx (%)	35.0 (± 2.1)	21.1 (± 1.0) **

Figure 5. Blood pressure and pressure waveforms of SPAK$^{L502A/L502A}$ mice. (**A**) Intravascular carotid measurements of systemic systolic blood pressure (SBP) and diastolic blood pressure (DBP), and heart rate (HR) determined by ECG R-R wave interval in mice under general anaesthesia. (**B**) Pulse waveform analysis reveals no change in pulse pressure (PP) (SBP–DBP) but does show decreased augmentation pressure (AP) (SBP–anacrotic notch [AN] pressure), dicrotic notch (DN) pressure and MAP (1/3 × SBP + 2/3 × DBP) in the SPAK$^{L502A/L502A}$ versus wild type. This hypotensive phenotype is in part owing to changes in vascular contractility in SPAK$^{L502A/L502A}$ mice as evidenced by their lower augmentation index (AIx) [AP/PP], a marker of arterial stiffness, and is further supported by a decrease in their diastolic pressure decay time constant ($\tau_{bourgeois}$) (1/slope of diastolic pressure decay; measured 30 ms after DN and 20 ms before end DBP), a surrogate marker of decreased vascular resistance. Bars are mean ± SEM, $n = 8–9$. Significant differences from the SPAK wild type are shown by: *$P < 0.02$, **$P < 0.001$.

Plasmids

C-terminal human SPAK, full length, N-, C-terminal mouse SPAKs were amplified employing SuperScript III (Invitrogen) from placenta total RNA (Stratagene) using appropriate oligonucleotides. The RT–PCR products were ligated into pCR2.1-TOPO vector and sequenced. The sequence-verified SPAKs were sub-cloned into bacterial (pGEX-6P-1) and mammalian (pCMV5) expression vectors using BamHI and NotI. Required amino acid mutations were introduced into the pCR2.1-TOPO clone using site-directed mutagenesis by QuikChange method (Stratagene) but substituting the Taq enzyme with KOD Hot Start DNA polymerase (Novagen). All DNA plasmids used in this study are listed in Supplementary Material, Table S1. Oligonucleotides were obtained from Invitrogen Life Sciences. DNA sequencing was performed by The Sequencing Service, College of Life Sciences, University of Dundee (www.dnaseq.co.uk). All recombinant proteins, plasmids and antibodies generated for the present study are available on request and are described in additional detail on our website for reagents (https://mrcppureagents.dundee.ac.uk/).

Expression and purification of proteins in *Escherichia coli*

All pGEX-6P-1 constructs encoding expression of recombinant with N-terminal Glutathione-S-Transferase (GST) tags were transformed into BL21 *E. coli* cells, and 1-l cultures were grown at 37°C in Luria Broth containing 100 µg/ml ampicillin until the absorbance at 600 nm was 0.8. Isopropyl ß-D-thiogalactopyranoside (30 µM) was then added, and the cells were cultured for a further 18 h at 26°C. Cells were isolated by centrifugation, resuspended in 40 ml of ice-cold lysis buffer and lysed in one round of freeze/thawing, followed by sonication (Branson Digital Sonifier; ten 15-s pulses with a setting of 45% amplitude) to fragment DNA. Lysates were centrifuged at 4°C for 15 min at 26 00 *g*. The GST-SPAK recombinant proteins were affinity-purified on 0.5 ml glutathione–Sepharose and eluted in buffer A containing 0.27 M sucrose and 20 mM glutathione.

Fluorescence polarization

Fluorescence polarization measurements were performed at 25°C with purified SPAK proteins in 50 mM Tris–HCl, pH 7.5, 150 mM NaCl and 2 mM DTT. The concentration of the SPAK proteins was determined by measuring their absorbance at 280 nm and calculated using the molar absorption coefficient determined by the ProtParam Online tool (55). All peptides [SEEGKP QLVGRFQVTSSK (EP4543) and SEEGKPQLVGAFQVTSSK (EP4544)] contained an N-terminal linker required for conjugating to the Lumio Green fluorophore (CCPGCCGGGG) and were initially resuspended in 50 mM ammonium bicarbonate, pH 8. Peptide labelling was achieved by incubating 10 nM of each peptide in a 0.5 ml reaction mixture of 20 µM Lumio Green in 25 mM Tris–HCl, pH 7.5, 200 mM NaCl and 5 mM 2-mercaptoethanol. Reactions were left to proceed in the dark for 2 h. The peptides were dialysed for 4 h into 25 mM Tris–HCl, pH 7.5, 200 mM NaCl and 5 mM 2-mercaptoethanol using a Micro DispoDIALYZER with a 100-Da molecular-mass cut-off (Harvard Apparatus) and then for another 12 h with changed buffer. For fluorescence polarization, mixtures were set up containing the indicated concentration of protein, 10 nM Lumio-Green-labelled peptide in a final volume of 30 µl. All individual bindings were performed in duplicate with at least 12 data points per curve. Fluorescence polarization measures were made using a BMG PheraStar plate reader, with an excitation wavelength of 485 nm and an emission wavelength of 538 nm, and measurements were corrected to the fluorescent probe alone. Data analysis and graphing were then performed in GraphPad Prism6; a one-site-specific binding

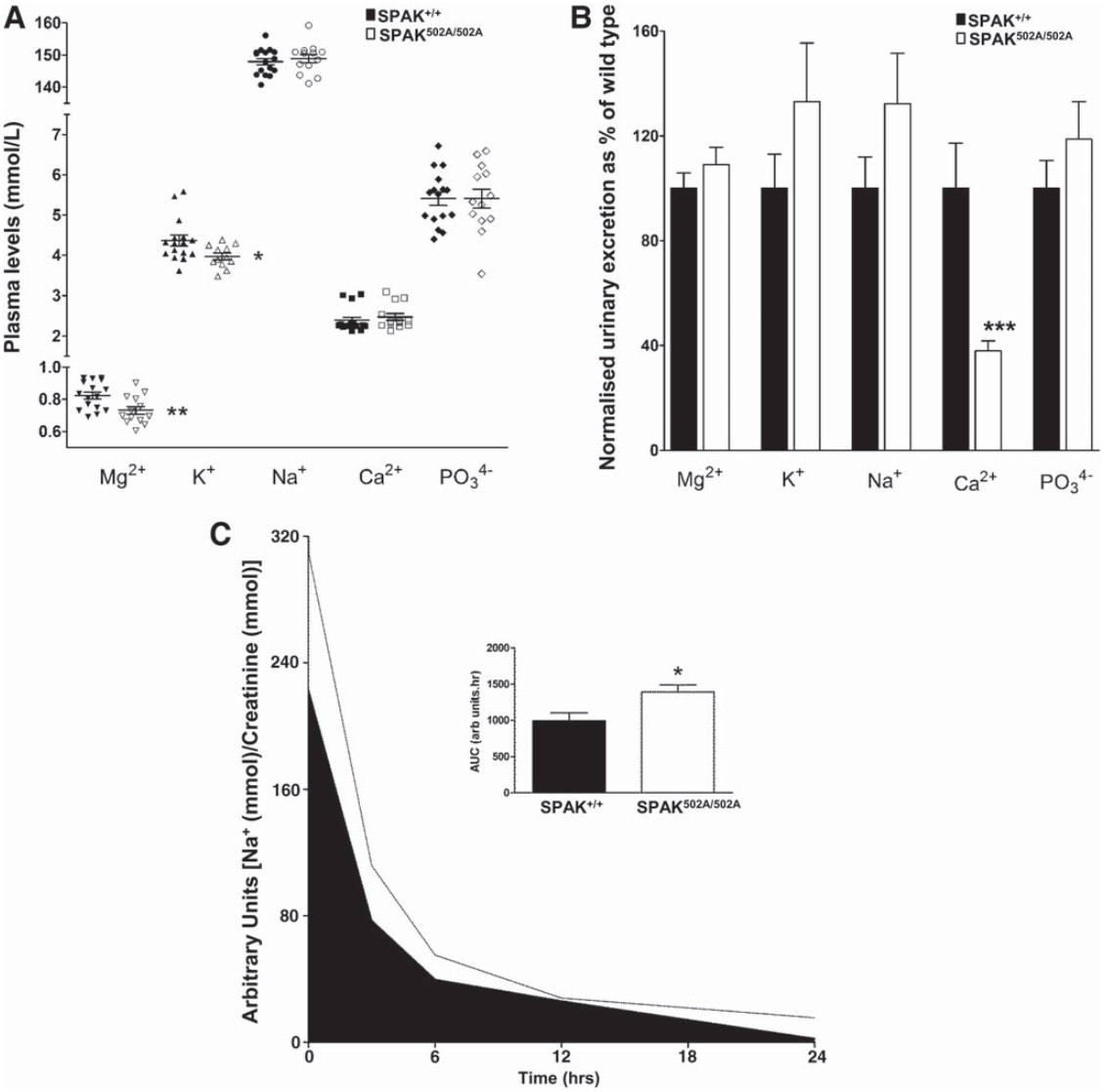

Figure 6. Plasma and urine electrolyte levels of SPAK$^{L502A/L502A}$ mice. (**A**) Plasma electrolytes ($n = 12$–16 per genotype per electrolyte) and (**B**) creatinine normalised urinary electrolytes ($n = 16$–18 per genotype per electrolyte). (**C**) Urinary Na^+ excretion expressed as mmol Na^+/mmol creatinine at various time points after switching from a 3% w/w to a 0.03% w/w salt diet. Inset (C) shows the areas under the two curves (AUC) ($n = 16$ per genotype). Bars are mean ± SEM. Significant differences from the SPAK wild type are shown by: *$P < 0.02$, **$P < 0.01$, ***$P < 0.005$.

model was assumed ($Y = B_{max} * X/[K_d + X]$) and the fitted dissociation constant computed. All experimental bindings were repeated at least twice and comparable results to those shown in the present study were obtained.

Cell culture and transfections

HEK293 (human embryonic kidney 293) cells were cultured on 10-cm-diameter dishes in DMEM supplemented with 10% (v/v) foetal bovine serum, 2 mM L-glutamine, 100 U/ml penicillin and 0.1 mg/ml streptomycin. For transfection experiments, each dish of adherent HEK293 cells was transfected with 20 μl of 1 mg/ml polyethylenimine (Polysciences) and 5–10 μg of plasmid DNA as described previously (56). Thirty-six hours post-transfection, cells were lysed in 0.3 ml of ice-cold lysis buffer/dish, lysates were clarified by centrifugation at 4°C for 15 min at 26 000*g* and the supernatants were frozen in aliquots in liquid nitrogen and stored at −20°C. Protein concentrations were determined using the Bradford method.

Buffers

Lysis buffer was 50 mM Tris–HCl, pH 7.5, 1 mM EGTA, 1 mM EDTA, 50 mM sodium fluoride, 5 mM sodium pyrophosphate, 1 mM sodium orthovanadate, 1% (w/v) NP-40 or 1% (w/v) Triton X-100, 0.27 M sucrose, 0.1% (v/v) 2-mercaptoethanol and protease inhibitors (one tablet per 50 ml). Buffer A was 50 mM Tris–HCl, pH 7.5, 0.1 mM EGTA and 0.1% (v/v) 2-mercaptoethanol. TBS-Tween buffer (TTBS) was Tris–HCl, pH 7.5, 0.15 M NaCl and 0.2% (v/v) Tween-20. SDS sample buffer was 1× NuPAGE LDS sample buffer (Invitrogen), containing 1% (v/v) 2-mercaptoethanol.

Antibodies

The following antibodies were raised in sheep and affinity purified on the appropriate antigen by the Division of Signal Transduction Therapy Unit at the University of Dundee: WNK1-total antibody (residues 2360–2382 of human WNK1, S62B), WNK4-total antibody (residues 1221–1243 of human WNK4, S064B),

WNK4 N-terminal antibody (residues 1–14 of mouse WNK4, S726D), SPAK-mouse antibody (2–76 of mouse SPAK, S668D), OSR1 mouse antibody (389–408 of mouse OSR1, SAHLPQPAGQ MPTQPAQVSL, S149C), SPAK/OSR1 (T-loop) phospho-Thr233/Thr185 antibody (226–238 of human SPAK or residues 178–190 of human OSR1, TRNKVRKpTFVGTP, S204C), SPAK/OSR1 (S-motif) phospho-Ser373/Ser325 antibody (367–379 of human SPAK, RRVPGSpSGHLHKT, which is highly similar to residues 319–331 of human OSR1 in which the sequence is RRVPG SpSGRLHKT, S670B), SPAK phospho-Thr233 antibody (226–238 of human SPAK, TRNKVRKpTFVGTP, S668B), NKCC1 phospho-Thr203 + Thr207 + Thr212 (residues 198–217 of human NKCC1, HYYYDpTHTNpTYYLRpTFGHNT, S763B), NKCC1 phospho-Thr 212 + Thr 217 (residues 208–223 of human NKCC1, YYLRpT FGHNpTMDAVPR, S063D), NKCC1-total antibody (residues 1–260 of shark NKCC1, S841B), NCC phospho-Thr46 + Thr50 + Thr55 antibody (residues 41–60 of human NCC phosphorylated at Thr46 + Thr50 + Thr55, HPSHLpTHSSpTFCMRpTFGYNT, S908B), NCC phospho-Thr46 antibody (residues 40–54 of human NCC phosphorylated at Thr46, SHPSHLpTHSSTFCMRRR, S241C), NCC phospho-Thr60 antibody (residues 54–66 of human NCC phosphorylated at Thr60, RTFGYNpTIDVVPT, S995B), NCC phospho-Ser91 antibody (residues 85–97 of human NCC phosphorylated at Ser91, CTLADLHpSFLKQEGRR, S996B), NCC-total antibody (residues 906–925 of human NCC, CHTKRFEDMIAPFRLNDGFKD, S965B), NKCC2 phospho-Thr100 (residues 94–106 of human NKCC2, NTYYLQpTFGHNTM, S431C), NKCC2 phospho-Ser130 (residues 123–137 of human NKCC2, GPKVNRPpSLLEIHEQ, S888C), NKCC2 phospho-Ser91 (residues 86–97 of human NKCC2, RRFHAYD pSHTNTYYRR, S451C), NKCC2-total antibody (residues 1–174 of human NKCC2, S838B), GST-total antibody (raised against the glutathione S-transferase protein, S902A) and ERK1 total antibody (full-length human ERK1 protein, S221B). The anti-GAPDH antibody (ab8245), anti-NCC-total [SLC12A3] (AB95302) and the anti-parvalbumin antibody (ab11427) were purchased from Abcam. Anti-PVALB (Parvalbumin PV25) from Swant. Anti-NKCC2-total (LS-C313275) from LifeSpan BioSciences. The anti-ERK1/2 antibody (9102) was purchased from Cell Signalling Technology. The anti-FLAG antibody (F1804) was purchased from Sigma–Aldrich. Secondary antibodies coupled to horseradish peroxidase used for immunoblotting were obtained from Pierce. Fluorochrome-conjugated secondary antibodies for immunofluorescent confocal microscopy were obtained from Life Technologies and Abcam. Pre-immune IgG used in control immunoprecipitation experiments were affinity purified from pre-immune serum using protein G-Sepharose.

Immunoprecipitation and assay of SPAK

One milligram of clarified cell lysate was incubated with 5 µg of the SPAK/OSR1 (total) antibody conjugated to 5 µl of protein G-Sepharose and incubated for 2 h at 4°C with gentle agitation. The immunoprecipitates were washed twice with 1 ml of lysis buffer containing 0.5 M NaCl and twice with 1 ml of buffer A. The SPAK/OSR1 immunoprecipitates were assayed with the CATCHtide peptide substrate (RRHYYYDTHTNTYYLRTFGHN TRR) that encompasses the SPAK/OSR1 phosphorylation sites on NKCC1 (3). Assays were set up in a total volume of 50 µl in buffer A containing 10 mM $MgCl_2$, 0.1 mM [γ32P]ATP and 300 µM CATCHtide (37). After incubation for 30 min at 30°C, the reaction mixture was applied onto P81 phosphocellulose paper, the papers were washed in phosphoric acid and incorporation of 32P-radioactivity in CATCHtide was quantified by Cerenkov counting.

Immunoblotting and total-antibody immunoprecipitation

Cell lysates (15 µg) in SDS sample buffer were subjected to electrophoresis on polyacrylamide gels and transferred to nitrocellulose membranes. The membranes were incubated for 30 min with TBS-T containing 5% (w/v) skim milk. The membranes were then immunoblotted in 5% (w/v) skim milk in TBS-T with the indicated primary antibodies overnight at 4°C. Sheep antibodies were used at a concentration of 1–2 µg/ml. The incubation with phospho-specific sheep antibodies was performed with the addition of 10 µg/ml of the dephospho-peptide antigen used to raise the antibody. The blots were then washed six times with TBS-T and incubated for 1 h at room temperature with secondary HRP-conjugated antibodies diluted 5000-fold in 5% (w/v) skim milk in TBS-T. After repeating the washing steps, the signal was detected with enhanced chemiluminescence reagent. Immunoblots were developed using a film automatic processor (SRX-101; Konica Minolta Medical), and films were scanned with a 600-dpi resolution on a scanner (PowerLook 1000; UMAX). Figures were generated using Photoshop/Illustrator (Adobe). For total-antibody immunoprecipitation NCC, NKCC1 and NKCC2 were immunoprecipitated from indicated kidney extracts. A 2 mg aliquot of the indicated clarified kidney extract were incubated with 15 µg of the indicated total NCC, NKCC1 and NKCC2 antibodies conjugated to 15 µl of protein-G–Sepharose. Incubation was for 2 h at 4°C with gentle agitation, and the immunoprecipitates were washed three times with 1 ml of lysis buffer containing 0.15 M NaCl and twice with 1 ml of buffer A. Bound proteins were eluted with 1× lithium dodecyl sulphate (LDS) sample buffer.

Generation and genotyping of SPAK knock-in mice

The knock-in mice were generated by TaconicArtemis (http://www.taconic.com/wmspage.cfm?parm1=1453) as described in Figure 2A. The knock-in mice were generated and maintained on an inbred C57BL/6J background. Genotyping was performed by PCR using genomic DNA isolated from tails or embryonic membranes. For the SPAK mice, Primer 1 (5′ TCT GTA AGC TCA TTT ATG TAG TCA CC 3′) and Primer 2 (P2: 5′ CAA GTG AGT GAG TGA ATA CAG CC 3′) were used to detect the wild-type and knock-in alleles as described in Figure 2A. The PCR programme consisted of 2 min at 95°C, 30 s at 95°C, 1 min at 60°C and 1 min at 72°C: 35 cycles; 10 min at 72°C. DNA sequencing was performed by The Sequencing Service, College of Life Sciences, University of Dundee, UK (www.dnaseq.co.uk).

Mice were maintained under specific pathogen-free conditions, and all procedures were carried out in accordance with the regulations set by the Universities of Cambridge and Dundee, and the United Kingdom Home Office.

Sample preparation and immunostaining for imaging

Harvested mouse tissues were immersion fixed in fresh 4% (w/v) formaldehyde-PBS pH 6.9 for 16 h at 37°C and washed three times in PBS and stored at 4°C until paraffin embedded. Five-micrometre sections were deparaffinised in Histoclear (National Diagnostics) and rehydrated in graded methanol steps. An antigen retrieval step was performed with R-Universal buffer in the 2100 antigen retriever for a single heat-pressure cycle (Aptum Biologics). Sections were permeabilised with 0.05% (v/v) Triton X-100–PBS for 20 min and blocked for 1 h at 37°C with 2% (v/v) donkey serum in 0.05% (v/v) Triton X-100–PBS. Primary antibodies were incubated overnight for 16 h at 4°C at the following concentrations diluted in 1% (v/v) donkey serum in 0.05% (v/v)

Triton X-100–PBS: 2 μg/ml for pNCC T46, tNCC, pNKCC2 S91, tNKCC2 and 4 μg/ml for WNK4 N-terminal and 1:2000 for PVALB. Phospho-specific antibodies included the addition of 10 μg/ml of the non-phospho peptide used to raise the antibody per 2 μg/ml of antibody used. Negative controls omitted the primary antibody and were processed in parallel (Supplementary Material, Fig. S3). Slides were then washed for 20 min in 0.05% (v/v) Triton X-100–PBS and incubated in secondary antibody for 1 h at 37°C. Pre-absorbed donkey IgG-conjugated Alexa Fluor 488, 633 and 647 secondary antibodies (Life Technologies/Abcam) were used at 1:200 diluted in 1% (v/v) donkey serum in 0.05% (v/v) Triton X-100–PBS for immunofluorescent labelling. Slides were washed as mentioned earlier, counterstained using Sytox orange nucleic acid stain (S11368—Life Technologies) and mounted using Prolong gold antifade (P36930—Life Technologies) and shielded from light.

Image acquisition and processing

Immunofluorescent images were acquired on the Leica TCS SP2 laser-scanning confocal with 488-, 543-, 633-nm laser lines mounted on an upright Leica DM RXA fluorescent microscope using an HC PL FLUOTAR 20X/0.5NA objective. Acquisition parameters were as follows: 12-bit, 1024 × 1024 pixels, 2× digital zoom, 800 Hz scan speed, 4-line Kalman filtering, sequential (by line) channel imaging and 10 slice z-stack of 5 μm.

In FIJI image analysis software, fluorescent z-stacks underwent background subtraction (1000px radius rolling ball, no smoothing) and average intensity z-projection. Brightness and contrast were adjusted by linear histogram stretching to enhance visibility. Any images to be compared with one another were processed evenly across the whole image in parallel, the exception to this were nuclei images where brightness and contrast were performed on each image independently to ensure the best visibility.

In vivo pulse waveform analysis and BP measurements

Animals were anaesthetized with isoflurane on 100% O_2 (induction: 3%, maintenance: 1.75%) and placed on a self-regulating rectal probe-coupled heat mat (TC-1000; CWE) to maintain a body temperature of 37°C. Heart rate was measured by the R-R wave interval from ECG Lead II using an animal bio amp (FE136; AD Instruments) with needle electrodes inserted into fore and hind limbs (MLA1213; AD Instruments). The right carotid artery was catheterized with a 1F Mikro-Tip pressure transducer (SPR-1000; Millar) connected to a bridge amp (FE221; AD Instruments) and powerlab system (PL3504/P; AD Instruments). When the animals had stabilized, measurements were taken at 2000 samples/s using lab chart version 7/8 pro (AD Instruments) to record ECG and BP pulse waveforms.

Data processing and analysis was performed in Lab chart 8 pro. Using the BP add-on, systolic, diastolic and dicrotic notch BPs were automatically detected per beat (beats with respiratory-induced artefact were gated out of the analysis using the beats classifier). Mean arterial pressure (MAP) was calculated as (1/3 systolic pressure + 2/3 diastolic pressure) and pulse pressure as (systolic pressure – diastolic pressure). A macro was scripted to detect the anacrotic notch, by using the third zero value crossing the fourth derivative of the pressure (57). The augmentation pressure was calculated as (systolic pressure – anacrotic notch pressure) and augmentation index as (augmentation pressure/pulse pressure). A macro was scripted to measure the slope of the diastolic pressure decay, 30 ms after the dicrotic notch and 20 ms before the end diastolic pressure (to avoid perturbations caused by aortic valve opening/closing). The reciprocal of this slope (ignoring the sign) was calculated from the 20% trimmed mean values to determine the time decay constant of the diastolic pressure decay ($\tau_{bourgeois}$), which correlates with vascular resistance (41). Data collection and analysis was carried out in a blinded fashion throughout.

Plasma and urine electrolyte measurements

Animal were placed on a 3% w/w Na diet for 14 days with urine and plasma samples collected on between Days 7 and 10 for baseline. On Day 14, mice were switched onto a 0.03% w/w Na diet with urine samples collected at 0, 3, 6, 12, 24 h after Na-diet switch. Spot urine was collected from awake mice following spontaneous micturition on handling over a sheet of Saran® wrap or Parafilm®. Samples were then divided and one sample received acidification with HNO_3 to a final concentration of 1% v/v to prevent precipitation of electrolytes, before both were stored at –80°C. Blood was collected by saphenous venepuncture in awake restrained animals, and plasma was separated by using Microvette® CB 300 LH (Sarstedt) centrifuged at 2000*g* for 5 min before storage at –80°C.

Plasma and urine (non-acidified) creatinine levels were assayed in the core Core Biochemical Assay Laboratory, Addenbrooke's Hospital, Cambridge, UK. Plasma and urine (acidified) samples were diluted 1:1000 using ultra-pure polished water containing 1% v/v HNO_3. Cations were then measured using an inductively coupled plasma—optical emission spectrometry (Perkin Elmer ICP-OES Analyser) with known standards and pre-set elemental spectra. Data collection and analysis was carried out in a blinded fashion throughout.

Statistical analysis

Data are presented as mean ± SEM, with n representing the number of analysed mice. Mean values were compared by the Student's *t*-test for paired or unpaired observations where appropriate, using SigmaStat Program (Jandel Scientific, Chicago, IL, USA) or GraphPad Prism5, or by ANOVA with *post hoc* testing using version 15 of SPSS software. A $P < 0.05$ was considered statistically significant.

Supplementary Material

Supplementary Material is available at *HMG* online.

Authors' Contributions

J.Z. carried out the experiments given in Figures 1, 2, 3, Supplementary Material, Figs S1 and S2. K.S. carried out the experiments given in Figures 4, 5, 6, Supplementary Material, Figs S3 and S4. J.Z. provided assistance with the experiments given in Figures 4, 5 and 6. T.M. performed the cDNA cloning. J.Z., K.S., K.M. O. and D.R.A. planned the experiments, analysed the results and wrote the paper.

Acknowledgement

We express gratitude to Gail Gilmour and Elaine Forsyth for aid with the management of mouse colonies and genotyping and the excellent technical support of the MRC-Protein Phosphorylation and Ubiquitylation Unit (PPU) DNA Sequencing Service (coordinated by Nicholas Helps), the MRC-PPU tissue-culture team (coordinated by Kirsten Airey and Janis Stark), the Division of Signal Transduction Therapy (DSTT) protein production, antibody

purification teams (coordinated by Hilary McLauchlan and James Hastie), the Cambridge Geography Science Laboratories (coordinated by Chris Rolfe, Steve Boreham and Samantha Smith) and Addenbrooke's Core Biochemical Assay Laboratory (coordinated by Keith Burling and Peter Barker).

Conflict of Interest statement. None declared.

Funding

This work was supported by the Medical Research Council, British Heart foundation (a PhD studentship to K.S. and PG 13 89 30577), and the pharmaceutical companies supporting the Division of Signal Transduction Therapy Unit (AstraZeneca, Boehringer-Ingelheim, GlaxoSmithKline, Merck KGaA, Janssen Pharmaceutica and Pfizer). Funding to pay the Open Access publication charges for this article was provided by the University of Cambridge RCUK and COAF block grants.

References

1. Delpire, E. and Gagnon, K.B. (2008) SPAK and OSR1: STE20 kinases involved in the regulation of ion homoeostasis and volume control in mammalian cells. *Biochem. J.*, **409**, 321–331.
2. Richardson, C. and Alessi, D.R. (2008) The regulation of salt transport and blood pressure by the WNK-SPAK/OSR1 signalling pathway. *J. Cell. Sci.*, **121**, 3293–3304.
3. Vitari, A.C., Deak, M., Morrice, N.A. and Alessi, D.R. (2005) The WNK1 and WNK4 protein kinases that are mutated in Gordon's hypertension syndrome phosphorylate and activate SPAK and OSR1 protein kinases. *Biochem. J.*, **391**, 17–24.
4. Moriguchi, T., Urushiyama, S., Hisamoto, N., Iemura, S., Uchida, S., Natsume, T., Matsumoto, K. and Shibuya, H. (2005) WNK1 regulates phosphorylation of cation-chloride-coupled cotransporters via the STE20-related kinases, SPAK and OSR1. *J. Biol. Chem.*, **280**, 42685–42693.
5. Filippi, B.M., de Los Heros, P., Mehellou, Y., Navratilova, I., Gourlay, R., Deak, M., Plater, L., Toth, R., Zeqiraj, E. and Alessi, D.R. (2011) MO25 is a master regulator of SPAK/OSR1 and MST3/MST4/YSK1 protein kinases. *EMBO J.*, **30**, 1730–1741.
6. Piechotta, K., Lu, J. and Delpire, E. (2002) Cation chloride cotransporters interact with the stress-related kinases Ste20-related proline-alanine-rich kinase (SPAK) and oxidative stress response 1 (OSR1). *J. Biol. Chem.*, **277**, 50812–50819.
7. Gagnon, K.B., England, R. and Delpire, E. (2006) Volume sensitivity of cation-Cl- cotransporters is modulated by the interaction of two kinases: Ste20-related proline-alanine-rich kinase and WNK4. *Am. J. Physiol. Cell Physiol.*, **290**, C134–C142.
8. Anselmo, A.N., Earnest, S., Chen, W., Juang, Y.C., Kim, S.C., Zhao, Y. and Cobb, M.H. (2006) WNK1 and OSR1 regulate the Na^+, K^+, $2Cl^-$ cotransporter in HeLa cells. *Proc. Natl Acad. Sci. USA*, **103**, 10883–10888.
9. Richardson, C., Sakamoto, K., de los Heros, P., Deak, M., Campbell, D.G., Prescott, A.R. and Alessi, D.R. (2011) Regulation of the NKCC2 ion cotransporter by SPAK-OSR1-dependent and -independent pathways. *J. Cell. Sci.*, **124**, 789–800.
10. Richardson, C., Rafiqi, F.H., Karlsson, H.K., Moleleki, N., Vandewalle, A., Campbell, D.G., Morrice, N.A. and Alessi, D.R. (2008) Activation of the thiazide-sensitive Na+-Cl- cotransporter by the WNK-regulated kinases SPAK and OSR1. *J. Cell. Sci.*, **121**, 675–684.
11. de Los Heros, P., Alessi, D.R., Gourlay, R., Campbell, D.G., Deak, M., Macartney, T.J., Kahle, K.T. and Zhang, J. (2014) The WNK-regulated SPAK/OSR1 kinases directly phosphorylate and inhibit the K^+-Cl^- co-transporters. *Biochem. J.*, **458**, 559–573.
12. Gagnon, K.B. and Delpire, E. (2013) Physiology of SLC12 transporters: lessons from inherited human genetic mutations and genetically engineered mouse knockouts. *Am. J. Physiol. Cell Physiol.*, **304**, C693–C714.
13. Arroyo, J.P., Kahle, K.T. and Gamba, G. (2013) The SLC12 family of electroneutral cation-coupled chloride cotransporters. *Mol. Asp. Med.*, **34**, 288–298.
14. Kahle, K.T., Rinehart, J. and Lifton, R.P. (2010) Phosphoregulation of the Na-K-2Cl and K-Cl cotransporters by the WNK kinases. *Biochim. Biophys. Acta*, **1802**, 1150–1158.
15. Kahle, K.T., Ring, A.M. and Lifton, R.P. (2008) Molecular physiology of the WNK kinases. *Annu. Rev. Physiol.*, **70**, 329–355.
16. Alessi, D.R., Zhang, J., Khanna, A., Hochdorfer, T., Shang, Y. and Kahle, K.T. (2014) The WNK-SPAK/OSR1 pathway: master regulator of cation-chloride cotransporters. *Sci. Signal.*, **7**, re3.
17. Wilson, F.H., Disse-Nicodeme, S., Choate, K.A., Ishikawa, K., Nelson-Williams, C., Desitter, I., Gunel, M., Milford, D.V., Lipkin, G.W., Achard, J.M. *et al.* (2001) Human hypertension caused by mutations in WNK kinases. *Science*, **293**, 1107–1112.
18. Boyden, L.M., Choi, M., Choate, K.A., Nelson-Williams, C.J., Farhi, A., Toka, H.R., Tikhonova, I.R., Bjornson, R., Mane, S.M., Colussi, G. *et al.* (2012) Mutations in kelch-like 3 and cullin 3 cause hypertension and electrolyte abnormalities. *Nature*, **482**, 98–102.
19. Ohta, A., Schumacher, F.R., Mehellou, Y., Johnson, C., Knebel, A., Macartney, T.J., Wood, N.T., Alessi, D.R. and Kurz, T. (2013) The CUL3-KLHL3 E3 ligase complex mutated in Gordon's hypertension syndrome interacts with and ubiquitylates WNK isoforms: disease-causing mutations in KLHL3 and WNK4 disrupt interaction. *Biochem. J.*, **451**, 111–122.
20. Wakabayashi, M., Mori, T., Isobe, K., Sohara, E., Susa, K., Araki, Y., Chiga, M., Kikuchi, E., Nomura, N., Mori, Y. *et al.* (2013) Impaired KLHL3-mediated ubiquitination of WNK4 causes human hypertension. *Cell. Rep.*, **3**, 858–868.
21. Shibata, S., Zhang, J., Puthumana, J., Stone, K.L. and Lifton, R.P. (2013) Kelch-like 3 and Cullin 3 regulate electrolyte homeostasis via ubiquitination and degradation of WNK4. *Proc. Natl Acad. Sci. USA*, **110**, 7838–7843.
22. Louis-Dit-Picard, H., Barc, J., Trujillano, D., Miserey-Lenkei, S., Bouatia-Naji, N., Pylypenko, O., Beaurain, G., Bonnefond, A., Sand, O., Simian, C. *et al.* (2012) KLHL3 mutations cause familial hyperkalemic hypertension by impairing ion transport in the distal nephron. *Nat. Genet.*, **44**, **456**–460. S451–453.
23. Schumacher, F.R., Sorrell, F.J., Alessi, D.R., Bullock, A.N. and Kurz, T. (2014) Structural and biochemical characterization of the KLHL3-WNK kinase interaction important in blood pressure regulation. *Biochem. J.*, **460**, 237–246.
24. Simon, D.B., Nelson-Williams, C., Bia, M.J., Ellison, D., Karet, F.E., Molina, A.M., Vaara, I., Iwata, F., Cushner, H.M., Koolen, M. *et al.* (1996) Gitelman's variant of Bartter's syndrome, inherited hypokalaemic alkalosis, is caused by mutations in the thiazide-sensitive Na-Cl cotransporter. *Nat. Genet.*, **12**, 24–30.
25. Lin, S.H., Shiang, J.C., Huang, C.C., Yang, S.S., Hsu, Y.J. and Cheng, C.J. (2005) Phenotype and genotype analysis in Chinese patients with Gitelman's syndrome. *J. Clin. Endocrinol. Metab.*, **90**, 2500–2507.
26. Shao, L., Ren, H., Wang, W., Zhang, W., Feng, X., Li, X. and Chen, N. (2008) Novel SLC12A3 mutations in Chinese patients with Gitelman's Syndrome. *Nephron. Physiol.*, **108**, p29–p36.

27. Yang, S.S., Lo, Y.F., Wu, C.C., Lin, S.W., Yeh, C.J., Chu, P., Sytwu, H.K., Uchida, S., Sasaki, S. and Lin, S.H. (2010) SPAK-knockout mice manifest Gitelman Syndrome and impaired vasoconstriction. *J. Am. Soc. Nephrol.*, **21**, 1868–1877.
28. McCormick, J.A., Mutig, K., Nelson, J.H., Saritas, T., Hoorn, E.J., Yang, C.L., Rogers, S., Curry, J., Delpire, E., Bachmann, S. *et al.* (2011) A SPAK isoform switch modulates renal salt transport and blood pressure. *Cell. Metab.*, **14**, 352–364.
29. Grimm, P.R., Taneja, T.K., Liu, J., Coleman, R., Chen, Y.Y., Delpire, E., Wade, J.B. and Welling, P.A. (2012) SPAK isoforms and OSR1 regulate sodium-chloride co-transporters in a nephron-specific manner. *J. Biol. Chem.*, **287**, 37673–37690.
30. Rafiqi, F.H., Zuber, A.M., Glover, M., Richardson, C., Fleming, S., Jovanovic, S., Jovanovic, A., O'Shaughnessy, K.M. and Alessi, D.R. (2010) Role of the WNK-activated SPAK kinase in regulating blood pressure. *EMBO Mol. Med.*, **2**, 63–75.
31. Chiga, M., Rafiqi, F.H., Alessi, D.R., Sohara, E., Ohta, A., Rai, T., Sasaki, S. and Uchida, S. (2011) Phenotypes of pseudohypoaldosteronism type II caused by the WNK4 D561A missense mutation are dependent on the WNK-OSR1/SPAK kinase cascade. *J. Cell Sci.*, **124**, 1391–1395.
32. Wang, Y., O'Connell, J.R., McArdle, P.F., Wade, J.B., Dorff, S.E., Shah, S.J., Shi, X., Pan, L., Rampersaud, E., Shen, H. *et al.* (2009) From the cover: whole-genome association study identifies STK39 as a hypertension susceptibility gene. *Proc. Natl Acad. Sci. USA*, **106**, 226–231.
33. Gordon, R.D. and Hodsman, G.P. (1986) The syndrome of hypertension and hyperkalaemia without renal failure: long term correction by thiazide diuretic. *Scott. Med. J.*, **31**, 43–44.
34. Gordon, R.D., Klemm, S.A., Tunny, T.J. and Stowasser, M. (1995) Gordon's syndrome: A sodium-volume-dependent form of hypertension with a genetic basis. In Laragh, J.H. and Brenner, B.M. (eds) Hypertension: pathophysiology, diagnosis, and management. Raven Press, New York, pp 2111–2123.
35. Glover, M. and O'Shaughnessy, K.M. (2011) SPAK and WNK kinases: a new target for blood pressure treatment? *Curr. Opin. Nephrol. Hypertens.*, **20**, 16–22.
36. Cohen, P. and Alessi, D.R. (2013) Kinase drug discovery—what's next in the field? *ACS Chem. Biol.*, **8**, 96–104.
37. Vitari, A.C., Thastrup, J., Rafiqi, F.H., Deak, M., Morrice, N.A., Karlsson, H.K. and Alessi, D.R. (2006) Functional interactions of the SPAK/OSR1 kinases with their upstream activator WNK1 and downstream substrate NKCC1. *Biochem. J.*, **397**, 223–231.
38. Gagnon, K.B., England, R. and Delpire, E. (2007) A single binding motif is required for SPAK activation of the Na-K-2Cl cotransporter. *Cell Physiol. Biochem.*, **20**, 131–142.
39. Mori, T., Kikuchi, E., Watanabe, Y., Fujii, S., Ishigami-Yuasa, M., Kagechika, H., Sohara, E., Rai, T., Sasaki, S. and Uchida, S. (2013) Chemical library screening for WNK signalling inhibitors using fluorescence correlation spectroscopy. *Biochem. J.*, **455**, 339–345.
40. Villa, F., Goebel, J., Rafiqi, F.H., Deak, M., Thastrup, J., Alessi, D.R. and van Aalten, D.M. (2007) Structural insights into the recognition of substrates and activators by the OSR1 kinase. *EMBO Rep.*, **8**, 839–845.
41. Bourgeois, M.J., Gilbert, B.K., Donald, D.E. and Wood, E.H. (1974) Characteristics of aortic diastolic pressure decay with application to the continuous monitoring of changes in peripheral vascular resistance. *Circ. Res.*, **35**, 56–66.
42. Safar, M.E. (2001) Systolic blood pressure, pulse pressure and arterial stiffness as cardiovascular risk factors. *Curr. Opin. Nephrol. Hypertens.*, **10**, 257–261.
43. Yang, C.L., Zhu, X. and Ellison, D.H. (2007) The thiazide-sensitive Na-Cl cotransporter is regulated by a WNK kinase signaling complex. *J Clin Invest*, **117**, 3403–3411.
44. Bettmann, M. (1988) Ionic versus nonionic contrast agents and their effects on blood components. Clinical summary and conclusions. *Invest. Radiol.*, **23**(Suppl 2), S378–S380.
45. Kemter, E., Rathkolb, B., Bankir, L., Schrewe, A., Hans, W., Landbrecht, C., Klaften, M., Ivandic, B., Fuchs, H., Gailus-Durner, V. *et al.* (2010) Mutation of the Na(+)-K(+)-2Cl(-) cotransporter NKCC2 in mice is associated with severe polyuria and a urea-selective concentrating defect without hyperreninemia. *Am. J. Physiol. Renal Physiol.*, **298**, F1405–F1415.
46. Knoers, N.V., de Jong, J.C., Meij, I.C., Van Den Heuvel, L.P. and Bindels, R.J. (2003) Genetic renal disorders with hypomagnesemia and hypocalciuria. *J. Nephrol.*, **16**, 293–296.
47. Loffing, J., Vallon, V., Loffing-Cueni, D., Aregger, F., Richter, K., Pietri, L., Bloch-Faure, M., Hoenderop, J.G., Shull, G.E., Meneton, P. *et al.* (2004) Altered renal distal tubule structure and renal Na(+) and Ca(2+) handling in a mouse model for Gitelman's syndrome. *J. Am. Soc. Nephrol.*, **15**, 2276–2288.
48. Belge, H., Gailly, P., Schwaller, B., Loffing, J., Debaix, H., Riveira-Munoz, E., Beauwens, R., Devogelaer, J.P., Hoenderop, J.G., Bindels, R.J. *et al.* (2007) Renal expression of parvalbumin is critical for NaCl handling and response to diuretics. *Proc. Natl Acad. Sci. USA*, **104**, 14849–14854.
49. Prasad, V., Bodi, I., Meyer, J.W., Wang, Y., Ashraf, M., Engle, S.J., Doetschman, T., Sisco, K., Nieman, M.L., Miller, M.L. *et al.* (2008) Impaired cardiac contractility in mice lacking both the AE3 Cl^-/$HCO3^-$ exchanger and the NKCC1 Na+-K+-2Cl-cotransporter: effects on Ca2+ handling and protein phosphatases. *J. Biol. Chem.*, **283**, 31303–31314.
50. Crilly, M.A. (2014) Adjusting the aortic augmentation index for the resting heart rate. *J. Atheroscler. Thromb.*, **21**, 378–380.
51. Ye, Z.Y., Li, D.P., Byun, H.S., Li, L. and Pan, H.L. (2012) NKCC1 upregulation disrupts chloride homeostasis in the hypothalamus and increases neuronal activity-sympathetic drive in hypertension. *J. Neurosci.*, **32**, 8560–8568.
52. Bergaya, S., Faure, S., Baudrie, V., Rio, M., Escoubet, B., Bonnin, P., Henrion, D., Loirand, G., Achard, J.M., Jeunemaitre, X. *et al.* (2011) WNK1 regulates vasoconstriction and blood pressure response to alpha 1-adrenergic stimulation in mice. *Hypertension*, **58**, 439–445.
53. Zeniya, M., Sohara, E., Kita, S., Iwamoto, T., Susa, K., Mori, T., Oi, K., Chiga, M., Takahashi, D., Yang, S.S. *et al.* (2013) Dietary salt intake regulates WNK3-SPAK-NKCC1 phosphorylation cascade in mouse aorta through angiotensin II. *Hypertension*, **62**, 872–878.
54. Meyer, J.W., Flagella, M., Sutliff, R.L., Lorenz, J.N., Nieman, M.L., Weber, C.S., Paul, R.J. and Shull, G.E. (2002) Decreased blood pressure and vascular smooth muscle tone in mice lacking basolateral Na(+)-K(+)-2Cl(-) cotransporter. *Am. J. Physiol. Heart Circ. Physiol.*, **283**, H1846–H1855.
55. Gasteiger, E., Jung, E. and Bairoch, A. (2001) SWISS-PROT: connecting biomolecular knowledge via a protein database. *Curr. Issues Mol. Biol.*, **3**, 47–55.
56. Durocher, Y., Perret, S. and Kamen, A. (2002) High-level and high-throughput recombinant protein production by transient transfection of suspension-growing human 293-EBNA1 cells. *Nucl. Acids Res.*, **30**, E9.
57. Kelly, R., Hayward, C., Avolio, A. and O'Rourke, M. (1989) Noninvasive determination of age-related changes in the human arterial pulse. *Circulation*, **80**, 1652–1659.

Supplementary Figure Legends

Figure S1. **Generation and characterisation of specific SPAK antibodies**. The N-SPAK antibody was generated by ligating cDNA corresponding to amino acids 2–74 of mouse SPAK downstream of the GST open reading frame in the pGEX-6P-1 vector. The resulting fusion protein was injected into sheep to produce polyclonal antibodies. HEK293 cells were transfected with the constructs encoding the full-length mouse FLAG-tagged SPAK wild type and SPAK L502A. 36 h post transfection, the lysates were subjected to immunoblotting with the indicated antibodies. The indicated amounts of recombinant mouse full-length GST-SPAK protein were subjected to immunoblot analysis on HEK293 cell lysates (A) and kidney lysates (B) with the newly generated SPAK and OSR1 mouse antibodies described in the Materials and Methods.

Figure S2. **Quantitative real-time PCR analysis of sodium ion co-transporter expression in the kidney**. Total RNA was purified from wild type and $SPAK^{L502A/L502A}$ mice kidneys using RNeasy kits (Qiagen) and reverse transcribed using iScript (Biorad). mRNA levels of SPAK, OSR1, NKCC1, NKCC2 and NCC were assessed by using Sybrgreen-based quantitative real-time PCR according to manufacturer's instructions. The levels were quantified from five separate mice and each PCR was performed in triplicate. Results were normalized to 18S rRNA expression and levels are presented relative to wild type expression. Primer sequences used are shown in Supplementary Table S3.

Figure S3. **Cardiac ventricular mass**. The weight of the Left Ventricle and Septum combined (LV+S) are expressed as a % of bodyweight (BW). Bars are mean±SEM n=14-16. Significant differences from the SPAK wild type are shown by: * P<0.02.

Figure S4. **Representative pseudocoloured average intensity z projections of immunofluorescent stained kidney sections**. (A) Immunolocalisation of WNK4 in the DCT marked by tNCC and TAL marked by NKCC2 (n=4 per genotype. Scale bar = 50μm). (B) Primary antibody negative controls for each staining set (Scale bar = 100μm).

Supplementary Table S1. **Breeding of SPAK knock-in mice**. Matings for SPAK were set up as outlined above and the progeny were genotyped as described in the methods. The percentage of each genotype observed is indicated in parenthesis followed by its expected Mendelian frequency.

Supplementary Table S2. **Summary of the purified proteins used in this study**. The DSTT DU number, purification system and affinity tags are used in Figure 1 and Figure S1.

Supplementary Table S3. **Primer sequences used for quantitative PCR undertaken in this study**.

Supplementary Figure S1

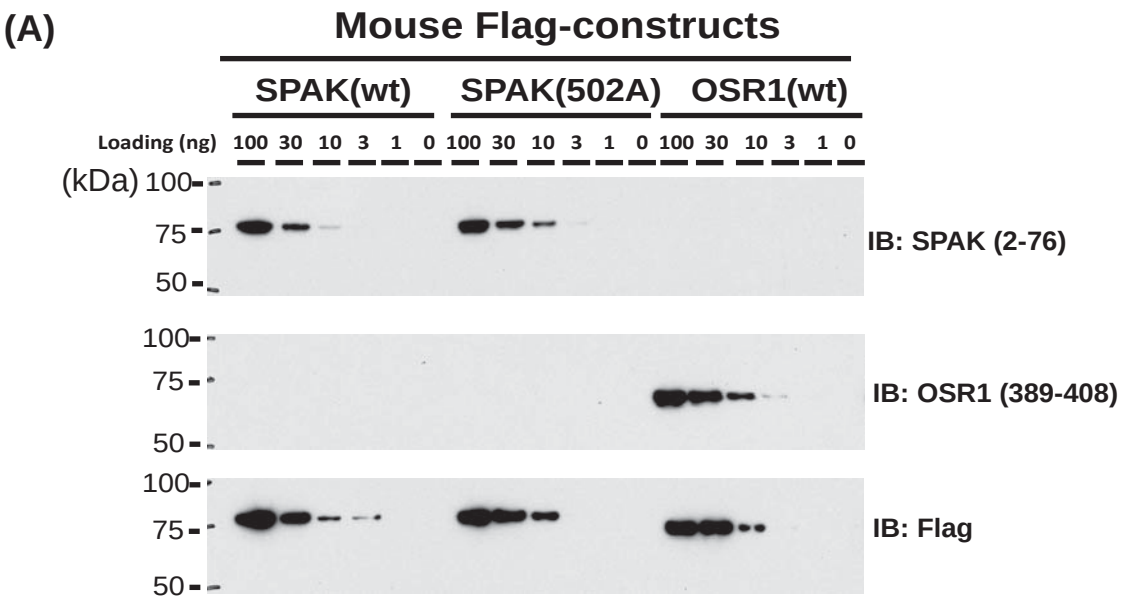

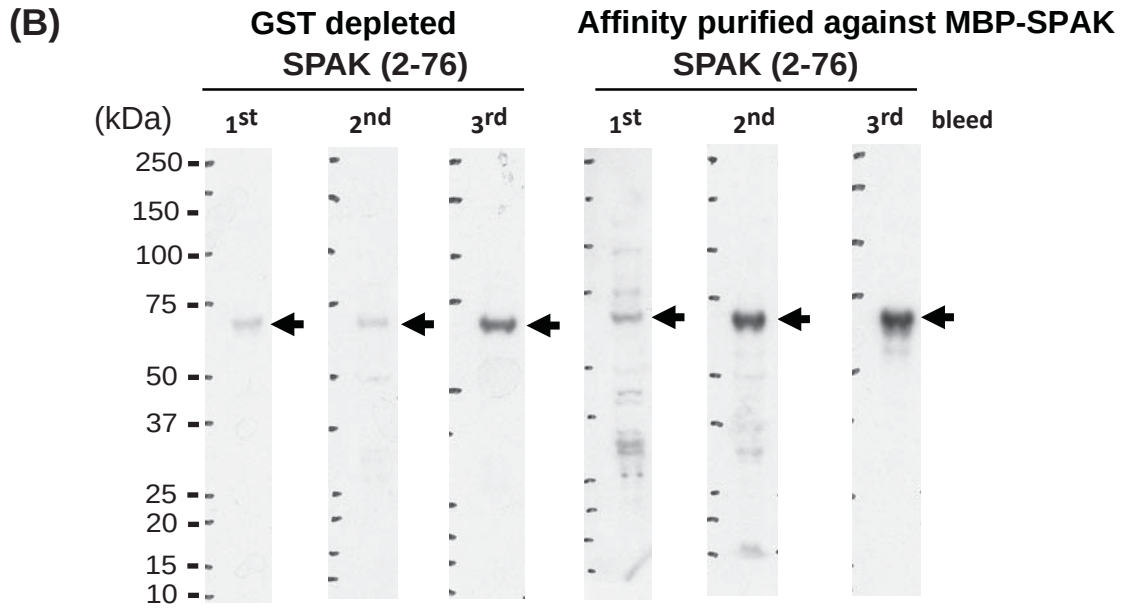

Supplementary Figure S2

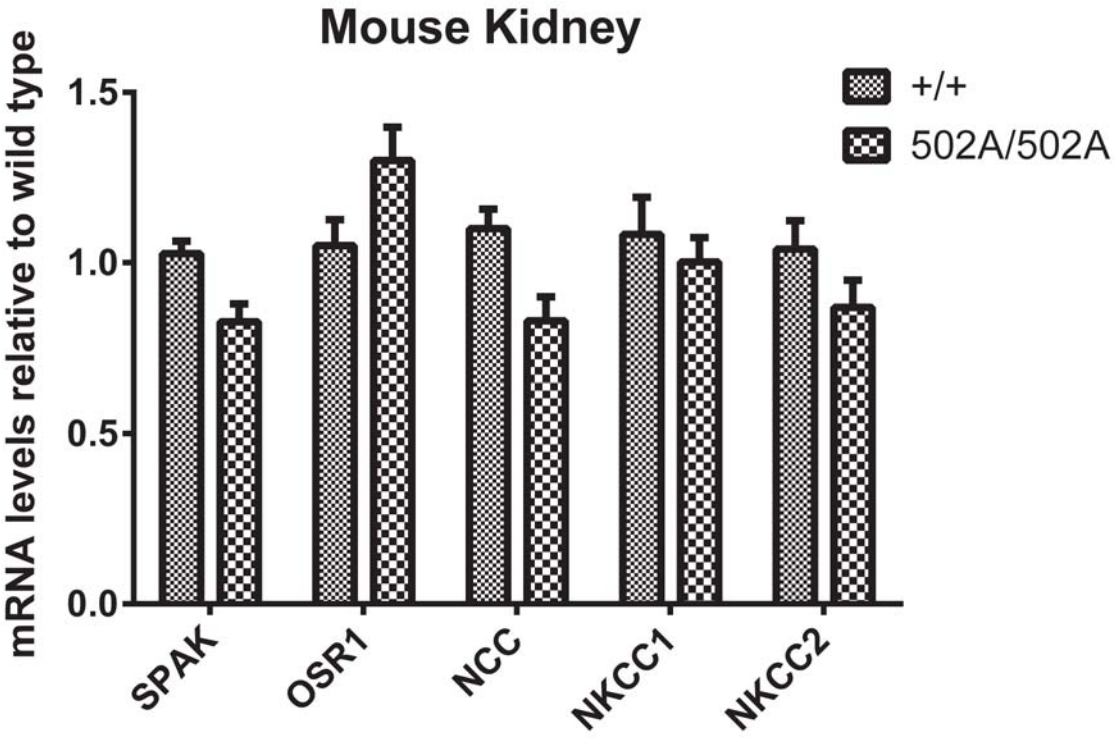

Supplementary Figure S3

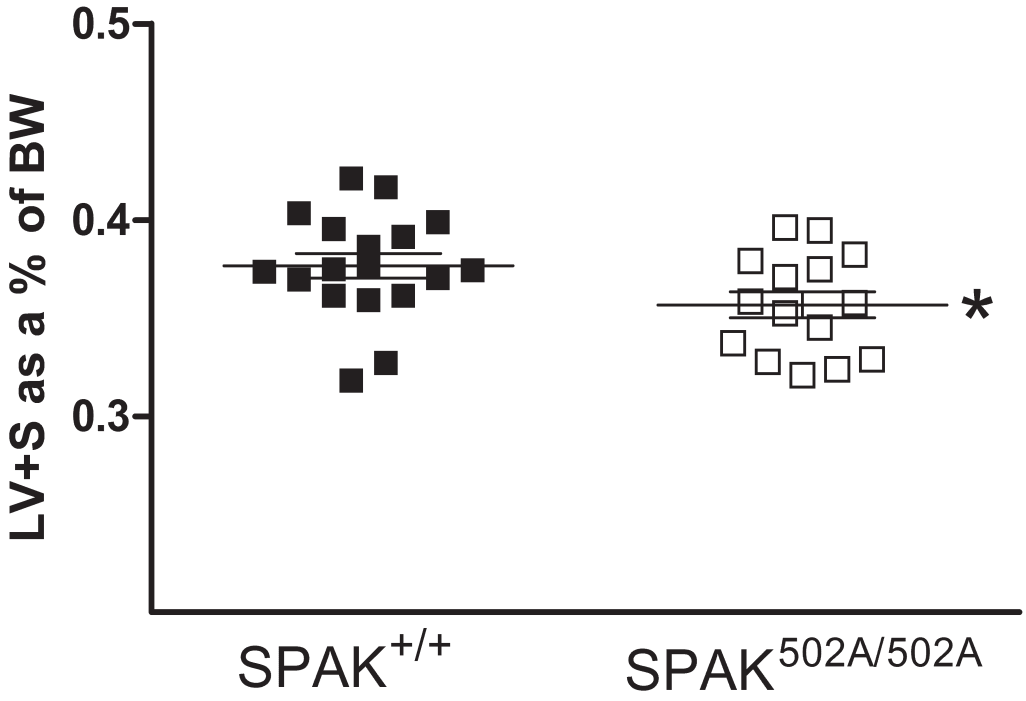

Supplementary Figure S4

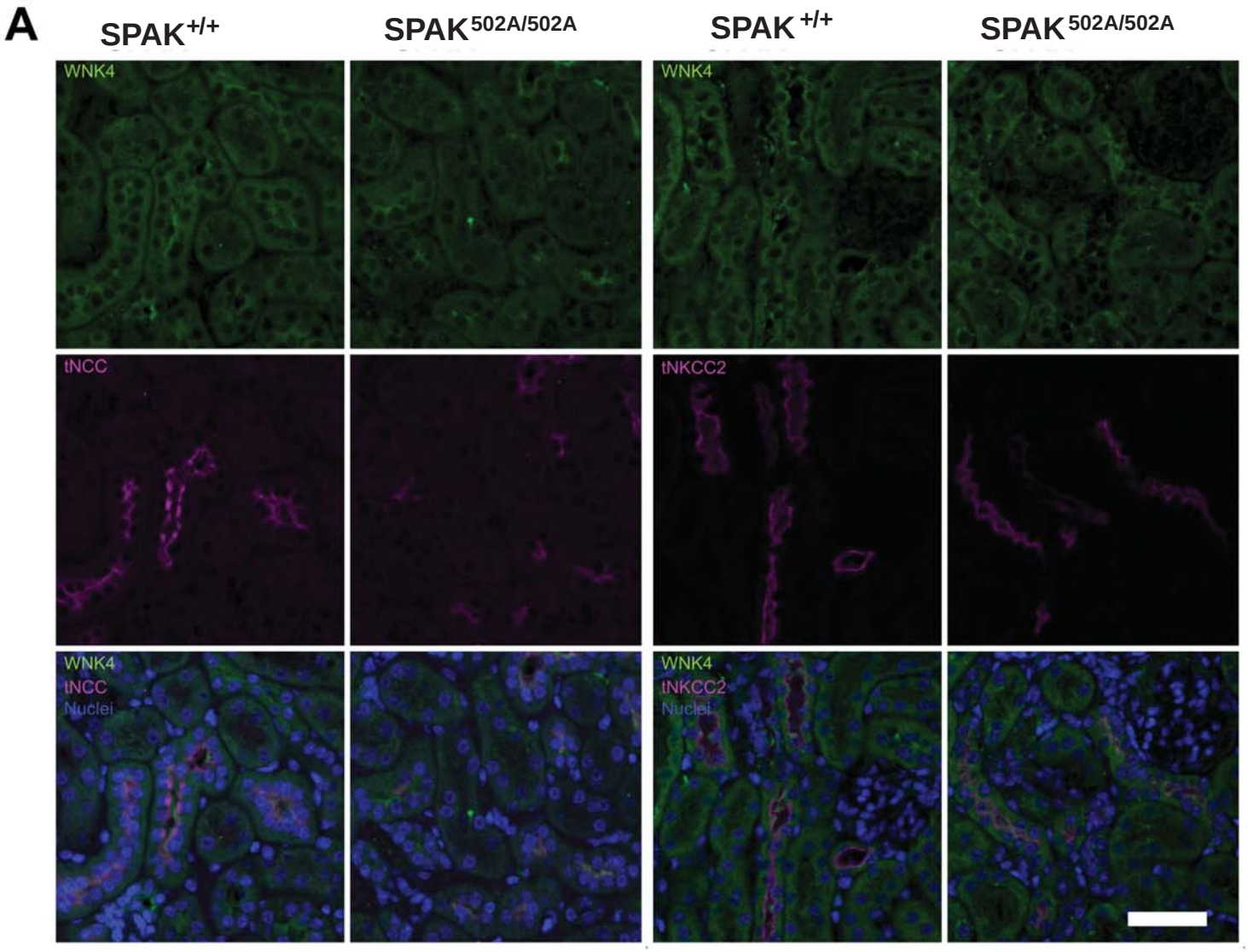

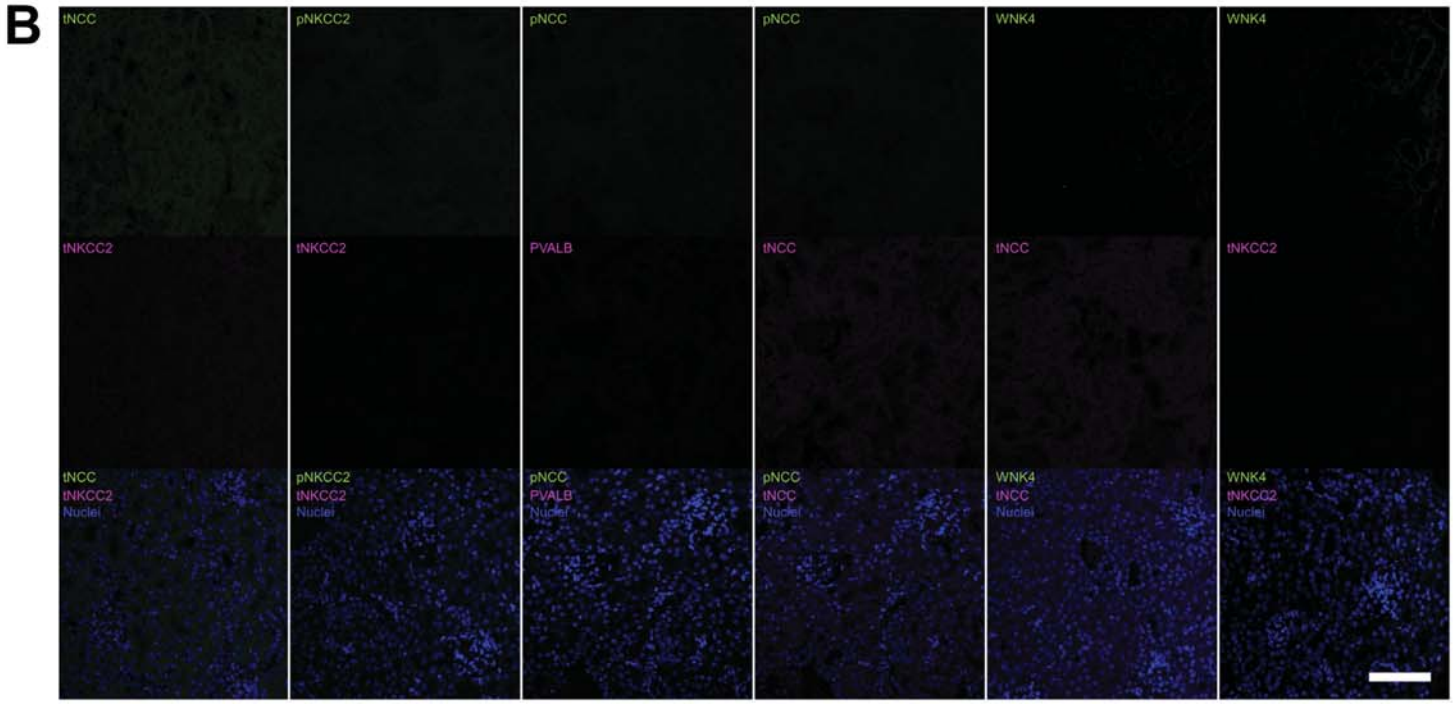

Supplementary Table S1

Cross	Genotype		Number Born (%)	Expected Mendelian Frequency (%)
SPAK (+/502A) OSR1 (+/+)	SPAK (+/+)	OSR1 (+/+)	94 (30%)	25
SPAK (+/502A) OSR1 (+/+)	SPAK (+/502A)	OSR1 (+/+)	180 (57%)	50
	SPAK (502A/502A)	OSR1 (+/+)	42 (13%)	25

Supplementary Table S2

Kinase/protein	DU number	Expression system	Affinity tag
GST-SPAK 452 – 545 (end)	DU41572	Bacteria	GST
GST-SPAK 452-end L491A	DU41619	Bacteria	GST
GST-mSPAK 2-74	DU44920	Bacteria	GST
GST-mSPAK 424-556	DU44891	Bacteria	GST
MBP-mSPAK 2-74	DU48033	Bacteria	MBP
MBP-mSPAK 424-556	DU48034	Bacteria	MBP
FLAG-mSPAK	DU48072	HEK293	FLAG
FLAG-mSPAK Opt L502A	DU48455	HEK293	FLAG

Supplementary Table S3

Symbol	Protein	Use	Sense primer (5`-3`)	Antisense primer (5`-3`)
SPAK	SPAK	PCR	TCTGTAAGCTCATTTATGTAGTCACC P1: STK39 6062_39	CAAGTGAGTGAGTGAATACAGCC P1: STK39 6062_40
SPAK	SPAK	q-PCR	GTCTAGGACATGATGGTATGG	CCAACATGGGGTACCAACAAATGC
OSR1	OSR1	q-PCR	CGCTGCAGTCTCCTGTCATCTG	CAGAGTGAGGTCTAGGACAGCCAGG
SLC12A1	NKCC2	q-PCR	TTGGATATAACCCACGCCTTTACG	GCCATGCCGCTGTTCATCTC
SLC12A2	NKCC1	q-PCR	GCAGATCCTCAGTCAGCCATAC	TCCCGAACAACACACGAACC
SLC12A3	NCC	q-PCR	CGGGGTTTGTGTCATGAGGATG	TTGTATCAATGCCTCTGGGGTTG
18S	18S rRNA	q-PCR	GTAACCCGTTGAACCCCATT	CCATCCAATCGGTAGTAGCG

APPENDIX 5

Macro scripts used in data analysis:

- ADI LabChart Macro Script for Augmentation Pressure
- ADI LabChart Macro Script for τBourgeois
- FIJI/ImageJ Macro Script for 3 Channel Z-stacks from the Leica SP2
- FIJI/ImageJ Macro Script for Drawing Divisions on Registered Image Stacks

ADI LabChart Macro Script for Augmentation Pressure

```
Sub Augmentation_BP_v2 ()

	startRec = Doc.SelectionStartRecord
	startOffset = Doc.SelectionStartOffset
	endRec = Doc.SelectionEndRecord
	endOffset = Doc.SelectionEndOffset
	If Not (startRec = kEndRecordIndex) Then
		Call Doc.SetSelectionRange (startRec, startOffset, startRec, startOffset)
	End If

	If (endRec > startRec) Or (endOffset > startOffset) Then
		Do While (IsCurrentSelectionWithin (startRec, startOffset, endRec,
endOffset) = True)

			' Begin Find
			ChannelIndex = 0
			SetAction = kSetActivePoint
			SelectMode = kSelectAround
			SelectTime = 1
			DataDisplayMode = kViewDataVisible
			SelectAll = False
			Direction = kSearchForward
			FindType = "Local minima"
			FindData = "NoiseThreshold=0.01;"
			Call Doc.Find (ChannelIndex, SetAction, SelectMode, SelectTime,
DataDisplayMode, SelectAll, Direction, FindType, FindData)
			' End Find

			' The function below will return true if the last operation failed,
which will cause the current loop to exit
			If (Services.ShouldExitCurrentRepeat()) Then Exit Do
			If Not (IsCurrentSelectionWithin (startRec, startOffset, endRec,
endOffset) = True) Then Exit Do


			' Begin Find
			ChannelIndex = 9
			SetAction = kSetActivePoint
			SelectMode = kSelectAround
			SelectTime = 1
			DataDisplayMode = kViewDataVisible
			SelectAll = False
			Direction = kSearchForward
			FindType = "Local maxima"
			FindData = "NoiseThreshold=0.05;"
			Call Doc.Find (ChannelIndex, SetAction, SelectMode, SelectTime,
DataDisplayMode, SelectAll, Direction, FindType, FindData)
			' End Find

			' The function below will return true if the last operation failed,
which will cause the current loop to exit
			If (Services.ShouldExitCurrentRepeat()) Then Exit Do
			If Not (IsCurrentSelectionWithin (startRec, startOffset, endRec,
endOffset) = True) Then Exit Do


			' Begin Find
			ChannelIndex = 9
			SetAction = kSetActivePoint
			SelectMode = kSelectAround
			SelectTime = 1
			DataDisplayMode = kViewDataVisible
			SelectAll = False
			Direction = kSearchForward
			FindType = "Data below"
			FindData = "Limit=0;"
```

```
                    Call Doc.Find (ChannelIndex, SetAction, SelectMode, SelectTime,
DataDisplayMode, SelectAll, Direction, FindType, FindData)
                    ' End Find

                    ' The function below will return true if the last operation failed,
which will cause the current loop to exit
                    If (Services.ShouldExitCurrentRepeat()) Then Exit Do
                    If Not (IsCurrentSelectionWithin (startRec, startOffset, endRec,
endOffset) = True) Then Exit Do


                    ' Begin Find
                    ChannelIndex = 0
                    SetAction = kSetToPreviousPoint
                    SelectMode = kSelectAround
                    SelectTime = 1
                    DataDisplayMode = kViewDataVisible
                    SelectAll = False
                    Direction = kSearchForward
                    FindType = "Local maxima"
                    FindData = "NoiseThreshold=0.005;"
                    Call Doc.Find (ChannelIndex, SetAction, SelectMode, SelectTime,
DataDisplayMode, SelectAll, Direction, FindType, FindData)
                    ' End Find

                    ' The function below will return true if the last operation failed,
which will cause the current loop to exit
                    If (Services.ShouldExitCurrentRepeat()) Then Exit Do
                    If Not (IsCurrentSelectionWithin (startRec, startOffset, endRec,
endOffset) = True) Then Exit Do

                    Call Doc.AddToDataPad ()
                    If Not (IsCurrentSelectionWithin (startRec, startOffset, endRec,
endOffset) = True) Then Exit Do

            Loop
       End If

       If Not (startRec = kEndRecordIndex) Then
              Call Doc.SetSelectionRange (endRec, endOffset, endRec, endOffset)
       End If

End Sub
```

ADI LabChart Macro Script for $\tau_{Bourgeois}$

```
Sub T_Bourgeois_v3 ()

	startRec = Doc.SelectionStartRecord
	startOffset = Doc.SelectionStartOffset
	endRec = Doc.SelectionEndRecord
	endOffset = Doc.SelectionEndOffset
	If Not (startRec = kEndRecordIndex) Then
		Call Doc.SetSelectionRange (startRec, startOffset, startRec, startOffset)
	End If

	If (endRec > startRec) Or (endOffset > startOffset) Then
		Do While (IsCurrentSelectionWithin (startRec, startOffset, endRec,
endOffset) = True)

			' Begin Find
			ChannelIndex = 10
			SetAction = kSetActivePoint
			SelectMode = kSelectAround
			SelectTime = 1
			DataDisplayMode = kViewDataVisible
			SelectAll = False
			Direction = kSearchForward
			FindType = "Local maxima"
			FindData = "NoiseThreshold=0.05;"
			Call Doc.Find (ChannelIndex, SetAction, SelectMode, SelectTime,
DataDisplayMode, SelectAll, Direction, FindType, FindData)
			' End Find

			' The function below will return true if the last operation failed,
which will cause the current loop to exit
			If (Services.ShouldExitCurrentRepeat()) Then Exit Do
			If Not (IsCurrentSelectionWithin (startRec, startOffset, endRec,
endOffset) = True) Then Exit Do

			Call Doc.SetRightXCompression (5, False, "Chart View")
			If Not (IsCurrentSelectionWithin (startRec, startOffset, endRec,
endOffset) = True) Then Exit Do

			Call Doc.SetRightXCompression (2, False, "Chart View")
			If Not (IsCurrentSelectionWithin (startRec, startOffset, endRec,
endOffset) = True) Then Exit Do

			Call Doc.SetRightXPos (2220892, "Chart View")
			If Not (IsCurrentSelectionWithin (startRec, startOffset, endRec,
endOffset) = True) Then Exit Do

			Call Doc.SetRightXPos (2221024, "Chart View")
			If Not (IsCurrentSelectionWithin (startRec, startOffset, endRec,
endOffset) = True) Then Exit Do

			Call Doc.SetRightXPos (2221156, "Chart View")
			If Not (IsCurrentSelectionWithin (startRec, startOffset, endRec,
endOffset) = True) Then Exit Do


			' Begin Find
			ChannelIndex = 10
			SetAction = kSetActivePoint
			SelectMode = kSelectAround
			SelectTime = 1
			DataDisplayMode = kViewDataVisible
			SelectAll = False
			Direction = kSearchForward
			FindType = "Local minima"
			FindData = "NoiseThreshold=0.0001;"
			Call Doc.Find (ChannelIndex, SetAction, SelectMode, SelectTime,
DataDisplayMode, SelectAll, Direction, FindType, FindData)
```

```
                    ' End Find

                    ' The function below will return true if the last operation failed,
which will cause the current loop to exit
                    If (Services.ShouldExitCurrentRepeat()) Then Exit Do
                    If Not (IsCurrentSelectionWithin (startRec, startOffset, endRec,
endOffset) = True) Then Exit Do


                    ' Begin Find
                    ChannelIndex = 10
                    SetAction = kSetActivePoint
                    SelectMode = kSelectAround
                    SelectTime = 1
                    DataDisplayMode = kViewDataVisible
                    SelectAll = False
                    Direction = kSearchForward
                    FindType = "Move forward"
                    FindData = "AmountToMove=0.02;"
                    Call Doc.Find (ChannelIndex, SetAction, SelectMode, SelectTime,
DataDisplayMode, SelectAll, Direction, FindType, FindData)
                    ' End Find

                    ' The function below will return true if the last operation failed,
which will cause the current loop to exit
                    If (Services.ShouldExitCurrentRepeat()) Then Exit Do
                    If Not (IsCurrentSelectionWithin (startRec, startOffset, endRec,
endOffset) = True) Then Exit Do

                    Call Doc.AddCommentAtInsertionPoint (10, "start")
                    If Not (IsCurrentSelectionWithin (startRec, startOffset, endRec,
endOffset) = True) Then Exit Do


                    ' Begin Find
                    ChannelIndex = 10
                    SetAction = kSetActivePoint
                    SelectMode = kSelectAround
                    SelectTime = 1
                    DataDisplayMode = kViewDataVisible
                    SelectAll = False
                    Direction = kSearchForward
                    FindType = "Local minima"
                    FindData = "NoiseThreshold=0.001;"
                    Call Doc.Find (ChannelIndex, SetAction, SelectMode, SelectTime,
DataDisplayMode, SelectAll, Direction, FindType, FindData)
                    ' End Find

                    ' The function below will return true if the last operation failed,
which will cause the current loop to exit
                    If (Services.ShouldExitCurrentRepeat()) Then Exit Do
                    If Not (IsCurrentSelectionWithin (startRec, startOffset, endRec,
endOffset) = True) Then Exit Do


                    ' Begin Find
                    ChannelIndex = 10
                    SetAction = kSetActivePoint
                    SelectMode = kSelectAround
                    SelectTime = 1
                    DataDisplayMode = kViewDataVisible
                    SelectAll = False
                    Direction = kSearchForward
                    FindType = "Move backward"
                    FindData = "AmountToMove=0.015;"
                    Call Doc.Find (ChannelIndex, SetAction, SelectMode, SelectTime,
DataDisplayMode, SelectAll, Direction, FindType, FindData)
                    ' End Find

                    ' The function below will return true if the last operation failed,
which will cause the current loop to exit
                    If (Services.ShouldExitCurrentRepeat()) Then Exit Do
```

```
                    If Not (IsCurrentSelectionWithin (startRec, startOffset, endRec,
endOffset) = True) Then Exit Do

                    Call Doc.AddCommentAtInsertionPoint (10, "end")
                    If Not (IsCurrentSelectionWithin (startRec, startOffset, endRec,
endOffset) = True) Then Exit Do

              Loop
       End If

       If Not (startRec = kEndRecordIndex) Then
              Call Doc.SetSelectionRange (endRec, endOffset, endRec, endOffset)
       End If


' Move the insertion point to the beginning of the file
       Call Doc.SelectChannel(-1, True)
       Call Doc.SetSelectionTime(0, 0, 0, 0)

       Do While True


              ' Begin Find
              ChannelIndex = 10
              SetAction = kSetActivePoint
              SelectMode = kSelectAround
              SelectTime = 1
              DataDisplayMode = kViewDataVisible
              SelectAll = False
              Direction = kSearchForward
              FindType = "Search for comment"
              FindData = "JustThisChannel=0;WhatToLookFor=start;"
              Call Doc.Find (ChannelIndex, SetAction, SelectMode, SelectTime,
DataDisplayMode, SelectAll, Direction, FindType, FindData)
              ' End Find

              ' The function below will return true if the last operation failed, which
will cause the current loop to exit
              If (Services.ShouldExitCurrentRepeat()) Then Exit Do

              ' Begin Find
              ChannelIndex = 10
              SetAction = kSetToPreviousPoint
              SelectMode = kSelectAround
              SelectTime = 1
              DataDisplayMode = kViewDataVisible
              SelectAll = False
              Direction = kSearchForward
              FindType = "Search for comment"
              FindData = "JustThisChannel=0;WhatToLookFor=end;"
              Call Doc.Find (ChannelIndex, SetAction, SelectMode, SelectTime,
DataDisplayMode, SelectAll, Direction, FindType, FindData)
              ' End Find

              ' The function below will return true if the last operation failed, which
will cause the current loop to exit
              If (Services.ShouldExitCurrentRepeat()) Then Exit Do
              Call Doc.AddToDataPad ()
       Loop



End Sub
```

FIJI/ImageJ Macro Script for 3 Channel Z-stacks from the Leica SP2

```
run("Image Sequence...",
"open=[C:\\Users\\Keith\\Desktop\\Imaging\\Processing\\Macro\\default.tif] number=1000
starting=1 increment=1 scale=100 file=[] or=[] sort");

saveAs("Tiff", "C:\\Users\\Keith\\Desktop\\Imaging\\Processing\\Macro\\Steps\\1 -
Stack.tif");




run("8-bit");

saveAs("Tiff", "C:\\Users\\Keith\\Desktop\\Imaging\\Processing\\Macro\\Steps\\2 - 8bit.tif");




selectWindow("2 - 8bit.tif");

run("Slice Keeper", "first=1 last=1000 increment=3");

saveAs("Tiff", "C:\\Users\\Keith\\Desktop\\Imaging\\Processing\\Macro\\Steps\\3a - Slice
Keeper (1-1000-3).tif");


run("Subtract Background...", "rolling=100 disable stack");

saveAs("Tiff", "C:\\Users\\Keith\\Desktop\\Imaging\\Processing\\Macro\\Steps\\4a - Subtract
Background (rolling 100 - disable smoothing).tif");


run("Z Project...", "start=1 stop=1000 projection=[Average Intensity]");

saveAs("Tiff", "C:\\Users\\Keith\\Desktop\\Imaging\\Processing\\Macro\\Steps\\5a - Z
Project (average intensity).tif");


selectWindow("4a - Subtract Background (rolling 100 - disable smoothing).tif");

close();
```

```
selectWindow("2 - 8bit.tif");

run("Slice Keeper", "first=2 last=1000 increment=3");

saveAs("Tiff", "C:\\Users\\Keith\\Desktop\\Imaging\\Processing\\Macro\\Steps\\3b - Slice Keeper (2-1000-3).tif");


run("Subtract Background...", "rolling=100 disable stack");

saveAs("Tiff", "C:\\Users\\Keith\\Desktop\\Imaging\\Processing\\Macro\\Steps\\4b - Subtract Background (rolling 100 - disable smoothing).tif");


run("Z Project...", "start=1 stop=1000 projection=[Average Intensity]");

saveAs("Tiff", "C:\\Users\\Keith\\Desktop\\Imaging\\Processing\\Macro\\Steps\\5b - Z Project (average intensity).tif");


selectWindow("4b - Subtract Background (rolling 100 - disable smoothing).tif");

close();




selectWindow("2 - 8bit.tif");

run("Slice Keeper", "first=3 last=1000 increment=3");

saveAs("Tiff", "C:\\Users\\Keith\\Desktop\\Imaging\\Processing\\Macro\\Steps\\3c - Slice Keeper (3-1000-3).tif");


run("Subtract Background...", "rolling=100 disable stack");

saveAs("Tiff", "C:\\Users\\Keith\\Desktop\\Imaging\\Processing\\Macro\\Steps\\4c - Subtract Background (rolling 100 - disable smoothing).tif");


run("Z Project...", "start=1 stop=1000 projection=[Average Intensity]");

saveAs("Tiff", "C:\\Users\\Keith\\Desktop\\Imaging\\Processing\\Macro\\Steps\\5c - Z Project (average intensity).tif");
```

```
selectWindow("4c - Subtract Background (rolling 100 - disable smoothing).tif");

close();




selectWindow("2 - 8bit.tif");

close();




run("Merge Channels...", "red=[5a - Z Project (average intensity).tif] green=[5b - Z Project (average intensity).tif] blue=[5c - Z Project (average intensity).tif] gray=*None* keep");

saveAs("Tiff", "C:\\Users\\Keith\\Desktop\\Imaging\\Processing\\Macro\\Steps\\5-1abc - RGB Merge Channels.tif");

run("Merge Channels...", "red=[5a - Z Project (average intensity).tif] green=[5c - Z Project (average intensity).tif] blue=[5b - Z Project (average intensity).tif] gray=*None* keep");

saveAs("Tiff", "C:\\Users\\Keith\\Desktop\\Imaging\\Processing\\Macro\\Steps\\5-1acb - RGB Merge Channels.tif");

run("Merge Channels...", "red=[5b - Z Project (average intensity).tif] green=[5a - Z Project (average intensity).tif] blue=[5c - Z Project (average intensity).tif] gray=*None* keep");

saveAs("Tiff", "C:\\Users\\Keith\\Desktop\\Imaging\\Processing\\Macro\\Steps\\5-1bac - RGB Merge Channels.tif");

run("Merge Channels...", "red=[5b - Z Project (average intensity).tif] green=[5c - Z Project (average intensity).tif] blue=[5a - Z Project (average intensity).tif] gray=*None* keep");

saveAs("Tiff", "C:\\Users\\Keith\\Desktop\\Imaging\\Processing\\Macro\\Steps\\5-1bca - RGB Merge Channels.tif");

run("Merge Channels...", "red=[5c - Z Project (average intensity).tif] green=[5a - Z Project (average intensity).tif] blue=[5b - Z Project (average intensity).tif] gray=*None* keep");

saveAs("Tiff", "C:\\Users\\Keith\\Desktop\\Imaging\\Processing\\Macro\\Steps\\5-1cab - RGB Merge Channels.tif");

run("Merge Channels...", "red=[5c - Z Project (average intensity).tif] green=[5b - Z Project (average intensity).tif] blue=[5a - Z Project (average intensity).tif] gray=*None* ");

saveAs("Tiff", "C:\\Users\\Keith\\Desktop\\Imaging\\Processing\\Macro\\Steps\\5-1cba - RGB Merge Channels.tif");
```

```
run("Images to Stack", "name=Stack title=[] use");

run("Make Montage...", "columns=3 rows=2 scale=1 first=1 last=6 increment=1 border=0
font=60 label");

saveAs("Tiff", "C:\\Users\\Keith\\Desktop\\Imaging\\Processing\\Macro\\Steps\\5-2 -
Montage RGB combinations.tif");


selectWindow("Stack");

close();
```

FIJI/ImageJ Macro Script for Drawing Divisions on Registered Images Stacks

```
run("Set Scale...", "distance=0 known=0 pixel=1 unit=pixel");

getDimensions(width, height, channelCount, sliceCount, frameCount);

x_width=(width);
y_height=(height);

for (i = 0; i < sliceCount; i++) {

        makeLine(x_width-x_width, y_height-y_height, x_width/1, y_height/1); run("Draw");
        makeLine(x_width/1, y_height-y_height, x_width-x_width, y_height/1); run("Draw");

        makeLine(x_width/2, y_height-y_height, x_width/2, y_height/1); run("Draw");
        makeLine(x_width/1, y_height/2, x_width-x_width, y_height/2); run("Draw");

        makeLine(x_width/4, y_height-y_height, (x_width/4)*3, y_height/1); run("Draw");
        makeLine(x_width/1, y_height/4, x_width-x_width, (y_height/4)*3); run("Draw");

        makeLine((x_width/4)*3, y_height-y_height, x_width/4, y_height/1); run("Draw");
        makeLine(x_width/1, (y_height/4)*3, x_width-x_width, y_height/4); run("Draw");
}
```